The man behind the Pluto mission p. 1414

Advancing research integrity and reproducibility pp. 1420 & 1422

The disappearing warming hiatus p. 1469

Science

$10
26 JUNE 2015
sciencemag.org

AAAS

The developing heart

Identifying when cells commit to becoming cardiac myocytes p. 1444

CONTENTS

26 JUNE 2015 • VOLUME 348 • ISSUE 6242

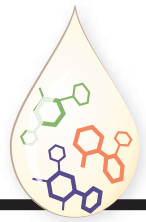

1427 Milk sugars balance baby's gut microbes

1411

NEWS

IN BRIEF

1404 Roundup of the week's news

IN DEPTH

1406 SURVIVING EBOLA SURVIVAL
After recovering from Ebola, some patients are struggling with other health problems *By K. Kupferschmidt*

1407 AN ENHANCED VIEW OF GENE CONTROL
Chromosomal loops and domains help enhancers turn on genes *By E. Pennisi*

1409 BREAKING THE LIGHT BARRIER
Trick for pushing more bits through optical fibers could ease looming "capacity crunch" *By R. F. Service*
▸ REPORT P. 1445

1410 TAPPING A NUCLEAR TEST BAN TREASURE-TROVE
Treaty chief offers academics surveillance data *By D. Clery*

FEATURES

1411 THE CANCER TEST
A nonprofit's effort to replicate 50 top cancer papers is shaking up labs *By J. Kaiser*
▸ EDITORIAL P. 1403; PERSPECTIVES PP. 1420 & 1422

1414 MISSION CONTROLLER
How Alan Stern's tenacity, drive, and command got a NASA spacecraft to Pluto *By E. Hand*

1419 Alan Stern's worldly ventures
By E. Hand
▸ VIDEO

INSIGHTS

PERSPECTIVES

1420 SELF-CORRECTION IN SCIENCE AT WORK
Improve incentives to support research integrity *By B. Alberts* et al.
▸ EDITORIAL P. 1403; NEWS STORY P. 1411; PERSPECTIVE P. 1422

1422 PROMOTING AN OPEN RESEARCH CULTURE
Author guidelines for journals could help to promote transparency, openness, and reproducibility *By B. A. Nosek* et al.
▸ EDITORIAL P. 1403; NEWS STORY P. 1411; PERSPECTIVE P. 1420

1425 ECOLOGICAL COMMUNITIES BY DESIGN
Synthetic ecology requires knowledge of how microbial comunities function *By J. K. Fredrickson*

1427 MOTHER'S LITTLEST HELPERS
Breastmilk nourishes the microbes colonizing the neonatal intestinal tract *By K. Hinde and Z. T. Lewis*

1429 BEARING DOWN ON HYDROGEN
Shockwaves are used to turn deuterium into a liquid metal *By G. J. Ackland*
▸ REPORT P. 1455

1430 WHO CAN CLEAVE DMSP?
A DMSP lyase from an abundant marine eukaryote differs fundamentally from known bacterial enzymes *By A. W. B. Johnston*
▸ REPORT P. 1466

1432 TOPOLOGY, SPIN, AND LIGHT
Evanescent solutions to Maxwell's equations correspond to surface modes with strong spin-momentum locking *By M. Stone*
▸ REPORT P. 1448

1433 A HUSH FOR TRANSGENE EXPRESSION
A protein complex represses genes that insert into heterochromatin *By T. R. Brummelkamp and B. van Steensel*
▸ REPORT P. 1481

BOOKS *ET AL.*

1435 RADIUM AND THE SECRET OF LIFE
By L. A. Campos, reviewed by H. A. Curry

1436 TEACHING ONLINE
By C. H. Major, reviewed by E. Dolan

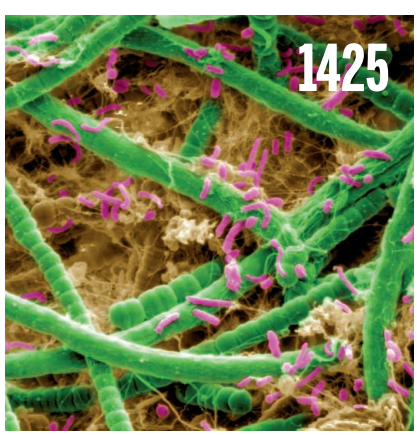

1425

Science Staff 1402
AAAS News & Notes 1439
New Products 1493
Science Careers 1494

Published by AAAS

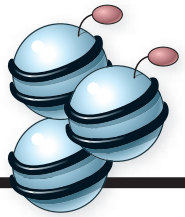

1433 & 1481

HUSHing gene expression

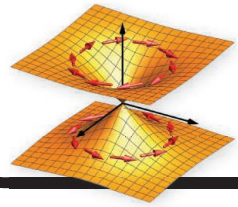

1432 & 1448

Quantum effects shining through

LETTERS

1437 APPLYING ANTIBIOTICS LESSONS TO ANTIVIRALS
By D. W. Martin Jr.

1437 RESPONSE
By E. Bekerman and S. Einav

1437 CHINA LEGITIMIZES IVORY, AGAIN
By J. Zhan and Q. Weng

1438 TECHNICAL COMMENT ABSTRACTS

RESEARCH

IN BRIEF

1440 From *Science* and other journals

REVIEW

1443 EMBRYO DEVELOPMENT
BMP gradients: A paradigm for morphogen-mediated developmental patterning *E. Bier and E. M. De Robertis*
REVIEW SUMMARY; FOR FULL TEXT: dx.doi.org/10.1126/science.aaa5838

RESEARCH ARTICLE

1444 HEART DEVELOPMENT
Integration of Bmp and Wnt signaling by Hopx specifies commitment of cardiomyoblasts *R. Jain* et al.
RESEARCH ARTICLE SUMMARY; FOR FULL TEXT: dx.doi.org/10.1126/science.aaa6071

REPORTS

1445 APPLIED OPTICS
Overcoming Kerr-induced capacity limit in optical fiber transmission *E. Temprana* et al.
▸ NEWS STORY P. 1409

1448 OPTICS
Quantum spin Hall effect of light *K. Y. Bliokh* et al.
▸ PERSPECTIVE P. 1432

1451 3D LITHOGRAPHY
Atomic gold–enabled three-dimensional lithography for silicon mesostructures *Z. Luo* et al.

1455 HIGH-PRESSURE PHYSICS
Direct observation of an abrupt insulator-to-metal transition in dense liquid deuterium *M. D. Knudson* et al.
▸ PERSPECTIVE P. 1429; PODCAST

1460 CORAL REEFS
Genomic determinants of coral heat tolerance across latitudes *G. B. Dixon* et al.

1463 PHOTOSYNTHESIS
A 12 Å carotenoid translocation in a photoswitch associated with cyanobacterial photoprotection *R. L. Leverenz* et al.

1466 MARINE SULFUR CYCLE
Identification of the algal dimethyl sulfide–releasing enzyme: A missing link in the marine sulfur cycle *U. Alcolombri* et al.
▸ PERSPECTIVE P. 1430

1469 CLIMATE CHANGE
Possible artifacts of data biases in the recent global surface warming hiatus *T. R. Karl* et al.

1472 BRAIN CIRCUITS
A parvalbumin-positive excitatory visual pathway to trigger fear responses in mice *C. Shang* et al.

1477 STRUCTURAL BIOLOGY
A Cas9–guide RNA complex preorganized for target DNA recognition *F. Jiang* et al.

1481 GENE SILENCING
Epigenetic silencing by the HUSH complex mediates position-effect variegation in human cells *I. A. Tchasovnikarova* et al.
▸ PERSPECTIVE P. 1433

1486 RNA BIOCHEMISTRY
Factor-dependent processivity in human eIF4A DEAD-box helicase *C. García-García* et al.

1488 GENE REGULATION
Discrete functions of nuclear receptor Rev-erbα couple metabolism to the clock *Y. Zhang* et al.

DEPARTMENTS

1403 EDITORIAL
Solving reproducibility *By Stuart Buck*
▸ NEWS STORY P. 1411; PERSPECTIVES PP. 1420 & 1422

1506 WORKING LIFE
The health of those who study health *By Rachel Bernstein*

ON THE COVER

Immunofluorescence microscopy identifies an intermediate cell in the cardiomyocyte lineage. An image of the heart of a 14.5-day mouse embryo shows this intermediate—progenitor derivatives expressing Hopx (red)—and the differentiated myocytes expressing troponin (green). Jain *et al.* demonstrate that Hopx-expressing cells promote cardiomyocyte commitment by coordinating signaling pathways in the progenitor niche. See page 1444 and dx.doi.org/10.1126/science.aaa6071. *Image: Epstein laboratory*

SCIENCE (ISSN 0036-8075) is published weekly on Friday, except the last week in December, by the American Association for the Advancement of Science, 1200 New York Avenue, NW, Washington, DC 20005. Periodicals mail postage (publication No. 484460) paid at Washington, DC, and additional mailing offices.

Copyright © 2015 by the American Association for the Advancement of Science. The title SCIENCE is a registered trademark of the AAAS.

Domestic individual membership and subscription (51 issues): $153 ($74 allocated to subscription). Domestic institutional subscription (51 issues): $1282; Foreign postage extra: Mexico, Caribbean (surface mail) $55; other countries (air assist delivery) $85. First class, airmail, student, and emeritus rates on request. Canadian rates with GST available upon request, GST #1254 88122. Publications Mail Agreement Number 1069624. **Printed in the U.S.A.**
Change of address: Allow 4 weeks, giving old and new addresses and 8-digit account number. **Postmaster:** Send change of address to AAAS, P.O. Box 96178, Washington, DC 20090–6178. **Single-copy sales:** $10.00 current issue, $15.00 back issue prepaid includes surface postage; bulk rates on request.

Authorization to photocopy material for internal or personal use under circumstances not falling within the fair use provisions of the Copyright Act is granted by AAAS to libraries and other users registered with the Copyright Clearance Center (CCC) Transactional Reporting Service, provided that $30.00 per article is paid directly to CCC, 222 Rosewood Drive, Danvers, MA 01923. The identification code for *Science* is 0036-8075. *Science* is indexed in the *Reader's Guide to Periodical Literature* and in several specialized indexes.

Science
AAAS
1200 New York Avenue, NW, Washington, DC 20005
Bateman House, 82-88 Hills Road, Cambridge, UK CB2 1LQ

Editor-in-Chief Marcia McNutt
Executive Editor Monica M. Bradford **News Editor** Tim Appenzeller
Managing Editor, Research Journals Katrina L. Kelner
Deputy Editors Barbara R. Jasny, Andrew M. Sugden(UK), Valda J. Vinson, Jake S. Yeston

Research and Insights

SR. EDITORS Caroline Ash(UK), Gilbert J. Chin, Lisa D. Chong, Julia Fahrenkamp-Uppenbrink(UK), Pamela J. Hines, Stella M. Hurtley(UK), Paula A. Kiberstis, Marc S. Lavine(Canada), Kristen L. Mueller, Ian S. Osborne(UK), Beverly A. Purnell, L. Bryan Ray, Guy Riddihough, H. Jesse Smith, Jelena Stajic, Peter Stern(UK), Phillip D. Szuromi, Brad Wible, Nicholas S. Wigginton, Laura M. Zahn **ASSOCIATE EDITORS** Brent Grocholski, Sacha Vignieri **ASSOCIATE BOOK REVIEW EDITOR** Valerie B. Thompson **ASSOCIATE LETTERS EDITOR** Jennifer Sills **CHIEF CONTENT PRODUCTION EDITOR** Cara Tate **SR. CONTENT PRODUCTION EDITORS** Harry Jach **CONTENT PRODUCTION EDITORS** Jeffrey E. Cook, Chris Filiatreau, Cynthia Howe, Lauren Kmec, Barbara P. Ordway **SR. EDITORIAL COORDINATORS** Carolyn Kyle, Beverly Shields **EDITORIAL COORDINATORS** Ramatoulaye Diop, Joi S. Granger, Lisa Johnson, Anita Wynn **PUBLICATIONS ASSISTANTS** Aneera Dobbins, Jeffrey Hearn, Dona Mathieu, Le-Toya Mayne Flood, Shannon McMahon, Scott Miller, Jerry Richardson, Rachel Roberts(UK), Alice Whaley(UK), Brian White **EXECUTIVE ASSISTANT** Anna Bashkirova **ADMINISTRATIVE SUPPORT** Janet Clements(UK), Monika Magon(UK, Intern), Lizanne Newton(UK), Maryrose Madrid, John Wood(UK)

News

NEWS MANAGING EDITOR John Travis **INTERNATIONAL EDITOR** Richard Stone **DEPUTY NEWS EDITORS** Daniel Clery(UK), Robert Coontz, Elizabeth Culotta, David Grimm, David Malakoff, Leslie Roberts **CONTRIBUING EDITOR** Martin Enserink(Europe) **SR. CORRESPONDENTS** Jeffrey Mervis, Elizabeth Pennisi **NEWS WRITERS** Adrian Cho, Jon Cohen, Jennifer Couzin-Frankel, Carolyn Gramling, Eric Hand, Jocelyn Kaiser, Catherine Matacic, Kelly Servick, Robert F. Service, Erik Stokstad(Cambridge, UK), Emily Underwood **INTERNS** Emily Conover, Emily DeMarco **CONTRIBUTING CORRESPONDENTS** Michael Balter(Paris), John Bohannon, Ann Gibbons, Mara Hvistendahl, Sam Kean, Richard A. Kerr, Eli Kintisch, Kai Kupferschmidt(Berlin), Andrew Lawler, Christina Larson(Beijing), Mitch Leslie, Charles C. Mann, Eliot Marshall, Virginia Morell, Dennis Normile(Tokyo), Heather Pringle, Tania Rabesandratana(London), Gretchen Vogel(Berlin), Lizzie Wade(Mexico City) **CAREERS** Jim Austin(Editor), Donisha Adams, Rachel Bernstein **COPY EDITORS** Kara Estelle (Chief), Julia Cole, Jennifer Levin **ADMINISTRATIVE SUPPORT** Jessica Williams

Executive Publisher Rush D. Holt
Publisher Kent R. Anderson **Chief Digital Media Officer** Rob Covey

BUSINESS OPERATIONS AND ADMINISTRATION DIRECTOR Sarah Whalen **BUSINESS SYSTEMS AND FINANCIAL ANALYSIS DIRECTOR** Randy Yi **MANAGER OF FULFILLMENT SYSTEMS** Neal Hawkins **SYSTEMS ANALYST** Nicole Mehmedovich **ASSISTANT DIRECTOR, BUSINESS OPERATIONS** Eric Knott **MANAGER, BUSINESS OPERATIONS** Jessica Tierney **BUSINESS ANALYSTS** Cory Lipman, Cooper Tilton, Celeste Troxler **FINANCIAL ANALYST** Robert Clark **RIGHTS AND PERMISSIONS ASSISTANT DIRECTOR** Emilie David **PERMISSIONS ASSOCIATE** Elizabeth Sandler **RIGHTS, CONTRACTS, AND LICENSING ASSOCIATE** Lili Kiser

MARKETING DIRECTOR Ian King **MARKETING MANAGER** Julianne Wielga **MARKETING ASSOCIATE** Elizabeth Sattler **SR. MARKETING EXECUTIVE** Jennifer Reeves **SR. ART ASSOCIATE, PROJECT MANAGER** Tzeitel Sorrosa **ART ASSOCIATE** Seil Lee **JR. ART ASSOCIATE** Kim Huynh **ASSISTANT COMMERCIAL EDITOR** Selby Frame **MARKETING PROJECT MANAGER** Angelissa McArthur **PROGRAM DIRECTOR, AAAS MEMBER CENTRAL** Peggy Mihelich **FULFILLMENT SYSTEMS AND OPERATIONS** membership@aaas.org **MANAGER, MEMBER SERVICES** Pat Butler **SPECIALISTS** LaToya Casteel, Terrance Morrison, Latasha Russell **MANAGER, DATA ENTRY** Mickie Napoleoni **DATA ENTRY SPECIALISTS** JJ Regan, Brenden Aquilino, Fiona Giblin

DIRECTOR, SITE LICENSING Tom Ryan **DIRECTOR, CORPORATE RELATIONS** Eileen Bernadette Moran **SR. PUBLISHER RELATIONS SPECIALIST** Kiki Forsythe **PUBLISHER RELATIONS MANAGER** Catherine Holland **PUBLISHER RELATIONS, EASTERN REGION** Keith Layson **PUBLISHER RELATIONS, WESTERN REGION** Ryan Rexroth **SALES RESEARCH COORDINATOR** Aiesha Marshall **MANAGER, SITE LICENSE OPERATIONS** Iquo Edim **SENIOR PRODUCTION SPECIALIST** Robert Koepke **SENIOR OPERATIONS ANALYST** Lana Guz **FULFILLMENT ANALYST** Judy Lillibridge **ASSOCIATE DIRECTOR, MARKETING** Christina Schlecht **MARKETING ASSOCIATES** Thomas Landreth, Isa Sesay-Bah

DIRECTOR OF WEB TECHNOLOGIES Ahmed Khadr **SR. DEVELOPER** Chris Coleman **DEVELOPERS** Dan Berger, Jimmy Marks **SR. PROJECT MANAGER** Trista Smith **SYSTEMS ENGINEER** Luke Johnson

CREATIVE DIRECTOR, MULTIMEDIA Martyn Green **DIRECTOR OF ANALYTICS** Enrique Gonzales **SR. WEB PRODUCER** Sarah Crespi **WEB PRODUCER** Alison Crawford **VIDEO PRODUCER** Nguyen Nguyen **SOCIAL MEDIA PRODUCER** Meghna Sachdev

DIRECTOR OF OPERATIONS PRINT AND ONLINE Lizabeth Harman **DIGITAL/PRINT STRATEGY MANAGER** Jason Hillman **QUALITY TECHNICAL MANAGER** Marcus Spiegler **DIGITAL PRODUCTION MANAGER** Lisa Stanford **ASSISTANT MANAGER DIGITAL/PRINT** Rebecca Doshi **DIGITAL MEDIA SPECIALIST** Tara Kelly **SENIOR CONTENT SPECIALISTS** Steve Forrester, Antoinette Hodal, Lori Murphy, Anthony Rosen **CONTENT SPECIALISTS** Jacob Hedrick, Kimberley Oster

DESIGN DIRECTOR Beth Rakouskas **DESIGN EDITOR** Marcy Atarod **SENIOR SCIENTIFIC ILLUSTRATORS** Chris Bickel, Katharine Sutliff **SCIENTIFIC ILLUSTRATOR** Valerie Altounian **SENIOR ART ASSOCIATES** Holly Bishop, Preston Huey **SENIOR DESIGNER** Garvin Grullón **DESIGNER** Chrystal Smith **SENIOR PHOTO EDITOR** William Douthitt **PHOTO EDITORS** Leslie Blizard, Christy Steele

DIRECTOR, GLOBAL COLLABORATION, CUSTOM PUBLICATIONS, ADVERTISING Bill Moran **EDITOR, CUSTOM PUBLISHING** Sean Sanders: 202-326-6430 **ASSISTANT EDITOR, CUSTOM PUBLISHING** Tianna Hicklin: 202-326-6463 **ADVERTISING MARKETING MANAGER** Justin Sawyers: 202-326-7061 science_advertising@aaas.org **ADVERTISING MARKETING ASSOCIATE** Javia Flemmings **ADVERTISING SUPPORT MANAGER** Karen Foote: 202-326-6740 **ADVERTISING PRODUCTION OPERATIONS MANAGER** Deborah Tompkins **SR. PRODUCTION SPECIALIST/GRAPHIC DESIGNER** Amy Hardcastle **PRODUCTION SPECIALIST** Yuse Lajiminmuhip **SR. TRAFFIC ASSOCIATE** Christine Hall **SALES COORDINATOR** Shirley Young **ASSOCIATE DIRECTOR, COLLABORATION, CUSTOM PUBLICATIONS/CHINA/TAIWAN/KOREA/SINGAPORE** Ruolei Wu: +86-186 0822 9345, rwu@aaas.org **COLLABORATION/CUSTOM PUBLICATIONS/JAPAN** Adarsh Sandhu + 81532-81-5142 asandhu@aaas.org **EAST COAST/E. CANADA** Laurie Faraday: 508-747-9395, FAX 617-507-8189 **WEST COAST/W. CANADA** Lynne Stickrod: 415-931-9782, FAX 415-520-6940 **MIDWEST** Jeffrey Dembksi: 847-498-4520 x3005, Steven Loerch: 847-498-4520 x3006 **UK EUROPE/ASIA** Roger Goncalves: TEL/FAX +41 43 243 1358 **JAPAN** Katsuyoshi Fukamizu(Tokyo): +81-3-3219-5777 kfukamizu@aaas.org **CHINA/TAIWAN** Ruolei Wu: +186-0082-9345

WORLDWIDE ASSOCIATE DIRECTOR OF SCIENCE CAREERS Tracy Holmes: +44 (0) 1223 326525, FAX +44 (0) 1223 326532 tholmes@science-int.co.uk **CLASSIFIED** advertise@sciencecareers.org **U.S. SALES** Tina Burks: 202-326-6577, Nancy Toema: 202-326-6578 **SALES ADMINISTRATOR** Marci Gallun **EUROPE/ROW SALES** Axel Gesatzki, Sarah Lelarge **SALES ASSISTANT** Kelly Grace **JAPAN** Hiroyuki Mashiki(Kyoto): +81-75-823-1109 hmashiki@aaas.org **CHINA/TAIWAN** Ruolei Wu: +86-186 0082 9345 rwu@aaas.org **MARKETING MANAGER** Allison Pritchard **MARKETING ASSOCIATE** Aimee Aponte

AAAS BOARD OF DIRECTORS RETIRING PRESIDENT, CHAIR Gerald R. Fink **PRESIDENT** Geraldine (Geri) Richmond **PRESIDENT-ELECT** Barbara A. Schaal **TREASURER** David Evans Shaw **CHIEF EXECUTIVE OFFICER** Rush D. Holt **BOARD** Bonnie L. Bassler, May R. Berenbaum, Carlos J. Bustamante, Stephen P.A. Fodor, Claire M. Fraser, Michael S. Gazzaniga, Laura H. Greene, Elizabeth Loftus, Mercedes Pascual

SUBSCRIPTION SERVICES For change of address, missing issues, new orders and renewals, and payment questions: 866-434-AAAS (2227) or 202-326-6417, FAX 202-842-1065. Mailing addresses: AAAS, P.O. Box 96178, Washington, DC 20090-6178 or AAAS Member Services, 1200 New York Avenue, NW, Washington, DC 20005

INSTITUTIONAL SITE LICENSES 202-326-6755 **REPRINTS:** Author Inquiries 800-635-7181 **COMMERCIAL INQUIRIES** 803-359-4578 **PERMISSIONS** 202-326-6765, permissions@aaas.org **AAAS Member Services** 202-326-6417 or http://membercentral.aaas.org/discounts

Science serves as a forum for discussion of important issues related to the advancement of science by publishing material on which a consensus has been reached as well as including the presentation of minority of conflicting points of view. Accordingly, all articles published in *Science*—including editorials, news and comment, and books reviews—are signed and reflect the individual views of the authors and not official points of view adopted by AAAS or the institutions with which the authors are affiliated.

INFORMATION FOR AUTHORS See pages 678 and 679 of the 6 February 2015 issue or access www.sciencemag.org/about/authors

SENIOR EDITORIAL BOARD

Gary King, *Harvard University*
Susan M. Rosenberg, *Baylor College of Medicine,* **Ali Shilatifard,** *Northwestern University Feinberg School of Medicine,* **Michael S. Turner**, *U. of Chicago*

BOARD OF REVIEWING EDITORS (Statistics board members indicated with **(S)**)

Adriano Aguzzi, *U. Hospital Zürich*
Takuzo Aida, *U. of Tokyo*
Leslie Aiello, *Wenner-Gren Foundation*
Judith Allen, *U. of Edinburgh*
Sonia Altizer, *U. of Georgia*
Sebastian Amigorena, *Institut Curie*
Kathryn Anderson, *Memorial Sloan-Kettering Cancer Center*
Meinrat O. Andreae, *Max-Planck Inst. Mainz*
Paola Arlotta, *Harvard U.*
Johan Auwerx, *EPFL*
David Awschalom, *U. of Chicago*
Jordi Bascompte, *Estación Biológica de Doñana CSIC*
Facundo Batista, *London Research Inst.*
Ray H. Baughman, *U. of Texas, Dallas*
David Baum, *U. of Wisconsin*
Carlo Beenakker, *Leiden U.*
Kamran Behnia, *ESPCI-ParisTech*
Yasmine Belkaid, *NIAID, NIH*
Philip Benfey, *Duke U.*
Stephen J. Benkovic, *Penn State U.*
May Berenbaum, *U. of Illinois*
Gabriele Bergers, *U. of California, San Francisco*
Bradley Bernstein, *Massachusettes General Hospital*
Peer Bork, *EMBL*
Bernard Bourdon, *Ecole Normale Supérieure de Lyon*
Chris Bowler, *École Normale Supérieure*
Ian Boyd, *U. of St. Andrews*
Emily Brodsky, *U. of California, Santa Cruz*
Ron Brookmeyer, *U. of California Los Angeles* **(S)**
Christian Büchel, *U. Hamburg-Eppendorf*
Joseph A. Burns, *Cornell U.*
Gyorgy Buzsaki, *New York U. School of Medicine*
Blanche Capel, *Duke U.*
Mats Carlsson, *U. of Oslo*
David Clapham, *Children's Hospital Boston*
David Clary, *U. of Oxford*
Joel Cohen, *Rockefeller U., Columbia U.*
James Collins, *Boston U.*
Robert Cook-Deegan, *Duke U.*
Alan Cowman, *Walter & Eliza Hall Inst.*
Robert H. Crabtree, *Yale U.*
Roberta Croce, *Vrije Universiteit*
Janet Currie, *Princeton U.*
Jeff L. Dangl, *U. of North Carolina*
Tom Daniel, *U. of Washington*
Frans de Waal, *Emory U.*
Stanislas Dehaene, *Collège de France*
Robert Desimone, *MIT*
Claude Desplan, *New York U.*
Ap Dijksterhuis, *Radboud U. of Nijmegen*
Dennis Discher, *U. of Pennsylvania*
Gerald W. Dorn II, *Washington U. School of Medicine*
Jennifer A. Doudna, *U. of California, Berkeley*
Bruce Dunn, *U. of California, Los Angeles*
Christopher Dye, *WHO*
Todd Ehlers, *U. of Tuebingen*
David Ehrhardt, *Carnegie Inst. of Washington*
Tim Elston, *U. of North Carolina at Chapel Hill*
Gerhard Ertl, *Fritz-Haber-Institut, Berlin*
Barry Everitt, *U. of Cambridge*
Ernst Fehr, *U. of Zurich*
Anne C. Ferguson-Smith, *U. of Cambridge*
Michael Feuer, *The George Washington U.*
Toren Finkel, *NHLBI, NIH*
Kate Fitzgerald, *U. of Massachusetts*
Peter Fratzl, *Max-Planck Inst.*
Elaine Fuchs, *Rockefeller U.*
Daniel Geschwind, *UCLA*
Andrew Gewirth, *U. of Illinois*
Karl-Heinz Glassmeier, *TU Braunschweig*
Ramon Gonzalez, *Rice U.*
Julia R. Greer, *Caltech*
Elizabeth Grove, *U. of Chicago*
Nicolas Gruber, *ETH Zurich*
Kip Guy, *St. Jude's Children's Research Hospital*
Taekjip Ha, *U. of Illinois at Urbana-Champaign*
Christian Haass, *Ludwig Maximilians U.*
Steven Hahn, *Fred Hutchinson Cancer Research Center*
Michael Hasselmo, *Boston U.*
Martin Heimann, *Max-Planck Inst. Jena*
Yka Helariutta, *U. of Cambridge*
James A. Hendler, *Rensselaer Polytechnic Inst.*
Janet G. Hering, *Swiss Fed. Inst. of Aquatic Science & Technology*
Kai-Uwe Hinrichs, *U. of Bremen*
Kei Hirose, *Tokyo Inst. of Technology*
David Hodell, *U. of Cambridge*
David Holden, *Imperial College*
Lora Hooper, *UT Southwestern Medical Ctr. at Dallas*
Raymond Huey, *U. of Washington*
Steven Jacobsen, *U. of California, Los Angeles*
Kai Johnsson, *EPFL Lausanne*
Peter Jonas, *Inst. of Science & Technology (IST) Austria*
Matt Kaeberlein, *U. of Washington*
William Kaelin Jr., *Dana-Farber Cancer Inst.*
Daniel Kahne, *Harvard U.*
Daniel Kammen, *U. of California, Berkeley*
Masashi Kawasaki, *U. of Tokyo*
V. Narry Kim, *Seoul National U.*
Joel Kingsolver, *U. of North Carolina at Chapel Hill*
Robert Kingston, *Harvard Medical School*
Etienne Koechlin, *Ecole Normale Supérieure*
Alexander Kolodkin, *Johns Hopkins U.*
Alberto R. Kornblihtt, *U. of Buenos Aires*
Leonid Kruglyak, *UCLA*
Thomas Langer, *U. of Cologne*
Mitchell A. Lazar, *U. of Pennsylvania*
David Lazer, *Harvard U.*
Thomas Lecuit, *IBDM*
Virginia Lee, *U. of Pennsylvania*
Stanley Lemon, *U. of North Carolina at Chapel Hill*
Ottoline Leyser, *Cambridge U.*
Marcia C. Linn, *U. of California, Berkeley*
Jianguo Liu, *Michigan State U.*
Luis Liz-Marzan, *CIC biomaGUNE*
Jonathan Losos, *Harvard U.*
Ke Lu, *Chinese Acad. of Sciences*
Christian Lüscher, *U. of Geneva*
Laura Machesky, *CRUK Beatson Inst. for Cancer Research*
Anne Magurran, *U. of St. Andrews*
Oscar Marin, *CSIC & U. Miguel Hernández*
Charles Marshall, *U. of California, Berkeley*
C. Robertson McClung, *Dartmouth College*
Graham Medley, *U. of Warwick*
Tom Misteli, *NCI*
Yasushi Miyashita, *U. of Tokyo*
Mary Ann Moran, *U. of Georgia*
Richard Morris, *U. of Edinburgh*
Alison Motsinger-Reif, *NC State U.* **(S)**
Sean Munro, *MRC Lab. of Molecular Biology*
Thomas Murray, *The Hastings Center*
James Nelson, *Stanford U. School of Med.*
Daniel Neumark, *U. of California, Berkeley*
Kitty Nijmeijer, *U. of Twente*
Pär Nordlund, *Karolinska Inst.*
Helga Nowotny, *European Research Advisory Board*
Ben Olken, *MIT*
Joe Orenstein, *U. of California Berkeley & Lawrence Berkeley National Lab*
Harry Orr, *U. of Minnesota*
Andrew Oswald, *U. of Warwick*
Steve Palumbi, *Stanford U.*
Jane Parker, *Max-Planck Inst. of Plant Breeding Research*
Giovanni Parmigiani, *Dana-Farber Cancer Inst.* **(S)**
Donald R. Paul, *U. of Texas, Austin*
John H. J. Petrini, *Memorial Sloan-Kettering Cancer Center*
Joshua Plotkin, *U. of Pennsylvania*
Albert Polman, *FOM Institute AMOLF*
Philippe Poulin, *CNRS*
Jonathan Pritchard, *Stanford U.*
David Randall, *Colorado State U.*
Colin Renfrew, *U. of Cambridge*
Felix Rey, *Institut Pasteur*
Trevor Robbins, *U. of Cambridge*
Jim Roberts, *Fred Hutchinson Cancer Research Ctr.*
Barbara A. Romanowicz, *U. of California,Berkeley*
Jens Rostrup-Nielsen, *Haldor Topsoe*
Mike Ryan, *U. of Texas, Austin*
Mitinori Saitou, *Kyoto U.*
Shimon Sakaguchi, *Kyoto U.*
Miquel Salmeron, *Lawrence Berkeley National Lab*
Jürgen Sandkühler, *Medical U. of Vienna*
Alexander Schier, *Harvard U.*
Randy Seeley, *U. of Cincinnati*
Vladimir Shalaev, *Purdue U.*
Robert Siliciano, *Johns Hopkins School of Medicine*
Denis Simon, *Arizona State U.*
Alison Smith, *John Innes Centre*
Richard Smith, *U. of North Carolina* **(S)**
John Speakman, *U. of Aberdeen*
Allan C. Spradling, *Carnegie Institution of Washington*
Jonathan Sprent, *Garvan Inst. of Medical Research*
Eric Steig, *U. of Washington*
Paula Stephan, *Georgia State U. and National Bureau of Economic Research*
Molly Stevens, *Imperial College London*
V. S. Subrahmanian, *U. of Maryland*
Ira Tabas, *Columbia U.*
Sarah Teichmann, *Cambridge U.*
John Thomas, *North Carolina State U.*
Shubha Tole, *Tata Institute of Fundamental Research*
Christopher Tyler-Smith, *The Wellcome Trust Sanger Inst.*
Herbert Virgin, *Washington U.*
Bert Vogelstein, *Johns Hopkins U.*
Cynthia Volkert, *U. of Göttingen*
Douglas Wallace, *Dalhousie U.*
David Wallach, *Weizmann Inst. of Science*
Ian Walmsley, *U. of Oxford*
Jane-Ling Wang, *U. of California, Davis*
David A. Wardle, *Swedish U. of Agric. Sciences*
David Waxman, *Fudan U.*
Jonathan Weissman, *U. of California, San Francisco*
Chris Wikle, *U. of Missouri* **(S)**
Ian A. Wilson, *The Scripps Res. Inst.* **(S)**
Timothy D. Wilson, *U. of Virginia*
Rosemary Wyse, *Johns Hopkins U.*
Jan Zaanen, *Leiden U.*
Kenneth Zaret, *U. of Pennsylvania School of Medicine*
Jonathan Zehr, *U. of California, Santa Cruz*
Len Zon, *Children's Hospital Boston*
Maria Zuber, *MIT*

BOOK REVIEW BOARD

David Bloom, *Harvard U.,* **Samuel Bowring,** *MIT,* **Angela Creager,** *Princeton U.,* **Richard Shweder,** *U. of Chicago,* **Ed Wasserman,** *DuPont*

EDITORIAL

Solving reproducibility

The reproducibility problem in science is a familiar issue, not only within the scientific community, but with the general public as well. Recent developments in social psychology (such as fraudulent research by D. Stapel) and cell biology (the Amgen Inc. and Bayer AG reports on how rarely they could reproduce published results) have become widely known. Nearly every field is affected, from clinical trials and neuroimaging, to economics and computer science. Obvious solutions include more research on statistical and behavioral fixes for irreproducibility, activism for policy changes, and demanding more preregistration and data sharing from grantees. Two Perspectives in this issue (pp. 1420 and 1422) describe how journals and academic institutions can foster a culture of reproducibility. Transparency is central to improving reproducibility, but it is expensive and time-consuming. What can be done to alleviate those obstacles?

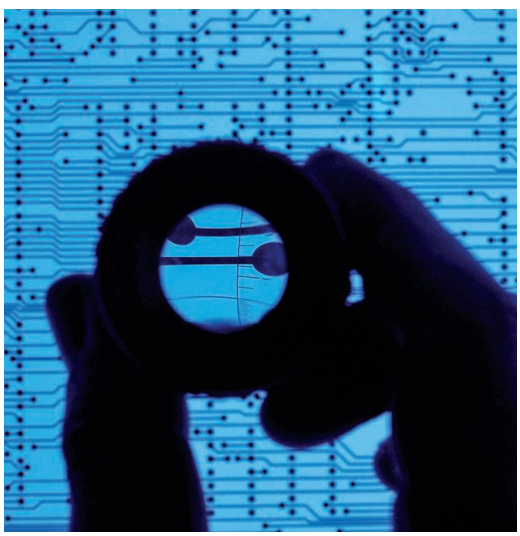

"Transparency is central to improving reproducibility..."

Most scientists aspire to greater transparency, but if being transparent taps into scarce grant money and requires extra work, it is unlikely that scientists will be able to live up to their own cherished values. Thus, one of the most effective ways to promote high-quality science is to create free open-source tools that give scientists easier and cheaper ways to incorporate transparency into their daily workflow: from open lab notebooks, to software that tracks every version of a data set, to dynamic document generation. Moreover, scientists who use open-source software are not locked into proprietary software platforms with unclear monetization plans. If philanthropy or government funds new tools that the open-source community can iterate and improve on, the per-dollar return on investment can far exceed the costs.

Infrastructural tools are now available, or in development, that should help to catalyze a change in scientific transparency. One example is the Open Science Framework (OSF), a free and open-source software platform for managing scientific workflow (supported by the Laura and John Arnold Foundation in partnership with the Center for Open Science). Among its many features, this platform can enable scientists to easily track the history of all versions of every document or data set and the exact contributions made by each team member. All project materials can be given persistent identifiers, and the tracking of provenance allows any subsequent research project to give proper credit to the original. Projects using this platform include the Shared Access Research Ecosystem project of the Association of Research Libraries and its partners. This project endeavors to connect scholarly metadata and allow the identification of various elements of a research project, such as grant proposals, journal articles, and data repository information.

Open-source platform innovations are growing. Other examples include the iPython project (supported largely by the Alfred P. Sloan Foundation), which offers a web-based computing notebook for users to create documents such as code, computational results, and narrative explanations. Although originally developed around the Python language, the project has expanded to cover other languages (such as R) under the banner of Project Jupyter. The Galaxy Project (funded by the U.S. National Science Foundation and others) provides a web-based platform for "data-intensive" biomedical research; and for managing bioinformatics and phylogenetic research on plants, there is the iPlant Collaborative.

The scientific community cannot depend entirely on volunteers or the private market to develop free platforms that address specialized scientific needs and encourage greater reproducibility. Ultimately, the infrastructure supporting science is a public good, just like the knowledge it produces. By supporting such infrastructure, the public and philanthropic sectors can make it painless for researchers to live up to their own values of openness and rigor.

– Stuart Buck

Stuart Buck is vice president of research integrity at the Laura and John Arnold Foundation, Houston, TX. E-mail: sbuck@arnoldfoundation.org

10.1126/science.aac8041

PHOTOS: (TOP RIGHT) LAURA AND JOHN ARNOLD FOUNDATION; (INSET) © EDWARD ROZZO/CORBIS

Downloaded from www.sciencemag.org on June 26, 2015

Published by AAAS

$95,000,000

Investment from pharmaceutical giant GlaxoSmithKline toward the new nonprofit Altius Institute for Biomedical Sciences, which will be devoted to studying gene regulation with the ultimate aim of treating diseases.

IN BRIEF

Kennewick Man was Native American

To scientists, this nearly complete skeleton, found in 1996 in Washington state, is the "Kennewick Man." To Native Americans, he is the "Ancient One." Eleven years ago, after Native Americans sought to gain custody of these 8500-year-old bones in order to rebury them, the federal courts ruled he was not related to any modern tribe. That gave scientists the right to study him, although several attempts to sequence his DNA had failed. But last week, researchers reported online in *Nature* that they have sequenced Kennewick Man's genome—and the results, they say, leave little room for doubt that he was a Native American. Kennewick Man, they found, is closely related to at least one of the five Washington-area tribes that claimed him: the Colville. The U.S. Army Corps of Engineers, which has custody of the skeleton, now says it will reopen the case for the Ancient One's repatriation to the tribes.

PHOTO: CHIP CLARK/SMITHSONIAN INSTITUTION

AROUND THE WORLD

Experts slam research whale kills

SAN DIEGO, CALIFORNIA | For the third time in 15 months, experts have concluded there is no justification for Japan to kill whales for research. Opinion was split in last week's report from the annual meeting of the Scientific Committee of the International Whaling Commission (IWC), but 44 scientists from 13 countries noted that "the need for lethal sampling has not been demonstrated." In 2014, The Hague–based International Court of Justice ordered Japan to halt its Antarctic Ocean research whaling program, stating that the lethal sampling was not justified. Japan drew up a new plan, which an IWC expert panel also rejected in February. Japan has not yet decided if it will resume killing whales as part of its Antarctic research whaling program, said Joji Morishita, the nation's representative to IWC, at a press conference this week—but, he said, IWC's Scientific Committee "does not have jurisdiction to approve or deny the research plan." The entire IWC will take up the issue when it meets in September 2016.
http://scim.ag/IWCreswhale

TMT construction to resume

MAUNA KEA, HAWAII | Astronomers have decided to restart construction of a controversial telescope in Hawaii that has been the subject of protests by Native Hawaiian groups (*Science*, 10 April, p. 160). At press time, the board planned to resume construction of the Thirty Meter Telescope (TMT) on the Mauna Kea volcano on Wednesday, 24 June, according to a statement issued 20 June by the telescope's governing board. "We are now comfortable that we can be better stewards and better neighbors during our temporary and limited use of this precious land," wrote Henry Yang, chair of the TMT International Observatory Board, in the statement. The move comes after Hawaii's governor, David Ige (D), announced measures on 26 May—including a call to remove about a quarter of Mauna Kea's 13 existing telescopes—aimed at addressing the concerns of Native Hawaiian

Downloaded from www.sciencemag.org on June 26, 2015

Published by AAAS

Africa's vulture populations plummet

One of nature's best scavengers is under serious threat in Africa. Populations of seven species of vulture have fallen by 80% or more over three generations, qualifying the majority of Africa's species as critically endangered, scientists reported online last week in *Conservation Letters*. Despite their gloomy reputation, vultures provide valuable services; by cleaning the carcasses of dead animals, for example, they keep numbers of feral dogs in check, reducing transmission rates for rabies. And Egyptian vultures (*Neophron percnopterus,* pictured) have been found to remove up to 22% of waste produced in towns along the Horn of Africa. The main threat to the vultures appears to be poison, the researchers found; vultures are often incidental victims when farmers target lions or hyenas by lacing carcasses with pesticides. Poachers aiming to hide their kills of rhinos and elephants are also increasingly shooting the birds circling overhead. **http://scim.ag/vulturepopul**

protesters who claim the mountain as sacred ground. **http://scim.ag/TMTrestart**

Company halts Ebola drug trial

PORT LOKO, SIERRA LEONE | A clinical trial of a promising Ebola drug has been stopped early after it apparently failed to show a benefit to patients. The drug, called TKM-Ebola-Guinea, is a set of small RNA molecules packaged in lipid nanoparticles. It interferes with Ebola genes and prevents the virus from replicating. In animal trials, the drug saved monkeys from an otherwise deadly dose of the virus. But on 19 June, Tekmira Pharmaceuticals, the company that makes the drug, announced that disappointing early results had prompted them to stop enrolling people in the trial, which originally aimed for 100 patients. Meanwhile, a trial of the other drug seen as the best shot at fighting Ebola, the antibody cocktail ZMapp, is expanding to Guinea after enrolling more than 30 patients in the United States, Liberia, and Sierra Leone. **http://scim.ag/TKMtrialend**

NEWSMAKERS

France fills top science policy post

French President François Hollande last week appointed political scientist **Thierry Mandon** as the new state secretary for higher education and research, a post that has been vacant since Geneviève Fioraso stepped down in March. The hiring delay sparked discontent among scientists, who said it betrayed a fundamental lack of interest in research. Mandon knows the research world well; he was president of Genopole, a biotechnology and genomics research cluster near Paris, from 1998 to 2014. Since June 2014, he has been state secretary for state reform and simplification, responsible for making French public authorities more efficient and user-friendly. He faces many challenges, including a recent €100 million cut in government funding for universities, which has fueled anxiety about the 2016 budget, currently under negotiation. **http://scim.ag/_Mandon**

FINDINGS

New Guinea flatworm invades U.S.

Nearly 2 years after its debut in Europe, an invasive flatworm with a taste for snails has arrived on the U.S. mainland. The New Guinea flatworm (*Platydemus manokwari*) is the only flatworm on the Global Invasive Species Database's list of 100 of the world's most dangerous invaders. Thought to originate from its namesake Pacific island, the predatory flatworm had been identified in 15 countries (including the United States, in Hawaii). Now, using molecular gene analysis and observations of the worm's color and shape, scientists have documented additional sightings, in Singapore, the Solomon Islands, New Caledonia, and the United States (Puerto Rico and Florida), they report this week in *PeerJ*. In particular, the discovery of the worm in several Miami gardens has some scientists raising the alarm, fearing that it is poised to spread throughout the U.S. mainland. However, freezing temperatures may help restrict the worm's range. **http://scim.ag/flatworminv**

A New Guinea flatworm snacking on a snail.

Running out of groundwater

Water levels in more than half of the world's 37 largest groundwater aquifers—a source of fresh water for hundreds of millions of people—are being depleted at alarming rates due to demands from agriculture, growing populations, and industry, suggest new data from the twin satellites of NASA's Gravity Recovery and Climate Experiment mission. Using slight changes in the gravitational tugs on the two satellites, researchers estimated how fast the basins were gaining or losing water. Of the 37 basins, 21 showed declining water levels from 2003 to 2013; eight of those weren't being naturally replenished at all, and another five only slightly replenished, the team reported online last week in two papers in *Water Resources Research*.

PHOTOS: (TOP TO BOTTOM) © KRYS BAILEY/ALAMY; PIERRE GROS

Published by AAAS

People who recovered from Ebola place handprints on a "survivor wall."

INFECTIOUS DISEASES

Surviving Ebola survival

After recovering from Ebola, some patients are struggling with other health problems

By **Kai Kupferschmidt**

The Ebola outbreak in West Africa is far from over. That is true for those still battling the deadly disease in Sierra Leone and in Guinea, where 24 new cases were confirmed last week, up from 12 cases 4 weeks ago. And it is true for the thousands who survived the infection but are reeling from the shock of their experiences and, in many instances, still suffering symptoms long after being declared free of the virus. Now, large studies have begun to catalog these sequelae and to help make sense of this "post-Ebola syndrome."

Foday Gallah, a 37-year-old Liberian ambulance worker, fell ill in August after picking up an Ebola-stricken child. He survived the disease but today suffers from memory problems and a chronic headache. His left knee hurts, his eyes burn, and he sometimes gets double vision.

Gallah's story is not unusual, says Mosoka Fallah, the principal investigator of the PREVAIL III study launched last week by the U.S. National Institute of Allergy and Infectious Diseases (NIAID) and the Liberian ministry of health. (PREVAIL I is an Ebola vaccine study; PREVAIL II is testing potential Ebola drugs.) Fallah hopes to enroll 1500 Ebola survivors and 6000 close contacts in the study.

> ***"Some of them have lost their jobs, they have been driven from their homes, relatives have abandoned them."***
>
> **Mosoka Fallah**, principal investigator of PREVAIL III

The group will examine not only the long-term health effects of contracting Ebola, but also whether survivors are protected from future infections and whether some may still be able to pass the virus on to others.

Several Ebola outbreaks have occurred in recent decades, and hundreds of infected people beat the virus. But more people have survived the current outbreak than all previous others combined. At least 16,000 people survived an infection in West Africa, the World Health Organization (WHO) estimates.

Earlier research has shown that Ebola survivors can have health problems even years after defeating the virus. One study, published earlier this year in *The Lancet Infectious Diseases*, examined survivors of a 2007 Ebola outbreak in Uganda that was caused by a less deadly species of the virus called Bundibugyo. In 2010, scientists went back to the area and compared 49 survivors with more than 200 uninfected contacts. They found that survivors were more likely to suffer from hearing loss, eye pain, blurred vision, difficulty sleeping, and other symptoms.

The same seems to be happening in West Africa. Fallah says that a survey among Ebola survivors found that one-third suffered from fatigue and one-fifth from hearing impairments, for instance. Doctors who treated infected health care workers flown

PHOTO: © MARCUS DIPAOLA/NURPHOTO/CORBIS

Downloaded from www.sciencemag.org on June 26, 2015

Published by AAAS

to Europe or the United States report the same. Anthony Fauci, who heads NIAID, has helped treat two Ebola patients in the United States. Both showed some symptoms even after they had fully recovered from the acute infection, he says. "When I call up colleagues and ask if they are running into the same problems, they say, 'Yes.'"

At least three explanations are possible, says Danielle Clark, an epidemiologist at the Naval Medical Research Center in Fort Detrick, Maryland, who headed the Bundibugyo study. The lingering symptoms may stem from cells and organs damaged by the virus before it was brought under control. They could be a side effect of the immune system battling the virus, or a sign the immune system has subsequently turned on its own body. In that scenario, the immune system does its job, recognizing certain structures on the virus and fighting off the invader, but then trains its weapons on noncombatants. "If there are structurally similar host molecules, the immune system gets confused and starts fighting that," Clark says.

The eye seems to be affected frequently, possibly because the immune system's reach does not normally extend to the organ. U.S. doctor and survivor Ian Crozier was found to have Ebola virus in his eye more than 2 months after the virus had disappeared from his blood.

Other viruses haunt people after they have recovered. Lassa virus infections can cause hearing loss, for instance, and dengue fever, chikungunya, and Rift Valley fever can all lead to chronic problems after the acute infection. "By studying Ebola, we may get insight into these other infections as well," Clark says, including who is particularly at risk for lingering symptoms.

The PREVAIL III study will follow participants for 5 years with a physical exam every 6 months. Investigators will collect blood as well as sweat, tears, and semen or cervical secretions from some survivors and from close contacts. INSERM, the French biomedical research agency, has already started a similar study in Guinea, called Postebogui, which aims to follow 450 patients for a year, checking them every 3 months. "We will also check contacts to see if there may have been silent infections and to understand when antibodies arise and for how long," says study coleader Eric Delaporte.

Indeed, one of the most pressing questions is whether the virus still lurks in some survivors and, if it does, whether that poses a risk to others. Ebola virus can persist in the seminal fluid of men who have cleared the virus from their blood. Before the outbreak in West Africa, the longest reported time was 82 days after symptom onset. But in one recent case, genetic material from Ebola virus was isolated from the semen of a survivor 199 days after symptom onset, prompting WHO to change its advice on sexual transmission. It now recommends that survivors use condoms until their semen has twice tested negative or for at least 6 months after symptom onset. If sexual transmission occurs, it is infrequent, says Dan Bausch, an infectious disease specialist at WHO in Geneva, Switzerland. Still, even a single case could lead to a new outbreak, he says. "I don't think we need to panic over that, but we need to recognize it."

Many survivors not only have to deal with the sequelae of the disease, but also with the psychological fallout of their traumatic experiences, Bausch says. "There is post-traumatic stress disorder, anxiety, depression. Those things are much harder for us to measure." Then there is stigmatization. "Some of them have lost their jobs, they have been driven from their homes, relatives have abandoned them," Fallah says. He hopes that studies such as PREVAIL III will increase knowledge about survivors and so help overcome unfounded fears. "Imagine you survive this terrible disease, then you come home and may have five or six family members dead and you are fighting with the consequences of Ebola and then the stigmatization as well," Bausch says.

The uncertainty is hard to bear, Gallah says. "We don't know what our life is going to be like for the next 5 or 6 or 10 years." He hopes he will be able to go back to work soon. "At least when I'm busy doing something, I feel OK. When I sit by myself, my mind just goes back to the terrible things I went through." ■

Ebola's lingering legacy

Some survivors are reporting symptoms long after the acute infection. Several studies are underway to assess how common this is and whether these people still harbor the virus.

- Eye inflammation, pressure, pain, blurred vision
- Hearing loss
- Headache, attention difficulties, memory problems
- Joint pain and stiffness, muscle weakness
- Erectile dysfunction
- Fatigue, difficulty sleeping

GENETICS

An enhanced view of gene control

Chromosomal loops and domains help enhancers turn on genes

By **Elizabeth Pennisi**, *in Cold Spring Harbor, New York*

Genes may be the stars in a cell's nucleus, but they would never shine without a strong supporting cast. Take the stretches of regulatory DNA called enhancers, which help turn genes on at the right times and places. Although researchers have scrutinized genes as closely as the paparazzi track Hollywood celebrities, enhancers have largely stayed in the background, their workings a mystery. A recent genetics meeting here signaled a change: In talk after talk, researchers described where and how these quiet fixers exert their influence.

One group showed how enhancers maintain the right level of sensitivity to other signals, so that they switch genes on only at the right times and places. Others explored how cells package genes and their enhancers so that they can work together properly, and how DNA forms loops that bring enhancers right to the target gene. The advances even point to strategies for exploiting these regulatory elements to treat disease, by switching off disease genes and turning up the activity of healthy ones.

"We've been talking about [enhancers] for a long time," says Susan Gasser, director of the Friedrich Miescher Institute for Biomedical Research in Basel, Switzerland. "But now we are really beginning to understand them."

One revelation is that it doesn't pay for an enhancer to be too good at its job. Enhancers switch on genes when transcription factors and other proteins bind to specific segments in the enhancer DNA. By tinkering with one enhancer's sequence, Michael Levine from the University of California, Berkeley, and his colleagues found that, in principle, enhancers could be more sensitive to the signals that activate them. They focused on the enhancer for *Otx*, a gene that plays a role in nervous system development.

The *Otx* enhancer attracts two proteins, each of which uses a different four-base

Published by AAAS

sequence as a landing site. In Levine's lab, Emma Farley randomly changed bases outside these proteins' binding sites. She made about a million variations of the *Otx* enhancer, linking each variant to another sequence that serves as an identifying "barcode" and to a reporter gene that indicated when the enhancer was active by producing a pigment. Tiny marine invertebrates called sea squirts can be made to take up DNA simply by applying a mild electric shock, so the researchers easily made many thousands of transgenic sea squirt embryos incorporating the various enhancers.

They found that enhancers can vary quite a bit and still work: About 100,000 variants produced detectable enhancer activity in some of the squirts' cells, and 20,000 invoked stronger or more consistent expression than the native sequence. The most active of these 20,000 enhancer variants had a particular DNA pattern, with identical bases on either side of each protein-binding site, Levine reported. Initially, he was puzzled that the native *Otx* enhancer doesn't have the same, seemingly optimal flanking bases. But further tests showed that the "optimal" enhancer actually isn't: It turned on *Otx* inappropriately, in the wrong tissues. In nature, "the enhancer is intentionally mediocre," Levine says. "There's a trade-off between [binding] levels and specificity." It makes sense, he adds: A hair-trigger switch that could be activated by stray protein molecules is as risky for an organism as a switch that does not turn on when it should.

Cells have a second strategy for ensuring that enhancers operate properly: packaging them relatively close to the genes they activate. Three years ago, Job Dekker, a biologist at the University of Massachusetts Medical School in Worcester, and others reported evidence that enhancer-gene connections were not scattered willy-nilly, but instead occur within "topologically associating domains," or TADs, distributed along each chromosome. Each TAD encompassed a handful of genes and dozens of enhancers, he and others estimated.

The proposal faced some skepticism, so Dekker took a close look at a much-studied gene, *CFTR*, that is mutated in people with cystic fibrosis. The gene, which encodes an ion channel, interacts with different enhancers in each of the five cell types his team looked at. In every case, the enhancers and the gene were all found within the same stretch of chromosome—the apparent TAD.

TADs may be a way of limiting a gene's exposure to spurious activation by the wrong enhancers, or they may help ensure that genes that need to work in synchrony do so, Dekker and others suggest. Either way, what's becoming clear, Levine says, is that the TAD "is a very fundamental unit of genome organization and function."

That still leaves a geometrical question: Enhancers and their target genes are often some distance apart in a TAD, so how do they get together? The answer appears to be that DNA loops within TADs juxtapose enhancers and genes. Dekker, for example, showed that three of the five studied cell types activate *CFTR*, but do so at different times and under different conditions and form different loops to bring the appropriate enhancers to the gene. They did these studies using a technique called chromosome conformation capture that detects what pieces of DNA are in close contact with one another.

Beyond offering new insight into the workings of the nucleus, such findings open the possibility of changing it. Molecular biologist Gerd Blobel of the Children's Hospital of Philadelphia in Pennsylvania, for example, detailed his ongoing efforts to modify a gene-enhancer loop as a treatment for sickle cell anemia.

In this disorder, a gene for making a subunit of the oxygen-carrying protein complex hemoglobin is defective, causing the production of misshapen red blood cells. But the body has another type of hemoglobin that's active only during fetal development. Several therapeutic strategies, including one on the market today, work by elevating production of fetal hemoglobin.

Last year, Blobel's team reported cell studies in which they down-regulated the production of adult hemoglobin and boosted fetal hemoglobin by altering the loop that normally brings an enhancer called LCR into contact with the adult hemoglobin gene. "It's not conventional gene therapy and it's not gene correction, but it's editing how the genome is folded," Blobel explains.

The technique involves making a two-fisted protein in which one "fist" is part of a zinc finger protein that recognizes and binds to the fetal hemoglobin gene, and a second "fist" is a segment of a cofactor protein that aids DNA looping. Adding this hybrid protein to cells causes the loop between the adult hemoglobin gene and the LCR enhancer to shift, activating less of the adult hemoglobin gene and more of the fetal one.

The treatment is less toxic to cells than pharmacological treatments that activate fetal hemoglobin, Blobel told the meeting. Now, his group has begun testing this approach in mice engineered to carry the human globin genes. "Changing [chromosome] organization to achieve the end result of gene [activity] reduction is a far reaching insight," says Bing Ren, a molecular geneticist at the San Diego, California, branch of the Ludwig Institute for Cancer Research. It could "represent a completely new set of therapeutic interventions."

Blobel's experiments also go a long way toward erasing lingering doubts about the importance of enhancer loops, several scientists noted. "We spent many years trying to prove that looping was a real phenomenon," says Kenneth Zaret, a molecular biologist at the University of Pennsylvania. Blobel's work "seals the deal." ■

In the loop

Chromosome regions called topologically associating domains concentrate genes and regulatory DNA known as enhancers. DNA loops then bring enhancers, with regulatory proteins, to a gene to turn it on. Tying enhancer activity to a reporter gene can reveal when it goes to work, as in sea squirt tadpoles (below, green).

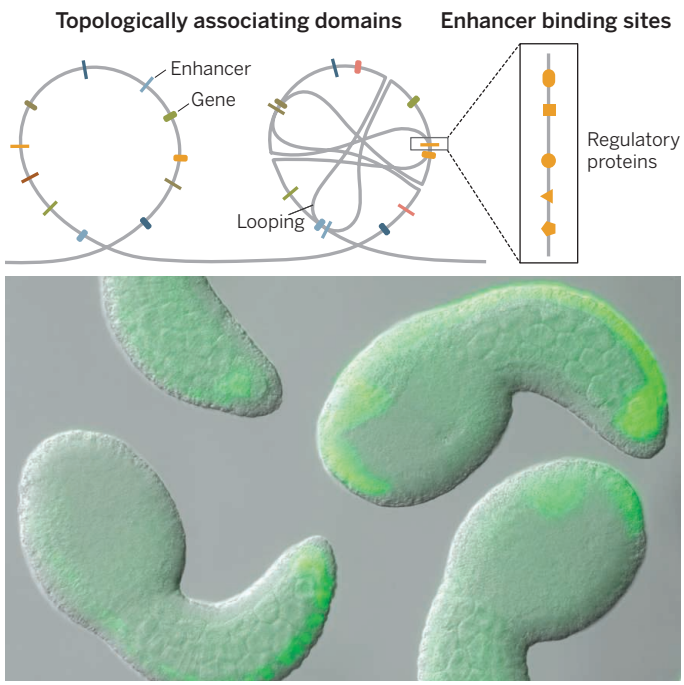

CREDITS: (PHOTO) EMMA FARLEY AND KATRINA OLSON; (ILLUSTRATION) EMMA FARLEY AND KATRINA OLSON, ADAPTED BY M. ATAROD/*SCIENCE*

Published by AAAS

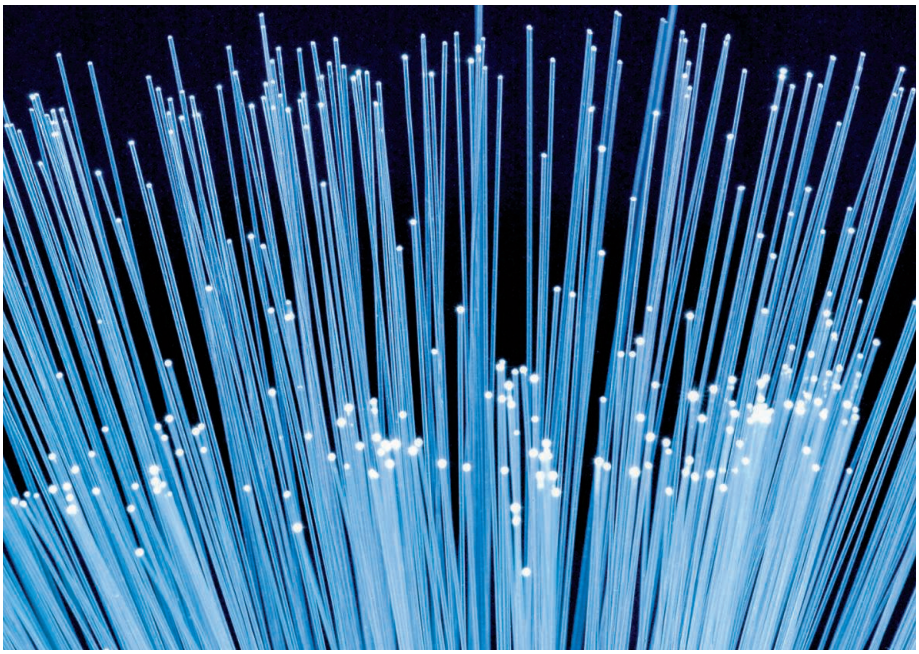

Light zipping through optical fibers can carry huge amounts of data, but errors creep in with distance.

OPTICS

Breaking the light barrier

Trick for pushing more bits through optical fibers could ease looming "capacity crunch"

By **Robert F. Service**

All those tweets, phone calls, YouTube cat videos, and Netflix downloads are causing serious congestion on our data highways. Traffic on the hair-like glass optical fibers that carry data around the globe has risen by about 60% per year since 2000. At that pace, today's fiber-optic networks could reach full capacity in just a couple of years, turning the Internet into a virtual Los Angeles traffic jam. "The capacity crunch is very real, and a big problem," says Peter Winzer, who heads optical transmission research at Bell Laboratories, an R&D arm of Alcatel-Lucent in Murray Hill, New Jersey.

But new work could push that crunch date back several years. On page 1445 this week in *Science*, researchers at the University of California, San Diego (UCSD), report a new scheme for sending digital data over fiber-optic lines that could boost capacity somewhere between two- and fourfold. Winzer, who was not involved in the work, calls it "a breakthrough as a science concept." Vijay Vusirikala, an optical network architect at Google in Mountain View, California, agrees. "Any technology that allows us to increase the capacity of fibers is really critical," Vusirikala says.

Optical fibers were first deployed in the 1980s because they promised to vastly increase network capacity. Before that, data traveled as analog signals over copper electrical wires. Fiber optics, which carries data as modulated pulses of light, has far higher carrying capacity, or bandwidth, than copper wires. That's because light pulses at different wavelengths, or colors, can travel independently down the same fiber with comparatively little crosstalk or interference. That allows engineers to send 100 or more separate data streams down a single fiber at the same time.

Those data streams are created by chip-based lasers that convert the electrical impulses from electronic devices into light, turning each wavelength on and off to create a rapid flicker of 1s and 0s. Today, engineers also modulate the shape of the pulses, their phase, their polarization, and their physical spacing in the fiber. At the far end of the optical highway, detectors turn the light pulses back into electrons. With the help of modern communications lasers and detectors, single fibers today carry 100 to 200 optical signals simultaneously, with an overall capacity of about 20 terabits (trillions of bits) per second.

The signals can travel great distances down a fiber without weakening. But over thousands of kilometers—say, from New York to Los Angeles—optical distortions creep in, causing errors to build up and degrade the data. They result from interference between the multiple signals at different wavelengths. As one signal propagates down the fiber, its electromagnetic wave causes electrons in the glass to shuffle around, a shift that affects the propagation of other light waves. The result is that the two starting light waves combine to create a third at a separate wavelength. The effect is very weak, but it builds up over long distances—especially in fibers carrying many wavelengths of light. "You get a progressively bigger problem with more and more channels and longer distances," says Stojan Radic, an electrical engineer and optical physicist at UCSD and an author of the new study.

To cope, every 1000 kilometers or so, long-haul networks must read the incoming signals and convert them to electrical signals so computer chips can weed out the distortions. The optical signals are then regenerated and sent on their way. That process slows data traffic, reducing capacity, and the equipment needed for it now accounts for approximately 80% of the cost of setting up new network infrastructure. As a result, Vusirikala says, "we try to avoid it at all costs."

Ever-faster fibers

Despite decades of soaring transmission rates, experts warn the "information highway" can't keep up with insatiable demand.

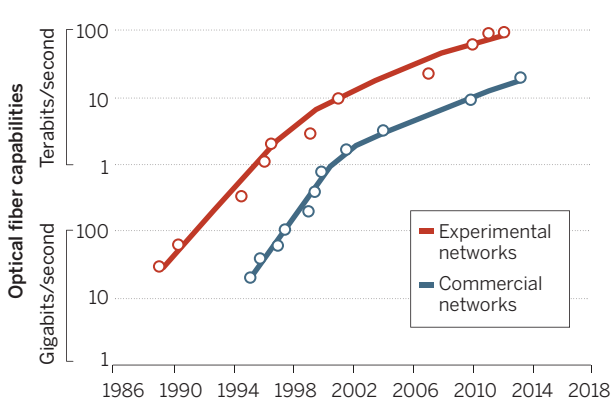

CREDITS: (PHOTO) PAUL RAPSON/SCIENCE SOURCE; (DATA) ADAPTED BY P. J. WINZER, *OPTICS AND PHOTONICS NEWS* (1 MARCH 2015) © OSA

Downloaded from www.sciencemag.org on June 26, 2015

Published by AAAS

Distortion would be easier to weed out if it were predictable, Radic says. If the lasers that encode the data produced photons at a single precise wavelength, for example, any distortion could simply be subtracted from the optical signal at the end of the long-haul fiber, with no need for regeneration en route. Unfortunately, real-world lasers vary in wavelength as they operate. The variation is tiny, just hundredths of a percent. But it creates a random backdrop that makes the distortion impossible to filter out.

Radic and his colleagues initially tried to solve the problem by making the lasers more stable, but the effort went nowhere. So they tried a different strategy: ensuring that the laser variation was predictable rather than random. Modern communication equipment typically uses several lasers to produce all the different wavelengths that are sent down the fiber. Instead, Radic's team used a device called a frequency comb to convert light from a single laser, at a single wavelength, into pulses at a range of different wavelengths. Each could then be modulated to carry a separate optical signal.

The upshot is that when the primary laser signal drifts from its original wavelength, each of the daughter pulses then drifts by the exact same amount, all in lockstep. That makes it straightforward to spot distortions and subtract them out. The consequence, Radic says, is that the technology can either pack twice as much data into a fiber or send signals twice as far before they need to be regenerated. Radic adds that his group already has a clear path to doubling this again.

"It's a very important step," Winzer says of the new work. However, he adds, "how practical it is remains to be seen." One issue, he notes, is that implementing this technology will require new chips for both data encoding and signal processing unlike any now available.

Even if the strategy does multiply the data capacity of existing fibers, eventually there will be no alternative to laying more highway, Winzer and others say. Those new cables could contain cutting-edge technology, such as "multimode" fibers with far higher bandwidth than the versions in the ground now. But laying new fiber is very expensive, and therefore the last resort. "Right now, the easiest thing is to mine more out of the existing fiber assets," Vusirikala says. If this new technology makes that possible, it will mean shorter waiting times for those cat videos to appear on your screen. Then again, there are times when a data traffic jam might not be such a bad thing. ■

Q&A

Tapping a nuclear test ban treasure-trove

Treaty chief offers academics surveillance data

By **Daniel Clery**

The Comprehensive Nuclear-Test-Ban Treaty (CTBT) has spawned a globe-girdling network of 300 detector stations that sniff out radionuclides, listen for low-frequency sounds, and record tremors—all to discern whether countries are carrying out clandestine nuclear weapons tests. And the treaty has not yet even come into force; the United States remains a prominent holdout. But the CTBT's $1 billion International Monitoring System is 90% complete and has scored notable successes. Among them: sizing up North Korea's nuclear tests, plotting the spread of radionuclides from the Fukushima nuclear accident, and tracking the spectacular Chelyabinsk meteorite as it broke up over Siberia in 2013.

CTBTO chief Lassina Zerbo is making test ban data more useful to more people.

This global stethoscope is amassing a treasure trove of data. Initially, the CTBT Organization (CTBTO), based in Vienna, didn't share, but after the 2004 Indian Ocean tsunami—when the monitoring system could have given an early warning—things have loosened up. Now, timely data are sent to tsunami warning centers in 13 countries, as well as to civil aviation authorities and nuclear regulators.

This glasnost is due in large part to Lassina Zerbo, director of CTBTO's International Data Centre from 2004 to 2013 and, since then, the organization's executive secretary. Zerbo spoke with *Science* on the eve of the 5th CTBT Science and Technology Conference. His comments have been edited for clarity and brevity.

Q: After the 2004 tsunami, how was wider use of CTBT data encouraged?

A: We got into a series of science and technology conferences whereby we try to think out of the box, moving away from our everyday work on nuclear test monitoring to see what the outside scientific community could do with the technology that we use.

Q: Where did that out-of-the-box thinking lead you?

A: We can detect plane crashes, like the one between Burkina Faso and Mali last July. That was detected by one of our stations in [Ivory Coast]. People want to go beyond that. In Burkina Faso last year, there was a local chief [who described] an explosion 150 meters from his house. Because he was from the opposition party, he was of the view that [the ruling party] sent a missile and it hit the house next to him. We found out [from ultrasound recordings] that it was from mine explosives that someone was keeping in his own house. There are many other examples.

Q: Are academic scientists using your data?

A: Absolutely. We now have 52 contracts [with institutions] and there are many more contracts that are yet to be signed. Now, we have individuals who are doing their own research who want to access our data.

Q: Are any data sets out of bounds?

A: No, I wouldn't say so. The out-of-bounds will be basically on the timeliness of the data. If an explosion happened now, we first have to say whether it's a manmade event or whether it's an earthquake. So if somebody had real-time access to our data, they could say to the media: "I have found that Burkina Faso has carried out a nuclear test explosion." We have to be very careful about real-time data. People don't realize what our radionuclide stations can detect: If you take, let's say, 0.1 grams of an isotope, evenly distributed around the globe, we are able to detect that. You see how crazy that is? It's beyond what you can imagine.

This is why I'm promoting opening up our data. People work with our data and improve the science and technology behind it—it helps us improve the processing as well as the sensitivity of our equipment. It's basically the cheapest consultants that you can get. You're not paying for it. ■

PHOTO: CTBTO/FLICKR

Published by AAAS

ILLUSTRATION: DAVIDE BONAZZI

THE CANCER TEST

A nonprofit's effort to replicate 50 top cancer papers is shaking up labs

By **Jocelyn Kaiser**

The email that arrived in Richard Young's inbox in October 2013 was polite but firm. The writer was part of a group of researchers who "are conducting a study to investigate the reproducibility of recent research findings in cancer biology." A paper that Young, a biologist at the Massachusetts Institute of Technology in Cambridge, had published in *Cell* in 2012 on how a protein called c-Myc spurs tumor growth was among 50 high-impact papers chosen for scrutiny by the Reproducibility Project: Cancer Biology. The group might need help with materials and advice on experimental design, the message said. It also promised that the project would "share our procedure" to ensure "a fair replication."

Young wrote back that a European lab had already published a replication of his study. No matter, the project's representative replied, they still wanted to repeat it. But they needed more information about the protocol. After weeks of emails back and forth and scrambling by graduate students and postdocs to spell out procedures in intricate detail, the group clarified that they did not want to replicate the 30 or so experiments in the *Cell* paper, but just four described in a single key figure. And those experiments would be performed not by another academic lab working in the same area, but by

Downloaded from www.sciencemag.org on June 26, 2015

Published by AAAS

Under the microscope

The Reproducibility Project: Cancer Biology compiled a list of 50 high-impact papers from 2010 to 2012 for replication. The top three studies for each year, listed here by impact rank and last corresponding author, cover topics from the biology of metastasis to drug resistance.

2010

1. ***Nature*, Noncoding role of mRNA in cancer**
   Pier Pandolfi, Harvard University and Beth Israel Deaconess Medical Center
2. ***Cell*, Chromatin-mediated drug resistance**
   Jeff Settleman, Massachusetts General Hospital
3. ***Nature*, Noncoding RNA and metastasis**
   Howard Chang, Stanford University

2011

1. ***Nature*, Brd4 as therapeutic target in leukemia**
   Christopher Vakoc, Cold Spring Harbor Laboratory
2. ***Cell*, New strategy to target c-Myc**
   Constantine Mitsiades, Dana-Farber Cancer Institute
3. ***Cell*, Stromal caveolin-1 and metastasis**
   Miguel Del Pozo, CNIC, Madrid

2012

1. ***Nature*, Genomic markers of cancer drug sensitivity**
   Cyril Benes, Massachusetts General Hospital
2. ***PNAS*, CD47-SIRPa interaction as drug target**
   Irving Weissman, Stanford
3. ***Nature*, Resistance to RAF inhibitors**
   Todd Golub, Broad Institute

an unnamed contract research organization.

This past January, the cancer reproducibility project published its protocol for replicating the experiments, and the waiting began for Young to see whether his work will hold up in their hands. He says that if the project does match his results, it will be unsurprising —the paper's findings have already been reproduced. If it doesn't, a lack of expertise in the replicating lab may be responsible. Either way, the project seems a waste of time, Young says. "I am a huge fan of reproducibility. But this mechanism is not the way to test it."

That is a typical reaction from investigators whose work is being scrutinized by the cancer reproducibility project, an ambitious, open-science effort to test whether key findings in *Science*, *Nature*, *Cell*, and other top journals can be reproduced by independent labs. Almost every scientist targeted by the project who spoke with *Science* agrees that studies in cancer biology, as in many other fields, too often turn out to be irreproducible, for reasons such as problematic reagents and the fickleness of biological systems. But few feel comfortable with this particular effort, which plans to announce its findings in coming months. Their reactions range from annoyance to anxiety to outrage. "It's an admirable, ambitious effort. I like the concept," says cancer geneticist Todd Golub of the Broad Institute in Cambridge, who has a paper on the group's list. But he is "concerned about a single group using scientists without deep expertise to reproduce decades of complicated, nuanced experiments."

Golub and others worry that if the cancer reproducibility project announces that many of the 50 studies failed its test, individual reputations will be damaged and public support for biomedical research undermined. "I really hope that these people are aware of how much responsibility they have," says cancer biologist Lars Zender of the University of Tübingen in Germany.

Timothy Errington, the reproducibility effort's manager at the nonprofit Center for Open Science in Charlottesville, Virginia, knows the scrutiny has unsettled the community. But, he says, the project is working hard to make sure that the labs have all the details they need to match the original studies. The effort will ultimately benefit the field, he says, by gauging the extent of the reproducibility problem in cancer biology. "Some see this as a threat, a way to disprove something. That's not what this is about."

> ***"Some see this as a threat, a way to disprove something. That's not what this is about."***
>
> **Timothy Errington**, Reproducibility Project: Cancer Biology

> ***"You can't give me and Julia Child the same recipe and expect an equally good meal."***
>
> **Jeff Settleman**, Calico Life Sciences

CONCERNS THAT MUCH PRECLINICAL research can't be reproduced are not new, but the spotlight turned to cancer biology 3 years ago, when a commentary in *Nature* reported that scientists from the biotech company Amgen could reproduce only six of 53 high-profile cancer papers. (Another firm, Bayer, had reported a 79% failure rate for a set of mostly cancer studies in 2011.) The Amgen piece argued that irreproducible data contributed to high drug development costs and failed clinical trials. Indeed, a year earlier Amgen had dropped an entire research effort to find drugs targeting a cancer protein called STK33 after it could not confirm key results in a *Cell* paper.

To the frustration of many, the commentary's co-authors Glenn Begley, who had left Amgen to become a consultant, and Lee Ellis of the University of Texas MD Anderson Cancer Center in Houston said confidentiality agreements with some labs barred them from sharing data from their replication efforts or even the titles of the papers. However, Begley, now at TetraLogic Pharmaceuticals in Malvern, Pennsylvania, wrote a follow-up commentary in *Nature* describing the six main problems he found, including a lack of proper controls, faulty statistics, and failure to validate reagents.

At about the same time, cancer biologist Elizabeth Iorns launched the Reproducibility Initiative, which offered to replicate life sciences experiments for a fee through a network of 1000 contract labs she had established, called Science Exchange (*Science*, 31 August 2012, p. 1031). Iorns was inspired by the fact that drug companies often used her network for replications, seeing a chance to avoid wasting money pursuing shaky science. But Iorns had to seek funding to examine academic research, starting with cancer biology. That led her to the Laura and John Arnold Foundation, which introduced her to the Center for Open Science, founded by University of Virginia (UVA) psychologist Brian Nosek to promote transparency in science.

Their collaboration was a new direction for Nosek's center, which had started out with a project to replicate psychology papers by recruiting volunteers from academia (*Science*, 30 March 2012, p. 1558). But for the

Published by AAAS

cancer research replications, which involved messy "wet" biology, organizers decided to pay labs belonging to the Science Exchange—contract labs or fee-based support labs at universities known as core facilities.

Some authors of the top 50 papers suggest that it's a conflict of interest for Iorns's own company to be getting the business. Iorns responds that her firm is not profiting, because it is donating its roughly 5% fee to the project. She says that organizing replication efforts through Science Exchange is faster and cheaper than through academic collaborations, and the results are less likely to be biased, because the scientists doing the work needn't worry about offending their peers with a negative result.

Errington was hired to run the cancer replication project just after completing a Ph.D. in microbiology at UVA. Iorns and a colleague had compiled a list of the 50 most widely cited cancer bio-logy studies from 2010 to 2012 (see table, p. 1412). The topics reflect the field's hottest areas, from new protein drug targets in tumors to the role of gut microbes in cancer. With $1.3 million from the Arnold foundation—which works out to $26,000 per paper, sufficient to replicate key experiments from each paper, Iorns says—and donations of reagents from companies, they sent off their first emails to corresponding authors and posted their progress online.

Early on, Begley, who had raised some of the initial objections about irreproducible papers, became disenchanted. He says some of the papers chosen have such serious flaws, such as a lack of appropriate controls, that attempting to replicate them is "a complete waste of time." He stepped down from the project's advisory board last year.

Amassing all the information needed to replicate an experiment and even figure out how many animals to use proved "more complex and time-consuming than we ever imagined," Iorns says. Principal investigators had to dig up notebooks and raw data files and track down long-gone postdocs and graduate students, and the project became mired in working out material transfer agreements with universities to share plasmids, cell lines, and mice.

To add rigor to the replications, the group decided to publish a peer-reviewed protocol for each experiment before the work began, through a partnership with the open-access journal *eLife*. This has enabled the original authors and outside scientists to provide critical input, Errington says. Charles Sawyers, a researcher at the Memorial Sloan Kettering Cancer Center in New York City and an *eLife* senior editor, says the journal's editors felt that participating would "ensure that the reproducibility experiments are well designed and that the results are as interpretable as possible." So far, the project has published 11 protocols. It hopes to release the first experimental results in *eLife* this fall and all 50 by the end of 2017.

ALTHOUGH ERRINGTON SAYS many labs have been "excited" and happy to participate, that is not what *Science* learned in interviews with about one-fourth of the principal investigators on the 50 papers. Many say the project has been a significant intrusion on their lab's time—typically 20, 30, or more emails over many months and the equivalent of up to 2 weeks of full-time work by a graduate student to fill in protocol details and get information from collaborators. Errington concedes that a few groups have balked and stopped communicating, at least temporarily.

For many scientists, the biggest concern is the nature of the labs that will conduct the replications. It's unrealistic to think contract labs or university core facilities can get the same results as a highly specialized team of academic researchers, they say. Often a graduate student has spent years perfecting a technique using novel protocols, Young says. "We brought together some of the most talented young scientists in the area of gene control and oncology to do these genomics studies. If I thought it was as simple as sending a protocol to a contract laboratory, I would certainly be conducting my research that way," he says.

Jeff Settleman, who left academia for industry 5 years ago and is now at Calico Life Sciences in South San Francisco, California, agrees. "You can't give me and Julia Child the same recipe and expect an equally good meal," he says. Settleman has two papers being replicated.

Academic labs approach replication differently. Levi Garraway of the Harvard University–affiliated Dana-Farber Cancer Institute in Boston, who also has two papers on the project's list, says that if a study doesn't initially hold up in another lab, they might send someone to the original lab to work side by side with the authors. But the cancer reproducibility project has no plans to visit the original lab, and any troubleshooting will be limited to making sure the same protocol is followed, Errington says. Erkki Ruoslahti of the Sanford-Burnham Medical Research Institute in San Diego, California, has a related worry: The lab replicating one of his mouse experiments will run that experiment just one time; he repeated it two or three times.

The scientists behind the cancer reproducibility project dismiss these criticisms. Iorns says the contract labs and core facilities "are highly trained" and often "have much more expertise" than the original investigators in the technique at hand. If a recipe has enough detail, two different cooks should be able to produce the exact same meal, she says.

She adds that the project will generate a vast data set that will allow those interested in reproducibility to examine "all kinds of variables" that determine whether an experiment can be repeated. And she argues that the time and effort it requires of the targeted researchers shows that their papers are short on key information. Researchers should be reporting every detail of an experiment when they publish, down to catalog and lot numbers for reagents and underlying data sets—if not in the paper, through links to other sites, she says: "The biggest lesson so far is that we should change the way that we publish our results."

But many cancer biologists say the solution is not another Amgen-like paper labeling many cancer studies as irreproducible—this time with the titles of the papers and their lead investigators. Instead, journals and reviewers should require more rigorously designed experiments and demand that key conclusions be adequately supported, Settleman says. Many journals are already beefing up review criteria, and the National Institutes of Health is taking steps to bolster reproducibility, for example, by asking study sections to scrutinize a proposal's experimental design. (On page 1422, Nosek and others, including *Science*'s editor-in-chief, suggest journal standards to increase reproducibility.)

Iorns agrees that such reforms are needed, but so is scrutiny of these high-profile papers, which are shaping the search for new cancer treatments. Instead of worrying about damaged reputations and threats to federal funding, the research community "should be worried about the consequences right *now*," she says—that pharmaceutical companies can't reproduce key cancer papers. "All we're saying is, there may be issues with being able to repeat this experiment in another lab. Hiding that is really the biggest mistake." ■

Repeat failures

6 of 53
Cancer papers that Amgen could reproduce

14 of 67
Biomedical papers that Bayer completely reproduced

55%
MD Anderson researchers who could not reproduce a published study

DATA: C. G. BEGLEY AND L. M. ELLIS, *NATURE* **483**, 7391 (29 MARCH 2012); F. PRINZ *ET AL.*, *NATURE REVIEWS DRUG DISCOVERY* **10**, 712 (SEPTEMBER 2011); A. MOBLEY *ET AL.*, *PLOS ONE* **8**, 5 (15 MAY 2013)

Published by AAAS

Alan Stern reviews spacecraft instructions outside New Horizons' mission control room.

PHOTO: PAUL FETTERS

Downloaded from www.sciencemag.org on June 26, 2015

Published by AAAS

MISSION CONTROLLER

How Alan Stern's tenacity, drive, and command got a NASA spacecraft to Pluto

By **Eric Hand**

The video cameras are poised. Alan Stern is loath to miss a cue. Dressed in all black, he strides across the parking lot. Short in stature, Stern has legs that move faster than most people's, and a mind that is generally several steps ahead, too. The camera crew, from the Japanese network NHK, is one of four following Stern, a planetary scientist from the Southwest Research Institute (SWRI) in Boulder, Colorado. They draw a bead on him for an early morning establishing shot. Stern executes a quick flyby. "Hi, Mom," he says, giving a thumbs-up as he enters the space science building at Johns Hopkins University's Applied Physics Laboratory (APL) in Laurel, Maryland.

Above him in the atrium dangles a half-size replica of New Horizons, a NASA spacecraft. Its life-size twin is now cruising through space nearly 5 billion kilometers from Earth, adding more than a million kilometers to its journey each day. The spacecraft is surprisingly small, not much bigger than Stern. But, like him, it is packed with purpose. It is swaddled in layers of foil to protect its instruments and computers from the searing cold. Solar panels would be pointless so far from the sun, and so an engine of radioactive plutonium pulses inside. The backside is dominated by a large radio dish, necessary to talk with Earth across an expanse that takes 4.5 hours for light to traverse.

New Horizons is closing in on Pluto, once thought to be the last of the planets and a lonely outpost on the solar system's edge. Discovered in 1930, Pluto has remained something of a cipher, despite the best efforts of telescopes in space and on the ground. Its changing atmosphere and variegated surface remain mysterious, and even its size is not precisely known. In 2006, Pluto was demoted to a dwarf planet, a move that still annoys Stern. Yet in a karmic reversal, Pluto's scientific and public popularity—its brand, Stern might say—has soared. Pluto is now not the final stop in the solar system, but a gatekeeper to a new frontier: the Kuiper belt, a region of thousands of small icy bodies beyond Neptune's orbit that was theorized by astronomer Gerard Kuiper in 1951 but confirmed only in 1992. No longer the smallest of the planets, Pluto is the king of the Kuiper belt.

On 14 July, New Horizons will zoom past it—50 years to the day after Mariner 4 flew

Published by AAAS

past Mars and returned the first pictures from another planet. Stern has been working toward this moment for half of that half-century: 10 years to muster political and scientific will for a mission, 5 years to build the spacecraft, and nearly 10 years to make the trip. He is the principal investigator for the $700 million mission—the largest and most expensive one ever controlled by a non-NASA employee. Now he is 99% of the way there.

Stern has traveled from Boulder to APL on this day in May to kick off the final science team meeting before the encounter. In a conference room, 50 people hunch over their laptops. On a screen overhead, a video rouses the team: an electronic anthem mashed-up with snippets of control room dialogue from the Apollo 11 moon mission. "Guidance? Go! Control? Go!" shout the ghosts of mission controllers past. Hal Weaver, the project scientist for the mission and a laid-back foil to Stern and his intensity, says, "Alan is going to have this choreographed." In the 30 days prior to reaching Pluto, Stern wants different pep songs played each morning.

Stern takes the podium. Although everything is going great, he says, there are things that could still go wrong. "If it's bugging you, let's make sure we bring it up," he says. His words are cautious, but his tone—commanding, emphatic, confident—is devoid of doubt. "We have the eyes of the world on this mission. It is unlike any other mission in recent history in terms of the expected level of attention. And in addition, we only get one shot at it. It's not an orbiter. It's not a lander." It's a flyby, at Mach 42, and Stern must wring as much out of the short-lived encounter as possible.

Landings on planets (and comets) advertise their complexity with parachutes and airbags, harpoons and retrorockets. Even orbiters, with the tricky, fiery burn of orbital insertion, contain an element of drama. In comparison, a flyby seems a walk in the park—just gravity in motion, and a few clicks of a camera shutter. So you'll forgive Stern for emphasizing how complicated the flyby actually is. In the 9 days of "core encounter"—7 days before closest approach on 14 July to 2 days after—New Horizons will run through 20,799 commands. It must scan the path ahead for hazardous debris, make minor trajectory corrections, and point instruments for 461 scientific observations as it passes within 12,500 kilometers of Pluto's surface. In the hours just after closest approach, the spacecraft must pass through two tiny keyholes in space—the shadows of Pluto and its largest moon, Charon—so that it can use the eclipsed sun as a backlight to examine the thin ring of atmosphere around each body. As it leaves the system of five moons (at last count), New Horizons will continue to stare, and image Pluto's dark side by Charon's moonlight. "Despite the fact that we've done a lot of practicing, we can't simulate everything," Stern says. "My biggest concern is what we haven't thought of."

There are 249 contingency plans in place, attempts to identify—and then mitigate—all known risks. They include not just risks to the spacecraft, like clouds of debris lurking among Pluto's moons, but also those on the ground. Should something happen to the main mission control room, for example, New Horizons can be operated from a backup building at APL. There is even a backup to the backup: The team has prepped a minimalist control room—basically a New Horizons–compatible computer—at the Jet Propulsion Laboratory (JPL) in Pasadena, California.

Scientific enthusiasm at age 6.

And, oh, the practicing. Stern boasts of having performed 35 operational readiness tests—dress rehearsals for various aspects of the mission. In the biggest of these tests, 2 years ago, the spacecraft was put through the motions of its 9-day encounter, somewhere in the void between Uranus and Neptune, its instruments successfully returning precisely framed pictures of empty space. It's not just about smooth operations; the team has also practiced making a splash. There have been three so-called *New York Times* readiness tests, in which the science team interpreted fake data on the fly, under time constraints, and produced press releases meant to be headline-worthy. To help, Stern hired six journalists, had them sign nondisclosure agreements, and embedded them within the science team. "I'd never heard of it," Weaver says. "Several of us pushed back and said, 'You know, we're literate people. We can write our captions.'" Stern was unpersuaded.

One does not get to the edge of the solar system by leaving things to chance. "This mission would not be flying unless he had shoved it down the throat of NASA," says Stern's longtime SWRI colleague, Hal Levison. "His force of will and his tenacity played a role in what's happening right now."

SOL ALAN STERN WAS BORN on 22 November 1957, in New Orleans, Louisiana, the first of three children for Leonard and Joel Stern. He was a fussy baby, difficult to put down to bed. Taking him outside to see the moon seemed to induce sleep. "After many, many repeated applications of that, the first word out of his mouth was 'moon,'" says Leonard Stern, his father. "Not 'mama' or 'dada,' but 'moon.'"

His fascination with celestial objects was galvanized by the space race of the 1960s. He sneaked out of bed to watch late-night TV broadcasts of the Gemini and Mercury flights. He exhausted the local library's selection of space books. He devoured the science fiction of Isaac Asimov and Arthur C. Clarke. But he wanted more. "During one of the Apollo missions, I saw Walter Cronkite showing off the flight plan," he says. "It just mesmerized me. All this detail! That's what I wanted." He requested the materials from NASA, but was told he had to be a journalist or an author. So in the early 1970s, he wrote a book—about a hypothetical mission to a comet. His grandfather's secretary typed up the 100-plus pages, and Stern sent it off to NASA. "Next thing you know, a box this big shows up at my house, filled with Apollo manuals." By then, the family had moved to Dallas, Texas, and Stern was enrolled at St. Mark's, a prep school with a planetarium, an observatory, and an astronomy club. "That is all my brother ate, drank, slept, and breathed," recalls his brother, Leonard "Happy" Stern. "Everything in his being was about how to be in space."

He was gaining other skill sets, too. In 1976, while NASA was landing the Viking probes on Mars, Stern finished his freshman year at the University of Texas (UT), Austin, and took a summer job selling Collier's Encyclopedias. After a tutorial from his father, a salesman for a chemical company, he spent a couple of months crisscrossing the state, knocking on doors. He netted several thousand dollars, enough to trade in his beat-up Buick Skyhawk for an Oldsmobile Cutlass.

Stern has told his father that 80% of what he does now is a sales game. "He learned that selling those encyclopedias, and he's

PHOTO: STERN FAMILY PHOTOGRAPH

Published by AAAS

Stern trains for suborbital space flight in an F-104 jet in 2012.

never forgotten it," Leonard says. Stern demurs. "I object to putting [the Pluto mission] on par with selling encyclopedias," he says. "If you equate the two, it does a disservice to all the other people involved."

Articulate in front of a microphone and at ease in front of a camera, Stern is an eager media subject, sometimes to the irritation of his colleagues. "He likes to generate press for himself, and he is sort of making [the mission] about him," says Levison, one of the few people confident enough in his friendship with Stern to say so. Stern is aware of the criticism, and he declared his qualms about this profile at the outset. "There has to be a recognition that it's not the Alan Stern mission," he said.

Besides honing his talent for persuasion, the young Stern was becoming a careful planner. After graduating from UT in 1978 as a physics major, Stern re-enrolled as a master's student, and roomed with his brother. Happy Stern recalls discovering Alan's day planner. It included not only a 5 a.m. wake up, but also entries, 5 minutes apart, for showering, brushing his teeth, and combing his hair. "You don't think this is a little strange here, pal?" Happy asked him. To this day, Stern carries a sheet of SWRI stationery with him 7 days a week, a black-inked to-do list on which every entry is to be scratched out in red ink by bedtime.

STERN GOT HIS FIRST TASTE of Pluto while a graduate student. Charon had just been discovered in 1978, and astronomers had seen hints that Pluto has an atmosphere—one that would experience strong seasons because of Pluto's highly elliptical orbit and large tilt to the sun. For his master's thesis, Stern modeled the range of atmospheric possibilities. The scope for creative work was enticing, he says. "It was like a green field. You could go anywhere with this."

Stern pursued a double master's, in aerospace engineering and planetary science, in hope of becoming an astronaut candidate. He also became a certified pilot and flight instructor. He met his wife, Carole, while teaching a ground-school flying class, and later proposed to her under the Saturn V rocket on display at NASA's Johnson Space Center in Houston, Texas. "You don't forget that, I'll tell ya," she says.

Stern never made the cut as an astronaut, in part because of a detached retina. So he did the next best thing: He built instruments for astronauts. By 1983, he was working as an engineer at the University of Colorado's Laboratory for Atmospheric and Space Physics. He became the project scientist for Spartan Halley, a small satellite designed to study Halley's Comet, and the principal investigator for the Comet Halley Active Monitoring Program, an experiment in which a crew member aboard the space shuttle would take pictures of the comet with a specially adapted 35-millimeter camera. Both instruments were loaded on the space shuttle Challenger for launch on 28 January 1986.

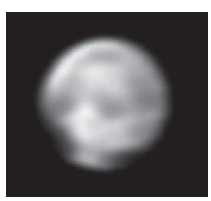

Pluto on 18 June at a distance of 31.5 million kilometers.

"Dick Scobee, Ron McNair, Judy Resnik, [Ellison] Onizuka, Mike Smith." Stern recites the names of five of the seven crew members who died that day when Challenger disintegrated just after launch, people he had trained and knew well. Stern was in Florida for the launch. Then he saw the disaster replayed again and again on the news. "Even if you tried, you couldn't get away from this," he says. It was not just a human loss for Stern, but also a professional disaster, his brother says. "Now he doesn't have a plan, and my brother had a plan for brushing his teeth. I think he was a little lost then."

Stern did not stay down for long. He published his first book, one that seemed to be something of a therapy session. It was called *The U.S. Space Program After Challenger: Where Are We Going?* Then he went back to school. He finished his Ph.D. in 1989, in just 3 years, writing a dissertation on the evolution of comets and their detectability around other stars. The scientifically minded engineer had become a scientist for life.

Not only that, but also a scientific empire builder. Knowing he was not cut out for an academic job—you can imagine his patience tested by faculty senate meetings—Stern found a home at SWRI headquarters in sleepy San Antonio, Texas. SWRI, a soft-money research institute, did most of its business with the Department of Defense. Stern made a pitch to his bosses to stake out a new SWRI outpost in Boulder, devoted to space science. Stern arrived in 1994—just him, a postdoctoral researcher, and a secretary. His first recruit was Levison, an expert on modeling planetary orbits and collisions. "A lot of people [at SWRI] were nervous

PHOTOS: (TOP TO BOTTOM) STARFIGHTERS INC.; NASA/JOHNS HOPKINS UNIVERSITY APPLIED PHYSICS LABORATORY/SOUTHWEST RESEARCH INSTITUTE

Published by AAAS

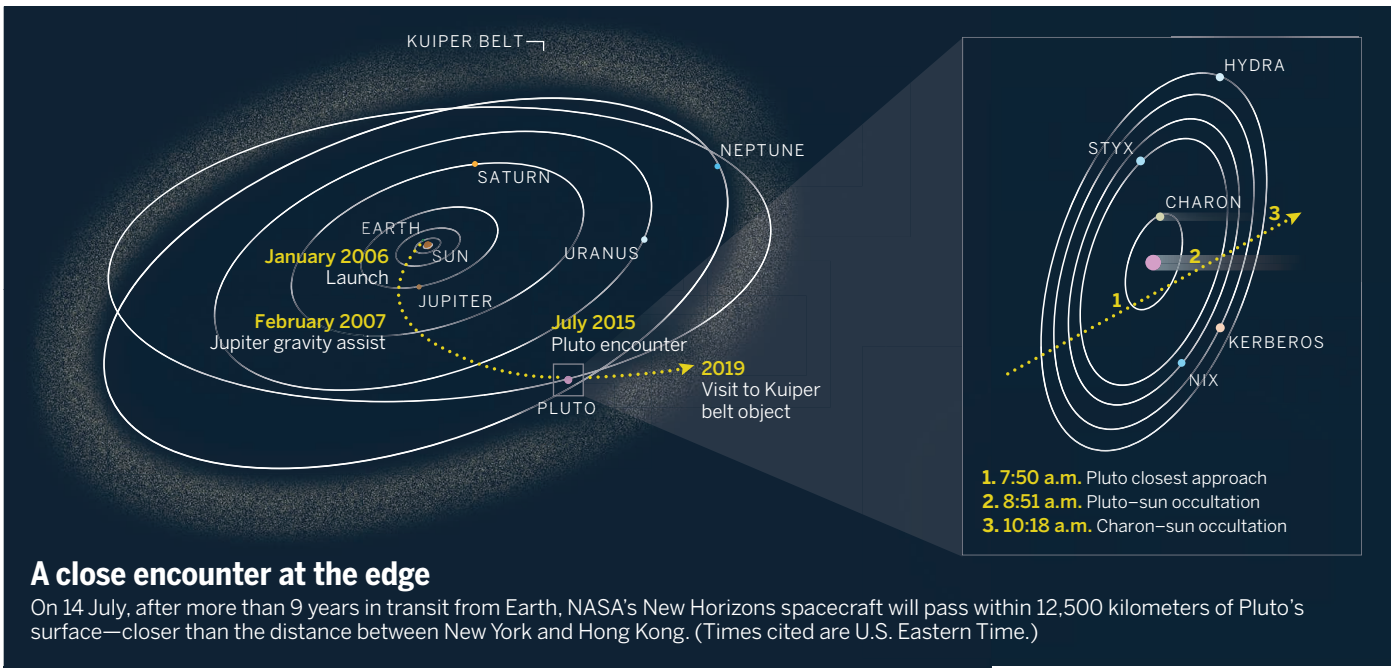

A close encounter at the edge

On 14 July, after more than 9 years in transit from Earth, NASA's New Horizons spacecraft will pass within 12,500 kilometers of Pluto's surface—closer than the distance between New York and Hong Kong. (Times cited are U.S. Eastern Time.)

about taking that sort of risk," Levison says. "Alan in his mastery of politics made it all work." The SWRI Boulder operation today employs 55 scientists and takes in $40 million a year in revenue.

AS STERN'S STAR ROSE, so did Pluto's. For the first 4 decades after its discovery, little could be said about Pluto except that it was small, reddish, and frigid. Even its orbit—observed so far only a third of the way through its 248-year circuit of the sun—was poorly understood. After Charon's discovery, astronomers could watch its dance with Pluto to calculate both bodies' masses. Then, in 1985, Charon and Pluto began eclipsing each other. Ground-based telescopes could barely resolve the two disks, but by measuring the peaks and dips of reflected light as the two orbs passed in and out of each other's shadows, astronomers discovered that Pluto was about half as big as previously thought, and brighter than Charon. In 1988, Pluto eclipsed a distant star, and the light shining around Pluto's edges afforded the first definitive evidence of an atmosphere.

Then came a sign that Pluto was not alone: the 1992 discovery of the first Kuiper belt object (KBO). Pluto, it seemed, represented a much larger class of icy bodies. And because KBOs are thought to be unaltered since the birth of the solar system 4.5 billion years ago, Pluto held the potential of unlocking insights into the earliest days of planet formation.

By the mid-1990s, astronomers were clamoring for a visit, and soon. In 1989, Pluto reached perihelion—the closest point to the sun in its elliptical orbit. Scientists wanted to get there before Pluto began its slow retreat from the sun and temperatures plummeted, collapsing its atmosphere into frozen nitrogen. What's more, a spacecraft launched between 2001 and 2006 could take advantage of Jupiter's gravity for a slingshot effect that would shave years off the trip.

The Pluto Kuiper Express, a mission concept led by JPL, got the farthest. But in 2000, NASA science chief Ed Weiler canceled the mission when its projected costs surpassed $1 billion. Later that year, Weiler was persuaded to try something different: a Pluto competition. A competition for low-cost planetary missions led by principal investigators from outside NASA, called Discovery, had already yielded innovative proposals costing just hundreds of millions of dollars, well short of the billion-dollar budget of a flagship NASA mission. With target costs in the half a billion dollar range, a Pluto competition would sit somewhere between a Discovery mission and a flagship. NASA announced the competition on 20 December 2000.

VIDEO

For a video interview with Alan Stern, see http://scim.ag/AlanStern.

Stamatios "Tom" Krimigis, then the space department head at APL, leaped at the chance. At that point, only JPL had been trusted to build and operate NASA's big planetary missions. But in 1996, APL had launched NASA's first Discovery mission, an asteroid orbiter. With JPL's budget-busting tendencies, Krimigis knew that APL would have a chance. And he knew exactly who should lead the proposal: Alan Stern. "He was the personification of the Pluto mission," Krimigis says. "He was single-minded, and I liked his style."

The duo inked an agreement 2 days after the NASA announcement and began assembling their team. The final proposal was due on 18 September 2001—1 week after the terrorist attacks in New York City. With APL shut down, Stern created a "war room" in a nearby hotel to put the finishing touches on it. In the end, though, it wasn't much of a competition, Weiler says. "Alan was the clear winner."

That was just the beginning of the fight. The Bush administration had installed a new NASA administrator, Sean O'Keefe, who was no fan of the mission, and was instead pushing the idea of nuclear fission–powered spacecraft. When the federal budget request for 2003 came out, in February 2002, the administration had zeroed out the Pluto mission, effectively canceling it.

Weiler challenged Stern to rally planetary scientists' support for the mission in the decadal survey, a once-a-decade, prioritized wish list that's meant to reflect science's unified voice. For months, Stern lobbied tirelessly. When the report appeared in July 2002, the Pluto mission held the top spot in the medium-size mission category, ahead of missions to the moon and to Jupiter. "That's what really broke the logjam," Weiler says. "My administration was not going to fight that."

Stern's team raced to build New Horizons before the gravity assist window closed. The finished spacecraft carried seven instruments, including a student-built interplanetary dust counter and a sensor to mea-

DIAGRAM: G. GRULLÓN/SCIENCE

Published by AAAS

sure the energy of particles escaping from Pluto's atmosphere. Novelties were also stowed aboard: cremated ashes of Pluto's discoverer, Clyde Tombaugh; an old U.S. stamp of Pluto with the caption "Not yet explored"; a piece of SpaceShipOne, private space company Virgin Galactic's first suborbital space vehicle; and two quarters: one from Maryland, whose Senator Barbara Mikulski had given the mission crucial support at its lowest ebb, and one from Florida, where then-Governor Jeb Bush had signed off on the launch of the plutonium-laden spacecraft.

On 13 January 2006, Stern, wearing a clean-room suit and a radiation counter, went to the top of an Atlas V rocket to take one last look. The probe had just been filled with plutonium. Stern posed for a picture, and New Horizons was shut within the payload bay. The Atlas had been souped up with extra boosters and a never-before-used third stage. Six days later, it launched like a bottle rocket, going supersonic within 30 seconds. "This was not a stately shuttle launch," Stern says. New Horizons left Earth faster than any spacecraft ever before.

WITH 9 YEARS TO GO until Pluto arrival, Stern suddenly had a lot more time on his hands. But not for long. In 2007, NASA Administrator Mike Griffin asked Stern to come to Washington, D.C., to lead the agency's $5 billion science division. Upon arrival, Stern asserted his vision of fiscal discipline. He came down hard on missions such as the exoplanet-hunting Kepler telescope, denying it extra funds. He tried to discipline NASA's costly array of Mars missions, too.

Stern speaks to the New Horizons science team in May.

PHOTO: PAUL FETTERS

Curiosity, the $2.5 billion, JPL-built Mars rover, was running hundreds of millions of dollars over budget in an effort to meet a 2009 launch window. Stern wanted to limit the pain to JPL and, more generally, to the Mars program, to ensure that other science wouldn't suffer. In March 2008, he had a subordinate dispatch a letter to JPL ordering it to hold $4 million of money planned for two operating rovers, Spirit and Opportunity, as a reserve for Curiosity. Stern was soon accused of shutting down the beloved older rovers. Griffin, learning about the letter from the media, reversed the decision.

Stern says the $4 million was just a footnote; he and Griffin disagreed more generally over how to apportion the pain of Curiosity cost overruns. "I said, 'You need to find someone else who can deal with that, because I can't stomach it,'" Stern says. He offered his resignation, and Griffin accepted it.

Weiler returned to Washington to resume his old job. Stern had overestimated the power of the position, Weiler says: "He had a hard time realizing you get to make very, very few decisions."

It was the second time in Stern's life that he had suffered a big loss. Once again, he dusted himself off. He returned to SWRI as a half-time employee. His other time was spent consulting for commercial space companies such as Virgin Galactic and Blue Origin and also setting up a few of his own—some of which have raised eyebrows (see sidebar, right).

But for now, Stern's focus is squarely on Pluto. He will be living out of a hotel near APL for the coming weeks, enduring 4:30 a.m. wake-ups and battling his inbox, which at its peak reaches 500 emails a day. At the science team meeting, Stern is about to leave the podium and retreat to a corner table. There, flanked by his assistant, he will whipsaw between email, Twitter, Facebook, and Space.com, one eye always on the proceedings. But before he sits down, he leaves his troops with one last thought. "I said this when we won the project," he says. "It's true again. Our time is finally here."

STERN'S RESTLESSNESS has many people wondering what he will do after the Pluto mission. That won't be for a while. In August, the team will choose the mission's next target: a small KBO. There are two candidates, each about 50 kilometers across and reachable in 2019. New Horizons' next milestone will occur in the late 2040s, when it crosses the edge of the solar system, where the thin wind of particles from the sun peters out—though the spacecraft's plutonium engine will have faded away a decade earlier. After exiting the solar system, New Horizons will wander the galaxy interminably, a relic that will outlive Earth, when the sun goes red giant and swallows it up.

Leonard Stern sees a similar inexhaustibility in his son. "I don't see Alan cutting back. He's just not built that way. I think he thinks there's just so much more that he needs to know. Nobody's driving him but himself." ■

Alan Stern's worldly ventures

By **Eric Hand**

Alan Stern's salesmanship helped get New Horizons to Pluto. He has a few other things for sale as well: a trip to the moon for $1.55 billion, and naming rights to a crater on Mars for $5. Those are the signature products of Golden Spike and Uwingu, two of his companies. Golden Spike plans to send a two-seat lander to the moon, staging material in Earth orbit using commercial rockets. Governments with space ambitions—the target customers—have not lined up to buy tickets, but Stern insists that the company has made progress. "Absence of evidence is not evidence of absence," he says.

Uwingu has had more immediate impact, albeit on a smaller scale. Uwingu raises money for space research through campaigns, such as selling naming rights to martian craters on an unofficial Uwingu map (the bigger the crater, the more expensive the name). Founded in 2012 with a nearly $80,000 crowdsourcing campaign, Uwingu is a for-profit company. Half of the revenues go into a fund for scientific grants—between $130,000 and $150,000 in 2014, Stern says.

Stern and other workers each pay themselves about 1% of the other half of the take. "It's a very small amount of money," he says. Asked if the naming campaigns are a way to poke at the authority of the International Astronomical Union, which is officially in charge of crater names and which rankled Stern by reclassifying Pluto as a dwarf planet in 2006, he says, "honestly, I get a chuckle when I hear that."

Ralph McNutt, a New Horizons scientist at the Johns Hopkins University Applied Physics Laboratory in Laurel, Maryland, says that as an entrepreneur, Stern takes the buckshot approach, throwing up ideas, unsure which ones will stick. "If anybody can pull a rabbit out of the hat in all of this, it's Alan," he says. "But sometimes, I'm not sure if there's a rabbit." ■

Published by AAAS

Design principles for synthetic ecology p. 1425 ▸

Whacking hydrogen into metal p. 1429

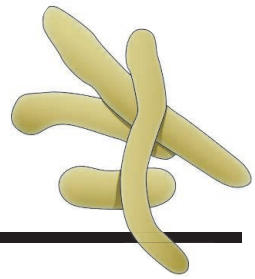

SCIENTIFIC INTEGRITY

Self-correction in science at work

Improve incentives to support research integrity

By **Bruce Alberts,[1] Ralph J. Cicerone,[2] Stephen E. Fienberg,[3] Alexander Kamb,[4] Marcia McNutt,[5]* Robert M. Nerem,[6] Randy Schekman,[7] Richard Shiffrin,[8] Victoria Stodden,[9] Subra Suresh,[10] Maria T. Zuber,[11] Barbara Kline Pope,[12] Kathleen Hall Jamieson[13,14]**

Week after week, news outlets carry word of new scientific discoveries, but the media sometimes give suspect science equal play with substantive discoveries. Careful qualifications about what is known are lost in categorical headlines. Rare instances of misconduct or instances of irreproducibility are translated into concerns that science is broken. The October 2013 *Economist* headline proclaimed "Trouble at the lab: Scientists like to think of science as self-correcting. To an alarming degree, it is not" (*1*). Yet, that article is also rich with instances of science both policing itself, which is how the problems came to *The Economist's* attention in the first place, and addressing discovered lapses and irreproducibility concerns. In light of such issues and efforts, the U.S. National Academy of Sciences (NAS) and the Annenberg Retreat at Sunnylands convened our group to examine ways to remove some of the current disincentives to high standards of integrity in science.

Like all human endeavors, science is imperfect. However, as Robert Merton noted more than half a century ago "the activities of scientists are subject to rigorous policing, to a degree perhaps unparalleled in any other field of activity" (*2*). As a result, as Popper argued, "science is one of the very few human activities—perhaps the only one—in which errors are systematically criticized and fairly often, in time, corrected" (*3*). Instances in which scientists detect and address flaws in work constitute evidence of success, not failure, because they demonstrate the underlying protective mechanisms of science at work.

POLICY

Still, as in any human venture, science writ large does not always live up to its ideals. Although attempts to replicate the 1998 Wakefield study alleging an association between autism and the MMR (measles,

ILLUSTRATION: DAVIDE BONAZZI

Downloaded from www.sciencemag.org on June 26, 2015

Published by AAAS

mumps, and rubella) vaccine quickly discredited the work, it took far too long—12 years—for *The Lancet* to retract that fatally flawed article. By contrast, problems flagged in the January 2014 Obokata pluripotent stem cell papers led to a prompt investigation by the research institute and *Nature* retracting the papers by July 2014.

Leaders in the research community are responsible for ensuring that management systems keep pace with revolutions in research capacity and methods. Consistent with their self-correcting norm, scientists are actively addressing the disconcerting rise in irreproducible findings and retractions. As the *Economist* article itself noted, *PLOS One* and *Science Exchange* had begun an initiative "through which life scientists can pay to have their work validated by an independent lab"; *Nature* had initiated an 18-point checklist for authors "to ensure that all technical and statistical information that is crucial to an experiment's reproducibility or that might introduce bias is published"; and *Perspectives on Psychological Science* developed "a section devoted to replications" (*1*). Conferences such as the Association for Computing Machinery's Special Interest Group on Management of Data have begun to require reproducibility in accepted papers. After Obokata, *Nature* announced measures to increase the likelihood that misrepresented visuals will be detected in the review process (*4*). Other efforts include tighter financial disclosure rules, journal guidelines mandating increased transparency [see Nosek *et al*., page 1422 in this issue (*5*)], and increased data disclosure (*6*). Innovations such as Cross Mark and Retraction Watch have made it easier for scholars to purge retracted work from the scholarly dialogue.

INCENTIVES FOR QUALITY AND CORRECTION. Nosek and his colleagues have argued that some key incentive structures embraced by academia are counterproductive. Researchers are encouraged to publish novel, positive results and to warehouse any negative findings (*7*). Cash bonuses paid in a number of countries have increased the number of submissions to prestigious journals (*8*), and in some instances that work has been fraudulent. Growing numbers of biomedical students funded by the U.S. National Institutes of Health contribute to a pipeline of researchers in serial postdoctoral positions, as well as to declining morale and ever-lengthening time until researchers obtain their first independent research grant.

We believe that incentives should be changed so that scholars are rewarded for publishing well rather than often. In tenure cases at universities, as in grant submissions, the candidate should be evaluated on the importance of a select set of work, instead of using the number of publications or impact rating of a journal as a surrogate for quality. This practice is used in nominations for election to the NAS and selecting honorees in professional societies.

The peer-review process should do a better job of mentoring young reviewers, increasing the clarity and quality of editorial response, and uncovering instances in which a reviewer is biased for or against a particular work. Although this may add to the reviewers' burden, one solution, used by *eLife*, is for reviewers to share their comments with each other and collaborate on a response before sending comments to the author with the editorial decision. *Science*'s cross-review, in which reviews are exchanged between reviewers, allows editors to capture broader input on the reviews before returning them to the authors. Were some reform to be implemented to address bias in reviewing, along with an incentive structure that rewards publishing quality rather than quantity, we suspect that the integrity of science could be better protected at no net increased cost in reviewers' time.

"Ensuring that the integrity of science is protected is the responsibility of many stakeholders."

Reliance on the term "retraction" may create a disincentive to act in the best interests of science. The word "retraction," with its negative connotation, covers withdrawal of scholarship both for inadvertent error and for misconduct. Yet, voluntary withdrawal of findings by a researcher eager to correct an unintended mistake is laudatory, in contrast to involuntary withdrawal by a duplicitous researcher who has published fraudulent claims. Alternative nomenclature such as "voluntary withdrawal" and "withdrawal for cause" might remove stigma from the former while upping it for the latter. "Voluntary withdrawal" would be for papers that are wrong in major respects, cannot be fixed with just a correction, but are not a result of fraud or misconduct. Authors would be encouraged to take this route to avoid leaving confusing papers in the literature and to preserve their reputations. Ideally, some statute of limitations should be placed on voluntary withdrawals. "Withdrawal for cause" would be invoked any time fraud or misconduct taints the published literature. There should be no statute of limitations on withdrawal for cause.

In a similar vein, "conflict of interest" implies that disclosed relationships are corruptive. Adopting more neutral language such as "disclosure of relevant relationships" may encourage more complete compliance without implying that all disclosed associations are sinister.

INVESTIGATION AND EDUCATION. Authoritative and timely investigations into allegations of misconduct are critical to ensuring that flawed findings, which because of fraud or misconduct cannot be redeemed, are formally decertified. Because journals lack the wherewithal to investigate allegations of misconduct in published research, they rely on scholars' home institutions to address such concerns. Funding agencies often play an oversight role. In cases in which the institution is unwilling, conflicted, or incapable of investigating, consequential flawed findings might linger in the literature. A more robust structural solution is needed.

Even when institutions, funders, and journals work in good faith to address misconduct and ensure the accuracy of the research record, they can be overwhelmed by the growing number of allegations, the expense and complexity of investigations, the difficulties in addressing misconduct in international and cross-disciplinary collaborations, and the emergence of technologies that make it easier both to commit misconduct and to detect it. The investigating unit should be respected, neutral, nimble, have wide access to necessary expertise, and be capable of responding regardless of the funding source.

Ensuring that the integrity of science is protected is the responsibility of many stakeholders. In 1992, the NAS called for an independent Scientific Integrity Advisory Board to exercise leadership in addressing ethical issues in research conduct (*9*). Although not implemented, if such an entity were instituted, it could serve as a respected

[1]University of California, San Francisco, CA, USA. [2]National Academy of Sciences, Washington, DC, USA. [3]Carnegie Mellon University, Pittsburgh, PA, USA. [4]Discovery Research, Amgen Inc., Thousand Oaks, CA, USA. [5]Science, American Association for the Advancement of Science, Washington, DC, USA. [6]Georgia Institute of Technology, Atlanta, GA, USA. [7]Howard Hughes Medical Institute and University of California, Berkeley, CA, USA. [8]Indiana University, Bloomington, IN, USA. [9]University of Illinois at Urbana-Champaign, Champaign, IL, USA. [10]Carnegie Mellon University, Pittsburgh, PA, USA. [11]Massachusetts Institute of Technology, Cambridge, MA, USA. [12]National Academies Press, National Academy of Sciences, National Academy of Engineering, Institute of Medicine, National Research Council, Washington, DC, USA. [13]Annenberg Retreat at Sunnylands, Rancho Mirage, CA, USA. [14]Annenberg Public Policy Center, University of Pennsylvania, Philadelphia, PA, USA. *Corresponding author. E-mail: mmcnutt@aaas.org

Published by AAAS

and neutral resource that supports and complements efforts of the research enterprise and its key stakeholders.

Universities should insist that their faculties and students are schooled in the ethics of research, their publications feature neither honorific nor ghost authors, their public information offices avoid hype in publicizing findings, and suspect research is promptly and thoroughly investigated. All researchers need to realize that the best scientific practice is produced when, like Darwin, they persistently search for flaws in their arguments. Because inherent variability in biological systems makes it possible for researchers to explore different sets of conditions until the expected (and rewarded) result is obtained, the need for vigilant self-critique may be especially great in research with direct application to human disease. We encourage each branch of science to invest in case studies identifying what went wrong in a selected subset of nonreproducible publications—enlisting social scientists and experts in the respective fields to interview those who were involved (and perhaps examining lab notebooks or redoing statistical analyses), with the hope of deriving general principles for improving science in each field.

"Instances in which scientists detect and address flaws in work constitute evidence of success, not failure."

Industry should publish its failed efforts to reproduce scientific findings and join scientists in the academy in making the case for the importance of scientific work. Scientific associations should continue to communicate science as a way of knowing, and educate their members in ways to more effectively communicate key scientific findings to broader publics. Journals should continue to ask for higher standards of transparency and reproducibility.

We recognize that incentives can backfire. Still, because those such as enhanced social image and forms of public recognition (*10*, *11*) can increase productive social behavior (*12*), we believe that replacing the stigma of retraction with language that lauds reporting of unintended errors in a publication will increase that behavior. Because sustaining a good reputation can incentivize cooperative behavior (*13*), we anticipate that our proposed changes in the review process will not only increase the quality of the final product but also expose efforts to sabotage independent review. To ensure that such incentives not only advance our objectives but above all do no harm, we urge that each be scrutinized and evaluated before being broadly implemented.

Will past be prologue? If science is to enhance its capacities to improve our understanding of ourselves and our world, protect the hard-earned trust and esteem in which society holds it, and preserve its role as a driver of our economy, scientists must safeguard its rigor and reliability in the face of challenges posed by a research ecosystem that is evolving in dramatic and sometimes unsettling ways. To do this, the scientific research community needs to be involved in an ongoing dialogue. We hope that this essay and the report *The Integrity of Science* (*14*), forthcoming in 2015, will serve as catalysts for such a dialogue.

Asked at the close of the U.S. Constitutional Convention of 1787 whether the deliberations had produced a republic or a monarchy, Benjamin Franklin said "A Republic, if you can keep it." Just as preserving a system of government requires ongoing dedication and vigilance, so too does protecting the integrity of science. ■

REFERENCES AND NOTES

1. Trouble at the lab, *The Economist*, 19 October 2013; www.economist.com/news/briefing/21588057-scientists-think-science-self-correcting-alarming-degree-it-not-trouble.
2. R. Merton, *The Sociology of Science: Theoretical and Empirical Investigations* (University of Chicago Press, Chicago, 1973), p. 276.
3. K. Popper, *Conjectures and Refutations: The Growth of Scientific Knowledge* (Routledge, London, 1963), p. 293.
4. Editorial Board, *Nature* **511**, 5 (2014); www.nature.com/news/stap-retracted-1.15488.
5. B. A. Nosek *et al.*, *Science* **348**, 1422 (2015).
6. Institute of Medicine, *Discussion Framework for Clinical Trial Data Sharing: Guiding Principles, Elements, and Activities* (National Academies Press, Washington, DC, 2014).
7. B. Nosek, J. Spies, M. Motyl, *Perspect. Psychol. Sci.* **7**, 615 (2012).
8. C. Franzoni, G. Scellato, P. Stephan, *Science* **333**, 702 (2011).
9. National Academy of Sciences, National Academy of Engineering, and Institute of Medicine, *Responsible Science, Volume I: Ensuring the Integrity of the Research Process* (National Academies Press, Washington, DC, 1992).
10. N. Lacetera, M. Macis, *J. Econ. Behav. Organ.* **76**, 225 (2010).
11. D. Karlan, M. McConnell, *J. Econ. Behav. Organ.* **106**, 402 (2014).
12. R. Thaler, C. Sunstein, *Nudge: Improving Decisions About Health, Wealth and Happiness* (Yale Univ. Press, New Haven, CT, 2009).
13. T. Pfeiffer, L. Tran, C. Krumme, D. Rand, *J. R. Soc. Interface* **2012**, rsif20120332 (2012).
14. Committee on Science, Engineering, and Public Policy of the National Academy of Sciences, National Academy of Engineering, and Institute of Medicine, *The Integrity of Science* (National Academies Press, forthcoming). http://www8.nationalacademies.org/cp/projectview.aspx?key=49387.

10.1126/science.aab3847

SCIENTIFIC STANDARDS

Promoting an open research culture

Author guidelines for journals could help to promote transparency, openness, and reproducibility

By **B. A. Nosek,* G. Alter, G. C. Banks, D. Borsboom, S. D. Bowman, S. J. Breckler, S. Buck, C. D. Chambers, G. Chin, G. Christensen, M. Contestabile, A. Dafoe, E. Eich, J. Freese, R. Glennerster, D. Goroff, D. P. Green, B. Hesse, M. Humphreys, J. Ishiyama, D. Karlan, A. Kraut, A. Lupia, P. Mabry, T. A. Madon, N. Malhotra, E. Mayo-Wilson, M. McNutt, E. Miguel, E. Levy Paluck, U. Simonsohn, C. Soderberg, B. A. Spellman, J. Turitto, G. VandenBos, S. Vazire, E. J. Wagenmakers, R. Wilson, T. Yarkoni**

POLICY

Transparency, openness, and reproducibility are readily recognized as vital features of science (*1*, *2*). When asked, most scientists embrace these features as disciplinary norms and values (*3*). Therefore, one might expect that these valued features would be routine in daily practice. Yet, a growing body of evidence suggests that this is not the case (*4*–*6*).

A likely culprit for this disconnect is an academic reward system that does not sufficiently incentivize open practices (*7*). In the present reward system, emphasis on innovation may undermine practices that support verification. Too often, publication requirements (whether actual or perceived) fail to encourage transparent, open, and reproducible science (*2*, *4*, *8*, *9*). For example, in a transparent science, both null results and statistically significant results are made available and help others more accurately assess the evidence base for a phenomenon. In the present culture, however, null results are published less frequently than statistically significant results (*10*) and are, therefore, more likely inaccessible and lost in the "file drawer" (*11*).

The situation is a classic collective action problem. Many individual researchers lack

Downloaded from www.sciencemag.org on June 26, 2015

Published by AAAS

strong incentives to be more transparent, even though the credibility of science would benefit if everyone were more transparent. Unfortunately, there is no centralized means of aligning individual and communal incentives via universal scientific policies and procedures. Universities, granting agencies, and publishers each create different incentives for researchers. With all of this complexity, nudging scientific practices toward greater openness requires complementary and coordinated efforts from all stakeholders.

THE TRANSPARENCY AND OPENNESS PROMOTION GUIDELINES. The Transparency and Openness Promotion (TOP) Committee met at the Center for Open Science in Charlottesville, Virginia, in November 2014 to address one important element of the incentive systems: journals' procedures and policies for publication. The committee consisted of disciplinary leaders, journal editors, funding agency representatives, and disciplinary experts largely from the social and behavioral sciences. By developing shared standards for open practices across journals, we hope to translate scientific norms and values into concrete actions and change the current incentive structures to drive researchers' behavior toward more openness. Although there are some idiosyncratic issues by discipline, we sought to produce guidelines that focus on the commonalities across disciplines.

Standards. There are eight standards in the TOP guidelines; each moves scientific communication toward greater openness. These standards are modular, facilitating adoption in whole or in part. However, they also complement each other, in that commitment to one standard may facilitate adoption of others. Moreover, the guidelines are sensitive to barriers to openness by articulating, for example, a process for exceptions to sharing because of ethical issues, intellectual property concerns, or availability of necessary resources. The complete guidelines are available in the TOP information commons at http://cos.io/top, along with a list of signatories that numbered 86 journals and 26 organizations as of 15 June 2015. The table provides a summary of the guidelines.

First, two standards reward researchers for the time and effort they have spent engaging in open practices. (i) Citation standards extend current article citation norms to data, code, and research materials. Regular and rigorous citation of these materials credit them as original intellectual contributions. (ii) Replication standards recognize the value of replication for independent verification of research results and identify the conditions under which replication studies will be published in the journal. To progress, science needs both innovation and self-correction; replication offers opportunities for self-correction to more efficiently identify promising research directions.

Second, four standards describe what openness means across the scientific process so that research can be reproduced and evaluated. Reproducibility increases confidence in results and also allows scholars to learn more about what results do and do not mean. (i) Design standards increase transparency about the research process and reduce vague or incomplete reporting of the methodology. (ii) Research materials standards encourage the provision of all elements of that methodology. (iii) Data sharing standards incentivize authors to make data available in trusted repositories such as Dataverse, Dryad, the Interuniversity Consortium for Political and Social Research (ICPSR), the Open Science Framework, or the Qualitative Data Repository. (iv) Analytic methods standards do the same for the code comprising the statistical models or simulations conducted for the research. Many discipline-specific standards for disclosure exist, particularly for clinical trials and health research more generally (e.g., www.equator-network.org). Many more are emerging for other disciplines, such as those developed by *Psychological Science* (*12*).

Finally, two standards address the values resulting from preregistration. (i) Standards for preregistration of studies facilitate the discovery of research, even unpublished research, by ensuring that the existence of the study is recorded in a public registry. (ii) Preregistration of analysis plans certify the distinction between confirmatory and exploratory research, or what is also called hypothesis-testing versus hypothesis-generating research. Making transparent the distinction between confirmatory and exploratory methods can enhance reproducibility (*3*, *13*, *14*).

Levels. The TOP Committee recognized that not all of the standards are applicable to all journals or all disciplines. Therefore, rather than advocating for a single set of guidelines, the TOP Committee defined

*Corresponding author. E-mail: nosek@virginia.edu
Affiliations for the authors, all of whom are members of the TOP Guidelines Committee, are given in the supplementary materials.

ILLUSTRATION: DAVIDE BONAZZI

Published by AAAS

three levels for each standard. Level 1 is designed to have little to no barrier to adoption while also offering an incentive for openness. For example, under the analytic methods (code) sharing standard, authors must state in the text whether and where code is available. Level 2 has stronger expectations for authors but usually avoids adding resource costs to editors or publishers that adopt the standard. In Level 2, journals would require code to be deposited in a trusted repository and check that the link appears in the article and resolves to the correct location. Level 3 is the strongest standard but also may present some barriers to implementation for some journals. For example, the journals *Political Analysis* and *Quarterly Journal of Political Science* require authors to provide their code for review, and editors reproduce the reported analyses publication. In the table, we provide "Level 0" for comparison of common journal policies that do not meet the transparency standards.

Adoption. Defining multiple levels and distinct standards facilitates informed decision-making by journals. It also acknowledges the variation in evolving norms about research transparency. Depending on the discipline or publishing format, some of the standards may not be relevant for a journal. Journal and publisher decisions can be based on many factors—including their readiness to adopt modest to stronger transparency standards for authors, internal journal operations, and disciplinary norms and expectations. For example, in economics, many highly visible journals such as *American Economic Review* have already adopted strong policies requiring data sharing, whereas few psychology journals have comparable requirements.

In this way, the levels are designed to facilitate the gradual adoption of best practices. Journals may begin with a standard that rewards adherence, perhaps as a step toward requiring the practice. For example, *Psychological Science* awards badges for "open data," "open materials," and "preregistration" (*12*), and approximately 25% of accepted articles earned at least one badge in the first year of operation.

The Level 1 guidelines are designed to have minimal effect on journal efficiency and workflow while also having a measurable impact on transparency. Moreover, although higher levels may require greater implementation effort up front, such efforts may benefit publishers and editors and the quality of publications by, for example, re-

Summary of the eight standards and three levels of the TOP guidelines

Levels 1 to 3 are increasingly stringent for each standard. Level 0 offers a comparison that does not meet the standard.

	LEVEL 0	LEVEL 1	LEVEL 2	LEVEL 3
Citation standards	Journal encourages citation of data, code, and materials—or says nothing.	Journal describes citation of data in guidelines to authors with clear rules and examples.	Article provides appropriate citation for data and materials used, consistent with journal's author guidelines.	Article is not published until appropriate citation for data and materials is provided that follows journal's author guidelines.
Data transparency	Journal encourages data sharing—or says nothing.	Article states whether data are available and, if so, where to access them.	Data must be posted to a trusted repository. Exceptions must be identified at article submission.	Data must be posted to a trusted repository, and reported analyses will be reproduced independently before publication.
Analytic methods (code) transparency	Journal encourages code sharing—or says nothing.	Article states whether code is available and, if so, where to access them.	Code must be posted to a trusted repository. Exceptions must be identified at article submission.	Code must be posted to a trusted repository, and reported analyses will be reproduced independently before publication.
Research materials transparency	Journal encourages materials sharing—or says nothing	Article states whether materials are available and, if so, where to access them.	Materials must be posted to a trusted repository. Exceptions must be identified at article submission.	Materials must be posted to a trusted repository, and reported analyses will be reproduced independently before publication.
Design and analysis transparency	Journal encourages design and analysis transparency or says nothing.	Journal articulates design transparency standards.	Journal requires adherence to design transparency standards for review and publication.	Journal requires and enforces adherence to design transparency standards for review and publication.
Preregistration of studies	Journal says nothing.	Journal encourages preregistration of studies and provides link in article to preregistration if it exists.	Journal encourages preregistration of studies and provides link in article and certification of meeting preregistration badge requirements.	Journal requires preregistration of studies and provides link and badge in article to meeting requirements.
Preregistration of analysis plans	Journal says nothing.	Journal encourages preanalysis plans and provides link in article to registered analysis plan if it exists.	Journal encourages preanalysis plans and provides link in article and certification of meeting registered analysis plan badge requirements.	Journal requires preregistration of studies with analysis plans and provides link and badge in article to meeting requirements.
Replication	Journal discourages submission of replication studies—or says nothing.	Journal encourages submission of replication studies.	Journal encourages submission of replication studies and conducts blind review of results.	Journal uses Registered Reports as a submission option for replication studies with peer review before observing the study outcomes.

Published by AAAS

ducing time spent on communication with authors and reviewers, improving standards of reporting, increasing detectability of errors before publication, and ensuring that publication-related data are accessible for a long time.

Evaluation and revision. An information commons and support team at the Center for Open Science is available (top@cos.io) to assist journals in selection and adoption of standards and will track adoption across journals. Moreover, adopting journals may suggest revisions that improve the guidelines or make them more flexible or adaptable for the needs of particular subdisciplines.

The present version of the guidelines is not the last word on standards for openness in science. As with any research enterprise, the available empirical evidence will expand with application and use of these guidelines. To reflect this evolutionary process, the guidelines are accompanied by a version number and will be improved as experience with them accumulates.

Conclusion. The journal article is central to the research communication process. Guidelines for authors define what aspects of the research process should be made available to the community to evaluate, critique, reuse, and extend. Scientists recognize the value of transparency, openness, and reproducibility. Improvement of journal policies can help those values become more evident in daily practice and ultimately improve the public trust in science, and science itself. ■

REFERENCES AND NOTES

1. M. McNutt, *Science* **343**, 229 (2014).
2. E. Miguel *et al.*, *Science* **343**, 30 (2014).
3. M. S. Anderson, B. C. Martinson, R. De Vries, *J. Empir. Res. Hum. Res. Ethics* **2**, 3 (2007).
4. J. P. A. Ioannidis, M. R. Munafò, P. Fusar-Poli, B. A. Nosek, S. P. David, *Trends Cogn. Sci.* **18**, 235 (2014).
5. L. K. John, G. Loewenstein, D. Prelec, *Psychol. Sci.* **23**, 524 (2012).
6. E. H. O'Boyle Jr., G. C. Banks, E. Gonzalez-Mule, *J. Manage.* 10.1177/0149206314527133 (2014).
7. B. A. Nosek, J. R. Spies, M. Motyl, *Perspect. Psychol. Sci.* **7**, 615 (2012).
8. J. B. Asendorpf *et al.*, *Eur. J. Pers.* **27**, 108 (2013).
9. J. P. Simmons, L. D. Nelson, U. Simonsohn, *Psychol. Sci.* **22**, 1359 (2011).
10. A. Franco, N. Malhotra, G. Simonovits, *Science* **345**, 1502 (2014).
11. R. Rosenthal, *Psychol. Bull.* **86**, 638 (1979).
12. E. Eich, *Psychol. Sci.* **25**, 3 (2014).
13. E.-J. Wagenmakers, R. Wetzels, D. Borsboom, H. L. van der Maas, R. A. Kievit, *Perspect. Psychol. Sci.* **7**, 632 (2012).
14. C. D. Chambers, *Cortex* **49**, 609 (2013).

ACKNOWLEDGMENTS

This work was supported by the Laura and John Arnold Foundation.

SUPPLEMENTARY MATERIALS

www.sciencemag.org/content/348/6242/1422/suppl/DC1

10.1126/science.aab2374

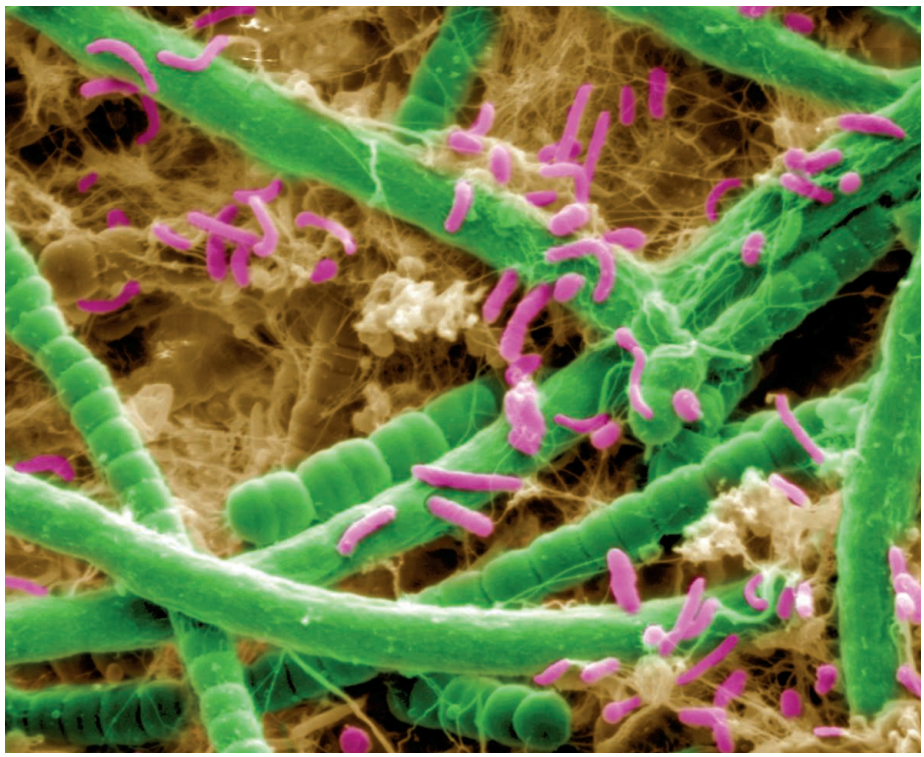

PHOTO: ALICE DOHNALKOVA/PNNL

Learning from nature. Photomicrograph of cyanobacterial-heterotroph microbial consortia derived from a phototrophic microbial mat community from a saline lake. Emerging understanding of cooperative mechanisms in such communities may be helpful in the design of synthetic communities for use in biotechnology.

ECOLOGY

Ecological communities by design

Synthetic ecology requires knowledge of how microbial communities function

By **James K. Fredrickson**

In synthetic ecology, a nascent offshoot of synthetic biology, scientists aim to design and construct microbial communities with desirable properties. Such mixed populations of microorganisms can simultaneously perform otherwise incompatible functions (*1*). Compared with individual organisms, they can also better resist losses in function as a result of environmental perturbation or invasion by other species (*2*). Synthetic ecology may thus be a promising approach for developing robust, stable biotechnological processes, such as the conversion of cellulosic biomass to biofuels (*3*). However, achieving this will require detailed knowledge of the principles that guide the structure and function of microbial communities (see the image).

Recent work with synthetic communities is shedding light on microbial interactions that may lead to new principles for community design and engineering. In game theory, cooperators provide publicly available goods that benefit all, whereas cheaters exploit those goods without reciprocation. The tragedy of the commons predicts that cheaters are more fit than cooperators, eventually destroying the cooperation. Yet, this is not borne out by observations. For example, using a synthetic consortium of genetically modified yeast to represent cooperators and cheaters, Waite and Shou (*4*) found that, although initially less fit than cheaters, cooperators rapidly dominated in a fraction of the cultures. The evolved cooperators harbored mutations allowing them to grow at much lower nutrient concentrations than their ancestor. This suggests that the tragedy of the commons can be avoided

Published by AAAS

if, during adaptation, the fitness gain of cooperators exceeds that of the cheaters by at least the cost of cooperation (see the figure).

The work by Asfahl *et al.* provides another example of deferring the tragedy of the commons via nonsocial adaptation (*5*). The opportunistic pathogen *Pseudomonas aeruginosa* uses diffusible signaling molecules, in a process known as quorum sensing (QS), to regulate public goods—resources that can benefit the entire community. Under growth conditions that require QS-regulated public goods, mutations in the transcriptional regulator *psdR* give rise to a nonsocial adaptation. This mutation has no effect on public goods expression; rather, it increases the fitness of individuals harboring the mutation by improving intracellular metabolism of the goods. Although the adapted population is still subject to invasion by cheaters, the mutation affords a higher fitness (growth rate) that increases the population's tolerance of cheaters, thus maintaining cooperative behavior. This suggests that fitness adaptations are a fundamental mechanism by which cooperative communities can be maintained under the persistent threat of cheaters.

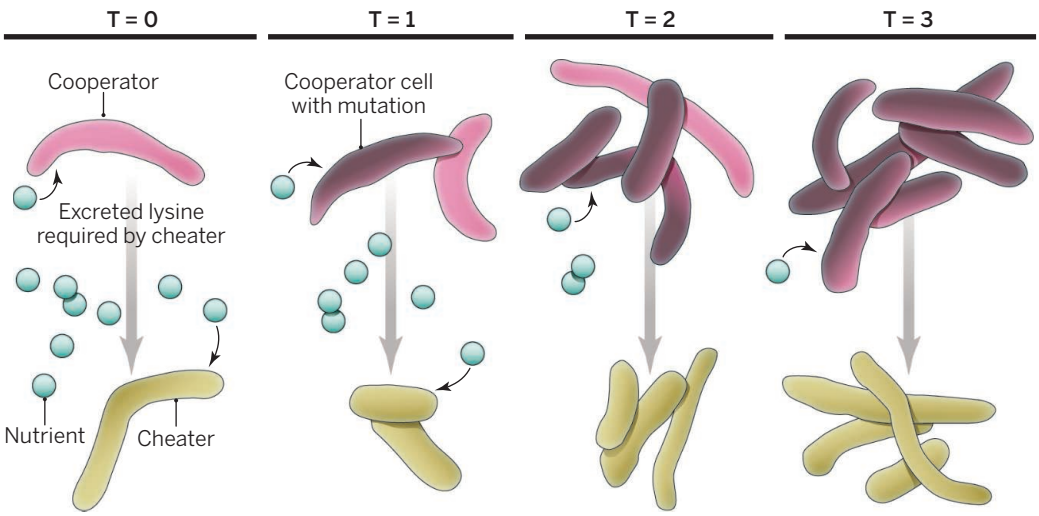

Adaptive race. In cooperative communities, cheaters use common goods without paying the cost to produce them. In the absence of adaptation or adaptive mutations, the cheaters eventually win out but cause the system to collapse. In synthetic communities of cooperators that excrete lysine and cheaters that require lysine, both species adapt to cope with limited resources. In the example shown, a mutation in a cooperator allows the mutated strain to outcompete its ancestors over time. This mechanism explains why cooperating microbial communities can persist in changing environments. For further details, see (*4*).

Microbial communities also cooperate through metabolic cross-feeding or syntrophy, where one organism synthesizes a compound that another organism requires but cannot produce. For example, amino acids and sugar exchange are common mutualistic interactions in co-occurring subcommunities from different habitats (*6*). In a recent study, Mee *et al.* (*7*) explored the basic principles of syntrophic exchange in synthetic communities consisting of *Escherichia coli* mutants auxotrophic for different amino acids. They found that stronger cooperative interactions were promoted between cells exchanging metabolically expensive amino acids compared to those that are cheaper to synthesize. Hence, amino acid auxotrophy may be a common strategy by which microbial communities lessen the collective metabolic burden of biosynthesis and stabilize cooperation. Further evidence for this comes from the persistence of metabolic cooperation between different *E. coli* amino acid auxotrophs in adaptively evolved cocultures (*8*).

Inherent to community productivity is the question of what maintains cross-feeding in the presence of metabolically independent noncooperators. Pande *et al.* (*9*) addressed this question with synthetic communities of *E. coli* that had been genetically modified to require uptake of certain amino acids for growth and to release other amino acids into the environment. Most cross-feeding consortia grew more rapidly than the parental bacterium that could synthesize all the amino acids needed for growth; this was the case even when the consortia were cultivated with the parent and therefore in direct competition for nutrients. The authors attributed the greater fitness of the cooperating consortia to a metabolic division of labor. Here, the added costs of producing an excess of one or more amino acids to benefit the community were more than compensated for by the reduced costs incurred by not having to synthesize all amino acids de novo. The loss of specific biosynthetic functions can give rise to stable metabolic interactions that benefit the interacting organisms. This likely explains why amino acid exchange is common among members of microbial communities throughout the biosphere (*7*).

In some cases, the interactions between community members that give rise to higher-order properties emerge only when distinct physical structures are formed. A coculture of *P. aeruginosa*, *Pseudomonas protegens*, and *Klebsiella pneumoniae* forms a mixed-species biofilm that collectively exhibits greater resistance to antimicrobials (tobramycin and sodium dodecyl sulfate) than do biofilms of the individual species (*10*). Furthermore, when the mixed culture is grown planktonically and treated with tobramycim, only the more resistant *P. protegens* survive. The results indicate that species composition and spatial organization can affect higher-order properties such as stress resistance. It remains unclear how the spatial organization of different species in mixed biofilms helps to make them resilient.

Model systems derived from natural communities have tremendous untapped potential to uncover the genetic, biochemical, and evolutionary bases for ecological interactions at play in more complex systems (*11*). Microbial oxygenic phototrophs are ubiquitous worldwide and host diverse microbes that can influence the physiology and ecology of the host. Sison-Mangus *et al.* (*12*) investigated how coadaptation affects the interactions between *Pseudo-nitzschia*, a genus of marine diatoms, and the bacteria associated with them. They discovered that individual species of the diatom harbor phylogenetically distinct bacterial communities and that the communities associated with species that produce the toxin domoic acid are less diverse. Transplant experiments to assess coevolution effects on host fitness revealed that bacteria conferred stronger fitness to their natural host than to non-native diatoms. That some organisms may select for specific microbes they host, possibly through metabolite secretion, suggests this may be an effective approach for designing synthetic communities.

Colonization resistance, defined as the capacity for the native community to resist invasion, is thought to be a major function of the microbiome. To explore mecha-

Pacific Northwest National Laboratory (PNNL), Richland, WA 99352, USA. E-mail: jim.fredrickson@pnnl.gov

Published by AAAS

nisms of colonization resistance, He *et al.* (*13*) investigated a community cultivated from mouse oral cavity that could detect the presence of *E. coli* and enhance its lethality toward the invader by elevating H_2O_2 production (*14*). Using information from the simplified oral microbiome, the authors constructed a synthetic consortia consisting of three mice oral bacterial species from previous studies and used it to investigate colonization resistance mechanisms. Their results revealed the roles of the three species: *Streptococcus saprophyticus* functions as a sensor by detecting *E. coli* lipopolysaccharide, whereas *Streptococcus infantis* serves as a mediator that detects a diffusible signal from the sensor and relays information to the killer (*Staphylococcus sanguinus*), which turns on H_2O_2 production. These mechanistic details of interactions provide insight into how microbiomes might be designed and engineered to resist invasion.

Substantial challenges remain before synthetic ecology can be successfully applied to biotechnologies such as consolidated bioprocessing of lignocellulosic biomass for biofuel production. For example, it remains to be shown how interactions among community members drive assembly and structure and how these interactions give rise to higher-order properties. To gain a better understanding of these processes, scientists must identify and quantify the numerous biomolecules produced and secreted by microbes in communities and link the exchanges of these molecules to specific organisms and the genes involved in production and consumption. ■

REFERENCES AND NOTES

1. D. R. Johnson, F. Goldschmidt, E. E. Lilja, M. Ackermann, *ISME J.* **6**, 1985 (2012).
2. K. Brenner, L. You, F. H. Arnold, *Trends Biotechnol.* **26**, 483 (2008).
3. J. J. Minty *et al.*, *Proc. Natl. Acad. Sci. U.S.A.* **110**, 14592 (2013).
4. A. J. Waite, W. Shou, *Proc. Natl. Acad. Sci. U.S.A.* **109**, 19079 (2012).
5. K. L. Asfahl *et al.*, *ISME J.* 10.1038/ismej.2014.259 (2015).
6. A. Zelezniak *et al.*, *Proc. Natl. Acad. Sci. U.S.A.* **112**, 6449 (2015).
7. M. T. Mee, J. J. Collins, G. M. Church, H. H. Wang, *Proc. Natl. Acad. Sci. U.S.A.* **111**, E2149 (2014).
8. X. Zhang, J. L. Reed, *PLOS ONE* **9**, e108297 (2014).
9. S. Pande *et al.*, *ISME J.* **8**, 953 (2014).
10. K. W. Lee *et al.*, *ISME J.* **8**, 894 (2014).
11. C. M. Jessup *et al.*, *Trends Ecol. Evol.* **19**, 189 (2004).
12. M. P. Sison-Mangus, S. Jiang, K. N. Tran, R. M. Kudela, *ISME J.* **8**, 63 (2014).
13. X. He *et al.*, *ISME J.* **8**, 564 (2014).
14. X. He *et al.*, *Microb. Ecol.* **60**, 655 (2010).

ACKNOWLEDGMENTS

This work was supported by the U.S. Department of Energy, Office of Biological and Environmental Research (BER), as part of BER's Genomic Science Program (GSP). This contribution originates from the GSP Foundational Scientific Focus Area at the PNNL. Image courtesy of A. Dohnalkova, PNNL.

10.1126/science.aab0946

MICROBIOTA

Mother's littlest helpers

Breastmilk nourishes the microbes colonizing the neonatal intestinal tract

By **Katie Hinde**[1] *and* **Zachery T. Lewis**[2]

Commensal bacteria underlie, in part, our nutritional status, immune function, and psychological well-being. The trillions of beneficial microbes within our intestinal tract convert dietary nutrients, inhibit pathogen colonization, regulate immune processes, and produce neural signals (*1*, *2*). Advances in our understanding of the importance of microbes have motivated the commercial development of products intended to boost "good" commensals and confer health benefits. Probiotic dietary supplements contain live beneficial microbes hoped to subsequently colonize the gut. Prebiotic nutrients are thought to enhance good gastrointestinal microflora by preferentially nourishing beneficial microbes. Even "psychobiotics" are being explored to ameliorate symptoms of psychiatric illness. These live organisms influence the brain through metabolites and neuroactive compounds in rodent models and preliminary human studies (*3*). How to most effectively be the landscape architects of our microbial community, however, often remains unclear. An opportunity to gain insights into how natural selection has shaped the coevolution of hosts and microbes can be found in mammalian mother-infant dyads, as our microbiota are ecologically engineered by mothers and breastmilk. Such insights can be leveraged to improve clinical management and nutritional technologies, enhancing human health not just in infancy, but across the life course (*4*, *5*).

Establishment and maintenance of the microbial community within the human infant gut vary as a function of bacterial exposure, successful colonization, and sustained nutrition. Perinatal exposure is a function of highly variable birth experiences within and across cultures, from Cesarian delivery in a hospital surgical suite to a vaginal birth in a traditional village home (*1*, *2*, *5*). As such, microbial transfer from the surrounding people, animals, and surfaces to the neonate varies substantially. Microbes are also present in breastmilk and may contribute to the developing infant gut microbiome, but this is currently an open question. The origin of these milk microbes may lie in the established pathways of surface skin contamination and retrograde flow (salivary backwash) as a result of the intra-oral vacuum dynamics of suckling (*6*), or via the more speculative translocation to milk through a gut-mammary route (*5*, *7*).

Once breastmilk is in the intestinal environment of an infant, intense microbial competition exists for both space and nutrients. The major available carbon source, human milk glycans, are complex oligosaccharide and glycoconjugate compounds that typically pass undigested from the infant stomach because eutherian mammals (those with a placenta) lack enzymes to cleave them (*8*, *9*). Investigations of the structure of milk oligosaccharides reveal that human milk has a greater diversity (>200 isomers), more complexity, and higher abundance than the milk of other primates, including all of the great apes (*4*, *8*). Importantly, certain oligosaccharides that dominate human milk, but are absent or rare in other primates, are the preferred food of *Bifidobacterium*, the most prevalent microbial clade in the healthy infant gut (*8*).

> ***"...our microbiota are ecologically engineered by mothers and breastmilk."***

Bifidobacterium was first described as a major member of the infant gut community over 40 years ago. More recently, it was demonstrated that the model "breastfed-infant-type" bifidobacteria, *B. longum* subsp. *infantis,* has genes encoding proteins predicted to bind, import, cleave, and metabolize the major oligosaccharides present in human milk (*10*). Variation in the oligosaccharide profile in breast milk (within and among mothers) influences the timing and type of microbial community established in an infant, both at the level of broad microbial clades and among bifidobacterial species (*11*). Bifidobacterial consumption of oligosaccharides produces short-chain fatty acids such as acetate and butyrate, some of which are used as a fuel source by infant

[1]*Department of Human Evolutionary Biology, Harvard University, Boston, MA, USA.* [2]*Department of Food Science and Technology, University of California–Davis, Davis, CA, USA.* *E-mail: khinde@fas.harvard.edu*

Downloaded from www.sciencemag.org on June 26, 2015

Published by AAAS

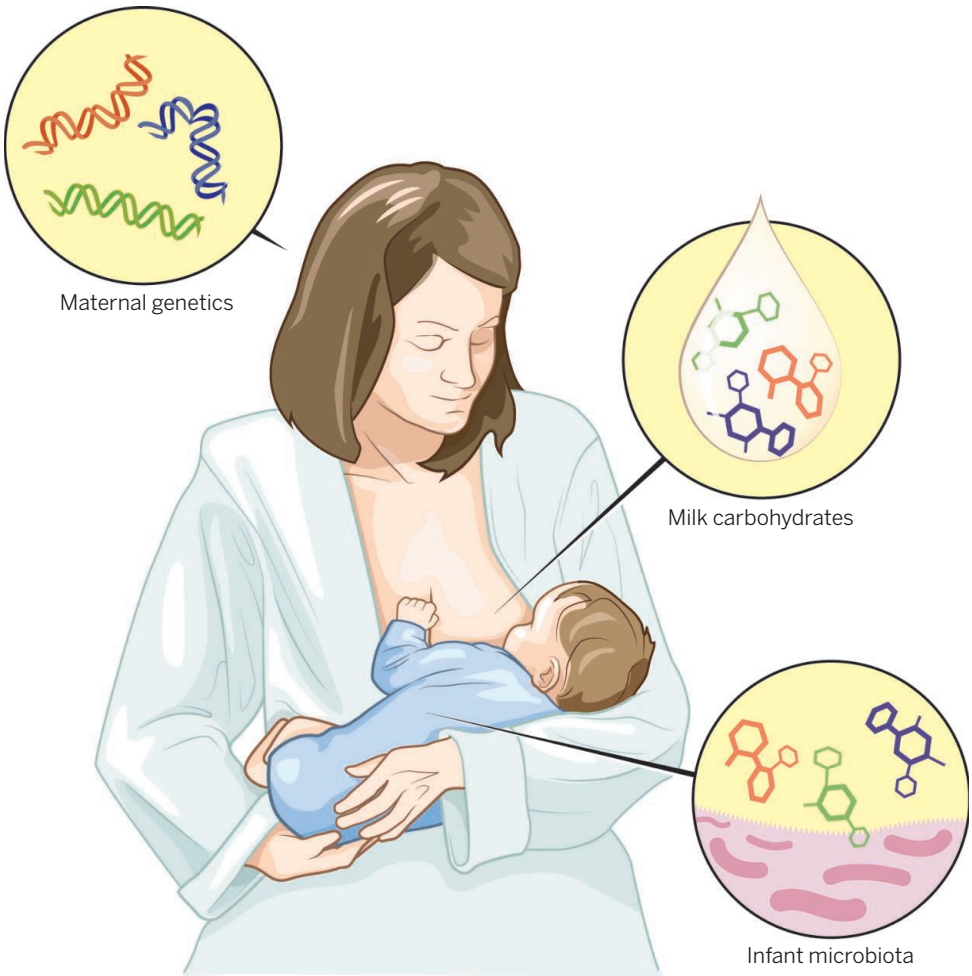

Of milk and microbes. The oligosaccharide content of a mother's breastmilk may influence the gut microbiota—and consequently, the health and well-being—of an infant.

colonocytes, can aid the infant's immune system, and can create a low environmental pH in the gastrointestinal tract that is hostile to some pathogens (*1*, *5*).

To date, the most studied variation in milk oligosaccharide profile has been the presence, abundance, and composition of fucosylated oligosaccharides. Mutations of the *FUT2* "secretor" gene influence the structure of milk oligosaccharides by preventing 2′ fucosylation (*11*). In a sample of mothers from a WEIRD population (Western, educated, industrialized, rich, democratic), bifidobacteria were established earlier and more often in infants breastfed by mothers without mutations in *FUT2* (*11*). Although maternal genotype influences the carbohydrate support of bacteria in the infant intestinal tract, whether infant genotype or gene expression influences the intestinal environment for hosting microbes has not been described. How infants are agents in their own development, as well as the potential outcomes when there is concordance or discordance between the mother's and infant's genotypes, are topics of future research.

Bifidobacterial preponderance, particularly of "breastfed-infant-type" species, is associated with better infant health and development. Bifidobacteria seemingly aid in the proper function of intestinal epithelial cells, enhancing barrier function and inducing anti-inflammatory signaling (*5*). Recently, Bangladeshi infants colonized by high amounts of *B. longum* subsp. *infantis* were shown to have a larger thymus (where lymphocytes mature) and multiple indicators of better cell-mediated immunity (*12*). These infants had better peripheral T cell response to *Staphylococcus* enterotoxin B and better T cell response following vaccination against the oral polio virus and tetanus toxoid. Because infant and child vaccination is a central component of public health, minimizing microbial dysbiosis is likely an important feature of the success of vaccination campaigns.

Ongoing and future studies that systematically integrate the use of probiotics, prebiotics, and breastmilk (or donor milk feeding) will yield necessary guidance on improving bacterial colonization and health outcomes of hospitalized preterm and low–birth weight newborns. Preliminary studies have revealed that the administration of probiotics and exclusive breastmilk feeding reduce the risk of neonatal mortality and incidence of necrotizing enterocolitis, a dangerous disease caused in part by microbial dysbiosis (*13*, *14*). Exfoliated intestinal epithelial cells recovered from feces now allow researchers to evaluate how gene expression underlying intestinal cell proliferation, differentiation, and barrier function is affected by microbial activity. Such shed cells have demonstrated that breastfeeding influences gene expression in the neonatal intestinal tract (*15*).

Natural selection generates adaptations by acting on traits characterized by variation, heritability, and differential fitness outcomes. Indeed, the human milk glycan system shows clear evidence of divergence and expansion since the last common ancestor with our primate relatives, suggesting strong selection on the coevolution of human milk and microbes (see the figure). The infant intestinal microbiota's ability to metabolize, and the adaptive capacity of mothers to synthesize, human milk glycans possibly coevolved in response to selective regimes that exerted new pressures on immunity and digestion in human evolutionary history. Key candidates for such selective pressures are transitions to subsistence agriculture and animal domestication. These cultural practices are associated with increased sedentism and population density, altered dietary nutrition, and intensified zoonotic and communicable disease transmission. Embracing evolutionary and cultural ecology perspectives will enhance our understanding of mother's littlest helpers and hopefully improve clinical interventions and public health. ■

REFERENCES

1. M. A. Martin, D. A. Sela, in *Building Babies* (Springer, New York, 2013), pp. 233–256.
2. G. A. W. Rook *et al.*, *Clin. Exp. Immunol.* **177**, 1 (2014).
3. C. R. Allen-Blevins, D. A. Sela, K. Hinde, *Evol. Med. Public Health* **2015**, 106 (2015).
4. K. Hinde, J. B. German, *J. Sci. Food Agric.* **92**, 2219 (2012).
5. P. D. Houghteling, W. A. Walker, *J. Ped. Gastro. Nutr.* **60**, 294 (2015).
6. D. T. Geddes *et al.*, *Early Hum. Dev.* **84**, 471 (2008).
7. L. J. Funkhouser, S. R. Bordenstein, *PLOS Biol.* **11**, e1001631 (2013).
8. T. Urashima, M. Messer, O. T. Oftedal, in *Evolutionary Biology: Genome Evolution, Speciation, Coevolution and Origin of Life* (Springer International Publishing, New York, 2014), pp. 3–33.
9. L. Bode, *Glycobiology* **22**, 1147 (2012).
10. D. A. Sela *et al.*, *Proc. Natl. Acad. Sci. U.S.A.* **105**, 18964 (2008).
11. Z. T. Lewis *et al.*, *Microbiome* **3**, 13 (2015).
12. M. N. Huda *et al.*, *Pediatrics* **134**, e362 (2014).
13. K. AlFaleh, J. Anabrees, *Evid. Based Child Health* **9**, 584 (2014).
14. T. J. Johnson *et al.*, *Neonatology* **107**, 271 (2015).
15. S. M. Donovan *et al.*, *FEBS Lett.* **588**, 4112 (2014).

10.1126/science.aac7436

ILLUSTRATION: V. ALTOUNIAN/*SCIENCE*

Published by AAAS

MATERIALS SCIENCE

Bearing down on hydrogen

Shockwaves are used to turn deuterium into a liquid metal

By **Graeme J. Ackland**

Under high pressure, electrons can be squeezed out of the covalent bond that holds the hydrogen molecule together. Under these conditions, condensed hydrogen can become metallic, but the pressures required can be obtained only through the gravitational field of gas giant planets, or fleetingly in shock waves. On page 1455 of this issue, Knudson *et al.* (*1*) report experiments using the Z machine at Sandia National Laboratories that uses an aluminum plate propelled by giant capacitors to generate concentrated shock waves in a tiny sample (*2*). They observe metallic liquid hydrogen at pressures around 300 GPa and temperatures between 1000 and 2000 K created for a tenth of a microsecond. By shock wave standards, that is remarkably cold and slow.

It took 50 years from prediction to discovery of the Higgs boson. By comparison, after 80 years, the most famous conjecture in condensed-matter physics remains unproven. In 1935, Hillard Huntington and Eugene Wigner calculated the properties of metallic hydrogen (*3*). Based on a nearly free electron picture, they calculated that a simple atomic structure (body-centered cubic) would be some 10-fold denser than cold molecular hydrogen. Ignorant of the compressibility, they stated that the required pressures would be above 25 GPa, an impossible pressure in those days.

It turned out, however, that the compressibility of hydrogen is much lower than they had guessed, and to reach the needed density, a pressure of 350 GPa would be required. They also underestimated the ingenuity of experimentalists, as such "impossible" pressures are now obtained by two separate methods: shock compression and diamond anvil cells.

It was previously assumed that at high pressures, hydrogen behaves like the other group I elements. When sufficient mechanical energy is applied, hydrogen would transition from a molecular insulator to an atomic metal. Curiously, it turns out that group I elements do the opposite, changing from metal to insulator under pressure. They do this by becoming electrides: pseudo-ionic compounds in which valence electrons become localized in interstitial sites between the ions (*4*). Moreover, just as the idea that atomic structures need not be metallic was taking hold, calculations on hydrogen started to predict that some molecular structures may be metallic (*5*).

Adding to this conceptual confusion is that the hydrogen atom is light enough that its quantum-mechanical wavelength approaches the interatomic spacing. The nuclei must then be treated as indistinguishable quantum particles, which has led to the prediction of exotic phases of matter such as superfluids or superconductors (*6*). Under such conditions, the behavior of deuterium (as used by Knudson *et al.*) would be different because of its higher mass and bosonic nucleus. At high temperatures, the difference between deuterium and hydrogen is likely to be smaller. Traditional shock experiments can only traverse a particular set of isentropic pressure (P), temperature (T) states, and these are different for hydrogen and deuterium. The shaped pulses of the Z machine allow a range of PT space to be explored.

The structure of solid hydrogen up to pressures of 250 GPa is well established (*7*) (see the figure). Phase I is a hexagonal close-packed molecular liquid. Here, the high-school image of H_2 as a dumbbell molecule is misleading. According to quantum mechanics, at low pressure, H_2 behaves as a free rotor, pointing in all directions with the same probability. Phase I can therefore be thought of as the close packing of spherical molecules. As pressure increases, the molecules interact, and at low temperature, this leads to a broken symmetry phase II, where the rotation has stopped. At high temperature, the melt line shows a maximum around 900 K and 70 GPa. As the pressure is increased further, the melting temperature drops, meaning that the liquid is denser than the close-packed crystal (*8*, *9*).

Under further pressure increase, according to theory, a new motif appears—groups of three hydrogen molecules arrange themselves into hexagonal trimers. The electrons are not yet dissociated, and the structure remains nonmetallic, but the covalent bonding is much weaker. In the low-temperature phase III, all molecules are in such trimers. However, at high temperature, phase IV appears to comprise alternating layers of trimers and relatively freely rotating molecules. This is found in simulation, and evidenced

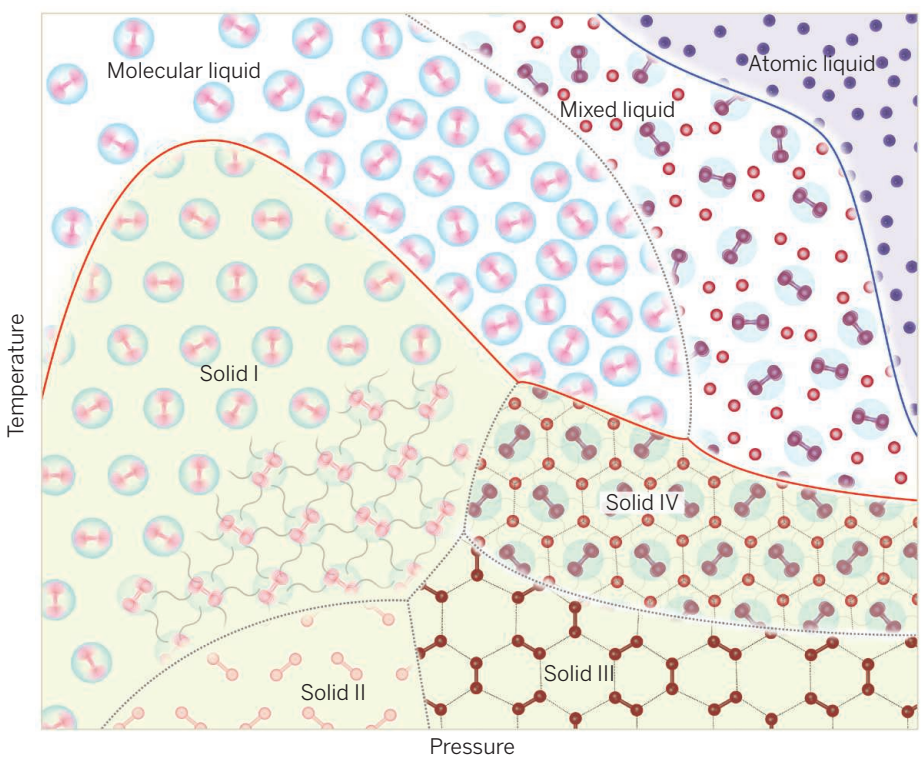

Schematic phase diagram of hydrogen. The figure shows the four known solid phases I to IV and two observed liquid phases, together with the predicted atomic liquid. Blue rings imply rotating quantum molecules, wiggly lines imply entangled rotor state, and solid bonds are where calculation shows a covalent bond.

Centre for Science at Extreme Conditions (CSEC), School of Physics and Astronomy, University of Edinburgh, Edinburgh EH9 3FD, UK. E-mail: gjackland@ed.ac.uk

ILLUSTRATION: IOAN-BOGDAN MAGDAU/THE UNIVERSITY OF EDINBURGH, SCHOOL OF PHYSICS AND ASTRONOMY

Downloaded from www.sciencemag.org on June 26, 2015

Published by AAAS

experimentally by the appearance of two distinct molecular vibration frequencies (*10*, *11*). If one treats the atoms in the trimer layer as small spheres, and the free molecules as large spheres, the average structure as seen in molecular dynamics calculation corresponds to the densest possible packing for such hard spheres. The notion that at high pressure hydrogen simply adopts the most efficient packing structure is compelling.

Although there are many theoretical predictions, no metallic solid phase of hydrogen has yet been produced. Nor is it resolved whether the melting temperature continues to drop, perhaps to zero in a quantum superfluid, or rises again when metallic phases occur.

Returning to the liquid phase, the diagnostic technique used by Knudson *et al.* essentially looks for the reflection of visible light from the interface between the deuterium sample and its aluminum holder. The first strong signal is the drop in reflectivity around 120 GPa. This is not a structural transition; the bandgap is small enough that visible light is absorbed. Then, at a pressure between 280 to 300 GPa, the reflected light reappears, implying that hydrogen has turned into a shiny metal in a transformation that is primarily driven by compression rather than heating. Simulations in these conditions suggest the onset of molecular dissociation; however, the calculated metallization pressure depends sensitively on the approximations made in the calculation (*1*, *8*, *12*–*14*).

Thus, it appears that metallization occurs at lower pressures in the liquid than in the solid. The high temperature probably helps: At very high temperatures like those obtained in a nuclear fusion device, deuterium forms a plasma in which the electrons are boiled off rather than squeezed out. Despite static compression beyond values of Knudson *et al.*, no solid hydrogen metal has yet been made, and so Wigner and Huntington's prediction still awaits its proof. ■

REFERENCES

1. M. D. Knudson *et al.*, *Science* **348**, 1455 (2015).
2. M. Matzen *et al.*, *Phys. Plasmas* **12**, 055503 (2005).
3. E. Wigner, H. B. Huntington, *J. Chem. Phys.* **3**, 764 (1935).
4. M. Marqués *et al.*, *Phys. Rev. Lett.* **106**, 095502 (2011).
5. C. J. Pickard, R. J. Needs, *Nat. Phys.* **3**, 473 (2007).
6. E. Babaev *et al.*, *Nature* **431**, 666 (2004).
7. J. M. McMahon *et al.*, *Rev. Mod. Phys.* **84**, 1607 (2012).
8. J. Chen *et al.*, *Nat. Commun.* **4**, 2064 (2013).
9. R. T. Howie, P. Dalladay-Simpson, E. Gregoryanz, *Nat. Mater.* **14**, 495 (2015).
10. I. B. Magdau, G. J. Ackland, *Phys. Rev. B* **87**, 174110 (2013).
11. R. T. Howie *et al.*, *Phys. Rev. Lett.* **108**, 125501 (2012).
12. I. Tamblyn, S. A. Bonev, *Phys. Rev. Lett.* **104**, 065702 (2010).
13. M. A. Morales, C. Pierleoni, E. Schwegler, D. M. Ceperley, *Proc. Natl. Acad. Sci. U.S.A.* **107**, 12799 (2010).
14. M. A. Morales, J. M. McMahon, C. Pierleoni, D. M. Ceperley, *Phys. Rev. Lett.* **110**, 065702 (2013).

10.1126/science.aac6626

BIOGEOCHEMISTRY

Who can cleave DMSP?

A DMSP lyase from an abundant marine eukaryote differs fundamentally from known bacterial enzymes

By **Andrew W. B. Johnston**

Marine organisms play a key role in the global sulfur cycle by producing dimethyl sulfide (DMS), a volatile compound that is emitted into the atmosphere. On page 1466 of this issue, Alcolombri *et al.* (*1*) report how the abundant marine phytoplankton *Emiliania huxleyi* (see the image) produces DMS from dimethylsulfoniopropionate (DMSP). Using a series of classical biochemical approaches, augmented by genomic and proteomic analyses, the authors isolated the enzyme and corresponding gene (termed *Alma1*) that cleaves DMSP into acrylate and DMS. They also found a functional Alma1-like enzyme in a dinoflagellate, a very different type of abundant single-cell marine plankton, emphasizing the widespread importance of this newly discovered DMSP lyase.

DMSP is one of the most important and abundant organic molecules in the world (*2*), with a billion metric tons made and turned over every year. A signature molecule for life at sea, it is produced by marine macroalgae as well as by single-cell phytoplankton species, such as diatoms, dinoflagellates, and—as in this case—the haptophyte *E. huxleyi*. It most likely serves to protect organisms to survive osmotic stress, although other functions have been suggested, ranging from defense against grazing to protection against oxidative and other stresses.

When Challenger and Simpson first identified DMSP in 1948 in the red alga *Polysiphonia* (*3*), they recognized it as the chemical progenitor of the volatile DMS known to emanate from these seaweeds (*4*). Shortly afterwards, Cantoni and Anderson isolated an enzyme from these algae that was able to cleave DMSP; consistent with findings on Alma1, this lyase required reducing agents to maintain activity in vitro and was associated with an insoluble subcellular fraction, possibly the chloroplast (*5*).

The cleavage products are also of interest, particularly the volatile DMS, at least 10 million metric tons of which are released into the atmosphere annually. DMS is a component of the tangy aroma of the seaside and functions as a chemical attractant

School of Biological Sciences, University of East Anglia, UK. E-mail: a.johnston@uea.ac.uk

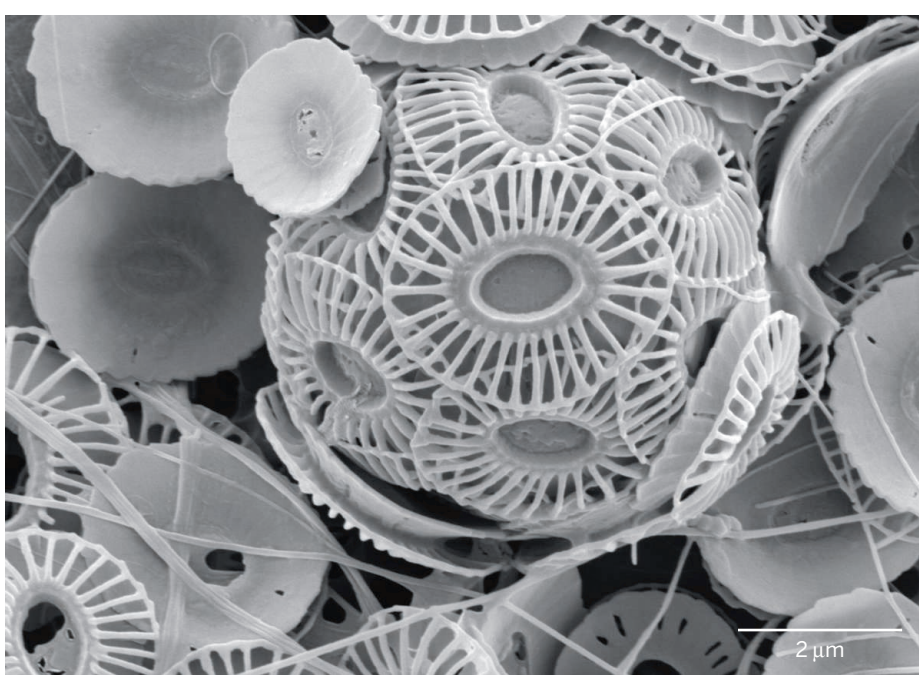

DMS producer. Micrograph of a single cell of *E. huxleyi*, which cleaves DMSP to produce DMS.

PHOTO: ALEX POULTON/NATIONAL OCEANOGRAPHY CENTRE, SOUTHAMPTON

Published by AAAS

Cliffs at Hunstanton, Norfolk, England. The upper band of white chalk comprises accumulated calciferous coccolithophore skeletons. The foreground boulders are covered with gutweed (*U. intestinalis*), a green alga that makes DMSP and in which DMSP lyase activity has been described (*12*) but the corresponding gene has not yet been identified.

PHOTO: DAVE BYFORD PHOTOGRAPHY AND VIDEO

that guides various marine animals—including some sea birds, invertebrates, and even mammals—toward potential food supplies (*6*). Not only does the release of DMS into the atmosphere contribute substantially to the global flux of sulfur from sea to air and back to land via precipitation (*7*) but also DMS oxidation products act as condensation nuclei, causing water molecules to coalesce, with possible effects on local climate through enhanced cloud formation (*8*).

We already see some of the power that can come from the basic molecular knowledge provided by Alcolombri *et al.*'s study. For example, cultures of different strains of *E. huxleyi* vary markedly in their DMSP cleavage activities (*9*); the new results suggest that this is almost certainly a result of different levels of expression of the Alma1 enzyme. Alcolombri *et al.* found and ratified the enzymatic activity of an Alma1 homolog in the DMSP-producing (and cleaving) endosymbiotic *Symbiodinium*, a photosynthetic dinoflagellate that is key to the health of corals. This organism is taxonomically very distant from haptophytes, suggestive of long-range horizontal gene transfer. The *Alma1* gene contains two introns and is located in the nucleus. This clearly rules out the possibility that the gene was obtained from any bacteria that might inadvertently have been in the *E. huxleyi* culture. This is important, given that the oceans are awash with many different classes of bacteria that can cleave DMSP into DMS and acrylate, using a plethora of enzymes (*10*, *11*). It is now clear that DMSP lyases exist in both eukaryotes and bacteria, but they must function in different ways, because Alma1 bears no resemblance to any of the known bacterial lyases.

The wider questions now concern the relative contributions of bacteria and eukaryotes in the cleavage of DMSP and the ways in which these may be affected by and impinge on environmental parameters. It is intriguing that *E. huxleyi* (and other marine plankton) not only make DMSP but also cleave a fraction of this. What endogenous and/or external factors trigger this ability, and what is its adaptive function? And what of those other algae that make DMSP and in which DMSP lyase activity has been documented, such as those in the genus *Ulva* (*12*)? These include the familiar sea lettuce and the gutweed, seen on coastal rocks (see the photo). To date, their available sequences contain no convincing homologs of the Alma1 polypeptide. These and other algae may contain yet other forms of enzymes that can claim to be DMSP lyases. ■

REFERENCES

1. U. Alcolombri *et al.*, *Science* **348**, 1466 (2015).
2. R. P. Kiene, L. J. Linn, J. A. Bruton, *J. Sea Res.* **43**, 209 (2000).
3. F. Challenger, M. I. Simpson, *J. Chem. Soc.* **3**, 1591 (1948).
4. P. Haas, *Biochem. J.* **29**, 1297 (1935).
5. G. L. Cantoni, D. G. Anderson, *J. Biol. Chem.* **222**, 171 (1956).
6. G. A. Nevitt, *Integr. Comp. Biol.* **51**, 819 (2011).
7. A. J. Kettle, M. O. Andreae, *J. Geophys. Res. Atmos.* **105**, 26793 (2000).
8. R. Simó, *Trends Ecol. Evol.* **16**, 287 (2001).
9. M. Steinke, G. V. Wolfe, G. O. Kirst, *Mar. Ecol. Prog. Ser.* **175**, 215 (1998).
10. A. R. J. Curson, J. D. Todd, M. J. Sullivan, A. W. B. Johnston, *Nat. Rev. Microbiol.* **9**, 849 (2011).
11. M. A. Moran, C. R. Reisch, R. P. Kiene, W. B. Whitman, *Annu. Rev. Mar. Sci.* **4**, 523 (2012).
12. M. P. de Souza, Y. P. Chen, D. C. Yoch, *Planta* **199**, 433 (1996).

10.1126/science.aac5661

Published by AAAS

OPTICS

Topology, spin, and light

Evanescent solutions to Maxwell's equations correspond to surface modes with strong spin-momentum locking

By **Michael Stone**

Ocean waves form between air and water, and both winds and currents decay exponentially with distance from the water surface. Similar evanescent surface waves may occur whenever two substances with differing physical properties meet—but some are special cases because they must exist for topological reasons. Such mandated surface modes occur in the low-energy quasiparticle spectrum of p-wave superconductors and superfluids and constitute the defining feature of the electronic properties of topological insulators. On page 1448 of this issue, Bliokh *et al.* (*1*) suggest that we add evanescent solutions of Maxwell's equations to this list of special cases, and in particular, the coupled oscillations of the electromagnetic field and the near-surface electrons in a metal that are known as surface plasmon-polaritons.

These optical modes have been known for some time; what is new here is the claim that they bear a close analogy to electron waves of topological origin. Topological surface modes in electronic systems originate in the way in which the Bloch wave functions in the bulk of the material are linked together. This linking is characterized by topological invariants that cannot change unless some interband energy gap closes (for example, if the energy levels of the conduction and valence band electrons cross at some particle momentum).

In topological insulators (*2*), there is an energy gap between the valence bands occupied by electrons and the empty conduction bands. The bulk of the material is an insulator, but the surface states have no energy gap and the surface is conducting. The gaplessness arises because the linking means that we cannot break the solid into a collection of disconnected atoms without closing the energy gap. The outside of the material looks to the interior electrons as a disconnected part, so the gap must close at the surface.

The low-energy surface electrons typically obey a Weyl equation, which is the "half-Dirac" equation that describes massless neutrinos with a definite handedness. The graph of the energy versus momentum of a particle obeying the Weyl equation forms a cone with the positive and negative energy state touching at a single "Weyl point" (see the figure). A full Dirac equation for massless particles falls apart into a pair of Weyl equations with opposite handedness. Adding a mass term to a Dirac pair of Weyl fermions couples the left- and right-handed modes and opens a gap between the upper and lower cones in the energy spectrum. In the absence of an opposite-handed Weyl mode, no gap can open. Weyl equations also appear in a class of topological materials called Weyl semimetals (*3*). In this case, the low-energy electrons in the interior obey Weyl equations. In a Weyl semimetal, there is an even number of points in momentum space where the conduction and valence band touch and where the wave functions obey a Weyl equation. These materials also have gapless surface states, where the momenta of the zero-energy states lie on "Fermi arcs" that connect the projections of left- and right-handed Weyl points onto the surface.

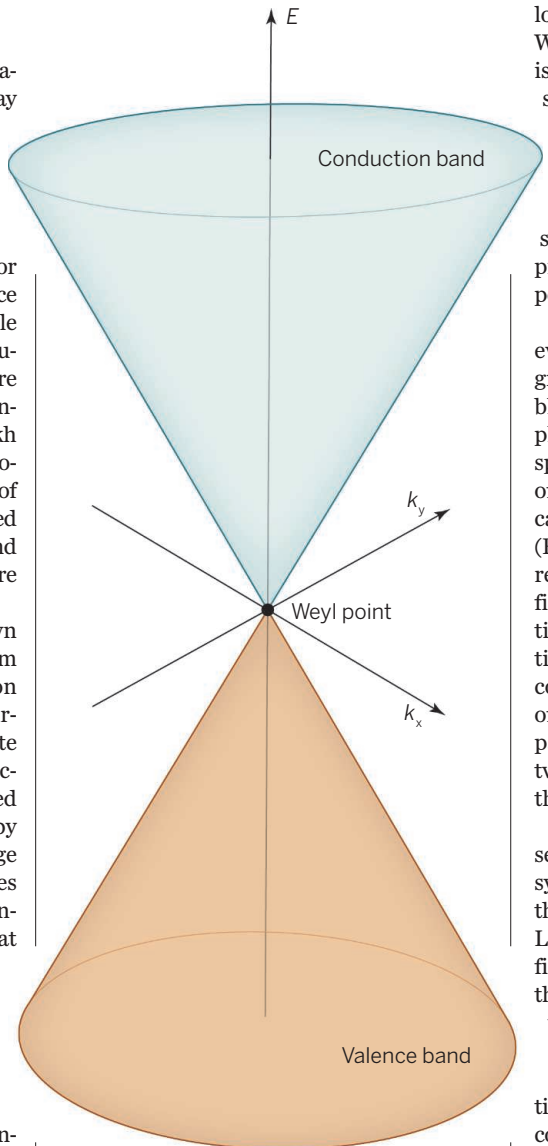

A Weyl point. The energy-momentum relation near a Weyl point is seen in the surface states of a topological insulator, the bulk states of a Weyl semimetal, the evanescent plasmon-polaritons, and the theoretical study of Bliokh *et al*. Near such a point with momentum $\mathbf{p} = \mathbf{p}_0$, the energy is given by $E(\mathbf{p}) = \pm\text{const.}\,|\mathbf{k}|$, where $\mathbf{k} = \mathbf{p} - \mathbf{p}_0$.

Interest in the topological character of evanescent optical modes arises from a growing appreciation of the close resemblance of the wave equations for the spin-1 photon and the spin-½ electron—and how spin has similar effects on the dynamics of both. The free-space Maxwell equations can be rewritten in "Riemann-Silberstein" (RS) form (*4*) where four equations for the real-valued electric field **E** and magnetic field **B** reduce to two complex-valued equations, one for the right-handed combination $\mathbf{E} + i\mathbf{cB}$ and one for the left-handed combination $\mathbf{E} - i\mathbf{cB}$, where c is the speed of light. The RS equations look like a Dirac pair of Weyl equations except that two-by-two spin-½ Pauli matrices are replaced by three-by-three spin-1 equivalents.

As a result of their close resemblance, the semiclassical equations of motion for both systems contain anomalous velocity terms that are momentum-space analogs of the Lorentz force, but with the electromagnetic field replaced by the same Berry curvature that provides the topological invariant in the Weyl semimetals. In particle physics and condensed matter systems, this anomalous velocity is responsible for the violation of Liouville's theorem on phase space conservation at a Weyl point, and hence for the chiral anomaly that violates the separate conservation of the number of left- and right-handed particles even in the absence of a mass (*5*). In optics, the anomalous velocity is responsible for the spin-Hall effect of light and related effects (*6*).

A key characteristic of topological surface states is that the spin degree of freedom is locked in a fixed relation to the direction of the momentum. This same feature appears in all evanescent wave solutions to Maxwell's equations. Furthermore, the solution to each of the right- or left-chirality free-space RS equations has topological invariant or Chern

Department of Physics, University of Illinois, Urbana, IL 61801, USA. E-mail: m-stone5@illinois.edu

Downloaded from www.sciencemag.org on June 26, 2015

Published by AAAS

number $C = 2$ (twice as large as the $C = 1$ of the spin-½ equation), which again suggests that the boundary of free space should host topological modes.

Evanescent electromagnetic waves are trapped at any surface where the sign of one or both of the permittivity ε or the permeability μ changes from positive to negative and so couples the left- and right-handed Weyl-like equations. A sign change in ε occurs, for example, at the surface of a metal at frequencies below the electron plasma frequency ε_p, and the resulting modes are the surface plasmon-polaritons. These modes have a nonzero spin angular momentum that always lies to the right of their direction of propagation. This spin-momentum locking leads to fascinating directional scattering effects when the plasmon-polaritons run into surface defects (*7*).

In the topological interpretation, the interior or "bulk" of the topological system is free space, so the RS system is an analog of a Weyl semimetal (see the figure). It is really a Dirac semimetal (*8*), where the two Weyl points coincide to make a Dirac point. There can be no Fermi arcs connecting these coincident points. Instead, the low-energy polariton modes appear to connect the zero-momentum Dirac point with another Dirac point at infinite momentum.

Surface states are intimately connected with anomalous conservation laws: In topological insulators, a Berry curvature gives rise to Hall-like currents in the bulk, and where these currents meet the surface, they donate their spin or electric charge to the surface states. The bulk is invisible to the surface states because they cannot access it. To the surface states, the arriving charge anomalously violates the conservation of charge or spin (*9*). In a Weyl semimetal, there are anomalies at each Weyl point where particles can flow to the conduction band from the valence band, or vice versa. In this case, the semimetal Fermi arcs are there to provide the return flow on the surface (*10*). It is interesting to speculate that a similar interpretation might be found for the optical surface modes. ■

REFERENCES

1. K. Y. Bliokh, D. Smirnova, F. Nori, *Science* **348**, 1448 (2015).
2. X.-L. Qi, S.-C. Zhang, *Rev. Mod. Phys.* **83**, 1057 (2011).
3. X. Wan, A. M. Turner, A. Vishwanath, S. Y. Savrasov, *Phys. Rev. B* **83**, 205101 (2011).
4. I. Białynicki-Birula, in *Progress in Optics, Vol. 36*, E. Wolf, Ed. (Elsevier, Amsterdam, 1996), pp. 245–294.
5. M. A. Stephanov, Y. Yin, *Phys. Rev. Lett.* **109**, 162001 (2012).
6. M. Onodaet al., *Phys. Rev. Lett.* **93**, 083901 (2004).
7. D. O'Connor *et al.*, *Nat. Commun.* **5**, 5327 (2104).
8. S. M. Young *et al.*, *Phys. Rev. Lett.* **108**, 140405 (2012).
9. C. G. Callan Jr., J. A. Harvey, *Nucl. Phys. B* **250**, 427 (1985).
10. F. D. M. Haldane, http://arxiv.org/abs/1401.0529 (2014).

10.1126/science.aac4368

ILLUSTRATION: C. BICKEL/*SCIENCE*

GENE REGULATION

A HUSH for transgene expression

A protein complex represses genes that insert into heterochromatin

By **Thijn R. Brummelkamp**[1] *and* **Bas van Steensel**[2]

The introduction of an extra gene into a genome—transgenesis—is frequently used as an experimental approach to study gene function but also has applications in biotechnology and gene therapy efforts. In mammalian cells, transgenes are often integrated in a random manner leading to variable levels of expression, with differences as great as three orders of magnitude depending on the integration site (*1*). The complications of unpredictable levels of transgene expression are well recognized, but the mechanisms leading to variable expression are poorly understood. On page 1481 of this issue, Tchasovnikarova *et al.* (*2*) determine that a protein complex silences extra genes that are inserted into heterochromatin, regions of compacted DNA. This represents a new aspect of gene regulation that depends on chromatin context.

The prevailing thought is that the local chromatin environment at the site of transgene integration affects its activity. Gene introduction in the fly *Drosophila melanogaster* and other model organisms can lead to heterogeneous expression levels, referred to as position-effect variegation. In position-effect variegation, the transgene is thought to be silenced as a result of spreading of heterochromatin from neighboring sequences into the transgene (see the first figure). It remains unclear to what extent this relates to transgene silencing in mammals, and whether transgenes are silenced through multiple mechanisms or a dominant process operational at many different genomic locations.

Tchasovnikarova *et al.* took a genetic approach to identify regulators of transgene silencing in human cells, using a retrovirus to integrate the transgene into the genome. Random integration of a green fluorescent protein (GFP) reporter transgene into the human cell line resulted in cells with highly divergent GFP expression levels. The authors purified the subpopulation of cells with very low GFP expression, which they presumed was the result of transgene repression. To identify proteins responsible for this repression, they subjected these cells to random mutagenesis. Here, a key trick was the choice of human KBM7 cells as a model system (*3*): These cells are almost completely haploid, and hence a single mutation in a gene can have a profound effect because there is no second copy of the gene. Tchasovnikarova *et al.* collected the mutant cells in which GFP was thus reactivated and used high-throughput sequencing to identify the mutated genes.

This approach identified genes encoding the proteins SET domain, bifurcated 1 (SETDB1), transgenic activation repressor (TASOR), M-phase phosphoprotein 8 (MPP8), and periphilin. Through biochemical approaches, the authors found that the latter three proteins form a complex dubbed the human silencing hub (HUSH). This complex in turn interacts with SETDB1 (see the second figure). Thus, the results of the genetic screen nicely dovetailed with biochemical data.

Previously, all three HUSH subunits, among numerous other factors, were

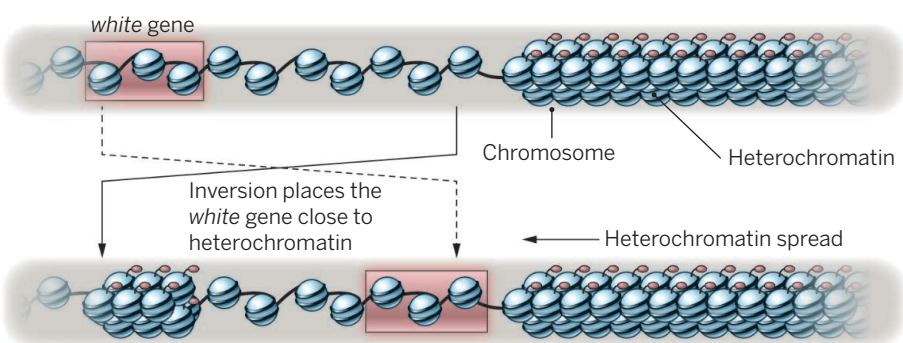

Classic position-effect variegation. An early observation in *Drosophila* involved a chromosomal inversion in which an active eye color gene (*white*) is brought into close proximity to a heterochromatic chromosomal region, leading to repression of *white* by the spreading of heterochromatin into the gene.

Published by AAAS

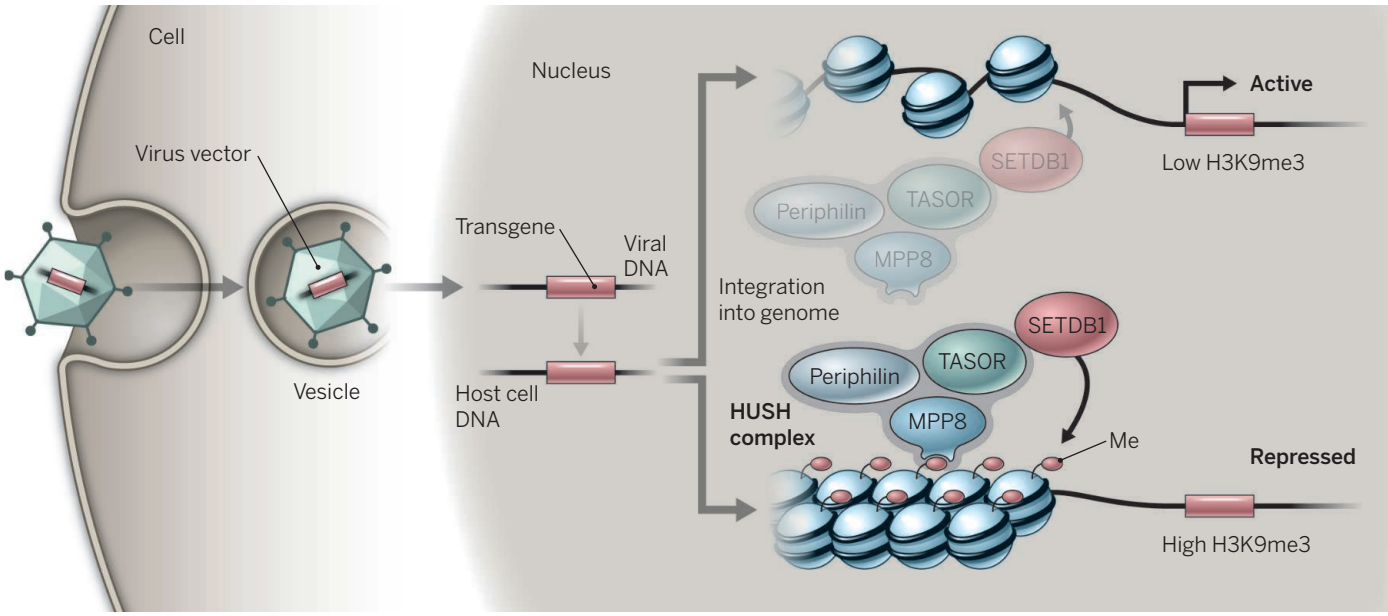

Transgene repression by HUSH. Viral genome integration into the host cell genome results in transgenes that are variably expressed. The HUSH complex, with SETDB1, is important for transgene repression. Genomic regions harboring inactive transgenes are characterized by high amounts of the H3K9me3 histone mark. Me, methylation.

identified in protein complexes that recognize trimethylated lysine 9 of histone H3 (H3K9me3) (*4*). Histones form the essential packaging proteins of chromatin, and H3K9me3 has been implicated in the formation of heterochromatin. MPP8 has a chromodomain, a protein domain that binds to H3K9me3, suggesting a possible mechanism by which HUSH is targeted to chromatin. Indeed, Tchasovnikarova *et al.* show that the binding of TASOR to chromatin and H3K9me3 peptides was dependent on MPP8, which required its chromodomain for transgene repression. Nevertheless, in the absence of other HUSH subunits, periphilin could still bind to chromatin, indicating that it could independently assist in maintaining the HUSH complex bound to the transgene.

Interestingly, SETDB1 is an enzyme that trimethylates H3K9. By binding to H3K9me3 and recruiting SETDB1 as a modifier for the same mark, the HUSH complex shows mechanistic similarities to the well-studied complex of the chromodomain protein heterochromatin protein 1 (HP1), which also binds to H3K9me3, as well as to a H3K9 trimethyltransferase called suppressor of variegation 3-9 [SU(VAR)3-9 in *Drosophila*]. These factors have been implicated in PEV, and the positive feedback loop that they form is thought to enable spreading of heterochromatin along the same DNA strand (*5*).

[1]*Division of Biochemistry and Division of Gene Regulation, Netherlands Cancer Institute, 1066 CX Amsterdam, Netherlands.* [2]*Department of Cell Biology, Erasmus University Medical Center, 3015 GE Rotterdam, Netherlands*
E-mail: t.brummelkamp@nki.nl; b.v.steensel@nki.nl

Why are only certain transgenes subjected to the HUSH silencing mechanism and others not? Comparison of the genomic integration sites of repressed and active transgenes revealed a striking pattern: The reporter gene was silenced most strongly when inserted into genomic regions covered by H3K9me3. In some instances, constituents of the HUSH complex were also found at these sites prior to transgene insertion. A mechanistic implication of these findings is that the silenced transgenes probably do not recruit the HUSH complex autonomously, but instead are "invaded" by HUSH, SETDB1, and H3K9me3 that are already present at the insertion site, similar to the previously observed spreading of other types of heterochromatin along a DNA strand.

Because many different protein complexes repress genes, it is somewhat unexpected that the HUSH complex affects the majority of repressed transgenes. This could mean that the HUSH complex covers a relatively large fraction of the genome. Genome-wide chromatin maps of HUSH occupancy may address this further.

These results show an interesting contrast with the well-studied silencing of retrovirus integrations in embryonic stem cells (*6*). In this case, specific elements in the viral DNA are recognized by sequence-specific DNA binding factors, which in turn recruit a silencing complex containing SETDB1, HP1, and another protein called tripartite motif-containing 28 (TRIM28) [also known as Krüppel associated box (KRAB)–associated protein-1 (KAP1)]. HUSH repression in KBM7 cells does not require KAP1 or HP1. Thus, silencing of foreign DNA can be carried out through distinct complexes that may each act in certain cell types. Given that HUSH repressed transgenes in three tested human cell lines, it will be interesting to learn more about its division of labor with other silencing mechanisms across human cell types.

PEV has also been observed in mice, and large-scale mutagenesis has identified the gene products involved (*7*, *8*). These include mouse homologs of TASOR and SETDB1, but remarkably also of SU(VAR)3-9 and KAP1, indicating that at least in some cases the different protein complexes may collaborate. However, it is unclear whether this occurs broadly, because only a single mouse locus exhibiting PEV was studied. Tchasovnikarova *et al.* elegantly optimized their screen for the identification of broadly acting factors by using a polyclonal population of cells carrying a repressed reporter gene integrated at many positions. It appears that the HUSH complex is a widely active repressor complex that was not studied much before, but now appears to have a major role in somatic transgene silencing in diverse mammalian contexts. ■

REFERENCES

1. W. Akhtar *et al.*, *Cell* **154**, 914 (2013).
2. I. A. Tchasovnikarova *et al.*, *Science* **348**, 1481 (2015).
3. J. E. Carette *et al.*, *Science* **326**, 1231 (2009).
4. H. C. Eberl, C. G. Spruijt, C. D. Kelstrup, M. Vermeulen, M. Mann, *Mol. Cell* **49**, 368 (2013).
5. J. C. Eissenberg, S. C. Elgin, *Trends Genet.* **30**, 103 (2014).
6. S. Schlesinger, S. P. Goff, *Mol. Cell. Biol.* **35**, 770 (2015).
7. L. Daxinger *et al.*, *Genome Biol.* **14**, R96 (2013).
8. S. K. Harten *et al.*, *Mamm. Genome* **25**, 293 (2014).

10.1126/science.aac6529

ILLUSTRATION: C. BICKEL/*SCIENCE*

Published by AAAS

HISTORY OF SCIENCE

The living element

Radium played an important, but often forgotten, role in life sciences research in the early 20th century

By **Helen Anne Curry**

Radium and the Secret of Life
Luis A. Campos
University of Chicago Press, 2015. 386 pp.

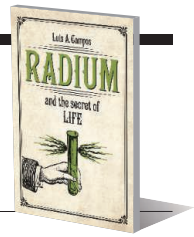

"If anything in the world is alive, is not radium alive?" asked the physician and journalist C. W. Saleeby in 1906. Writing at the height of a radium craze that swept across Europe and America in the early 20th century, Saleeby was one of many observers who connected radium and radioactivity to the mysteries of life. Physicists advanced a vitalized language of atomic change, referring to the "birth" of atoms and the "evolution" of elements. Many people speculated, often wildly, on the potential vitalizing effects of radium on plants, animals, and people, while biologists took up experiments meant to reveal that very capacity. Metaphorical and material couplings of radium and life abounded. These couplings—and the curious, marvelous, and mostly forgotten scientific investigations that emanated from them—are the subject of the historian Luis A. Campos's fascinating history of radium and its uses in biological experimentation.

Plants treated with radium (right) appear to dwarf untreated plants (left).

PHOTO: COURTESY OF PAUL FRAME. OAK RIDGE ASSOCIATED UNIVERSITIES. AND PATRICK MCDERMOTT. RUTGERS UNIVERSITY

Consider the Cambridge physicist John Burke, who, in 1905, announced that he had produced bacteria-like growths by dropping a piece of radium salt into a test tube filled with beef bouillon. Burke dubbed the tiny formations "radiobes." Although he acknowledged that they were unlike any known living creature, he felt that they nonetheless fell "within the realm of biology." He speculated that the radiobes might be a kind of proto-life, something from which life as we know it had once arisen. Burke and his radiobes sparked a media frenzy. Many scientists were less sanguine about these experiments and found reasons to dismiss both the importance of the radiobes and Burke's interpretations of the nature of life—but not before he had opened the conceptual door to a new experimental approach to study the historical origin of life.

Other experimentalists working at the "radium-life nexus" took the application of radium in new directions, attempting to solve still other conundrums of biological change and bringing myriad physical concepts to bear on biological questions in the process. The botanist Daniel MacDougal incorporated radium into his experimental studies of evolution in 1904. He hoped that the transmuting element might prove a useful tool for generating biological transmutation. Perhaps, he speculated, it would reveal how an organism sometimes made the leap to become a novel species. Later, the geneticists Thomas Hunt Morgan and Albert Blakeslee considered how radiant atoms could be used to investigate chromosomes and genes, the so-called atoms of heredity. They hoped that the biological effects of radium might resolve the mystery of evolutionary control, enabling scientists to generate heritable changes at will. Campos convincingly argues that these experiments with radium chased the secret of creating and controlling life from organism to chromosome to gene and, finally, to DNA.

By writing the story of radium back into the history of early genetics, Campos upends some of its standard tales. Take, for example, his account of Hermann Muller, the Nobel Prize–winning *Drosophila* geneticist. Muller is widely held to have been the first person to induce mutation through radiation treatment in a series of x-ray experiments that he conducted in 1927. As Campos shows, it was Muller's elaborate experimental protocols and effective self-promotion that helped him to secure this title. Previously, mutation had had a capacious definition, encompassing changes in organisms, chromosomes, and genes, but after Muller, it signified genic change alone. This shift rendered earlier experiments in induced mutation with radium invisible or irrelevant.

Throughout the book, Campos remains attentive to what he calls the "generative power of metaphor," exploring routes by which the descriptive analogies drawn between radioactivity and life—such as the transmutation of elements versus that of species or genes—were made material in experimental systems. He finds that the very words that scientists used to characterize the objects of their scrutiny played an important role in determining which methods and tools were best suited for investigating these entities.

Alive to the notion that metaphors are more than mere description, Campos turns their power to the practice of history, too, showing, in conclusion, how the metaphors of radioactivity contribute to novel modes of historical investigation and interpretation. Rather than provide a decisive end point to his narrative, he traces an "asymptotic process of decay" of the associations made between radium and life. From Campos's exploration of these ever-disintegrating residues emerge some of his most provocative claims. For example, he proposes that radiation genetics and the target theory of genetic change might be better understood as "curious decay products" of earlier studies, rather than the result of an imposition of physics on biology, as is often suggested. Handling his subject with care, and exploiting its unique properties at every turn, Campos demonstrates radium's capacity to reveal the secrets of science and history alike.

The reviewer is in the Department of History and Philosophy of Science, University of Cambridge, Cambridge CB2 3RH, UK. E-mail: hac44@cam.ac.uk

10.1126/science.aab3104

Downloaded from www.sciencemag.org on June 26, 2015

Published by AAAS

EDUCATION

Best practices for digital teaching

A handbook for the 21st-century educator

By **Erin Dolan**

Anyone teaching a course at a university is likely to have a notion of what face-to-face teaching should look like through his or her experience as a student, as a teacher, and through depictions in media. Yet as Claire Howell Major points out in her book *Teaching Online*, most of us do not have similar notions for online courses because we have little to no experience with them. She aims to provide the guidance needed to envision and implement online teaching.

Major frames *Teaching Online* from the perspective of change, focusing on how teaching and learning are different in online environments and how faculty can recognize, understand, and manage these differences. Each chapter includes personal narratives from instructors, education researchers, and instructional designers, as well as concrete strategies for tackling fundamental issues in online teaching.

The book's narratives and strategies are grounded in educational research, which provides the evidence base for recommendations on how to assess one's readiness for teaching online, establish an online presence, use universal design principles to create accessible websites, and establish norms in an online course. Extensive footnotes steer readers to additional resources and examples. The main strength of the book is this integration of theoretical, empirical, and practical perspectives.

Much of the book's guidance on how to design and teach an online course also applies to face-to-face teaching. For example, in teaching an online course, one has to consider how to know that students are learning. The same is true for face-to-face courses. Teaching online raises interesting questions about what the "signals" of learning will be and how they will be mediated by technology. These signals could be reduced because we cannot see a student's puzzlement or moment of understanding, or amplified because we can gauge a student's understanding from written responses on a course discussion board. One hopes that addressing these questions will drive faculty to question their ideas about learning cues in face-to-face environments as well.

In general, the text favors an audience with some knowledge of pedagogy. However, nonspecialists should resist the urge to reject the book out of hand. Rather, consider following Major's recommendation to read the chapters out of order. For example, start with chapter 1 for an overview of the changes inherent to teaching online, skip to chapters 4 to 6 for information about course planning and intellectual property, review chapters 7 to 12 for discussion of cross-cutting themes such as time management and communication, and end with chapters 2 and 3 for a more rarefied discussion of teaching and learning.

Compelling anecdotes and evidence-based approaches prepare educators to tackle online teaching.

> ***"Much of the book's guidance on how to design and teach an online course also applies to face-to-face teaching."***

Teaching Online
A Guide to Theory, Research, and Practice
Claire Howell Major
Johns Hopkins University Press, 2015. 330 pp.

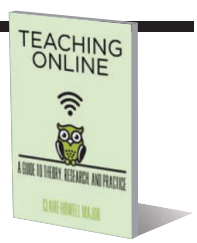

Education faculty are likely to engage in the kind of reflection on teaching and learning that this book aims to encourage. The real opportunity is to reach beyond this group to disciplinary faculty, such as scientists, mathematicians, engineers, social scientists, and humanists. Yet, disappointingly few of the narratives are authored by faculty outside of education or technology. This is the main limitation of the book.

Many studies and multiple meta-analyses (summarized in chapter 3) have shown that students in online courses realize the same, if not better, outcomes as compared to students in face-to-face courses. This means that we can move beyond the debate of whether teaching online is good or bad, to how to do it well. In other words, what instructional strategies, patterns of interaction and engagement, and supporting facilities are necessary and sufficient for students to learn? Addressing these questions in the process of developing and implementing online courses may be a powerful catalyst for promoting broader teaching change.

10.1126/science.aab3320

The reviewer is at the Texas Institute for Discovery Education in Science, College of Natural Sciences, University of Texas, Austin, TX 78712, USA. E-mail: edolan@austin.utexas.edu

PHOTO: ARIEL SKELLEY/CORBIS IMAGES

Downloaded from www.sciencemag.org on June 26, 2015

Published by AAAS

Applying antibiotics lessons to antivirals

READING THE PERSPECTIVE "Combating emerging viral threats" by E. Bekerman and S. Einav (17 April, p. 282), I was struck by the call for broad-spectrum antiviral drugs, given the recognition of the problems caused by broad-spectrum antibacterial drugs (*1*) and the recent clarion calls for precision medicine (*2*). "One drug, one bug" antibiotics, along with appropriate point-of-intervention diagnostics, would mitigate the spread of drug resistance. The same is likely to be true for antivirals.

Furthermore, "one drug, multiple bugs" (broad-spectrum) antibiotics damage the highly diverse populations of bacteria in and on our body. These microbiota are becoming increasingly appreciated as critical for health. Damage to the gut microbiota, particularly during early development, has lasting negative consequences for maturation and function of the immune and central nervous systems (*3*). The gut microbiota similarly harbor viral components important for health (*4*). Broad-spectrum antivirals are likely to damage these viral components of our gut microbiota.

IMAGE: © ROEL SMART/ISTOCKPHOTO.COM

Today's slow and expensive drug development process pressures industry to seek one drug for multiple bugs. However, efforts to manage viral infections, as for bacterial infections, should not focus on broad-spectrum agents but on technology platforms that allow the discovery, development, manufacturing, and regulatory approval of multiple precision antiviral agents, each targeting only one bug. Such drugs could be developed, produced, and approved expeditiously and cost-effectively, as the world has managed to achieve effectively for annual influenza vaccines in most years.

David W. Martin Jr.

AvidBiotics Corporation, South San Francisco, CA 94080, USA. E-mail: dmartin@avidbiotics.com

REFERENCES

1. Center for Disease Control and Prevention, "Antibiotic resistance threats in the United States, 2013" (2013); www.cdc.gov/drugresistance/threat-report-2013/.
2. The White House, Fact Sheet: President Obama's Precision Medicine Initiative (www.whitehouse.gov/the-press-office/2015/01/30/fact-sheet-president-obama-s-precision-medicine-initiative).
3. M. J. Blaser, *Missing Microbes* (Henry Holt and Company, New York, 2014).
4. H. W. Virgin, *Cell* **157**, 142 (2014).

Response

The main arguments against broad-spectrum therapies presented by Martin are based on the pitfalls of this approach with antibiotics. However, the spread of resistance in bacteria to which Martin refers is not directly applicable to viral resistance. Bacteria can spread antibiotic resistance either vertically by passing the antibiotic resistance genes to new generations or horizontally by sharing or exchanging antibiotic resistance genes through gene transfer mechanisms between even distantly related species (*1*). In contrast, the evolution of drug resistance within viruses is governed by their intrinsically error-prone replication. Hence, the likelihood that a virus develops resistance to a broad-spectrum agent is comparable to that of developing resistance to a therapeutic targeting a single virus. We therefore disagree with the statement that precision medicine for antivirals would mitigate the spread of drug resistance. Broad-spectrum host-targeted approaches with higher genetic barriers to resistance offer a more feasible approach to limiting antiviral resistance than do precisely targeted antivirals.

The prior antibiotic efforts have saved millions of lives to date. They are likely a major contributor to the markedly extended life span in developed countries over the past century. Thus, while the overuse and misuse of antibiotics warrant scrutiny, the emergence of resistance is not an indication that this strategy failed.

Understanding of the virome and its role (both beneficial and detrimental) in human disease is in its infancy (*2*). We agree with Martin that broad-spectrum antiviral therapies may affect the human virome. Nevertheless, this potential concern needs to be offset by the tremendous cost and difficulty of developing drugs targeting individual viruses. The biggest success story in the past decade has been the development of targeted antivirals against hepatitis C virus (HCV). However, it took many billions of dollars and more than a decade to achieve this, and drug access has now become a major challenge (*3*). HCV is a single virus. The list of emerging and reemerging viruses that represent major threats to global health keeps increasing. More than 11,000 individuals died from the recent Ebola outbreak, and a greater number of patients die from dengue and other emerging viral infections every year. Therefore, as we wrote in our Perspective, we advocate combining specific development approaches with broad-spectrum approaches to enable global health protection and national security readiness more rapidly.

We too recognize the value of precision medicine (*4*). Nevertheless, the need for novel antivirals is broad and urgent. We should therefore not let precision medicine distract from lower-cost and effective population-wide interventions (*5*).

Elena Bekerman and Shirit Einav*

Department of Medicine/Division of Infectious Diseases, Department of Microbiology and Immunology, Stanford University School of Medicine, Stanford, CA 94305, USA.

*Corresponding author. E-mail: seinav@stanford.edu

REFERENCES

1. J. Davies, *Science* **264**, 375 (1994).
2. H. W. Virgin, *Cell* **157**, 142 (2014).
3. A. Hill, G. Cooke, *Science* **345**, 141 (2014).
4. F. S. Collins, H. Varmus, *N. Engl. J. Med.* **372**, 793 (2015).
5. J. H. Coote, M. J. Joyner, *Lancet* **385**, 1617 (2015).

China legitimizes ivory, again

IN THE PAST, the Chinese ivory industry was licensed to purchase a certain quota of ivory on the grounds of "the inheritance of

Downloaded from www.sciencemag.org on June 26, 2015

Published by AAAS

traditional ivory arts." Rather than helping to slow the decline of elephant populations, the policy served as a permanent protective umbrella for the illegal ivory trade (*1*). Unfortunately, there are no plans to change the situation for the better. On 11 May 2015, the China State Forestry Administration announced that 34 enterprises were authorized to produce ivory products, and 130 enterprises were certified for ivory trading. The count is down from 37 and 145 (*2*), respectively, in 2013, but the decrease will not change the effect of the policy. Once again, the Chinese government has legitimized ivory trade in China.

China has attempted to regulate the ivory trade through franchise and collection certificate systems for ivory products, but to no avail. As long as some ivory is legal, even artificial ivory may not help; traders can claim that illegal ivory is artificial to regulators and that artificial ivory is authentic to buyers, thereby increasing total ivory trade and hastening the extinction of African elephants (*3*). Classifying even a portion of authentic ivory as legitimate may result in misinformation for consumers regarding illegal ivory trading. An inquiry conducted by the International Fund for Animal Welfare indicates that more than 70% of the Chinese public is unaware that ivory is acquired at the cost of elephant slaughter (*4*) or that much of the revenue supports terrorist groups (*4*).

The European Union and the United States, both as contracting parties of the Convention on International Trade of Endangered Species, have already banned the import of commercial ivory products. We call on the Chinese government to likewise ban international and commercial trade with a firmer hand, in order to stem the excessive consumption of ivory products and protect African elephants.

Jinqi Zhan and Qiang Weng*

College of Biological Sciences and Biotechnology, Beijing Forestry University, Beijing 100083, China.

*Corresponding author. E-mail: qiangweng@bjfu.edu.cn

REFERENCES

1. S. Huang, Q. Weng, *Science* **343**, 611 (2014).
2. "Ivory import should be banned, legitimate import aggravates smuggling," opinion.huanqiu.com (27 February 2015); http://opinion.huanqiu.com/opinion_china/2015-02/5767016.html [in Chinese].
3. Z. M. Zhou, *Nature* **507**, 40 (2014).
4. "Blood ivory," *South. Wkly.* (15 November 2013); www.infzm.com/content/95931 [in Chinese].

TECHNICAL COMMENT ABSTRACTS

Comment on "Global diversity and geography of soil fungi"

Christopher W. Schadt and Anna Rosling

Tedersoo *et al.* (Research Article, 28 November 2014, p. 1078) present a compelling study regarding patterns of biodiversity of fungi, carried out at a scale unprecedented to date for fungal biogeographical studies. The study demonstrates strong global biogeographic patterns in richness and community composition of soil fungi. What concerns us with the study is what we do not see. Unfortunately, this study underestimates the fungal diversity of one key group of soil fungi due to reliance on a single primer with known flaws.

Full text at http://dx.doi.org/10.1126/science.aaa4269

Comment on "Number-space mapping in the newborn chick resembles humans' mental number line"

Madhur Mangalam and Shraddha Madhav Karve

Rugani *et al.* (Reports, 30 January 3015, p. 534) tested 3-day-old domestic chicks using an innovative experimental setup and demonstrate the presence of the mental number line. We raise concerns regarding this conclusion by highlighting the possible loopholes in the experimental design and the data analysis procedures. We further suggest auxiliary experiments that can substantiate the authors' claim.

Full text at http://dx.doi.org/10.1126/science.aaa8577

Comment on "Number-space mapping in the newborn chick resembles humans' mental number line"

Christopher Harshaw

Rugani *et al.* (Reports, 30 January 2015, p. 534) presented evidence that domestic chicks employ a "mental number line." I argue that the hypothesis testing used to support this claim unjustifiably assumes that domestic chicks are unbiased when choosing between identical stimuli presented to their left and right.

Full text at http://dx.doi.org/10.1126/science.aaa9565

Response to Comments on "Number-space mapping in the newborn chick resembles humans' mental number line"

Rosa Rugani, Giorgio Vallortigara, Konstantinos Priftis, Lucia Regolin

Mangalam and Karve raise concerns on whether our results demonstrate a mental number line, suggesting auxiliary experiments. Further data analyses show that their methodological concerns are not founded. Harshaw suggests that a side bias could have affected our results. We show that this concern is also unfounded.

Full text at http://dx.doi.org/10.1126/science.aab0002

Published by AAAS

TECHNICAL COMMENT

FUNGAL BIOGEOGRAPHY

Comment on "Global diversity and geography of soil fungi"

Christopher W. Schadt[1,2] and Anna Rosling[3]

Tedersoo *et al*. (Research Article, 28 November 2014, p. 1078) present a compelling study regarding patterns of biodiversity of fungi, carried out at a scale unprecedented to date for fungal biogeographical studies. The study demonstrates strong global biogeographic patterns in richness and community composition of soil fungi. What concerns us with the study is what we do not see. Unfortunately, this study underestimates the fungal diversity of one key group of soil fungi due to reliance on a single primer with known flaws.

The internal transcribed spacer (ITS) region of the ribosomal RNA (rRNA) operon has been a de facto barcode for fungal taxonomy and ecology for 25 years since seminal publications by White *et al*. (*1*) and Gardes *et al*. (*2*). Although these primers have been valuable for describing fungal diversity both taxonomically and ecologically, unfortunately like almost any single primer set, they cannot capture all diversity in the fungal kingdom in an unbiased fashion. Tedersoo *et al*. (*3*) correctly acknowledge in the main text that the Tulasnellaceae and Microsporidia will not be amplified with their chosen primer set. They have also taken considerable care to include variants of the forward ITS3 primer to increase the representativeness of amplicon pools and describe these variants in their supplementary materials. However, it was previously shown by Rosling *et al*. (*4*), in the paper describing this new class (*Archaeorhizomycetes*) and cited by Tedersoo *et al*., that the ITS4 reverse primer has at least two mismatches to all known species in the class. These mismatches have been shown to result in at least a 10-fold underrepresentation of Archeaorhizomycetes in artificial communities using known DNA template amounts from isolates (*5*), and as a consequence other taxa in the artificial community also appeared to be more abundant than they were.

[1]Biosciences Division, Oak Ridge National Laboratory, Oak Ridge, TN, USA. [2]Department of Microbiology, University of Tennessee, Knoxville, TN, USA. [3]Department of Evolutionary Biology, Uppsala University, Uppsala, Sweden.
E-mail: schadtcw@ornl.gov (C.W.S.); anna.rosling@ebc.uu.se (A.R.)

The *Archaeorhizomycetes* are a widespread, highly diverse, and ancient class of the Ascomycota documented in more than 100 studies of soil fungal communities (*6*). These fungi were first identified from 28*S* rRNA gene sequences from tundra soils in 2003 (*7*) and subsequently shown to be globally distributed in soil rRNA gene studies by Porter *et al*. (*8*) and expanded upon by Rosling *et al*. (*4*) and Menkis *et al*. (*6*). Using perfectly matched large subunit primers, *Archaeorhizomycetes* are shown to be dominant in many soils, typically comprising >10% of rRNA gene sequences recovered (*8*) and in one case >90% (*9*). In another specific example, Taylor and co-workers (*10*) performed extensive studies of soil fungal communities in Alaska using primers unbiased against amplification of *Archaeorhizomycetes*. In Alaska, at least 53 putative species-level operational taxonomic units (OTUs) of *Archaeorhizomycetes* could be identified, with diversity ranging from 2 to 25 OTUs per sample. Several of these putative species-level groups were among the most abundant OTUs across Alaska (*11*) and comprised at least 5% of the species richness of Alaskan soil fungal communities. In their current study, Tedersoo and colleagues identify only two OTUs belonging to the *Archaeorhizomycetes* in one out of two Alaskan sites studied, and thus *Archaeorhizomycetes* are reported in their paper to represent only ~0.3% of the fungal diversity in arctic tundra samples. In contrast, previous reports of alpine and arctic tundra samples revealed >10% overall relative abundance of the *Archaeorhizomycetes* class when suitable primers were used (*7*, *11*). It should also be noted that as all studies of rRNA gene diversity are inherently semiquantitative (based on relative abundances), a likely 10-fold underestimation of diversity and abundance of the class *Archaeorhizomycetes* would affect the ratios of other functional and phylogenetic classes. Tedersoo *et al*. specifically discuss the patterns of *Archaeorhizomycete* diversity and abundance at the global scale in several instances within the paper but do not acknowledge the likely bias created by mismatched polymerase chain reaction (PCR) primer. Thus, *Archaeorhizomycetes* are not low-diversity, low-abundance soil fungi as described in (*3*), but in fact quite the opposite.

Although it is apparent that the authors used a single ITS4 primer variant to facilitate inclusion of the barcode tag sequences for multiplexing samples, this is no longer necessary because methods now exist for adding barcode tags after amplification (*12*). With the rapid advancement in parallelization and throughput of samples enabled by current sequencing technologies, the use of multiple primer sets or primer variants is achievable and advisable. The biases of PCR primers for studies of "unknown" organisms in bacterial and fungal ecology have been widely reported, and the continued reliance on single primer sets and variants for such studies compromises our understanding of the diversity and biogeography of microorganisms. It is also incumbent upon microbial ecologists to interpret patterns conservatively, especially given known biases.

REFERENCES

1. T. J. White, T. Bruns, S. J. W. T. Lee, J. W. Taylor, *PCR Protocols* **18**, 315–322 (1990).
2. M. Gardes, T. J. White, J. A. Fortin, T. D. Bruns, J. W. Taylor, *Can. J. Bot.* **69**, 180–190 (1991).
3. L. Tedersoo *et al*., *Science* **346**, 1256688 (2014).
4. A. Rosling *et al*., *Science* **333**, 876–879 (2011).
5. K. Ihrmark *et al*., *FEMS Microbiol. Ecol.* **82**, 666–677 (2012).
6. A. Menkis, H. Urbina, T. Y. James, A. Rosling, *Fungal Biology* **118**, 943–955 (2014).
7. C. W. Schadt, A. P. Martin, D. A. Lipson, S. K. Schmidt, *Science* **301**, 1359–1361 (2003).
8. T. M. Porter *et al*., *Mol. Phylogenet. Evol.* **46**, 635–644 (2008).
9. H. F. Castro, A. T. Classen, E. E. Austin, R. J. Norby, C. W. Schadt, *Appl. Environ. Microbiol.* **76**, 999–1007 (2010).
10. D. L. Taylor *et al*., *Ecol. Monogr.* **84**, 3–20 (2014).
11. A. Rosling, I. Timling, D. L. Taylor, in *Genomics of Soil- and Plant-Associated Fungi*, B. A. Horwitz, P. K. Mukherjee, M. Mukherjee, C. P. Kubicek, Eds. (Springer, Heidelberg, Germany, 2013), pp. 333–349.
12. D. S. Lundberg, S. Yourstone, P. Mieczkowski, C. D. Jones, J. L. Dangl, *Nat. Methods* **10**, 999–1002 (2013).

11 December 2014; accepted 15 April 2015
10.1126/science.aaa4269

Downloaded from www.sciencemag.org on June 26, 2015

TECHNICAL COMMENT

ANIMAL COGNITION

Comment on "Number-space mapping in the newborn chick resembles humans' mental number line"

Madhur Mangalam[1]* and Shraddha Madhav Karve[2]

Rugani *et al*. (Reports, 30 January 3015, p. 534) tested 3-day-old domestic chicks using an innovative experimental setup and demonstrate the presence of the mental number line. We raise concerns regarding this conclusion by highlighting the possible loopholes in the experimental design and the data analysis procedures. We further suggest auxiliary experiments that can substantiate the authors' claim.

Empirical evidence supports the possibility that humans represent numbers along a mental number line (MNL) in ascending order from left to right (*1*). The origin of this MNL, however, is contentious. Interspecific comparison of numerical competence among humans and nonhuman animals suggests a continuous and nonverbal representation of numbers (*2*). Rugani *et al*. (*3*) tested the existence of the MNL in 3-day-old domestic chicks. An initial training phase involving a reward association with a certain number was followed by a test phase in which the same subjects are challenged by a number smaller or larger than the one used for training. The authors concluded that the subjects associated smaller numbers with the left space and larger numbers with the right space during the test phase. Additionally, this bias was displayed according to the relative magnitude of the challenge and was not an absolute bias toward a certain number.

Experiment 1 tested 15 subjects with numbers "2" and "8" after training with "5," and experiment 2 tested 12 subjects with numbers "8" and "32" after training with "20." In both experiments, half of the subjects were tested for the smaller number first, and the other half were tested for the larger number first (five trials each). The results are shown to be independent of the order of testing; thus, the authors consider each of the $2 \times 5 = 10$ trials to be independent.

There are confounds that possibly violate the assumption of the 10 trials to be independent.

Several studies have demonstrated that young chicks show lateral biases at spatial tasks (*4*–*6*). Any such bias is likely to be exaggerated as an artifact when the same subject is used repeatedly. Simply put, 70% of 15 subjects × 5 trials—that is, ~53 out of 75—is significant (binomial test with hypothetical probability of success = 0.5; $P < 0.001$), but 70% of 15 subjects × 1 trial—that is, ~11 out of 15—is not (binomial test, $P = 0.119$). One can argue that if such bias exists, it will manifest in the second set of trials as well, with the subject showing bias inconsistent with the MNL. However, once the chicks associate the smaller number 2 with the left space (which is not unlikely after five consecutive trials), just changing the stimulus to 8 can result in a move toward the right space, possibly because of the discrepancy in the association and the novelty factor (*6*). The same can also be true for the group of subjects challenged with the larger number stimulus 8 in the first place. Thus, the assumption of the 10 trials being independent is objectionable.

Moreover, the data on chicks choosing either the left or the right space follows the binomial distribution; the use of the Mann-Whitney *U* test is likely to be erroneous. Although according to the Mann-Whitney *U* test, the two data sets: (6, 6, 6, 6, 6, 6, 6, 6, 6, 6) and (5, 5, 5, 5, 5, 5, 5, 5, 5, 5) are different ($U = 0$; df = 19; $P < 0.001$), they are not different according to a binomial test (binomial test: 60/100; $P = 0.060$). For the same reason, studies on manual asymmetries in nonhuman primates use binomial *z* scores to examine individual-level biases; the *z* test is then used to examine population-level biases (*7*).

The concerns we have raised suggest that the evidence for the presence of the MNL in chicks might be insufficient currently.

In addition to the existing set of experiments, we would like to suggest a parallel set of experiments involving a blank panel. Apart from substantiating the current findings, these experiments will give a clue to the presence of zero in the MNL. Train the chicks with a blank panel and then test them with number panels; in another experiment, train the chicks with a number panel and then test them with blank panels. If one assumes the absence of the concept of zero in chicks, there should be no bias in either experiment, which would support the findings of Rugani *et al*. (*3*). However, a strong bias in these experiments will substantiate the authors' claim, with a startling proposition that chicks have some parallel to zero in the MNL.

[1]Department of Psychology, University of Georgia, Athens, GA 30602, USA. [2]Indian Institute of Science Education and Research Pune, Pune 411 008, India.
*Corresponding author. E-mail: madhur.mangalam@uga.edu

REFERENCES

1. S. Dehaene, *The Number Sense* (Oxford Univ. Press, New York, 2011).
2. D. B. Haun, F. M. Jordan, G. Vallortigara, N. S. Clayton, *Trends Cogn. Sci.* **14**, 552–560 (2010).
3. R. Rugani, G. Vallortigara, K. Priftis, L. Regolin, *Science* **347**, 534–536 (2015).
4. G. Vallortigara, L. Regolin, G. Bortolomiol, L. Tommasi, *Behav. Brain Res.* **74**, 135–143 (1996).
5. L. Regolin, G. Vallortigara, *Behav. Processes* **37**, 67–74 (1996).
6. M. Dharmaretnam, L. J. Rogers, *Behav. Brain Res.* **162**, 62–70 (2005).
7. E. V. Lonsdorf, W. D. Hopkins, *Proc. Natl. Acad. Sci. U.S.A.* **102**, 12634–12638 (2005).

18 February 2015; accepted 7 May 2015
10.1126/science.aaa8577

Downloaded from www.sciencemag.org on June 26, 2015

TECHNICAL COMMENT

ANIMAL COGNITION

Comment on "Number-space mapping in the newborn chick resembles humans' mental number line"

Christopher Harshaw

Rugani *et al*. (Reports, 30 January 2015, p. 534) presented evidence that domestic chicks employ a "mental number line." I argue that the hypothesis testing used to support this claim unjustifiably assumes that domestic chicks are unbiased when choosing between identical stimuli presented to their left and right.

Rugani *et al*. (*1*) presented evidence in support of the claim that domestic chicks (*Gallus gallus domesticus*) employ a "mental number line" similar to that used by most, but not all, humans. This Comment will focus on a critical flaw in the study's design and statistical analysis. I argue that Rugani *et al*. failed to measure, model, or control for the significant side biases displayed by precocial birds, including the domestic chicks used in their study (*2*–*9*).

Precocial chicks possess highly lateralized brains and, consequently, show strong motor and perceptual biases (*10*)—biases often more extreme than human analogs (e.g., pseudoneglect). For example, chicks show significant bias for turning left at the intersection of a T maze (*4*, *6*, *9*, *11*), in addition to task-dependent preferences for foot and eye use (*2*, *3*, *5*). Such biases are sculpted by normally occurring pre- and perinatal experience, including both differential exposure of the hemispheres to audiovisual stimulation prenatally (*4*, *7*, *11*, *12*) and the repetitive turning movements necessary for chicks to successfully hatch from the egg (*6*, *9*). As a consequence, as many as 67 to 90% of domestic chicks display significant side biases in tasks requiring a locomotor response (*4*, *6*, *9*).

Side biases are less consequential in experiments involving choice between nonidentical stimuli, because counterbalancing can be used to distribute error stemming from such bias between stimuli and competing hypotheses. In contrast, in designs involving choice between identical stimuli presented to the left and right of the subject, such as employed by Rugani *et al*., side biases require far closer attention, as the problem of dissociating side bias from experimental effect becomes central to the ability to draw meaningful conclusions. There are several acceptable ways of accomplishing this. One is to provide independent trials in which bias is measured (e.g., a series of trials similar, although not identical, to testing, covering the range of stimuli in the study) and correcting for bias on a chick-by-chick basis. Another approach is to test a more sophisticated model that includes a bias parameter, as is common in many operant paradigms involving choice [e.g., *13*)]. Finally, the null hypotheses tested could be adjusted to reflect the average bias in a particular population. In the latter case, a result would be declared significant only if it exceeded this average expected bias.

None of these approaches were taken by Rugani *et al*., who instead relied on single-sample *t* tests evaluated against a null hypothesis of 0.5 (50% left, 50% right) for all of their key comparisons. As noted previously, there is nevertheless a strong a priori reason to expect motor and perceptual biases under the conditions used in this study [e.g., (*4*, *6*, *9*)]. Evidence of side bias is also detectable in Rugani *et al*. For example, the average absolute deviation from 50/50 responding across all 10 trials for each chick was 12.7% ± 1.1%, indicating that most chicks exhibited some degree of bias ($t = 11.5$, $P < 0.00001$). If the conservative approach of adjusting the null hypotheses tested to reflect the average absolute bias displayed by chicks in each experiment (i.e., testing a chance-plus-bias model) were taken, a significant difference would have been found only for the small numerosity trial of experiment 3b ($t = 2.12$, $P < 0.03$) and large numerosity trials of experiments 2, 3a, and 3c ($t = -2.61$, $P < 0.02$; $t = -3.66$, $P < 0.002$; and $t = -1.79$, $P < 0.05$, respectively; one-tailed testing).

If a stricter bias criterion were applied—for example, ≥70% choices on a single side, then 60% of chicks (9 out of 15) in experiment 1 and 34.4% of chicks across all experiments exhibited bias. Theoretically, this would not present a serious challenge to the conclusions of the study if such biases were symmetrical around a mean of 0.50 and affected both major hypotheses equally. With respect to the first consideration, the majority of chicks (63.6%) that met the stricter bias criterion (i.e., ≥70%) exhibited rightward bias. Considering all subjects, the average proportion of choices made to the right across all experiments was 0.522 ± 0.019, indicating a similar, albeit weaker bias ($t = -1.147$, $P = 0.26$). This bias was largest in experiment 3a, in which the proportion of choices to the right was 0.571 ± 0.037—a borderline significant difference from 0.5 ($t = -1.92$, $P = 0.081$). Did bias affect both hypotheses equally? Figure 1 displays the percentage of chick choices to the left and right on small and large trials, respectively, plotted both against the absolute value of chick bias (A and B) and side bias relative to predicted outcomes (C and D). As can be seen, the absolute value of chick bias appears to have significantly influenced the outcome on small ($r = -0.277$, $P < 0.03$) but not large ($r = -0.042$, $P = 0.742$) trials (upper panels), whereas the direction of bias correlated significantly with predicted outcomes on both trial types (lower panels).

The foregoing analyses demonstrate that there was unaccounted bias in Rugani *et al*. that differentially affected the study's two major predictions. That is, rightward bias likely inflated chick performance on large numerosity trials and interfered with chick performance on small numerosity trials. Given that there is no choice test between identical stimuli presented to the left and right of a domestic chick in which significant bias would not be expected a priori, the hypotheses tested by Rugani *et al*. are closer to statistical "straw men" than empirically meaningful. Both the training that chicks underwent before testing and the logic of the series of experiments are irrelevant to this consideration. Nevertheless, it should be noted that the analyses presented here are by no means ideal, given that the measures of bias employed are necessarily confounded by any experimental (i.e., training-induced) effect present.

Department of Psychological and Brain Sciences, Indiana University, Bloomington, IN 47405, USA.
E-mail: charshaw@indiana.edu

REFERENCES AND NOTES

1. R. Rugani, G. Vallortigara, K. Priftis, L. Regolin, *Science* **347**, 534–536 (2015).
2. L. J. Rogers, L. Workman, *Anim. Behav.* **45**, 409–411 (1993).
3. G. Vallortigara, L. Regolin, G. Bortolomiol, L. Tommasi, *Behav. Brain Res.* **74**, 135–143 (1996).
4. M. B. Casey, S. Karpinski, *Psychol. Rec.* **49**, 67–74 (1999).
5. L. Tommasi, G. Vallortigara, *Laterality* **4**, 89–95 (1999).
6. M. B. Casey, C. M. Martino, *Dev. Psychobiol.* **37**, 13–24 (2000).
7. M. Koshiba, S. Nakamura, C. Deng, L. J. Rogers, *Neurosci. Lett.* **336**, 81–84 (2003).
8. R. J. Andrew, A. N. B. Johnston, A. Robins, L. J. Rogers, *Behav. Brain Res.* **155**, 67–76 (2004).
9. M. B. Casey, *Dev. Psychobiol.* **47**, 123–135 (2005).
10. L. J. Rogers, *Brain Res. Bull.* **76**, 235–244 (2008).
11. M. B. Casey, R. Lickliter, *Dev. Psychobiol.* **32**, 327–338 (1998).
12. C. Deng, L. J. Rogers, *Behav. Brain Res.* **134**, 375–385 (2002).
13. J. E. Mazur, *Psychol. Rev.* **108**, 96–112 (2001).

ACKNOWLEDGMENTS

I thank M. Casey, J. Spencer, D. Landy, M. Blumberg, B. Lickliter, C. Allen, and J. de Leeuw for helpful feedback on a previous draft.

19 February 2015; accepted 7 May 2015
10.1126/science.aaa9565

Downloaded from www.sciencemag.org on June 26, 2015

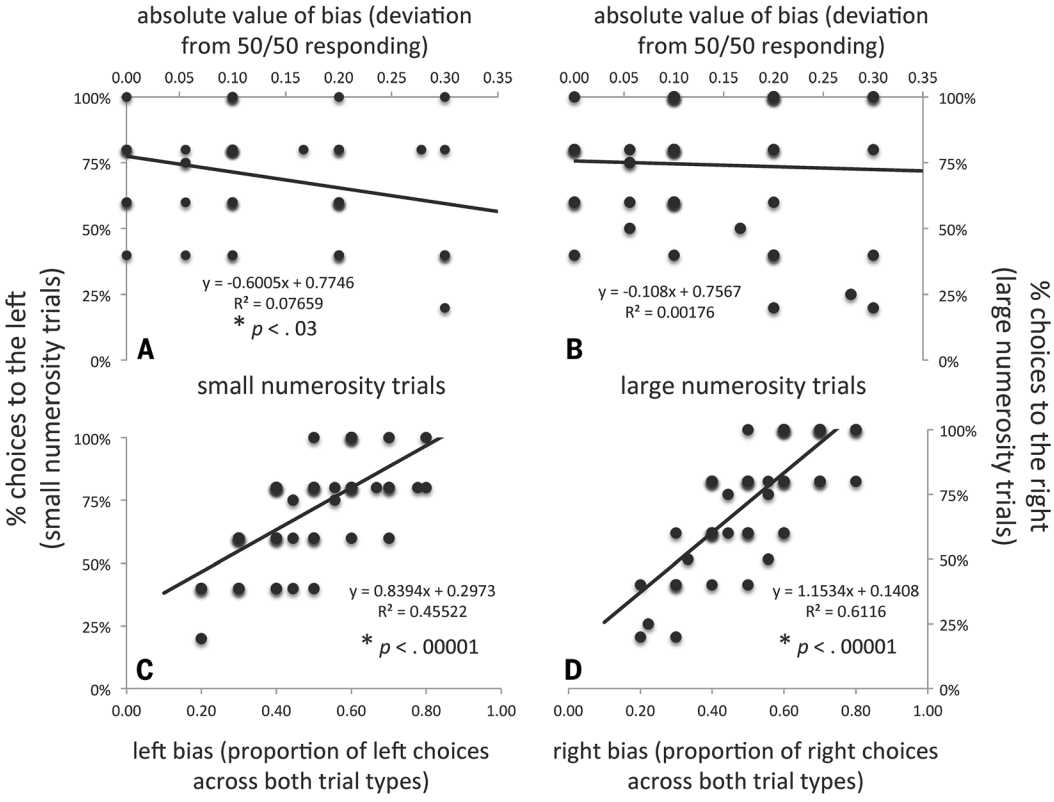

Fig. 1. An illustration of the effects of side bias on the two predicted outcomes of the study. The choice of "left" on small numerosity trials (**A** and **C**) and the choice of "right" on large numerosity trials (**B** and **D**). In (A) and (B), the *x* axis depicts the absolute value of chick bias (i.e., the absolute value of 0.5 minus the proportion of choices made to the left). In (C) and (D), the *x* axis depicts the strength of side bias relative to the predicted direction. An asterisk indicates a significant Pearson's correlation. As can be seen, the absolute value of chick bias appears to have had a significant effect on the outcome of small but not large numerosity trials [(A) and (B)], whereas the direction of chick bias correlates strongly with predicted outcomes on both trial types [(C) and (D)].

TECHNICAL RESPONSE

ANIMAL COGNITION

Response to Comments on "Number-space mapping in the newborn chick resembles humans' mental number line"

Rosa Rugani,[1,2]* Giorgio Vallortigara,[1] Konstantinos Priftis,[2] Lucia Regolin[2]

Mangalam and Karve raise concerns on whether our results demonstrate a mental number line, suggesting auxiliary experiments. Further data analyses show that their methodological concerns are not founded. Harshaw suggests that a side bias could have affected our results. We show that this concern is also unfounded.

Mangalam and Karve claim that some confounds may violate the assumption of trials' independency of the measures and criticize the use of the Mann-Whitney test instead of the binomial test (*1*). We have now analyzed chicks' performance focusing on the first trial only, as this cannot be influenced by any previous trials. We computed the number of chicks that chose the left panel on the first trial in the small number test and the number of chicks that selected the right panel in the first trial of the large number test. We applied the binomial test. Chicks significantly circumnavigated the left panel in the small number test (experiment 1: 14/15, $P < 0.01$; experiment 2: 10/12, $P = 0.04$; experiment 3: 31/37, $P < 0.01$) and the right panel in the large number test (experiment 1: 12/15, $P = 0.04$; experiment 2: 12/12, $P < 0.01$; experiment 3: 32/37, $P < 0.01$).

When, in a further analysis, we selectively considered the first trial of the first test performed, chicks significantly chose the left panel in the small number test (experiment 1: 7/8; experiment. 2: 5/6; experiment 3: 16/20; overall 28/34, $P < 0.01$) and the right panel in the large number test (experiment 1: 5/7; experiment 2: 6/6; experiment 3: 13/17; overall 24/30, $P < 0.01$).

[1]Center for Mind/Brain Sciences, University of Trento, Rovereto (Trento), Italy. [2]Department of General Psychology, University of Padova, Padova, Italy.
*Corresponding author. E-mail: rosa.rugani@unitn.it or rosa.rugani@unipd.it

Mangalam and Karve pointed out that the bias may be related to feeding, with a preferential activation of the right eye (left hemisphere) at the population level. It should be noted that in the paper they quoted (*2*), selective lateralization for food discrimination and antipredatory responses were simultaneously assessed. Note, also, that the opposite bias is reported in feeding tasks (*3*). Once a given number is associated with food, the reinforcement expectation may increase in front of larger numbers. Let us arbitrarily suppose the existence of a rightward bias because of use of the right eye in association with feeding during training. The right bias would be somewhat amplified in the large number test. When chicks are subsequently presented with the small number test, the bias would turn to a left bias for some reason, as Mangalam and Karve advocate (namely, a discrepancy in the association or a novelty factor). Whatever the reason for the change in the bias between the first and second tests, there would be reasons to expect that such a shift involved only one direction (plausibly the left one, because of right-hemisphere involvement in response to novelty (*4*). Instead, the direction of the bias we found, already on the very first test, was opposite depending on initial training: Chicks trained on 5 associated 8 with the right; chicks trained on 20 associated 8 with the left.

With reference to the experiments with zero, there is a problem when using a blank panel, namely, the change in continuous physical variables, which would obviously be impossible to control.

In sum, the alternative hypothesis suggested by Mangalam and Karve would at most explain only the data of those subjects that first underwent the "large number test." It would not explain the preferential choice of the left side for the "small number test," in particular when this was the first test administered.

Harshaw considers crucial the role of side biases displayed by individual chicks (*5*). He computes an index of bias that could be negative (leftward bias), positive (rightward bias), or equal to 0 (absence of any bias). The overall bias in our sample (mean = 0.02; SE = 0.02; $t = 1.15$; $P = 0.26$) demonstrates Harshaw's concerns to be unfounded. In his comment, Harshaw averaged the absolute values of left and right biases, resulting in an overall bias cumulating left and right tendencies as if all chicks had a rightward bias. Correlations reported in his figure 1 (*5*) are misleading, as absolute values are represented along the x axis.

Concerning Harshaw's "stricter bias" (arbitrarily fixed at "≥70% choices on a single side"), his claim that it "would not present a serious challenge to the conclusions of the study if such biases were symmetrical around the mean of 0.50" is rhetorical. Harshaw in fact fails to conclude that of the 22 chicks displaying the bias (34.40% of the 64 subjects), 14 subjects had a right "bias" and 8 subjects a left "bias" (binomial test 14 versus 8, $P = 0.29$). The difference is not significant, so this bias could not have influenced our results.

Overall alternative interpretations to the idea of a mental number line are of course yet possible. However, up to now, our number-space mapping hypothesis (*6*) is the only one that optimally fits our results.

REFERENCES AND NOTES

1. M. Mangalam, S. M. Karve, *Science* **348**, 1438 (2015).
2. M. Dharmaretnam, L. J. Rogers, *Behav. Brain Res.* **162**, 62–70 (2005).
3. B. Diekamp, L. Regolin, O. Güntürkün, G. Vallortigara, *Curr. Biol.* **15**, R372–R373 (2005).
4. J. N. Daisley, E. Mascalzoni, O. Rosa Salva, R. Rugani, L. Regolin, *Philos. Trans. R. Soc. B* **364**, 965–981 (2009).
5. C. Harshaw, *Science* **348**, 1438 (2015).
6. R. Rugani, G. Vallortigara, K. Priftis, L. Regolin, *Science* **347**, 534–536 (2015).

ACKNOWLEDGMENTS

We thank P. Bolzon for helpful support with the statistical analyses.

12 March 2015; accepted 7 May 2015
10.1126/science.aab0002

Downloaded from www.sciencemag.org on June 26, 2015

Breaking through the polycarbonate ceiling

By **Kathy Wren**

While visiting Cambodia as a U.S. science envoy, AAAS President Geri Richmond met with girls learning to use tablets at the Hun Sen Anuwat School.

PHOTO: COURTESY GERI RICHMOND

Many people describe the obstacles to women's professional advancement as a "glass ceiling," but chemist and AAAS President Geri Richmond chooses her materials-based metaphors more carefully.

Unlike glass, which can be shattered, "polycarbonate is one of our most robust polymers, so you bounce off it," said Richmond, who is also a U.S. science envoy as well as presidential chair and professor of chemistry at the University of Oregon. Those who encounter a polycarbonate ceiling blocking career advancement must find creative ways around it, she added.

A longtime leader in the effort to enhance diversity in the science, technology, mathematics, and engineering (STEM) workforce, AAAS is continuing to help women and other underrepresented groups transcend the polycarbonate ceiling, guided by Richmond and other members of the AAAS leadership team, including Shirley Malcom, director of AAAS Education and Human Resources (EHR). Malcom, who this month received the UCLA Medal in part for her efforts to diversify the science community, serves as co-chair of the Gender Advisory Board of the UN Commission on Science and Technology for Development and of Gender InSITE, a global campaign to deploy science and technology to help improve the lives and status of girls and women.

A variety of AAAS projects currently offer early-career support for women, minorities, and persons with disabilities, through conferences, awards, internships, and other activities. Additional efforts, including a newly enhanced program supporting international collaboration by women researchers, are focusing on later-career needs.

Ultimately, "our institutions must transform to support values of excellence as well as diversity, equity, and inclusion," Malcom said. "We need to go after the institutional barriers that keep women in marginalized positions within science, in the United States and beyond."

Describing the realization that led her to found COACh, a career-training and networking program for women scientists and engineers in the United States and developing countries, Richmond recalled a time in the 1990s when she was seeing the careers of her women colleagues stalling unexpectedly: "They were publishing, they were getting grants, they were keeping their research groups going, but they were hitting this polycarbonate ceiling. They weren't getting the invited talks. They weren't getting the distinguished lectureships. They weren't getting the offers from other universities that you would see the men get, yet they were equally capable."

Collaborating internationally can often lead to new professional opportunities, but extended travel can be difficult for mothers with young children or others with family obligations. Through surveys and focus groups, the AAAS Women's International Scientific Cooperation (WISC) project concluded that requiring shorter stays abroad, as compared to other international travel grants, would make international collaborations more accessible for women.

Through a follow-up program, Mentoring Women in International Research Collaborations (MWIRC) in STEM, AAAS has thus far administered 15 grants of $20,000 each, with funding from the National Science Foundation. The program has ramped up in recent months, with a new travel award that sent two women scientists to the international Gender Summit in Cape Town in April and will send 12 more participants to the next three Summits.

The program has also rolled out a new website and is conducting webinars for awardees to share experiences and advice.

MWIRC support has made a marked impact on the career of Delaram Kahrobaei, a computer scientist at the City University of New York (CUNY), who collaborated with a mathematician colleague at Universitat Politècnica de Catalunya in Barcelona. Since traveling to Spain, Kahrobaei and two graduate students have published papers, established a seminar based on their findings, and given a variety of conference presentations. In a 20 May AAAS webinar, Kahrobaei said that these developments contributed to her recent promotion to full professorship. CUNY "looks very favorably on international collaboration," she said.

Other AAAS activities aim to make science and technology careers more inclusive at the early-career level, such as the Entry-Point! internships for students with disabilities and the Emerging Researchers National Conference in STEM hosted by AAAS and the National Science Foundation. AAAS also administers the annual L'Oréal awards, which provide grants to women doing postdoctoral research. And, starting this month, AAAS's Marion Milligan Mason Fund will provide three grants of $50,000 every other year to women researchers engaged in basic research in the chemical sciences.

At the AAAS Annual Meeting, EHR organizes an intergenerational networking breakfast for women and minority attendees, which includes a ceremony honoring early-career women scholars from developing countries who are receiving awards from the Elsevier Foundation, with The World Academy of Sciences and the Organization for Women Scientists for the Developing World. ■

Downloaded from www.sciencemag.org on June 26, 2015

Published by AAAS

RESEARCH

Evanescent modes of Maxwell equations

Bliokh et al., *p. 1448*

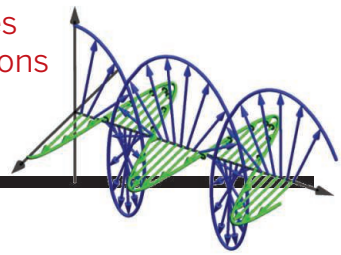

IN *SCIENCE* JOURNALS

Edited by **Stella Hurtley**

Corals inherit heat tolerance in northern Great Barrier Reef

CORAL REEFS

Some like it hot

Coral reefs are threatened by increasing temperatures. Acute temperature increases stress and damage corals. However, more gradual temperature changes can result in adaptation and subsequent tolerance for higher temperatures. Dixon *et al*. show that the heat tolerance that currently exists across coral populations from different latitudes can be inherited. Thus, natural variation in temperature tolerance may facilitate rapid adaptation among corals as our climate warms. — SNV

Science, this issue p. 1460

3D LITHOGRAPHY

Complex shapes from chemical lithography

Lithographic printing of semiconductors builds up complex patterns one layer at a time. The process involves multiple steps to mask, print, and etch each layer. Luo *et al.* tweaked the same process used to grow silicon nanowires to pattern them into complex three-dimensional (3D) shapes. Gold acted as a catalyst to grow and elongate silicon nanowires from the vapor phase. Varying the pressure of the growth process altered the rate of gold diffusion along the surface of the wire. Upon etching the wires, the non-uniform coating of gold acted as a lithographic mask. The authors were thus able to make complex-shaped silicon spicules with a series of ridges and notches by strictly chemical means. — MSL

Science, this issue p. 1451

MATERIALS CHEMISTRY

A green way to clean up an oil spill

Cleaning thin films of light crude oil from the marine environment is a herculean task. Currently, silicone-based compounds are used, which can leave a permanent residue. Inspired by the natural pigments in plants, John *et al.* developed a plant-based oil-cleaning agent. The product functions as a "green" chemical herder to retract thin oil layers into a thickened mass suitable for recovery or burning. The biodegradable agent was as good as synthetic chemicals at corralling oil and left no residual contamination. — ZHK

Sci. Adv. 10.1126. sciadv.1400265 (2015)

GENE REGULATION

Multitasking around the clock

Chronic disruption of our circadian rhythms—for example, through shift work—may increase the risk of metabolic disease. Zhang *et al.* found that a multitasking transcription factor called Rev-erb-α regulates expression of both clock and metabolic genes through distinct mechanisms. At clock genes, it binds directly to a specific DNA sequence, displacing a competing transcription factor. At metabolic genes, it interacts not with DNA but with other transcription factors that regulate metabolic gene expression in a tissue-specific manner. — PAK

Science, this issue p. 1488

BRAIN CIRCUITS

Looming in on the threat-response circuit

What are the neural elements that transmit threat-relevant inputs in the brain? Shang *et al.*

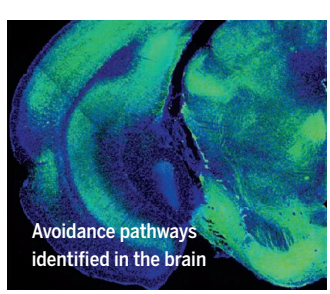

Avoidance pathways identified in the brain

IMAGES: (TOP TO BOTTOM) BLIOKH *ET AL.*; LINE K. BAY/AUSTRALIAN INSTITUTE OF MARINE SCIENCE; SHANG *ET AL.*

Downloaded from www.sciencemag.org on June 26, 2015

Published by AAAS

systematically identified the key neuronal subtypes in the mouse superior colliculus underlying active avoidance and defensive-like behaviors. They found a pathway that responded to looming objects, linking input from the retina to the fear center in the brain. — PRS

Science, this issue p. 1472

DERMATOLOGY

B12 boosts acne via the microbiota

Low doses of vitamin B12 supplements can help acne, but in higher doses the same supplement can cause acne flare-ups. Why? Kang *et al.* show that transcriptional changes in the resident microbes of the skin enhance B12-induced acne. Supplementing patients with the vitamin reduced the expression of B12-synthesis genes in *Propionibacterium acnes.* This altered the transcriptome of the skin microbiota, driving production of inflammation-inducing porphyrins. — ACC

Sci. Transl. Med. **7**, 293ra103 (2015).

STRUCTURAL BIOLOGY

An RNA seed poised to meet its target

The CRISPR-Cas system in prokaryotes precisely identifies infecting parasitic DNAs and viruses and destroys them. The CRISPR-Cas system has been adapted for facile genome editing, heralding a new age in molecular biology. Jiang *et al*. show that the Cas9 nuclease adopts a distinct confirmation when it binds to the targeting guide RNA. The guide RNA then assumes a preordered shape. This RNA "seed region" is thus poised to initiate recognition of the DNA target sequence. — GR

Science, this issue p. 1477

PHOTOSYNTHESIS

Protection from too much light

Photosynthetic organisms protect themselves from too much light using pigment photoswitches that absorb excess energy. Leverenz *et al*. analyzed the structure of an active, energy-dissipating form of the orange carotenoid protein (OCP) from a cyanobacterium. When activated by excess light, OCP moves its hydrophobic carotenoid pigment 12 Å within the protein to accommodate nonphotochemical quenching by the broader photosynthetic antenna complex. — NW

Science, this issue p. 1463

CLIMATE CHANGE

Walking back talk of the end of warming

Previous analyses of global temperature trends during the first decade of the 21st century seemed to indicate that warming had stalled. This allowed critics of the idea of global warming to claim that concern about climate change was misplaced. Karl *et al.* now show that temperatures did not plateau as thought and that the supposed warming "hiatus" is just an artifact of earlier analyses. Warming has continued at a pace similar to that of the last half of the 20th century, and the slowdown was just an illusion. — HJS

Science, this issue p. 1469

APPLIED OPTICS

Getting around the capacity crunch

The growing appetite for an ever-faster Internet and enhanced long-haul communication requires the pumping of more light down optic fibers. However, light-induced nonlinearities limit how much light can be pumped into the fiber without compromising the signal. This limitation has led to the prospect of a "capacity crunch." Temprana *et al*. eliminated the effects of nonlinearity by using digital back-propagation methods with mutually coherent laser pulses from a single frequency comb. — ISO

Science, this issue p. 1445

IN OTHER JOURNALS

Edited by **Sacha Vignieri** *and* **Jessse Smith**

Animal domestication altered the human diet and may have done the same to our genome

HUMAN GENETICS

Cultural imprints on the human genome

As modern humans and society evolved, animal husbandry and farming changed the way humans eat. Valente *et al*. investigated how differences in diet may have played a role in human evolution. Examining the genetics of African populations with different modes of subsistence, as compared to Europeans, the authors identify selection on gene variants postulated to be adaptive for different diets. However, the degree to which these signals are associated with diet, rather than other environmental factors and evolutionary forces, requires further study. This highlights the difficultly of identifying how human culture has affected our genome. — LMZ

BMC Genet. 10.1186/s12863-015-0212-1 (2015).

DNA BINDING

A sex-determining interaction

Across much of the animal kingdom, DMRT proteins are involved in regulating sexual development. In humans, DMRT1 both activates a male sex-determining gene and deactivates female sex-determining genes. Murphy *et al.* report a crystal structure showing three DNA binding DM domains,

PHOTO: BORSEV/ISTOCKPHOTO

Published by AAAS

ALSO IN *SCIENCE* JOURNALS

Edited by **Stella Hurtley**

EMBRYO DEVELOPMENT

BMP mophogens direct growth and fate

As shown in classic fate-mapping studies, tissues and organs arise from specific regions of the embryo. Work over the past few decades has identified molecular players directing this choreographed development. Bone morphogenetic proteins (BMPs) and their antagonists establish domains in developing embryos. Bier and De Robertis review historical events for key discoveries in this area. They go on to lay out the current understanding of how diffusible morphogens form gradients to subdivide germ layers into distinct territories and organize body axes, regulate growth, and maintain stem cell niches. — BAP

Science, this issue p. 1443

HEART DEVELOPMENT

Making cardiomyocytes

In the heart, multiple cell types work together. Cardiac progenitor cells give rise to cardiomyocyte, endothelial, or smooth muscle lineages. However, the identity of a marker specific to cardiomyocyte formation has been elusive. Jain *et al*. now identify a specialized progenitor population that is committed exclusively to forming cardiomyocytes. They also identify the niche signals that promote lineage commitment and the mechanisms involved in making cardiomyocytes. The findings may help in the development of future cell-based regenerative therapeutics for heart disease. — BAP

Science, this issue p. 1444

OPTICS

A quantum twist on classical optics

Interpreting recent experimental results of light interactions with matter shows that the classical Maxwell theory of light has intrinsic quantum spin Hall effect properties even in free space. Complex effects in condensed-matter systems can often find analogs in cleaner optical systems. Bliokh *et al*. argue that the optical systems exhibiting such complex phenomena should also be simpler (see the Perspective by Stone). Their theoretical study shows that free-space light has a nonzero topological spin Chern number and thus should have counterpropagating surface modes. Such modes are actually well known and can be described as evanescent modes of Maxwell equations. — ISO

Science, this issue p. 1448; see also p. 1432

HIGH-PRESSURE PHYSICS

Driving liquid deuterium into metal

Quick and powerful compression can force materials to change their properties dramatically. Knudson *et al*. compressed liquid deuterium to extreme temperatures and pressures using high-energy magnetic pulses at the Sandia Z-machine (see the Perspective by Ackland). Deuterium began to reflect like a mirror during compression, as the electrical conductivity sharply increased. The observed conditions for metallization of deuterium and hydrogen help us to build theoretical models for the universe's most abundant element. This a our understanding of the internal layering of gas giant planets such as Jupiter and Saturn. — BG

Science, this issue p. 1455; see also p. 1429

MARINE SULFUR CYCLE

Sourcing the smell of the seaside

Marine phytoplankton plays a critical role in the global sulfur cycle. Algae, for instance, are the main source of the aromatic compound dimethylsulfide (DMS) released from the oceans into the atmosphere. Alcolombri *et al*. identified the lyase enzyme responsible for DMS production in the bloom-forming marine phytoplankton *Emiliania huxleyi* (see the Perspective by Johnston). The presence of this gene in other globally distributed phytoplankton and corals suggests that it may serve as a reliable indicator of DMS production across diverse phyla. Because DMS gets oxidized to sulfur aerosols, which act as cloud condensation nuclei, this enzyme is a key global biogeochemical catalyst. — NW

Science, this issue p. 1466; see also p. 1430

GENE SILENCING

Keeping quiet one gene at a time

Chromosomal DNA comes in two flavors—euchromatin, which contains most of the expressed genes, and heterochromatin, which usually remains quiet. But what keeps genes within heterochromatin silent? Tchasovnikarova *et al*. examined the basis for this type of silencing in mammalian cells (see the Perspective by Brummelkamp). They identified a complex of proteins in human cells they called HUSH that kept particular parts of the genome silent by changing associated histone methylation marks. — SMH

Science, this issue p. 1481, see also p. 1433

RNA BIOCHEMISTRY

Unwinding RNA for protein synthesis

During the first steps of protein synthesis, the small subunit of the ribosome scans the 5′ end of the mRNA, looking for the protein start codon. This process involves one of the translation initiation factors, eIF4A, which helps to remove any RNA structures that might impede the ribosome's search. García-García *et al*. used single-molecule optical trap assays to show that eIF4A, in combination with two other translation initiation factors, is able to continuously and directionally unwind a double-stranded RNA hairpin. The factors unwound RNA in steps roughly equal to a turn of the RNA double helix. — GR

Science, this issue p. 1486

SYNTHETIC ECOLOGY

More than the sum of its parts

How do microbial strains and species interact and survive in microbial communities? The answer may help scientists to devise biotechnological processes; e.g., for creating biofuels from biomass. In a Perspective, Fredrickson highlights recent insights into the cooperative mechanisms that help microbial communities to thrive. Different species often share the work of producing essential compounds such as amino acids. Cooperating cells can evolve to outcompete cheaters that exploit such common goods without reciprocation. Spatial organization is also important; for example, in helping mixed biofilms to resist antimicrobials. — JFU

Science, this issue p. 1425

MICROBIOTA

Benefits of breastfeeding

Dietary changes that boost good microflora in our gut are of great health interest, but it is unclear how to best sculpt this microbial community to our benefit. In a Perspective, Hinde and Lewis take an evolutionary view of the infant gut microbiome and breastfeeding for insights into optimizing interventions. *Bifidobacterium* is the major microbial clade in the healthy infant gut. These bacteria

Published by AAAS

metabolize the oligosaccharides most prevalent in human milk, generating byproducts that aid the developing gut and immune system. Natural selection may have favored the coevolution of human milk and a healthy gut microbiota in response to regimes that exerted pressure on immunity and digestion — LDC

Science, this issue p. 1427

DRUG DISCOVERY

Finding better immunosuppressants

The immunosuppressant cyclosporin A (CsA) prevents organ rejection in transplant patients. CsA inhibits the phosphatase calcineurin and prevents the activation of the NFAT transcription factors, both of which are required for T cell proliferation. However, CsA also prevents calcineurin from binding to other targets, leading to many side effects. Matsoukas *et al*. identified compounds that displaced NFAT from calcineurin-NFAT complexes without inhibiting the activity of the phosphatase. Four of these compounds blocked the expression of NFAT target genes and inhibited the proliferation of human $CD4^+$ T cells, and may be good leads for further testing as immunosuppressants. — JFF

Sci. Signal. **8**, ra63 (2015).

Published by AAAS

systematically identified the key neuronal subtypes in the mouse superior colliculus underlying active avoidance and defensive-like behaviors. They found a pathway that responded to looming objects, linking input from the retina to the fear center in the brain. — PRS

Science, this issue p. 1472

DERMATOLOGY

B12 boosts acne via the microbiota

Low doses of vitamin B12 supplements can help acne, but in higher doses the same supplement can cause acne flare-ups. Why? Kang *et al.* show that transcriptional changes in the resident microbes of the skin enhance B12-induced acne. Supplementing patients with the vitamin reduced the expression of B12-synthesis genes in *Propionibacterium acnes.* This altered the transcriptome of the skin microbiota, driving production of inflammation-inducing porphyrins. — ACC

Sci. Transl. Med. **7**, 293ra103 (2015).

STRUCTURAL BIOLOGY

An RNA seed poised to meet its target

The CRISPR-Cas system in prokaryotes precisely identifies infecting parasitic DNAs and viruses and destroys them. The CRISPR-Cas system has been adapted for facile genome editing, heralding a new age in molecular biology. Jiang *et al*. show that the Cas9 nuclease adopts a distinct confirmation when it binds to the targeting guide RNA. The guide RNA then assumes a preordered shape. This RNA "seed region" is thus poised to initiate recognition of the DNA target sequence. — GR

Science, this issue p. 1477

PHOTOSYNTHESIS

Protection from too much light

Photosynthetic organisms protect themselves from too much light using pigment photoswitches that absorb excess energy. Leverenz *et al*. analyzed the structure of an active, energy-dissipating form of the orange carotenoid protein (OCP) from a cyanobacterium. When activated by excess light, OCP moves its hydrophobic carotenoid pigment 12 Å within the protein to accommodate nonphotochemical quenching by the broader photosynthetic antenna complex. — NW

Science, this issue p. 1463

CLIMATE CHANGE

Walking back talk of the end of warming

Previous analyses of global temperature trends during the first decade of the 21st century seemed to indicate that warming had stalled. This allowed critics of the idea of global warming to claim that concern about climate change was misplaced. Karl *et al.* now show that temperatures did not plateau as thought and that the supposed warming "hiatus" is just an artifact of earlier analyses. Warming has continued at a pace similar to that of the last half of the 20th century, and the slowdown was just an illusion. — HJS

Science, this issue p. 1469

APPLIED OPTICS

Getting around the capacity crunch

The growing appetite for an ever-faster Internet and enhanced long-haul communication requires the pumping of more light down optic fibers. However, light-induced nonlinearities limit how much light can be pumped into the fiber without compromising the signal. This limitation has led to the prospect of a "capacity crunch." Temprana *et al*. eliminated the effects of nonlinearity by using digital back-propagation methods with mutually coherent laser pulses from a single frequency comb. — ISO

Science, this issue p. 1445

IN OTHER JOURNALS

Edited by **Sacha Vignieri** *and* **Jessse Smith**

Animal domestication altered the human diet and may have done the same to our genome

HUMAN GENETICS

Cultural imprints on the human genome

As modern humans and society evolved, animal husbandry and farming changed the way humans eat. Valente *et al*. investigated how differences in diet may have played a role in human evolution. Examining the genetics of African populations with different modes of subsistence, as compared to Europeans, the authors identify selection on gene variants postulated to be adaptive for different diets. However, the degree to which these signals are associated with diet, rather than other environmental factors and evolutionary forces, requires further study. This highlights the difficultly of identifying how human culture has affected our genome. — LMZ

BMC Genet. 10.1186/s12863-015-0212-1 (2015).

DNA BINDING

A sex-determining interaction

Across much of the animal kingdom, DMRT proteins are involved in regulating sexual development. In humans, DMRT1 both activates a male sex-determining gene and deactivates female sex-determining genes. Murphy *et al.* report a crystal structure showing three DNA binding DM domains,

PHOTO: BORSEV/ISTOCKPHOTO

Downloaded from www.sciencemag.org on June 26, 2015

Published by AAAS

A methyl donor can reduce an addict's urge for ever more cocaine

NEUROSCIENCE

A new way to reduce drug seeking

Relapse is a serious problem for many individuals trying to recover from addiction. Because DNA methylation regulates neural functions associated with synaptic plasticity, learning, and memory, Wright *et al.* investigated its role in sensitization to cocaine and reinstatement to cocaine and associated cues. A methyl donor, L-methionine, reduced behavioral sensitization to the locomotor-activating and drug-seeking effects of chronic cocaine use. L-methionine also blocked a cocaine-induced marker of neuronal activation after reinstatement in the nucleus accumbens and the medial prefrontal cortex, two brain regions responsible for drug seeking and relapse. — PRS

J. Neurosci., **35,** 8948 (2015).

each comprising a zinc binding module followed by a recognition helix, bound to target DNA. Recognition helices from two domains lie antiparallel in a widened major groove. They find that DMRT1 can bind as a dimer, trimer, or tetramer in vitro and in vivo, with DNA sequence and shape dictating the binding mode. A mutation that causes male-to female sex reversal in humans reduces binding affinity and interferes with the binding stoichiometry of wild-type DMRT1. — VV

Nat. Struct. Mol. Biol. **22**, 442 (2015).

MICROBIOLOGY

How bladder cells kick out unwelcome intruders

The bladder epithelium acts as the front line of the urinary defense system against microbial infection. Miao *et al*. examined urine samples from humans and mice and the extracellular medium of cultured bladder epithelial cells after infection by uropathogenic *Escherichia coli*. Remarkably, they found numerous viable bacteria encased in host-derived membrane-bound vesicles. Intracellular bacteria were initially taken up by autophagosomes and targeted to lysosomes. The bacteria raised the normally low lysosomal pH, which might be expected to protect them from lysosomal degradation. However, the bladder cells sensed the neutralized lysosomes and exocytosed them, expelling the membrane-encased bacteria. The bacteria were thus incapable of reinfection, and the bladder cells defended against their unwelcome visitors. — SMH

Cell **161**, 1306 (2015).

PHYSICS

Seeing single fermions in optical lattices

Peeking directly into quantum matter as it undergoes phase transitions at low temperature has long been a goal of condensed-matter physicists. This intimate view was made possible by atomic physicists, who visualized individual atoms of ^{87}Rb in optical analogs of solid-state systems: optical lattices. But the relevant particle insolid-statesystemsisanelectron—a fermion—whereas an atom of ^{87}Rb is a boson. Visualizing single fermionic atoms in optical lattices presented considerable technical challenges; now, Cheuk *et al*., Parsons *et al*., and Haller *et al.* have achieved this goal using two different atomic species (fermionic ^{40}K and ^{6}Li) and two different cooling techniques. It is expected that these works will enable insight into the many-body behavior of fermions. — JS

Phys. Rev. Lett. **114**, 193001; 213002 (2015); arXiv:1503.02005.

ANALYTICAL CHEMISTRY

A faster way to weigh electrode products

It's becoming increasingly convenient to measure the mass of chemical compounds. Whereas mass spectrometry used to require intricate preparation, several current implementations can weigh molecules straight from a sample in open air. Brown *et al.* have now adapted one such technique to study the short-lived initial products of electrochemical oxidation reactions. Their apparatus incorporates a spinning platinum electrode that accumulates a thin film of the reaction medium on its surface. Application of voltage then generates charged products in that film that can be swept into the mass spectrometer within tens of milliseconds. The authors apply the technique to identify diimine intermediates in both uric acid and xanthine oxidations. — JSY

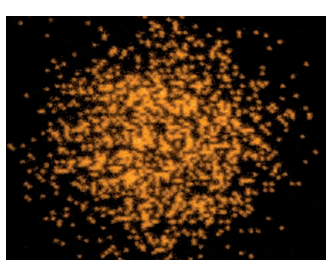

Fermonic ^{40}K atoms on a densely filled optical lattice

J. Am. Chem. Soc. 10.1021/jacs.5b03862 (2015).

EDUCATION

A PORTAAL to active learning

The shift from traditional lectures to active learning continues in science education. Eddy *et al.* report on the Practical Observation Rubric To Assess Active Learning (PORTAAL), a new assessment tool designed to help teachers implement active learning activities. A thorough review of the discipline-based education research literature led to the identification of 21 readily implemented elements shown to increase relevant learning goals with undergraduate students, which are now easily evaluated using PORTAAL. After only 5 hours of training, teachers can use PORTALL to measure how their teaching practices and classrooms align with research-supported best practices for active learning. Additionally, PORTAAL provides feedback and guidance to instructors, allowing them to improve their pedagogy. — MM

CBE Life Sci. Educ. **14**, ar23; 10.1187/cbe.14-06-0095 (2015).

PHOTOS: (TOP TO BOTTOM) GBRUNDIN /ISTOCKPHOTO; LAWRENCE CHEUK/MIT

Published by AAAS

REVIEW SUMMARY

EMBRYO DEVELOPMENT

BMP gradients: A paradigm for morphogen-mediated developmental patterning

Ethan Bier* and Edward M. De Robertis*

BACKGROUND: Classic embryological studies showed that diffusible factors (morphogens) influence cell fate during dorsal-ventral (DV) axis patterning. Subsequently, mathematical analyses applied reaction-diffusion equations in a theoretical framework to model how stable gradients of morphogenetic factors might be created in developing cell fields, according to the laws of physical chemistry. This work suggested mechanisms by which such gradients form and are read in a threshold-dependent fashion to establish distinct cellular responses. As highlighted in this Review, these pioneering experimental and intellectual insights laid the groundwork for more recent studies that have elucidated the mechanisms by which morphogen gradients are generated and stabilized by molecular feedback circuits.

ADVANCES: The molecular players involved in early DV patterning uncovered over the past two decades constitute a highly conserved cohort of extracellular factors that regulate bone morphogenetic protein (BMP) signaling. A key insight was the identification of the homologous proteins Short gastrulation (Sog) and Chordin as BMP-binding proteins in *Drosophila* and *Xenopus* 20 years ago. Since then, analysis of this patterning system has led to dramatic advances in our understanding of the molecular mechanisms regulating early DV axis specification. Elements of this pathway include secreted BMP ligands and BMP antagonists, as well as extracellular metalloproteinases that cleave and inactivate BMP antagonists. Identification of these and other accessory proteins provided strong support for the proposal that an inversion of the DV axis had occurred between arthropods and vertebrates. Analysis of how these components are deployed in an array of species with divergent developmental strategies has deepened our understanding of this ancestral DV patterning biochemical pathway. These comparative studies have shed light on the broader question of a how a conserved core pathway can be modified during evolution to accommodate different forms of embryogenesis while maintaining common output effector functions. In addition, advances in computational analysis have provided the necessary tools to analyze BMP-mediated signaling in quantitative terms and have provided important insights into how this patterning process is integrated with cell proliferation and tissue growth. One such insight is the identification of expanders (such as Pentagone and Sizzled), which are secreted molecules typically produced at the low end of a gradient that stabilize the ligand, scaling the gradient to the growth of tissues.

ON OUR WEB SITE

Read the full article at http://dx.doi.org/10.1126/science.aaa5838

OUTLOOK: An important unanswered question is how morphogen gradients form and function reliably in the face of intrinsic signal-degrading processes to achieve consistent developmental patterning and growth. One testable hypothesis, based on the "wisdom of crowds" concept, that may shed light on this challenging problem is that several independent features of morphogen gradients can be read in parallel by cells and can also serve as inputs to an array of feedback modules that integrate instantaneous levels of signaling, perform time averaging of signals, and act locally to coordinate signaling between neighboring cells. A consensus-based estimate of the relative position of a cell may be reached by deploying multiple parallel feedback modules. In addition, it will be important to determine the roles of mechanisms, such as free or facilitated diffusion in the extracellular space; exosomes; and cytonemes in morphogen gradient function. Understanding the mechanisms by which morphogen-mediated patterning systems evolve to maintain key elements of overall body design while allowing for a marked diversity in the spatial deployment of various subsets of signaling components is another compelling challenge. Such studies should better illuminate the precise nature of highly constrained developmental processes and delineate more fluid features of the networks that permit remodeling of core components to meet the specialized selective needs of particular organisms. These future studies should refine and strengthen one of the best paradigms for understanding development. ■

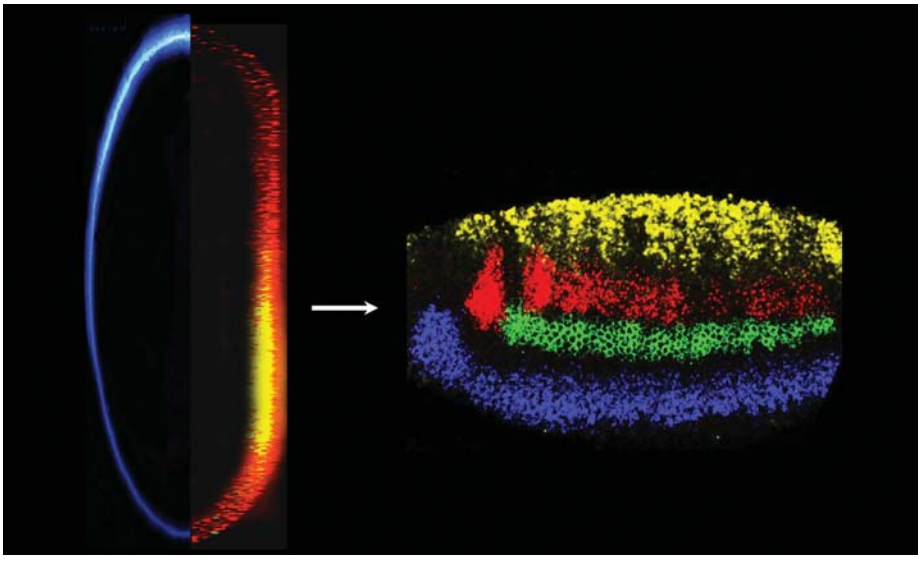

Conserved BMP-mediated patterning of the DV axis. Gradients of proteins in vertebrates (left: blue Chordin stain) and invertebrates (left: red/yellow Sog stain) initiate patterning along the DV axis. These gradients are then read to establish distinct zones of gene expression within the central nervous system (right: *dpp*, yellow; *msh*, red; *ind*, green; *vnd*, blue).

CREDITS: CHORDIN GRADIENT (LEFT) COLORED AND MODIFIED BY PHOTOSHOP FROM FIG. 3A OF J. L. PLOUHINEC *ET AL.*, *PROC. NATL. ACAD. SCI. U.S.A.* **110**, 20372–20379 (2013); SOG GRADIENT (RIGHT) MODIFIED BY PHOTOSHOP FROM FIG. 1B″ OF S. SRINIVASAN *ET AL.*, *DEV. CELL* **2**, 91–101 (2002)

The list of author affiliations is available in the full article online.
*Corresponding author. E-mail: ebier@ucsd.edu (E.B.); ederobertis@mednet.ucla.edu (E.M.D.R.)
Cite this article as E. Bier, E. M. De Robertis, *Science* **348**, aaa5838 (2015). DOI: 10.1126/science.aaa5838

Downloaded from www.sciencemag.org on June 26, 2015

REVIEW

EMBRYO DEVELOPMENT

BMP gradients: A paradigm for morphogen-mediated developmental patterning

Ethan Bier[1]* and Edward M. De Robertis[2,3]*

Bone morphogenetic proteins (BMPs) act in dose-dependent fashion to regulate cell fate choices in a myriad of developmental contexts. In early vertebrate and invertebrate embryos, BMPs and their antagonists establish epidermal versus central nervous system domains. In this highly conserved system, BMP antagonists mediate the neural-inductive activities proposed by Hans Spemann and Hilde Mangold nearly a century ago. BMPs distributed in gradients subsequently function as morphogens to subdivide the three germ layers into distinct territories and act to organize body axes, regulate growth, maintain stem cell niches, or signal inductively across germ layers. In this Review, we summarize the variety of mechanisms that contribute to generating reliable developmental responses to BMP gradients and other morphogen systems.

A major question in developmental biology is how information provided in a fertilized egg can trigger the chain of events leading cells in the embryo to adopt different developmental fates and to do so with great reliability. Classic fate-mapping studies revealed that cells in different regions of the embryo predictably give rise to specific tissues or organs. But how is this diversification of cell potential achieved in a self-regulating system? Hans Spemann addressed this question by conducting a series of illuminating experiments in which he transplanted tissue fragments between donor and recipient amphibian embryos of different pigmentation. Most transplants resulted in the cells adopting the fate of the surrounding cells of the recipient (for example, neural plate or epidermis). However, embryos that received a graft of the dorsal blastopore lip, which Spemann later named the organizer, developed a twinned (or secondary) body axis, indicating that there was something special about this region (Fig. 1, A and B). An important question raised by these early embryological experiments (*1*), which was subsequently addressed by Spemann's graduate student Hilde Mangold, was how did the transplanted organizer tissue lead to such whole-scale reprogramming of the embryo? Did the transplanted cells change fate to give rise to different cells comprising the full duplicated axis or did they alter the behavior of neighboring recipient cells? By using pigmented and unpigmented amphibian eggs as donors and hosts, Mangold demonstrated that unpigmented donor dorsal tissue gave rise to notochord in the duplicated axis, as it would ordinarily do in an undisturbed embryo (*2*) (Fig. 1B). However, ectodermal derivatives, including the central nervous system (CNS), were derived from host tissue, which suggested that the transplanted mesoderm cells produced signals that redirected the developmental trajectories of adjacent host cells. Subsequent "tissue sandwich" experiments (in which ectodermal cells were brought into contact with various mesodermal derivatives) revealed that these hypothetical diffusible signals capable of inducing a secondary neural axis were elaborated by dorsal mesodermal cells. These signals were termed "neural-inducing" factors. Spemann received the Nobel Prize for medicine in 1935. Tragically, Hilde Mangold died in a kitchen stove accident in 1924 and so was not recognized for her research.

In the early 1990s, vertebrate neural-inducing signals produced by Spemann's organizer were identified and found to act by inhibiting the bone morphogenetic protein (BMP) signaling pathway. Parallel studies in the fruitfly similarly identified conserved BMP signaling elements essential for patterning the dorsal-ventral (DV) axis [reviewed in (*3*, *4*)]. Together, these breakthroughs established a paradigm for studying diffusible developmental signals.

Morphogens

The British mathematician Alan Turing, who cracked the Nazi Enigma code during World War II and later developed the theoretical framework for computers, proposed that information to generate complex anatomical structures might be provided by the diffusion of hypothetical substances he called "morphogens" (*5*). Turing formulated a general partial differential equation to quantitatively describe the changes in the concentration of a morphogen over time (Fig. 1C): Following Fick's law of diffusion, this equation states that the change in morphogen concentration (C) over time (δt) is proportional to its diffusion rate (D) and to the second derivative in space of the morphogen concentration ($\nabla^2 C$). In addition, the change in morphogen concentration is a function (F) of all of the chemical reactions it undergoes (e.g., synthesis, degradation, and association or dissociation with other proteins such as antagonists).

From this initial insight, many reaction-diffusion computer models have been derived to explain the behavior of developing systems. Francis Crick considered a special case in which one group of cells (the source) secretes a factor that diffuses into adjacent regions (the sink), where it is either counteracted or degraded (*6*) (Fig. 1E). Crick proposed that this so-called adjacent source-sink configuration can create concentration gradients of the morphogen, whose shapes remain stable over time. These gradients could then exert various effects on developing cells. Another key advance was the realization that a pair of morphogens composed of an activator and an inhibitor can generate stable patterns (*7*), provided that they originate from the same source and that the inhibitor is more diffusible (Fig. 1D). The activator turns on its own production and also the synthesis of the inhibitor, which in turn represses the activator. Stable patterns result because the inhibitor diffuses faster than the activator, turning it off in the periphery. It is amazing that these powerful mathematical frameworks for understanding long-range reaction-diffusion of morphogens were offered at a time when the chemical nature of not even a single morphogen was known. Many of these principles have now been confirmed by the BMP/Dpp and Chordin/Sog morphogenetic system (see below).

French flag model

Lewis Wolpert suggested a simple visually evocative idea, often referred to as the "French flag model," for how a morphogen gradient can subdivide a field of otherwise equivalent cells into distinct regions (*8*) (Fig. 1F). In this model, morphogens act in a threshold-dependent fashion to control expression of distinct sets of genes in broad zones, each domain corresponding to a fixed range of morphogen level. These primary response genes in turn specify particular cell fates (e.g., transcription factors) or trigger secondary patterning events by signaling to adjacent domains (e.g., secreted signals). Important mechanistic questions for such models are how cells detect abrupt threshold levels of the morphogen and then how they execute distinct responses in a coherent fashion. One general feature of many primary response genes that helps resolve borders is cross-inhibition between factors produced in neighboring domains. Although such reciprocal inhibitory interactions can act as a toggle switch to convert smooth gradients into

[1]Section of Cell and Developmental Biology, University of California, San Diego, La Jolla, CA 92095-0349, USA.
[2]Howard Hughes Medical Institute, University of California, Los Angeles, Los Angeles, CA 90095-1662, USA.
[3]Department of Biological Chemistry, University of California, Los Angeles, Los Angeles, CA 90095-1662, USA.
*Corresponding author. E-mail: ebier@ucsd.edu (E.B.); ederobertis@mednet.ucla.edu (E.M.D.R.)

sharp on-off responses, it remains to be determined how given thresholds are accurately read from individual to individual and how "salt-and-pepper" responses are avoided along borders within a given embryo. As discussed in more detail below, several additional homeostatic mechanisms are likely to be at play, including: differential timing of gene responses; transiently acting prepatterns that bias cells to respond differently to a given level of morphogen; growth of the tissue (with or without corresponding changes in the length scale of the gradient); the ability of cells to read other aspects of a gradient, including its slope; inflections in the gradient (second derivative terms); integrated effects of the gradient; and noise, which can trigger differential signaling between neighboring cells at the tail end of a gradient.

BMP-mediated patterning of the embryonic DV axis

Two of the most noteworthy and well-studied examples of conservation of developmental patterning mechanisms are specification of segmental identities along the anterior-posterior (AP) axis by *Hox* genes (*9*) and subdivision of the DV axis into distinct ectodermal domains by graded BMP signaling (*10*). The notable homologies in DV patterning were first revealed through comparisons of this process in *Drosophila* and *Xenopus*, and informative variations on this theme have subsequently been provided by analysis of a broad range of animal species (see below).

All-or-none BMP signaling during Drosophila neural induction

In *Drosophila*, DV patterning is initiated by a ventral-to-dorsal gradient of the maternally provided morphogen Dorsal (Dl), an NFκB-related transcription factor that specifies mesoderm (e.g., somatic muscle, heart) at high levels, neuroectoderm (e.g., ventral epidermis and CNS) at moderate levels, and dorsal epidermis and an extra-embryonic tissue known as the amnioserosa by its absence (*11*). Primary Dl response

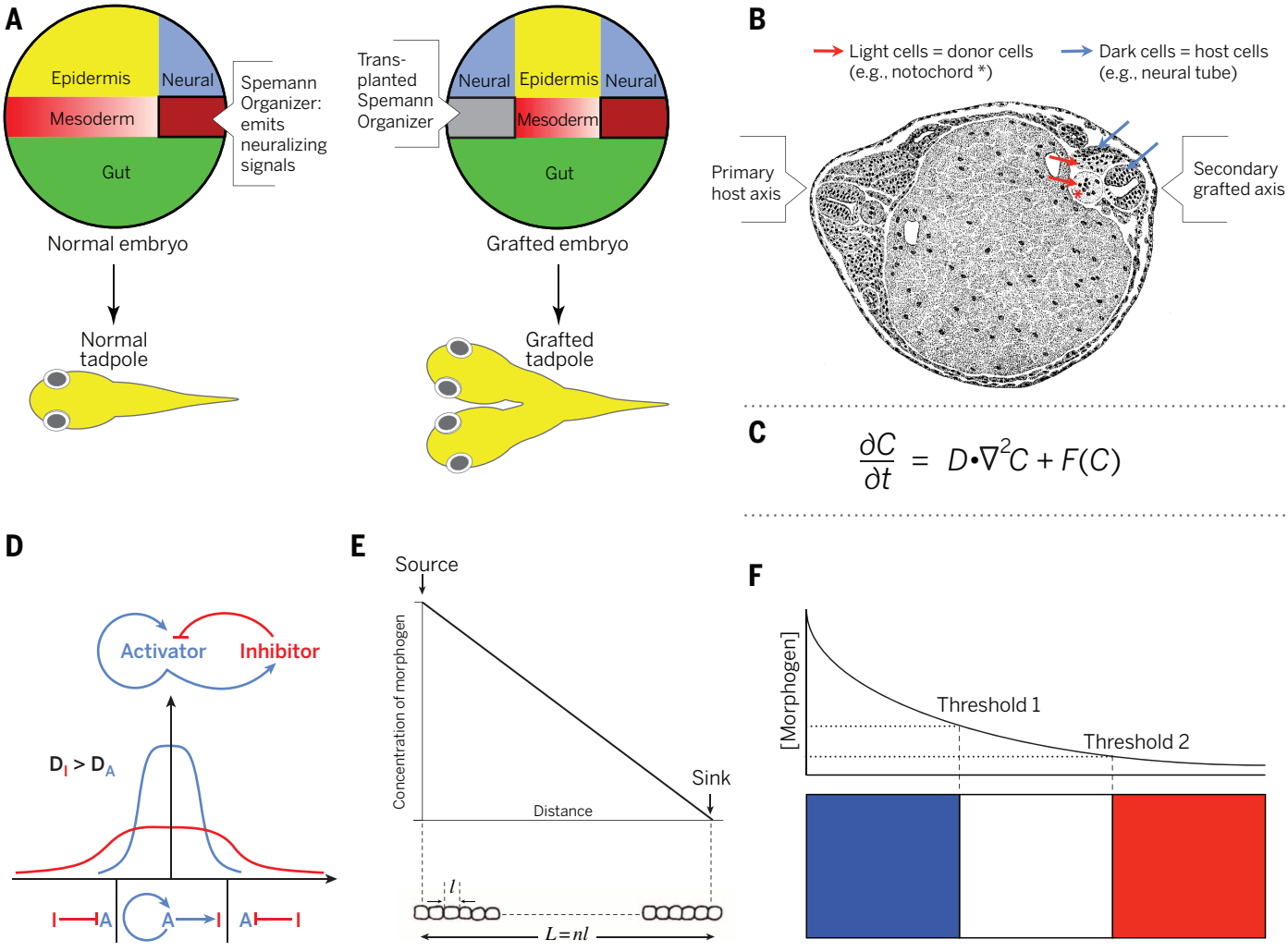

Fig. 1. Morphogens. (**A**) Diagram of organizer graft experiment. The gray area indicates the ventral mesodermal location of the Spemann organizer graft that leads to embryos developing duplicated neural axes. Grafts of tissue taken from other regions of the embryo typically had little, if any, effect. (**B**) Transplantation of the dorsal mesoderm (Spemann organizer) dissected from the blastopore of a donor embryo into the ventral mesoderm of a host embryo results in an embryo with a double axis. In the induced secondary axis, the lightly pigmented donor cells (red arrows) generate mesodermal structures (notochord: asterisk and somites), whereas host tissue forms the nervous system (blue arrows). (**C**) Turing's basic reaction-diffusion equation describing how a morphogen is governed by Fick's law (see text). *C*, morphogen concentration; *t*, time; *D*, diffusion rate; $\nabla^2 C$, second derivative in space of the morphogen concentration; *F*, function. (**D**) Formation of a stable morphogen gradient via a reaction-diffusion mechanism based on two factors [activator (A) and inhibitor (I)]. The activator increases the level of the inhibitor, whereas the inhibitor negatively turns off the activator and is more diffusible than the activator. D_I, diffusion coefficient of inhibitor; D_A, diffusion coefficient of activator. (**E**) A source and sink of a morphogen can create a stable concentration gradient (as proposed by F. Crick). *L*, full length of tissue; *n*, number of cells; *l*, size of a single cell. (**F**) French flag model in which two different threshold concentrations of a morphogen elicit three distinct responses. [Credits: (A) redrawn from figure 5.3 of (*114*); (B) figure 24 of (*2*); (D) figure 1 of (*40*); (E) figure 1 of (*6*)]

genes in dorsal and lateral regions of the embryo include genes involved in establishing a gradient of BMP signaling.

As summarized in Fig. 2A, two *Drosophila* BMP-related proteins—Decapentaplegic (Dpp, a BMP2/4 ortholog) and Screw (Scw, a BMP5/7 homolog)—signal via heterotetrameric BMP receptors to phosphorylate and activate the transcription factor Mad in the cytoplasm (or SMADs

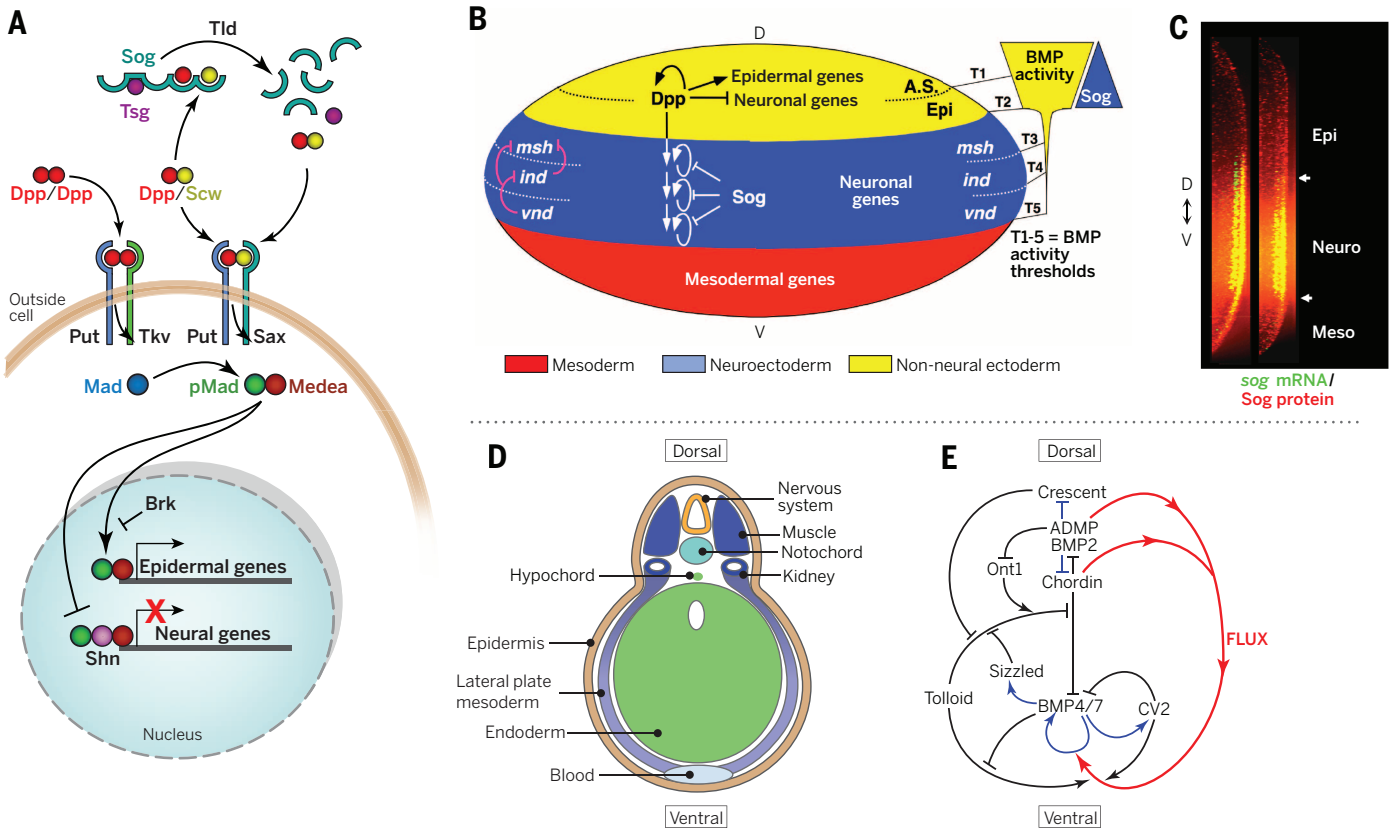

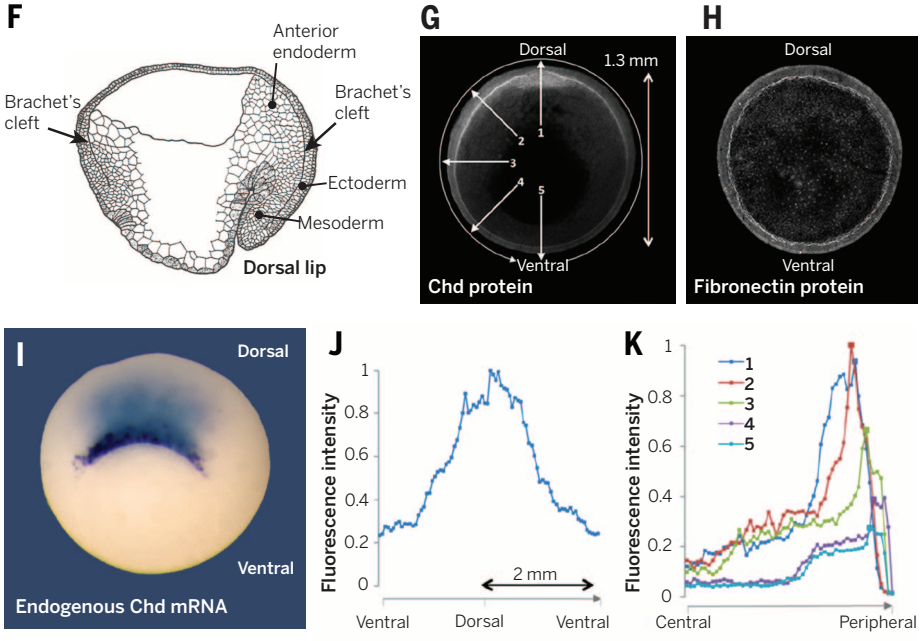

Fig. 2. BMP patterning during neural induction in *Drosophila* and *Xenopus*. (**A**) Diagram of BMP signaling components in *Drosophila*. See text for details. (**B**) Diagram of an early blastoderm-stage *Drosophila* embryo showing subdivision of the DV axis into mesoderm, neuroectoderm, and epidermis. (Right) A high-level BMP activity gradient in dorsal Dpp-expressing cells is created in response to an inverse Sog gradient (emanating from the neuroectoderm) that subdivides the epidermal region into amnioserosa and epidermis proper (thresholds T1 and T2, respectively). A low-level BMP gradient in the neuroectoderm helps partition this region into the three domains expressing the neural identity genes *msh*, *ind*, and *vnd* (thresholds T3 to T5, respectively). (Left) The neural identity genes engage in ventral-dominant repression wherein Vnd inhibits *ind* and *msh* and Ind inhibits *msh*. (**C**) Sog protein gradient viewed in cross section at two successive stages in the blastoderm embryo (left, when Sog protein is first expressed; right, 15 min later). (**D**) Stereotypical DV tissue types of the vertebrate body plan. (**E**) BMP activity along the DV axis results from a series of direct protein-protein interactions between Chordin and other partners (black arrows), transcriptional regulation (blue arrows), and protein flux (red arrows). The entire embryo participates in forming the BMP gradient, which results from the dueling activities of the dorsal and ventral signaling centers. (**F**) Diagram of a sagittal section of a *Xenopus* gastrula (as proposed by P. Nieuwkoop). Brachet's cleft is the narrow cavity that separates the mesendoderm from the ectoderm, encircling the entire DV axis (arrows). (**G**) The Chordin protein gradient spans the entire DV axis. (**H**) Distribution of Fibronectin protein in a comparable embryo is uniform. (**I**) Chordin mRNA is transcribed only on the dorsal side. (**J**) Protein quantification along the DV Brachet's cleft; the gradient forms over 2 mm. (**K**) Chordin fluorescence in radial tracings along the numbered arrows indicated in (G). [Credits: (C) figure 1, b′ and b″, of (*22*); (E to K) from (*40*)]

in vertebrates). Phosphorylated Mad (pMAD ≈ vertebrate pSMAD1/5/8) complexes with a related cofactor Medea (≈ vertebrate SMAD4), enters the nucleus, and activates some target genes (e.g., epidermal genes activated by binding of Mad/Medea complexes to cis-regulatory DNA sequences) but represses expression of other genes [e.g., neuronal genes repressed via a trimeric transcriptional complex consisting of Mad, Medea, and a zinc finger protein Schnurri (Shn)] (*12*). An important feature of this dual action of BMP signaling is that activation of epidermal genes (mediated by activation elements) (*13*) requires much higher levels of BMP signaling (achieved only dorsally where BMPs are produced) than repression of neuronal genes [mediated by silencing elements (SEs)] (*11*, *12*).

Several extracellular proteins regulate BMP signaling (Fig. 2B). In the lateral neuroectoderm, the BMP antagonist short gastrulation (Sog = Chordin) is secreted. In the dorsal epidermis, Dpp, the metalloproteinase Tolloid (Tld), and a cofactor Twisted gastrulation (Tsg) are produced. BMP receptor subunits, Mad, Medea, Shn, and Scw are ubiquitously expressed, although some of these factors are up-regulated in specific patterns [reviewed in (*14*–*17*)]. Dpp and Sog play key roles within their respective domains of expression to stabilize epidermal versus neuroectodermal cell fates, respectively, and also to diffuse into adjacent domains to form gradients that influence patterning therein.

The first stage of BMP patterning in the *Drosophila* ectoderm, analogous to vertebrate neural induction, relies on the all-or-none effect of high-level BMP signaling in the dorsal epidermis to repress expression of neuronal genes in that region. Thus, in *dpp*-mutant embryos, neuroblast-specifying genes such as those of the Achaete-Scute complex are ectopically expressed in the dorsal epidermis (*18*). Strong Dpp signaling also activates expression of epidermal targets, including the *dpp* gene itself (referred to as autoactivation). Because BMP receptors are present throughout the embryo, coupled Dpp diffusion and autoactivation creates a positive-feedback loop with the potential for spreading Dpp expression invasively from the epidermis into the neuroectoderm (*19*). The BMP antagonist Sog plays a key role in protecting the neuroectoderm from such Dpp invasion by preventing BMP signaling from reaching the high levels required to trigger autoactivation (however, graded low-level BMP signaling is likely to be present in the neuroectoderm; see below). BMP signals are also blocked in the *Drosophila* neuroectoderm by the transcriptional repressor Brinker (*20*). In summary, strong BMP signaling in the *Drosophila* epidermis represses expression of neural genes, and this effect is blocked by BMP antagonists in the neuroectoderm.

Graded high-level BMP-mediated activation patterns the dorsal epidermis

In addition to its all-or-none repression of neural genes dorsally, graded high-level BMP signaling activates nested patterns of epidermal gene expression and partitions the dorsal region into the epidermis proper (dorsolateral portion) and the amnioserosa (dorsal portion). This BMP activity gradient forms primarily in response to an inverse protein gradient of the BMP antagonist Sog. Sog is secreted from the neuroectoderm, diffuses into the dorsal region (Fig. 2, B and C), and binds preferentially to Dpp:Scw heterodimers (the most potent BMP ligand), thereby blocking BMP's access to its receptors (*21*). Creation of the Sog protein gradient (Fig. 2C), which is highest near the source of Sog and diminishes toward the dorsal midline, requires activity of the Tld protease (*22*). Tld can cleave and inactivate Sog (*23*) (and can also generate alternative forms of Sog; see below). Because Tld is expressed in dorsal cells, a classical source-sink configuration is established wherein Sog diffusing from a ventral source is degraded dorsally by Tld. Tld cleavage of Sog requires binding of Dpp:Scw, Tsg, and Sog to form a trimeric complex. This trimeric complex may help concentrate Dpp:Scw heterodimers along the dorsal midline by a shuttling mechanism wherein Sog binding to Dpp:Scw prevents receptor-mediated clearance of the ligand while at the same time transporting Dpp:Scw dorsally. Cleavage of Sog by Tld then releases Dpp:Scw to signal (*21*, *24*). In addition to these purely diffusion-based mechanisms, which are thought to occur in the thin layer of perivitelline fluid between the embryo and surrounding vitelline membrane, there is evidence for endocytosis playing a role as a sink for Sog (*22*), for extracellular matrix (ECM) interactions (*25*–*27*), intracellular regulation of SMADs via linker phosphorylation (*28*), secondary signal-dependent augmentation of BMP signaling in dorsal-most cells (*29*, *30*), and feed-forward cooperation between SMADs and the primary BMP target gene *zen* to regulate gene expression in the amnioserosa (*31*), acting in concert to steepen the BMP activity gradient.

Graded low-level BMP-mediated repression patterns the neuroectoderm

A steep low-level BMP gradient is likely to form within the lateral neuroectoderm of the *Drosophila* embryo as a consequence of Dpp diffusing in from the dorsal epidermis and being bound and sequestered by high levels of Sog (i.e., the epidermis is the source of Dpp, and Sog is the Dpp sink in the neuroectoderm). Several types of Sog:Dpp complexes may contribute to a BMP sink, including secreted full-length Sog (preferentially binding Dpp:Scw heterodimers); truncated forms of Sog, known as "Supersog," that bind and inhibit the activity of Dpp:Dpp homodimers (*25*, *32*, *33*); and forms of Sog (or Supersog) that associate with membranes via palmitoylation of a type II secretion signal (*34*). Although this hypothetical BMP activity gradient has not been directly visualized (probably due to its very low levels), genetic evidence suggests that such a gradient plays a role in subdividing the neuroectoderm into nonoverlapping domains that give rise to three primary rows of CNS neuroblasts (*35*). Neuronal fates in these three domains are specified by so-called neural identity genes, which encode the homeobox proteins Vnd (ventral row-one neuroblasts), Ind (intermediate or medial row-two neuroblasts), and Msh (dorsal row-three neuroblasts) (Fig. 3A). Neural identity genes engage in a vectorial form of cross-inhibition wherein more ventral genes repress expression of more dorsal genes (e.g., Vnd inhibits *ind* and *msh*; Ind inhibits *msh*) (*36*) (Fig. 2B). This ventral-dominant chain of repression results in sharp mutually exclusive patterns of neural identity gene expression.

Genetic analysis of BMP patterning in the neuroectoderm under conditions where it was possible to parse the effects of this morphogen from those of Dorsal revealed that BMPs repress neural identity genes in a dose-dependent fashion such that *ind* is repressed more efficiently than *msh* (*35*). Strong repression of *ind* in dorsal neuroectodermal cells near the epidermal source of Dpp relieves Ind-dependent repression of *msh* in a dorsal-most stripe of neuroectodermal cells. Consistent with these genetic findings, biochemical studies have identified SEs mediating BMP repression in cis-regulatory modules (CRMs) of the *msh* versus *ind* genes. Mad/Med/Shn complexes bind with higher affinity to an SE site in the *ind* CRM than to those in the *msh* CRM (*37*). This difference in binding affinities is relevant in vivo because replacing an *msh* Mad/Med/Shn binding site with the *ind* site results in Dpp-dependent repression of *msh*-reporter gene expression in its normal neuroectodermal domain (*37*), providing a rare example of this direct mechanism in setting a threshold response to a morphogen.

These studies show that in *Drosophila*, the maternal Dl gradient is interpreted by the Dpp/Sog morphogens to elicit the differentiation of at least five ectodermal cell types: two in the epidermal domain that are distinguished by differing levels of high BMP signaling (amnioserosa and epidermis proper) and three subdivisions within the CNS (i.e., the Vnd, Ind, and Msh domains) giving rise to neuroblasts in rows one through three.

DV patterning in Xenopus

A gradient of BMP and Chordin signaling also controls DV histotypes in vertebrates, coordinately determining cell differentiation in the ectoderm, mesoderm, and endoderm germ layers. Low BMP levels cause differentiation of ectoderm to CNS, intermediate levels to neural crest, and high levels to epidermis. In the mesoderm, low BMP gives rise to notochord, at slightly higher levels to skeletal muscle (in segmental structures called somites), then kidney (each segment develops a kidney tubule in the embryo); lateral plate (which gives rise to the body wall); and, at the highest BMP levels, to blood (Fig. 2D). DV differentiation of the endoderm is similarly regulated. These tissues represent the invariant body plan shared by all vertebrates. This raises the question of how many morphogen gradients exist. Is there one gradient per germ layer? How would each gradient be regulated coordinately so that a perfectly harmonious embryo is formed every time? The mechanisms involved are self-organizing because if blastula embryos are cut in half, the part containing the organizer can

rescale into a well-proportioned embryo, or, if cut sagittally, the entire missing half can regenerate, forming identical twins (*38*).

Because the embryo has only one chance to allocate these tissue types correctly, it is not surprising that the DV gradient is tightly regulated. The organizer secretes the BMP antagonists Noggin, Follistatin, and Chordin, and if all three are knocked down with morpholino oligonucleotides, the embryo lacks all dorsal structures (*39*). A large network of Chordin-interacting extracellular proteins has been isolated from the *Xenopus* embryo, with key supporting insights coming from zebrafish genetics. Using a combination of biochemistry with purified proteins and embryological studies involving the depletion of multiple gene products with morpholinos and transplantation experiments, it was possible to construct the biochemical pathway shown in Fig. 2E (*40*). All of its components are secreted proteins that are able to directly interact with each other, forming feedback loops of activators and inhibitors synthesized by cells in the dorsal and ventral poles of the embryo.

Chordin, the homolog of Sog, is a morphogen secreted very abundantly by the organizer. It binds to both dorsal (BMP2 and ADMP) and ventral (BMP4/7) BMPs. Tsg, which is expressed ventrally, greatly facilitates the binding of Chordin to BMPs. Studies in zebrafish have shown that heterodimers of BMP2b:BMP7 can activate BMP signaling in the context of the embryo, whereas the respective homodimers do not (*41*). This effect is due to the recruitment of two distinct type I BMP receptors and is markedly similar to *Drosophila* DV patterning in which Sog preferentially binds Dpp:Scw heterodimers, which constitute the most potent signaling ligands. The rate-limiting step in the pathway is the secreted metalloproteinase Tolloid [called Xolloid-related (Xlr) in *Xenopus*] that specifically cleaves Chordin at two particular sites, releasing active BMPs in the ventral side of the embryo (*42*). Tolloid activity is highly regulated. First, it is inhibited by Sizzled, a ventral sFRP (secreted Frizzled-related protein) that functions as a competitive inhibitor of Tolloid, indirectly inhibiting BMP by stabilizing Chordin (*43*). Second, Tolloid protease activity is noncompetitively inhibited by BMPs that directly bind to its noncatalytic CUB domains, explaining the antimorphic (low-BMP) effects of some mutations in *Drosophila* (*44*). Third, the dorsally produced Olfactomedin-related Ont-1 adaptor bridges the binding of Chordin and Tolloid, facilitating Chordin degradation in the dorsal side (*45*). Finally, the Sizzled homolog Crescent acts as an inhibitor of Tolloid on the dorsal side (Fig. 2E). The ventral side produces Crossveinless 2 (CV2, also known as Bmper), an antagonist with BMP-binding domains similar to those of Chordin that does not diffuse and remains on the surface of the cells that produce it. CV2 binds Chordin/BMP with high affinity, concentrating these complexes on the ventral side where they can be cleaved by Tolloid (*46*). The pro-BMP effects of CV2 in the *Drosophila* wing (*47*) may similarly be explained by the concentration of diffusing Dpp/Sog complexes in CV2-expression regions.

For every action in the dorsal side, there is a corresponding reaction in the ventral side. Chordin transcription is activated by high Nodal and low BMP signals. Recent work in zebrafish has shown that microinjection of two different animal pole cells with Nodal and BMP mRNA at the 128-cell stage is sufficient to induce a complete secondary axis (*48*). Self-organization in the *Xenopus* embryo results from the dorsal and ventral genes being under opposite transcriptional control: When BMP levels are lowered, synthesis of dorsal BMPs (ADMP, BMP2) is increased, and at high BMP levels, feedback inhibitors such as Sizzled dampen the signal (and expand the gradient; see below).

Many of the secreted proteins in the feedback loops of the DV pathway react directly with each other as imagined by Turing (*5*). For example, Tolloid and Sizzled constitute a classical activator-inhibitor pair arising from the same cellular source: Xlr activates BMP signaling (indirectly, by degrading Chordin), which promotes Sizzled transcription, and Sizzled protein would in turn diffuse, turning off Tolloid activity in the periphery. The evolutionary conservation of the DV-interacting proteins (such as BMP/Dpp, Chordin/Sog, Tsg, and CV2)—on opposite sides of the embryo—in *Drosophila* and *Xenopus* provides molecular support for the 1822 proposal by French naturalist Etienne Geoffroy Saint-Hilaire that an inversion of the DV body plan has taken place (*49*).

The Chordin gradient

Using an improved immunolocalization method it has recently become possible to visualize the endogenous Chordin gradient in the *Xenopus* gastrula (*40*). Chordin was found to diffuse within the narrow space that separates the ectoderm from anterior endoderm and mesoderm (Fig. 2, F and G). In amphibian embryos, this virtual cavity is called Brachet's cleft (in honor of the Belgian embryologist). However, all vertebrate embryos have an ECM containing fibronectin and other proteins between the ectoderm and mesoderm. Therefore, Brachet's cleft is not an amphibian-specific structure. Confocal optical sections reveal a smooth gradient of Chordin, extending from the organizer to the ventral side through this ECM (Fig. 2, G, J, and K). Chordin protein diffuses far from the Spemann organizer cells in which it is transcribed (Fig. 2I). The Chordin morphogen gradient extends over a distance of 2 mm (the *Xenopus* gastrula has a diameter of 1.3 mm) in this signaling highway between the ectoderm and

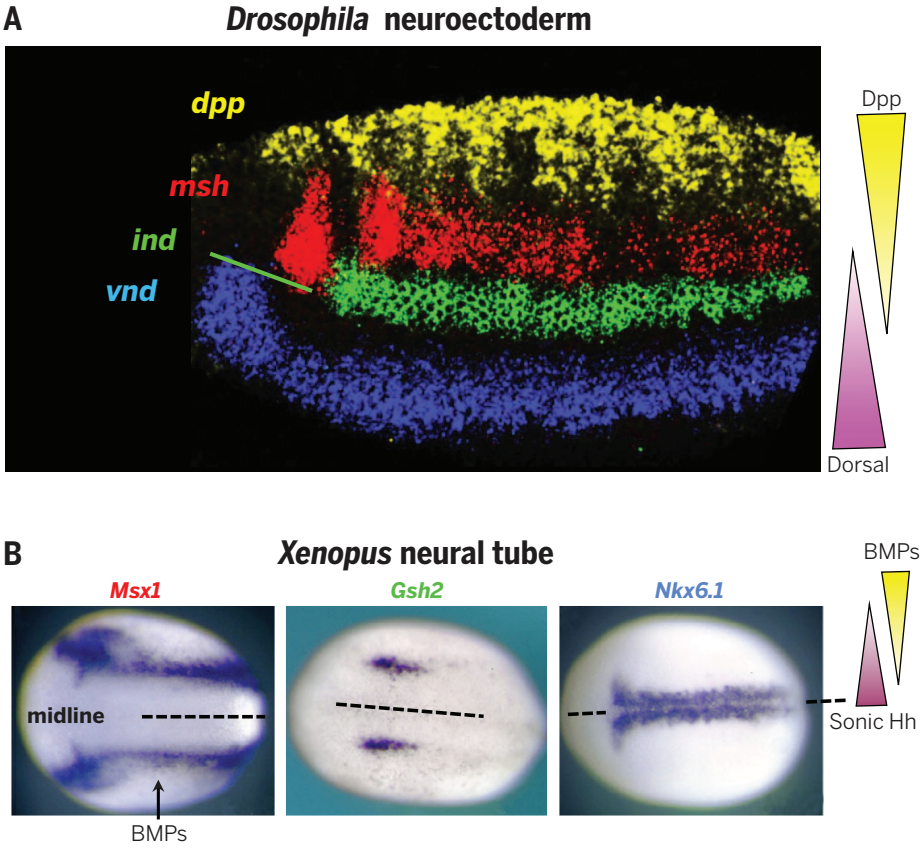

Fig. 3. BMP-mediated patterning in the CNS of *Drosophila* and vertebrates. (**A**) Expression patterns of the neural identity genes *vnd* (blue), *ind* (green), and *msh* (red) in a *Drosophila* blastoderm embryo relative to the BMP (*dpp*, yellow) and Dorsal gradients. (**B**) Expression patterns of *Xenopus Msx1* (≈ *msh*), *Gsh2* (≈ *ind*), and Nkx6.1 (≈ vnd) at the open neural plate stage relative to the BMP and Sonic Hedgehog gradients. [Credits: (A) modified figure 1b of (*115*); (B) assembled from panels B (*Gsh2*), K (*Nkx6.1*), and L (*Msx1*) of figure 4 from (*116*)]

endomesoderm (Fig. 2, J and K). The Chordin gradient rescales in bisected embryos, and a second long-distance gradient is seen emanating from Spemann organizer grafts (*40*). Chordin protein must reach very high concentrations in the confines of Brachet's cleft. From this ECM, Chordin protein could pattern both the ectoderm and the mesoderm; for example, causing CNS induction in the overlying ectoderm.

During gastrulation the germ layers undergo extensive morphogenetic movements, and cells might read their positional information directly from the Chordin/BMP gradient contained in the Brachet's cleft ECM. The gradient would be generated by the facilitated diffusion of Chordin from the organizer to regions of lower concentration (carrying with it BMPs made in more dorsal regions) and the sink provided by its degradation by Tolloid in ventral regions. The location of this gradient may explain why the ectoderm and mesoderm respond coordinately to BMPs during development. Diffusion of overexpressed epitope-tagged Nodal and Lefty has also been reported in the ECM flanking both sides of the lateral plate mesoderm in *Xenopus* tailbud tadpoles (*50*), suggesting that diffusion of morphogens through ECM, separating cell layers, might be a more general phenomenon in development. In *Drosophila*, the Sog/Dpp gradient most likely forms in the perivitelline space; at this time, it is unclear whether this extracellular space has any topological homology to Brachet's cleft.

BMP patterning of the vertebrate dorsal-lateral CNS

After neural induction and involution of the mesoderm, the neural plate invaginates to form the neural tube, which comes to lie between the overlying epidermis and the ventral notochord. BMPs initially produced by epidermal cells diffuse into the dorsal CNS and activate autonomous expression of BMPs within the neural tube. These BMPs then diffuse ventrally to create an activity gradient that has been proposed to activate neural genes (such as Msx1/2) dorsally and to repress genes expressed more ventrally in response to Hedgehog signaling [reviewed in (*51*, *52*)]. A notable parallel between patterning of the vertebrate and *Drosophila* CNS is that orthologs of the *Drosophila* neural identity genes are expressed in the same order relative to the epidermal source of BMPs: *Msx1,2* (= *msh*) dorsally; *Gsh1,2* (= *ind*) laterally, and *Nkx2.2/Nkx6.1* (= Vnd) in the ventral neural tube (Fig. 3, A and B). These relative gene expression domains are also shared with the annelid worm *Platyneris dumerilli* (*53*), suggesting that the CNS of *Urbilateria*, the common ancestor of bilaterians, had at least three subdivisions corresponding to primary rows of neuronal progenitors (*54*). How BMP-mediated regulation of this conserved suite of gene expression may have evolved is discussed further below.

Quantitative modeling of morphogen gradient formation and activity

The panoply of mechanistic experimental data summarized above has spurred development of increasingly complete and predictive mathematical models of BMP-mediated patterning (*16*, *29*, *55*–*58*). In several instances, these models have suggested potential new network behaviors that have subsequently been tested experimentally and verified. This modeling can help address questions such as how a morphogen gradient leads to reliable patterning and how patterning can be coupled to growth in some cases (*59*). These are nontrivial problems for several reasons. First, it is difficult to imagine mechanisms by which a single morphogen could specify thresholds varying over two or more orders of magnitude in concentration. Second, there is great variability and fluctuation in many cellular functions such as changes in cell shape, size, surface-to-volume ratio, number of cell-surface receptors, protein concentrations based on transcriptional interruption during cell division and transcriptional bursting, and noise that is inherent to all of these and other processes required for cells to measure and respond to a given level of morphogen. Yet, despite these considerable signal-degrading factors, embryos and appendages develop with marked fidelity and are surprisingly resistant to a variety of experimental perturbations (e.g., scaling the overall shape of structures with great accuracy in the face of major alterations in the size of those structures). We consider here several mechanisms for creating and responding to morphogen gradients, as well as homeostatic corrective mechanisms, which, in aggregate, may help account for how such reproducible patterning is achieved.

Creating morphogen gradients

Although beyond the scope of the current Review, several different mechanisms have been proposed for the creation of stable morphogen gradients (Fig. 4). Perhaps the most obvious and commonly considered mechanism is free diffusion of the secreted morphogen in the extracellular space (Fig. 4A). Models assuming extracellular diffusion of BMPs and other morphogens (e.g., Wnts and Hedgehog-related factors) are consistent with experimental observations in diverse systems. Additionally, there is direct evidence for such a simple mechanism in forming BMP activity gradients in the *Xenopus* gastrula (see above) and the *Drosophila* wing imaginal disc (*60*, *61*), as well as indirect modeling support in other systems (*62*). There is also evidence for other means of morphogen transport (Fig. 4B), including vesicle-bound release from cells (exosomes or argosomes) (*63*, *64*), transcytosis, movement or migration of morphogen-producing cells (*65*), and direct long-distance cell-to-cell contacts mediated by filopodia-like processes called cytonemes (*66*–*71*). Cytonemes can extend, in a directed fashion, more than 100 μm from a cell and can mediate reception of specific morphogen signals [e.g., Dpp versus Hh or FGF (*67*)] (Fig. 4C). In the case of migrating tracheal cells in the *Drosophila* wing imaginal disc, mutations that inhibit the formation of cytonemes abrogate the ability of tracheal cells to respond to Dpp produced in the wing disc epithelium (*66*), strongly suggesting that these cytoplasmic extensions play an essential role in this form of inductive signaling.

Activity gradients of a morphogen can also be created by temporal mechanisms. One class of time-integrating mechanisms is for cells to retain a "memory" of having been exposed to a certain level of morphogen in the past. Such memory can be accomplished directly by perdurance of a morphogen within a cell (e.g., low turnover rate) or indirectly via the activation of a stable switch of some kind. For example, in the case of Hh signaling in the *Drosophila* wing imaginal disc, the width of the Hh responsive domain (six to eight cells) remains constant during the growth of the wing disc, whereas cells at the outer edge of the Hh receptive domain move out of range as the disc grows (*72*). In this situation, if memory of the Hh signal fades on a time scale on the order of the growth rate, then a gradient of Hh response will be observed in cells lying anterior to those currently receiving the diffusible signal. Similarly, in the case of Wg signaling, a tethered form of the ligand can largely replace the function of the normally secreted form in long-range patterning, partly due to the formation of a crude activity gradient that likely reflects memory of contact-mediated signaling and cell displacement during tissue growth (*73*).

Transient patterning events may also seed the outcome of bistable cell fate choices. For example, differences in the genomic length of a locus result in differential temporal delays in gene activation or repression and can lead to the formation of transient spatial gradients (*74*), which in principle could bias the outcome of stable cross-regulatory interactions among those genes. Indeed, the length of target genes of several morphogen gradients (including Dpp) in the *Drosophila* embryo and wing disc follows an ordered trend with respect to the morphogen-defined axes (*74*). Differential delays in the responses of particular genes to a morphogen may also occur [e.g., a DV progression of neural identity gene expression in both *Drosophila* and vertebrates (*75*–*77*)]. Determining the contributions of such diverse spatial and temporal mechanisms for creating gradients of morphogen activity in different developmental settings is one the most important challenges for future studies.

Responding to morphogen gradients

In French flag models, the salient feature of the morphogen gradient read by cells is the absolute level of the morphogen. Mathematical models built around this simple premise have revealed trade-offs in patterning performance regarding parameters such as peak ligand or receptor levels, receptor turnover, receptor occupancy, or ligand diffusion length scale (*58*, *78*). Thus, parameter sets that do well in one part of the gradient typically lead to poor or mediocre performance in other regions. However, by nature a gradient has other features that cells could also detect, including its slope, inflection points, and temporal elements (e.g., the time derivative of a signal or its integrated levels). Different levels of signal-to-noise could also be used, in principle, to estimate

distances far from a source of morphogen because stochastic differences in signaling between neighboring cells should be graded toward the tail end of a gradient. Parallel processing of these various features of a gradient may allow cells to detect their positions across the full expanse of the gradient (Fig. 5A).

Homeostatic feedback mechanisms

It has become increasingly evident that homeostatic feedback mechanisms play a key role in establishing and maintaining reproducible morphogen gradients in the face of challenges such as tissue growth, noise, morphogenetic movements, and variable environmental inputs (e.g., nutrient availability, temperature). Expanders such as Sizzled in *Xenopus* embryos (Fig. 2E) or Pentagone (Fig. 5B) in *Drosophila* wing discs [reviewed in (*14*, *55*)] provide examples of factors that can scale the gradient length constant to the growth of tissues. Expanders, which are typically produced at the low end of a gradient (by virtue of having their expression inhibited by morphogen signaling) and are highly diffusible, bind to ligands and stabilize them [e.g., by preventing their degradation (*79*)]. The stabilizing effect of Pentagone, which may act via its interaction with the glypican Dally (*80*) (a Dpp co-receptor), allows Dpp to travel further as the tissue grows (Fig. 5B), thereby increasing the gradient length constant and scaling the patterning response.

Local interactions between cells can also act homeostatically to integrate growth or environmental

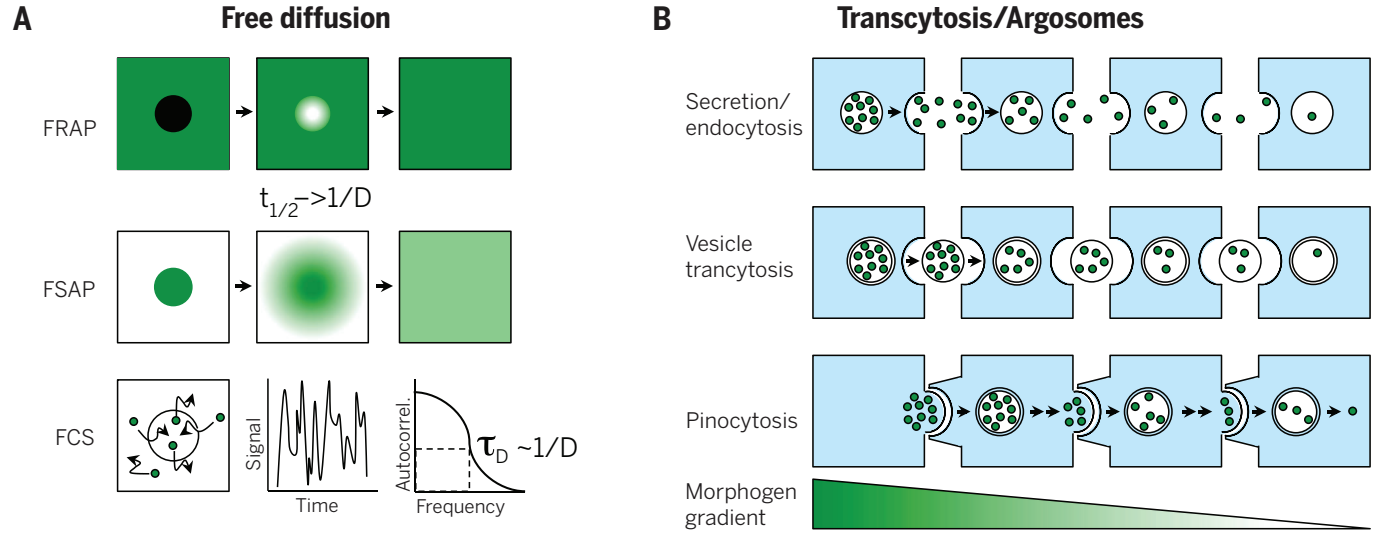

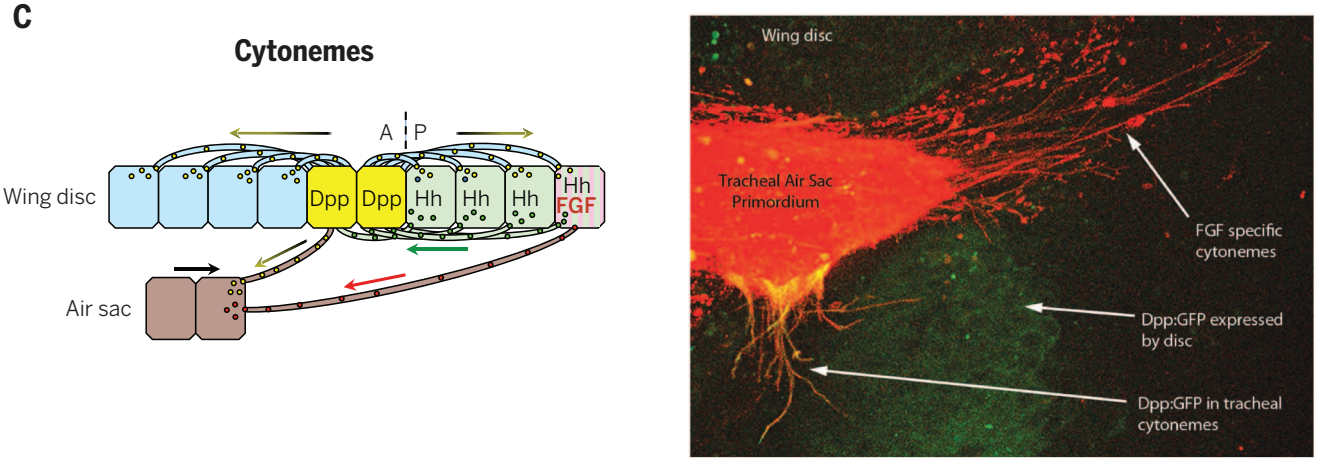

Fig. 4. Mechanisms of morphogen movement. (**A**) Methods for measuring free diffusion of a morphogen. Fluorescence recovery after photobleaching (FRAP) provides an estimate for 1/*D* approximately equal to the half time required to regain fluorescence in a region after photobleaching of a fluorophore-tagged morphogen. Fluorescence spread after photoconversion (FSAP) provides a reciprocal estimate of the dispersion rate after activation of a fluorophore-tagged morphogen. Fluorescence correlation spectroscopy (FCS) measures small fluctuations in fluorescence signals within small regions of extracellular space, which, when analyzed, statistically reveal the number of particles moving in and out of that region, thus allowing an estimate of the diffusion constant. For a more in depth treatment, see (*62*). τ_D, diffusion time. (**B**) Diagram summarizing potential mechanisms of active morphogen transport between cells, including secretion from one cell and reuptake via endocytosis by a neighbor, transcytosis of vesicles, and pinocytosis of a protrusion from one cell by a neighboring cell. (**C**) Cytonemes either transport receptor-ligand complexes back to the cell body or export ligands for release and reuptake at a distance from a signal-producing cell. (Left) Diagram summarizing cytoneme-mediated transport of Dpp, Hh, and FGF ligands in the developing *Drosophila* wing primordium. Within the wing disc monolayer, Hh is transported from producing cells in the posterior compartment to six to eight cell diameters into the anterior compartment. Cells in peripheral regions of the disc send cytonemes toward the center of the disc, where they contact Dpp-producing cells and endocytosis Dpp: Receptor complexes and transport them back to the cell body (*117*). (Right) Air sac cells, a migrating outpocketing of the tracheal system, extend independent classes of cytonemes to contact the overlying wing disc to respond to either Dpp or FGF (*66*). [Credits: (A) adapted from content in boxes 5 and 6 of (*62*); (C) left panel modified and assembled from components in figure 1D of (*117*), right panel from (*66*)]

systems with morphogen-mediated patterning to achieve accurate scaling of morphological structures, as in bisected *Xenopus* embryos that develop into normal tadpoles of half size. Signaling systems—such as the planar polarity and Fat/Yorkie pathways, as well as lateral inhibitory interactions (e.g., Notch signaling)—provide such feedback for patterning [reviewed in (*14*, *81*)].

Integration of multiple developmental cues

The Victorian polymath Francis Galton introduced the concept of the "wisdom of crowds or vox populi" by asking a crowd of 800 people attending a country fair to guess the weight of an ox. Astonishingly, the average of the individual guesses differed from the actual weight (1198 pounds) by only 1 pound (<0.1%), with the median guess being off by only 9 pounds (<1%) (*82*). The accuracy of this collective estimation, which has been put forward as an argument in favor of democracy and other forms of plurality (*83*), was predicated on each member of the crowd having an informed but independent basis for guessing, no prior communication between members of the crowd, and a mechanism to collate these guesses to generate a consensus (average or median estimate). Might a similar strategy help to explain the ability of cells to guess their place in a morphogen gradient? This could be the case if cells possess mechanisms to integrate the variety of potential parallel-acting mechanisms for generating a gradient (e.g., facilitated diffusion, exosomes, cytonemes), each of which could be read independently by distinct compartmentalized receptor complexes, as well as the diversity of gradient information that could impinge on each particular readout of the gradient (e.g., the magnitude, integral, and derivative of the signal) and homeostatic network interactions (e.g., cross-regulation between genes receiving distinct sets of gradient inputs, as well as proportional, integrated, and derivative feedback compensation). Such a consensus-based estimate of position in a morphogen gradient might perform well in establishing the relative position of a cell and, in conjunction with local regulation of secondary feedback signals (e.g., planar signals,

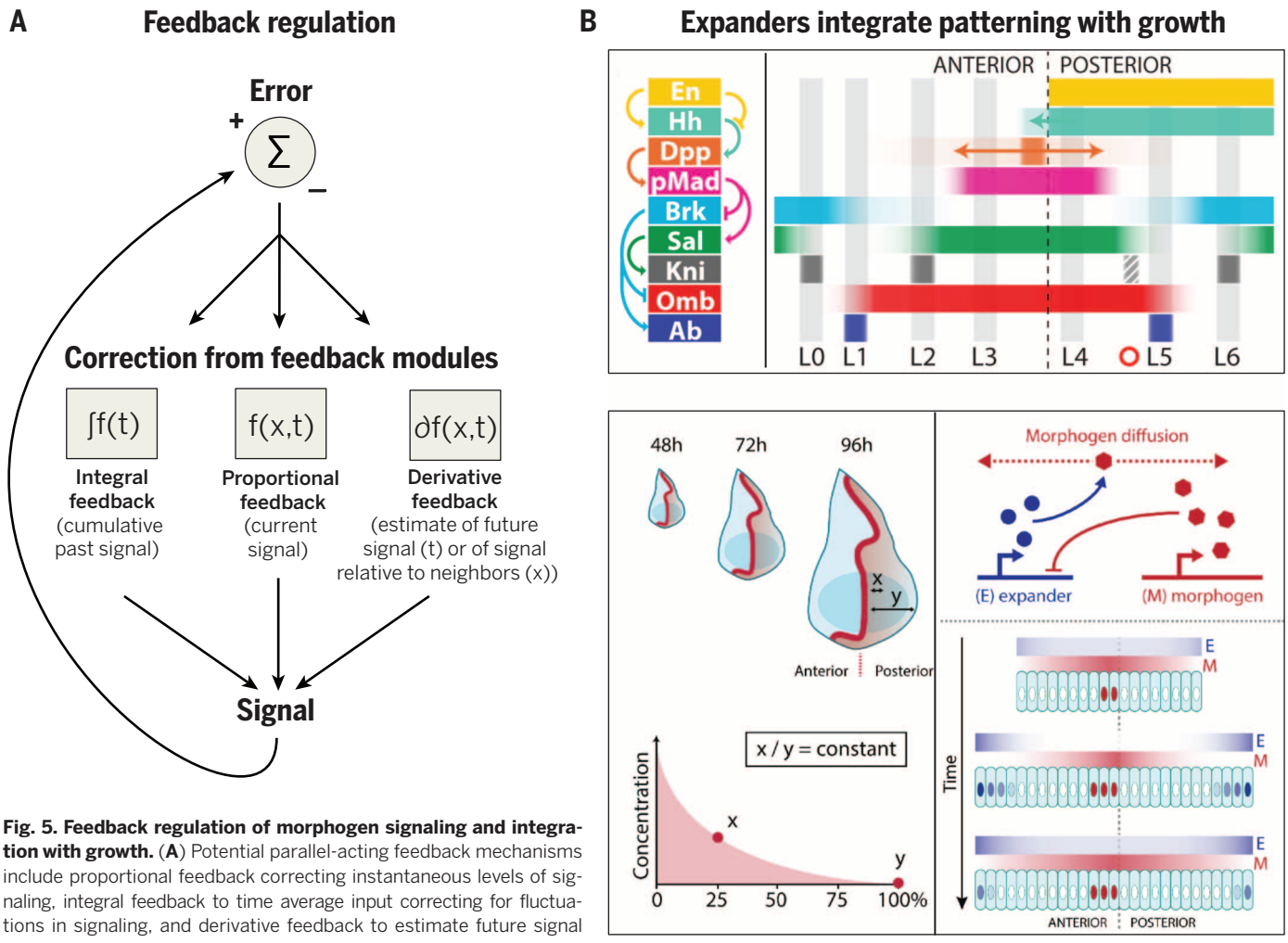

Fig. 5. Feedback regulation of morphogen signaling and integration with growth. (**A**) Potential parallel-acting feedback mechanisms include proportional feedback correcting instantaneous levels of signaling, integral feedback to time average input correcting for fluctuations in signaling, and derivative feedback to estimate future signal strength and to integrate signaling locally in space. (**B**) Integration of patterning and growth. (Top) Scheme diagramming the gene regulatory network (left) controlling BMP-mediated anterior-posterior patterning in the wing imaginal disc (right). Briefly, the Engrailed (En) transcription factor activates Hh expression in the posterior compartment. Hh then diffuses anteriorly to activate Dpp expression in a central stripe. Dpp diffuses both anteriorly and posteriorly to activate genes such as *spalt* (*sal*) and *omb* in a threshold-dependent fashion. Wing vein primordia (numbered L1 to L6) are then induced along specific gene expression boundaries (e.g., the L2 vein anterior to the *sal* expression domain and the L5 vein along the posterior *omb* border) (*59*, *61*, *118*). (Lower Left) BMP-mediated patterning in the growing wing imaginal disc (≈1000-fold increase in cell number). The disc increases in size, whereas relative positions of gene expression patterns remain constant (i.e., *X*/*Y* = constant), indicating that the length constant of the Dpp gradient increases as the disc expands. (Lower Right) The expander Pentagone contributes to scaling in the wing disc. Pentagone expression (in blue) is repressed by Dpp (in red) signaling, but it protects Dpp from receptor-mediated endocytosis, thereby allowing it to diffuse a greater distance. As the disc grows, Dpp-mediated inhibition weakens at the periphery of the disc, allowing expression of Pentagone, which in turn facilitates diffusion of Dpp. [Credits: (B) drawn and provided by Valentino Gantz]

lateral inhibitory factors, expanders), may iteratively provide the necessary corrections to achieve proper scaling. Identifying cellular mechanisms for integrating such hypothetical consensus-based integration of diverse gradient estimates and determining whether cells in different developmental contexts employ distinct guessing algorithms (e.g., does inductive cell signaling rely more on cytonemes, whereas long-range patterning depends primarily on facilitated diffusion?) will be important steps in assessing the validity of this hypothesis.

Evolution and diversification of DV patterning systems

As mentioned earlier, the role of polarized BMP signaling in establishing the DV axis is one the best examples for evolutionary conservation of a developmental patterning system. For example, injection of *Drosophila sog* mRNA into ventral regions of a *Xenopus* embryo lead to axis duplications similar to those observed with injection of chordin mRNA or transplantation of the Spemann organizer (*84*, *85*). Similarly, vertebrate BMP pathway components are active in *Drosophila* and, in the case of BMP2, can even rescue *dpp*-null mutants to full viability (*86*). This high degree of functional conservation, in combination with the similar relative expression patterns of pathway components in organisms spanning a broad range of phyla, provides one of the best examples of a conserved developmental system.

Ancestral role of BMP-mediated axial patterning

Studies across a broad spectrum of organisms have provided further evidence for the conserved role of BMP signaling in DV patterning and subdivision of the embryo into neural versus epidermal domains (i.e., neural induction in the broadest sense). Thus, BMPs and their antagonists define epidermal versus neural cell fates in arthropods [e.g., basal insects (*87*) and spiders (*88*)], lophotrochozoa [e.g., planaria (*89*–*91*) and polychaete annelids (*53*)], and deuterostomes [echinoderms (*91*) and nonvertebrate chordates; e.g., amphioxus (*93*)] [reviewed in (*4*, *94*)].

BMPs and their antagonists are also expressed in localized patterns in diploblast embryos (i.e., cnidarians, the sister group to bilateria, comprising jellyfish, sea anemones, corals, and hydra) where they play an important role in establishing primary body axes (*95*, *96*). As diploblasts have diffuse nerve nets, the presence of polarized BMP signaling in these species suggests that axial patterning by BMPs preceded centralization of the nervous system. During gastrulation, the *Nematostella* (sea anemone) gastrula embryo forms a directive axis that expresses *Chordin, Dpp*, and *BMP5-8* on one side and the BMP *GDF-like* and the BMP antagonist *Gremlin* on the opposite side. Although Chordin and Dpp are secreted by the same group of cells (Fig. 6), signaling by phospho-Smad1/5 takes place in the opposite side, where likely Dpp:BMP5-8 dimers are liberated from Chordin inhibition by Tolloid (*95*). This ancestral long-distance signaling pathway has marked similarities to the ones present in *Xenopus*, zebrafish, and *Drosophila*, except that in *Nematostella* this gradient also controls the expression of *Hox* genes.

A variety of evidence suggests that the role for BMPs in specifying epidermis and a condensed nervous system arose in an uribilaterian ancestor. First, as mentioned above, BMPs perform these two functions in diverse organisms spanning all three major bilaterian branches. Second, neural identity genes are expressed in a conserved series of DV domains in much the same fashion that *Hox* genes are expressed along the AP axis. Third, species with condensed CNS organization are present within the great majority of the 30 bilaterian phyla (*97*). Many phyla also contain organisms with simpler body designs, which are likely to have arisen secondarily as derived simplifications of the basal body plan. For example, in hemichordates, which have a diffuse

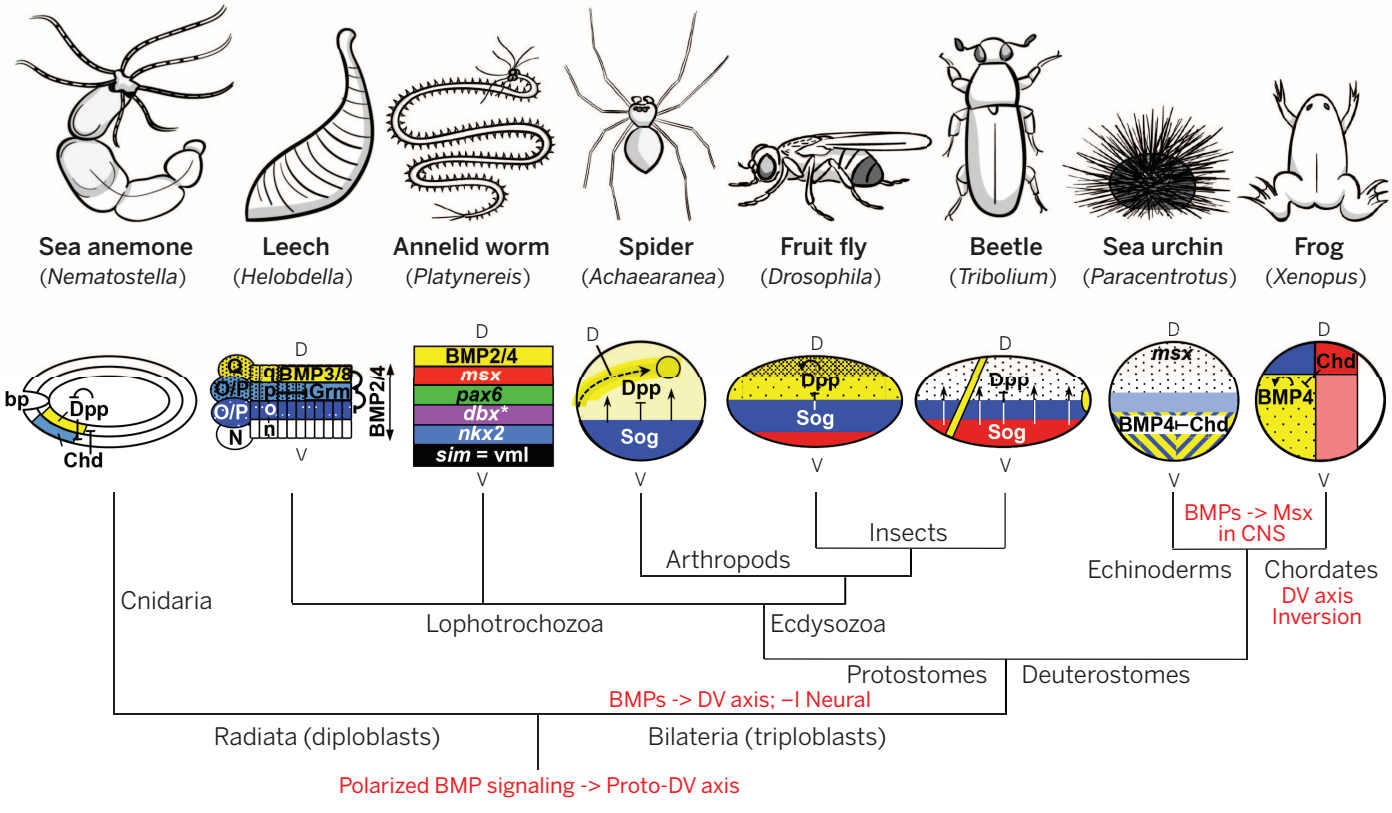

Fig. 6. Evo-devo analysis of BMP-mediated patterning of the DV axis. Phylogeny of select organisms in which BMP signaling has been studied is shown. Despite many alterations in expression patterns of BMPs and their antagonists, the developmental outcome of this signaling pathway has remained conserved across these diverse organisms (e.g., BMP signaling suppresses neural fates). Red text indicates nodes at which specific changes in BMP signaling may have occurred. [Credits: Evolutionary diagram modified and expanded from figure 1 of (*94*). Sketches of organisms drawn and provided by Valentino Gantz]

nerve network, suppression of neuronal development by the BMP gradient has been lost. However, the components of this pathway are still expressed in a polarized pattern, which suggests that they are required for other DV patterning functions such as determining the ventral position of the mouth (*98*).

Evolvability of BMP-mediated patterning

Although, as argued above, it seems likely that BMP-mediated axial patterning is an ancestral trait, there is also a marked degree of flexibility in how particular BMP pathway components are deployed to achieve the common goal of generating epidermis in regions with high levels of BMP signaling and neuroectoderm in regions of low signaling (Fig. 6). For example, in more primitive insects (e.g., beetles), the source of BMPs is not localized along the DV axis, but ventrally produced Sog helps BMPs diffuse to the dorsal side of the embryo (*99*) as it also does in *Drosophila* (*21*, *24*, *29*, *57*, *100*–*106*). Also, in more primitive dipterans such as the scuttle fly, the BMP gradient is broken into two peaks that define distinct tissues in this species, the amnion versus the serosa, in contrast to *Drosophila* with single blended extra-embryonic tissue, the amnioserosa (*107*). In spiders, a cluster of Dpp-producing mesenchymal migratory cells leaves a trail of signaling that specifies the future dorsal midline that may be contacted by epithelial cells via cytonemes (*108*). In the mouse, *chordin* knockout causes only minor phenotypes in the prechordal midline, but in combination with *noggin* knockouts, the forebrain fails to develop (*109*). Thus, in mammals, which have a slower development and lack epiboly movements over a yolk mass (which requires the maintenance of a constant gradient), redundant BMP antagonists increase in developmental importance. In sea urchin embryos, BMPs and Chordin (Chd/Sog) are coexpressed (orally) (as is the case for ADMP, BMP2, and Chordin in *Xenopus*), and the BMP activity gradient forms as a consequence of differences in BMP and Chordin diffusion (*92*). This strategy is analogous to that of sea anemone embryos in which Dpp and Chordin are expressed in the same cells and the key regulator of the system is the shuttling of Chordin (*95*). However, some animals such as annelids seem to have lost *chordin* from their genome, and other BMP antagonists such as Noggin and Gremlin are brought into play (*110*, *111*). In the case of the leech, DV patterning is regulated by BMPs inducing only immediately adjacent cells and up-regulating the BMP antagonist Gremlin (*94*, *111*). These evolutionary developmental biology ("evo-devo") studies have revealed a high degree of evolvability in the ancestral Sog/Chordin/BMP DV patterning gradient.

There is also evidence for evolvability of BMP signaling in CNS patterning. Although BMP activity gradients are consistently oriented with respect to the epidermis and subdomains of the CNS in diverse organisms, it appears that they achieve this conserved output by alternative mechanisms. As summarized above, BMPs act during CNS patterning in *Drosophila* as they do earlier in neural induction to repress expression of neural genes, whereas in vertebrates the consensus view has been that BMPs activate genes in dorsal and lateral regions of the spinal cord (*51*). Analysis of cis-regulatory elements responsible for BMP-mediated regulation of the paralogous *Drosophila msh* and zebrafish *msxB* genes in the dorsal CNS supports opposite modes of BMP regulation (*37*). Mutation of BMP-responsive SMAD sites leads to derepression of *msh* reporter gene expression in the epidermis in *Drosophila*, whereas a comparable mutation results in the loss of *msxB* reporter gene expression in zebrafish. Thus, BMPs can act by opposite mechanisms (weak repression versus weak activation) to achieve the same gene expression output pattern.

Conclusions and future perspectives

Over the past two decades, the molecular basis for classic embryological observations has been elucidated in great detail and has led to testable quantitative network models for BMP-mediated regulation of DV patterning. This progress notwithstanding, several important questions remain. Perhaps foremost among them is how network models can account for the nearly invariant morphologies of fully developed organisms and how such reproducible patterning is achieved in the face of considerable difficulties in accurately reading morphogen activity across the broad range of graded concentrations, which engenders unavoidable tradeoffs. Such models must also cope with inherent variations in critical parameters arising from both intrinsic noise and environmental variation, which can result in substantial perturbations, as illustrated by embryos of vastly different sizes or developing at different temperatures, forming correctly proportioned adults. It will be interesting to see whether models based on the "wisdom of crowds" concept shed light on this problem. Experimental tests of such models should account for various forms of potential parallel genetic circuitry (or redundancy) that are integral to this line of thinking. Thus, the loss of single or even multiple circuits may not have a major effect on morphology, but the roles of these circuits might be revealed in sensitized backgrounds where other critical elements are weakened. A salient example of such redundancy is the ability of a membrane-tethered form of Wg alone to sustain viability and generate almost normal patterning (*73*), whereas it is nearly certain that diffusible forms of the protein also normally play a role in patterning. Additionally, new quantitative approaches integrated with cutting-edge imaging methods should be considered, such as using Bayesian statistical models to reveal potential links in gene regulatory networks by examining the effects of many (hundreds) modest perturbations of the system (e.g., heterozygosity or duplication of each gene in the network) on multiple gene expression markers in vivo across fields of developing cells [e.g., (*112*, *113*)].

Other important questions include how different stable BMP signaling networks are deployed within an organism to accomplish distinct patterning events and how interactions within these networks can change during evolution while retaining similar developmental outputs. With regard to adaptation of BMP signaling networks to different developmental contexts, an intriguing question is whether different modes of BMP transport dominate in particular settings. For example, might free diffusion facilitated by a sink be a dominant mechanism for dispersing ligands between cell sheets, whereas cytonemes offer a preferred mode of transport for other types of inductive signaling (e.g., during Dpp-dependent induction of the *Drosophila* midgut or in maintenance of local stem niches)? Mutants selectively inhibiting the formation of cytonemes dedicated to specific signaling pathways will provide important new insights into this mode of ligand transport and reception.

Comparative studies of BMP regulatory networks (such as that involved in early embryonic DV patterning and neural induction) in additional species would also be of interest, as well as further analysis of BMP-dependent CNS patterning, as discussed above. An interesting question in this regard is whether critical changes in a network are accomplished at the level of alterations in cis-regulatory elements that shift patterns of gene expression or by the addition or subtraction of specific proteins from the system, such as expanders or other factors mediating feedback interactions. Clearly, many interesting and important questions remain in this paradigm-setting field.

REFERENCES AND NOTES

1. V. Hamburger, *The Heritage of Experimental Embryology: Hans Spemann and the Organizer* (Oxford Univ. Press, Oxford, 1988).
2. H. M. Spemann, H. Mangold, Uber induction von embryonanlagen durch implantation artfremder organis atoren. *W. Roux' Arch. Ent. Org.* **100**, 599–638 (1924) [translated and reprinted in *Int. J. Dev. Biol.* **45**, 15 (2001)].
3. E. M. De Robertis, Evo-devo: Variations on ancestral themes. *Cell* **132**, 185–195 (2008). doi: 10.1016/j.cell.2008.01.003; pmid: 18243095
4. C. M. Mizutani, E. Bier, EvoD/Vo: The origins of BMP signalling in the neuroectoderm. *Nat. Rev. Genet.* **9**, 663–677 (2008). doi: 10.1038/nrg2417; pmid: 18679435
5. A. Turing, The chemical basis of morphogenesis. *Philos. Trans. R. Soc. London Ser. B* **237**, 37–72 (1952). doi: 10.1098/rstb.1952.0012
6. F. Crick, Diffusion in embryogenesis. *Nature* **225**, 420–422 (1970). doi: 10.1038/225420a0; pmid: 5411117
7. A. Gierer, H. Meinhardt, A theory of biological pattern formation. *Kybernetik* **12**, 30–39 (1972). doi: 10.1007/BF00289234; pmid: 4663624
8. L. Wolpert, Positional information and the spatial pattern of cellular differentiation. *J. Theor. Biol.* **25**, 1–47 (1969). doi: 10.1016/S0022-5193(69)80016-0; pmid: 4390734
9. P. W. Holland, Evolution of homeobox genes. *WIREs Dev. Biol.* **2**, 31–45 (2013). doi: 10.1002/wdev.78
10. S. J. Gould, *The Structure of Evolutionary Theory* (Harvard Univ. Press, Cambridge, MA, 2002).
11. A. Stathopoulos, M. Levine, Dorsal gradient networks in the *Drosophila* embryo. *Dev. Biol.* **246**, 57–67 (2002). doi: 10.1006/dbio.2002.0652; pmid: 12027434
12. S. Ross, C. S. Hill, How the Smads regulate transcription. *Int. J. Biochem. Cell Biol.* **40**, 383–408 (2008). doi: 10.1016/j.biocel.2007.09.006; pmid: 18061509
13. A. Weiss *et al.*, A conserved activation element in BMP signaling during *Drosophila* development. *Nat. Struct. Mol. Biol.* **17**, 69–76 (2010). doi: 10.1038/nsmb.1715; pmid: 20010841
14. F. Hamaratoglu, M. Affolter, G. Pyrowolakis, Dpp/BMP signaling in flies: From molecules to biology. *Semin. Cell Dev. Biol.* **32**, 128–136 (2014). doi: 10.1016/j.semcdb.2014.04.036; pmid: 24813173

15. H. Araujo, M. R. Fontenele, R. N. da Fonseca, Position matters: Variability in the spatial pattern of BMP modulators generates functional diversity. *Genesis* **49**, 698–718 (2011). doi: 10.1002/dvg.20778; pmid: 21671348
16. L. Zakin, E. M. De Robertis, Extracellular regulation of BMP signaling. *Curr. Biol.* **20**, R89–R92 (2010). doi: 10.1016/j.cub.2009.11.021; pmid: 20144774
17. D. Umulis, M. B. O'Connor, S. S. Blair, The extracellular regulation of bone morphogenetic protein signaling. *Development* **136**, 3715–3728 (2009). doi: 10.1242/dev.031534; pmid: 19855014
18. V. Francois, M. Solloway, J. W. O'Neill, J. Emery, E. Bier, Dorsal-ventral patterning of the *Drosophila* embryo depends on a putative negative growth factor encoded by the *short gastrulation* gene. *Genes Dev.* **8**, 2602–2616 (1994). doi: 10.1101/gad.8.21.2602; pmid: 7958919
19. B. Biehs, V. François, E. Bier, The *Drosophila short gastrulation* gene prevents Dpp from autoactivating and suppressing neurogenesis in the neuroectoderm. *Genes Dev.* **10**, 2922–2934 (1996). doi: 10.1101/gad.10.22.2922; pmid: 8918893
20. A. Jaźwińska, C. Rushlow, S. Roth, The role of brinker in mediating the graded response to Dpp in early *Drosophila* embryos. *Development* **126**, 3323–3334 (1999). pmid: 10393112
21. O. Shimmi, D. Umulis, H. Othmer, M. B. O'Connor, Facilitated transport of a Dpp/Scw heterodimer by Sog/Tsg leads to robust patterning of the *Drosophila* blastoderm embryo. *Cell* **120**, 873–886 (2005). doi: 10.1016/j.cell.2005.02.009; pmid: 15797386
22. S. Srinivasan, K. E. Rashka, E. Bier, Creation of a Sog morphogen gradient in the *Drosophila* embryo. *Dev. Cell* **2**, 91–101 (2002). doi: 10.1016/S1534-5807(01)00097-1; pmid: 11782317
23. G. Marqués *et al*., Production of a DPP activity gradient in the early *Drosophila* embryo through the opposing actions of the SOG and TLD proteins. *Cell* **91**, 417–426 (1997). doi: 10.1016/S0092-8674(00)80425-0; pmid: 9363950
24. Y. C. Wang, E. L. Ferguson, Spatial bistability of Dpp-receptor interactions during *Drosophila* dorsal-ventral patterning. *Nature* **434**, 229–234 (2005). doi: 10.1038/nature03318; pmid: 15759004
25. E. Negreiros, M. Fontenele, A. R. Câmara, H. Araujo, αPS1βPS integrin receptors regulate the differential distribution of Sog fragments in polarized epithelia. *Genesis* **48**, 31–43 (2010). pmid: 20017203
26. H. Araujo, E. Negreiros, E. Bier, Integrins modulate Sog activity in the *Drosophila* wing. *Development* **130**, 3851–3864 (2003). doi: 10.1242/dev.00613; pmid: 12835400
27. A. Sawala, C. Sutcliffe, H. L. Ashe, Multistep molecular mechanism for bone morphogenetic protein extracellular transport in the *Drosophila* embryo. *Proc. Natl. Acad. Sci. U.S.A.* **109**, 11222–11227 (2012). doi: 10.1073/pnas.1202781109; pmid: 22733779
28. A. Aleman *et al*., Mad linker phosphorylations control the intensity and range of the BMP-activity gradient in developing *Drosophila* tissues. *Sci. Rep.* **4**, 6927 (2014). doi: 10.1038/srep06927; pmid: 25377173
29. D. M. Umulis, O. Shimmi, M. B. O'Connor, H. G. Othmer, Organism-scale modeling of early *Drosophila* patterning via bone morphogenetic proteins. *Dev. Cell* **18**, 260–274 (2010). doi: 10.1016/j.devcel.2010.01.006; pmid: 20159596
30. J. Gavin-Smyth, Y. C. Wang, I. Butler, E. L. Ferguson, A genetic network conferring canalization to a bistable patterning system in *Drosophila*. *Curr. Biol.* **23**, 2296–2302 (2013). doi: 10.1016/j.cub.2013.09.055; pmid: 24184102
31. H. L. Liang, M. Xu, Y. C. Chuang, C. Rushlow, Response to the BMP gradient requires highly combinatorial inputs from multiple patterning systems in the *Drosophila* embryo. *Development* **139**, 1956–1964 (2012). doi: 10.1242/dev.079772; pmid: 22513375
32. K. Yu *et al*., Processing of the *Drosophila* Sog protein creates a novel BMP inhibitory activity. *Development* **127**, 2143–2154 (2000). pmid: 10769238
33. K. Carneiro *et al*., Graded maternal short gastrulation protein contributes to embryonic dorsal-ventral patterning by delayed induction. *Dev. Biol.* **296**, 203–218 (2006). doi: 10.1016/j.ydbio.2006.04.453; pmid: 16781701
34. K.-H. Kang, E. Bier, dHIP14-dependent palmitoylation promotes secretion of the BMP antagonist Sog. *Dev. Biol.* **346**, 1–10 (2010). doi: 10.1016/j.ydbio.2010.06.024; pmid: 20599894
35. C. M. Mizutani, N. Meyer, H. Roelink, E. Bier, Threshold-dependent BMP-mediated repression: A model for a conserved mechanism that patterns the neuroectoderm. *PLOS Biol.* **4**, e313 (2006). doi: 10.1371/journal.pbio.0040313; pmid: 16968133
36. J. Cowden, M. Levine, Ventral dominance governs sequential patterns of gene expression across the dorsal-ventral axis of the neuroectoderm in the *Drosophila* embryo. *Dev. Biol.* **262**, 335–349 (2003). doi: 10.1016/S0012-1606(03)00395-6; pmid: 14550796
37. F. F. Esteves *et al*., BMPs regulate *msx* gene expression in the dorsal neuroectoderm of *Drosophila* and vertebrates by distinct mechanisms. *PLOS Genet.* **10**, e1004625 (2014). doi: 10.1371/journal.pgen.1004625; pmid: 25210771
38. E. M. De Robertis, H. Kuroda, Dorsal-ventral patterning and neural induction in *Xenopus* embryos. *Annu. Rev. Cell Dev. Biol.* **20**, 285–308 (2004). doi: 10.1146/annurev.cellbio.20.011403.154124; pmid: 15473842
39. M. K. Khokha, J. Yeh, T. C. Grammer, R. M. Harland, Depletion of three BMP antagonists from Spemann's organizer leads to a catastrophic loss of dorsal structures. *Dev. Cell* **8**, 401–411 (2005). doi: 10.1016/j.devcel.2005.01.013; pmid: 15737935
40. J. L. Plouhinec, L. Zakin, Y. Moriyama, E. M. De Robertis, Chordin forms a self-organizing morphogen gradient in the extracellular space between ectoderm and mesoderm in the *Xenopus* embryo. *Proc. Natl. Acad. Sci. U.S.A.* **110**, 20372–20379 (2013). doi: 10.1073/pnas.1319745110; pmid: 24284174
41. S. C. Little, M. C. Mullins, Bone morphogenetic protein heterodimers assemble heteromeric type I receptor complexes to pattern the dorsoventral axis. *Nat. Cell Biol.* **11**, 637–643 (2009). doi: 10.1038/ncb1870; pmid: 19377468
42. S. Piccolo *et al*., Cleavage of Chordin by Xolloid metalloprotease suggests a role for proteolytic processing in the regulation of Spemann organizer activity. *Cell* **91**, 407–416 (1997). doi: 10.1016/S0092-8674(00)80424-9; pmid: 9363949
43. H. X. Lee, A. L. Ambrosio, B. Reversade, E. M. De Robertis, Embryonic dorsal-ventral signaling: Secreted frizzled-related proteins as inhibitors of tolloid proteinases. *Cell* **124**, 147–159 (2006). doi: 10.1016/j.cell.2005.12.018; pmid: 16413488
44. H. X. Lee, F. A. Mendes, J. L. Plouhinec, E. M. De Robertis, Enzymatic regulation of pattern: BMP4 binds CUB domains of Tolloids and inhibits proteinase activity. *Genes Dev.* **23**, 2551–2562 (2009). doi: 10.1101/gad.1839309; pmid: 19884260
45. H. Inomata, T. Haraguchi, Y. Sasai, Robust stability of the embryonic axial pattern requires a secreted scaffold for chordin degradation. *Cell* **134**, 854–865 (2008). doi: 10.1016/j.cell.2008.07.008; pmid: 18775317
46. A. L. Ambrosio *et al*., Crossveinless-2 is a BMP feedback inhibitor that binds Chordin/BMP to regulate *Xenopus* embryonic patterning. *Dev. Cell* **15**, 248–260 (2008). doi: 10.1016/j.devcel.2008.06.013; pmid: 18694564
47. A. Ralston, S. S. Blair, Long-range Dpp signaling is regulated to restrict BMP signaling to a crossvein competent zone. *Dev. Biol.* **280**, 187–200 (2005). doi: 10.1016/j.ydbio.2005.01.018; pmid: 15766758
48. P. F. Xu, N. Houssin, K. F. Ferri-Lagneau, B. Thisse, C. Thisse, Construction of a vertebrate embryo from two opposing morphogen gradients. *Science* **344**, 87–89 (2014). doi: 10.1126/science.1248252; pmid: 24700857
49. T. A. Appel, *The Cuvier-Geoffroy Debate: French Biology in the Decades Before Darwin* (Oxford Univ. Press, Oxford, 1987).
50. L. Marjoram, C. Wright, Rapid differential transport of Nodal and Lefty on sulfated proteoglycan-rich extracellular matrix regulates left-right asymmetry in *Xenopus*. *Development* **138**, 475–485 (2011). doi: 10.1242/dev.056010; pmid: 21205792
51. K. J. Lee, T. M. Jessell, The specification of dorsal cell fates in the vertebrate central nervous system. *Annu. Rev. Neurosci.* **22**, 261–294 (1999). doi: 10.1146/annurev.neuro.22.1.261; pmid: 10202540
52. I. Patten, M. Placzek, Opponent activities of Shh and BMP signaling during floor plate induction in vivo. *Curr. Biol.* **12**, 47–52 (2002). doi: 10.1016/S0960-9822(01)00631-5; pmid: 11790302
53. A. S. Denes *et al*., Molecular architecture of annelid nerve cord supports common origin of nervous system centralization in bilateria. *Cell* **129**, 277–288 (2007). doi: 10.1016/j.cell.2007.02.040; pmid: 17448990
54. D. Arendt, A. S. Denes, G. Jékely, K. Tessmar-Raible, The evolution of nervous system centralization. *Philos. Trans. R. Soc. London Ser. B* **363**, 1523–1528 (2008). doi: 10.1098/rstb.2007.2242; pmid: 18192182
55. D. Ben-Zvi, A. Fainsod, B. Z. Shilo, N. Barkai, Scaling of dorsal-ventral patterning in the *Xenopus* laevis embryo. *BioEssays* **36**, 151–156 (2014). doi: 10.1002/bies.201300136; pmid: 24323952
56. Y. T. Zhang, A. D. Lander, Q. Nie, Computational analysis of BMP gradients in dorsal-ventral patterning of the zebrafish embryo. *J. Theor. Biol.* **248**, 579–589 (2007). doi: 10.1016/j.jtbi.2007.05.026; pmid: 17673236
57. C. M. Mizutani *et al*., Formation of the BMP activity gradient in the *Drosophila* embryo. *Dev. Cell* **8**, 915–924 (2005). doi: 10.1016/j.devcel.2005.04.009; pmid: 15935780
58. A. D. Lander, Pattern, growth, and control. *Cell* **144**, 955–969 (2011). doi: 10.1016/j.cell.2011.03.009; pmid: 21414486
59. S. Restrepo, J. J. Zartman, K. Basler, Coordination of patterning and growth by the morphogen DPP. *Curr. Biol.* **24**, R245–R255 (2014). doi: 10.1016/j.cub.2014.01.055; pmid: 24650915
60. D. Nellen, R. Burke, G. Struhl, K. Basler, Direct and long-range action of a DPP morphogen gradient. *Cell* **85**, 357–368 (1996). doi: 10.1016/S0092-8674(00)81114-9; pmid: 8616891
61. S. Zhou *et al*., Free extracellular diffusion creates the Dpp morphogen gradient of the *Drosophila* wing disc. *Curr. Biol.* **22**, 668–675 (2012). doi: 10.1016/j.cub.2012.02.065; pmid: 22445299
62. P. Müller, K. W. Rogers, S. R. Yu, M. Brand, A. F. Schier, Morphogen transport. *Development* **140**, 1621–1638 (2013). doi: 10.1242/dev.083519; pmid: 23533171
63. J. L. Erickson, Formation and maintenance of morphogen gradients: An essential role for the endomembrane system in *Drosophila melanogaster* wing development. *Fly* **5**, 266–271 (2011). doi: 10.4161/fly.5.3.16542; pmid: 21654212
64. V. Greco, M. Hannus, S. Eaton, Argosomes: A potential vehicle for the spread of morphogens through epithelia. *Cell* **106**, 633–645 (2001). doi: 10.1016/S0092-8674(01)00484-6; pmid: 11551510
65. S. Pfeiffer, C. Alexandre, M. Calleja, J. P. Vincent, The progeny of wingless-expressing cells deliver the signal at a distance in *Drosophila* embryos. *Curr. Biol.* **10**, 321–324 (2000). doi: 10.1016/S0960-9822(00)00381-X; pmid: 10744976
66. S. Roy, H. Huang, S. Liu, T. B. Kornberg, Cytoneme-mediated contact-dependent transport of the *Drosophila* decapentaplegic signaling protein. *Science* **343**, 1244624 (2014). doi: 10.1126/science.1244624; pmid: 24385607
67. S. Roy, F. Hsiung, T. B. Kornberg, Specificity of *Drosophila* cytonemes for distinct signaling pathways. *Science* **332**, 354–358 (2011). doi: 10.1126/science.1198949; pmid: 21493861
68. F. Hsiung, F.-A. Ramirez-Weber, D. D. Iwaki, T. B. Kornberg, Dependence of *Drosophila* wing imaginal disc cytonemes on Decapentaplegic. *Nature* **437**, 560–563 (2005). doi: 10.1038/nature03951; pmid: 16177792
69. M. Sato, T. B. Kornberg, FGF is an essential mitogen and chemoattractant for the air sacs of the *Drosophila* tracheal system. *Dev. Cell* **3**, 195–207 (2002). doi: 10.1016/S1534-5807(02)00202-2; pmid: 12194851
70. F. A. Ramírez-Weber, T. B. Kornberg, Cytonemes: Cellular processes that project to the principal signaling center in *Drosophila* imaginal discs. *Cell* **97**, 599–607 (1999). doi: 10.1016/S0092-8674(00)80771-0; pmid: 10367889
71. T. A. Sanders, E. Llagostera, M. Barna, Specialized filopodia direct long-range transport of SHH during vertebrate tissue patterning. *Nature* **497**, 628–632 (2013). doi: 10.1038/nature12157; pmid: 23624372
72. M. Nahmad, A. Stathopoulos, Dynamic interpretation of hedgehog signaling in the *Drosophila* wing disc. *PLOS Biol.* **7**, e1000202 (2009). doi: 10.1371/journal.pbio.1000202; pmid: 19787036
73. C. Alexandre, A. Baena-Lopez, J. P. Vincent, Patterning and growth control by membrane-tethered Wingless. *Nature* **505**, 180–185 (2014). doi: 10.1038/nature12879; pmid: 24390349
74. P. McHale *et al*., Gene length may contribute to graded transcriptional responses in the *Drosophila* embryo. *Dev. Biol.* **360**, 230–240 (2011). doi: 10.1016/j.ydbio.2011.08.016; pmid: 21920356
75. E. Kutejova, J. Briscoe, A. Kicheva, Temporal dynamics of patterning by morphogen gradients. *Curr. Opin. Genet. Dev.* **19**, 315–322 (2009). doi: 10.1016/j.gde.2009.05.004; pmid: 19596567
76. K. F. Liem Jr., G. Tremml, T. M. Jessell, A role for the roof plate and its resident TGFβ-related proteins in neuronal patterning in the dorsal spinal cord. *Cell* **91**, 127–138 (1997). doi: 10.1016/S0092-8674(01)80015-5; pmid: 9335341

77. M. Lek *et al*., A homeodomain feedback circuit underlies step-function interpretation of a Shh morphogen gradient during ventral neural patterning. *Development* **137**, 4051–4060 (2010). doi: 10.1242/dev.054288; pmid: 21062862
78. A. D. Lander, W. C. Lo, Q. Nie, F. Y. Wan, The measure of success: Constraints, objectives, and tradeoffs in morphogen-mediated patterning. *Cold Spring Harb. Perspect. Biol.* **1**, a002022 (2009). doi: 10.1101/cshperspect.a002022; pmid: 20066078
79. F. Hamaratoglu, A. M. de Lachapelle, G. Pyrowolakis, S. Bergmann, M. Affolter, Dpp signaling activity requires Pentagone to scale with tissue size in the growing *Drosophila* wing imaginal disc. *PLOS Biol.* **9**, e1001182 (2011). doi: 10.1371/journal.pbio.1001182; pmid: 22039350
80. R. Vuilleumier *et al*., Control of Dpp morphogen signalling by a secreted feedback regulator. *Nat. Cell Biol.* **12**, 611–617 (2010). doi: 10.1038/ncb2064; pmid: 20453847
81. L. A. Baena-Lopez, H. Nojima, J. P. Vincent, Integration of morphogen signalling within the growth regulatory network. *Curr. Opin. Cell Biol.* **24**, 166–172 (2012). doi: 10.1016/j.ceb.2011.12.010; pmid: 22257639
82. F. Galton, Vox populi. *Nature* **75**, 450–451 (1907).
83. J. Surowiecki, *The Wisdom of Crowds* (Anchor Books/Random House, New York, 2004).
84. S. A. Holley *et al*., A conserved system for dorsal-ventral patterning in insects and vertebrates involving sog and *chordin*. *Nature* **376**, 249–253 (1995). doi: 10.1038/376249a0; pmid: 7617035
85. J. Schmidt, V. Francois, E. Bier, D. Kimelman, *Drosophila* short gastrulation induces an ectopic axis in *Xenopus*: Evidence for conserved mechanisms of dorsal-ventral patterning. *Development* **121**, 4319–4328 (1995). pmid: 8575332
86. R. W. Padgett, J. M. Wozney, W. M. Gelbart, Human BMP sequences can confer normal dorsal-ventral patterning in the *Drosophila* embryo. *Proc. Natl. Acad. Sci. U.S.A.* **90**, 2905–2909 (1993). doi: 10.1073/pnas.90.7.2905; pmid: 8464906
87. Y. Goltsev *et al*., Evolution of the dorsal-ventral patterning network in the mosquito, *Anopheles gambiae*. *Development* **134**, 2415–2424 (2007). doi: 10.1242/dev.02863; pmid: 17522157
88. Y. Akiyama-Oda, H. Oda, Axis specification in the spider embryo: Dpp is required for radial-to-axial symmetry transformation and sog for ventral patterning. *Development* **133**, 2347–2357 (2006). doi: 10.1242/dev.02400; pmid: 16720876
89. M. D. Molina *et al*., Noggin and noggin-like genes control dorsoventral axis regeneration in planarians. *Curr. Biol.* **21**, 300–305 (2011). doi: 10.1016/j.cub.2011.01.016; pmid: 21295481
90. M. A. Gaviño, P. W. Reddien, A Bmp/Admp regulatory circuit controls maintenance and regeneration of dorsal-ventral polarity in planarians. *Curr. Biol.* **21**, 294–299 (2011). doi: 10.1016/j.cub.2011.01.017; pmid: 21295483
91. P. W. Reddien, A. L. Bermange, A. M. Kicza, A. Sánchez Alvarado, BMP signaling regulates the dorsal planarian midline and is needed for asymmetric regeneration. *Development* **134**, 4043–4051 (2007). doi: 10.1242/dev.007138; pmid: 17942485
92. F. Lapraz, L. Besnardeau, T. Lepage, Patterning of the dorsal-ventral axis in echinoderms: Insights into the evolution of the BMP-chordin signaling network. *PLOS Biol.* **7**, e1000248 (2009). doi: 10.1371/journal.pbio.1000248; pmid: 19956794
93. J. K. Yu *et al*., Axial patterning in cephalochordates and the evolution of the organizer. *Nature* **445**, 613–617 (2007). doi: 10.1038/nature05472; pmid: 17237766
94. E. Bier, Evolution of development: Diversified dorsoventral patterning. *Curr. Biol.* **21**, R591–R594 (2011). doi: 10.1016/j.cub.2011.06.037; pmid: 21820625
95. G. Genikhovich *et al*., Axis patterning by BMPs: Cnidarian network reveals evolutionary constraints. *Cell Rep.* **10**, 1646–1654 (2015). doi: 10.1016/j.celrep.2015.02.035
96. C. Niehrs, On growth and form: A Cartesian coordinate system of Wnt and BMP signaling specifies bilaterian body axes. *Development* **137**, 845–857 (2010). doi: 10.1242/dev.039651; pmid: 20179091
97. J. W. Valentine, *On The Origin of Phyla* (Univ. of Chicago Press, Chicago, ed. 1, 2004).
98. C. J. Lowe *et al*., Dorsoventral patterning in hemichordates: Insights into early chordate evolution. *PLOS Biol.* **4**, e291 (2006). doi: 10.1371/journal.pbio.0040291; pmid: 16933975
99. M. van der Zee, O. Stockhammer, C. von Levetzow, R. Nunes da Fonseca, S. Roth, Sog/Chordin is required for ventral-to-dorsal Dpp/BMP transport and head formation in a short germ insect. *Proc. Natl. Acad. Sci. U.S.A.* **103**, 16307–16312 (2006). doi: 10.1073/pnas.0605154103; pmid: 17050690
100. H. L. Ashe, M. Levine, Local inhibition and long-range enhancement of Dpp signal transduction by Sog. *Nature* **398**, 427–431 (1999). doi: 10.1038/18892; pmid: 10201373
101. E. Bier, Developmental biology: A unity of opposites. *Nature* **398**, 375–376 (1999). pmid: 10201364
102. K. Yu *et al*., Cysteine repeat domains and adjacent sequences determine distinct bone morphogenetic protein modulatory activities of the *Drosophila* Sog protein. *Genetics* **166**, 1323–1336 (2004). doi: 10.1534/genetics.166.3.1323; pmid: 15082551
103. E. Decotto, E. L. Ferguson, A positive role for Short gastrulation in modulating BMP signaling during dorsoventral patterning in the *Drosophila* embryo. *Development* **128**, 3831–3841 (2001). pmid: 11585808
104. E. L. Ferguson, K. V. Anderson, Localized enhancement and repression of the activity of the TGF-β family member, *decapentaplegic*, is necessary for dorsal-ventral pattern formation in the *Drosophila* embryo. *Development* **114**, 583–597 (1992). pmid: 1618130
105. E. L. Ferguson, Conservation of dorsal-ventral patterning in arthropods and chordates. *Curr. Opin. Genet. Dev.* **6**, 424–431 (1996). doi: 10.1016/S0959-437X(96)80063-3; pmid: 8791529
106. D. M. Umulis, M. Serpe, M. B. O'Connor, H. G. Othmer, Robust, bistable patterning of the dorsal surface of the *Drosophila* embryo. *Proc. Natl. Acad. Sci. U.S.A.* **103**, 11613–11618 (2006). doi: 10.1073/pnas.0510398103; pmid: 16864795
107. A. M. Rafiqi, C. H. Park, C. W. Kwan, S. Lemke, U. Schmidt-Ott, BMP-dependent serosa and amnion specification in the scuttle fly *Megaselia abdita*. *Development* **139**, 3373–3382 (2012). doi: 10.1242/dev.083873; pmid: 22874914
108. Y. Akiyama-Oda, H. Oda, Early patterning of the spider embryo: A cluster of mesenchymal cells at the cumulus produces Dpp signals received by germ disc epithelial cells. *Development* **130**, 1735–1747 (2003). doi: 10.1242/dev.00390; pmid: 12642480
109. D. Bachiller *et al*., The organizer factors Chordin and Noggin are required for mouse forebrain development. *Nature* **403**, 658–661 (2000). doi: 10.1038/35001072; pmid: 10688202
110. A. Lauri *et al*., Development of the annelid axochord: Insights into notochord evolution. *Science* **345**, 1365–1368 (2014). pmid: 25214631
111. D. H. Kuo, D. A. Weisblat, A new molecular logic for BMP-mediated dorsoventral patterning in the leech *Helobdella*. *Curr. Biol.* **21**, 1282–1288 (2011). doi: 10.1016/j.cub.2011.06.024; pmid: 21782437
112. S. V. Nuzhdin *et al*., Natural genetic variation in transcriptome reflects network structure inferred with major effect mutations: Insulin/TOR and associated phenotypes in *Drosophila melanogaster*. *BMC Genomics* **10**, 124 (2009). doi: 10.1186/1471-2164-10-124; pmid: 19317915
113. I. Dworkin *et al*., The effects of weak genetic perturbations on the transcriptome of the wing imaginal disc and its association with wing shape in *Drosophila melanogaster*. *Genetics* **187**, 1171–1184 (2011). doi: 10.1534/genetics.110.125922; pmid: 21288875
114. E. Bier, *The Coiled Spring: How Life Begins* (Cold Spring Harbor Laboratory Press, Cold Spring Harbor, New York, ed. 1, 2000).
115. D. Kosman *et al*., Multiplex detection of RNA expression in *Drosophila* embryos. *Science* **305**, 846 (2004). doi: 10.1126/science.1099247; pmid: 15297669
116. J. C. Illes, E. Winterbottom, H. V. Isaacs, Cloning and expression analysis of the anterior parahox genes, *Gsh1* and *Gsh2* from *Xenopus tropicalis*. *Dev. Dyn.* **238**, 194–203 (2009). doi: 10.1002/dvdy.21816; pmid: 19097192
117. T. B. Kornberg, S. Roy, Cytonemes as specialized signaling filopodia. *Development* **141**, 729–736 (2014). doi: 10.1242/dev.086223; pmid: 24496611
118. E. Bier, Drawing lines in the *Drosophila* wing: Initiation of wing vein development. *Curr. Opin. Genet. Dev.* **10**, 393–398 (2000). doi: 10.1016/S0959-437X(00)00102-7; pmid: 10889058

ACKNOWLEDGMENTS

We thank V. Gantz for kindly providing the illustrations of organisms depicted in Fig. 6 and for the schematics of wing growth and BMP-mediated patterning shown in Fig. 5B. E.B. acknowledges funding support from NIH grant NS29870, and E.M.D.R. is a Howard Hughes Medical Institute Investigator.

10.1126/science.aaa5838

RESEARCH ARTICLE SUMMARY

HEART DEVELOPMENT

Integration of Bmp and Wnt signaling by Hopx specifies commitment of cardiomyoblasts

Rajan Jain, Deqiang Li, Mudit Gupta, Lauren J. Manderfield, Jamie L. Ifkovits, Qiaohong Wang, Feiyan Liu, Ying Liu, Andrey Poleshko, Arun Padmanabhan, Jeffrey C. Raum, Li Li, Edward E. Morrisey, Min Min Lu, Kyoung-Jae Won, Jonathan A. Epstein*

INTRODUCTION: Cardiac progenitor cells are multipotent, and lineage analyses of murine and chick cardiac development have demonstrated that these cells give rise to the cardiac endothelium, smooth muscle, and cardiomyocytes. However, the mechanisms governing commitment to the myocyte lineage in vivo remain largely unknown. Further understanding of these mechanisms, and of the identity of progenitors committed to the myocyte lineage, may advance cardiac regenerative therapies.

RATIONALE: Hopx is an atypical homeodomain expressed in cardiac mesoderm shortly after cardiac progenitor cells are first evident. Previous studies have demonstrated that Hopx functions as a nuclear transcription co-repressor and is expressed in adult, +4 intestinal stem cells and hair follicle bulge stem cells. We compare lineage tracing of multipotent cardiac progenitor cells marked by Islet1 and Nkx2-5 expression with lineage tracing of Hopx$^+$ cells. We also perform functional studies of Hopx from endogenous tissue and differentiated embryoid bodies to identify mechanisms promoting commitment and myogenesis.

RESULTS: We define and characterize a Hopx-expressing cardiomyoblast intermediate that is committed to the cardiomyocyte fate. Hopx$^+$ is initially expressed in a subset of cardiac progenitor cells residing in the precardiac mesoderm prior to the expression of troponin T, a component of the contractile sarcomere apparatus of myocytes. Lineage-tracing experiments demonstrate that Hopx$^+$ cells give rise to cardiac myocytes exclusively. Early Hopx$^+$ cardiomyoblasts expand during cardiogenesis.

Overexpression of Hopx in cardiac progenitor cells leads to an increase in myocytes, whereas Hopx deficiency compromises myogenesis. Whole-genome analysis reveals that Hopx occupies regulatory regions of multiple Wnt-related genes, and *Hopx*$^{-/-}$ cardiac tissues are characterized by an expansion of Wnt signaling. Restoration of Wnt levels during differentiation of *Hopx*$^{-/-}$ embryoid bodies partially rescues myogenesis. Wnt signaling is a potent regulator of stemness of cardiac progenitor cells, and our data suggest that Hopx promotes myogenesis by repressing Wnt signaling.

ON OUR WEB SITE

Read the full article at http://dx.doi.org/10.1126/science.aaa6071

Cardiac progenitor cells down-regulate Wnt signaling as they enter the cardiac outflow tract, coincident with the expression of Hopx. The outflow tract is also enriched for bone morphogenetic protein (Bmp) signaling, known to influence differentiation of myocytes. Hopx physically interacts with activated Smad complexes in vitro and in vivo. Exogenous Bmp4 represses Wnt signaling in cardiac explants, and Bmp4-mediated Wnt repression requires Hopx. Thus, Hopx functions to couple Bmp signaling to repression of Wnt.

CONCLUSION: Our work defines an intermediate cardiac progenitor that expresses Hopx and is committed exclusively to the myocyte fate. Therefore, akin to an erythroblast in hematopoietic differentiation, we have termed these committed cardiac progenitor cells "cardiomyoblasts." The ability to identify committed, but undifferentiated, cardiomyocyte precursors may facilitate development of cardiac regenerative therapies, including those using embryonic stem cells and induced pluripotent stem cells.

Hopx functions to promote myogenesis by physically interacting with Smad proteins to repress Wnt signaling. Our findings raise the possibility that Hopx-mediated integration of Bmp signaling to repress Wnt may be active in other progenitor populations and may potentially underlie the tumor suppressor function of Hopx. ■

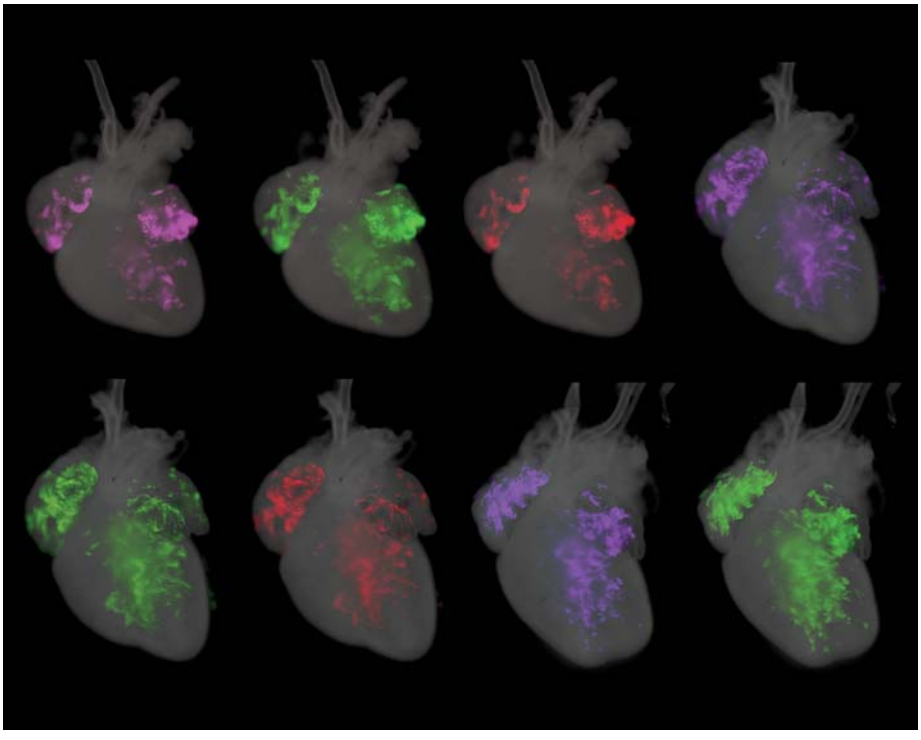

Lineage tracing of Hopx$^+$ cells. Images depicting lineage tracing of early Hopx$^+$ cardiomyoblasts that give rise to myocytes in the left ventricle and atria. Some images are duplicated and pseudocolored.

The list of author affiliations is available in the full article online.
*Corresponding author. E-mail: epsteinj@upenn.edu
Cite this article as R. Jain *et al.*, *Science* **348**, aaa6071 (2015).
DOI: 10.1126/science.aaa6071

Downloaded from www.sciencemag.org on June 26, 2015

RESEARCH ARTICLE

HEART DEVELOPMENT

Integration of Bmp and Wnt signaling by Hopx specifies commitment of cardiomyoblasts

Rajan Jain,[1]* Deqiang Li,[1]* Mudit Gupta,[1] Lauren J. Manderfield,[1] Jamie L. Ifkovits,[1]† Qiaohong Wang,[1] Feiyan Liu,[1] Ying Liu,[1] Andrey Poleshko,[1] Arun Padmanabhan,[1]‡ Jeffrey C. Raum,[2] Li Li,[1] Edward E. Morrisey,[1] Min Min Lu,[1] Kyoung-Jae Won,[2] Jonathan A. Epstein[1]§

Cardiac progenitor cells are multipotent and give rise to cardiac endothelium, smooth muscle, and cardiomyocytes. Here, we define and characterize the cardiomyoblast intermediate that is committed to the cardiomyocyte fate, and we characterize the niche signals that regulate commitment. Cardiomyoblasts express Hopx, which functions to coordinate local Bmp signals to inhibit the Wnt pathway, thus promoting cardiomyogenesis. Hopx integrates Bmp and Wnt signaling by physically interacting with activated Smads and repressing Wnt genes. The identification of the committed cardiomyoblast that retains proliferative potential will inform cardiac regenerative therapeutics. In addition, Bmp signals characterize adult stem cell niches in other tissues where Hopx-mediated inhibition of Wnt is likely to contribute to stem cell quiescence and to explain the role of Hopx as a tumor suppressor.

Lineage analyses during cardiac development in the chick and mouse over the past two decades have demonstrated that at least two pools of progenitor cells contribute to the heart (*1*). Cardiac progenitor cells (CPCs) derived from the cardiac crescent, or the first heart field (FHF), express *Nkx2-5* and contribute to a primitive heart tube. After subsequent looping of the heart tube, additional progenitor cells are added to the arterial and venous poles of the heart from the second heart field (SHF). SHF cells arise just medial and posterior to the FHF in the cardiac crescent and populate the pharyngeal arches and dorsomedial mesoderm before migration into the heart proper (*2*, *3*).

Studies modeling cardiac development using differentiation of embryonic stem (ES) cell–derived embryoid bodies (EBs) have demonstrated that SHF progenitors, marked by *Islet1* (*Isl1*) expression (*4*), are multipotent, with potential for differentiation into cardiomyocyte, endothelial, or smooth muscle lineages (*5*–*7*). Wnt signaling is necessary to promote and expand multipotent CPCs (*8*–*10*), and subsequent differentiation of cardiac myocytes is influenced by bone morphogenetic protein (Bmp) signaling and Wnt inhibition (*11*, *12*). However, the implications of these studies for in vivo cardiogenesis are unknown. The characteristics of an embryonic CPC niche are poorly described, and the degree to which CPCs remain uncommitted during mid- and late gestation has been unclear. For example, recent reports using inducible lineage tracing of early cardiac progenitors, marked by Mesp1 expression, suggest the existence of a relatively small pool of multipotent progenitors in vivo and that at least some of these become committed at very early stages, perhaps soon after gastrulation (*13*, *14*). Efforts to fully characterize the signaling pathways active during cell fate decisions in vivo have been hampered, at least in part, by the lack of specific markers of lineage commitment.

Here, we report that CPCs committed to the myocyte lineage can be prospectively identified before the expression of sarcomere genes on the basis of Hopx expression, an atypical homeodomain protein expressed during early cardiac development and in multiple stem cell populations (*15*–*19*). Akin to an erythroblast in hematopoietic differentiation, we have termed these committed CPCs "cardiomyoblasts." We show that SHF-derived cardiomyoblasts are specified in the distal outflow tract (OFT) within a zone of high Bmp and low Wnt signaling. Finally, we show that Hopx not only marks commitment, but that it also promotes myogenesis by interacting with an activated-Smad complex to repress Wnt.

Cardiomyoblasts are defined by Hopx expression

At early stages of cardiac development, *Nkx2-5* and *Isl1* mark populations of CPCs (*2*, *4*), and *Hopx* expression initiates shortly after *Nkx2-5* in precardiac mesoderm (*15*). We used a knock-in allele in which Hopx is epitope tagged and green fluorescent protein (GFP) is expressed in Hopx$^+$ cells (*18*) to determine that Hopx is expressed in a subset of CPCs at embryonic day 8.0 (E8.0) and E8.5 in the FHF and SHF, respectively (Fig. 1, A and B). As SHF progenitors enter the distal OFT, Isl1 expression is gradually extinguished and Hopx expression initiates, providing a restricted region of coexpression in the distal OFT (Fig. 1B). Fate mapping using *Nkx2-5$^{Cre/+}$* and cre-dependent reporter mice indicates that essentially the entire late-gestation heart derives from *Nkx2-5$^+$* precursors, including myocytes, smooth muscle, endothelium, and epicardium (Fig. 1C). Isl1$^+$ cells also give rise to smooth muscle, endothelium, myocytes, and epicardium, but some of the left ventricle myocardium and atria, derived from the FHF, is not labeled in *Isl1* fate-mapping experiments (Fig. 1D). Lineage-tracing experiments using a *Hopx$^{Cre/+}$* allele, in which we inserted cre following an internal ribosomal entry sequence (IRES) so as to avoid perturbing *Hopx* expression (*20*), demonstrate labeling in all four cardiac chambers (Fig. 1E and fig. S1, A and B). However, in contrast to *Nkx2-5* and *Isl1*, *Hopx* derivatives within the heart are entirely restricted to cardiac myocytes (Fig. 1E and fig. S2). Some cardiac fibroblasts derive from *Nkx2-5*- and *Isl1*-expressing precursors, but *Hopx$^+$* cells do not give rise to fibroblasts in the heart (fig. S2). Most cardiac myocytes derive from *Hopx$^+$* precursors, although some specialized myocytes surrounding the pulmonary veins and within the interatrial septum are not derived from Hopx$^+$ cells (fig. S3). Analysis of E9.5 *Nkx2-5$^{Cre/+}$*; *R26$^{Tom/+}$*; *Hopx$^{3XFlag/+}$* embryos reveals that all Hopx$^+$ cardiomyocytes at this time point derive from *Nkx2-5$^+$* precursors (Fig. 1F). Flow cytometry analysis of dissociated postnatal day 2 (P2) hearts, expressing a reporter allele, confirms the multilineage contribution of *Nkx2-5* and *Isl1*, in contrast to *Hopx$^+$* cells (fig. S4). We do not detect Hopx in any nonmyocyte cell types within the heart, consistent with our lineage-tracing data (fig. S5).

To confirm the fate of the earliest Hopx$^+$-expressing cells, we used a tamoxifen-inducible *Hopx* allele (*Hopx$^{ERCre/+}$*) (*19*). Low doses of tamoxifen induction in *Hopx$^{ERCre/+}$*; *R26$^{Tom/+}$* embryos reveal that single E8.25 *Hopx$^+$* cardiomyoblasts expand to form clusters of myocytes by E18.5 (Fig. 2, A and B) and that Hopx$^+$ cardiomyoblasts express markers of proliferation at early embryonic time points (fig. S6). In addition, inducing cre recombinase activity with a single dose of tamoxifen at E8.25, a time point correlating with Hopx expression within a subset of *Nkx2-5$^+$* progenitors, demonstrates lineage-labeled myocytes primarily in the left ventricle and both atria at E18.5 (Fig. 2C). However, similar lineage tracing of E9.25 Hopx$^+$ cells demonstrates that cardiomyoblasts expressing Hopx at this later time point contribute to myocytes in both ventricles and both atria (Fig. 2D). Taken together, these results establish that cardiac Hopx expression identifies a pool of progenitors committed entirely to the myocyte lineage (e.g., cardiomyoblasts) and that *Hopx$^+$* cardiomyoblasts expand during cardiogenesis. In addition, our results suggest that commitment of FHF and

[1]Department of Cell and Developmental Biology, Penn Cardiovascular Institute, Institute of Regenerative Medicine, Perelman School of Medicine at the University of Pennsylvania, Philadelphia, PA 19104, USA. [2]Department of Genetics, Institute for Diabetes, Obesity, and Metabolism, Perelman School of Medicine at the University of Pennsylvania, Philadelphia, PA 19104, USA.
*These authors contributed equally to this work. †Present address: GlaxoSmithKline, 1250 South Collegeville Road, Mail Code 12-L16E, Collegeville, PA 19426, USA. ‡Present address: Massachusetts General Hospital, 55 Fruit Street, Boston, MA 02114, USA.
§Corresponding author. E-mail: epsteinj@upenn.edu

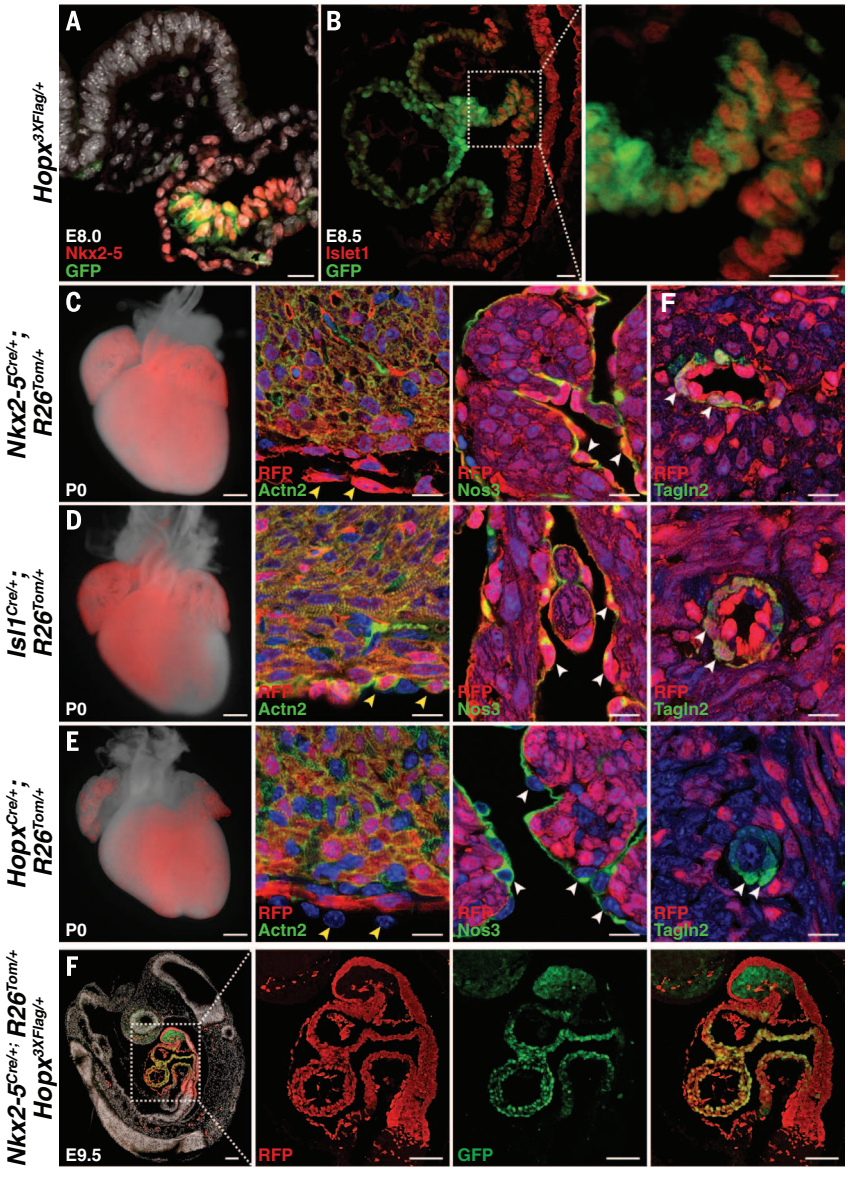

Fig. 1. Prospective identification of cardiomyoblasts. (**A**) A subset of E8.0 Nkx2-5^{+} cells in the FHF precardiac mesoderm express Hopx. (**B**) A subset of E8.5 Isl1^{+} SHF cells in the OFT express Hopx (inset highlights distal OFT). (**C** and **D**) *Nkx2-5*$^{+}$ (C) and *Isl1*$^{+}$ (D) cells give rise to myocytes (Actn2^{+}), epicardium (yellow arrowheads), endothelium (Nos3^{+}, white arrowheads), and smooth muscle (Tagln2^{+}, white arrowheads) at P0. (**E**) *Hopx*$^{+}$ cells give rise to myocytes, not epicardium (yellow arrowheads), endothelium (Nos3, white arrowheads), or smooth muscle (Tagln2, white arrowheads) at P0. (**F**) Hopx^{+} cells (GFP^{+}) derive from *Nkx2-5*$^{+}$ cells (RFP^{+}, red fluorescent protein) (E9.5, sagittal section). Scale bars: 500 μm [(C to E), whole mount], 100 μm (F), 25 μm (A and B), 10 μm [(C to E), histology].

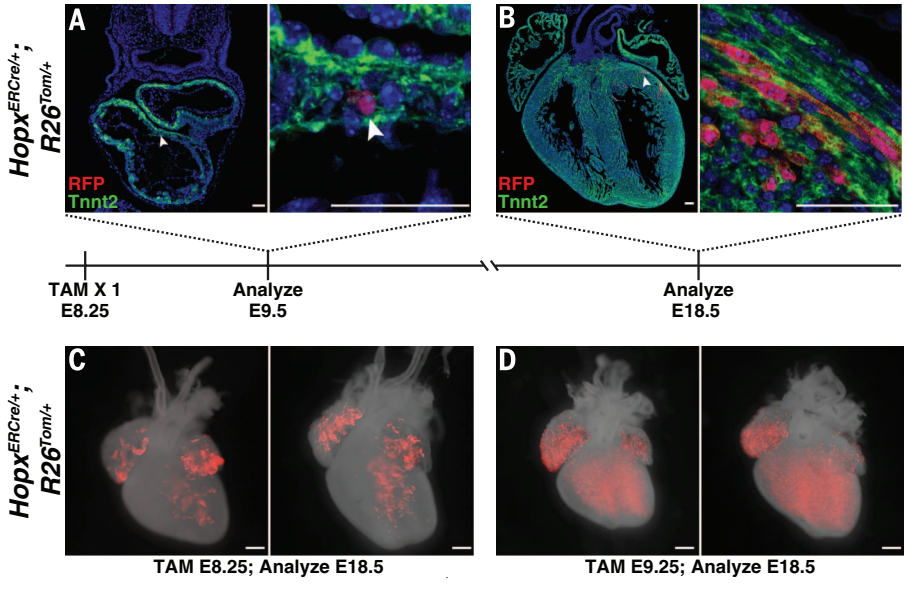

Fig. 2. Cardiomyoblasts expand during cardiogenesis. (**A** and **B**) E8.25 *Hopx*$^{ERCre/+}$; *R26*$^{Tom/+}$ embryos were induced with tamoxifen and harvested at E9.5 (A) and E18.5 (B). Individual *Hopx*-derived cells are labeled at E9.5 [(A and B) area highlighted by arrowhead is magnified on the right]. At E18.5, clusters of myocytes are identified (B). (**C** and **D**) *Hopx*$^{ERCre/+}$; *R26*$^{Tom/+}$ embryos were induced with tamoxifen at E8.25 (C) or E9.25 (D) and analyzed at E18.5 ($n \geq 2$ litters per time point; two examples at each time point shown). Scale bars: 500 μm (C and D) and 50 μm (A and B).

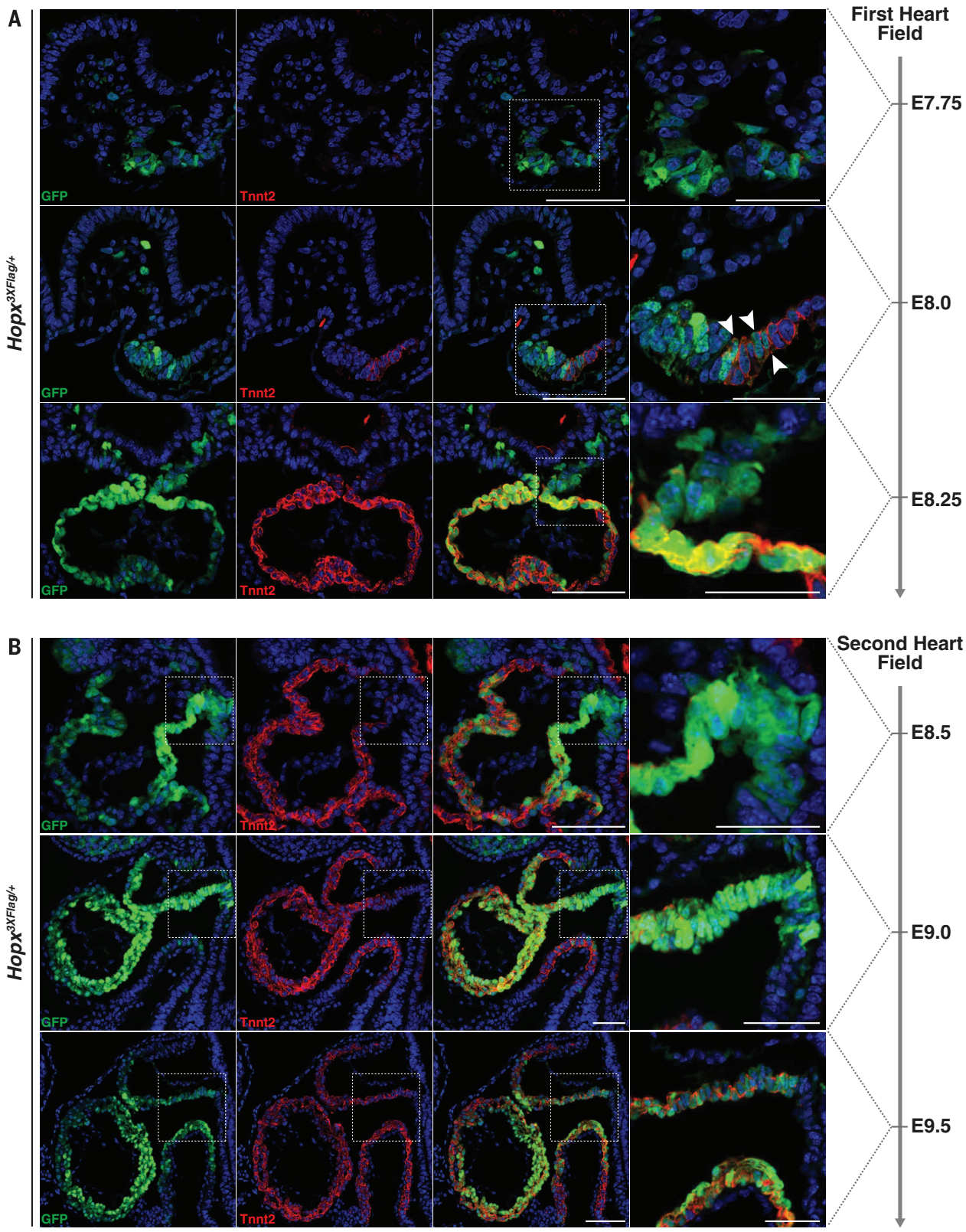

Fig. 3. Hopx expression precedes troponin expression. (**A**) Hopx expression precedes Tnnt2 expression in the precardiac mesoderm/FHF at early time points during cardiac development. Hopx^{+}, Tnnt2^{+} cells are identified a few hours later (white arrowheads). (**B**). The distal OFT and SHF mesoderm harbor Hopx^{+}, Tnnt2^{-} cells at early time points during cardiac development. Scale bars: 100 μm except right-most panels/insets, which are 50 μm.

SHF CPCs occurs at distinct time points during cardiogenesis.

Hopx promotes myogenesis by inhibiting Wnt signaling

Hopx is expressed early during cardiomyocyte differentiation and precedes that of troponin T (Tnnt2) in both the FHF and SHF (Fig. 3, A and B). To examine the function of Hopx during cardiomyogenesis, we overexpressed Hopx at various time points of ES cell differentiation. *Hopx* is normally detectable by day 5, before *Tnnt2* and *Myh6* are expressed by maturing EBs (fig. S7A). Using established protocols (*11*, *21*), we differentiated ES cells into EBs and expressed Hopx starting on day 4. Flow cytometry analyses of the resulting cultures at day 7 and day 11 indicate that precocious expression of Hopx induces a significant increase in the number of Tnnt2$^+$ cells (Fig. 4A). When Hopx is induced only 1 day later, at day 5, no statistically significant increase in cardiomyogenesis is observed (Fig. 4A).

We performed reciprocal loss-of-function experiments by generating embryonic stem cells (ESCs) from *Hopx*$^{-/-}$ and littermate *Hopx*$^{+/-}$ blastocysts and differentiating them into cardiac cell types (*20*). *Axin2* and *Nkx2-5* are each expressed at comparable levels when we compared *Hopx*$^{-/-}$ and *Hopx*$^{+/-}$ EBs at days 3 and 4.75 (fig. S7B). However, there is a marked reduction in the number of Tnnt2$^+$ cells and beating foci upon differentiation of *Hopx*$^{-/-}$ EBs compared to *Hopx*$^{+/-}$ EBs (Fig. 4B). We performed microarrays from *Hopx*$^{-/-}$ and *Hopx*$^{+/-}$ EBs (day 8, $n = 3$), and multiple myocyte-related genes are down-regulated in *Hopx*$^{-/-}$ EBs compared to *Hopx*$^{+/-}$ control EBs [table S1; e.g., *Myh6* –30.3×, *Myh7* –30.3×, *Mybpc3* –13.0×, *Ttn* –7.0×, *Tnnt2* –5.5×, *Nkx2-5* –3.984×; false discovery rate (FDR) cutoff = 10%]. Gene Ontology analysis of the top 3000 genes that are down-regulated confirmed enrichment for families of genes related to heart development and myogenesis (Fig. 4C). Although sarcomere genes are expressed in *Hopx*$^{-/-}$ hearts, the onset of Tnnt2 expression is delayed in SHF myoblasts as they enter the OFT, as evidenced by a lack of Tnnt2 expression in Nkx2-5$^+$ precursors within the distal OFT of *Hopx*$^{-/-}$ versus *Hopx*$^{+/+}$ hearts at E9.5 (Fig. 4D). The eventual expression of sarcomere genes in *Hopx* mutants suggests that redundant pathways exist for activation of the myogenic program.

To further define the role of Hopx during myogenesis, we defined the genomic regions occupied by Hopx by performing chromatin immunoprecipitation followed by massively paralleled sequencing (ChIP-seq). Although Hopx does not bind to DNA directly (*22*), it can interact with corepressor complexes to inhibit gene expression. We performed ChIP-seq analysis of pooled chromatin derived from ~35 E9.5 microdissected murine embryonic hearts (table S2). KEGG analysis of the genes associated with the strongest 3000 peaks suggested that Hopx occupancy was enriched in genomic regions proximal to Wnt family member genes ($P = 3.9 \times 10^{-4}$), and the Wnt signaling pathway was the top hit with PANTHER analysis ($P = 1.2 \times 10^{-3}$).

We independently validated Hopx occupancy close to several Wnt ligand transcriptional start sites by ChIP-QPCR (quantitative polymerase chain reaction) (Fig. 5A). Consistent with the known function of Hopx as a transcriptional repressor (*15*), many of these ligands, including *Wnt2*, *Wnt5b*, and *Wnt6*, are expressed at higher levels at day 8 of differentiation in *Hopx*$^{-/-}$ EBs compared to *Hopx*$^{+/-}$ EBs (Fig. 5B). *Axin2* and *Isl1*, both target genes of canonical Wnt signaling (*23*, *24*), are expressed at significantly higher levels in E9.5 *Hopx*$^{-/-}$ hearts, as compared to littermate controls (Fig. 5C). Immunohistochemistry of E9.5 to E10.5 control OFTs reveals that the distal OFT is a transition zone in which Axin2 and Isl1 expression diminish while Hopx expression is activated (Fig. 5D). In *Hopx*$^{-/-}$ embryos, Wnt signaling, as represented by Axin2 and Isl1 expression, is expanded into the proximal OFT compared to littermate controls (Fig. 5E). Overexpression of Hopx in EBs reduces *Axin2* expression, whereas a mutant form of Hopx that does not effectively interact with Smad4 (discussed further below) does not have this effect

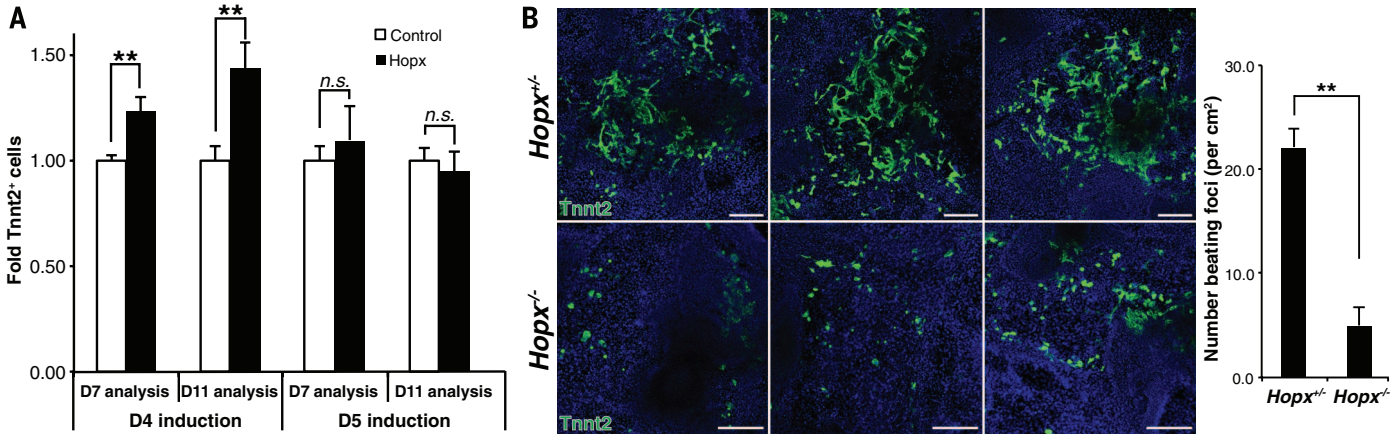

C

	Term	p-value
1	**Heart development**	**2.2E-11**
2	**Vasculature development**	**4.3E-8**
3	**Blood vessel development**	**5.0E-8**
4	**Blood vessel morphogenesis**	**6.4E-8**
5	**Muscle organ development**	**1.3E-7**
6	**Muscle cell differentiation**	**3.2E-7**
7	**Actin filament -based process**	**3.9E-7**
8	Lipid process	4.7E-7
9	**Cardiac muscle development**	**6.3E-7**
10	Lipid localization	7.9E-7

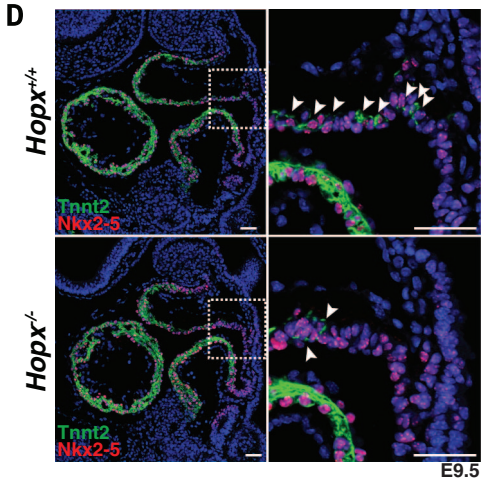

Fig. 4. Hopx promotes myogenesis. (**A**) Precocious expression of Hopx in CPCs at day 4 of EB differentiation results in more Tnnt2$^+$ cells measured by flow cytometry. (**B**) Differentiation of *Hopx*$^{-/-}$ EBs results in fewer Tnnt2$^+$ cells and fewer beating foci compared to *Hopx*$^{+/-}$ EBs (day 10). Images from three different replicates are shown. (**C**) Gene Ontology analysis from microarrays done with triplicate samples of *Hopx*$^{-/-}$ versus *Hopx*$^{+/-}$ EBs (top 3000 genes down-regulated, ranked by fold change, FDR cutoff = 10%, day 8, GOTERM_BP_FAT). (**D**) Paucity of Tnnt2$^+$ cells (arrowheads) in the distal OFT *Hopx*$^{-/-}$ compared to *Hopx*$^{+/+}$ embryos (E9.5). ** $P < 0.05$; n.s., not significant. Scale bars: 500 μm (B), 50 μm (D).

(fig. S7C). These data suggest that Hopx represses Wnt signaling during cardiogenesis.

During ES cell differentiation into cardiomyocytes, Hopx also functions to repress Wnt. KEGG analysis of the up-regulated genes in *Hopx*$^{-/-}$ versus *Hopx*$^{+/-}$ day 8 EB microarrays confirms overrepresentation of the Wnt signaling pathway in *Hopx*$^{-/-}$ cells ($P = 1.4 \times 10^{-3}$). EBs lacking *Hopx* show an increase in *Axin2* and significant impairment of sarcomere gene expression at day 8 of differentiation (Fig. 5F). Addition of XAV939, a potent inhibitor of Wnt signaling, at day 5 of differentiation to *Hopx*$^{-/-}$ EBs restores *Axin2* to control levels and partially rescues sarcomere gene expression. *Nkx2-5* is expressed by CPCs, and its expression markedly increases over the course of cardiac differentiation of EBs (*21*). Differentiating *Hopx*$^{-/-}$ EBs, however, fail to up-regulate *Nkx2-5* normally. Inhibition of Wnt in *Hopx*$^{-/-}$ EBs rescues *Nkx2-5* to levels found in controls (Fig. 5F). Microarray analysis (table S3, $n = 3$) confirms that expression of multiple sarcomere genes is rescued upon Wnt inhibition (Fig. 5G; e.g., *Myh6*, *Myh7*, *Myl7*, *Myl3*, *Tnnc1*,

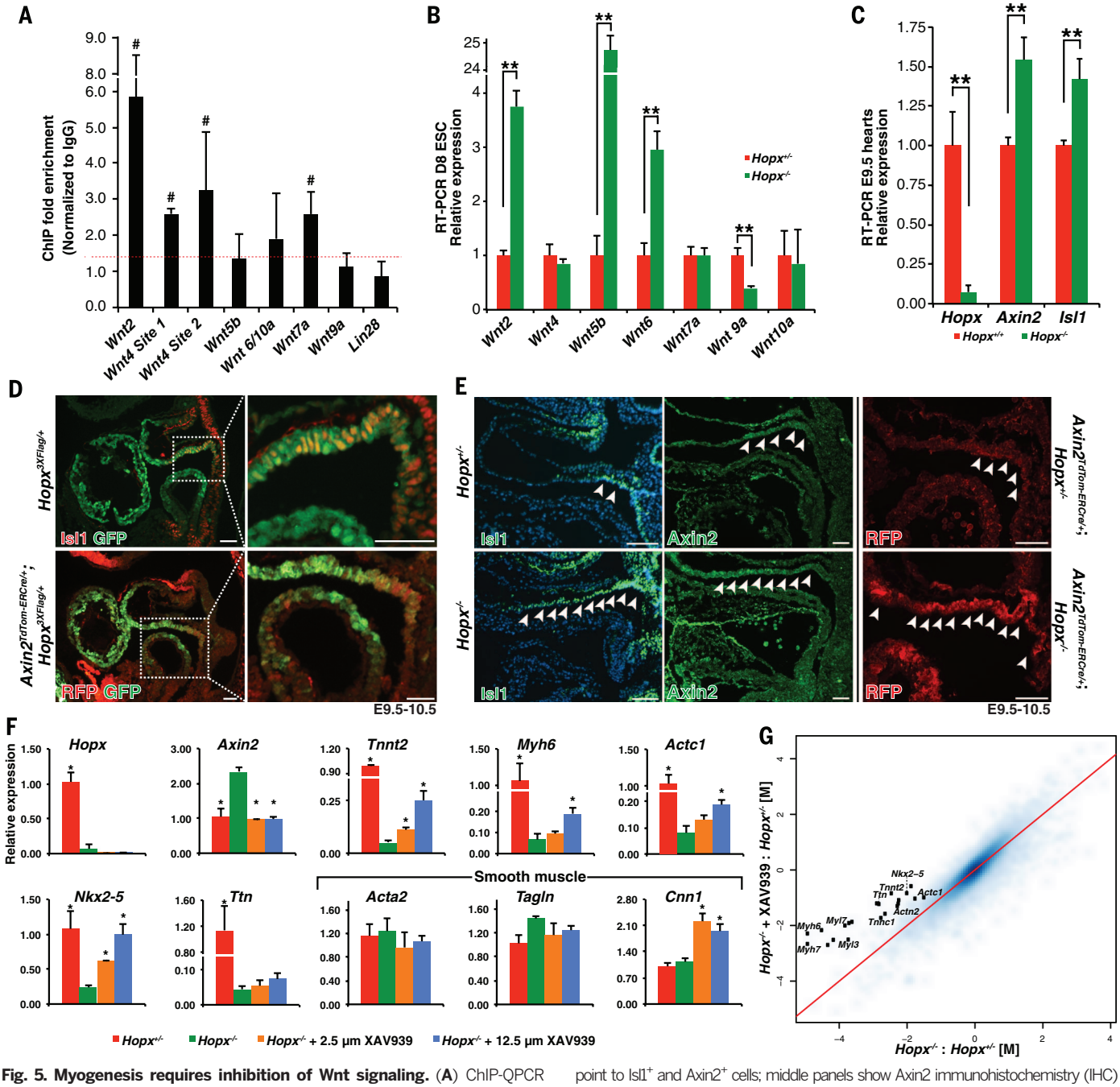

Fig. 5. Myogenesis requires inhibition of Wnt signaling. (**A**) ChIP-QPCR from E9.5 hearts. *Wnt2*, *Wnt4* sites 1 and 2, and *Wnt7a* demonstrate greater than 1.4× enrichment (red dashed line) over immunoglobulin G (IgG) in all replicates (denoted by #, $n \geq 3$ replicates). (**B**) Expression analysis of *Hopx*$^{-/-}$ versus *Hopx*$^{+/-}$ EBs (day 8). (**C**) QRT-PCR from littermate E9.5 microdissected hearts. (**D**) Isl1 (upper panels) and Axin2 (lower panels, RFP expression reflects *Axin2* in an *Axin2*$^{TdTom\text{-}ERCre/+}$ embryo, sagittal sections) are each coexpressed with Hopx in the cardiac OFT. (**E**) Isl1 and Axin2 expression is expanded in *Hopx*$^{-/-}$ [arrowheads point to Isl1^{+} and Axin2^{+} cells; middle panels show Axin2 immunohistochemistry (IHC) (green), and right panels show RFP IHC in *Axin2*$^{TdTom\text{-}ERCre/+}$ embryos]. (**F**) QRT-PCR analyses of *Hopx*$^{+/-}$ day 8 EBs (red) or *Hopx*$^{-/-}$ EBs (green) with either 2.5 µM (orange) or 12.5 µM (blue) XAV939 (*$P < 0.05$ in comparison to *Hopx*$^{-/-}$). (**G**) Comparison of the $\log_2$-transformed fold change (M) of genes differentially expressed in *Hopx*$^{-/-}$ versus *Hopx*$^{+/-}$ EBs (*x* axis) versus *Hopx*$^{-/-}$ + 12.5 µm XAV939 versus *Hopx*$^{+/-}$ (*y* axis) ($n = 3$ samples). Sarcomere-related genes annotated with black dots. Genes above the red line are partially normalized by Wnt inhibition. ** $P < 0.05$. Scale bars, 50 µm.

Actn2, *Actc1*). Taken together, these data suggest that Hopx repression of Wnt signaling promotes cardiomyogenesis.

Hopx interacts with Smad4

We purified Hopx-containing protein complexes from E9.5 *Hopx*$^{3XFlag/+}$ murine hearts and identified protein components by mass spectrometry. Numerous members of the Mi-2/NuRD (nucleosome remodeling deacetylase) complex were identified (e.g., Hdac1, Hdac2, Rbbp4/7, MTA 1/2/3, and MBD3), consistent with the known association of Hopx with Hdac2 (*22*). In addition, Smad4 was identified as a Hopx-interacting protein. This finding is of particular interest because *Bmp4*, phospho-Smad1/5/8, and, to a lesser extent, *Bmp2* are expressed in the OFT at E9.5, as we confirmed (Fig. 6A and fig. S8A). We confirmed the interaction between Hopx and Smad4 by coimmunoprecipitation of both factors overexpressed in 293Tx cells in the presence of increasing concentrations of recombinant Bmp4 and performing coimmunoprecipitation experiments. An interaction between Hopx and Smad4 that is dependent upon the presence of Bmp4 is detectable (Fig. 6B). Further, we confirmed that endogenous Hopx interacts with an activated Smad complex (Smad4 and phospho-Smad1/5/8) in coimmunoprecipitation experiments from E9.5 to E10 whole-embryo lysates (Fig. 6C and fig. S8B).

We have previously determined the structure of Hopx by nuclear magnetic resonance (NMR) spectroscopy, demonstrating a helix-turn-helix motif (*22*). Residues within the first and second α helix that are located close to one another were shown to be important for Hopx-mediated transcriptional repression, as were a distinct cluster of residues at the C terminus (shown in green, Fig. 6D). We mutated amino acids in the first and second helix and at the C terminus and assayed whether the mutants could interact with Smad4 using an in situ proximity ligation assay (Fig. 6, E to I). We confirmed expression of Hopx constructs (fig. S8, C and D) and specificity of the proximity ligation assay (fig. S8E). Consistent with the coimmunoprecipitation experiments (Fig. 6B), the Smad4 interaction with Hopx is enhanced by Bmp4 (Fig. 6, E and F). The Smad4-Hopx interaction is diminished by mutation of residues at the C terminus of Hopx, but not by mutations in helix 1 or 2 (Fig. 6, G to I). Consistent with a physical interaction between Hopx and Smad4, we detect enrichment of Smad4 occupancy by ChIP at Wnt ligand loci that are also occupied by Hopx (fig. S8F).

Hopx integrates Bmp and Wnt signaling

The data presented thus far indicate that Hopx expression defines a cardiomyoblast and that Hopx modulates cardiomyogenesis by repressing Wnt signaling. Further, Hopx can interact with an activated Smad complex. In murine EBs, myogenesis requires inhibition of Wnt and is promoted by activation of Bmp (*9*, *11*, *25*–*27*). Hence, we

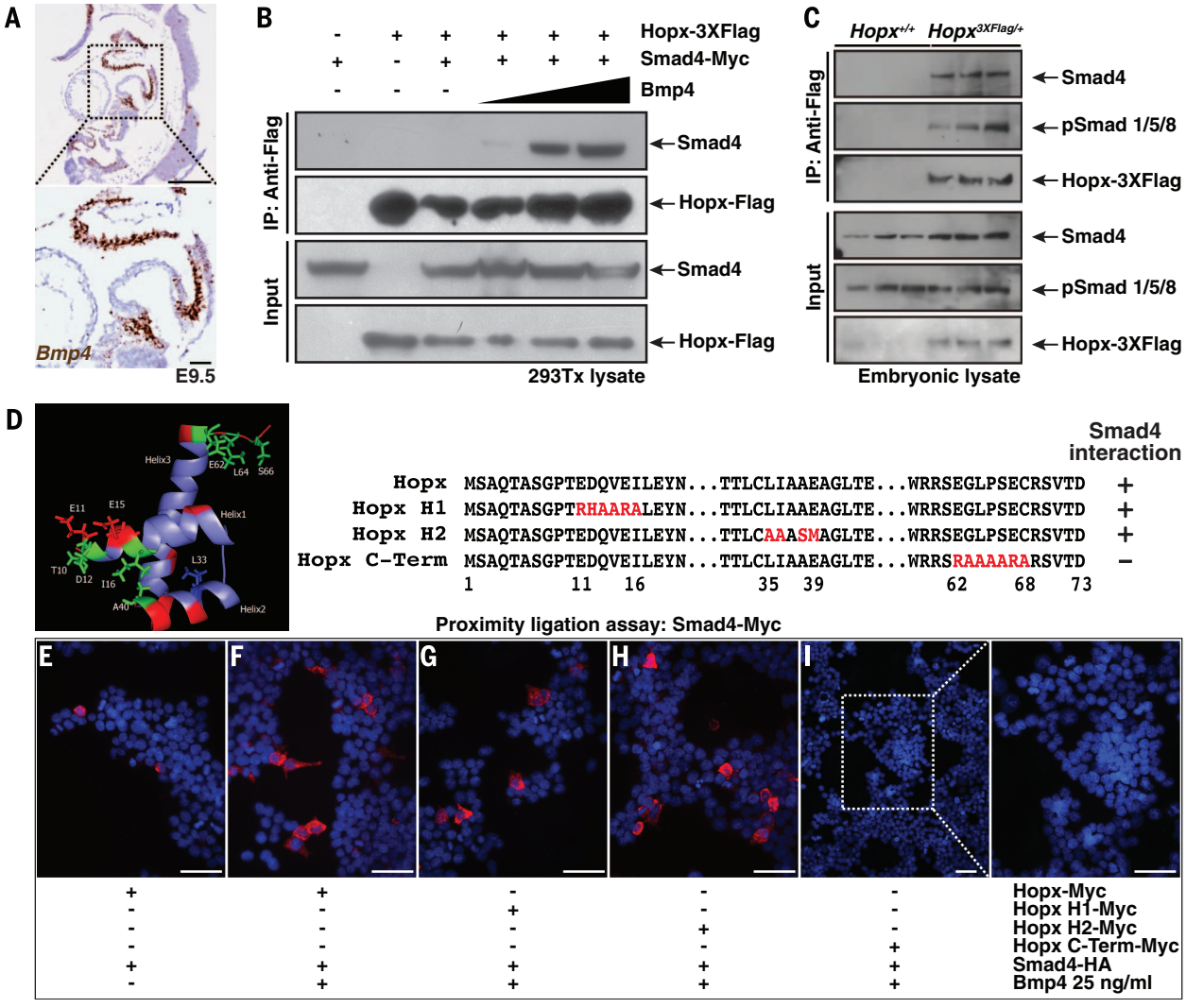

Fig. 6. Hopx interacts with an activated Smad complex. (**A**) *Bmp4* expression in control E9.5 heart (RNAscope in situ hybridization, brown; sagittal section). Inset focuses on outflow and inflow tracts. (**B**) Hopx coimmunoprecipitates with Smad4 in 293Tx cells in a Bmp4-dependent manner (0, 2, 10, 25 ng of Bmp4 per milliliter, 7.5% input). (**C**) Hopx coimmunoprecipitates with Smad4 and phospho-Smad1/5/8 in vivo (E9.5 to E10 tissue lysates, three independent examples of each genotype shown, 7.5% input). (**D**) NMR structure of Hopx (*22*) and schema of mutant constructs. (**E** to **I**) Proximity ligation assay using transfected 293Tx cells. Presence of Bmp4 and transfected plasmids is indicated. Bets representative images from $n = 3$ experiments shown. Scale bars: 250 μm [(A), top] and 50 μm [(A), bottom, and (E) to (I)].

sought to determine if Hopx functions to integrate Bmp signaling with Wnt repression.

First, we confirmed that *Bmp4* and *Bmp2* levels are unchanged in *Hopx*$^{-/-}$ embryonic hearts by in situ hybridization and quantitative real-time (QRT)–PCR (Fig. 7A). Protein expression and nuclear localization of Smad4 and phosphorylated Smad1/5/8 are also unchanged (Fig. 7A). Once in the nucleus, the active Smad complex functions to enhance transcription of Bmp target genes such as *Msx1*. Control (wild-type) E9.5 cardiac explants respond to exogenous Bmp4 by up-regulating *Msx1* in a dose-dependent fashion (Fig. 7B). A similar response is seen in *Hopx*$^{-/-}$ explants, indicating an intact Bmp response system (Fig. 7B).

Bmp signaling can result in repression of Wnt activity in various tissues, although the mechanism has been unclear (*28*–*31*). Addition of recombinant Bmp4 decreases *Axin2* expression in *Hopx*$^{+/+}$ cardiac explants compared to vehicle-treated controls (Fig. 7C, white bars). However, *Axin2* expression in *Hopx*$^{-/-}$ explants is relatively unresponsive to Bmp4 (Fig. 7C, black bars). We also tested whether Hopx participates in Bmp-mediated Wnt inhibition during cardiac differentiation of EBs (Fig. 7D). Bmp4 treatment of *Hopx*$^{+/-}$ EBs starting at day 5 results in a 60% decrease in *Axin2* by day 10 of differentiation compared to vehicle-treated EBs (white bars, Fig. 7D). However, Bmp4 minimally affects *Axin2* expression in *Hopx*$^{-/-}$ EBs (black bars, Fig. 7D). These data suggest that Hopx is required for Bmp-mediated repression of Wnt signaling during cardiogenesis.

Discussion

Here, we have shown that CPCs that express *Hopx* are irreversibly committed to the myocyte lineage, thereby defining progenitor cells that we call cardiomyoblasts. *Hopx* expression not only marks cardiomyoblasts, but it also functions to enhance cardiomyogenesis by linking Bmp signaling with repression of Wnt. A subset of committed myoblasts derived from the FHF express *Hcn4,* which is also expressed by endothelial cells during cardiac development (*32*, *33*). However, the lack of

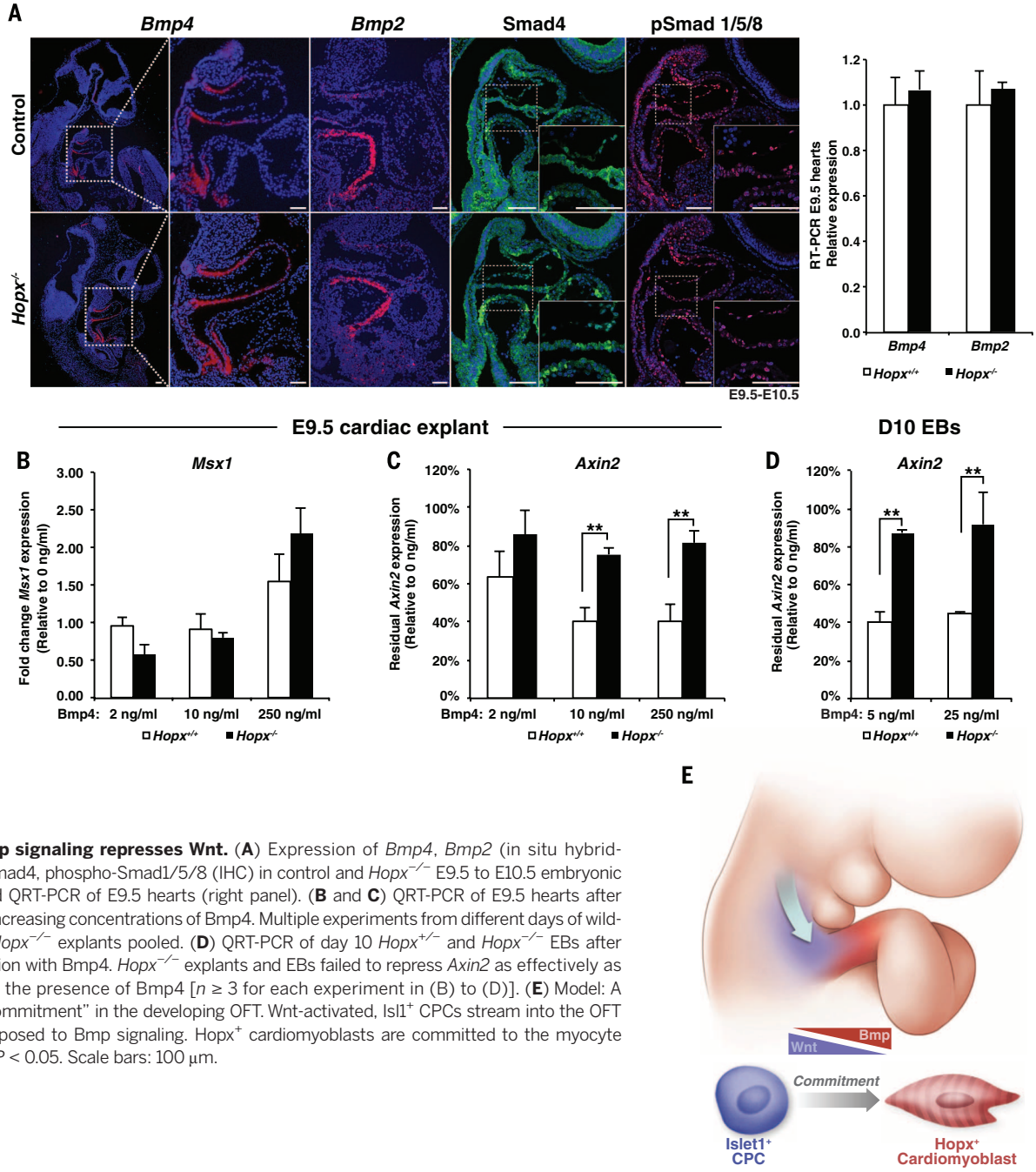

Fig. 7. Bmp signaling represses Wnt. (**A**) Expression of *Bmp4*, *Bmp2* (in situ hybridization), Smad4, phospho-Smad1/5/8 (IHC) in control and *Hopx*$^{-/-}$ E9.5 to E10.5 embryonic hearts, and QRT-PCR of E9.5 hearts (right panel). (**B** and **C**) QRT-PCR of E9.5 hearts after culture in increasing concentrations of Bmp4. Multiple experiments from different days of wild-type and *Hopx*$^{-/-}$ explants pooled. (**D**) QRT-PCR of day 10 *Hopx*$^{+/-}$ and *Hopx*$^{-/-}$ EBs after differentiation with Bmp4. *Hopx*$^{-/-}$ explants and EBs failed to repress *Axin2* as effectively as controls in the presence of Bmp4 [$n \geq 3$ for each experiment in (B) to (D)]. (**E**) Model: A "zone of commitment" in the developing OFT. Wnt-activated, Isl1^{+} CPCs stream into the OFT and are exposed to Bmp signaling. Hopx^{+} cardiomyoblasts are committed to the myocyte lineage. $^{**}P < 0.05$. Scale bars: 100 μm.

a definitive marker of a cardiomyoblast has hampered a detailed analysis of cardiomyocyte commitment. Our studies provide such a marker and reveal that commitment of FHF and SHF CPCs occurs at distinct time points and in different locations during cardiogenesis. In the SHF, Isl1^{+}, Wnt-activated CPCs stream into the OFT from the surrounding mesoderm, where they encounter local Bmp4 signals. CPCs then express Hopx, downregulate Wnt, and become committed to the myocyte fate. Thus, the distal OFT is a "zone of commitment" in the developing heart (Fig. 7E).

Markers of lineage commitment, and the signals that modulate lineage decisions, are likely to inform regenerative and stem cell approaches for cardiac disease. In the hematopoietic system, detailed understanding of these processes has allowed for definitive identification of various progenitor cells of the blood lineages, leading to the development of important therapies for human diseases (e.g., erythropoietin and granulocyte-macrophage colony-stimulating factor). The ability to identify committed, but undifferentiated, cardiomyocyte precursors may facilitate development of cardiac regenerative therapies, including those using ES and induced pluripotent stem cells (*34*).

Reciprocal signaling between Bmp and Wnt has been recognized in multiple progenitor populations (*28*–*31*, *35*). However, the mechanisms that coordinate these pathways in progenitor cell niches have remained elusive. Our current work raises the possibility that Hopx-mediated integration of Bmp signaling to repress Wnt may be active in other progenitor populations. For example, Hopx is expressed by +4 stem cells in the intestine (*19*), where niche Bmp signals repress Wnt (*28*, *36*). Recent work by the Fuchs laboratory also suggests that balance between Bmp and Wnt signaling influences the fate of hair follicle cells as they differentiate into various progeny lineages (*35*) and Hopx may play a role in this process (*18*). *HOPX* is a tumor suppressor gene implicated in colorectal and other cancers (*37*, *38*). Hijacking of developmental pathways is emerging as a potent mechanism of carcinogenesis (*39*). Loss of Hopx in cancer stem cells could result in uncoupling of niche-mediated Bmp signaling and quiescence through loss of Wnt repression.

Finally, although *Hopx* deficiency leads to thinned myocardium and cardiac rupture in a portion of embryos, cardiomyogenesis is not altogether blocked. Inhibition of Wnt signaling in SHF cardiomyoblasts is delayed but not completely prevented, and some *Hopx*$^{-/-}$ mice live to adulthood. This suggests that, not surprisingly, alternative mechanisms reinforce Wnt repression independent of Hopx (*40*). Further insights into the mechanisms that coordinate signaling in the niche are likely to inform our ability to harness the potential of regenerative medicine.

REFERENCES AND NOTES

1. J. A. Epstein, Franklin H. Epstein Lecture. Cardiac development and implications for heart disease. *N. Engl. J. Med.* **363**, 1638–1647 (2010). doi: 10.1056/NEJMra1003941; pmid: 20961247
2. R. G. Kelly, N. A. Brown, M. E. Buckingham, The arterial pole of the mouse heart forms from Fgf10-expressing cells in pharyngeal mesoderm. *Dev. Cell* **1**, 435–440 (2001). doi: 10.1016/S1534-5807(01)00040-5; pmid: 11702954
3. K. L. Waldo *et al*., Conotruncal myocardium arises from a secondary heart field. *Development* **128**, 3179–3188 (2001). pmid: 11688566
4. C. L. Cai *et al*., Isl1 identifies a cardiac progenitor population that proliferates prior to differentiation and contributes a majority of cells to the heart. *Dev. Cell* **5**, 877–889 (2003). doi: 10.1016/S1534-5807(03)00363-0; pmid: 14667410
5. S. J. Kattman, T. L. Huber, G. M. Keller, Multipotent flk-1+ cardiovascular progenitor cells give rise to the cardiomyocyte, endothelial, and vascular smooth muscle lineages. *Dev. Cell* **11**, 723–732 (2006). doi: 10.1016/j.devcel.2006.10.002; pmid: 17084363
6. A. Moretti *et al*., Multipotent embryonic isl1+ progenitor cells lead to cardiac, smooth muscle, and endothelial cell diversification. *Cell* **127**, 1151–1165 (2006). doi: 10.1016/j.cell.2006.10.029; pmid: 17123592
7. S. M. Wu *et al*., Developmental origin of a bipotential myocardial and smooth muscle cell precursor in the mammalian heart. *Cell* **127**, 1137–1150 (2006). doi: 10.1016/j.cell.2006.10.028; pmid: 17123591
8. P. Gadue, T. L. Huber, P. J. Paddison, G. M. Keller, Wnt and TGF-beta signaling are required for the induction of an in vitro model of primitive streak formation using embryonic stem cells. *Proc. Natl. Acad. Sci. U.S.A.* **103**, 16806–16811 (2006). doi: 10.1073/pnas.0603916103; pmid: 17077151
9. A. T. Naito *et al*., Developmental stage-specific biphasic roles of Wnt/beta-catenin signaling in cardiomyogenesis and hematopoiesis. *Proc. Natl. Acad. Sci. U.S.A.* **103**, 19812–19817 (2006). pmid: 17170140
10. S. L. Paige *et al*., Endogenous Wnt/beta-catenin signaling is required for cardiac differentiation in human embryonic stem cells. *PLOS ONE* **5**, e11134 (2010). doi: 10.1371/journal.pone.0011134; pmid: 20559569
11. S. J. Kattman *et al*., Stage-specific optimization of activin/nodal and BMP signaling promotes cardiac differentiation of mouse and human pluripotent stem cell lines. *Cell Stem Cell* **8**, 228–240 (2011). doi: 10.1016/j.stem.2010.12.008; pmid: 21295278
12. M. C. Nostro, X. Cheng, G. M. Keller, P. Gadue, Wnt, activin, and BMP signaling regulate distinct stages in the developmental pathway from embryonic stem cells to blood. *Cell Stem Cell* **2**, 60–71 (2008). doi: 10.1016/j.stem.2007.10.011; pmid: 18371422
13. F. Lescroart *et al*., Early lineage restriction in temporally distinct populations of Mesp1 progenitors during mammalian heart development. *Nat. Cell Biol.* **16**, 829–840 (2014). doi: 10.1038/ncb3024; pmid: 25150979
14. W. P. Devine, J. D. Wythe, M. George, K. Koshiba-Takeuchi, B. G. Bruneau, Early patterning and specification of cardiac progenitors in gastrulating mesoderm. *eLife* **3**, e03848 (2014). doi: 10.7554/eLife.03848; pmid: 25296024
15. F. Chen *et al*., Hop is an unusual homeobox gene that modulates cardiac development. *Cell* **110**, 713–723 (2002). doi: 10.1016/S0092-8674(02)00932-7; pmid: 12297045
16. A. De Toni *et al*., Regulation of survival in adult hippocampal and glioblastoma stem cell lineages by the homeodomain-only protein HOP. *Neural Dev.* **3**, 13 (2008). doi: 10.1186/1749-8104-3-13; pmid: 18507846
17. C. H. Shin *et al*., Modulation of cardiac growth and development by HOP, an unusual homeodomain protein. *Cell* **110**, 725–735 (2002). doi: 10.1016/S0092-8674(02)00933-9; pmid: 12297046
18. N. Takeda *et al*., Hopx expression defines a subset of multipotent hair follicle stem cells and a progenitor population primed to give rise to K6+ niche cells. *Development* **140**, 1655–1664 (2013). doi: 10.1242/dev.093005; pmid: 23487314
19. N. Takeda *et al*., Interconversion between intestinal stem cell populations in distinct niches. *Science* **334**, 1420–1424 (2011). doi: 10.1126/science.1213214; pmid: 22075725
20. Information on materials and methods is available on *Science* Online.
21. N. Christoforou *et al*., Mouse ES cell-derived cardiac precursor cells are multipotent and facilitate identification of novel cardiac genes. *J. Clin. Invest.* **118**, 894–903 (2008). pmid: 18246200
22. H. Kook *et al*., Analysis of the structure and function of the transcriptional coregulator HOP. *Biochemistry* **45**, 10584–10590 (2006). doi: 10.1021/bi060641s; pmid: 16939210
23. L. Lin *et al*., Beta-catenin directly regulates Islet1 expression in cardiovascular progenitors and is required for multiple aspects of cardiogenesis. *Proc. Natl. Acad. Sci. U.S.A.* **104**, 9313–9318 (2007). doi: 10.1073/pnas.0700923104; pmid: 17519333
24. E. D. Cohen *et al*., Wnt/beta-catenin signaling promotes expansion of Isl-1-positive cardiac progenitor cells through regulation of FGF signaling. *J. Clin. Invest.* **117**, 1794–1804 (2007). doi: 10.1172/JCI31731; pmid: 17607356
25. E. Cagavi *et al*., Functional cardiomyocytes derived from Isl1 cardiac progenitors via Bmp4 stimulation. *PLOS ONE* **9**, e110752 (2014). doi: 10.1371/journal.pone.0110752; pmid: 25522363
26. S. Y. Lim *et al*., Enhancing human cardiomyocyte differentiation from induced pluripotent stem cells with trichostatin A. *Methods Mol. Biol.* (2014). pmid: 25520285
27. S. Ueno *et al*., Biphasic role for Wnt/beta-catenin signaling in cardiac specification in zebrafish and embryonic stem cells. *Proc. Natl. Acad. Sci. U.S.A.* **104**, 9685–9690 (2007). doi: 10.1073/pnas.0702859104; pmid: 17522258
28. X. C. He *et al*., BMP signaling inhibits intestinal stem cell self-renewal through suppression of Wnt-beta-catenin signaling. *Nat. Genet.* **36**, 1117–1121 (2004). doi: 10.1038/ng1430; pmid: 15378062
29. E. Kandyba *et al*., Competitive balance of intrabulge BMP/Wnt signaling reveals a robust gene network ruling stem cell homeostasis and cyclic activation. *Proc. Natl. Acad. Sci. U.S.A.* **110**, 1351–1356 (2013). doi: 10.1073/pnas.1121312110; pmid: 23292934
30. M. V. Plikus *et al*., Cyclic dermal BMP signalling regulates stem cell activation during hair regeneration. *Nature* **451**, 340–344 (2008). doi: 10.1038/nature06457; pmid: 18202659
31. J. Song *et al*., Smad1 transcription factor integrates BMP2 and Wnt3a signals in migrating cardiac progenitor cells. *Proc. Natl. Acad. Sci. U.S.A.* **111**, 7337–7342 (2014). doi: 10.1073/pnas.1321764111; pmid: 24808138
32. X. Liang *et al*., HCN4 dynamically marks the first heart field and conduction system precursors. *Circ. Res.* **113**, 399–407 (2013). doi: 10.1161/CIRCRESAHA.113.301588; pmid: 23743334
33. D. Später *et al*., A HCN4+ cardiomyogenic progenitor derived from the first heart field and human pluripotent stem cells. *Nat. Cell Biol.* **15**, 1098–1106 (2013). doi: 10.1038/ncb2824; pmid: 23974038
34. J. J. Chong *et al*., Human embryonic-stem-cell-derived cardiomyocytes regenerate non-human primate hearts. *Nature* **510**, 273–277 (2014). doi: 10.1038/nature13233; pmid: 24776797
35. M. Genander *et al*., BMP signaling and its pSMAD1/5 target genes differentially regulate hair follicle stem cell lineages. *Cell Stem Cell* **15**, 619–633 (2014). doi: 10.1016/j.stem.2014.09.009; pmid: 25312496
36. N. Li *et al*., Single-cell analysis of proxy reporter allele-marked epithelial cells establishes intestinal stem cell hierarchy. *Stem Cell Rep.* **3**, 876–891 (2014). doi: 10.1016/j.stemcr.2014.09.011; pmid: 25418730
37. W. K. Cheung *et al*., Control of alveolar differentiation by the lineage transcription factors GATA6 and HOPX inhibits lung adenocarcinoma metastasis. *Cancer Cell* **23**, 725–738 (2013). doi: 10.1016/j.ccr.2013.04.009; pmid: 23707782
38. K. Yamashita, H. Katoh, M. Watanabe, The homeobox only protein homeobox (HOPX) and colorectal cancer. *Int. J. Mol. Sci.* **14**, 23231–23243 (2013). doi: 10.3390/ijms141223231; pmid: 24287901
39. C. Karamboulas, L. Ailles, Developmental signaling pathways in cancer stem cells of solid tumors. *Biochim. Biophys. Acta* **1830**, 2481–2495 (2013). doi: 10.1016/j.bbagen.2012.11.008; pmid: 23196196
40. D. J. O'Connell *et al*., A Wnt-bmp feedback circuit controls intertissue signaling dynamics in tooth organogenesis. *Sci. Signal.* **5**, ra4 (2012).pmid: 22234613

ACKNOWLEDGMENTS

We thank the Epstein laboratory, S. Evans, R. Schwartz, N. Palpant, and C. Murry for helpful discussions and sharing of reagents; H. Aghajanian for critical reading of the manuscript; and J. Schug and the Next Generation Sequencing Core for sequencing, ChIP-seq analysis, and microarray analysis. Data associated with this manuscript are available in Gene Expression Omnibus (GSE67254). We thank J. LeLay for help with initial ChIP-seq experiments, J. Jeong and S. Eun Kwon for help with bioinformatic analyses, the Wistar Proteomics Core for mass spectrometry analysis, the Penn Cell and Developmental Biology Microscopy Core for microscopy help, and L. Guo for artistic help with the model figure. The work was supported by NIH K08 HL119553-02 to R.J., NIH 5-T32-GM-007170 to M.G., NIH U01 HL100405, R01 HL071546, the Cotswold Foundation, and the Spain Fund for Regenerative Cardiology to J.A.E.

SUPPLEMENTARY MATERIALS

www.sciencemag.org/content/348/6242/aaa6071/suppl/DC1
Materials and Methods
Figs. S1 to S8
Tables S1 to S3
References (*41*–*51*)
4 January 2015; accepted 29 April 2015
10.1126/science.aaa6071

REPORTS

APPLIED OPTICS

Overcoming Kerr-induced capacity limit in optical fiber transmission

E. Temprana,[1] E. Myslivets,[1] B.P.-P. Kuo,[1] L. Liu,[1] V. Ataie,[1] N. Alic,[2]* S. Radic[1,2]

Nonlinear optical response of silica imposes a fundamental limit on the information transfer capacity in optical fibers. Communication beyond this limit requires higher signal power and suppression of nonlinear distortions to prevent irreversible information loss. The nonlinear interaction in silica is a deterministic phenomenon that can, in principle, be completely reversed. However, attempts to remove the effects of nonlinear propagation have led to only modest improvements, and the precise physical mechanism preventing nonlinear cancellation remains unknown. We demonstrate that optical carrier stability plays a critical role in canceling Kerr-induced distortions and that nonlinear wave interaction in silica can be substantially reverted if optical carriers possess a sufficient degree of mutual coherence. These measurements indicate that fiber information capacity can be notably increased over previous estimates.

High-capacity optical communication is made possible by a nearly ideal physical platform: An exceptionally low fiber attenuation ($\alpha = 4.6 \times 10^{-5}$ m^{-1}) (*1*) is matched by a small nonlinear refractive index ($n_2 = 2.5 \times 10^{-20}$ m^2 W^{-1}) in silica (*2*). However, over sufficiently long transmission distances, this combination of near-transparency and low nonlinearity still leads to a distributed, Kerr-mediated wave interaction that degrades (*3*) the optical signal. The nonlinear impairment has been identified as the primary physical mechanism (*4*–*6*) that imposes a strict limit on the achievable information capacity in optical fiber transmission. This limit is specific to the optically guided channel and has no direct analog in either wireless (*7*) or free-space photon communications (*8*). At present, the fiber capacity limit is engineered by compromising between the optical power and acceptable nonlinear distortions (*5*). To reach the full potential of this transmission medium, a true linear ($n_2 = 0$) waveguide should be realized in order to suppress the onset of the nonlinear distortion. Unfortunately, the latter is an unphysical requirement (*2*). Consequently, a suppression or outright cancellation of the nonlinear impairment in optical fibers is seen as the main challenge in multiple disciplines (*4*–*6*, *9*–*12*) that are hampered by the waveguide's nonlinear response to the propagating electromagnetic waves. Here, we demonstrate nonlinear impairment compensation by inverting the effects of distributed, nonlinear interaction among multiple frequency-stabilized optical signals. We show that the nonlinear noise-imposed uncertainty remains the only physical mechanism on the path to Shannon-limited fiber communication.

The precise knowledge of the optical carrier frequency is critical for a successful inversion of the nonlinear interaction effects. To clarify this important requirement, consider the interaction of N copolarized frequency modes in a single-mode waveguide, described by a set of coupled scalar nonlinear Schrödinger (NLS) relations (*2*):

$$\frac{\partial A_l}{\partial z} + \frac{1}{v_{gl}(\omega_l)}\frac{\partial A_l}{\partial t} - i\sum_{k=2}^{3}\left[\frac{i^k}{k!}\beta_{kl}\frac{\partial^k A_l}{\partial t^k}\right] + \frac{\alpha_l}{2}A_l = i\gamma\left(|A_l|^2 + 2\sum_{m\neq l}|A_m|^2\right)A_l, l = 1, \ldots, N \quad (1)$$

where A_l represents the mode complex amplitude (each having carrier frequency ω_l), γ is the nonlinear coefficient, and α_l, v_{gl}, and β_{kl} are the mode attenuation, group velocities, and dispersion orders, respectively. The latter is defined by the standard expansion: $\beta_k = d^k n(\omega)/d\omega^k$, where n is the effective waveguide refractive index.

The wave interaction defined by Eq. 1 is deterministic and stable (*13*, *14*), allowing, in principle, for computational inversion of distributed Kerr interaction. Indeed, this notion was the basis for recent nonlinear cancellation (NLC) efforts that solved the inverse-propagating NLS relation (*15*, *16*). However, in practice these attempts have led to a limited impairment suppression (*17*–*19*). We note that a separate class of nonlinear mitigation research, not considered here, relies on phase conjugation (*20*, *21*) that can rely on free-running transmitters. These approaches, however, have restricted applicability because they require symmetrical power evolution (*20*), vanishing third-order dispersion, or a trade-off of spectral efficiency for performance (*21*, *22*).

In contrast, the NLC that relies on the Eq. 1 inversion faces a fundamental challenge that was not addressed in prior experimental studies. As predicted by a recent theoretical study (*23*), the NLS inversion requires precise knowledge of modal carrier frequencies. During propagation, any frequency uncertainty is mapped to mode velocity ambiguity via waveguide chromatic dispersion (*23*), as illustrated in Fig. 1. Although Kerr-mediated process is deterministic, the resulting nonlinear interaction appears random and leads to an underestimation of the transmission information capacity. Indeed, the experimental demonstrations to date (*17*, *18*) have relied on uncorrelated (free-running) emitters, inherently reducing the modal frequency (and phase) stability. In this case, the carrier frequency uncertainty is transformed to a stochastically varying walk-off rate between the modes, leading to a diverging inversion of Eq. 1. Consequently, the reversibility of multi-frequency nonlinear interaction mandates a high degree of mutual coherence and the knowledge of the carrier offset from the absolute reference.

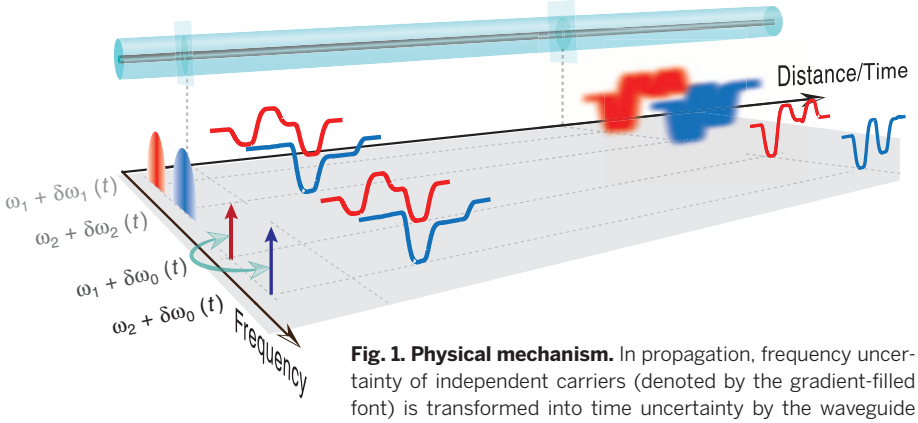

Fig. 1. Physical mechanism. In propagation, frequency uncertainty of independent carriers (denoted by the gradient-filled font) is transformed into time uncertainty by the waveguide chromatic dispersion, making the nonlinear interaction appear as stochastic. In contrast, mutually coherent carriers (denoted by the solid font) produce consistent deterministic interaction, amenable to nonlinear impairment reversal.

[1]Department of Electrical and Computer Engineering, University of California, San Diego, La Jolla, CA 92093, USA. [2]Qualcomm Institute, University of California, San Diego, La Jolla, CA 92093, USA.
*Corresponding author. E-mail: nalic@ucsd.edu

Downloaded from www.sciencemag.org on June 26, 2015

Recognizing this basic requirement, we devised NLC experiments to quantify the role of mutually correlated emitters. Specifically, the carrier frequencies were referenced to a parametric frequency comb derived from a single, continuous-wave master oscillator (*24*). In contrast to postcompensation techniques (*15*–*19*), predistorted channel launch results in signal reception that is free from nonlinear modal crosstalk (*23*). The respective input waveforms were synthesized by inverting the NLS propagation model given by Eq. 1 (*25*).

As with any Kerr-mediated interaction, the presence of noise limits the ideal distortion reversal. Consequently, the NLC compensation is demonstrated in two distinct experiments. The first experiment illustrates Kerr-inversion physics and nonlinear reversal in a pump-probe configuration in the absence of noise. Both the intense (pump) and weak (probe) waves had a high signal-to-noise ratio (SNR) and propagated over a short, nearly lossless, highly nonlinear fiber (HNLF) segment to guarantee that Kerr-induced impairment would dominate over stochastic, noise-induced distortion. Pump and probe waves, separated by 30 nm, were derived from the parametric comb source and had SNR of more than 40 dB. The pump and probe were launched into a HNLF 1100 m in length, with nonlinear parameter of 7 W^{-1} km^{-1}, dispersive parameters β_2 = 37.9 ps^2/km and β_3 = –0.06 ps^3/km, and transmission loss α = 0.6 dB/km. This segment was specifically selected to guarantee a sufficient walk-off between the pump and probe and to provide a clear distinction among the nonlinear interaction mechanisms. The pump beam, centered at 1588 nm, was amplified to a power level of 250 mW and was amplitude-modulated to achieve strong cross-phase modulation (CPM) (*2*, *3*). The signal wave, centered at 1558 nm and copolarized with the pump, had two orders of magnitude less power (1 mW) and was amplitude-modulated, as shown in Fig. 2. The weak (probe) wave experienced considerable distortion (red curve in Fig. 2A) that could be completely reversed by NLC in the high-SNR regime, erasing any distinction between the launched (black) and compensated (green) waveforms (*25*). This contrast is even more apparent in the spectral domain (Fig. 2B).

In the second experiment, we demonstrated the reversal of nonlinear distortion in a three-channel coherent wavelength division multiplex (WDM) transmission. In this case, the NLC is performed in a loop (*26*) emulating a modern communication link: Signal is sent over a total distance of 1020 km and re-amplified periodically after each span of 85 km of the standard single-mode fiber, as shown in Fig. 3. To gauge the role of frequency stabilization in the inversion of Eq. 1, we performed the first measurement with lasers with uncorrelated carrier frequencies. The emitters were modulated at four amplitude levels in each electric field quadrature, generating a (two-dimensional) 16-level quadrature amplitude modulation (*27*) (16-QAM) at 16 GBaud rate. In this case, the optimal channel launch power was 200 μW (Fig. 4A). The second measurement was performed with mutually coherent channels by deriving carriers from frequency comb tones centered at 1549.3 nm and separated by 25 GHz. Each carrier was independently modulated by synchronized patterns, imparting real and imaginary parts of the electric field defined by inversion of Eq. 1. The degree of nonlinear compensation is measured by the performance (*28*) of the central

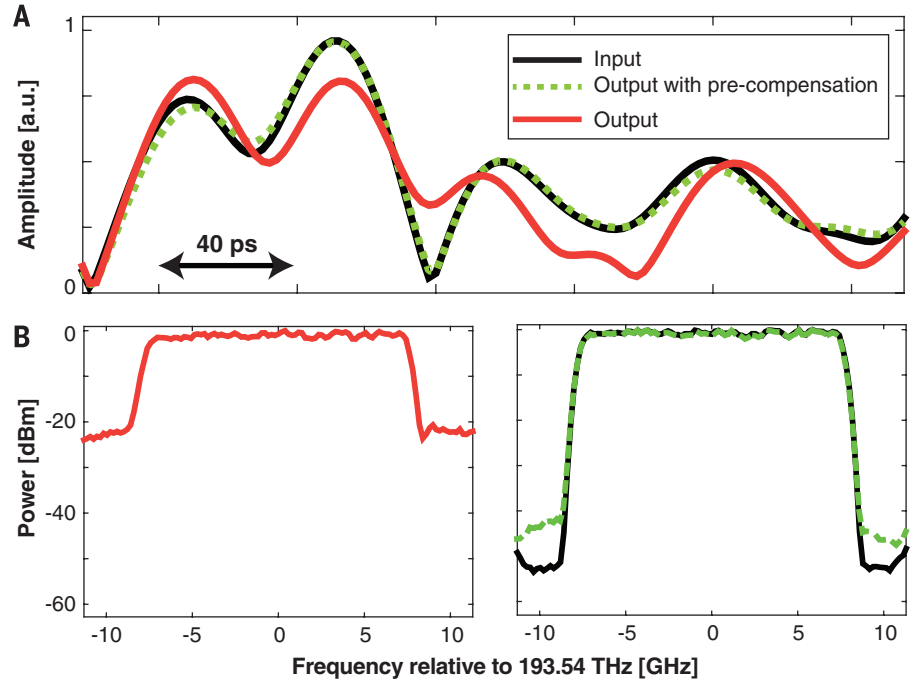

Fig. 2. Pump-probe cross-phase modulation compensation. (**A**) Time domain response. (**B**) The corresponding spectra with the color-coding scheme from (A).

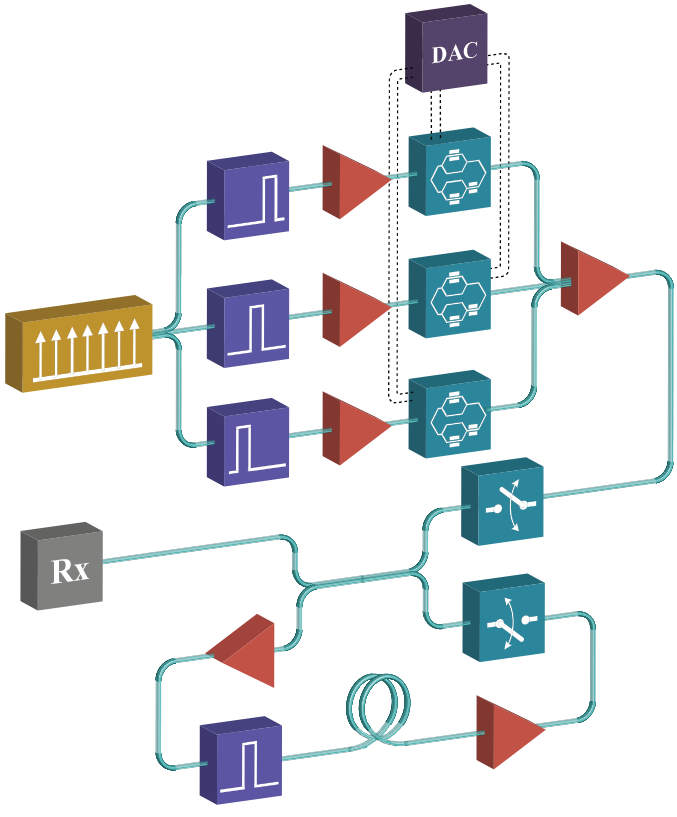

Fig. 3. Long–interaction length experimental setup. Recirculating loop-based transmission setup with recirculations 85 km in length, and comb lines used as mutually coherent signal carriers. DAC, digital-analog converter; Rx, coherent receiver.

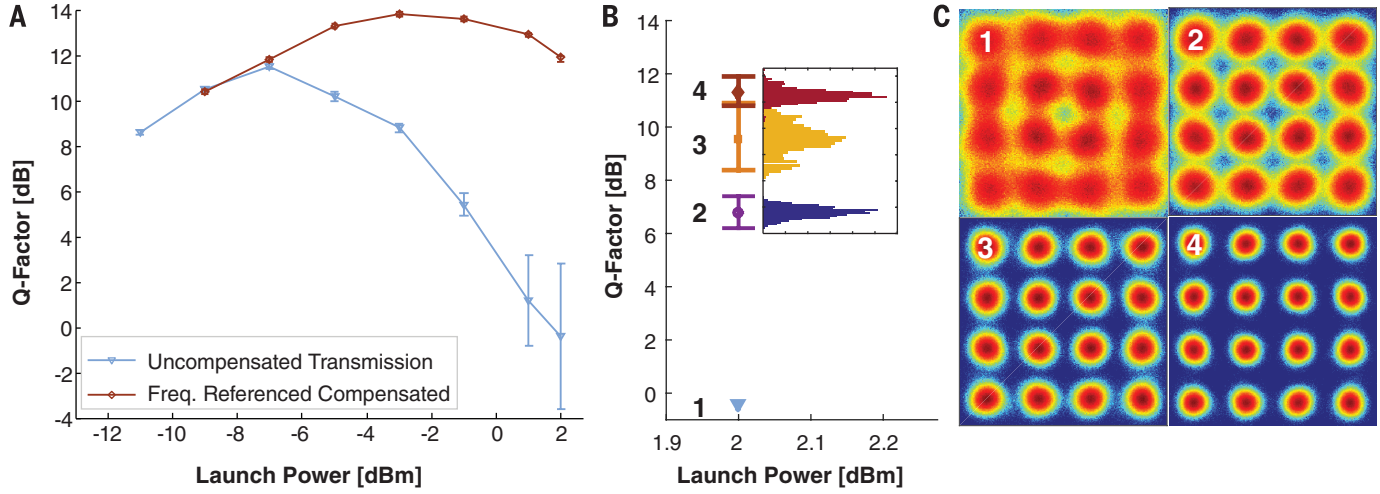

Fig. 4. Long-distance NLC characterization. (**A**) Received signal quality characterization after propagation for 1020 km. Error bars denote SD. (**B**) Middle channel performance and its variation over 2200 measurements for launch power of 2 dBm per span per channel for four mutual coherence configurations: b1, uncompensated nonlinear impairment; b2, NLC with uncorrelated carriers; b3, NLC with two mutually coherent carriers and (middle) one uncorrelated carrier; b4, NLC with (all) three mutually coherent carriers. (**C**) Constellation diagrams for the four mutual coherence configurations from (B).

channel at the loop output in terms of the Q factor

$$Q_{\mathrm{dB}} = 20 \cdot \log_{10}\left[\sqrt{2} \cdot \mathrm{erfc}^{-1}(2 \cdot \mathrm{BER})\right] \quad (2)$$

(*29*) while varying the signal launch powers from –9 to 2 dBm, where BER denotes the bit error ratio and erfc^{-1} is the inverse error function complement. The measurements in Fig. 4A clearly demonstrate the effective suppression of the nonlinear interaction: Even after distributed nonlinear interaction at a distance of 1020 km and an order of magnitude increase in the signal launch power, transmission quality (Q) is maintained. The saturation in performance (*30*, *31*) and its eventual decline are attributed to the Kerr-induced signal-noise interaction (*32*) (which is an inherent fundamental limit on the achievable performance), as well as the limitations of the experimental setup. No apparent jitter attributed to the Gordon-Haus effect (*33*) has been noticed in the experiments. It is nonetheless important to note a critical role of fast arbitrary waveform shaping, necessary to launch the inverted NLS solution. Electronic generators capable of operating over tens of GHz necessary to match a high-capacity coherent channel have become available only recently (*34*).

To further corroborate the critical importance of frequency referencing and its impact on the nonlinearity compensation ability, we repeated the experiment with three frequency-uncorrelated (free-running) carriers with linewidths of ~100 kHz and with a combination of correlated and uncorrelated carriers. The latter was realized by two comb-referenced channels while substituting the middle carrier by a single free-running laser. The performance of the system at the launch power of 1.6 mW (2 dBm) is shown in Fig. 4B, and the resulting constellation diagrams are given in Fig. 4C. The results in Fig. 4B clearly show that as the level of the mutual coherence between the interacting waves is increased (i.e., from the complete lack of coherence for three free-running oscillators, all the way to the fully frequency-referenced system), a qualitative improvement of the signal restoration is obtained, fully attesting to the gradual increase in the ability of the ensuing nonlinear interaction reversal. In particular, relative to the fully referenced system, the frequency uncertainty of only the middle carrier suffices to prevent a stable nonlinear compensation (Fig. 4B). Indeed, we observed a considerable variation of the output signal condition that is reflected by a widely varying figure of merit accumulated over 2200 measurements, as shown by the histogram in Fig. 4B (inset). [See (*25*) for additional measurements with free-running carriers.]

We note that the phases of the transmitters' paths, although frequency-referenced, were not stabilized in the experiment. As a consequence, the experimental results serve to corroborate the claim from (*23*) that phase of the carriers indeed plays only a minor role in an effective NLC. We emphasize that, contrary to the widespread opinion that nonlinear interaction reversal is only a matter of computation, our results clearly demonstrate that no amount of computational complexity can make up for the mutual coherence of the modes (in the interaction reversal). Although the second experiment encompasses three interacting modes, it qualitatively captures all of the relevant physical effects with the exception of polarization mode dispersion, whose random time variation will cause a variation in the nonlinear interaction in time and will affect the integrity of the interaction reversal, the quantification of which is beyond the scope of this report. The extension to higher mode counts, as well as to polarization multiplexed systems, is straightforward (*25*). We note that information capacity in the strict sense (*7*) cannot be measured experimentally. However, the experiments attest to the capacity increase beyond the currently accepted limits by demonstrating reversal of signal-signal interactions, assumed to be nonviable in previous information capacity treatments (*4*).

Our findings demonstrate the inversion of Kerr-induced interaction among multiple optical (frequency) modes in an optical fiber. The experiments have identified mutual carrier coherence as the critical requirement for substantial cancellation of nonlinear transmission effects. The compensation method relies on frequency comb–referenced carriers and enables an immediate increase of information capacity (*35*) and transmission reach in fiber communications beyond previously established limit estimates. By eliminating the stochastic contribution to Kerr-mediated wave interaction, this approach can be used to eliminate highly dissipative regeneration electronics from fiber networks and completely redefine the economy on which the present data traffic rests.

REFERENCES AND NOTES

1. Y. R. Shen, *Principles of Nonlinear Optics* (Wiley, New York, 1984).
2. G. P. Agrawal, *Nonlinear Fiber Optics* (Academic Press, San Diego, CA, ed. 2, 1995).
3. A. R. Chraplyvy, *J. Lightwave Technol.* **8**, 1548–1557 (1990).
4. P. P. Mitra, J. B. Stark, *Nature* **411**, 1027–1030 (2001).
5. R. J. Essiambre, G. Kramer, P. J. Winzer, G. J. Foschini, B. Goebel, *J. Lightwave Technol.* **28**, 662–701 (2010).
6. A. Mecozzi, R. J. Essiambre, *J. Lightwave Technol.* **30**, 2011–2024 (2012).
7. C. E. Shannon, *Bell Syst. Tech. J.* **27**, 379–423 (1948).
8. H. Hemmati, D. Caplan, in *Fiber Optic Telecommunications* (VIB, Oxford, 2013), pp. 121–162.
9. A. E. Kaplan, P. Meystre, *Opt. Lett.* **6**, 590–592 (1981).
10. P. A. Andrekson, M. Westlund, *Laser Photon. Rev.* **1**, 231–248 (2007).
11. C. J. McKinstrie, S. Radic, A. H. Gnauck, *Opt. Photon. News* **18**, 34–40 (2007).
12. K. Goda, K. K. Tsia, B. Jalali, *Nature* **458**, 1145–1149 (2009).
13. J. Yang, K. R. Akylas, *Stud. Appl. Math.* **111**, 359–375 (2003).
14. J. E. Prilepsky, S. A. Derevyanko, S. K. Turitsyn, *Opt. Express* **21**, 24344–24367 (2013).
15. X. Li *et al.*, *Opt. Express* **16**, 880–888 (2008).
16. E. Ip, J. M. Kahn, *J. Lightwave Technol.* **26**, 3416–3425 (2008).
17. K. Toyoda *et al.*, *Opt. Express* **20**, 19815–19821 (2012).

18. L. Dou *et al.*, in *Proc. ECOC2012*, paper Th.1.D.3 (2012).
19. N. K. Fontaine *et al.*, in *Proc. ECOC2013*, paper Mo.3.D.5 (2013).
20. K. Solis-Trapala, T. Inoue, S. Namiki, in *Proc. OFC2014*, paper W3F.8 (2014).
21. X. Liu, A. R. Chraplyvy, P. J. Winzer, R. W. Tkach, S. Chandrasekhar, *Nat. Photonics* **7**, 560–568 (2013).
22. T. Yoshida, T. Sugihara, K. Ishida, T. Mizuochi, in *Proc. OFC2014*, paper M3C.6 (2014).
23. N. Alic, E. Myslivets, E. Temprana, B. P. P. Kuo, S. Radic, *J. Lightwave Technol.* **32**, 2690–2698 (2014).
24. E. Myslivets, B. P. P. Kuo, N. Alic, S. Radic, *Opt. Express* **20**, 3331–3344 (2012).
25. See supplementary materials on *Science* Online.
26. N. S. Bergano, C. R. Davidson, *J. Lightwave Technol.* **13**, 879–888 (1995).
27. J. G. Proakis, M. Salehi, *Digital Communications* (McGraw-Hill, New York, ed. 5, 2007).
28. S. M. Berber, *IEEE Trans. Instrum. Meas.* **53**, 575–580 (2004).
29. N. S. Bergano, in *Fiber Optic Telecommunications IV* (Academic Press, San Diego, CA, 2002), pp. 154–197.
30. K. S. Turitsyn, S. A. Derevyanko, I. V. Yurkevich, S. K. Turitsyn, *Phys. Rev. Lett.* **91**, 203901 (2003).
31. E. Agrell, A. Alvarado, G. Durisi, M. Karlsson, *J. Lightwave Technol.* **32**, 2862–2876 (2014).
32. J. P. Gordon, L. F. Mollenauer, *Opt. Lett.* **15**, 1351–1353 (1990).
33. J. P. Gordon, H. A. Haus, *Opt. Lett.* **11**, 665–667 (1986).
34. www.fujitsu.com/downloads/MICRO/fme/documentation/c60.pdf
35. M. H. Taghavi, G. C. Papen, P. H. Siegel, *IEEE Trans. Inf. Theory* **52**, 5008–5022 (2006).

ACKNOWLEDGMENTS

We thank Sumitomo Electric Industries for fibers used in the experiments, and Google Inc. for support of this work. The University of California has filed a patent on the method and applications of frequency-referenced carriers for compensation of nonlinear impairments in transmission.

SUPPLEMENTARY MATERIALS

www.sciencemag.org/content/348/6242/1445/suppl/DC1
Materials and Methods
Supplementary Text
Figs. S1 to S4

22 March 2015; accepted 28 May 2015
10.1126/science.aab1781

OPTICS

Quantum spin Hall effect of light

Konstantin Y. Bliokh,[1,2]* Daria Smirnova,[2] Franco Nori[1,3]*

Maxwell's equations, formulated 150 years ago, ultimately describe properties of light, from classical electromagnetism to quantum and relativistic aspects. The latter ones result in remarkable geometric and topological phenomena related to the spin-1 massless nature of photons. By analyzing fundamental spin properties of Maxwell waves, we show that free-space light exhibits an intrinsic quantum spin Hall effect—surface modes with strong spin-momentum locking. These modes are evanescent waves that form, for example, surface plasmon-polaritons at vacuum-metal interfaces. Our findings illuminate the unusual transverse spin in evanescent waves and explain recent experiments that have demonstrated the transverse spin-direction locking in the excitation of surface optical modes. This deepens our understanding of Maxwell's theory, reveals analogies with topological insulators for electrons, and offers applications for robust spin-directional optical interfaces.

Solid-state physics exhibits a family of Hall effects with remarkable physical properties. The usual Hall effect (HE) and quantum Hall effect (QHE) appear in the presence of an external magnetic field, which breaks the time-reversal ($\mathcal{T}$) symmetry of the system. The HE induces charge current orthogonal to both the magnetic field and an applied electric field, whereas the QHE (*1*) involves distinct topological electron states, with unidirectional edge modes (charge-momentum locking), characterized by the topological Chern number (*2*).

The intrinsic spin Hall effect (SHE) can occur in $\mathcal{T}$-symmetric electron systems with spin-orbit interactions. It produces a spin-dependent transport of electrons orthogonal to the external driving force (*3*, *4*). There is also the quantum spin Hall effect (QSHE) (*5*, *6*), which is characterized by unidirectional edge spin transport—edge states with opposite spins propagating in opposite directions. Such topological states with spin-momentum locking gave rise to a new class of materials: topological insulators (*7*, *8*).

Alongside the extensive condensed-matter studies of electron Hall effects, their photonic counterparts have been found in various optical systems. In particular, both the HE (*9*) and the QHE with unidirectional edge propagation (*10*, *11*) have been reported in magneto-optical systems with broken $\mathcal{T}$-symmetry. Furthermore, because photons are relativistic spin-1 particles, they naturally exhibit intrinsic spin-orbit interaction effects, including Berry phase (*12*) and the SHE (*13*–*15*) stemming from fundamental spin properties of Maxwell equations (*16*).

The only missing part in the above optical Hall effects is the QSHE for photons. Recently, it was suggested that photonic topological insulators can be created in complex metamaterials structures (*17*–*19*). Here, we show that pure free-space light already possesses intrinsic QSHE, and simple natural materials (such as metals supporting surface plasmon-polariton modes) exhibit some features that resemble topological insulators. We show that the recently discovered transverse spin in evanescent waves (*20*, *21*) and spin-controlled unidirectional excitation of surface or waveguide modes (*22*–*27*) can be interpreted as manifestations of the QSHE of light.

Propagating (bulk) free-space modes of Maxwell equations are polarized plane waves. Introducing the complex amplitude $\mathbf{E}(\mathbf{r})$ of the harmonic electric field $\mathbf{E}(\mathbf{r},t) = \mathrm{Re}[\mathbf{E}(\mathbf{r})e^{-i\omega t}]$, the plane-wave solution with wave vector $\mathbf{k} = k\bar{\mathbf{z}}$ is

$$\mathbf{E} \propto \mathbf{e}\,\exp(ikz),\ \mathbf{e} = \alpha\bar{\mathbf{x}} + \beta\bar{\mathbf{y}} \qquad (1)$$

Here, $k = \omega/c$, $\mathbf{e}$ is the complex unit polarization vector ($|\alpha|^2 + |\beta|^2 = 1$), whereas $\bar{\mathbf{x}}$, $\bar{\mathbf{y}}$, and $\bar{\mathbf{z}}$ denote the unit vectors of the corresponding axes. The Jones vector $\xi = (\alpha,\beta)^T$ is a three-dimensional (3D) spinor, which describes the SU(2) polarization state of light. The spin states of propagating light are circular polarizations $\xi = (1, \pm i)^T/\sqrt{2}$, with helicities $\sigma \equiv 2\mathrm{Im}(\alpha^*\beta) = \pm 1$. According to the massless nature of photons, the plane-wave spin is directed along the wave vector: $\mathbf{S} = \sigma\mathbf{k}/k$ [we consider the spin density per photon in $\hbar = 1$ units (supplementary text)].

Generalizing Eq. 1 to an arbitrary direction of propagation, the polarization vector becomes momentum-dependent: $\mathbf{e}(\mathbf{k})$. Namely, it is tangent to the $\mathbf{k}$-space sphere because of the transversality condition $\mathbf{E}\cdot\mathbf{k} = 0$. This spherical $\mathbf{k}$-space geometry underlies the spin-orbit interaction of light (*12*–*16*). In particular, introducing the helicity basis of circular polarizations $\mathbf{e}^\sigma(\mathbf{k})$ (*16*), one can calculate the Berry connection $\mathbf{A}^{\sigma\sigma'} = -i\mathbf{e}^\sigma\cdot(\nabla_\mathbf{k})\mathbf{e}^{\sigma'}$ and curvature $\mathbf{F}^{\sigma\sigma'} = \nabla_\mathbf{k}\times\mathbf{A}^{\sigma\sigma'}$ for photons. In agreement with the helicity-degenerate light-cone spectrum of photons, the Berry curvature is diagonal, $\mathbf{F}^{\sigma\sigma'} = \delta^{\sigma\sigma'}\mathbf{F}^\sigma$, and it forms two monopoles at the Dirac-point origin of the momentum space (*12*–*16*):

$$\mathbf{F}^\sigma = \sigma\frac{\mathbf{k}}{k^3},\ \sigma = \pm 1 \qquad (2)$$

This curvature is responsible for the spin-redirection Berry phase and the SHE in optics (*12*–*16*).

We define the topological Chern numbers for the two helicity states $C^\sigma = \frac{1}{2\pi}\oint\mathbf{F}^\sigma d^2\mathbf{k}$, where the integral is taken over the $\mathbf{k}$-space sphere. The Chern numbers are meaningful in systems with Abelian Berry phases, such as 2D systems with the conserved spin component along the third dimension (*7*, *8*, *28*). This is also the case for photons having Abelian Berry phase, 2D polarization on the $\mathbf{k}$-space sphere, and conserved radial $\mathbf{k}$-component of the spin (helicity) (*29*). The monopole curvature (Eq. 2) yields $C^\sigma = 2\sigma$. The total

[1]Center for Emergent Matter Science, RIKEN, Wako-shi, Saitama 351-0198, Japan. [2]Nonlinear Physics Centre, Research School of Physics and Engineering, The Australian National University, Canberra, ACT 0200, Australia. [3]Department of Physics, University of Michigan, Ann Arbor, MI 48109-1040, USA.
*Corresponding author. E-mail: k.bliokh@gmail.com (K.Y.B.); fnori@riken.jp (F.N.)

Chern number $C = \sum_{\sigma=\pm1} C^{\sigma}$ and the spin Chern number $C_{\text{spin}} = \sum_{\sigma=\pm1} \sigma C^{\sigma}$ characterize the photonic QHE and QSHE properties (*7*, *8*, *28*):

$$C = 0, C_{\text{spin}} = 4 \quad (3)$$

The physical meaning of the Chern numbers is the number of edge modes with fixed direction of propagation. The vanishing total Chern number (Eq. 3) reflects the $\mathcal{T}$-symmetry of Maxwell equations and the absence of the QHE for free-space photons. At the same time, the nonzero spin Chern number (Eq. 3) implies that free-space light has two pairs of QSHE modes—edge counter propagating modes with opposite spins. Furthermore, the value $C_{\text{spin}} = 4$ implies that the topological $\mathbb{Z}_2$ invariant, associated with the $\mathcal{T}$-symmetry, vanishes: $\nu = \frac{C_{\text{spin}}}{2} \bmod 2 = 0$. This means that surface modes of Maxwell equations are not helical fermions (*30*) as, for example, surface states of the Dirac equation (*31*, *32*).

Nonetheless, nontrivial QSHE states of light exist, and they are well known. The photonic edge states of a bounded segment of free space are evanescent waves. For instance, assuming the $x = 0$ boundary, with free space at $x > 0$, the generic evanescent-wave solution of Maxwell equations can be written as (*21*)

$$\mathbf{E}_{\text{evan}} \propto \mathbf{e}_{\text{evan}} \exp(ik_z z - \kappa x),$$
$$\mathbf{e}_{\text{evan}} = \alpha\bar{\mathbf{x}} + \beta\frac{k}{k_z}\bar{\mathbf{y}} - i\alpha\frac{\kappa}{k_z}\bar{\mathbf{z}} \quad (4)$$

Here, the spinor $\xi = (\alpha, \beta)^T$ still characterizes the wave polarization states. The wave (Eq. 4) propagates along the z axis with wave number $k_z > k$ and decays exponentially away from the boundary with decrement $\kappa = \sqrt{k_z^2 - k^2}$.

One can consider the evanescent wave (Eq. 4) as a plane wave with the complex wave vector $\mathbf{k} = k_z\bar{\mathbf{z}} + i\kappa\bar{\mathbf{x}}$. The transversality condition $\mathbf{E} \cdot \mathbf{k} = 0$ generates the imaginary longitudinal z-component in the polarization vector $\mathbf{e}_{\text{evan}}$, in contrast to the purely transverse polarization $\mathbf{e}$ in propagating waves (Eq. 1). This component produces a (x, z)–plane rotation of the electric or magnetic fields and generates unusual transverse spin in evanescent waves (Fig. 1) (*20*, *21*). This transverse spin is independent of the polarization ξ and can be written as

$$\mathbf{S}_{\perp} = \frac{\text{Re}\mathbf{k} \times \text{Im}\mathbf{k}}{(\text{Re}\mathbf{k})^2} \quad (5)$$

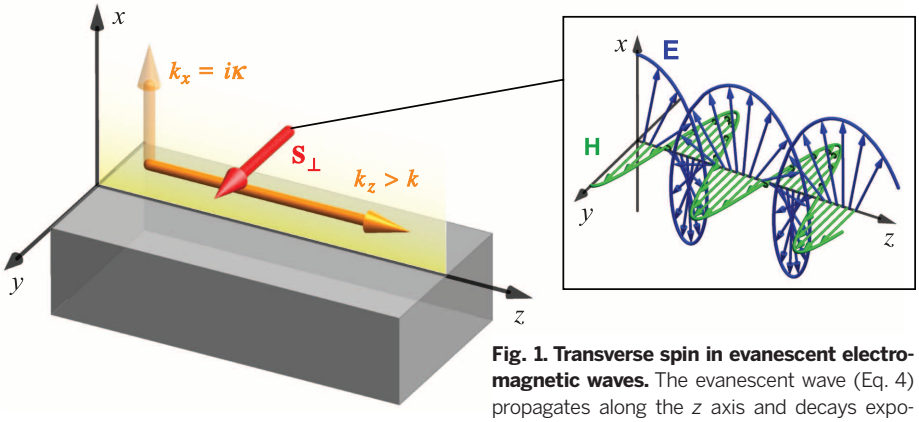

Fig. 1. Transverse spin in evanescent electromagnetic waves. The evanescent wave (Eq. 4) propagates along the z axis and decays exponentially in the $x > 0$ semi-space. (Inset) The instantaneous distributions of the electric and magnetic wave fields for the case of linear transverse-magnetic polarization, $\xi = (1, 0)^T$. The cycloidal (x, z)–plane rotation of the electric field generates the transverse spin $\mathbf{S}_{\perp}$ (Eq. 5) (*20*, *21*). The sign of the transverse spin depends on the direction of propagation of the evanescent wave.

Equation 5 demonstrates spin-momentum locking, similar to that in the QSHE and 3D topological insulators for electrons (*5*–*8*). In particular, the z-propagating evanescent waves with $k_z > 0$ and $k_z < 0$ will have opposite transverse spins $S_y > 0$ and $S_y < 0$ (Figs. 2 to 4). Thus, any interface between free space and a medium supporting surface or guided modes with evanescent tails (Eq. 4) exhibits counter propagating opposite-spin edge modes—the QSHE of light. This is the first key point of our work.

In agreement with $C_{\text{spin}} = 4$, there are two pairs of QSHE modes in free space because the evanescent waves (Eq. 4) are double-degenerate with respect to the helicities $\sigma = \pm1$. However, the existence of surface modes in Maxwell equations requires a planar interface between the vacuum and a medium characterized by a permittivity ε and permeability μ. Such interface breaks the dual symmetry between the electric and magnetic properties: $\varepsilon \neq \mu$ (*29*). This breaks the polarization degeneracy, and only a single polarization survives in the surface modes. For example, only transverse-magnetic surface waves exist at the interface with a medium with $\mu = 1$ and $\varepsilon < -1$. Calculating the spectrum, polarization, and spin of these surface modes of Maxwell equations, we obtain (supplementary text):

$$\omega_{\text{surf}} = \sqrt{\frac{1+\varepsilon}{\varepsilon}}\, k_{\text{surf}}, \xi_{\text{surf}} = \begin{pmatrix} 1 \\ 0 \end{pmatrix},$$
$$\langle \mathbf{S}_{\text{surf}} \rangle = \frac{1}{\sqrt{-\varepsilon}} \bar{\mathbf{k}}_{\text{surf}} \times \bar{\mathbf{n}}. \quad (6)$$

Here, $\bar{\mathbf{k}}_{\text{surf}}$ and $\bar{\mathbf{n}}$ are the unit vectors of the propagation direction and the outer normal of the medium, respectively, and we calculated the mean (integral) spin per one surface-mode particle. The momentum-dependent spin $\langle \mathbf{S}_{\text{surf}} \rangle$ originates from the transverse spin (Eq. 5) of evanescent waves.

Equations. 5 and 6 determine the momentum locking of the spin $\mathbf{S}$ but not of the polarization spinor ξ (Fig. 2A). Polarization specifically corresponds to spin for nonrelativistic electrons, but for relativistic particles these are different notions. The surface modes of Maxwell equations have momentum-dependent spin $\mathbf{S}_{\text{surf}}$ but fixed spinor ξ_{surf} (Eq. 6). The latter corresponds to the trivial $\mathbb{Z}_2$ invariant $\nu = 0$ and shows that surface

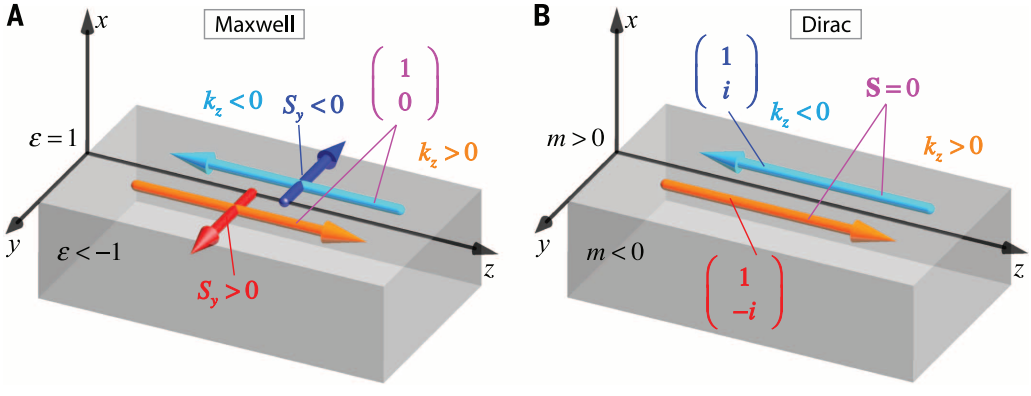

Fig. 2. Spin and spinor properties of Maxwell and Dirac surface modes. (**A**) Surface modes of Maxwell equations propagating along the interface between the vacuum and a nontransparent medium with $\mu = 1$, $\varepsilon < -1$. These surface waves have fixed polarization $\xi_{\text{surf}} = (1, 0)^T$ but opposite transverse spins $\mathbf{S}$ locked to opposite wave momenta (Eqs. 5 and 6). (**B**) Topological surface modes of the Dirac equation at the interface between positive-mass and negative-mass regions (*31*, *32*). These modes exhibit locking between their momenta and spinors: Orthogonal polarizations propagate in opposite directions. However, the expectation value of their spin vanishes: $\mathbf{S}_{\text{surf}} = 0$ (supplementary text).

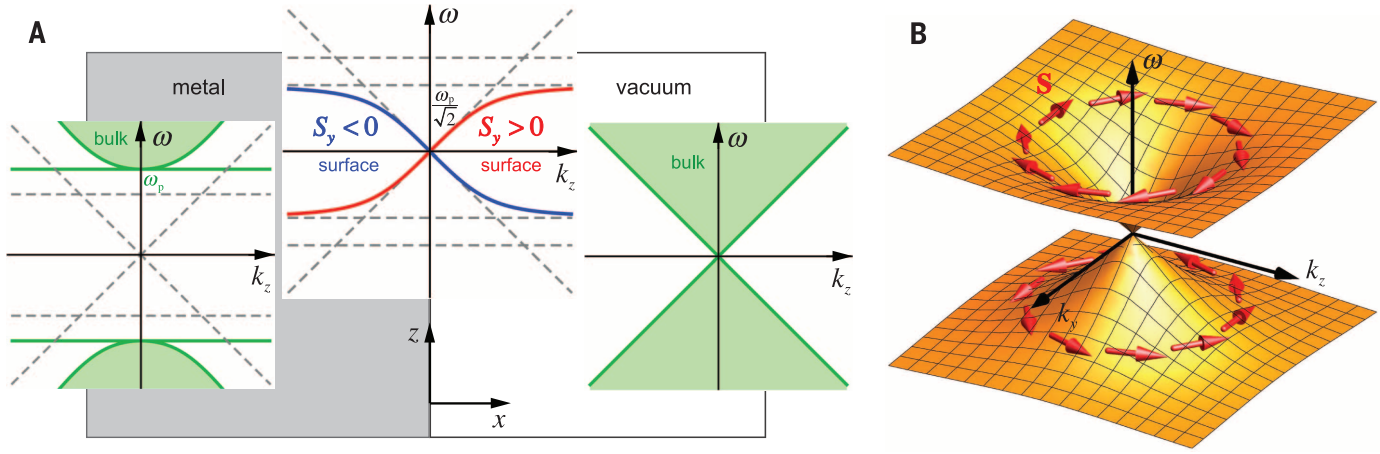

Fig. 3. Dispersion and spin-momentum locking of surface plasmon-polaritons. (**A**) Dispersion of bulk and surface modes at the vacuum-metal interface. SPPs exist inside the gap of the metal bulk spectrum and have spin-momentum locking associated with the transverse spin (Eqs. 5 and 6). (**B**) The two-dimensional dispersion of the same SPP mode exhibits a vortex spin texture similar to that for surface states of a 3D topological insulator (*7*, *8*).

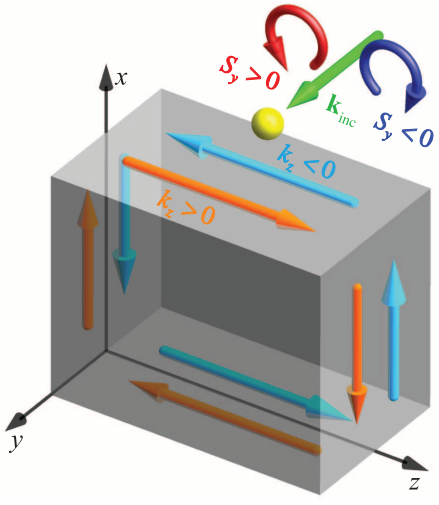

Fig. 4. Schematic of experiments demonstrating the QSHE of light. The incident *y*-propagating light (green) is coupled to surface modes with evanescent free-space tails via some scatterer (such as a nanoparticle). Depending on the spin of the incident light, $\mathbf{S}_{inc} = \sigma\bar{\mathbf{y}}$ (the helicity $\sigma = \pm 1$ is shown here by the circular-polarization arrows), surface waves with opposite propagation directions $\bar{\mathbf{k}}_{surf} = \pm\bar{\mathbf{z}}$ are excited (*22*–*27*).

Maxwell modes are bosons rather than helical fermions (*30*). Nonetheless, these modes provide the unidirectional edge spin transport (QSHE) because of the spin $\mathbf{S}_{surf}$. Precisely the opposite situation takes place in one of the main models for 3D electron topological insulators: the Dirac equation with surface modes at the interface between positive-mass and negative-mass regions (Fig. 2B) (*31*, *32*). In this case, spinor-momentum locking occurs, which corresponds to the topological $\mathbb{Z}_2$ invariant $\nu = 1$. However, surprisingly, the expectation value of the spin of the surface Dirac modes vanishes because of the mutual cancellation of the polarization-dependent and polarization-independent (similar to Eq. 5) contributions (supplementary text). Thus, one can say that surface Maxwell modes exhibit unidirectional spin transport (QSHE) but with trivial $\mathbb{Z}_2$ spinor properties, whereas the surface Dirac modes are topologically protected helical fermions that, however, do not transport spin. This is the second key point of our work.

Optical spin-momentum locking was recently observed in several experiments (*22*–*27*). An important example is provided by surface plasmon-polaritons (SPPs) at the vacuum-metal interface (*33*). Real metals are dispersive media with permittivity $\varepsilon(\omega) = 1 - \omega_p^2/\omega^2$, where ω_p is the plasma frequency. Metals are optical insulators at $\omega < \omega_p$, and at $\varepsilon < -1$ ($\omega < \omega_p/\sqrt{2}$), the vacuum-metal interface supports surface Maxwell modes—the SPPs (Fig. 3A). The metal becomes transparent at $\omega \geq \omega_p$, with bulk plasmons at $\omega = \omega_p$ and electromagnetic modes at $\omega > \omega_p$. As shown in Fig. 3A, the vacuum-metal interface resembles, by using condensed-matter analogies, the interface between a semimetal and an insulator. The SPP modes demonstrate spin-momentum locking (Eqs. 5 and 6) and nonremovable (because of the light-cone spectrum in vacuum) spectral degeneracy at $k = 0$, which are typical for electron QSHE states. Furthermore, plotting the SPP spectrum for a 2D surface of a 3D metal (Fig. 3B), one can see the conical spectrum and vortex spin texture analogous to those in 3D electron topological insulators (*7*, *8*), but without the helical-fermion spinor properties (Fig. 2).

A schematic of the experiments (*22*–*27*) is shown in Fig. 4, revealing spin-controlled unidirectional transport in electromagnetic surface or guided waves. A transversely propagating free-space light beam with the usual spin $\mathbf{S}_{inc} = \sigma\bar{\mathbf{y}}$ (helicity $\sigma = \pm 1$) was coupled to the evanescent tails of the SPP or waveguide modes via some scatterer (such as a nanoparticle or an atom). In doing so, the opposite incident-spin states $\mathbf{S}_{inc} = \pm\bar{\mathbf{y}}$ excited the surface or guided modes running in the opposite directions: $\bar{\mathbf{k}}_{surf} = \pm\bar{\mathbf{z}}$. This spin-direction correlation reached almost 100% efficiency in various systems, independently of their details. This proves the universal spin-momentum locking in optical surface waves—the QSHE of light.

Thus, we have shown that light has intrinsic QSHE features, which arise from the spin-orbit interactions of photons. The corresponding spin-momentum locking originates solely from the basic properties of evanescent waves in Maxwell equations and can be observed at any interface with the vacuum, which supports surface or guided waves. In particular, surface plasmon-polaritons at a metal-vacuum interface exhibit features similar to those of surface states of topological insulators (vortex spin texture at the conical dispersion). Because of their trivial spinor structure, surface electromagnetic states are not helical fermions and are not protected from backscattering. Nonetheless, they do provide robust unidirectional spin transport. Our work shows that recent experiments, demonstrating highly efficient spin-controlled unidirectional excitation of surface or guided modes, can be interpreted as observations of the QSHE of light. The transverse spin locked to the direction of propagation seems to be a universal feature of surface vector waves of different nature. It appears in Maxwell and Dirac equations, as well as in Rayleigh surface waves in elastic media and surface-water waves. This offers robust angular-momentum-to-direction coupling in various surface waves as well as analogies and generalizations involving quantum and classical wave theories.

REFERENCES AND NOTES

1. M. Stone, Ed., *The Quantum Hall Effect* (World Scientific, Singapore, 1992).
2. D. J. Thouless, M. Kohmoto, M. P. Nightingale, M. den Nijs, *Phys. Rev. Lett.* **49**, 405–408 (1982).
3. S. Murakami, N. Nagaosa, S.-C. Zhang, *Science* **301**, 1348–1351 (2003).
4. J. Sinova *et al.*, *Phys. Rev. Lett.* **92**, 126603 (2004).
5. C. L. Kane, E. J. Mele, *Phys. Rev. Lett.* **95**, 146802 (2005).
6. B. A. Bernevig, T. L. Hughes, S. C. Zhang, *Science* **314**, 1757–1761 (2006).
7. M. Z. Hasan, C. L. Kane, *Rev. Mod. Phys.* **82**, 3045–3067 (2010).
8. X.-L. Qi, S.-C. Zhang, *Rev. Mod. Phys.* **83**, 1057–1110 (2011).

9. G. L. J. A. Rikken, B. A. van Tiggelen, *Nature* **381**, 54–55 (1996).
10. F. D. M. Haldane, S. Raghu, *Phys. Rev. Lett.* **100**, 013904 (2008).
11. Z. Wang, Y. Chong, J. D. Joannopoulos, M. Soljacić, *Nature* **461**, 772–775 (2009).
12. R. Y. Chiao, Y.-S. Wu, *Phys. Rev. Lett.* **57**, 933–936 (1986).
13. K. Y. Bliokh, Y. P. Bliokh, *Phys. Lett. A* **333**, 181–186 (2004).
14. M. Onoda, S. Murakami, N. Nagaosa, *Phys. Rev. Lett.* **93**, 083901 (2004).
15. K. Y. Bliokh, A. Niv, V. Kleiner, E. Hasman, *Nat. Photonics* **2**, 748–753 (2008).
16. K. Y. Bliokh, M. A. Alonso, E. A. Ostrovskaya, A. Aiello, *Phys. Rev. A* **82**, 063825 (2010).
17. M. Hafezi, E. A. Demler, M. D. Lukin, J. M. Taylor, *Nat. Phys.* **7**, 907–912 (2011).
18. A. B. Khanikaev *et al*., *Nat. Mater.* **12**, 233–239 (2013).
19. M. C. Rechtsman *et al*., *Nature* **496**, 196–200 (2013).
20. K. Y. Bliokh, F. Nori, *Phys. Rev. A* **85**, 061801 (2012).
21. K. Y. Bliokh, A. Y. Bekshaev, F. Nori, *Nat. Commun.* **5**, 3300 (2014).
22. F. J. Rodríguez-Fortuño *et al*., *Science* **340**, 328–330 (2013).
23. J. Petersen, J. Volz, A. Rauschenbeutel, *Science* **346**, 67–71 (2014).
24. D. O'Connor, P. Ginzburg, F. J. Rodríguez-Fortuño, G. A. Wurtz, A. V. Zayats, *Nat. Commun.* **5**, 5327 (2014).
25. R. Mitsch, C. Sayrin, B. Albrecht, P. Schneeweiss, A. Rauschenbeutel, *Nat. Commun.* **5**, 5713 (2014).
26. B. le Feber, N. Rotenberg, L. Kuipers, *Nat. Commun.* **6**, 6695 (2015).
27. I. Söllner *et al*., arXiv:1406.4295v3 (2014).
28. D. N. Sheng, Z. Y. Weng, L. Sheng, F. D. M. Haldane, *Phys. Rev. Lett.* **97**, 036808 (2006).
29. I. Fernandez-Corbaton *et al*., *Phys. Rev. Lett.* **111**, 060401 (2013).
30. L. Lu, J. D. Joannopoulos, M. Soljačić, *Nat. Photonics* **8**, 821–829 (2014).
31. R. Jackiw, C. Rebbi, *Phys. Rev. D Part. Fields* **13**, 3398–3409 (1976).
32. A. P. Schnyder, S. Ryu, A. Furusaki, A. W. W. Ludwig, *Phys. Rev. B* **78**, 195125 (2008).
33. A. V. Zayats, I. I. Smolyaninov, A. A. Maradudin, *Phys. Rep.* **408**, 131–314 (2005).

ACKNOWLEDGMENTS

We are grateful to A. Furusaki, Y. Bliokh, E. Ostrovskaya, Y. Kivshar, and A. Khanikaev for fruitful discussions. This work was partially supported by the RIKEN iTHES Project, Multidisciplinary University Research Initiative Center for Dynamic Magneto-Optics (award number FA9550-14-1-0040), the Australian Research Council, Japan Society for the Promotion of Science–Russian Foundation for Basic Research contract 12-02-92100 and a Grant-in-Aid for Scientific Research (A).

SUPPLEMENTARY MATERIALS

www.sciencemag.org/content/348/6242/1448/suppl/DC1
Supplementary Text
Figs. S1 to S3
References (*34*–*40*)

19 February 2015; accepted 19 May 2015
10.1126/science.aaa9519

3D LITHOGRAPHY

Atomic gold–enabled three-dimensional lithography for silicon mesostructures

Zhiqiang Luo,[1]* Yuanwen Jiang,[1]* Benjamin D. Myers,[2,3] Dieter Isheim,[2,4] Jinsong Wu,[2,3] John F. Zimmerman,[1] Zongan Wang,[1] Qianqian Li,[2,3] Yucai Wang,[5] Xinqi Chen,[2,3] Vinayak P. Dravid,[2,3] David N. Seidman,[2,4] Bozhi Tian[1,5,6]†

Three-dimensional (3D) mesostructured semiconductors show promising properties and applications; however, to date, few methods exist to synthesize or fabricate such materials. Metal can diffuse along semiconductor surfaces, and even trace amounts can change the surface behavior. We exploited the phenomena for 3D mesoscale lithography, by showing one example where iterated deposition-diffusion-incorporation of gold over silicon nanowires forms etchant-resistant patterns. This process is facet-selective, producing mesostructured silicon spicules with skeletonlike morphology, 3D tectonic motifs, and reduced symmetries. Atom-probe tomography, coupled with other quantitative measurements, indicates the existence and the role of individual gold atoms in forming 3D lithographic resists. Compared to other more uniform silicon structures, the anisotropic spicule requires greater force for detachment from collagen hydrogels, suggesting enhanced interfacial interactions at the mesoscale.

Semiconductors with three-dimensional (3D) mesoscale features (*1*–*5*) are an emerging class of materials, with promising applications from stretchable bioelectronics (*3*) to alternative plasmonics and metamaterials (*6*). However, progress in this area has been impeded by challenges in chemical synthesis (*5*) and limitations in 3D fabrication methods (*1*, *2*, *4*, *7*). As a result, this area would benefit from new synthetic concepts or new components in lithography. One place to look for such inspiration is in biomaterials-based processes, which routinely assemble mesostructured materials.

In the growth of natural hard biomaterials, trace amounts of interfacial organic species are important components (*8*), yielding unusual 3D biomaterial shapes and properties. The application of trace organic molecules as components (e.g., an etching resist) in semiconductor-based lithography is hard to achieve, given that semiconductor processing typically involves either high-temperature gas-phase or harsh solution-phase preparations. However, inorganic species are much more stable and can be introduced as trace components into various semiconductors, as either impurities in the bulk volume (*9*–*11*) or as diffused species near the surface (*12*–*16*), with the latter holding great potential in 3D semiconductor lithography, given that surface diffusion is versatile and more controllable.

Here we focus on 3D mesoscale lithography of silicon (Si) nanowires with diffused gold (Au) (*13*, *14*, *17*), where Au originates from the nanoparticle catalyst used for nanowire nucleation and elongation [Fig. 1, supplementary materials (*18*), and fig. S1]. Because Au diffusion over Si surfaces is pressure-dependent (*16*), we first adopted periodic pressure modulation during Au-catalyzed Si nanowire synthesis to develop Au diffusion–induced patterns along nanowire sidewalls (figs. S1 to S3), where silane (SiH_4) and diborane (B_2H_6) were used as a Si precursor and a *p*-type dopant, respectively. Next, we revealed the Au-based patterns with anisotropic wet chemical etching in KOH solutions [materials and methods (*18*) and fig. S4]. The as-grown Si structures have rather uniform diameters except for periodic swells at the evacuation locations (figs. S2 and S3). After etching, we identified two Si mesostructures from the same growth batch: a type I spicule with platelike nodes and a type II spicule with triangle-shaped nodes (Fig. 1, A and B). Portions of the nanowire surfaces remained after etching, suggesting that the diffused Au acted as an etching resist. Both spicule structures show gradient, curved, and anisotropic surface textures. These formations are reminiscent of other complex nanowire morphologies (*19*–*24*) but are also similar to some naturally occurring hard materials, such as skeletons (*8*).

Transmission electron microscopy (TEM) images of *p*-type Si spicules (Fig. 1, C to F, and fig. S5) show that type I and type II structures grow along the <111> and <112> directions, respectively. Although type I is a single crystal, the type II spicule has a {111} twin plane (*11*), which separates subunits α and β (Fig. 1F, TB marks the twin boundary), as determined by the two sets of diffraction spots (Fig. 1F, magenta/white and blue/white dashed circles) in the selected area electron diffraction (SAED) pattern.

We used scanning TEM (STEM) for tomograms of mesostructured Si spicules (*18*) (Fig. 2, A and B, and fig. S6). In addition to the expected structural gradient and anisotropy, we revealed convex and

[1]Department of Chemistry, the University of Chicago, Chicago, IL 60637, USA. [2]Department of Materials Science and Engineering, Northwestern University, Evanston, IL 60208, USA. [3]Northwestern University Atomic and Nanoscale Characterization Experimental (NUANCE) Center, Northwestern University, Evanston, IL 60208, USA. [4]The Northwestern University Center for Atom-Probe Tomography (NUCAPT), Northwestern University, Evanston, IL 60208, USA. [5]The James Franck Institute, the University of Chicago, Chicago, IL 60637, USA. [6]The Institute for Biophysical Dynamics, Chicago, IL 60637, USA.
*These authors contributed equally to this work. †**Corresponding author. E-mail: btian@uchicago.edu**

concave components in both types of spicules. Combined with the faceted edges observed in TEM (yellow dashed lines, Fig. 1, C to E), we constructed curved anisotropic shells (magenta lines) and {111} facets-based polyhedron cores (type I: octahedron; type II: trigonal bipyramid, blue and green lines) as the coupled two principal "tectonic" motifs for individual nodes (Fig. 2, A and B, and fig. S7).

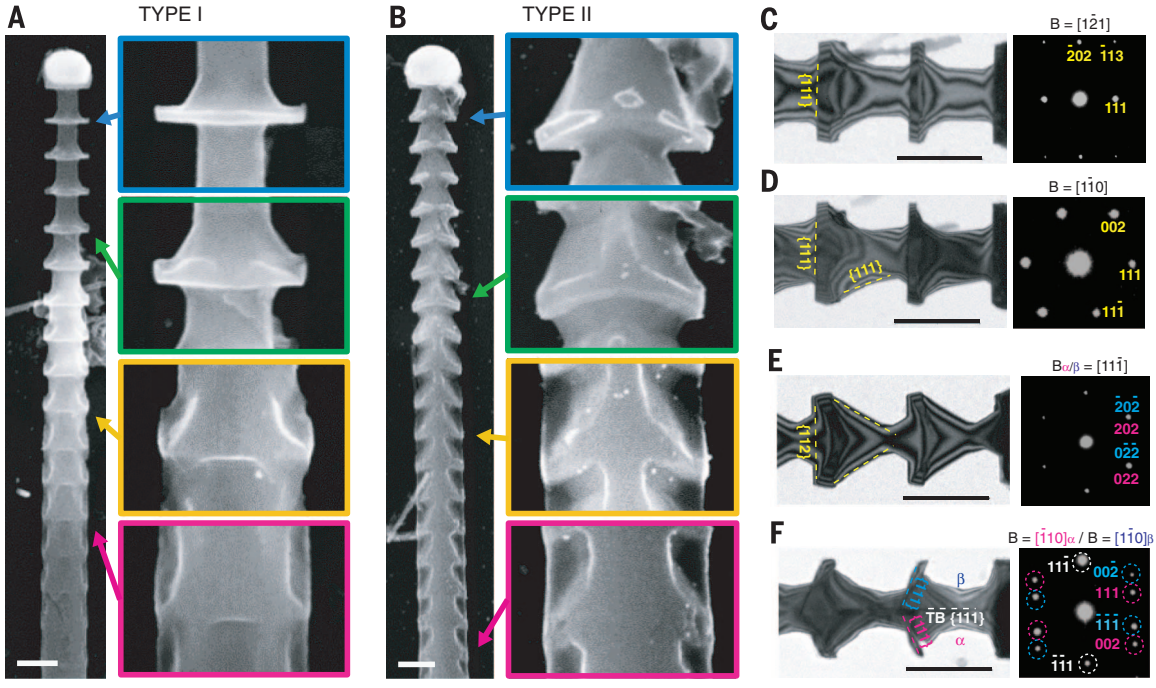

Fig. 1. Electron microscope images of type I (A, C, and D) and type II (B, E, and F) skeletonlike Si spicules. (A) and (B) SEM images. The righthand columns are zoomed-in views of individual segments shown in the lefthand columns. (C) to (F) TEM and SAED patterns of type I and type II structures, viewed from [1$\bar{2}$1] (C), [1$\bar{1}$0] (D), [11$\bar{1}$] (E), and $[\bar{1}10]_a/[1\bar{1}0]_b$ (F) zone axes. The numbers in SAED patterns are diffraction spots, which reveal [111] and $[112]_a/[\bar{1}\bar{1}2]_b$ growth orientations for type I and II structures. Magenta and blue in (E) and (F) highlight information from twinning subunits α and β, respectively. Scale bars, 200 nm.

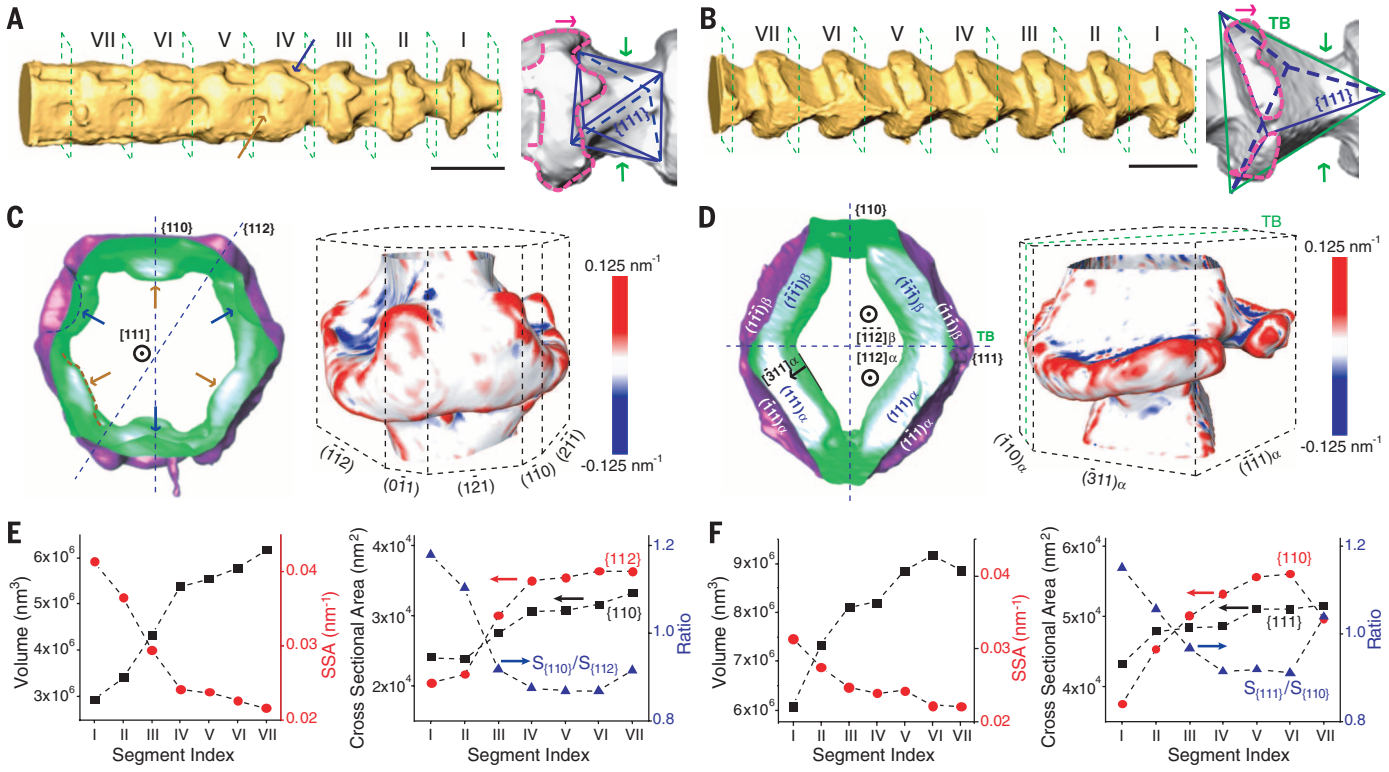

Fig. 2. Mesostructured Si spicules show defined motifs, pronounced curvature, anisotropy, and gradient. (**A** and **B**) STEM tomography of type I (A) and II (B) spicules, with polyhedron-curved shell models shown on the right. The blue and brown arrows in the STEM tomography mark two different concave features. The magenta and green arrows in the models suggest "morphogenesis" orientations for the two "tectonic" motifs. (**C** to **F**) Isosurfaces [(C) and (D), left], 3D curvature maps [(C) and (D), right], and quantitative analysis of gradient [(E) and (F)] in type I [(C) and (E)] and II [(D) and (F)] spicules. The segment indices are identical to those in (A) and (B). The numerical values in each segment were obtained using Amira 5.5 (FEI Visualization Sciences Group). Green and magenta in (C) mark the inside and outside surfaces, respectively. SSA, specific surface area. Scale bars in (A) and (B), 200 nm.

We analyzed the surfaces (*18*) and mean curvatures (the average of the two principal curvatures) of individual segments (Fig. 2, C and D). We confirmed that there were two groups of concave and highly curved patches in a type I spicule segment (segment IV, Fig. 2C, left)—lower (brown arrows) and higher (blue arrows) sets—consistent with the octahedron model (fig. S8). They are arranged with a threefold symmetry and were formed from selective etching of the left (Fig. 2A, brown arrow) and right (Fig. 2A, blue arrow) domains about the central plate, respectively (fig. S8). In contrast, a type II spicule segment (segment VI, Fig. 2D, left) is capped with {111} planes, and only one {110} mirror plane is observed. 3D mean curvature maps (segment I, Fig. 2, C and D, right) confirm the concave (blue) and convex (red) surfaces and show that large mean curvatures concentrate at the coupling regions between lateral shells and polyhedron cores (Fig. 2, A and B).

The individual segment volumes and specific surface areas (i.e., surface area/volume) generally increase and decrease, respectively, from segment I to VII in both structures (Fig. 2, E and F, left). These facts suggest that etching of Si and the corresponding porosity are more significant near the Au catalyst. The segment cross-sectional areas (Fig. 2, E and F, right; and fig. S9), {112} and {110} planes in the type I spicule, and {110} and {111} planes in the type II spicule, all generally increase from segment I to VII, suggesting a gradient in the pattern of etching resistance. The ratios of the two cross-sectional areas also change in different segments (Fig. 2, E and F, right), indicating nonuniform radial evolution of segment geometry.

To understand the pattern formation mechanism, we used x-ray photoelectron spectroscopy (XPS) to characterize Si surfaces before wet chemical etching (Fig. 3A). Deconvolution of Au 4*f* lines indicates the presence of two principal Au components in the detectable regime (<10 nm): metallic Au and intermetallic silicide-like Au (Fig. 3A, upper panel). For example, an Au 4*f* 7/2 peak at 84.0 eV with a full width at half maximum (FWHM) of 1.9 eV indicates metallic Au, whereas the one at 85.3 eV with a FWHM of 2.1 eV suggests the intermetallic Au species (*25*). The fact that intermetallic Au yields a notable XPS signal (area ratio: intermetallic/metallic ~ 1.068) suggests significant Au diffusion and subsequent incorporation into Si subsurface regions. To decouple the role of metallic Au from the intermetallic one in establishing the sculpted structure, we removed metallic Au with a standard gold etchant, as confirmed from XPS (Fig. 3A, lower panel). The primary sculpted structures are maintained after wet chemical etching (fig. S10), suggesting that intermetallic Au in the Si subsurface plays a major role as an etching resist.

Using laser-assisted local electrode atom-probe tomography (APT), we studied Au together with

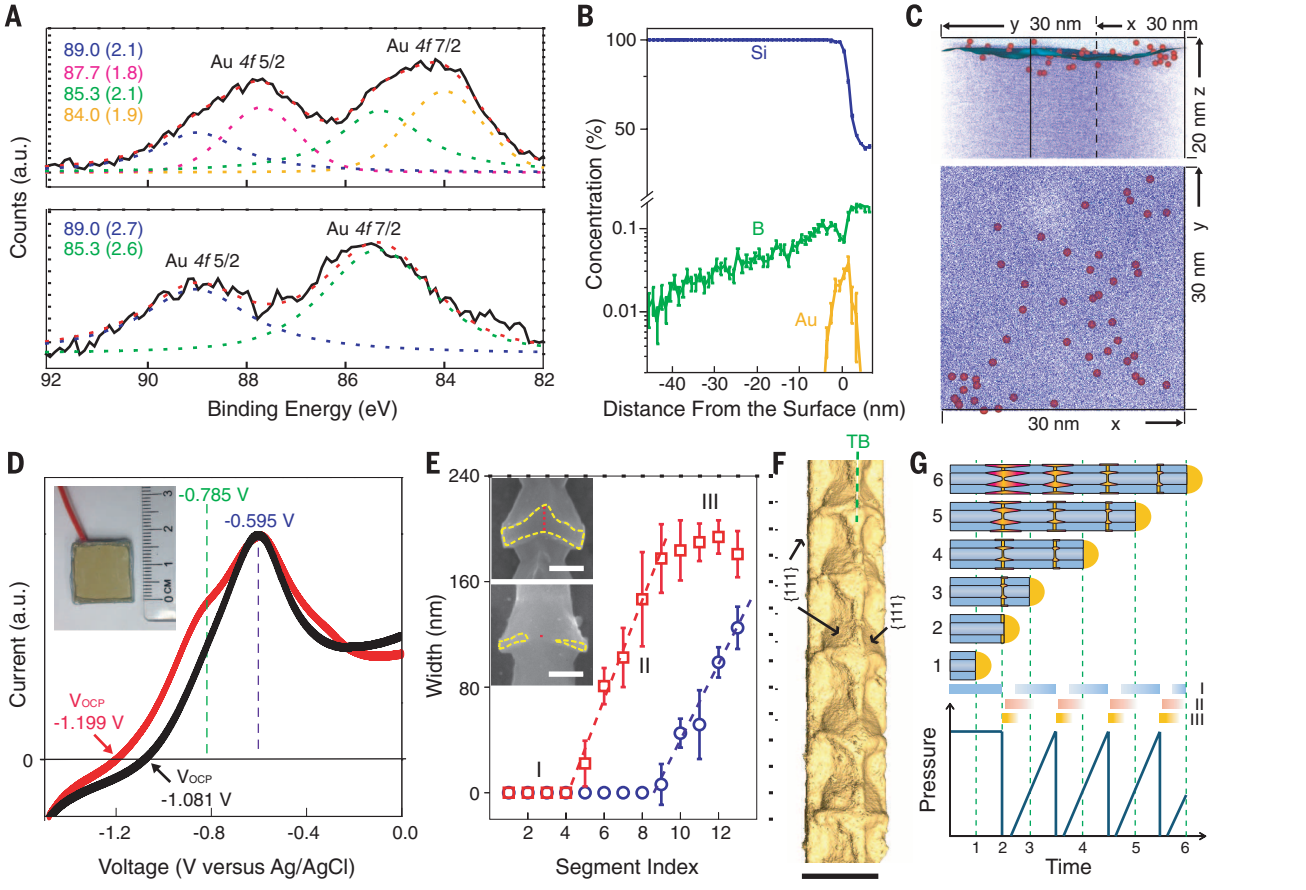

Fig. 3. Individual Au atoms can induce etching resist effect. (**A**) XPS spectra of modulated structures before silicon etching. Upper panel: Without metallic Au removal. Lower panel: With metallic Au removal. Insets show the binding energy and FWHM (in parenthesis) of deconvoluted peaks. (**B** and **C**) APT analysis. (B) Radial Si, B, and Au concentration profiles. (C) 3D chemical reconstruction viewed from parallel (upper panel) and perpendicular (lower panel) directions to the sample axis (fig. S12), showing the Si/SiO_2 interface (5% of O isosurface, blue/cyan) and Si (blue dots, 50%), Au (red dots, 100%), and O atoms (cyan dots, 50%). (**D**) Electrochemical current-voltage curves collected using pressure-modulated (black) and pressure-nonmodulated (red) Si structures as working electrodes. Metallic Au was removed with a gold etchant. The inset shows a device image, where the edge and back side of a Si wafer were passivated with epoxy. Two curves were normalized using the peak at −0.595 V. (**E**) The effect of diborane on spicule morphogenesis and Au diffusion profiles. Insets show SEM images of the sixth segment with 1:1000 (upper panel) and 1:4000 (lower panel) B:Si feeding ratios. Scale bars, 100 nm. (**F**) STEM tomography of an *n*-type, <112>-oriented Si spicule. The dashed line marks the {111} twin boundary (TB) based on its STEM imaging, and arrows highlight some exposed {111} facets. P:Si feeding ratio, 1:1000. Scale bar, 200 nm. (**G**) Schematic diagram illustrating the patterned interface formation. Graded color bands denote Si axial elongation (I, blue), Au deposition (III, orange), and diffusion (II, pink). The numbers indicate different stages during a typical growth period, and dashed lines mark the catalyst/Si interfaces at each stage.

other elements with subnanometer spatial resolution (figs. S11 to S15). A proximity histogram (Fig. 3B and fig. S13) (*18*, *26*), plotted along the spicule radial direction and collected from an etching-resistive portion (fig. S11), indicates a Au-enriched region localized at the Si/silica interface (the Si sidewall). The width of this region is ~7 nm. The Au peak concentration is ~370 atomic parts per million (ppm), which is less than that of boron (B) (~1370 atomic ppm in Si) but is substantially greater than the equilibrium Au concentration in bulk Si (*27*) and Si nanowires (*17*). The enhanced concentration of Au in the Si subsurface may be due to the kinetic trapping (*9*) of Au by radially deposited Si upon SiH_4 decomposition. A 3D, atom-by-atom chemical reconstruction from a 30 nm × 30 nm × 20 nm region (Fig. 3C) reveals that Au exists mostly as isolated atoms, instead of continuous Au films, which are routinely used as etch masks for Si. The incorporation of Au atoms in a Si matrix also explains the intermetallic Au feature in XPS (Fig. 3A).

Si wet chemical etching involves electron transfer at the solid/liquid interface (*28*). To answer how Au atoms induce an etch resist effect, we performed three-electrode electrochemical measurements (Fig. 3D) using pressure-modulated (black) and conventional nonmodulated (red) *p*-type Si nanowires as the working electrodes (Fig. 3D, inset), where bulk metallic Au (Au that is not incorporated in Si) was removed with a gold etchant. Representative current–versus-voltage scans recorded in 5% (weight by volume) KOH at room temperature (Fig. 3D) demonstrate that the open circuit potential (the potential difference between working and reference electrodes at the open-circuit state, V_{ocp}) shifted anodically (from –1.199 to –1.081 V) when pressure-induced Au diffusion was applied, suggesting more difficult etching. A passivation potential, ~–0.595V, appears in both pressure-modulated and nonmodulated samples and can be attributed to formation of a blocking oxide layer (*29*). However, in the conventional Si nanowire sample (red), we identified a shoulder peak centered around –0.785 V, which is not apparent in the Au-incorporated Si sample (black) and can be ascribed to an electrochemical process at Au-free Si nanowire surfaces. Because Au atoms are known to form recombination centers in Si, the random Au-based carrier traps effectively retard adjacent electron-based reactions (*28*, *29*) over the Au-incorporated nanowire shell region. This etching resist effect involves a shallow chemical reaction through individual atoms and is different from that in traditional silicon nitride (Si_xN_y) or Au film–based etching masks, where physical blockage by chemically inert materials plays a key role.

We studied the effect of a *p*-type dopant, B_2H_6, on the spicule morphologies. Results collected in <112> Si spicules (Fig. 3E) demonstrate that as B_2H_6 feeding increases from 1:4000 to 1:1000 (B:Si), the areas of Au-atom–decorated shells (enclosed in dashed yellow lines, Fig. 3E, inset) and the widths along the midline on the remaining {111} facets (dashed red lines, Fig. 3E, inset) increase. Additionally, the midline width versus segment plot (Fig. 3E) exhibits typically zero values in the segments closer to Au catalysts (phase I), followed by a linear increase (phase II, see linear fittings, Fig. 3E), and finally a plateau regime (phase III). The initial absence of Au-protected {111} facets suggests that in <112> Si spicules, {113} facets are the major Au deposition zones, whereas {111} facets are primarily used for Au diffusion and incorporation, which initiate at a later stage (figs. S16). The linear advance of the interface (i.e., $L \propto t$ or $L \propto n$, where n is the segment index) in phase II suggests that the patterned resist formation is a Au/Si reaction–limited process (*18*), because a diffusive one is usually described by nonlinear power laws ($L \propto t^{\alpha}$, $\alpha \leq 0.5$) (*12*). The plateau indicates the merging of Au-incorporated patterns from adjacent segments, after which interconnection is achieved. The higher feeding ratio of B:Si, 1:1000 (red) versus 1: 4000 (blue), yields a larger slope (i.e., 37.6 nm per segment versus 28.7 nm per segment) and an earlier onset (segment 5 versus 9) for the linear regions, suggesting that B_2H_6 can promote Au deposition, diffusion, and incorporation. A similar behavior was observed in <111> Si spicules, and we note that $\{11\bar{2}\}$ facets are primary Au deposition zones (fig. S17).

We tested the effect of an *n*-type dopant, phosphine (PH_3) (Fig. 3F and fig. S18). STEM tomography (Fig. 3F) displayed a mesostructure with less gradient. To achieve optimal growth, we identified an ~15°C higher growth temperature than when B_2H_6 was used, consistent with the fact that PH_3 and B_2H_6 can inhibit and enhance SiH_4 decomposition (*30*), respectively. Additionally, we needed to use an ~5 times longer evacuation time to promote Au coverage, suggesting that PH_3 is less effective than B_2H_6 in enabling the spreading of Au on Si surfaces (figs. S2 and S3) and that such spreading is critical for both efficient Au deposition and diffusion. Finally, if neither B_2H_6 nor PH_3 was added (i.e., intrinsic Si), we observed a larger number of isolated Au nanoparticles on the Si sidewalls (fig. S3), which yielded less-defined mesostructures upon etching (figs. S19 and S20).

We propose a modular deposition-diffusion-incorporation mechanism for patterned-interface (Figs. 1 to 3 and fig. S15) formation. Initially, the Si structure follows vapor-liquid-solid axial growth (Fig. 3G, 1). Upon evacuation, the growth stops (Fig. 3G, 2), and catalyst instability at a low pressure (~0.2 Torr) initiates Au deposition (Fig. 3G, III, graded orange band) and subsequent diffusion (Fig. 3G, II, graded pink band). During SiH_4 pressure recovery in the ramp period, the Au deposition and diffusion cease (*13*), while the Si growth rate increases (Fig. 3G, I, graded blue band) to form a new segment (Fig. 3G, 3). Decomposition of SiH_4 on the Si sidewalls assists robust incorporation of Au atoms into the Si subsurface. Iteration of this process (Fig. 3G, 4 to 6) generates the anisotropic and graded Au/Si interfaces, which

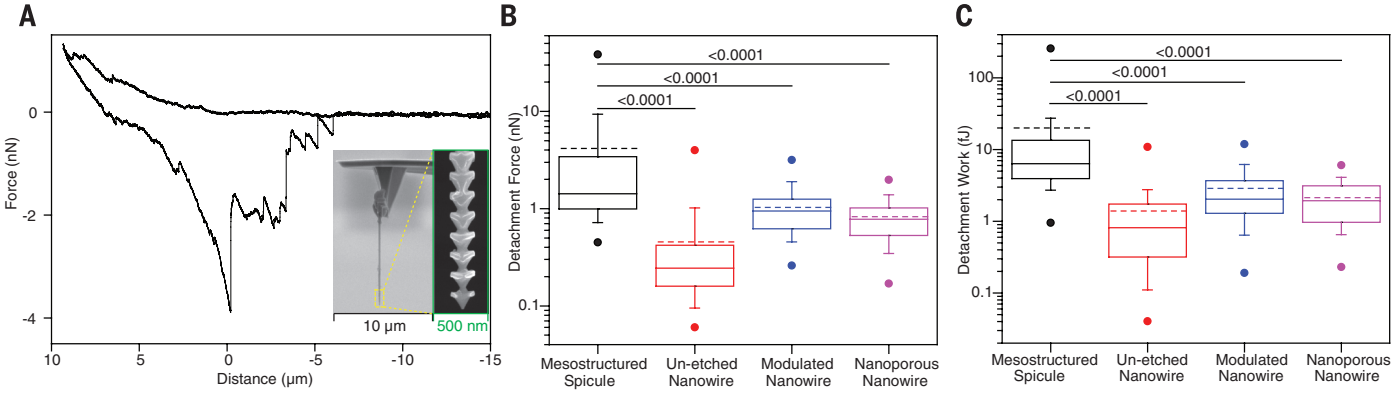

Fig. 4. Si spicules interact strongly with collagen hydrogel. (**A**) Representative *F-D* curves collected using an individual Si spicule as a probe. Insets displace the spicule-based AFM probe at different magnifications. More traces are shown in fig. S26. (**B** and **C**) Box-and-whisker plots of forces (B) and work (C) required to detach Si spicules (black), un-etched Si nanowires (red), diameter-modulated Si nanowires (blue), and nanoporous Si nanowires (purple). Half of the data points are within the box, and 80% are within the whiskers. Solid and dashed lines mark the median and mean, respectively. The dots represent maximum and minimum values. The means of detachment force are 4.16 nN (mesostructured spicule), 0.455 nN (un-etched nanowire), 1.03 nN (modulated nanowire), and 0.827 nN (nanoporous nanowire). The means of detachment work are 20.0 fJ (mesostructured spicule), 1.39 fJ (un-etched nanowire), 2.86 fJ (modulated nanowire), and 2.15 fJ (nanoporous nanowire). n = 50 *F-D* curves per probe, and numbers above bars indicate the *P* value of the Mann-Whitney test.

still shows decent resist quality after 10 months of storage in air (fig. S21). This proposed mechanism is further corroborated by the fact that (i) B-doped nanowires grown without pressure modulation only yielded uniform etching structures (fig. S22) (*18*,*19*); (ii) intentional gold diffusion only at the end of *p*-type nanowire synthesis also yielded etch resist (fig. S23); (iii) diffused Au did not recruit B (figs. S14 and S15), which is known to affect Si etching; and (iv) possible B incorporation directly from the gas phase is along the spicule radial direction, which is orthogonal to the direction for resist formation. Overall, we showed that dopant incorporation or nanowire initial morphology itself cannot yield the observed complex structures. The curvatures of the final spicules are defined by the shapes of patterned resists, curved catalyst/Si interfaces, crystallographic orientations, and etching conditions (fig. S24). The initial isolated Au nanoparticles play multiple roles, such as catalyzing Si growth, defining edge curvature, and supplying diffused Au atoms and clusters (fig. S25). Finally, we note that because metal diffusion along semiconductor surfaces is general, as in GaP-Au (*15*), GaAs-Au (*15*), and Si-In/Sn (*10*) systems, a similar patterning and lithography approach may be applied in other semiconductors.

The anisotropic mesoscale texture of Si spicules suggests that they may have different interactions with surrounding matrices such as hydrogels or biological tissues, as compared to other more isotropic Si structures such as diameter-modulated nanowires (*18*, *19*). To test this possibility, we first mounted single mesostructured Si spicules (<112>-oriented, *p*-type) onto atomic force microscopy (AFM) cantilever tips with a focused ion-beam system (Fig. 4A, inset). Next, by approaching/retracting the spicules to/from collagen type I hydrogel [materials and methods in (*18*) and fig. S26], we were able to monitor the force and work of the spicule-matrix interactions in both the forward and reverse directions. For each recording, we chose a fresh location over the hydrogel surface. To study the effects of probe geometry and surface, we performed control measurements (figs. S26 and S27) with an un-etched Si nanowire, a uniform diameter-modulated Si nanowire (*18*, *19*), and a nanoporous Si nanowire (*18*). A representative force-distance (*F-D*) curve recorded from the Si spicule probe exhibits a detachment force of ~3.9 nN and a detachment work of ~15.6 fJ (Fig. 4A). Statistical analyses of *F-D* measurements with the single Si spicule and different Si nanowire probes (Fig. 4, B and C; $n = 50$ *F-D* curves per probe) demonstrates that the anisotropic mesostructure, rather than surface area or nanoscale roughness, yields a major enhancement in detachment force and detachment work (figs. S26 and S27). The observation that the anisotropic spicule requires the largest detachment force from collagen is reminiscent of natural systems, such as a bee's stinger, which can become rooted in skin. This suggests the potential of adopting mesostructured Si spicules for building tight junctions with other soft materials, such as in tissue-interfacing adhesives or bioelectronics.

REFERENCES AND NOTES

1. S. Tawfick *et al.*, *Adv. Mater.* **24**, 1628–1674 (2012).
2. S. Xu *et al.*, *Science* **347**, 154–159 (2015).
3. J. A. Rogers, T. Someya, Y. Huang, *Science* **327**, 1603–1607 (2010).
4. V. B. Shenoy, D. H. Gracias, *MRS Bull.* **37**, 847–854 (2012).
5. S. Mann, G. A. Ozin, *Nature* **382**, 313–318 (1996).
6. G. V. Naik, V. M. Shalaev, A. Boltasseva, *Adv. Mater.* **25**, 3264–3294 (2013).
7. T. Ozel, G. R. Bourret, C. A. Mirkin, *Nat. Nanotechnol.* **10**, 319–324 (2015).
8. M. Cusack, A. Freer, *Chem. Rev.* **108**, 4433–4454 (2008).
9. O. Moutanabbir *et al.*, *Nature* **496**, 78–82 (2013).
10. W. H. Chen *et al.*, *Nat. Commun.* **5**, 4134 (2014).
11. E. R. Hemesath *et al.*, *Nano Lett.* **12**, 167–171 (2012).
12. N. Ferralis, F. El Gabaly, A. K. Schmid, R. Maboudian, C. Carraro, *Phys. Rev. Lett.* **103**, 256102 (2009).
13. P. Madras, E. Dailey, J. Drucker, *Nano Lett.* **10**, 1759–1763 (2010).
14. J. B. Hannon, S. Kodambaka, F. M. Ross, R. M. Tromp, *Nature* **440**, 69–71 (2006).
15. K. A. Dick, K. Deppert, L. Samuelson, L. R. Wallenberg, F. M. Ross, *Nano Lett.* **8**, 4087–4091 (2008).
16. M. I. den Hertog *et al.*, *Nano Lett.* **8**, 1544–1550 (2008).
17. J. E. Allen *et al.*, *Nat. Nanotechnol.* **3**, 168–173 (2008).
18. See the supplementary materials on *Science* Online.
19. J. D. Christesen, C. W. Pinion, E. M. Grumstrup, J. M. Papanikolas, J. F. Cahoon, *Nano Lett.* **13**, 6281–6286 (2013).
20. S. K. Lim, S. Crawford, G. Haberfehlner, S. Gradečak, *Nano Lett.* **13**, 331–336 (2013).
21. I. R. Musin, D. S. Boyuk, M. A. Filler, *J. Vac. Sci. Technol. B* **31**, 020603 (2013).
22. F. M. Ross, J. Tersoff, M. C. Reuter, *Phys. Rev. Lett.* **95**, 146104 (2005).
23. R. E. Algra *et al.*, *Nature* **456**, 369–372 (2008).
24. R. W. Day *et al.*, *Nat. Nanotechnol.* **10**, 345–352 (2015).
25. L. Zhao, A. C. L. Siu, J. A. Petrus, Z. He, K. T. Leung, *J. Am. Chem. Soc.* **129**, 5730–5734 (2007).
26. O. C. Hellman, J. A. Vandenbroucke, J. Rüsing, D. Isheim, D. N. Seidman, *Microsc. Microanal.* **6**, 437–444 (2000).
27. N. A. Stolwijk, B. Schuster, J. Holzl, H. Mehrer, W. Frank, *Physica B+C* **116**, 335–342 (1983).
28. H. Seidel, L. Csepregi, A. Heuberger, H. Baumgartel, *J. Electrochem. Soc.* **137**, 3612–3626 (1990).
29. L. C. Chen, M. J. Chen, C. H. Lien, C. C. Wan, *J. Electrochem. Soc.* **142**, 170–176 (1995).
30. B. Mehta, M. Tao, *J. Electrochem. Soc.* **152**, G309–G315 (2005).

ACKNOWLEDGMENTS

This work is supported by NSF [NSF CAREER, grant DMR-1254637; and NSF Materials Research Science and Engineering Centers (MRSEC), grant DMR-0820054], the Searle Scholars Foundation, the Air Force Office of Scientific Research (grant AFOSR FA9550-14-1-0175), and the University of Chicago startup fund. APT was performed at NUCAPT, whose APT was purchased and upgraded with funding from NSF–Major Research Instrumentation Program (grant DMR-0420532) and the Office of Naval Research–Defense University Research Instrumentation Program (grants N00014-0400798, N00014-0610539, and N00014-0910781). Instrumentation at NUCAPT was further upgraded by the Initiative for Sustainability and Energy at Northwestern. This work also made use of the EPIC facility (NUANCE Center–Northwestern University), which has received support from the NSF MRSEC program (grant NSF DMR-1121262) at the Materials Research Center and from the International Institute for Nanotechnology (IIN); and the State of Illinois, through the IIN. Part of this research is sponsored by the Air Force Research Laboratory (grant FA9550-12-1-0280). The authors thank L. Yu, Q. Guo, J. Jureller, J. Austin II, Y. Chen, S.-I. Baik, and T. A. Witten for technical support and stimulating discussion.

SUPPLEMENTARY MATERIALS

www.sciencemag.org/content/348/6242/1451/suppl/DC1
Materials and Methods
Supplementary Text
Figs. S1 to S27
References (*31*–*35*)

11 June 2014; accepted 19 May 2015
10.1126/science.1257278

HIGH-PRESSURE PHYSICS

Direct observation of an abrupt insulator-to-metal transition in dense liquid deuterium

M. D. Knudson,[1]* M. P. Desjarlais,[1] A. Becker,[2] R. W. Lemke,[1] K. R. Cochrane,[1] M. E. Savage,[1] D. E. Bliss,[1] T. R. Mattsson,[1] R. Redmer[2]

Eighty years ago, it was proposed that solid hydrogen would become metallic at sufficiently high density. Despite numerous investigations, this transition has not yet been experimentally observed. More recently, there has been much interest in the analog of this predicted metallic transition in the dense liquid, due to its relevance to planetary science. Here, we show direct observation of an abrupt insulator-to-metal transition in dense liquid deuterium. Experimental determination of the location of this transition provides a much-needed benchmark for theory and may constrain the region of hydrogen-helium immiscibility and the boundary-layer pressure in standard models of the internal structure of gas-giant planets.

In 1935, Wigner and Huntington (*1*) were the first to predict that when squeezed to sufficiently high density (ρ) and pressure (*P*), hydrogen would undergo a density-driven transition from an insulating, molecular solid to a conducting, atomic solid. Subsequently, this fundamental question of precisely how and at what *P* hydrogen metallizes at low temperature (*T*) has become one of the longest-standing open questions of high-pressure physics (*2*). More recently, there has been much interest in the analogous molecular insulator to atomic metal transition in the liquid at low *T* just above the melt line, largely due to its relevance to planetary science (*3*, *4*). A metallization transition in this region could provide a constraint for the

[1]Sandia National Laboratories, Albuquerque, NM, USA. [2]Institute of Physics, University of Rostock, Rostock, Germany.
*Corresponding author. E-mail: mdknuds@sandia.gov

Downloaded from www.sciencemag.org on June 26, 2015

low-*P* boundary of the region of hydrogen-helium immiscibility; first-principles calculations suggest that hydrogen metallization acts as a catalyst for hydrogen-helium demixing (*5*). This phenomenon, resulting in an additional energy source through latent heat and gravitational settling of helium, may play an important role in the evolution of the gas giants and has been proposed as a possible solution to the luminosity problem of Saturn (*3*, *4*). This phenomenon could also provide justification for the presence of a layer boundary in the interior of gas-giant planets, a necessary feature of the often-used three-layer model (*6*), which has shown reasonable success in describing observables of Jupiter and Saturn (*7*).

Experimental observation of this transition would also provide a benchmark for first-principles theoretical models of this phenomenon that fall into the category of density functional theory (DFT) within the generalized gradient approximation (GGA). Studies (*8*–*10*) using semilocal density functionals (DF), such as Perdew-Burke-Ernzerhof (PBE) (*11*), suggest the presence of a first-order liquid-liquid, insulator-to-metal transition (LL-IMT). The transition boundary in pressure-temperature (*PT*) space ends in a critical point at ~1500 to 2000 K, with negative slope (*dT*/*dP*) between ~2000 and 800 K and ~100 and 200 GPa (Fig. 1). This transition is predicted to be a ρ-driven dissociative transition in the liquid and appears similar to the so-called plasma phase transition (PPT) suggested to exist as a first-order transition in the partially ionized plasma domain at finite *T* (*12*, *13*). However, the DFT simulations predict this transition in the dense liquid at considerably lower *T* and higher *P*, analogous to the long-ago proposed IMT in the solid (*1*, *2*).

More recent studies (*14*, *15*) have looked at nonlocal functionals such as the hybrid Heyd-Scuseria-Ernzerhof (HSE) (*16*) and the van der Waals vdW-DF2 (*17*), as well as nuclear quantum effects (NQE) through the use of path integral molecular dynamics (PIMD) methods. We investigated vdW-DF2 and a second van der Waals functional, vdW-DF1 (*18*, *19*). These nonlocal DFs predict a transition *P* between ~200 and 400 GPa (Fig. 1) and also exhibit a critical point at ~2000 K (*18*). A phase boundary as high as ~400 to 600 GPa has been predicted using quantum Monte Carlo (QMC) techniques (*20*). Although all of these first-principles approaches exhibit a first-order LL-IMT in the warm dense fluid, the transition *P* and ρ are extremely sensitive to the choice of method and DF. This results in a predicted transition *P* that differs by as much as 400 to 500 GPa and a ρ at the transition of ~0.75 to 1.5 g/cc for hydrogen and ~1.5 to 3 g/cc for deuterium (figs. S19 and S20).

Earlier shock-wave reverberation experiments observed a continuous IMT via electrical conductivity measurements at ~140 GPa (measured) and ~3 kK (calculated) (*21*–*23*). In a similar *P* (calculated) and *T* (calculated) range, another group reported observation of an increase in ρ in conjunction with the continuous increase in conductivity (*24*). The IMT has also been explored in the predominately *T*-driven regime (~40 to 100 GPa and ~5 to 20 kK) through precompressed laser-shock experiments (*25*, *26*). However, these results are at considerably higher *T*, above the predicted critical points reported in the first-principles studies (figs. S19 and S20). High-*P* studies of the solid hydrogen phase diagram have not reported metallization (*2*, *27*). Static measurements have interpreted plateaus in the *T*-laser power curve as an observation of latent heat of a LL transition (*28*). However, the source of these plateaus could be due to changes in thermal conduction or the optical properties of the sample instead of a first-order transition (*29*).

Here, we present the results of a series of dynamic compression experiments on liquid deuterium performed at the Sandia Z machine (*30*), a pulsed-power generator capable of producing large pulsed currents (~20 MA) and magnetic field densities (~10 MG) within a low inductance load. These current and field densities produce magnetic pressures of several hundred GPa. The pulsed nature of the experiment allows inertia to hold the load assembly together for the duration of interest. With proper design of the experimental configuration and precise current pulse shaping, liquid deuterium samples were driven to more than 300 GPa while remaining below 1800 K. These experiments show a dramatic increase in reflectivity of the deuterium samples, indicative of an abrupt increase in conductivity between 280 and 305 GPa. We interpret this signal as evidence of an abrupt, ρ-driven LL-IMT.

Liquid deuterium samples were condensed in a cryocell (Fig. 2 and fig. S3) by filling a cavity with high-purity deuterium gas at 124 kPa (18 pounds per square inch) and cooling the cryocell to 22.0 ± 0.1 K, producing a quiescent liquid sample with nominal initial ρ of 0.167 g/cc (±0.4%). The cryocell was positioned a short distance from an aluminum electrode. Upon discharge of the accelerator capacitor banks, a shaped current pulse flowed through the experimental load. The initial increase in current accelerated the electrode across the gap, producing a shock within the front plate of the cryocell at impact, resulting in a series of shock-wave reverberations that stepwise-loaded the deuterium sample to ~800 to 1400 K, depending on the experiment. The subsequent increase in current drove a ramp compression wave into the cryocell, further compressing the deuterium sample along an isentrope to peak *P* and ρ of more than 300 GPa and 2 g/cc. Varying the magnitude of the initial shock enabled access to different *T* isentropes, allowing a range of *PT* space to be explored.

The liquid deuterium samples were diagnosed using fiber-optic–coupled diagnostics. A velocity interferometer (VISAR) (*31*) measured the velocity of the aluminum/deuterium and the deuterium/LiF interface (reflecting off an aluminum coating on the LiF window), using 532-nm laser light. Spectrally and temporally resolved reflectivity was measured using a spectrometer (450- to 650-nm bandwidth) coupled to a streak camera. The interferometer signal from the deuterium sample (Fig. 2) originally reflecting off the aluminum/deuterium interface is lost at ~2650 ns (~120 GPa). The signal suddenly reappears at ~2800 ns (~280 GPa), only to abruptly disappear again upon decompression at ~2880 ns (as *P* drops below ~280 GPa). In contrast, the interferometer signal reflecting from the deuterium/LiF interface is maintained throughout the experiment, albeit with a transient drop at ~2780 to 2800 ns that slightly precedes the reemergence of the signal originating from the aluminum/deuterium interface.

The spectral dependence of the reflected signal was obtained by determining the relative reflectivity with respect to aluminum (*18*) as a function of wavelength and time (Fig. 3). Before the loss of

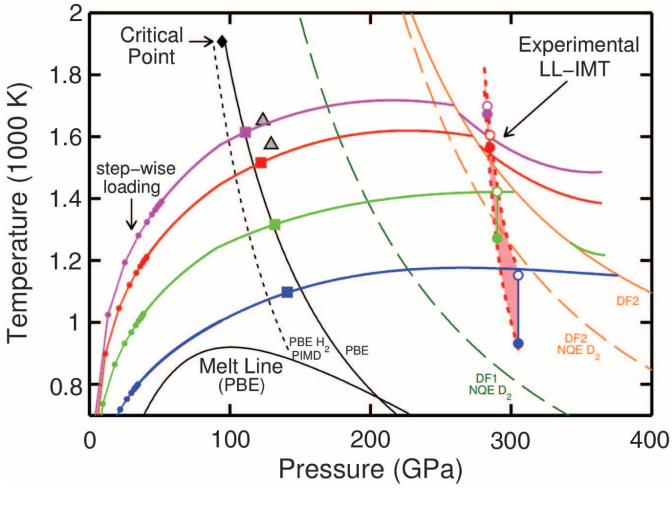

Fig. 1. Deuterium *PT* diagram. Melt line, (*9*). Theoretical LL-IMT phase boundaries: Black line, PBE (*9*); short dashed black line, PBE+PIMD (*15*); dashed green line, vdW-DF1+NQE for deuterium (this work); orange line, vdW-DF2 (this work); dashed orange line, vdW-DF2 +NQE for deuterium (this work). Experiment: gray triangles (*28*). The experimental *PT* paths from this work are shown as the nearly horizontal solid lines, the result of stepwise loading (shock reverberation) followed by ramp compression. The colored squares at ~120 to 150 GPa indicate where the deuterium is observed to become opaque as the band gap closes to ~2.1 eV. The shaded red region indicates the experimentally determined location of the LL-IMT. Open circles denote the estimated *T* at the phase boundary, neglecting any latent heat, and the closed circles include an estimate of the latent heat obtained by matching isentropes on either side of the phase boundary through thermodynamic integration using the vdW-DF2 functional (*18*). See (*18*) for an expanded version of this figure.

signal at ~120 GPa, the reflectivity ratio is essentially unity, indicating that the reflection is occurring at the aluminum/deuterium interface (i.e., the deuterium is transparent). Upon reappearance of the signal at ~280 GPa, a reflectivity ratio of just over 60% is observed throughout the visible range of 450 to 650 nm (1.9 to 2.75 eV) (Fig. 3C). DFT simulations of aluminum at these conditions (~1000 K and ~300 GPa) suggest an aluminum reflectivity in this wavelength range of ~72% (fig. S8). This implies an absolute reflectivity measurement in these experiments of ~45% in this wavelength range, consistent with DFT calculations for the atomic fluid phase of hydrogen (fig. S6).

This behavior suggests that, as deuterium is compressed above ~120 GPa, it loses transparency, indicating that the band gap closes to ~2 to 2.5 eV, resulting in strong absorption in the visible spectrum. The inferred band gap from a reanalysis of the Weir *et al.* experiments (*21*–*23*) is consistent with this picture (fig. S17B). Furthermore, DFT simulations of deuterium suggest a sharp increase in the absorption coefficient at a photon energy corresponding to the band gap. The band gap decreases with increasing P and drops below ~2 to 2.5 eV at ~125 to 150 GPa (fig. S9), in reasonable agreement with the experimental observations (fig. S10). Upon further increase in P, the observed sharp increase in deuterium reflectivity is indicative of an abrupt IMT. Consistent with DFT simulations in the metallic fluid, the observed reflectivity (Fig. 3C) is featureless over a broad energy range (1.9 to 2.75 eV). This increase in reflectivity in the visible is concurrent with a dramatic increase in the calculated DC conductivity. The observed absolute reflectivity of ~45% suggests DC conductivity of a few 10^5 S/m (fig. S7), the same magnitude as that observed by Weir *et al.*, albeit at considerably higher T.

The thermodynamic state of the bulk deuterium sample was determined through the measured apparent velocity at the deuterium/LiF interface and numerical simulations. Given the mechanical and optical response of LiF, one can determine P as a function of time, t [$P(t)$], which does not depend upon the deuterium equation of state (EOS), to a precision of ~2 to 3% at the aluminum/deuterium interface (*18*). The resulting $P(t)$ in the deuterium also provides $T(t)$ and $\rho(t)$ for a given deuterium EOS. We performed this using the Kerley03 EOS for deuterium (*32*) (figs. S11 and S12). The resulting PT paths show the majority of the T increase occurring during the first several shock reverberations (Fig. 1 and fig. S12). This happens well within the molecular fluid phase at relatively low P and ρ, where the Kerley03 EOS (*32*) reasonably reproduces Hugoniot measurements of deuterium (*33*, *34*).

DFT simulations suggest that dissociation becomes important at higher P and ρ (*2*). The Kerley03 EOS may not accurately describe the warm dense fluid in this region because it uses the chemical model representation, so we only rely on the EOS to calculate the state of the sample through the shock-wave reverberation portion of the experiment (up to 100 GPa). Further increases in T are modeled using DFT calculations with the vdW-DF2 functional (Fig. 1 and fig. S15). Although the initial trajectory of the DFT isentropes is similar to that of Kerley03, the increase in T with P begins to diminish, eventually becoming negative as the transition P is approached. This behavior is due to the emergence of dissociation, indicating that appreciable dissociation occurs before the first order LL-IMT. Despite exhibiting differences in $T(P)$ along the isentropes, $\rho(P)$ for the various DFT functionals and the Kerley03 EOS are quite similar, varying by only a few percent (*18*), reaching ~2.14 g/cc (~12.8-fold compression) at 320 GPa (fig. S13). Thus, despite not having a direct ρ measurement in these experiments, the measured $P(t)$ provides an accurate estimate of $\rho(t)$.

Several features become apparent when considering the observed optical changes with respect to the thermodynamic state of the deuterium sample (Fig. 4). The small but measurable increase in reflectivity that precedes the abrupt reflectivity increase appears to coincide with the transient drop in the interferometer signal from the aluminum/LiF interface (Fig. 2). This drop in signal is due to a transient loss of contrast in the interferometer system and is explained by the presence of velocity dispersion in the Doppler-shifted light (*18*). The results observed in these experiments are consistent with ~1% peak velocity dispersion (fig. S14), indicating a transient spatial velocity heterogeneity immediately before the substantial increase in reflectivity. This behavior suggests a small (~1 to 2%) ρ discontinuity between the molecular and atomic fluid, indicative of a first-order transition and the emergence of dissociation before the abrupt increase in reflectivity.

The asymmetry in the deuterium reflectivity with P (Fig. 4) is likely explained by the effects of thermal conduction. The observed reflectivity signal emanates from the deuterium/LiF interface, within a few hundred angstrom optical depth (*18*). Hydrodynamic simulations of the experimental configuration indicate a ΔT between the bulk deuterium and LiF of between 800 and 1400 K, depending on the experiment; deuterium is considerably more compressible than LiF, resulting in a much higher T with compression (fig. S15). Because both the molecular fluid and the LiF are poor thermal conductors, the interface T before metallization will be somewhere near the average T of the bulk deuterium and LiF, and a thermal gradient in the deuterium of several hundred K will develop. Upon metallization, the thermal conductivity of the atomic fluid will increase by roughly two orders of magnitude (as determined by vdW-DF2), and the thermal gradient will rapidly

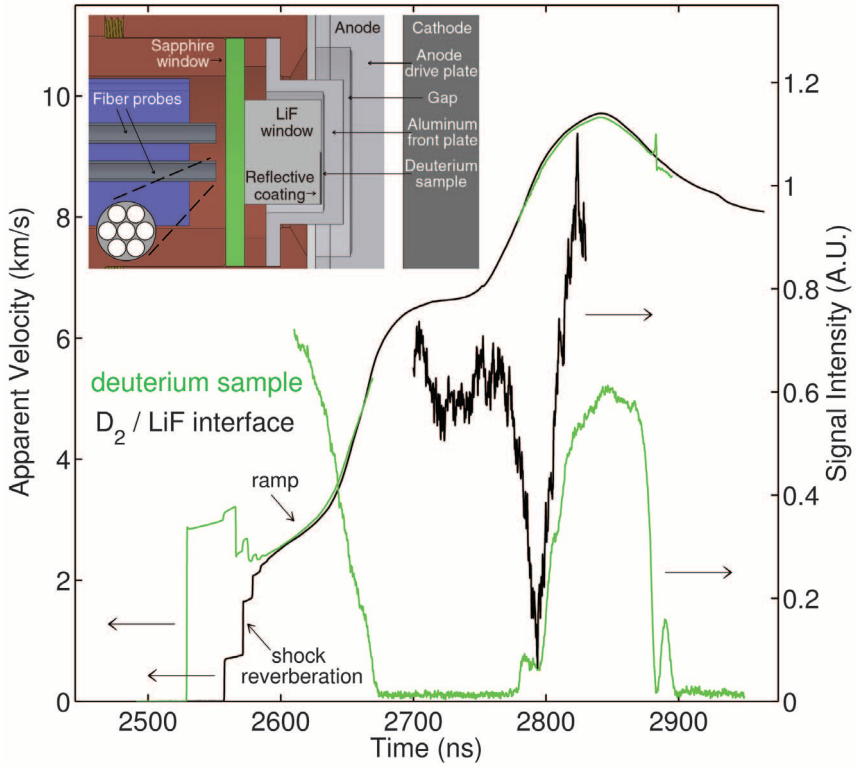

Fig. 2. Experimental profiles. Measured apparent velocities (left axis) from the deuterium sample, originally reflecting from the aluminum/deuterium interface (green line) and the reflective coating on the deuterium/LiF interface (black line). Data correspond to the green PT path in Fig. 1. Also shown are the magnitudes of the interferometer signals from these locations (right axis). The interferometer signal from the deuterium sample is lost as the deuterium becomes opaque due to the band gap closing to ~2.33 eV (the photon energy of the laser), recovers as the deuterium is driven across the IMT, and finally is lost again as the deuterium P drops back below the IMT. The interferometer signal at the deuterium/LiF interface is maintained throughout the duration of the experiment but shows a transient loss of contrast immediately before metallization, indicating the presence of spatial heterogeneity in velocity and, likely, ρ. Inset shows a schematic view of the experimental load (*18*).

diminish as the entire deuterium sample approaches the bulk deuterium T (fig. S16). Therefore, consistent with observation, the change in reflectivity should appear sluggish as P increases and rather sharp as P drops. Due to these effects, the clearest indication of P at the transition boundary corresponds to the abrupt drop in reflectivity upon release in P.

The oscillatory behavior of reflectivity upon further release in P is not fully understood. However, the oscillations are suggestive that the PT path in the experiment is not truly isentropic across the transition. If the transition were indeed first-order, it would not be unexpected in a dynamic experiment for the system to traverse the transition nonisentropically. Furthermore, the effects of thermal conduction at the deuterium/LiF interface may offset any T increase due to latent heat (fig. S16D), resulting in a PT path for deuterium near the interface that is more like an isotherm than an isentrope (*18*). Either of these effects could set up transient features that would oscillate as waves reflect back and forth across the sample cell, which at these conditions is on the order of 10 μm in thickness.

Given that the clearest signature of the transition is upon release in P, there is a complication in estimating T at the transition due to the latent heat. Because we cannot definitively state that the observed transition is first-order, nor can we conclude that a first-order transition would be traversed isentropically in such a dynamic experiment, we consider two extremes. As an upper bound for T at the transition, we consider T along the isentrope at P that coincides with the abrupt drop in reflectivity, neglecting any latent heat. As a lower bound, we use first-principles DFT simulations using the vdW-DF2 functional to estimate the latent heat across the transition through thermodynamic integration (*18*). The resulting bounds are connected by vertical lines in Fig. 1. We note that the effect of thermal conduction at the interface is a further complication in determining T at the transition. The ΔT between the bulk deuterium T and the interface T as P drops back across the transition can be a few hundred K for reasonable values of thermal conductivity of deuterium and LiF (fig. S16). This uncertainty would potentially result in a uniform shift in the boundary shown in Fig. 1 to lower T. Given the relative steepness in dT/dP of the experimentally determined boundary, the uncertainty in T does not result in an appreciable uncertainty in the boundary location in PT space.

With relatively weak dependence on T, as liquid deuterium is compressed to high P the band gap begins to decrease, reaching ~2 to 2.5 eV at ~120 to 150 GPa. The inferred band gap from a reanalysis of the Weir *et al.* experiments (*21*–*23*) is consistent with this picture. This vicinity where we observe extinction of our probe laser and broadband light is very close to where Dzyabura *et al.* (*28*) report the observation of latent heat in their experiments. Attenuation of light as the band gap begins to close, with stronger absorption at higher photon energies, might explain the observed plateau in the T-laser power curve. Upon further compression, signs of dissociation—as evidenced by the onset of reflectivity and the appearance of heterogeneity in velocity and, possibly, ρ—emerge at ~230 to 250 GPa. Finally, a very abrupt increase in reflectivity is observed at ~280 to 305 GPa, indicative of an IMT. The relative insensitivity of the transition to T suggests that this is a ρ-driven transition occurring at ~2 to 2.1 g/cc in deuterium. Although we cannot definitively state that this transition is first-order, the abruptness of the transition, the observed heterogeneity preceding the transition, and the transient oscillations in reflectivity upon release in P back across the transition all suggest that the transition is indeed first-order.

It is instructive to compare and contrast the present study with that performed by Weir *et al.* (*21*, *22*). Both studies used dynamic compression to reach the high-ρ, low-T region of the hydrogen phase diagram. Weir *et al.* were constrained by achievable end states in shock-wave reverberation experiments. By combining lower initial shocks with subsequent ramp compression, we were able to reach both higher ρ and lower T. Both studies

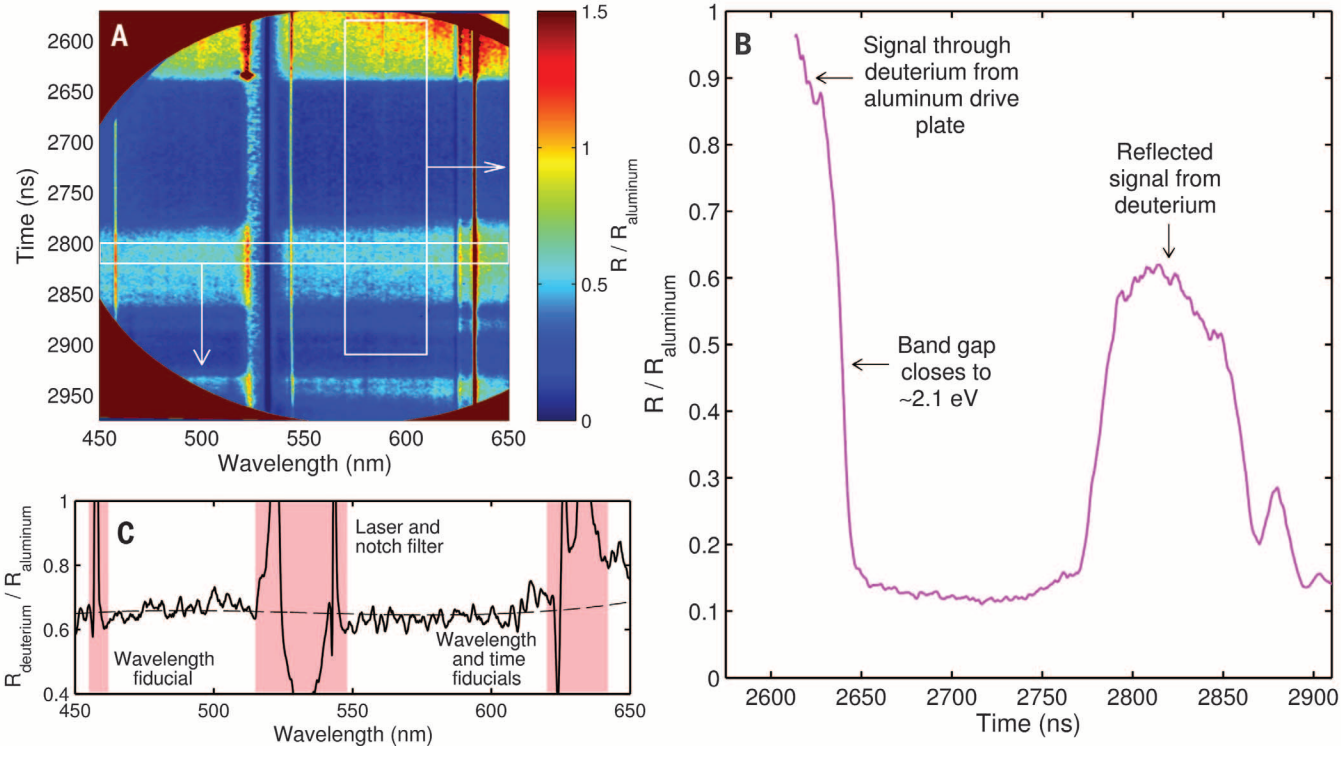

Fig. 3. Spectral and temporal dependence of reflected signal. (**A**) Measured reflectivity with respect to aluminum reflectivity versus both wavelength and time. Data corresponds to the magenta PT path in Fig. 1. (**B**) Line-out of reflectivity with respect to aluminum reflectivity (average over 570 to 610 nm, ~2.1 eV) versus time, showing that, early in time, the reflected signal originates at the aluminum/deuterium interface. Later in time, the deuterium becomes opaque as the band gap closes to ~2 to 2.5 eV and eventually reflective as the deuterium is driven above the IMT. Upon release back below the IMT, the reflectivity is lost. (**C**) Line-out of deuterium reflectivity with respect to aluminum reflectivity (average over 2800 to 2820 ns, during peak compression) versus wavelength, showing a featureless reflectivity ratio of over 60% throughout the visible spectrum. This corresponds to an absolute reflectivity of deuterium of ~45% in the metallic fluid phase (*18*).

measured P and relied on a deuterium EOS and numerical simulation to infer ρ and T. Weir *et al.* measured the DC conductivity at the end state of the shock reverberation and had to perform numerous experiments, each at subsequently higher ρ and T, making it difficult to isolate the relative contribution of ρ and T to the observed gradual increase in conductivity. By directly observing the deuterium sample throughout the experimental duration, we were able to monitor the optical properties of deuterium as a function of ρ at relatively constant T (Fig. 1). Our experiments reveal a very abrupt increase in optical reflectivity correlated with an equally abrupt increase in DC conductivity (as demonstrated in the corresponding DFT calculations), reaching values similar to those reported by Weir *et al.* The relative T insensitivity of this abrupt increase supports our assertion that, at the low T achieved in these experiments, deuterium undergoes a ρ-driven transition to a metallic fluid.

In this regime, the measured LL-IMT boundary P is well above the first-principles GGA predictions, well below the recently proposed QMC boundary, and is in best agreement with the two nonlocal van der Waals functionals. However, the experimentally determined dT/dP is much steeper. At the lowest T (~800 to 1000 K), the observed transition P is more consistent with the vdW-DF1 functional. This is in accordance with the suggestion that the vdW-DF1 functional is more accurate due to better agreement with QMC calculations at 0 K (*35*). However, our results at higher T suggest that this favorable comparison at 0 K may not hold at finite T. At higher T (~1800 K), the observed transition P is somewhat higher than that predicted by the vdW-DF2 functional. This behavior is similar to a detailed comparison of the various DFs with the Weir *et al.* (*21*, *22*) experiments, which probe the IMT at ~3000 K (fig. S18). Finally, Morales *et al.* (*15*) has shown good agreement between measured reflectance from precompressed laser-shock experiments (*25*, *26*) that probe the IMT at even higher T (~5 to 20 kK) to reflectance calculated at the relevant PT conditions using the vdW-DF2 functional. All of these comparisons suggest that the IMT is best described by the nonlocal van der Waals functionals, with perhaps a more complex T dependence, especially at low T (figs. S19 and S20).

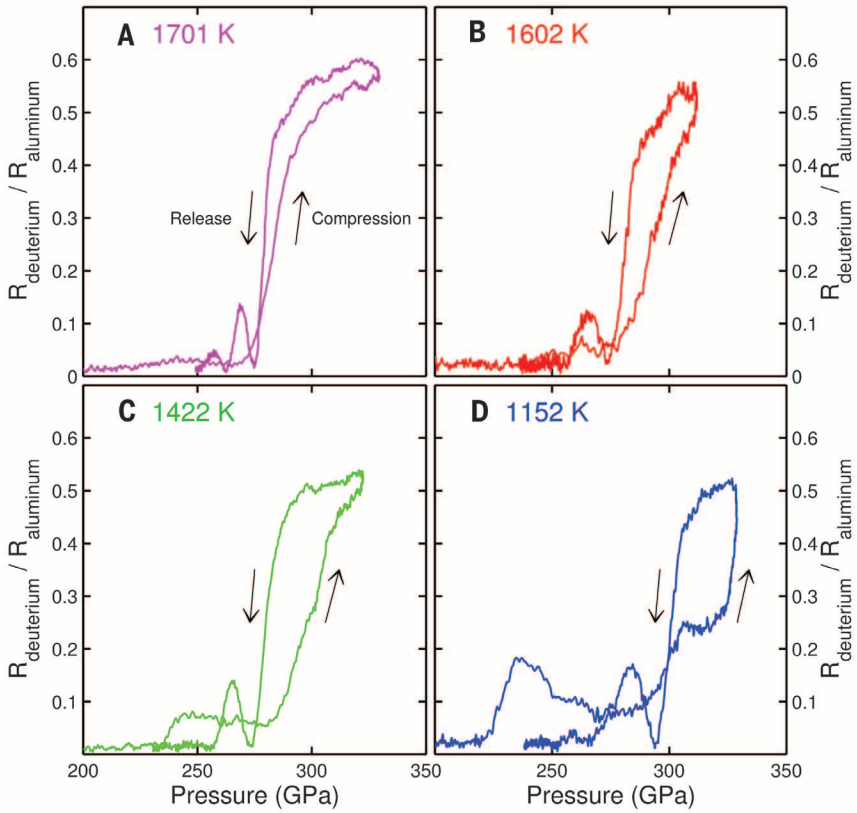

Fig. 4. Reflectivity versus *P*. Measured deuterium reflectivity with respect to aluminum reflectivity (from the interferometer) versus P for each experiment. (**A** to **D**) denote the highest- to lowest-T experiments, respectively. Colors correspond to the PT paths displayed in Fig. 1. T indicated in each panel corresponds to the estimated T at the phase boundary, neglecting any latent heat. All experiments show an asymmetry in the deuterium reflectivity with P; the drop in reflectivity upon P release is considerably sharper than the increase in reflectivity upon compression. This asymmetry, which is more pronounced at lower T, is likely due to the effects of thermal conduction (*18*). All experiments also show a small but measurable reflectivity that precedes the abrupt reflectivity increase, which again is more pronounced at lower T. Finally, all experiments show oscillatory behavior of the reflectivity upon further release of P below the IMT boundary.

In contrast to the gradual, continuous transitions observed in previous higher-T dynamic-compression experiments (*21*, *22*, *25*, *26*), we observe an abrupt LL-IMT at ~300 GPa and ~2 to 2.1 g/cc at low T. These results place a tight constraint on P and ρ of this transition in a regime that is strongly ρ-driven, is predicted to be first-order, and where the largest differences are observed for various first-principles methods and DFs. Furthermore, our results suggest why metallization has been challenging to observe in the solid, because the likely transition P exceeds what is currently achievable with static compression methods with hydrogen. Finally, these results imply that first-principles methods using semilocal DFs such as GGA considerably underestimate P for the LL-IMT in hydrogen at low T. Consequently, estimates for the low-P boundary of the region of hydrogen-helium immiscibility, which have been calculated using GGA (*5*), are likely also considerably underestimated. In addition to providing insight into one of the longest-standing open questions of high-pressure physics, our measurement of the metallization P of hydrogen in the warm dense liquid suggests that the low-P boundary of the immiscibility region should be at or above ~300 GPa. This boundary location will affect the fractions of Saturn and Jupiter that are thought to lie within the immiscibility region and will likely alter our understanding of the structure and evolution of these and other gas-giant planets.

REFERENCES AND NOTES

1. E. Wigner, H. B. Huntington, *J. Chem. Phys.* **3**, 764 (1935).
2. J. M. McMahon, M. A. Morales, C. Pierleoni, D. M. Ceperley, *Rev. Mod. Phys.* **84**, 1607–1653 (2012).
3. R. Smoluchowski, *Nature* **215**, 691–695 (1967).
4. E. E. Salpeter, *Astrophys. J.* **181**, L83 (1973).
5. W. Lorenzen, B. Holst, R. Redmer, *Phys. Rev. B* **84**, 235109 (2011).
6. T. Guillot, *Science* **286**, 72–77 (1999).
7. N. Nettelmann, A. Becker, B. Holst, R. Redmer, *Astrophys. J.* **750**, 52 (2012).
8. I. Tamblyn, S. A. Bonev, *Phys. Rev. Lett.* **104**, 065702 (2010).
9. M. A. Morales, C. Pierleoni, E. Schwegler, D. M. Ceperley, *Proc. Natl. Acad. Sci. U.S.A.* **107**, 12799–12803 (2010).
10. W. Lorenzen, B. Holst, R. Redmer, *Phys. Rev. B* **82**, 195107 (2010).
11. J. P. Perdew, K. Burke, M. Ernzerhof, *Phys. Rev. Lett.* **77**, 3865–3868 (1996).
12. L. D. Landau, Y. B. Zeldovich, *Acta Physico-Chimica U.S.S.R.* **18**, 380 (1943).
13. W. Ebeling, W. Richert, *Phys. Status Solidi B* **128**, 467–474 (1985).
14. W. Lorenzen, A. Becker, R. Redmer, Progress in warm dense matter and planetary physics, in *Frontiers and Challenges in Warm Dense Matter*, F. Graziani, M. P. Desjarlais, R. Redmer, S. B. Trickey, Eds. (Springer, Switzerland, 2014), pp. 203–234.
15. M. A. Morales, J. M. McMahon, C. Pierleoni, D. M. Ceperley, *Phys. Rev. Lett.* **110**, 065702 (2013).
16. J. Heyd, G. Scuseria, M. Ernzerhof, *J. Chem. Phys.* **118**, 8207 (2003).
17. K. Lee, E. D. Murray, L. Kong, B. I. Lundqvist, D. C. Langreth, *Phys. Rev. B* **82**, 081101 (2010).
18. Materials and methods are available as supplementary materials on *Science* Online.
19. M. Dion, H. Rydberg, E. Schröder, D. C. Langreth, B. I. Lundqvist, *Phys. Rev. Lett.* **92**, 246401 (2004).
20. G. Mazzola, S. Yunoki, S. Sorella, *Nat. Commun.* **5**, 3487 (2014).
21. S. T. Weir, A. C. Mitchell, W. J. Nellis, *Phys. Rev. Lett.* **76**, 1860–1863 (1996).
22. W. J. Nellis, S. T. Weir, A. C. Mitchell, *Phys. Rev. B* **59**, 3434–3449 (1999).
23. A reanalysis of the Weir *et al.* experiments (*18*) results in higher inferred T and a systematically larger band-gap energy (~1 eV larger) than those reported in (*21*, *22*).
24. V. E. Fortov *et al.*, *Phys. Rev. Lett.* **99**, 185001 (2007).

25. P. Loubeyre *et al.*, *High Press. Res.* **24**, 25–31 (2004).
26. P. Loubeyre *et al.*, *Phys. Rev. B* **86**, 144115 (2012).
27. A. F. Goncharov *et al.*, *Phys. Rev. B* **87**, 024101 (2013).
28. V. Dzyabura, M. Zaghoo, I. F. Silvera, *Proc. Natl. Acad. Sci. U.S.A.* **110**, 8040–8044 (2013).
29. Z. M. Geballe, R. Jeanloz, *J. Appl. Phys.* **111**, 123518 (2012).
30. M. Matzen *et al.*, *Phys. Plasmas* **12**, 055503 (2005).
31. L. M. Barker, R. E. Hollenbach, *J. Appl. Phys.* **43**, 4669 (1972).
32. G. I. Kerley, Equations of state for composite materials, *Technical Report No. SAND2003-3613*, Sandia National Laboratories (2003).
33. N. C. Holmes, M. Ross, W. J. Nellis, *Phys. Rev. B* **52**, 15835–15845 (1995).
34. J. E. Bailey *et al.*, *Phys. Rev. B* **78**, 144107 (2008).
35. R. C. Clay III *et al.*, *Phys. Rev. B* **89**, 184106 (2014).

ACKNOWLEDGMENTS

We acknowledge the crew of the Sandia Z facility for their contributions to these experiments; L. Shulenburger, J. Benage, and W. Lorenzen for numerous insightful discussions; and support from the Deutsche Forschungsgemeinschaft via SFB 652 and grant Re 882/11-2. A. Becker performed calculations at the North-German Supercomupting Alliance (HLRN). The experiments were performed as part of the Z Fundamental Science Program. Sandia National Laboratories is a multiprogram laboratory managed and operated by Sandia Corporation, a wholly owned subsidiary of Lockheed Martin Corporation, for the U.S. Department of Energy's National Nuclear Security Administration under contract DE-AC04-94AL85000. Data are available in the supplementary materials and upon request to mdknuds@sandia.gov.

SUPPLEMENTARY MATERIALS

www.sciencemag.org/content/348/6242/1455/suppl/DC1
Materials and Methods
Figs. S1 to S20
References (*36*–*71*)

22 January 2015; accepted 18 May 2015
10.1126/science.aaa7471

CORAL REEFS

Genomic determinants of coral heat tolerance across latitudes

Groves B. Dixon,[1] Sarah W. Davies,[1] Galina A. Aglyamova,[1] Eli Meyer,[2] Line K. Bay,[3]* Mikhail V. Matz[1]*

As global warming continues, reef-building corals could avoid local population declines through "genetic rescue" involving exchange of heat-tolerant genotypes across latitudes, but only if latitudinal variation in thermal tolerance is heritable. Here, we show an up–to–10-fold increase in odds of survival of coral larvae under heat stress when their parents come from a warmer lower-latitude location. Elevated thermal tolerance was associated with heritable differences in expression of oxidative, extracellular, transport, and mitochondrial functions that indicated a lack of prior stress. Moreover, two genomic regions strongly responded to selection for thermal tolerance in interlatitudinal crosses. These results demonstrate that variation in coral thermal tolerance across latitudes has a strong genetic basis and could serve as raw material for natural selection.

Worldwide, coral reefs are threatened by increasing temperatures associated with climate change (*1*, *2*). Models predict that even a modest increase in the thermal tolerance of reef-building corals over 40 to 80 years would lower their extinction risk dramatically (*3*). Corals are capable of physiological acclimatization to elevated temperature, and it has been argued that in such long-lived organisms acclimatization rather than genetic adaptation will play the leading role in their response to climate change (*4*). Here, we present data for the heritable basis of temperature tolerance that supports the potential for rapid adaptation at the genetic level based on standing genetic variation.

Many coral species maintain high genetic connectivity across thousands of kilometers and inhabit latitudinal ranges that span considerable temperature gradients (*5*, *6*). However, it remains unclear to what extent latitudinal variation in coral thermal physiology is heritable and could fuel genetic rescue via exchange of temperature-tolerant immigrants across latitudes (*7*). We used quantitative genetic, functional genomic, and quantitative trait loci analyses to address this question in *Acropora millepora* corals from thermally divergent locations separated by 5° of latitude: Princess Charlotte Bay (PCB) and Orpheus Island (OI, Fig. 1A).

Ten crosses were established according to a diallel scheme by cross-fertilizing gametes from four adult colonies from the two locations (Fig. 1B). Larval families were cultured in triplicate for 5 days until embryonic development was complete and sampled for tag-based RNA-sequencing analysis (*8*). Separately, larval crosses were scored for heat tolerance, measured as odds of survival after 27 and 31 hours at 35.5°C. The target temperature was reached by ramping over 12 hours at the rate of 0.63°C per hour, less than half of the warming rate on a reef flat during a tidal cycle (*4*).

Survival rates varied substantially among families (Fig. 1D). A mixed-effects generalized linear model with random effects of sire, dam, and their interaction as predictors indicated that the combined parental effects (i.e., broad-sense heritability) accounted for 87% of total deviance in odds of larval survival (Fig. 1E, 95% credible interval of the posterior: 72 to 99%). Proportions of deviance resulting from sire, dam, and their interaction were estimated at 11%, 66%, and 12%, respectively, although the credible intervals were wide because of the limited scope of our crossing design (Fig. 1E). Parents from the warmer location (PCB) conferred significantly higher thermo-tolerance to their offspring relative to parents from the cooler location (OI), with a PCB dam conferring a five-fold increase ($P_{MCMC} < 0.001$; MCMC, Markov chain Monte Carlo) and a PCB sire conferring an additional twofold increase ($P_{MCMC} = 0.048$) in survival odds (Fig. 1F).

To elucidate molecular processes underlying this variation, we identified genes whose expression before stress predicted the odds of larval survival under stress (Fig. 2A), which we term tolerance-associated genes (TAGs). At the 5% false discovery rate (FDR), 1973 TAGs were identified (Fig. 2B). In heat-tolerant larvae, gene ontology (GO) categories related to oxidoreductase activity and extracellular matrix were significantly enriched in the up-regulated gene set, whereas categories related to transmembrane transporter and motor activity were significantly enriched in the down-regulated gene set (Fig. 2C). An analysis of cellular component categories additionally revealed enrichment of nuclear-encoded mitochondrial membrane components (Fig. 2D and fig. S3), potentially a manifestation of mitochondrial variation that could contribute to the high maternal effect on heat tolerance (Fig. 1E).

Higher coral heat tolerance has been attributed to "frontloading," where elevated baseline expression of stress response genes primes the organism for stress (*9*). Alternatively, higher tolerance could be due to the lack of prior stress, in which case the expression of TAGs should be unrelated or opposite to the heat stress response. We compared the TAGs to gene expression in adult parental colonies after 3 days of heat stress (31.5°C, figs. S3 and S4) and to published data on larvae after 4 hours or 5 days of heat stress (*8*), based on patterns of up- and down-regulation within eukaryotic orthologous group (KOG) gene classes (*10*) (Fig. 3A). The adult heat stress response was quite similar to the 5-day larval heat stress response (Fig. 3B). The TAGs expression was significantly negatively correlated with long-term heat stress response in larvae (Fig. 3C) and in adults (albeit marginally significant: $P_{cor.test} = 0.06$). This indicates that the larval heat tolerance we detected most likely arose from the absence of preexisting stress, not from prior up-regulation of heat stress genes through frontloading.

The KOG class most enriched in up-regulated TAGs was energy production and conversion and encompassed mitochondrial proteins (Fig. 3A and fig. S3), further supporting the possible contribution of mitochondrial variation to the maternal effect on heat tolerance (Fig. 1E). Alternatively, maternal effect could be due to epigenetic modification

[1]Department of Integrative Biology, University of Texas at Austin, 205 W. 24th Street C0990, Austin, TX 78712, USA. [2]Department of Integrative Biology, Oregon State University, 3106 Cordley Hall, Corvallis, OR 97331, USA. [3]Australian Institute of Marine Science, PMB 3, Townsville MC, Queensland 4810, Australia.
*Corresponding author. E-mail: l.bay@aims.gov.au (L.K.B.); matz@utexas.edu (M.V.M.)

Downloaded from www.sciencemag.org on June 26, 2015

of the nuclear genome, in which case variation in TAGs expression would likely also be under maternal control. We undertook a weighted gene correlation network analysis (*11*) to investigate this possibility and found a predominance of genetic rather than maternal effects: Expression variation of over 2700 genes was transmitted from adult corals to their larval offspring irrespective of whether the adults were used as sires or as dams (fig. S6 and accompanying text). The number of genes affected by maternal effects ranged from none to nearly 2000 among dams, which would be surprising if maternal effects were due to ubiquitously present genome-wide epigenetic modifications. The best correlation with heat tolerance was observed for biparentally rather than maternally controlled genes (fig. S6, B to E), which corresponds well with the observation that higher heat tolerance was contributed by both PCB parents (Fig. 1F). However, because the strongest maternal effects both on gene expression and on larval heat tolerance were observed for the same parent (dam C), the role of epigenetic modifications cannot be ruled out.

To further demonstrate that larval heat tolerance has a genetic basis and can respond to selection, we quantified genomic effects of artificial selection by heat in two interlatitudinal reciprocal crosses (AC and CA). Selected samples consisted of the last 30 to 50 heat stress–surviving larvae out of the initial ~1000, whereas control samples consisted of 50 larvae from unstressed cultures. This experiment was performed with two culture replicates from each cross, resulting in eight compared groups. Larvae were individually genotyped (n = 326) by using 2bRAD methodology (*12*) to construct a genetic linkage map and to identify genomic regions displaying reproducible allele frequency shifts in response to heat selection.

The linkage map contained 1448 markers in 14 linkage groups (LGs) and had a total length of 1358 centimorgans (cM). In both crosses, the selection was predominantly against paternally derived haplotypes (fig. S7), resulting in markedly different genome-wide patterns of selection between reciprocal crosses (Fig. 4). The strength of negative selection, measured as a decrease in survival of larvae bearing the less-preferred haplotype, reached unity in LG 10 in the CA cross (i.e., the less-preferred haplotype was completely eliminated from the larval pool) and 0.91 in LG 5 in the AC cross. No statistically significant signatures of selection were observed when comparing pairs of unselected

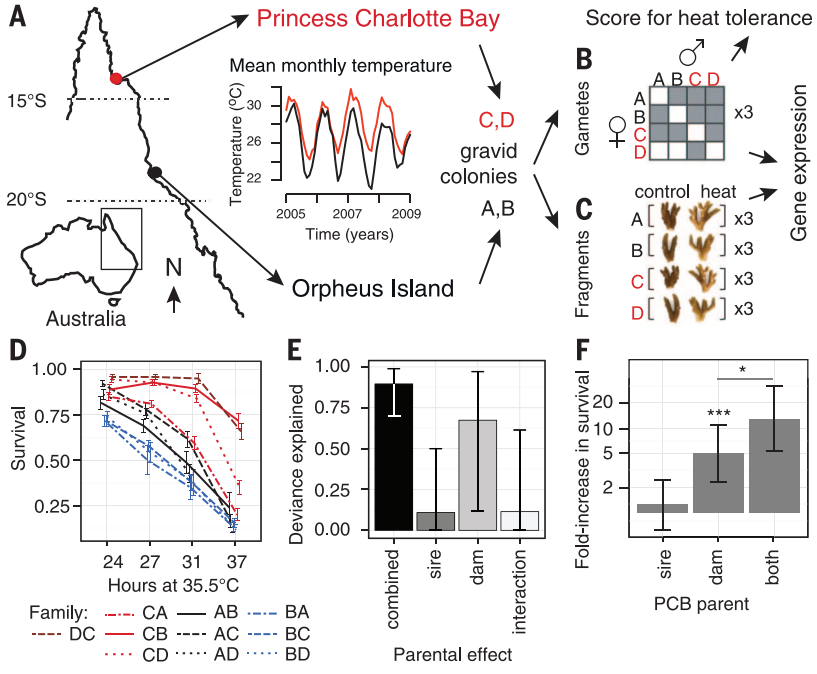

Fig. 1. Experimental design and quantitative genetics of larval heat tolerance. (**A**) Sampling locations and their annual temperature regimes on the Great Barrier Reef, Australia. (**B**) Crossing design matrix where solid squares represent established crosses. (**C**) Experimental design to quantify gene expression differences between parental colonies under heat stress (31.5°C for 3 days). (**D**) Mortality curves ± SE for each larval family. In the family identifier, the first letter is dam (mother); the second letter is sire (father). (**E**) Proportion of total deviance explained by parental effects. (**F**) Increase in odds of larval survival with parents from the warmer location (PCB) relative to the larvae with both parents from the cooler location (OI). ***P < 0.001, *P < 0.05. Whiskers on (E) and (F) denote 95% credible interval of the posterior.

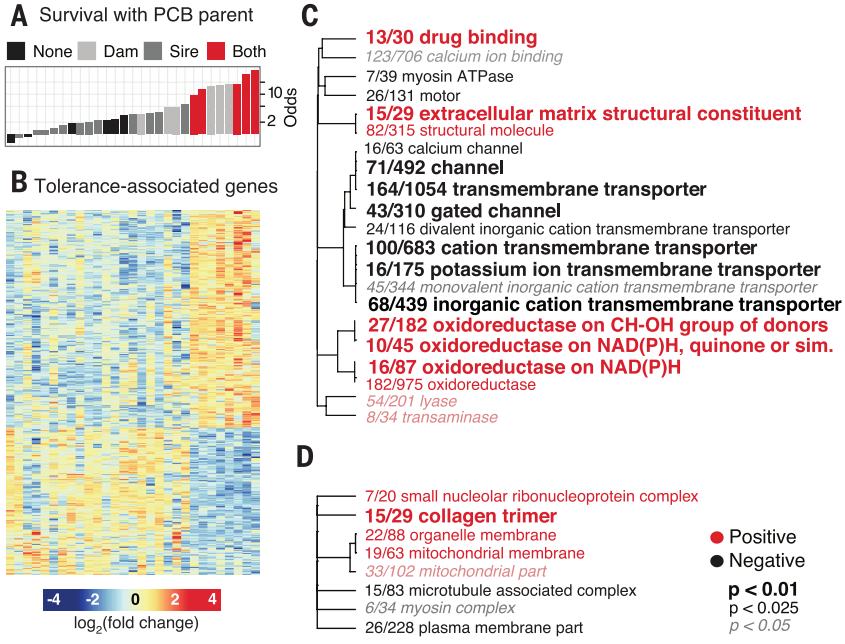

Fig. 2. Gene expression associated with larval heat tolerance. (**A**) Bar chart for survival odds under heat stress for each larval culture, ranked in increasing order. (**B**) Heat map of 1973 genes (rows) for which the expression before heat stress predicts the survival odds under stress. Columns are larval cultures ordered as in the bar chart above (A). (**C** and **D**) GO categories significantly enriched with genes either positively (red) or negatively (black) associated with heat tolerance. The dendrograms depict the sharing of genes between categories; the fractions correspond to genes with an unadjusted P < 0.05 relative to the total number of genes within the category. (C) Molecular function. ATPase, adenosine triphosphatase; NAD(P)H, reduced form of nicotinamide adenine dinucleotide. (D) Cellular component.

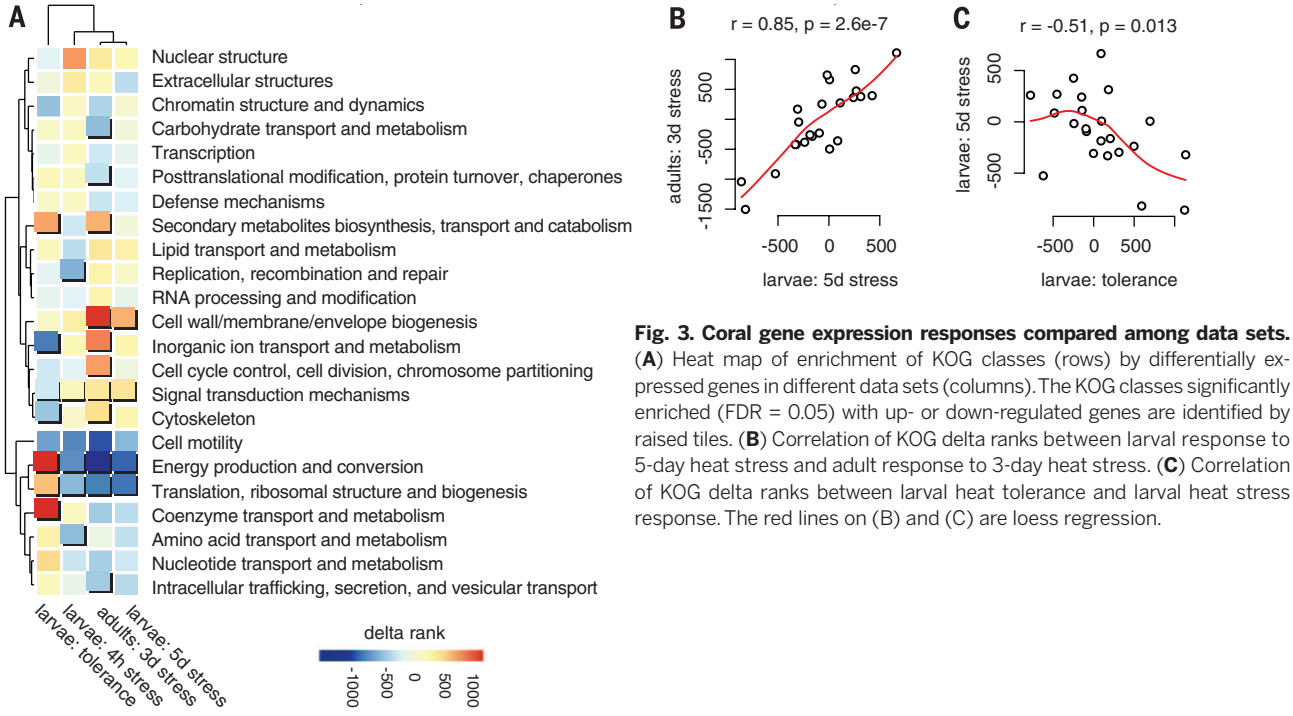

Fig. 3. Coral gene expression responses compared among data sets. (**A**) Heat map of enrichment of KOG classes (rows) by differentially expressed genes in different data sets (columns). The KOG classes significantly enriched (FDR = 0.05) with up- or down-regulated genes are identified by raised tiles. (**B**) Correlation of KOG delta ranks between larval response to 5-day heat stress and adult response to 3-day heat stress. (**C**) Correlation of KOG delta ranks between larval heat tolerance and larval heat stress response. The red lines on (B) and (C) are loess regression.

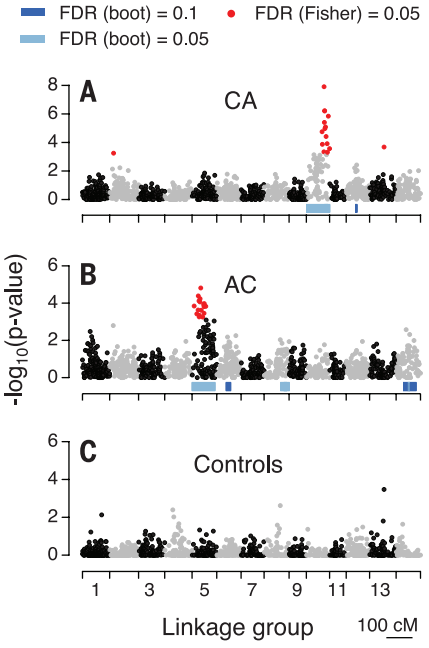

Fig. 4. Manhattan plot of allele frequency difference after selection by heat. (**A**) Selection effects in CA family. (**B**) Selection effects in AC family. (**C**) Differences in allele frequencies among control samples. Red points show markers at 5% FDR according to the Fisher's combined probability test; blue bars identify regions with significant clustering of such markers (according to 100,000 bootstrapped replicates).

samples (Fig. 4C). Selection against paternal haplotypes aligns well with the putative involvement of mitochondria in heat tolerance determination: Such selection could be due to poor compatibility of certain paternal nuclear alleles with maternal mitochondria under stress (*13*). There were two genes encoding mitochondrial transporters within 100 kilobases of the top marker under selection (CA cross, LG 10), one of which was significantly associated with larval heat tolerance at the gene expression level (fig. S8 and table S1).

Thermal tolerance measured in our experiments represents just one of many aspects of coral physiology potentially relevant for adaptation to climate change. For example, although molecular responses of larvae and adults to thermal stress are similar (Fig. 3B), larval thermal tolerance may not necessarily translate into adult thermal tolerance. Nonetheless, our study demonstrates heritability of coral stress-related phenotypic and molecular traits and thus highlights the adaptive potential stemming from standing genetic variation in coral metapopulations. Several lines of evidence point toward the importance of mitochondria and mitochondrial-nuclear interactions in determining heat tolerance, including its predominantly maternal inheritance (Fig. 1E), altered expression of mitochondrial proteins in heat-tolerant larvae (Fig. 2D and fig. S3), persistent selection against paternal haplotypes in reciprocal crosses under heat stress (Fig. 4 and fig. S7), and two genes encoding mitochondrial proteins in the vicinity of the major heat-selected marker (fig. S8). High maternal effect on larval thermal tolerance could also be partially due to epigenetic modification, which remains poorly understood in corals. Most importantly, the strong response of two genomic regions to heat selection (Fig. 4) directly confirms that natural variation in heat tolerance is both heritable and evolvable. The genetic rescue scenario, therefore, emerges as a plausible mechanism of rapid coral adaptation to climate change, especially if the natural connectivity of corals across latitudes is enhanced by assisted colonization efforts (*14*).

REFERENCES AND NOTES

1. T. P. Hughes *et al.*, *Science* **301**, 929–933 (2003).
2. O. Hoegh-Guldberg *et al.*, *Science* **318**, 1737–1742 (2007).
3. C. A. Logan, J. P. Dunne, C. M. Eakin, S. D. Donner, *Glob. Change Biol.* **20**, 125–139 (2014).
4. S. R. Palumbi, D. J. Barshis, N. Traylor-Knowles, R. A. Bay, *Science* **344**, 895–898 (2014).
5. D. J. Ayre, T. P. Hughes, *Evolution* **54**, 1590–1605 (2000).
6. M. J. H. Van Oppen, L. M. Peplow, S. Kininmonth, R. Berkelmans, *Mol. Ecol.* **20**, 4899–4914 (2011).
7. P. K. Ingvarsson, *Trends Ecol. Evol.* **16**, 62–63 (2001).
8. E. Meyer, G. V. Aglyamova, M. V. Matz, *Mol. Ecol.* **20**, 3599–3616 (2011).
9. D. J. Barshis *et al.*, *Proc. Natl. Acad. Sci. U.S.A.* **110**, 1387–1392 (2013).
10. R. L. Tatusov *et al.*, *BMC Bioinformatics* **4**, 41 (2003).
11. P. Langfelder, S. Horvath, *BMC Bioinformatics* **9**, 559 (2008).
12. S. Wang, E. Meyer, J. K. McKay, M. V. Matz, *Nat. Methods* **9**, 808–810 (2012).
13. L. A. Hoekstra, M. A. Siddiq, K. L. Montooth, *Genetics* **195**, 1129–1139 (2013).
14. O. Hoegh-Guldberg *et al.*, *Science* **321**, 345–346 (2008).

ACKNOWLEDGMENTS

We thank B. Willis (James Cook University) and group for logistical support during coral spawning. The bioinformatics analysis was performed with computational resources of the Texas Advanced Computer Center. This study was supported by grants from NSF (DEB-1054766) to M.V.M. and the Australian Institute of Marine Science to L.K.B. Sequencing data have been deposited to National Center for Biotechnology Information's Short Reads Archive (accession numbers PRJNA279192 and PRJNA279420); data sets and scripts have been deposited to Dryad (http://dx.doi.org/10.5061/dryad.g75nq).

SUPPLEMENTARY MATERIALS

www.sciencemag.org/content/348/6242/1460/suppl/DC1
Materials and Methods
Supplementary Text
Figs. S1 to S8
Table S1
Databases S1 and S3
Supplementary Data
References (*15*–*41*)

15 September 2014; accepted 8 May 2015
10.1126/science.1261224

PHOTOSYNTHESIS

A 12 Å carotenoid translocation in a photoswitch associated with cyanobacterial photoprotection

Ryan L. Leverenz,[1]* Markus Sutter,[1,2]* Adjélé Wilson,[3,4] Sayan Gupta,[5] Adrien Thurotte,[3,4] Céline Bourcier de Carbon,[3,4] Christopher J. Petzold,[2] Corie Ralston,[5] François Perreau,[6] Diana Kirilovsky,[3,4] Cheryl A. Kerfeld[1,2,7]†

Pigment-protein and pigment-pigment interactions are of fundamental importance to the light-harvesting and photoprotective functions essential to oxygenic photosynthesis. The orange carotenoid protein (OCP) functions as both a sensor of light and effector of photoprotective energy dissipation in cyanobacteria. We report the atomic-resolution structure of an active form of the OCP consisting of the N-terminal domain and a single noncovalently bound carotenoid pigment. The crystal structure, combined with additional solution-state structural data, reveals that OCP photoactivation is accompanied by a 12 angstrom translocation of the pigment within the protein and a reconfiguration of carotenoid-protein interactions. Our results identify the origin of the photochromic changes in the OCP triggered by light and reveal the structural determinants required for interaction with the light-harvesting antenna during photoprotection.

Photosynthetic organisms balance light harvesting against the toxic effects of oxidative intermediates produced under excess light (*1*). Thermal dissipation of excess absorbed energy—manifested as a quenching of antenna fluorescence known as nonphotochemical quenching (NPQ) (*2*, *3*)—is the predominant photoprotective mechanism. Carotenoid pigments play critical roles in NPQ (*2*–*11*), including a likely role as a direct quencher of excitation energy in "flexible" NPQ mechanisms (*4*) that operate reversibly on short time scales (seconds to minutes) and under dynamic light conditions (*6*–*11*).

In cyanobacteria, a relatively simple carotenoid-dependent NPQ mechanism is associated with the light-harvesting antenna protein complex, the phycobilisome (PB). Here, NPQ is triggered by photoactivation of the soluble orange carotenoid protein (OCP), a blue-light photoreceptor that noncovalently binds a single carotenoid (*3*). Activation of the OCP occurs when its dark (orange) state, OCP^O, absorbs blue light and forms the quenching active (red) state, OCP^R (*12*). OCP^R binds to the PB and initiates PB-associated NPQ (*12*, *13*). Structurally, the OCP is composed of two domains, a mixed α/β C-terminal domain (CTD) and a N-terminal domain (NTD) with an all α-helical fold unique to cyanobacteria (*14*) (fig. S1, A and B). A 4-keto carotenoid (fig. S1C) spans both domains (*14*, *15*) and is almost entirely enclosed by protein (4% solvent-exposed; fig. S1B). The isolated, carotenoid-binding NTD, referred to as the red carotenoid protein (RCP), functions as an effector domain; it binds to PBs and quenches PB fluorescence (*16*). The CTD serves as the regulatory (sensory) domain (*16*, *17*) conferring photochemical activity to the OCP and providing the site of interaction with the fluorescence recovery protein (FRP), which catalyzes the OCP^R-to-OCP^O conversion (*18*). In the absence of the CTD, the RCP is a constitutively active quencher; its activity and spectroscopic properties are essentially identical to those of OCP^R (*16*). However, dissociation or absence of the CTD would leave nearly half of the carotenoid accessible to solvent. This raises a fundamental question about how the hydrophobic carotenoid is structurally accommodated in OCP^R and RCP prior to interaction with the PB.

To probe the molecular details of carotenoid-protein interactions in RCP/OCP^R, we produced RCP by expressing a synthetic *rcp* gene [encoding residues 20 to 165 of *Synechocystis* PCC6803 (hereafter *Synechocystis*) OCP] in echinenone (ECN)– or canthaxanthin (CAN)–producing *E. coli* strains. In both strains, the OCP binds a mixture of CAN and ECN, with a higher relative amount of CAN binding in the CAN-producing strain (table S1). RCP_{CAN} (binding exclusively CAN) was more active than RCP_{ECN} (binding exclusively ECN) and induced PB fluorescence quenching comparable to that of RCP obtained by partial proteolysis (*16*) of the OCP purified from *Synechocystis* (fig. S2). Accordingly, we structurally characterized RCP_{CAN} and its cognate OCP.

The 1.90 Å resolution structure of *Synechocystis* OCP^O_{CAN} (table S2) aligns closely with the structure of *Synechocystis* OCP_{ECN} (*19*) [root mean square deviation (RMSD) 0.17 Å over 304 α-carbon atom pairs]. The carotenoid conformation is also consistent with previously reported OCP^O structures binding ECN (*19*) or hydroxyechinenone (*14*) (table S3), and there is well-defined electron density for each CAN carbonyl oxygen (Fig. 1A and fig. S4A). The OCP_{CAN} was photoactive and able to induce

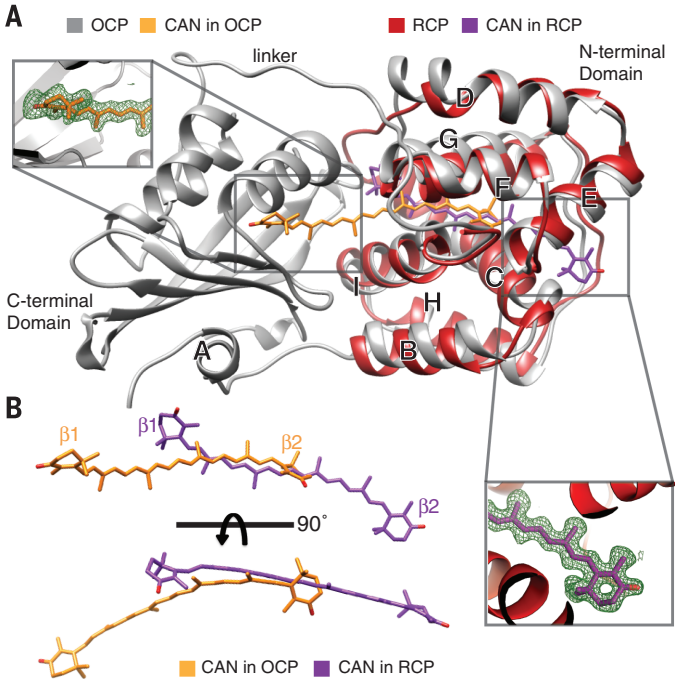

Fig. 1. Crystal structures of the orange carotenoid protein (OCP) and red carotenoid protein (RCP) binding canthaxanthin (CAN). (**A**) Superimposed ribbon structures of OCP_{CAN} (gray) and RCP_{CAN} (red). CAN is shown in orange sticks in OCP, purple sticks in RCP. Inset panels show representative electron density for the carotenoid in each structure (complete carotenoid $F_{obs} - F_{calc}$ maps are shown in fig. S4). (**B**) CAN structures in OCP and RCP show increased planarity of the polyene chain in RCP and distinctly different β-ring configurations.

[1]MSU-DOE Plant Research Laboratory, Michigan State University, East Lansing, MI 48824, USA. [2]Physical Biosciences Division, Lawrence Berkeley National Laboratory, Berkeley, CA 94720, USA. [3]Commissariat à l'Energie Atomique (CEA), Institut de Biologie et Technologies de Saclay (iBiTec-S), 91191 Gif-sur-Yvette, France. [4]Centre National de la Recherche Scientifique (CNRS), I2BC, UMR 9198, 91191 Gif-sur-Yvette, France. [5]Berkeley Center for Structural Biology, Physical Biosciences Division, Lawrence Berkeley National Laboratory, Berkeley, CA 94720, USA. [6]INRA, Institut Jean-Pierre Bourgin, UMR 1318, ERL CNRS 3559, Saclay Plant Sciences, RD10, F-78026 Versailles, France. [7]Department of Plant and Microbial Biology, University of California, Berkeley, CA 94720, USA.
*These authors contributed equally to this work. †Corresponding author. E-mail: ckerfeld@lbl.gov

Downloaded from www.sciencemag.org on June 26, 2015

PB fluorescence quenching (fig. S3). Moreover, the nearly identical UV-visible absorbance spectra for RCP_{CAN} and $OCP^{R}{}_{CAN}$ (fig. S2) indicates that the pigment-protein environments are comparable in $OCP^{R}{}_{CAN}$ and RCP_{CAN}, as reported for the *Arthrospira* homologs (*16*), substantiating their structural and functional homology.

We also determined the RCP_{CAN} structure to 1.54 Å resolution (table S2). The protein backbone of the RCP superimposes on the NTD of $OCP^{O}{}_{CAN}$ (Fig. 1A), with a RMSD of 1.24 Å (104 α-carbon pairs), indicating that large protein conformational changes in the NTD are not involved in PB binding or quenching. However, there is a remarkable difference in the position and conformation of the carotenoid in RCP in comparison to $OCP^{O}{}_{CAN}$. In the active form, the carotenoid is translocated more than 12 Å deeper into the NTD (Fig. 1, A and B). Due to the burrowing of the carotenoid into the NTD, it is only sparingly solvent-accessible (8% solvent-exposed) in RCP, specifically in the vicinity of the two terminal β-ionone rings (β1 and β2, Fig. 1B, Fig. 2A, and fig. S4). Each ring adopts different configurations about the C6-C7 (C6´-C7´) single bond in the two structures (Fig. 1B and Fig. 2A) and the out-of-plane torsions of each ring are decreased relative to those of CAN in OCP^{O} (table S3). The polyene chain is completely encompassed by protein; it assumes a highly planar conformation in RCP, whereas it is bowed and twisted in OCP^{O} (Fig. 1B and fig. S4). The increased planarity of the polyene and reduced β-ring torsions observed for CAN in RCP are consistent with previously published electronic absorption and Raman spectroscopy data that indicate extended effective π-conjugation and a planar all-trans configuration for the carotenoid in both quenching-active RCP and OCP^{R} (*12*, *16*).

The large displacement of the carotenoid has profound consequences for its interactions with the protein. Specifically, the amino acids comprising the CAN binding pockets in the OCP^{O} and RCP structures (Fig. 2A and table S4) occupy two distinct carotenoid-protein configurations (cpcs). In cpcO

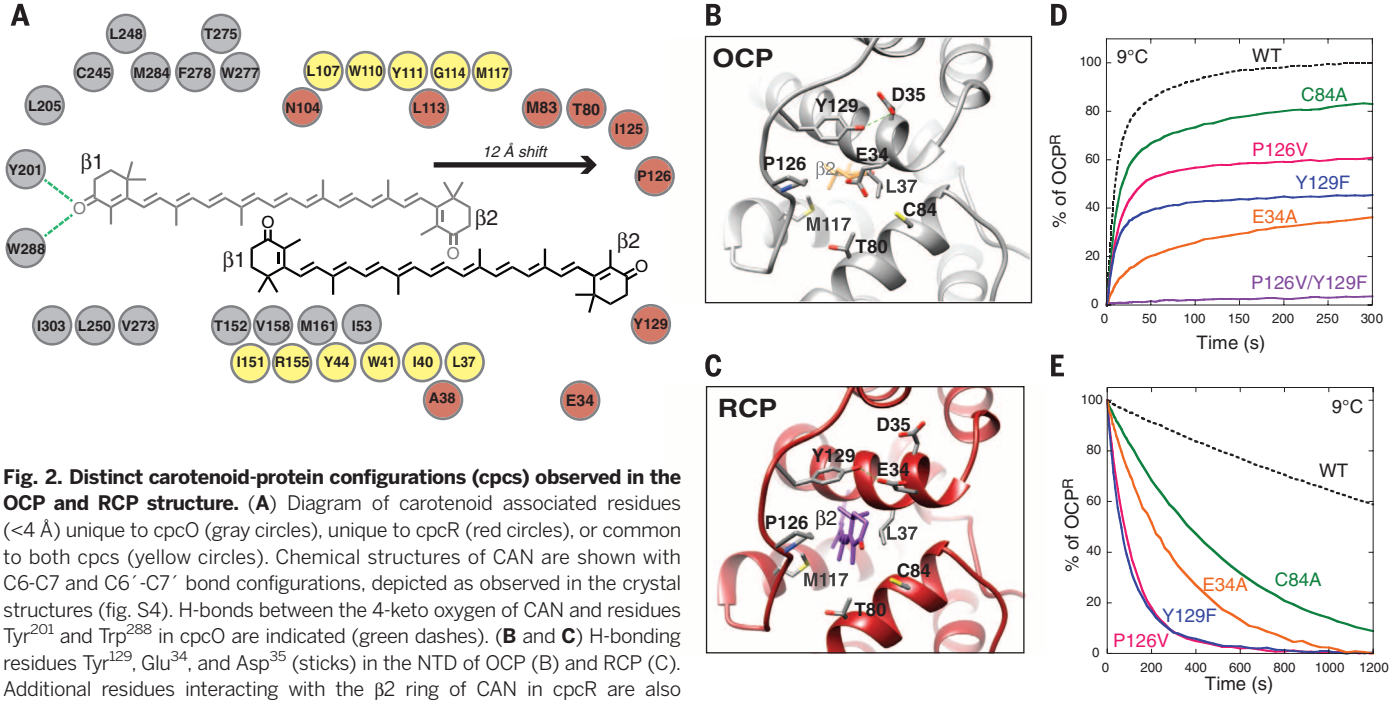

Fig. 2. Distinct carotenoid-protein configurations (cpcs) observed in the OCP and RCP structure. (**A**) Diagram of carotenoid associated residues (<4 Å) unique to cpcO (gray circles), unique to cpcR (red circles), or common to both cpcs (yellow circles). Chemical structures of CAN are shown with C6-C7 and C6´-C7´ bond configurations, depicted as observed in the crystal structures (fig. S4). H-bonds between the 4-keto oxygen of CAN and residues Tyr^{201} and Trp^{288} in cpcO are indicated (green dashes). (**B** and **C**) H-bonding residues Tyr^{129}, Glu^{34}, and Asp^{35} (sticks) in the NTD of OCP (B) and RCP (C). Additional residues interacting with the β2 ring of CAN in cpcR are also explicitly shown in both structures. (**D**) OCP^{O}-to-OCP^{R} conversion of OCP mutants at 9°C during 5 min of strong white-light illumination. (**E**) OCP^{R}-to-OCP^{O} dark recovery at 9°C for mutants in (D).

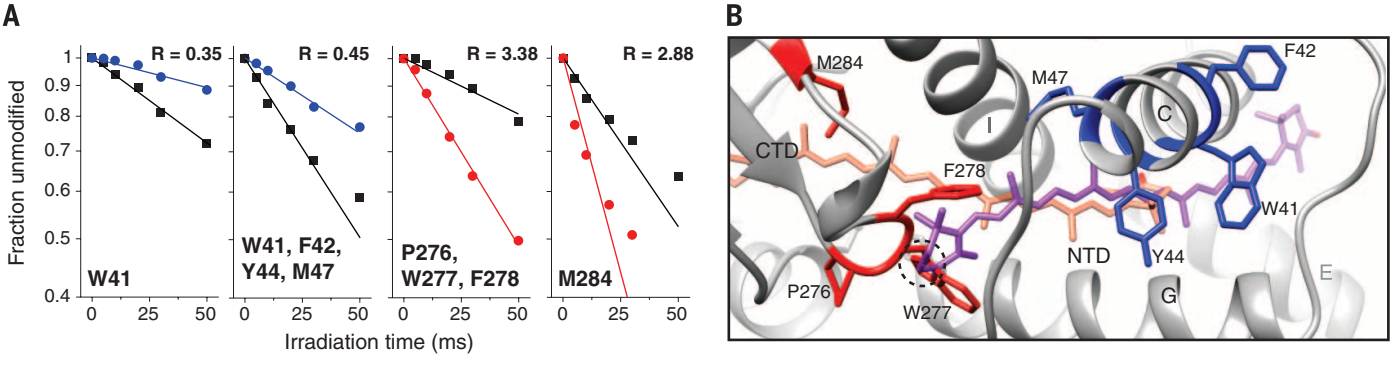

Fig. 3. Solvent accessibility changes in OCP_{CAN} as measured by x-ray hydroxyl radical footprinting. (**A**) Peptide modification as a function of x-ray irradiation dose for Trp^{41}, residue clusters Trp^{41}-Phe^{42}-Tyr^{44}-Met^{47} and Pro^{276}-Trp^{277}-Phe^{278}, and Met^{284} for dark-adapted (OCP^{O}, squares) and illuminated (OCP^{R}, circles) OCP_{CAN}. Solid lines represent single-exponential fits to the dose-dependent data. The ratio of the modification rates (R) indicates the change in relative SA. (**B**) Structural view (OCP_{CAN} structure) of CAN binding residues undergoing large (factor of >2) SA changes after illumination. CAN in cpcO (orange sticks) and CAN in cpcR (purple sticks) are both shown. CTD residues Pro^{276}, Trp^{277}, Phe^{278}, and Met^{284} (red sticks) exhibit a SA increase (R = 3.38, R = 2.88) in OCP^{R}, whereas residue Trp^{41} and residue cluster Trp^{41}-Phe^{42}-Tyr^{44}-Met^{47} (blue) exhibit SA decreases (R = 0.35, R = 0.45). A clash between $Trp^{277}$and CAN in cpcR is indicated (black circle).

(corresponding to CAN in OCP^O), 11 residues of the NTD are in close (<4 Å) proximity to the carotenoid. Retrospectively, the hydrophobic tunnel for translocation of the carotenoid further into the NTD is present in OCP^O (fig. S1B and fig. S5). In cpcR (CAN in RCP) an additional nine residues in this NTD "tunnel" interact with the carotenoid (Fig. 2A). Modest side chain conformational changes accompany translocation (Fig. 2B and fig. S5A). A perturbed local electrostatic environment for CAN in cpcR versus cpcO (fig. S5D), in addition to new H-bonding interactions between solvent and CAN's 4-keto groups in cpcR, likely contribute to altered photophysical properties of the carotenoid (i.e., stabilization of an intramolecular charge transfer state) that may be connected to quenching function (*20*).

The conservation of residues unique to cpcR observed in genes encoding for full-length OCPs (figs. S6 and S7) implicate the carotenoid shift as an integral part of OCP function. Several of the conserved residues within 4 Å of CAN in cpcR were probed by mutagenesis in the OCP. For certain mutations (i.e., $Glu^{34} \rightarrow$ Ala), the CAN:ECN binding ratio was observed to change markedly relative to the wild-type OCP (table S1), indicating that these residues influence carotenoid binding specificity in OCP. The OCP single mutants $Cys^{84} \rightarrow$ Ala, $Tyr^{129} \rightarrow$ Phe, $Pro^{126} \rightarrow$ Val, and $Glu^{34} \rightarrow$ Ala reduced the stability of the OCP^R form, as evidenced by decreased steady-state accumulation of OCP^R after illumination and accelerated OCP^R-to-OCP^O dark-reversion (Fig. 2, D and E); these mutants induced less than 40% PB quenching (fig. S8B). The OCP double mutant $Pro^{126} \rightarrow$ Val/$Tyr^{129} \rightarrow$ Phe remained orange even under prolonged, strong illumination (Fig. 2D and fig. S8), which suggests that these exposed residues, relatively distant from the carotenoid in cpcO, play a critical role in OCP photochemistry. Collectively, these results implicate the CAN-binding residues in cpcR (as observed in the RCP structure) in the stabilization of the carotenoid in the active OCP^R.

To obtain solution-state structural evidence for carotenoid translocation in the OCP^O-to-OCP^R photoconversion, we used x-ray hydroxyl radical footprinting mass spectrometry (XF-MS) to identify changes in side-chain solvent accessibility after illumination (*21*). X-ray dose response plots show that some of the largest solvent accessibility changes after photoconversion occurred in CAN binding residues (Fig. 3A and table S5). The largest solvent accessibility decreases are for peptides containing the NTD residue Trp^{41} (Fig. 3A). The decrease in solvent accessibility for this residue is consistent with an increased interaction with CAN due to CAN translocation. XF-MS analysis of RCP samples exhibited a similarly prominent SA decrease at Trp^{41} (table S5). Furthermore, CTD residues (Pro^{276}-Trp^{277}-Phe^{278} and Met^{284} in OCP^R; Fig. 3A) that contact the CAN polyene chain in cpcO (table S4) had a large increase in solvent accessibility. CAN translocation exposes these side chains to a solvent accessible region in the surface cleft between the CTD and NTD (fig. S1B). Correlated solvent accessibility changes in CAN binding CTD residues (increased solvent accessibility) and NTD residues (decreased solvent accessibility) support carotenoid translocation during OCP activation (Fig. 3B). XF-MS data also confirms that CAN translocation accompanies a separation of the CTD and NTD: The factor of 10 solvent accessibility increase in Arg^{155} (table S5) supports the proposed breakage of the Arg^{155}-Glu^{244} salt bridge in OCP^R (*17*, *22*).

Based on the observation of carotenoid translocation accompanying domain dissociation we propose the following sequence of events in the photoactivation of the OCP (Fig. 4A). Light absorption triggers structural changes in the carotenoid, perturbing its interaction with the CTD (e.g., perturbing H-bonds with Tyr^{201}/Trp^{288}). Light-induced displacement of the N-terminal αA helix from the CTD, proposed to occur based on structtural similarities to the Per-Arnt-Sim family of photosensors (*19*, *23*), has recently been demonstrated by chemical footprinting experiments (*17*). Analogous to the photochemical mechanism of PYP (*24*), it is possible that partial "ejection" of the carotenoid chromophore, driven by a transient, strained cis-carotenoid geometry may be coupled to CTD structural changes. An accompanying reorganization of side chain–pigment interactions has the net effect of destabilizing carotenoid binding in cpcO; translocation of the carotenoid drives the reconfiguration to cpcR. Chaotrope-induced formation of an activated state of the OCP suggests that the transition to cpcR can take place in the absence of light (*25*), implying that translocation may be largely driven by protein-carotenoid binding free energies. In contrast to cpcO, where the carotenoid serves as a structural element bridging the CTD and NTD, carotenoid translocation coupled with dissociation of the αA helix from the CTD (*17*) is required for full domain separation in OCP^R.

The separation of the NTD and CTD in OCP^R leads to solvent exposure of both CAN β rings. The regions surrounding the solvent-exposed β rings (β1, face 1; β2, face 2) include the two largest patches of conserved residues on the surface of RCP (fig. S7). Positive potential, in part due to the critical PB binding residue Arg^{155} (*22*), dominates face 1, whereas face 2 is relatively negatively charged (Fig. 4B). The distinct differences in surface charge between face 1 and face 2 suggest an electrostatically driven directionality in the NTD-PB interaction. Because the conformation of the NTD is essentially unchanged in the active form of the OCP, NTD-PB binding is likely tied to selective exposure of regions of the NTD occluded in OCP^O (face 1 and Arg^{155}), or to the carotenoid translocation itself.

NTD-PB interaction in the vicinity of the exposed β-ring would also be expected for carotenoid-dependent energy quenching, given the importance of interpigment distances in energy transfer efficiency (*26*). Although the atomic-resolution structure of the fully assembled PB is

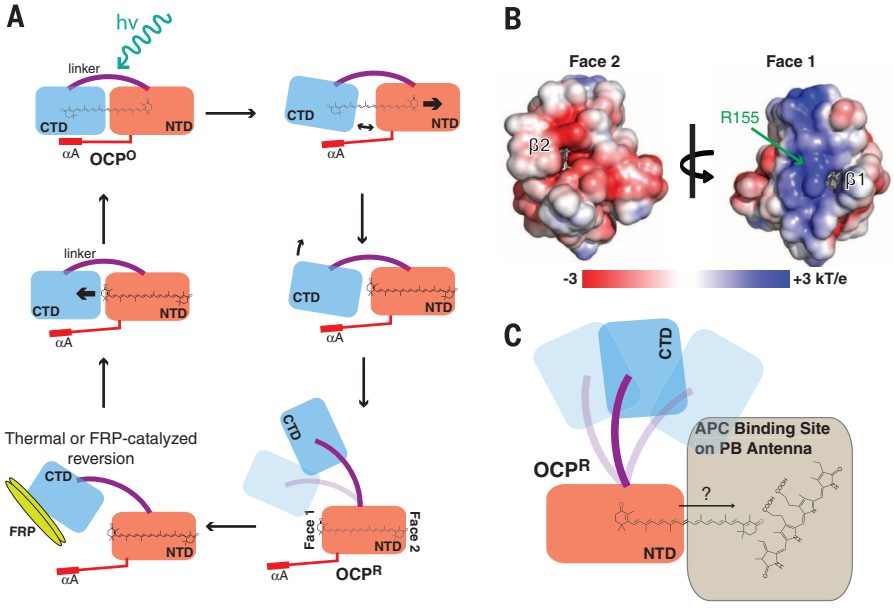

Fig. 4. Proposed models for OCP photoactivation and the site of OCP/RCP-phycobilisome interactions. (**A**) Proposed mechanism for OCP photochemistry, including carotenoid translocation, after light absorption by OCP^O (top left). Structural changes after absorption are localized primarily to the CTD (i.e., dissociation of the αA helix) and are coupled to the translocation (right). Translocation precedes complete NTD-CTD dissociation in OCP^R (bottom right). OCP^R reverts to OCP^O in darkness (thermal reversion) or when catalyzed by an interaction between the fluorescence recovery protein (FRP) and the CTD (*18*) (bottom left); subsequent protein refolding and carotenoid translocation into the CTD (middle left) restores the OCP^O ground state. (**B**) Electrostatic surface potential mapped on the RCP molecular surface colored from red to blue (−3 to +3 *kT/e*). (**C**) OCP:PB interaction illustrating binding at face 1 and a hypothetical carotenoid translocation after binding.

unknown, in silico docking simulations between RCP and PB subunits implicated in OCP-binding (*27*–*29*) show reduced bilin-carotenoid distances as compared to identical simulations with OCP^O (fig. S9A); RCP-PB complexes with face 1 CAN-bilin distances as low as 3.1 Å were identified (fig. S9B). Such close interaction would permit participation of the carotenoid in either direct bilin-carotenoid energy transfer (*20*) or charge transfer quenching mechanisms (*30*). The translocation observed concomitant with activation of the protein raises the possibility of additional carotenoid structural changes and/or movement after binding to the PB (Fig. 4C) to further reduce carotenoid-bilin distances or change the relative orientations of pigments in the OCP-PB complex. More broadly, the light-driven change in carotenoid-protein interactions observed in the OCP prompts a re-examination of other carotenoid binding protein complexes for the possibility of transient, activation-dependent movement of the non-covalently bound carotenoids in those systems.

REFERENCES AND NOTES

1. R. Croce, H. van Amerongen, *Nat. Chem. Biol.* **10**, 492–501 (2014).
2. P. Horton, A. V. Ruban, R. G. Walters, *Plant Physiol.* **106**, 415–420 (1994).
3. D. Kirilovsky, *Photosynth. Res.* **93**, 7–16 (2007).
4. K. K. Niyogi, T. B. Truong, *Curr. Opin. Plant Biol.* **16**, 307–314 (2013).
5. A. A. Pascal *et al.*, *Nature* **436**, 134–137 (2005).
6. H. Staleva *et al.*, *Nat. Chem. Biol.* **11**, 287–291 (2015).
7. H. A. Frank *et al.*, *Photosynth. Res.* **41**, 389–395 (1994).
8. T. K. Ahn *et al.*, *Science* **320**, 794–797 (2008).
9. A. V. Ruban *et al.*, *Nature* **450**, 575–578 (2007).
10. S. Bode *et al.*, *Proc. Natl. Acad. Sci. U.S.A.* **106**, 12311–12316 (2009).
11. P. J. Walla, C.-P. Holleboom, G. R. Fleming, in *Non-Photochemical Quenching and Energy Dissipation in Plants, Algae and Cyanobacteria*, B. Demmig-Adams, G. Garab, W. A. III, Govindjee, Eds. (Springer, Amsterdam, 2014), pp. 229–243.
12. A. Wilson *et al.*, *Proc. Natl. Acad. Sci. U.S.A.* **105**, 12075–12080 (2008).
13. M. Gwizdala, A. Wilson, D. Kirilovsky, *Plant Cell* **23**, 2631–2643 (2011).
14. C. A. Kerfeld *et al.*, *Structure* **11**, 55–65 (2003).
15. C. Punginelli, A. Wilson, J.-M. Routaboul, D. Kirilovsky, *Biochim. Biophys. Acta Bioenerg.* **1787**, 280–288 (2009).
16. R. L. Leverenz *et al.*, *Plant Cell* **26**, 426–437 (2014).
17. H. Liu *et al.*, *Biochim. Biophys. Acta Bioenerg.* **1837**, 1955–1963 (2014).
18. M. Sutter *et al.*, *Proc. Natl. Acad. Sci. U.S.A.* **110**, 10022–10027 (2013).
19. A. Wilson *et al.*, *J. Biol. Chem.* **285**, 18364–18375 (2010).
20. R. Berera *et al.*, *J. Phys. Chem. B* **116**, 2568–2574 (2012).
21. S. Gupta, R. D'Mello, M. R. Chance, *Proc. Natl. Acad. Sci. U.S.A.* **109**, 14882–14887 (2012).
22. A. Wilson *et al.*, *Plant Cell* **24**, 1972–1983 (2012).
23. C. A. Kerfeld, M. Alexandre, D. Kirilovsky, in *Carotenoids: Physical, Chemical and Biological Functions and Properties*, J.T. Landrum, Ed. (CRC Press, Boca Raton, FL, 2009), pp. 3–17.
24. U. K. Genick *et al.*, *Science* **275**, 1471–1475 (1997).
25. J. D. King, H. Liu, G. He, G. S. Orf, R. E. Blankenship, *FEBS Lett.* **588**, 4561–4565 (2014).
26. G. D. Scholes, K. P. Ghiggino, *J. Phys. Chem.* **98**, 4580–4590 (1994).
27. D. Jallet, M. Gwizdala, D. Kirilovsky, *Biochim. Biophys. Acta Bioenerg.* **1817**, 1418–1427 (2012).
28. D. Jallet *et al.*, *Plant Physiol.* **164**, 790–804 (2014).
29. H. Zhang *et al.*, *Biochemistry* **53**, 13–19 (2014).
30. L. Tian *et al.*, *J. Am. Chem. Soc.* **133**, 18304–18311 (2011).

ACKNOWLEDGMENTS

Supported by the U.S. Department of Energy (DOE), Basic Energy Sciences, award DE-FG02-91ER20021. We thank the staff at the Berkeley Center for Structural Biology, which is supported in part by the National Institute of General Medical Sciences and the Howard Hughes Medical Institute. We thank R. Celestre for assistance at beamline 5.3.1. The Advanced Light Source at Lawrence Berkeley National Laboratory is supported by the Office of Science, Office of Basic Energy Sciences, of the U.S. DOE under contract no. DE-AC02-05CH11231. This research used resources of the National Energy Research Scientific Computing Center, a DOE Office of Science User Facility supported by the Office of Science of the U.S. DOE under contract no. DE-AC02-05CH11231 and of the Joint BioEnergy Institute supported by the Office of Science, Office of Biological and Environmental Research, of the U.S. DOE under contract DE-AC02-05CH11231. A.W., A.T., C.B., and D.K. are supported by a grant from the Agence Nationale de la Recherche (ANR, project CYANOPROTECT), and used resources of CNRS and the Commissariat à l'Energie Atomique (CEA). We thank S. Cot for technical assistance. Coordinates have been deposited in the RCSB Protein Data Bank under accession codes 4XB4 (RCP_{CAN}) and 4XB5 (OCP_{CAN}).

SUPPLEMENTARY MATERIALS

www.sciencemag.org/content/348/6242/1463/suppl/DC1
Materials and Methods
Figs. S1 to S9
Tables S1 to S6
References (*31*–*47*)

19 January 2015; accepted 8 May 2015
10.1126/science.aaa7234

MARINE SULFUR CYCLE

Identification of the algal dimethyl sulfide–releasing enzyme: A missing link in the marine sulfur cycle

Uria Alcolombri,[1,2] Shifra Ben-Dor,[3] Ester Feldmesser,[4] Yishai Levin,[4] Dan S. Tawfik,[1]* Assaf Vardi[2]*

Algal blooms produce large amounts of dimethyl sulfide (DMS), a volatile with a diverse signaling role in marine food webs that is emitted to the atmosphere, where it can affect cloud formation. The algal enzymes responsible for forming DMS from dimethylsulfoniopropionate (DMSP) remain unidentified despite their critical role in the global sulfur cycle. We identified and characterized Alma1, a DMSP lyase from the bloom-forming algae *Emiliania huxleyi*. Alma1 is a tetrameric, redox-sensitive enzyme of the aspartate racemase superfamily. Recombinant Alma1 exhibits biochemical features identical to the DMSP lyase in *E. huxleyi*, and DMS released by various *E. huxleyi* isolates correlates with their Alma1 levels. Sequence homology searches suggest that *Alma1* represents a gene family present in major, globally distributed phytoplankton taxa and in other marine organisms.

Dimethylsulfoniopropionate (DMSP) is the major precursor of atmospheric dimethyl sulfide (DMS) and a key component of the ocean sulfur cycle. DMSP has been proposed to have physiological roles as an intracellular osmolyte and antioxidant (*1*) and also serves as an infochemical in interspecies predator-prey interactions, symbiosis, and pathogenicity (*2*–*5*). The volatile DMS is generated in oceans at remarkably high amounts, $>10^7$ tons per year. It is emitted to the atmosphere (*6*) by enzymes known as DMSP lyases and has a global role in atmosphere-ocean feedback processes (*7*, *8*). DMS also serves as a chemoattractant for phytoplankton, bacteria, zooplankton, fish, and sea birds (*3*, *9*, *10*). Several candidate DMSP lyases have been identified in marine bacteria (*11*, *12*); however, the identification of the algal DMSP lyase(s) is crucial for understanding the physiological roles of DMS, its oceanic origins, and the marine sulfur cycle (*12*–*14*) (Fig. 1).

We undertook a classical biochemical fractionation approach combined with shotgun proteomics to identify the DMSP lyase from *Emiliania huxleyi*. This coccolithophore algae is a well-established ecological model organism that forms massive oceanic blooms (*15*, *16*) and has high DMSP lyase activity (*17*). We based our search on two natural *E. huxleyi* isolates: NCMA373, which has a high level of DMSP lyase activity (*17*) (~10 fmol $cell^{-1}$ min^{-1}; herein, HL373), and NCMA374, which shows traces of activity (~2×10^{-3} fmol $cell^{-1}$ min^{-1}; LL374). Despite the different activity levels, both isolates have similar concentrations of intracellular DMSP (*17*).

Nearly all activity observed in the crude HL373 cell lysate was associated with the membrane fraction of the chloroplast and was retained by a 100-kD filter, indicating a relatively large enzyme or complex (fig. S1) [see the supplementary materials (SM)]. Because previous studies suggested antioxidant roles for DMSP and DMS (*1*) and

[1]Department of Biological Chemistry, Weizmann Institute of Science, Rehovot 76100, Israel. [2]Department of Plant and Environmental Sciences, Weizmann Institute of Science, Rehovot 76100, Israel. [3]Bioinformatics and Biological Computing Unit, Biological Services, Weizmann Institute of Science, Rehovot 76100, Israel. [4]Nancy and Stephen Grand Israel National Center for Personalized Medicine, Weizmann Institute of Science, Rehovot 76100, Israel.
*Corresponding authors. E-mail: assaf.vardi@weizmann.ac.il (A.V.); dan.tawfik@weizmann.ac.il (D.S.T.)

reported the redox sensitivity of DMSP lyases (*18*–*20*) (table S1), we tested the effect of thiol oxidation and alkylation on both the crude lysate and on the detergent-reconstituted fraction. In extracts, H_2O_2 and cysteine modifiers iodoacetamide (IAA) and Ellman's reagent inhibited DMSP lyase activity in a pH-dependent manner. Inhibition could be reversed by adding the reducing agent dithiothreitol (DTT) (Fig. 2A and fig. S1). Similar DMSP lyase biochemical properties were identified in the crude lysates of different algal species (*17*–*22*) (table S1).

Based on this proposed biochemical profile, we developed a protocol for the fractionation and enrichment for DMSP lyase, thus ensuring that the same enzyme is enriched throughout the procedure (fig. S2) (see the SM). Together with ion-exchange chromatography (fig. S3), we obtained ≥300-fold enrichment starting from crude cell lysate of *E. huxleyi* HL373 (table S2). To further visualize and identify the active enzyme, we developed an in-gel activity assay (Fig. 2B and fig. S4) (see the SM). DMSP lyase was primarily associated with a band size of ~90 kD, with an accompanying band between 130 and 250 kD (Fig. 2B). We performed shotgun liquid chromatography–tandem mass spectrometry–based proteomics analysis on bands showing lyase activity from HL373, as well as bands from LL374 corresponding to the same molecular weights but with no lyase activity. Bands from regions of the gel that showed no activity were similarly used as negative controls (fig. S4). We screened peptide sequences against a protein data set constructed from an RNA sequencing (RNA-seq) transcriptome of stationary and exponentially grown HL373 and LL374 cells (see the SM). Out of 46,400 putative transcripts, we obtained and filtered by annotation a set of 111 proteins whose peptides were identified in the MS analysis (table S3). These 111 candidates were scored using several criteria, primarily coverage (what fraction of the protein is covered by MS identified peptides) and differential transcript abundance between the HL373 and LL374 strains. Other criteria included a predicted transmembrane segment, transcript abundance, and predicted molecular weight (table S3).

Synthetic genes encoding the top five hits were overexpressed in *Escherichia coli* and tested for DMSP lyase activity. One of these examined genes, XP_005784450 (see table S3, contig comp92788_c0), named here *Alma1*, yielded high DMSP lyase activity. Accordingly, highly specific DMSP lyase activity was associated with the purified protein (450 μmol min^{-1} mg^{-1} of pure protein). Another gene, NW_005194698.1, locus 145357-146862 (see table S3, contig comp81698_c2), exhibited very low and inconsistent activity with intact *E. coli* cells, but we observed no activity in cell lysates and in the purified protein. *Alma1* is annotated in the *E. huxleyi* genome (*16*) as a hypothetical nuclear-encoded gene containing two introns, thus ruling out the possibility of a bacterial gene originating from a nonaxenic *E. huxleyi* culture (*11*). Furthermore, the *Alma1* gene shares no homology to any of the known bacterial DMSP lyase families. The biochemical profile of the recombinant Alma1 was identical to that of the protein mediating the DMSP lyase activity in *E. huxleyi* HL373 cell lysates (Fig. 2). Specifically, recombinant Alma1 was also found to be redox-sensitive in a pH-dependent manner, inhibited by cysteine modifiers, and metal-independent. Although Alma1 was purified from a chloroplast-rich fraction, and DMSP biosynthesis was predicted to be localized to the chloroplast in plants (*23*) and marine diatoms (*24*), we could not detect a canonical chloroplast-targeting sequence. Alma1 is natively a homotetramer, with an overall molecular weight of approximately 160 kD, as confirmed by gel filtration (fig. S5). Moreover, it also retained its activity upon acetone precipitation and hexane rinses, as observed in the algal isolated enzyme (fig. S1) (see the SM). Given that at least one bacterial DMSP lyase (DddD) is a CoA-transferase/lyase (*25*, *26*) and that *E. huxleyi* possesses a DddD homolog (*16*), we tested the effect of acetyl-CoA. We found no effect on Alma1's DMSP lyase activity, either with the *E. coli*–expressed enzyme or in HL373 lysates. Finally, by using ^{13}C-labeled DMSP, we determined that the product of catalysis was acrylate, as previously reported (*18*), and not 3-hydroxypropianate as the bacterial DddD product (*25*) (fig. S6).

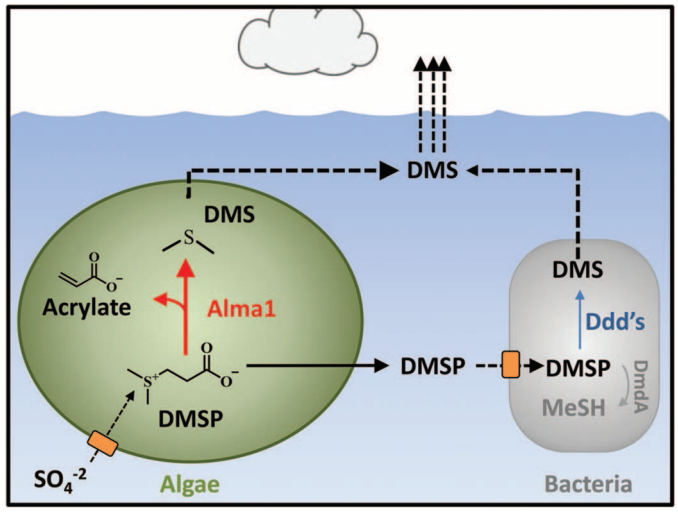

Fig. 1. DMSP catabolism in the ocean is mediated by both bacterial and algal DMSP lyases. DMSP is predominantly synthesized by algae. Under grazing or viral lysis, DMSP is released and catabolized by marine bacteria via demethylation (DmdA) or lyase activity (Ddd's). Alternatively, algal DMSP can be directly lysed by Alma1 (this study) to release acrylate and DMS, which is than emitted to the atmosphere (dashed line).

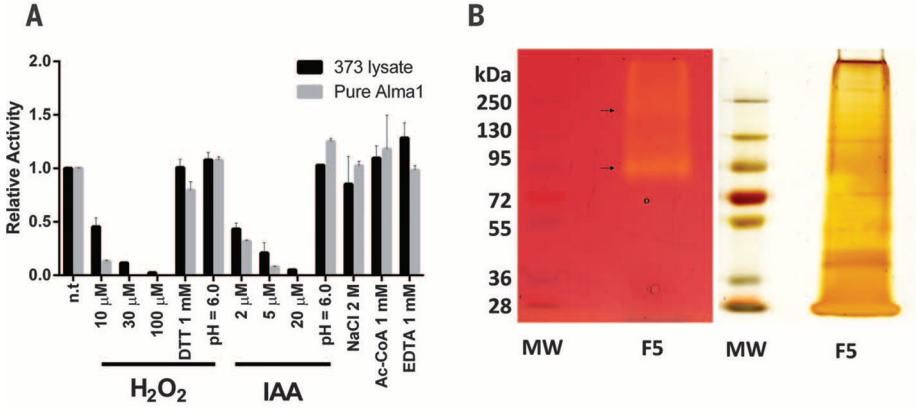

Fig. 2. Alma1 mediates the DMSP lyase activity in HL373 *Emiliania huxleyi*. (**A**) Biochemical profiling of the DMSP lyase activity observed in crude HL373 cell lysates (black bars) and in the recombinant *E. coli*–expressed Alma1 (gray bars). Initial enzymatic rates of DMS release were normalized to the rate in samples with no treatment (n.t.). Data are mean ± SD; $N \geq 2$. Reactions with H_2O_2 or IAA were performed at pH = 8.5 unless otherwise noted. Reactions performed at pH = 6.0 with 100 μM H_2O_2 or 20 μM iodoacetamide were normalized to no treatment at pH = 6.0. DTT relates to a sample treated first with 100 μM H_2O_2, followed by 1 mM DTT for 15 min. (**B**) Purified fraction was analyzed by in-gel activity assay. DMSP lyase activity causes proton release and was visualized by a pH indicator changing its color to yellow. The SDS–polyacrylamide gel electrophoresis gel was subsequently rinsed and silver-stained to detect the corresponding protein bands (right).

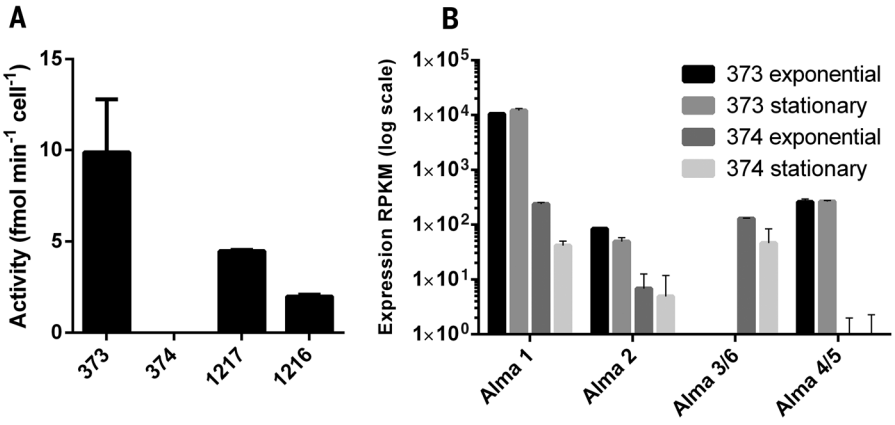

Fig. 3. Correlation between DMSP lyase activity and Alma1 mRNA expression level in different *E. huxleyi* strains. (**A**) The DMS release levels measured in the crude cell lysates of different *E. huxleyi* strains upon the addition of 10 mM DMSP. Data are mean ± SD; *N* = 2. (**B**) Relative expression of the different *Alma* genes in exponential or stationary-growth phase of strains HL373 (high DMSP lyase) and LL374 (low DMSP lyase). Data derived from RNA-seq transcriptome (see the SM). Expression is presented in RPKM (reads per kilobase per million). Data are mean ± SD; *N* = 2.

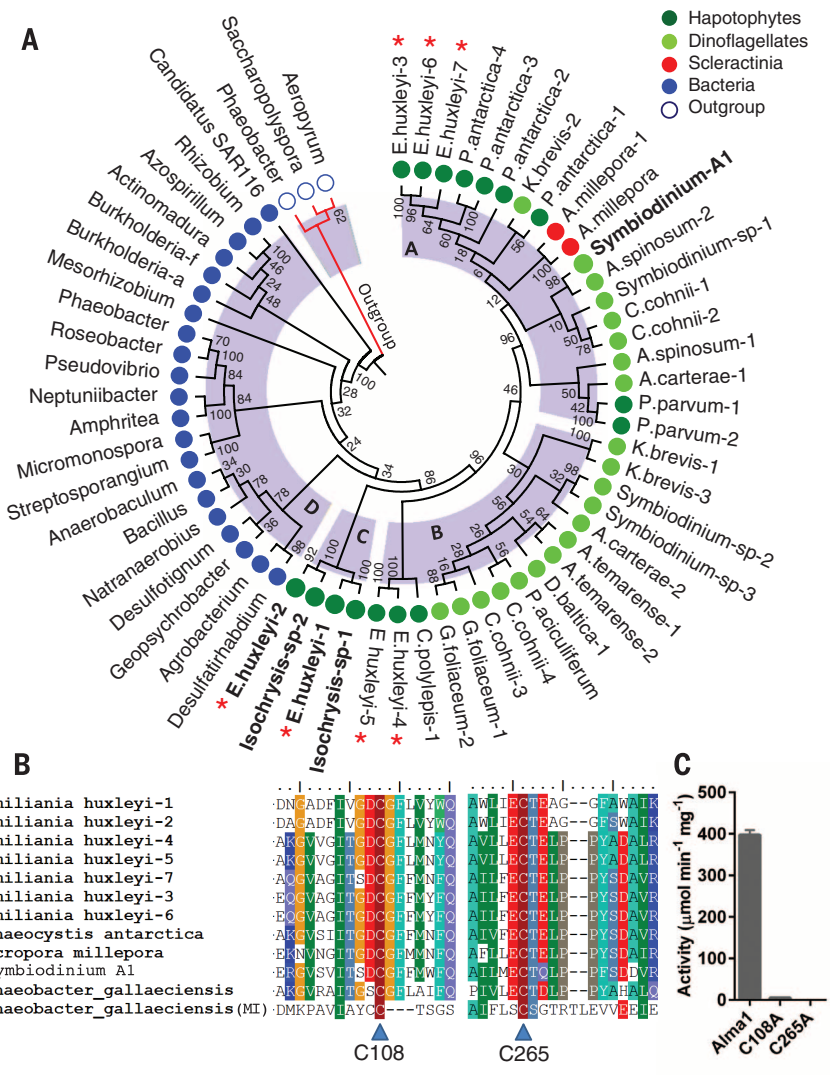

Fig. 4. A phylogenetic tree of the Alma family. (**A**) Schematic view of the maximum likelihood phylogenetic tree of the Alma1-like proteins identified in NCBI and in the Marine Microbial Eukaryote Transcriptome Sequencing Project (http://data.imicrobe.us/project/view/104). The seven *E. huxleyi* paralogs are marked with red stars. Genes with confirmed DMSP lyase activity are marked in bold (the *Isochrysis* sp. orthologs are ≥99% identical to *alma1* or *alma2* and are therefore confirmed by identity). Clades A to D are shaded in light blue. The outgroup is composed of representative maleate isomerases genes. (**B**) Representative alignment of Alma's active site residues. MI, maleate isomerase outgroup. (**C**) Specific DMSP lyase activity of recombinant Alma1 and its C108A and C265A mutants at 10 mM DMSP. Data are mean ± SD; *N* = 2.

The DMSP lyase activity levels in various *E. huxleyi* isolates correlated with protein abundance, as indicated by Western blot using antibody to recombinant Alma1 (fig. S7). Alma1's transcript levels were also up to 300 times as high in HL373 compared with LL374, consistent with 10,000-fold activity difference (Fig. 3) (*17*). Accordingly, the Alma1 peptides were only abundant in HL373 proteomics samples but could not be detected in LL374 samples (table S3). Similarly, 12 times higher mRNA levels of *Alma1* were observed in the haploid *E. huxleyi* strain RCC1217 compared with its related diploid strain *E. huxleyi* RCC1216 (*27*, *28*), whereas the DMSP lyase activities in these two strains differed by a factor of about 2.5 (Fig. 3A). Alma1 showed no substantial changes in enzymatic rate at salt concentrations up to 2 M and at pH 6 to 8 (Fig. 2A and fig. S8). The recombinant enzyme exhibited a specificity activity (k_{cat}/K_M) value of 0.8×10^5 M^{-1} s^{-1} (fig. S8), more than 1000 times higher than the characterized oceanic bacterial DMSP lyase DddP (*13*, *25*, *29*).

Based on the National Center for Biotechnology Information (NCBI) conserved domain database (CCD), Alma1 is a member of the Asp/Glu/hydantoin racemase superfamily (E-value = 8.33×10^{-25}) that comprises several enzyme families, including aspartate, glutamate, and hydantoin racemases, as well as maleate isomerase and arylmalonate decarboxylase. Phylogenetic analysis shows that Alma-like sequences are distinctly separated from maleate isomerases used here as an outgroup, even when genes from the same genome are included [e.g., *Phaeobacter gallaeciensis* has both maleate isomerases and Alma1-like putative DMSP lyases (Fig. 4A)]. All enzymes belonging to this racemase superfamily catalyze the abstraction and/or addition of a proton from a carbon next to a carboxylate. Accordingly, Alma1 catalyzes proton abstraction at the same position, resulting in a β-elimination and the release of DMS and acrylate. Crystal structures of various superfamily members indicate two active-site cysteines that catalyze proton abstraction and addition (and one cysteine only in decarboxylases). Alma1 and its identified orthologs possess both cysteines, C108 and C265 (Fig. 4, B and C, and fig. S8). Mutating cysteine 108 to alanine resulted in activity lower by a factor of

75, indicating that C108 is contributing but not crucial for catalysis. In contrast, mutating cysteine 265 to alanine resulted in complete loss of activity (Fig. 4C). These findings are in agreement with β-elimination demanding only one proton abstraction (as opposed to isomerization) and with C265 acting as the catalytic base.

The *E. huxleyi* genome has 7 *Alma* paralogs (see the SM) (Fig. 4A) (*16*). However, the transcriptome analysis indicates that *Alma1* is by far the most highly expressed *Alma* gene in HL*373* (≥40 times as much as all other paralogs) (Fig. 3). There appear to be four clades of *Alma* paralogs, with *Alma3/6* and *Alma7* (Clade A) being most closely related to *Alma* genes from *Phaeocystis antarctica*, another bloom-forming algal species that possesses high DMSP lyase activity and large DMS emissions (*20*, *22*). Clade A (Fig. 4A) also includes key algal species that are known to possess high DMSP lyase activity, dinoflagellates (e.g., *Symbiodinium* sp., a coral symbiont), other haptophytes (e.g., *Prymnesium parvum*) (*20*, *30*), and coral orthologs (*Acropora millepora*). Although DMSP can also be produced by corals (*31*), DMSP lyase activity is thought to be associated with symbiotic algae and/or associated bacteria and not with the coral itself (*32*). Within clade B (Fig. 4A), several *Alma* genes were found to have two Alma1-like domains fused in tandem, including *E. huxleyi Alma4/5* and the *Chrysochromulina polylepis* gene. Clade C (Fig. 4A) includes *E. huxleyi Alma1* and *Alma2* that also appear in the closely related *Isochrysis*. The more distant clade D comprises bacterial genes with ~30% identity to *Alma1*, but its relevance is yet to be determined. We synthesized five genes from across the phylogenetic tree and expressed them in *E. coli* (see the SM). Two genes, *E. huxleyi Alma2* (clade C) and *Symbiodinium*-A1 (clade A) were expressed at low levels, yet exhibited lyase activity upon feeding DMSP to *E. coli* culture (fig. S10). However, these two enzymes were not sufficiently stable to be purified.

The identification of the family members of the newly identified algal DMSP lyase in a wide range of marine organisms would enable better understanding of the physiological and signaling roles of DMS in algal resistance to viral infection, predation (*5*), and commensal (*14*) and symbiotic interaction (*31*). Although it is clear that DMS production by bacteria DMSP lyases has a fundamental role in the oceanic sulfur and carbon cycles, the newly revealed algal enzyme may allow quantification of the relative biogeochemical contribution of algae and bacteria to the global DMS production.

REFERENCES AND NOTES

1. W. Sunda, D. J. Kieber, R. P. Kiene, S. Huntsman, *Nature* **418**, 317–320 (2002).
2. E. Garcés, E. Alacid, A. Reñé, K. Petrou, R. Simó, *ISME J.* **7**, 1065–1068 (2013).
3. M. Garren *et al.*, *ISME J.* **8**, 999–1007 (2014).
4. J. Decelle *et al.*, *Proc. Natl. Acad. Sci. U.S.A.* **109**, 18000–18005 (2012).
5. G. V. Wolfe, M. Steinke, G. O. Kirst, *Nature* **387**, 894–897 (1997).
6. A. J. Kettle, M. O. Andreae, *J. Geophys. Res. Atmos.* **105** (D22), 26793–26808 (2000).
7. R. J. Charlson, J. E. Lovelock, M. O. Andreae, S. G. Warren, *Nature* **326**, 655–661 (1987).
8. P. K. Quinn, T. S. Bates, *Nature* **480**, 51–56 (2011).
9. J. R. Seymour, R. Simó, T. Ahmed, R. Stocker, *Science* **329**, 342–345 (2010).
10. M. S. Savoca, G. A. Nevitt, *Proc. Natl. Acad. Sci. U.S.A.* **111**, 4157–4161 (2014).
11. A. R. Curson, J. D. Todd, M. J. Sullivan, A. W. Johnston, *Nat. Rev. Microbiol.* **9**, 849–859 (2011).
12. C. R. Reisch, M. A. Moran, W. B. Whitman, *Front Microbiol* **2**, 172 (2011).
13. M. A. Moran, C. R. Reisch, R. P. Kiene, W. B. Whitman, *Annu. Rev. Mar. Sci.* **4**, 523–542 (2012).
14. R. Simó, *Trends Ecol. Evol.* **16**, 287–294 (2001).
15. W. M. Balch, P. M. Holligan, S. G. Ackleson, K. J. Voss, *Limnol. Oceanogr.* **36**, 629–643 (1991).
16. B. A. Read *et al.*, *Nature* **499**, 209–213 (2013).
17. M. Steinke, G. V. Wolfe, G. O. Kirst, *Mar. Ecol. Prog. Ser.* **175**, 215–225 (1998).
18. G. L. Cantoni, D. G. Anderson, *J. Biol. Chem.* **222**, 171–177 (1956).
19. M. P. de Souza, Y. P. Chen, D. C. Yoch, *Planta* **199**, 433–438 (1996).
20. J. Stefels, L. Dijkhuizen, *Mar. Ecol. Prog. Ser.* **131**, 307–313 (1996).
21. M. K. Nishiguchi, L. J. Goff, *J. Phycol.* **31**, 567–574 (1995).
22. B. R. Mohapatra, A. N. Rellinger, D. J. Kieber, R. P. Kiene, *Aquat. Biol.* **18**, 185–195 (2013).
23. J. Stefels, *J. Sea Res.* **43**, 183–197 (2000).
24. B. R. Lyon, P. A. Lee, J. M. Bennett, G. R. DiTullio, M. G. Janech, *Plant Physiol.* **157**, 1926–1941 (2011).
25. U. Alcolombri, P. Laurino, P. Lara-Astiaso, A. Vardi, D. S. Tawfik, *Biochemistry* **53**, 5473–5475 (2014).
26. J. D. Todd *et al.*, *Science* **315**, 666–669 (2007).
27. P. von Dassow *et al.*, *Genome Biol.* **10**, R114 (2009).
28. S. D. Rokitta *et al.*, *J. Phycol.* **47**, 829–838 (2011).
29. U. Alcolombri, M. Elias, A. Vardi, D. S. Tawfik, *Proc. Natl. Acad. Sci. U.S.A.* **111**, E2078–E2079 (2014).
30. A. M. N. Caruana, G. Malin, *Prog. Oceanogr.* **120**, 410–424 (2014).
31. J. B. Raina *et al.*, *Nature* **502**, 677–680 (2013).
32. J. B. Raina, E. A. Dinsdale, B. L. Willis, D. G. Bourne, *Trends Microbiol.* **18**, 101–108 (2010).

ACKNOWLEDGMENTS

We thank S. Albeck for assistance with the gel filtration analysis, S. Rosenwasser for important insights regarding the transcriptome de novo construction, U. Sheyn for assistance with the experimental setup for the transcriptome, A. Admon for mass spectrometry, P. Laurino for the nuclear magnetic resonance analysis, R. Hashayev for technical assistance with fractionation, and S. Graff for the graphic design. We gratefully acknowledge financial support from the Sasson and Marjorie Peress Philanthropic Fund to D.S.T. and from the European Research Council (ERC) StG (INFOTROPHIC grant 280991) to A.V. All data are available in the supplementary materials. Transcriptome sequences are deposited in NCBI's Sequence Read Archive, BioProjectID PRJNA283462. Author contributions: U.A., D.S.T, and A.V. conceived the project, designed the experiments, analyzed the data, and wrote the paper. U.A. performed the experiments. S.B.-D. and E.F. performed the transcriptome analyses. Y.L. performed the shotgun proteomics.

SUPPLEMENTARY MATERIALS

www.sciencemag.org/content/348/6242/1466/suppl/DC1
Materials and Methods
Figs. S1 to S10
Tables S1 to S3
References (*33*–*41*)

19 March 2015; accepted 15 May 2015
10.1126/science.aab1586

CLIMATE CHANGE

Possible artifacts of data biases in the recent global surface warming hiatus

Thomas R. Karl,[1]* Anthony Arguez,[1] Boyin Huang,[1] Jay H. Lawrimore,[1] James R. McMahon,[2] Matthew J. Menne,[1] Thomas C. Peterson,[1] Russell S. Vose,[1] Huai-Min Zhang[1]

Much study has been devoted to the possible causes of an apparent decrease in the upward trend of global surface temperatures since 1998, a phenomenon that has been dubbed the global warming "hiatus." Here, we present an updated global surface temperature analysis that reveals that global trends are higher than those reported by the Intergovernmental Panel on Climate Change, especially in recent decades, and that the central estimate for the rate of warming during the first 15 years of the 21st century is at least as great as the last half of the 20th century. These results do not support the notion of a "slowdown" in the increase of global surface temperature.

The Intergovernmental Panel on Climate Change (IPCC) Fifth Assessment Report (*1*) concluded that the global surface temperature "has shown a much smaller increasing linear trend over the past 15 years [1998–2012] than over the past 30 to 60 years." The more recent trend was "estimated to be around one-third to one-half of the trend over 1951–2012." The apparent slowdown was termed a "hiatus" and inspired a suite of physical explanations for its cause, including changes in radiative forcing, deep ocean heat uptake, and atmospheric circulation changes (*2*–*12*). Although these analyses and theories have considerable merit in helping to understand the global climate system, other important aspects of the "hiatus" related to observational biases in global surface temperature data have not received similar attention. In particular, residual data biases in the modern era could well have muted recent warming, and as stated by IPCC, the trend period itself was short and commenced with a strong El Niño

[1]National Oceanographic and Atmospheric Administration (NOAA), National Centers for Environmental Information (NCEI), Asheville, NC 28801, USA. [2]LMI, McLean, VA, USA.
*Corresponding author. E-mail: thomas.r.karl@noaa.gov

Downloaded from www.sciencemag.org on June 26, 2015

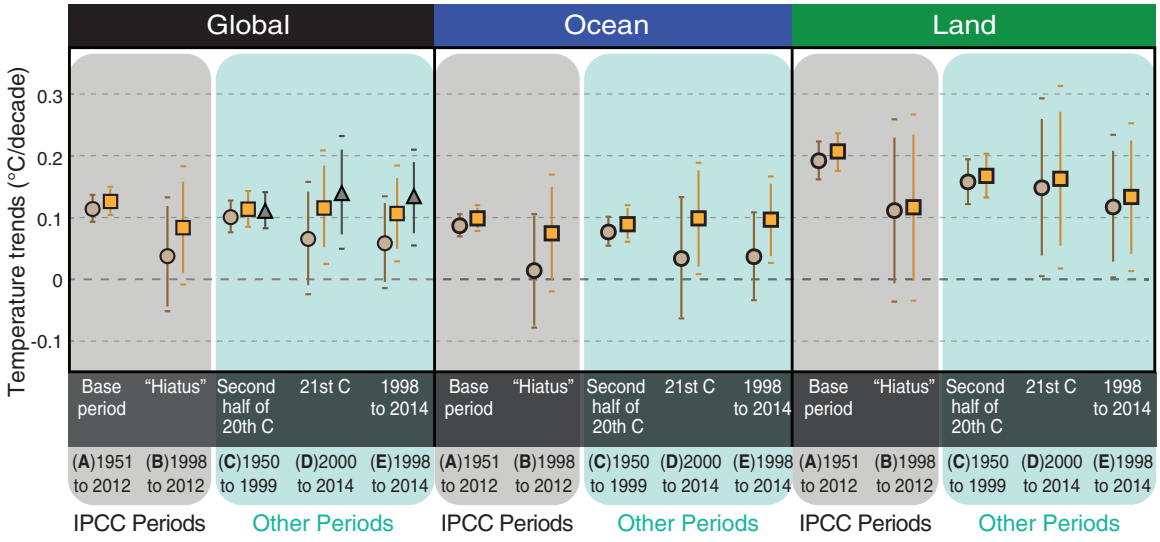

Fig. 1. Effect of new analysis on global surface temperature trends for several periods. Temperature trends are shown for data with the "new" analysis (squares) and "old" analysis (circles) for several periods of interest. Also indicated are global values calculated with the new corrections and the polar interpolation method (triangles). Consistent with the IPCC report (*1*), the error bars represent the 90% confidence intervals (CIs). The additional error associated with uncertainty of our corrections extends the 90% CI and is depicted with a horizontal dash. (**A** and **B**) The base period (1951–2012) and "hiatus" period used in IPCC (*1*). (**C**) An alternate base period, the second half of the 20th century. (**D**) The 21st century through 2014. (**E**) 1998 (a strong El Niño year) through the 21st century. Source data are provided in table S1.

in 1998. Given recent improvements in the observed record (*13*, *14*) and additional years of global data (including a record-warm 2014), we reexamine the observational evidence related to a "hiatus" in recent global surface warming.

The data used in our long-term global temperature analysis primarily involve surface air temperature observations taken at thousands of weather-observing stations over land, and for coverage across oceans, the data are sea surface temperature (SST) observations taken primarily by thousands of commercial ships and drifting surface buoys. These networks of observations are always undergoing change. Changes of particular importance include (i) an increasing amount of ocean data from buoys, which are slightly different than data from ships; (ii) an increasing amount of ship data from engine intake thermometers, which are slightly different than data from bucket seawater temperatures; and (iii) a large increase in land-station data, which enables better analysis of key regions that may be warming faster or slower than the global average. We address all three of these, none of which were included in our previous analysis used in the IPCC report (*1*).

First, several studies have examined the differences between buoy- and ship-based data, noting that the ship data are systematically warmer than the buoy data (*15*–*17*). This is particularly important because much of the sea surface is now sampled by both observing systems, and surface-drifting and moored buoys have increased the overall global coverage by up to 15% (supplementary materials). These changes have resulted in a time-dependent bias in the global SST record, and various corrections have been developed to account for the bias (*18*). Recently, a new correction (*13*) was developed and applied in the Extended Reconstructed Sea Surface Temperature (ERSST) data set version 4, which we used in our analysis. In essence, the bias correction involved

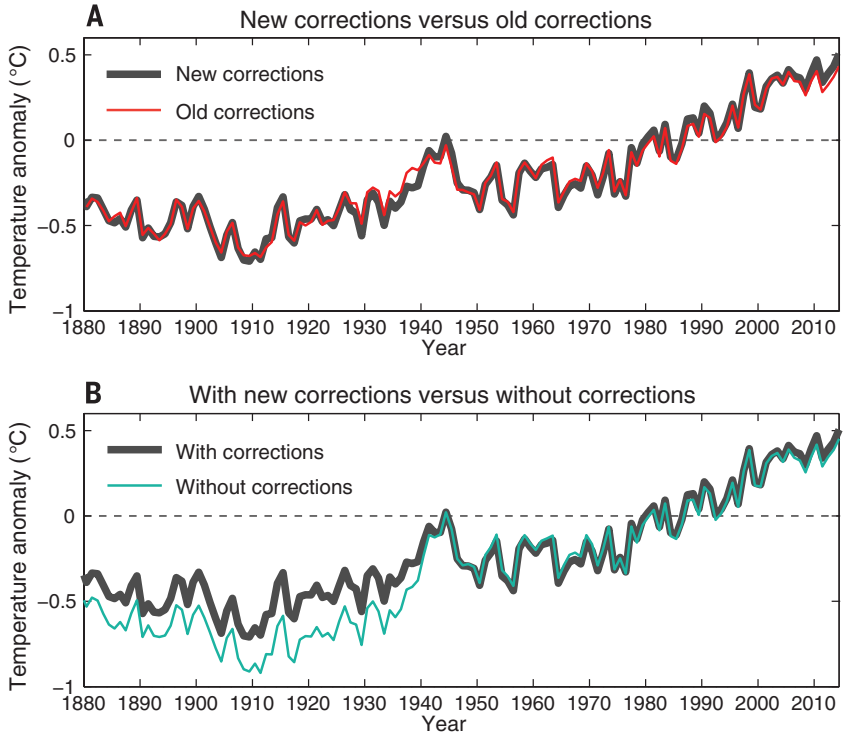

Fig. 2. Global (land and ocean) surface temperature anomaly time series with new analysis, old analysis, and with and without time-dependent bias corrections. (**A**) The new analysis (solid black) compared with the old analysis (red). (**B**) The new analysis (solid black) versus no corrections for time-dependent biases (blue).

calculating the average difference between collocated buoy and ship SSTs. The average difference globally was −0.12°C, a correction that is applied to the buoy SSTs at every grid cell in ERSST version 4. [IPCC (*1*) used a global analysis from the UK Met Office that found the same average ship-buoy difference globally, although the corrections applied in that analysis were equal to differences observed within each ocean basin (*18*).] More generally, buoy data have been proven to be more accurate and reliable than ship data, with better-known instrument characteristics and automated sampling (*16*). Therefore, ERSST version 4 also considers this smaller buoy uncertainty in the reconstruction (*13*).

Second, there was a large change in ship observations (from buckets to engine intake thermometers) that peaked around World War II. The

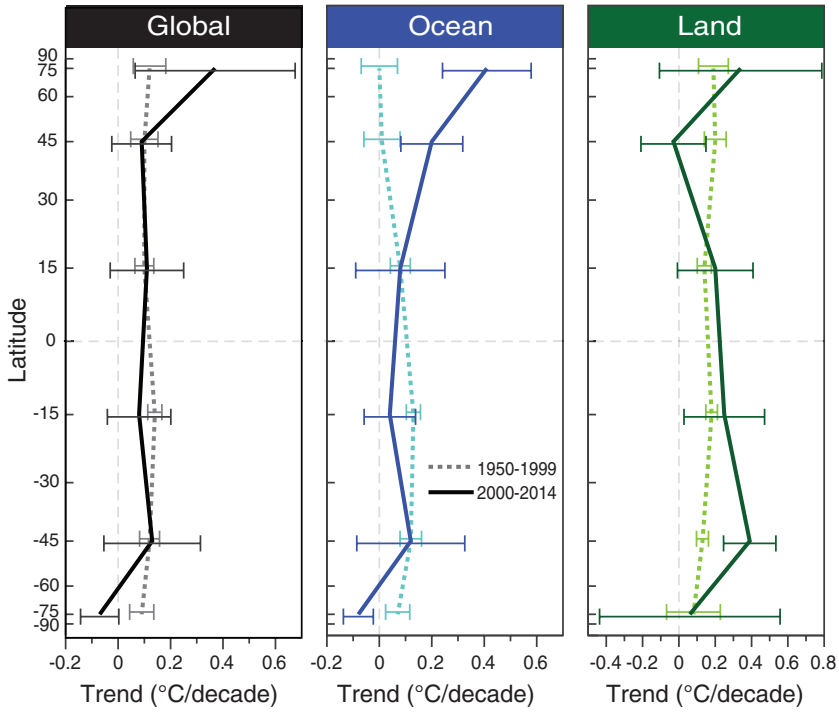

Fig. 3. Latitudinal profiles of surface temperature trends. Zonal mean trends and statistical uncertainty of the trend estimates for global, ocean, and land surface temperature, averaged in 30° latitudinal belts, for the second half of the 20th century (dashed) compared with the past 15 years (solid). Trends are cosine-weighted within latitude belts, and the vertical axis is on a sine scale so as to reflect the proportional surface area of the latitude bands. Only the uncertainty related to the trend estimates is provided because zonal standard errors of estimate are not available in contrast to the global averages.

previous version of ERSST assumed that no ship corrections were necessary after this time, but recently improved metadata (*18*) reveal that some ships continued to take bucket observations even up to the present day. Therefore, one of the improvements to ERSST version 4 is extending the ship-bias correction to the present, based on information derived from comparisons with night marine air temperatures. Of the 11 improvements in ERSST version 4 (*13*), the continuation of the ship correction had the largest impact on trends for the 2000–2014 time period, accounting for 0.030°C of the 0.064°C trend difference with version 3b. [The buoy offset correction contributed 0.014°C decade^{-1} to the difference, and the additional weight given to the buoys because of their greater accuracy contributed 0.012°C decade^{-1} (supplementary materials).]

Third, there have also been advancements in the calculation of land surface air temperatures (LSTs). The most important is the release of the International Surface Temperature Initiative (ISTI) databank (*14*, *19*), which forms the basis of the LST component of our new analysis. The ISTI databank integrates the Global Historical Climatology Network (GHCN)–Daily data set (*20*) with more than 40 other historical data sources, more than doubling the number of stations available. The resulting integration improves spatial coverage over many areas, including the Arctic, where temperatures have increased rapidly in recent decades (*1*). We applied the same methods used in our old analysis for quality control, time-dependent bias corrections, and other data processing steps (*21*) to the ISTI databank in order to address artificial shifts in the data caused by changes in, for example, station location, temperature instrumentation, observing practice, urbanization, and siting conditions. These corrections are essentially the same as those used in the GHCN–Monthly version 3 data set (*22*, *23*), which is updated operationally by the National Oceanographic and Atmospheric Administration's (NOAA's) National Centers for Environmental Information (NCEI). To obtain our new global analysis, the corrected ISTI land data (*14*) were systematically merged with ERSST version 4 (*13*), as described in the supplementary materials.

In addition to the three improvements just discussed, since the IPCC report (*1*) new analyses (*24*) have revealed that incomplete coverage over the Arctic has led to an underestimate of recent (since 1997) warming in the Hadley Centre/Climate Research Unit data used in the IPCC report (*1*). These analyses have surmised that incomplete Arctic coverage also affects the trends from our analysis as reported by IPCC (*1*). We address this issue as well.

Temperature trends in our old analysis and our new analysis are depicted in Fig. 1, supplemented with polar interpolation. (In this discussion, "old" refers to the analysis based on ERSST version 3b for ocean areas and GHCN–Monthly version 3 for land areas). For the most recent IPCC period (1998–2012), the new analysis exhibits more than twice as much warming as did the old analysis at the global scale (0.086° versus 0.039°C decade^{-1}) (table S1). This is clearly attributable to the new SST analysis, which itself has much higher trends (0.075° versus 0.014°C decade^{-1}). In contrast, trends in the new LST analysis are only slightly higher (0.117° versus 0.112°C decade^{-1}).

IPCC (*1*) acknowledged that trends since 1998 were tenuous because the period was short and commenced with a strong El Niño. Two additional years of data are now available to revisit this point, including a record-warm 2014, and trends computed through 2014 confirm the IPCC supposition. Specifically, the central trend estimate in our new analysis for 1998–2014 is 0.020°C decade^{-1} higher as compared with 1998–2012. Likewise, global trends for 2000–2014 are 0.030°C decade^{-1} higher than for 1998–2012. In other words, changing the start and end date by 2 years does in fact have a notable impact on the assessment of the rate of warming, but less compared with the impact of new time-dependent bias corrections.

Our analysis also suggests that short- and long-term warming rates are far more similar than previously estimated in IPCC's report (*1*). The difference between the trends in two periods used in IPCC's report (1998–2012 and 1951–2012) (*1*) is an illustrative metric: The trends for these two periods in the new analysis differ by 0.043°C decade^{-1} compared with 0.078°C decade^{-1} in the old analysis reported by IPCC (*1*). The smaller difference results from more warming in the new ocean analysis since 1998, reflecting the improved bias corrections in ERSST version 4. The new corrections show that the 90% confidence interval for 1998–2012 encompasses the best estimate of the trend for 1951–2012.

Also, the new global trends are statistically significant and positive at the 0.10 significance level for 1998–2012 (Fig. 1 and table S1) by using the approach described in (*25*) for determining trend uncertainty. In contrast, the IPCC report (*1*), which also used the approach in (*25*), reported no statistically significant trends for 1998–2012 in any of the three primary global surface temperature data sets. Moreover, for 1998–2014 our new global trend is 0.106° ± 0.058°C decade^{-1}, and for 2000–2014, it is 0.116° ± 0.067°C decade^{-1} (table S1). This is similar to the warming of the last half of the 20th century (Fig. 1). A more comprehensive approach for determining the 0.10 significance level (supplementary materials), which also accounts for the impact of annual errors of estimate on the trend, shows that the 1998–2014 and 2000–2014 trends (but not 1998–2012) were positive at the 0.10 significance level.

For the full period of record (1880–present) (Fig. 2), the new global analysis has essentially the same rate of warming as that of the previous analysis (0.068°C decade^{-1} and 0.065°C decade^{-1}, respectively) (table S1), reinforcing the point that the new corrections mainly have an impact in recent decades. However, it is also clear that the long-term trend would be significantly higher (0.085°C decade^{-1}) (Fig. 2B) without corrections for other historical biases, as described in (*26*).

There are important differences between the latitudinal structure of trends for the second half of the 20th century and for the 21st century (2000–2014) (Fig. 3). For example, the Arctic latitudes have shown strong warming trends both over the land and ocean since 2000, but during the latter half of the 20th century, the ocean trends in this area are near zero. The longer-term 50-year trend has more consistency in the rates of warming across all latitudes, and this is even more evident over the full period of record back to 1880 (fig. S1). There is a distinct Northern Hemisphere mid-latitude cooling in LST during the 21st century, which is also showing up in cooling of the cold extremes, as reported for the extreme minimum temperatures in this zone in (*27*). Atmospheric teleconnections and regional forcings could be relevant in understanding these short time-scale zonal trends. It is evident that in most latitude bands, the global trends in the past 15 years are comparable with trends in the preceding 50 years.

Last, we considered the impact of larger warming rates in high latitudes (*24*) on the overall global trend. To estimate the magnitude of the additional warming, we applied large-area interpolation over the poles using the limited observational data available. Results indicate that, indeed, additional global warming of a few hundredths of a degree Celsius per decade over the 21st century is evident (Fig. 1), providing further evidence against the notion of a recent warming "hiatus" (supplementary materials).

Newly corrected and updated global surface temperature data from NOAA's NCEI do not support the notion of a global warming "hiatus." As shown in Fig. 1, there is no discernable (statistical or otherwise) decrease in the rate of warming between the second half of the 20th century and the first 15 years of the 21st century. Our new analysis now shows that the trend over the period 1950–1999, a time widely agreed as having significant anthropogenic global warming (*1*), is 0.113°C decade^{-1}, which is virtually indistinguishable from the trend over the period 2000–2014 (0.116°C decade^{-1}). Even starting a trend calculation with 1998, the extremely warm El Niño year that is often used as the beginning of the "hiatus," our global temperature trend (1998–2014) is 0.106°C decade^{-1}—and we know that is an underestimate because of incomplete coverage over the Arctic. Indeed, according to our new analysis, the IPCC's (*1*) statement of 2 years ago—that the global surface temperature "has shown a much smaller increasing linear trend over the past 15 years than over the past 30 to 60 years"—is no longer valid.

REFERENCES AND NOTES

1. IPCC, *Climate Change 2013: The Physical Science Basis. Contribution of Working Group I to the Fifth Assessment Report of the Intergovernmental Panel on Climate Change*, T. F. Stocker, D. Qin, G.-K. Plattner, M. Tignor, S.K. Allen, J. Boschung, A. Nauels, Y. Xia, V. Bex, P.M. Midgley, Eds. (Cambridge Univ. Press, Cambridge, 2013).
2. G. A. Meehl, H. Teng, J. M. Arblaster, *Nature Clim. Change* **4**, 898–902 (2014).
3. G. A. Meehl, A. Hu, J. M. Arblaster, J. Fasullo, K. E. Trenberth, *J. Clim.* **26**, 7298–7310 (2013).
4. Y. Kosaka, S.-P. Xie, *Nature* **501**, 403–407 (2013).
5. M. H. England *et al.*, *Nature Clim. Change* **4**, 222–227 (2014).
6. B. D. Santer *et al.*, *Nat. Geosci.* **7**, 185–189 (2014).
7. G. A. Schmidt, D. T. Shindell, K. Tsigaridis, *Nat. Geosci.* **7**, 158–160 (2014).
8. J. Tollefson, *Nature* **505**, 276–278 (2014).
9. M. Watanabe *et al.*, *Geophys. Res. Lett.* **40**, 3175–3179 (2013).
10. J. C. Fyfe, N. P. Gillett, *Nature Clim. Change* **4**, 150–151 (2014).
11. K. E. Trenberth, J. T. Fasullo, M. A. Balmaseda, *J. Clim.* **27**, 3129–3144 (2014).
12. H. Ding, R. J. Greatbatch, M. Latif, W. Park, R. Gerdes, *J. Clim.* **26**, 7650–7661 (2013).
13. B. Huang *et al.*, *J. Clim.* **28**, 911–930 (2015).
14. J. J. Rennie *et al.*, *Geosci. Data J.* **1**, 75–102 (2014).
15. E. C. Kent, J. J. Kennedy, D. I. Berry, R. O. Smith, *Clim. Change* **1**, 718–728 (2010).
16. R. W. Reynolds, N. A. Rayner, T. M. Smith, D. C. Stokes, W. Wang, *J. Clim.* **15**, 1609–1625 (2002).
17. R. W. Reynolds, D. B. Chelton, *J. Clim.* **23**, 3545–3562 (2010).
18. J. J. Kennedy, N. A. Rayner, R. O. Smith, D. E. Parker, M. Saunby, *J. Geophys. Res. Atmos.* **116** (D14), D14104 (2011).
19. J. H. Lawrimore, J. J. Rennie, P. W. Thorne, *Eos* **94**, 61 (2014).
20. M. J. Menne, I. Durre, R. S. Vose, B. E. Gleason, T. G. Houston, *J. Atmos. Ocean. Technol.* **29**, 897–910 (2012).
21. M. J. Menne, C. N. Williams Jr., *J. Clim.* **22**, 1700–1717 (2009).
22. J. H. Lawrimore *et al.*, *J. Geophys. Res.* **116** (D19), D19121 (2011).
23. C. N. Williams, M. J. Menne, P. W. Thorne, *J. Geophys. Res.* **117** (D5), D05116 (2012).
24. K. Cowtan, R. G. Way, *Q. J. Roy. Met. Soc.* **140**, 1935–1944 (2014).
25. B. Santer *et al.*, *Int. J. Climatol.* **28**, 1703–1722 (2008).
26. T. M. Smith, R. W. Reynolds, *J. Clim.* **16**, 1495–1510 (2003).
27. J. Sillman, M. G. Donat, J. C. Fyfe, F. W. Zwiers, *Environ. Res. Lett.* **9**, 064023 (2014).

ACKNOWLEDGMENTS

We thank the many scientists at NCEI and at other institutions who routinely collect, archive, quality control, and provide access to the many complex data streams that go into the computation of the global surface temperature. In particular, we thank T. Boyer, B. Gleason, J. Matthews, J. Rennie, and C. Williams for their contributions to this analysis. We also thank J. Meehl and P. Duffy for constructive comments on an early version of this manuscript.

SUPPLEMENTARY MATERIALS

www.sciencemag.org/content/348/6242/1469/suppl/DC1
Materials and Methods
Fig. S1
Table S1
References (*28*–*38*)

23 December 2014; accepted 21 May 2015
Published online 4 June 2015;
10.1126/science.aaa5632

BRAIN CIRCUITS

A parvalbumin-positive excitatory visual pathway to trigger fear responses in mice

Congping Shang,[1,2] Zhihui Liu,[1] Zijun Chen,[1,2] Yingchao Shi,[1,2] Qian Wang,[1] Su Liu,[1] Dapeng Li,[1] Peng Cao[1]*

The fear responses to environmental threats play a fundamental role in survival. Little is known about the neural circuits specifically processing threat-relevant sensory information in the mammalian brain. We identified parvalbumin-positive (PV$^+$) excitatory projection neurons in mouse superior colliculus (SC) as a key neuronal subtype for detecting looming objects and triggering fear responses. These neurons, distributed predominantly in the superficial SC, divergently projected to different brain areas, including the parabigeminal nucleus (PBGN), an intermediate station leading to the amygdala. Activation of the PV$^+$ SC-PBGN pathway triggered fear responses, induced conditioned aversion, and caused depression-related behaviors. Approximately 20% of mice subjected to the fear-conditioning paradigm developed a generalized fear memory.

Environmental threats are detected by different sensory organs projecting to central brain areas to trigger fear responses (*1*, *2*). The superior colliculus (SC) is a retinal recipient structure (*3*, *4*) composed of different neuronal subtypes (*5*, *6*), including parvalbumin-positive (PV$^+$), somatostatin-positive (SST$^+$), and vasoactive intestinal peptide–positive (VIP$^+$) neurons (Fig. 1A and fig. S1). In addition to mediating orienting responses (*7*), the SC contributes to avoidance and defense-like behaviors (*8*–*11*). With an optogenetic approach (*12*–*14*), we found that activation of neurons expressing channelrhodopsin-2 (ChR2) in mouse SC triggered freezing that lasted 52.8 ± 5.3 s (n = 5 mice) (movie S1). This prompted us to systematically identify the key neuronal subtypes underlying this behavior.

By crossing Ai32 (*15*) with different Cre lines (Fig. 1B) (*16*, *17*), we expressed ChR2–enhanced yellow fluorescent protein (EYFP) in specific neuronal subtypes in the SC (Fig. 1C and fig. S1) and optogenetically elicited spikes in acute slices (Fig. 1D and fig. S1). Activation of SC PV$^+$ neurons, but not SST$^+$ or VIP$^+$ neurons, triggered impulsive escaping (1.18 ± 0.09 s) followed by long-lasting freezing (46.4 ± 2.8 s) (Fig. 1, E to G; fig. S1; and movie S2). To avoid activation of PV$^+$ retinal

[1]State Key Laboratory of Brain and Cognitive Sciences, Institute of Biophysics, Chinese Academy of Sciences, Beijing 100101, China. [2]University of Chinese Academy of Sciences, Beijing 100049, China.
*Corresponding author. E-mail: pcao@ibp.ac.cn

ganglion cells (RGCs) (*18*) by ferrule light, we injected adeno-associated virus (AAV) expressing double-floxed ChR2-mCherry (*12*) into the SC of *PV-ires-Cre* mice, resulting in specific expression of ChR2-mCherry in SC PV$^+$ neurons but not in PV$^+$ RGCs (Fig. 2A and fig. S2). The light triggered spikes from ChR2-mCherry–positive neurons in SC slices (Fig. 2B and fig. S2), elicited a similar stereotyped locomotor pattern (fig. S2 and movie S3), and increased the heart rate and plasma corticosterone levels that were not observed in mice with SC PV$^+$ neurons expressing mCherry (Fig. 2, C and D).

When facing threats, animals can either fight or flee. To test whether SC PV$^+$ neurons were involved in this behavioral dichotomy, we measured the durations of light-induced escaping (E) and freezing (F) and calculated their ratio (E/F ratio). We conducted a series of tests spanning 5 days (table S1). First, light stimulations with higher intensity or longer duration enhanced E/F ratios in the same male mice by prolonging escaping more strongly than freezing (Fig. 2, E and F). Second, light stimulations with higher frequency but similar total illumination time prolonged escaping and freezing proportionally (Fig. 2G). Third, both responses showed strong adaptation to repetitive light stimulations (every 5 min), with no significant change in E/F ratios across each stimulation (Fig. 2H). Finally, the same light stimulations elicited longer escaping and shorter freezing in female versus male mice, resulting in higher E/F ratios in females (Fig. 2I). The origin of these sexually dimorphic behaviors was further examined (supplementary text).

We next characterized the morphological and physiological properties of SC PV$^+$ neurons. They were predominantly but not exclusively distributed in the superficial gray (SuG) layer of the SC (Fig. 3A and fig. S3). Whole-cell recording of tdTomato-expressing PV$^+$ neurons in SC slices from *PV-ires-Cre; Ai9* mice (*19*) demonstrated that, distinct from V1 PV$^+$ interneurons with slow frequency adaptation (*20*), the SuG PV$^+$ neurons responded to depolarizing currents in a faster adaptation mode (Figs. 3, C and D, and fig. S3). SuG PV$^+$ neurons labeled with neurobiotin had parallel dendrites extending to the SC surface, presumably receiving inputs from RGCs (Fig. 3B and fig. S3). The postsynaptic currents from PV-negative neurons induced by optogenetic activation of PV$^+$ neurons expressing ChR2-mCherry were blocked by

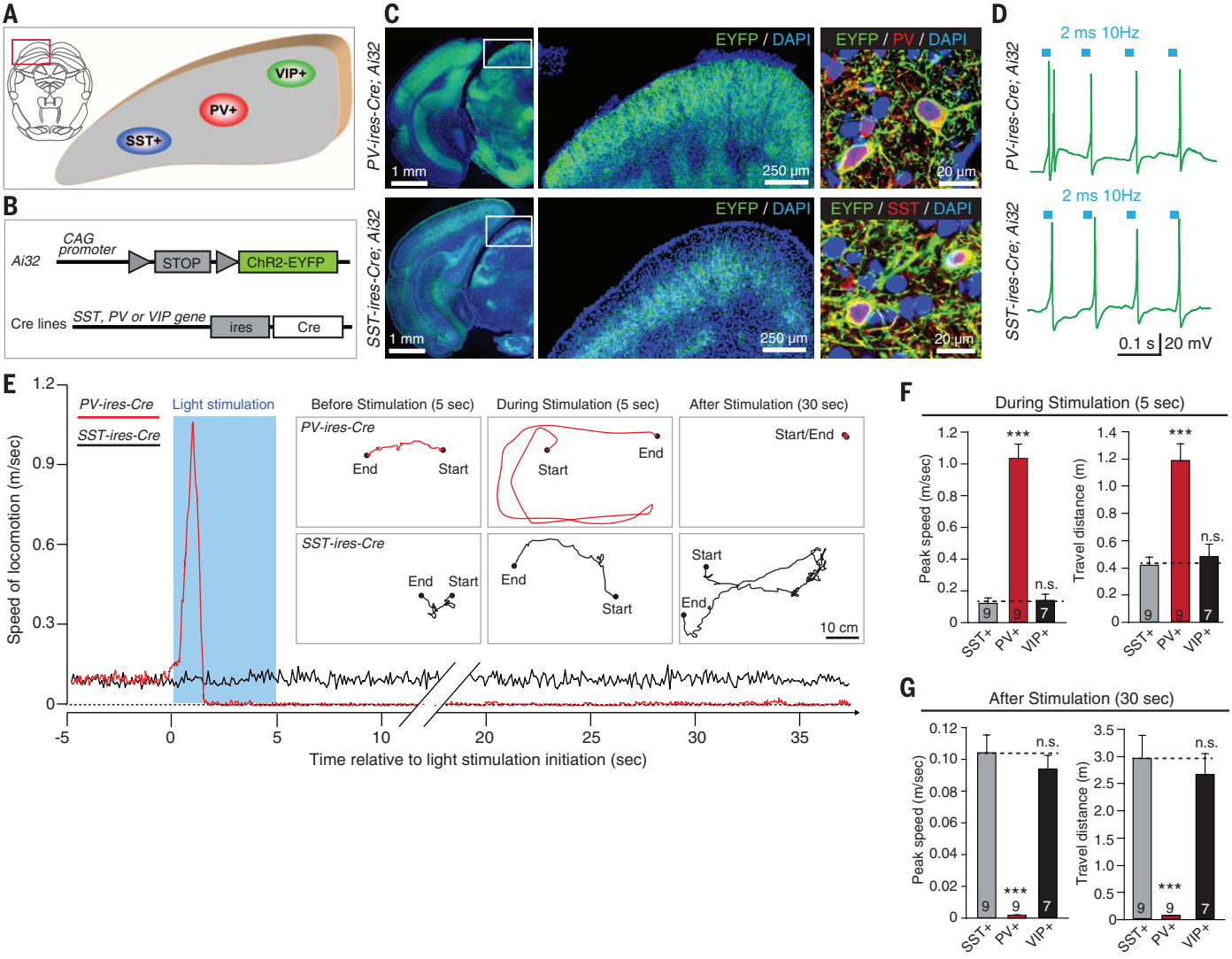

Fig. 1. Neuronal subtypes in the SC to trigger fear responses. (**A**) Diagram of different neuronal subtypes in the SC. (**B**) *Ai32* mice were crossed with different Cre lines. (**C**) Coronal micrographs showing ChR2-EYFP expressed in specific neuronal subtypes. DAPI, 4′,6-diamidino-2-phenylindole. (**D**) Light-induced spikes from ChR2-EYFP$^+$ neurons in acute slices. (**E**) Instantaneous locomotion speed before, during, and after light stimulation. (Inset) Locomotion trails from example mice. (**F** and **G**) Analyses of peak speed and travel distance during and after light stimulation. Data in (F) and (G) are means ± SEM (error bars); numbers of mice are in bars. Statistical analysis is *t* test (***$P < 0.001$; n.s. $P > 0.1$). Dashed lines in (F) and (G) indicate the control levels measured from behaviors after SC SST$^+$ neuron activation.

D-(−)-2-amino-5-phosphonopentanoic acid (APV) and 6-cyano-7-nitroquinoxaline-2,3-dione (CNQX), but not by picrotoxin (Fig. 3, E and F, and fig. S3), suggesting that these neurons were glutamatergic but did not release γ-aminobutyric acid. The SC PV$^+$ neurons in intermediate and deep layers of the SC were examined (supplementary text).

To test whether SC PV$^+$ neurons were involved in detecting collision threats in the visual field (*21*–*23*), we displayed a virtual soccer ball moving in controlled velocities and directions to the anaesthetized mice (Fig. 3J and fig. S4). The single-unit activity recorded with optrodes was quantitatively identified (*24*, *25*) as putative SC PV$^+$ neurons expressing ChR2-mCherry (Fig. 3, G to I). These putative PV$^+$ neurons (n = 9 cells) were strongly activated by the ball moving toward the animal but not by the motion in the other five directions (Fig. 3K). The response onset time before collision depended on the size and velocity of the ball (Fig. 3L) and was linearly correlated with the square root of the diameter/velocity (Fig. 3M). The response peak was close to the time to collision and was independent of the size and velocity of the soccer ball (Fig. 3N). In freely behaving mice, the escaping triggered by SC PV$^+$ neuron activation pointed to the side of the SC receiving light stimulation (movie S4).

We then determined the circuit mechanism underlying the fear responses mediated by SC PV$^+$ neurons. By injecting AAV expressing double-floxed monomeric green fluorescent protein (mGFP) into the SC of *PV-ires-Cre* mice, we specifically labeled SC PV$^+$ neurons (Fig. 4B and figs. S5 and S6) and observed axon terminals in the parabigeminal nucleus (PBGN), the pontine nucleus (Pn), and the dorsal lateral geniculate nucleus (DLGN) (Fig. 4, A and C). These projections were confirmed by retrograde tracing with cholera toxin B with Alexa Fluor-594 (CTB-594). CTB-594 injection into the PBGN (Fig. 4D) retrogradely labeled SC neurons predominantly in the ipsilateral SuG layer (Fig. 4E and fig. S7). A considerable proportion of CTB-labeled SC neurons (SC-PBGN: 52 ± 4.3%; SC-Pn: 31 ± 4.5%; SC-DLGN: 33 ± 3.8%, n = 3 mice) were positive for PV (Fig. 4F and fig. S7).

To determine which of these parallel projections (*26*) participated in the fear responses, we injected AAV expressing double-floxed ChR2-mCherry into the SC and implanted optic fibers in the PBGN or Pn (Fig. 4G) to locally stimulate the ChR2-mCherry–positive axon terminals. Activation of the PV$^+$ SC-PBGN pathway, but not the PV$^+$ SC-Pn pathway, triggered the stereotyped

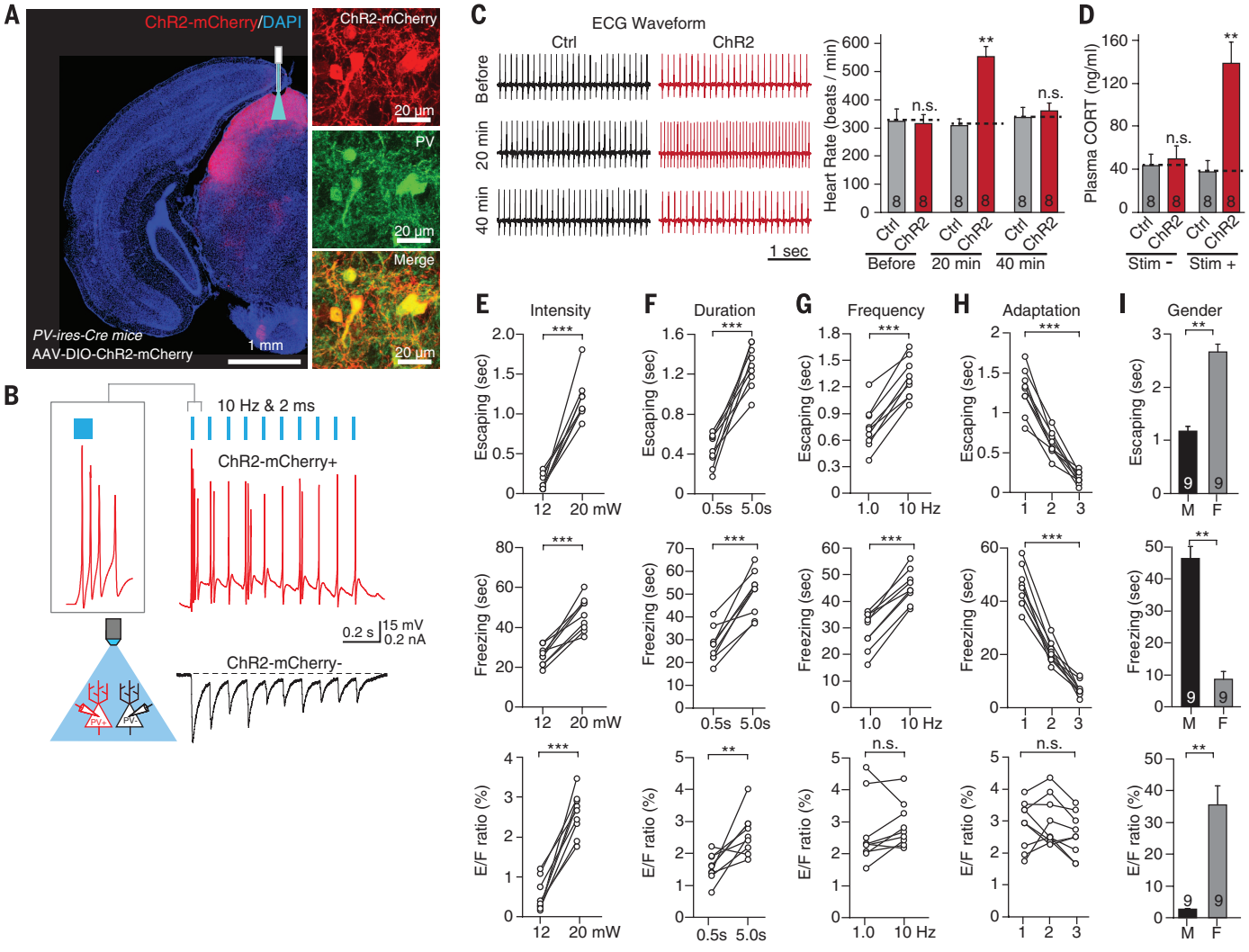

Fig. 2. Specific activation of SC PV$^+$ neurons induced fear responses. (**A**) Specific expression of ChR2-mCherry in SC PV$^+$ neurons of *PV-ires-Cre* mice. (**B**) The light-pulse train triggered spikes (red) from ChR2-mCherry–positive neurons and postsynaptic currents (black) from adjacent ChR2-mCherry–negative neurons. (**C**) Electrocardiographic traces and heart rate analyses from the anaesthetized mice before and after light stimulations. Ctrl, control. (**D**) Analyses of plasma corticosterone concentration in response to light stimulation. (**E** to **I**) Durations of escaping, freezing, and E/F ratios, were plotted as functions of stimulation intensity, duration, frequency, repetition, and sex in mice with SC PV$^+$ neurons expressing ChR2-mCherry. Data in (C) to (I) are means ± SEM (error bars); numbers of mice are in bars. Statistical analysis is t test (***P < 0.001; **P < 0.01; n.s. P > 0.1). Dashed lines indicate the levels measured from control mice. M, male; F, female.

escaping-freezing locomotor pattern (Fig. 4, H to J; fig. S9, and movie S5). We examined whether PBGN projected to the amygdala by anterograde and retrograde tracings. Local injection of AAV-SynaptoTag (*27*) in the PBGN and its adjacent region strongly labeled axon terminals positive for synaptobrevin-2–EGFP in the central amygdaloid nucleus (*28*, *29*), whereas CTB-594 injection in the amygdala retrogradely labeled neurons in the PBGN (fig. S8). Finally, the relation between PV$^+$ SC-PBGN pathway activation and the affective state of mice was explored (supplementary text and figs. S10 to S12). Taken together, these data revealed a PV$^+$ excitatory visual pathway to trigger stereotyped fear responses in mice.

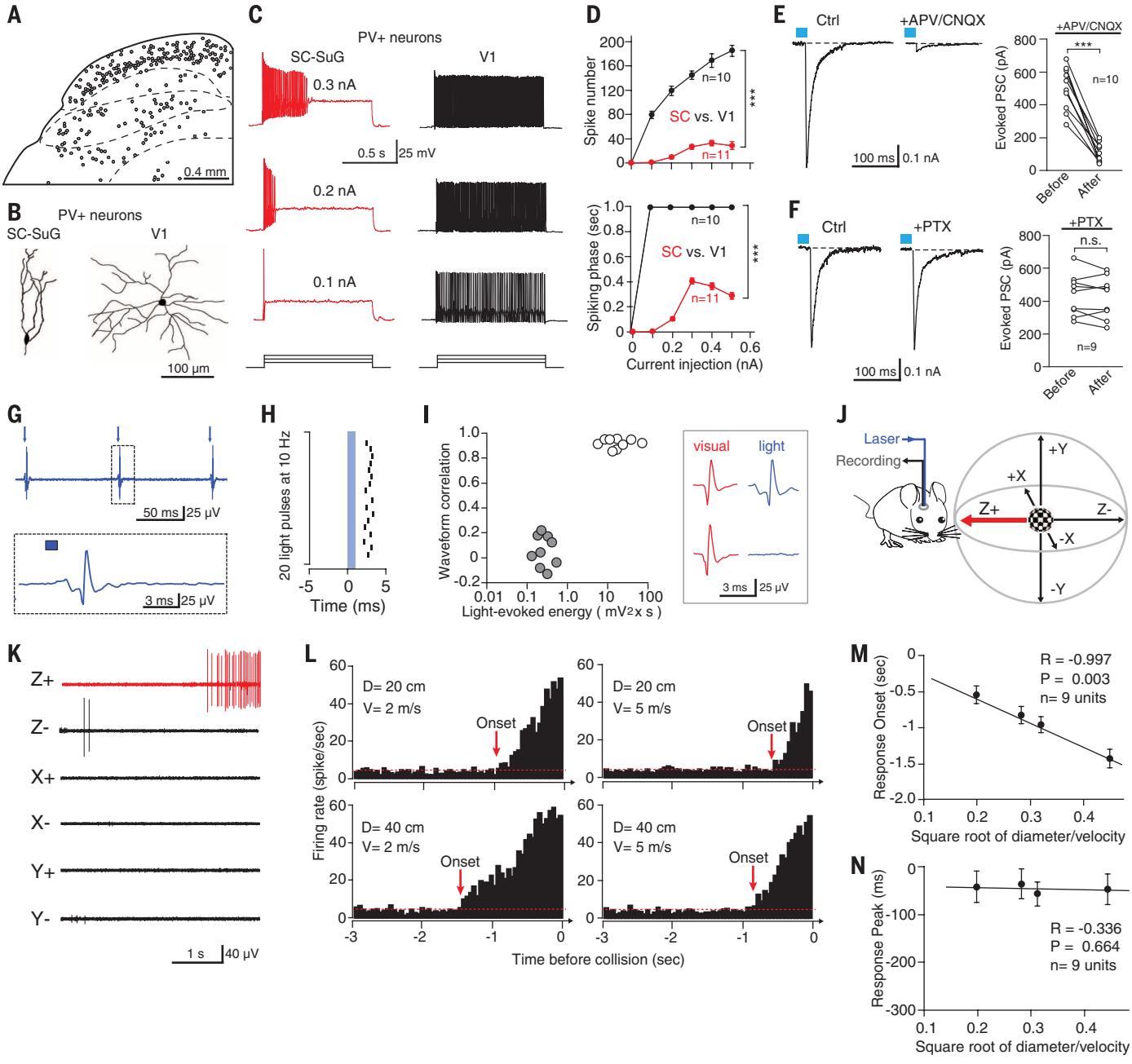

Fig. 3. Morphological and physiological properties of SC PV$^+$ neurons. (**A**) Layer-specific distribution of SC PV$^+$ neurons. (**B**) Neurobiotin-labeled PV$^+$ neurons in the SC SuG layer and V1. (**C**) Spike firings of PV$^+$ neurons in the SC and V1 to depolarizing currents. (**D**) Analyses of spike number and spiking phase as a function of current intensity. n, number of cells. (**E** and **F**) Effects of CNQX (20 μM)/APV (50 μM) (E) and picrotoxin (50 μM) (F) on the postsynaptic currents (PSC) induced by light stimulation. n, number of cells. (**G**) Single-unit activity recorded from a putative SC PV$^+$ neuron triggered by light pulses (arrows, 1 ms at 10 Hz). (**H**) Raster plot showing the latency of light-evoked spikes relative to the light pulses (0 ms). (**I**) Distributional plot (left) and example spikes (right) evoked by visual stimuli and light showing quantitative identification of PV-positive and PV-negative units based on the waveform correlation and energy of light-evoked spikes. (**J**) A virtual soccer ball flying toward the eye of an anaesthetized mouse. (**K**) Example single-unit traces from a putative SC PV$^+$ neuron in response to the soccer ball (20 cm in diameter) moving in six directions at 2 m/s. (**L**) Peristimulus time histograms of a PV$^+$ neuron to looming stimuli with controlled velocities (V) (2 and 5 m/sec) and diameters (D) (20 and 40 cm). Arrows indicate response onset time. (**M** and **N**) Correlation analyses of response onset time (M) and response peak time (N) of SC PV$^+$ neurons and the square root of diameter/velocity of the looming ball. Data are means ± SEM (error bars); numbers of cells or units are in graphs. Statistical analyses are *t* test and one-way analysis of variance (***$P < 0.001$; n.s. $P > 0.1$). R, correlation coefficient.

Our data lead to the following conclusions. First, the SC PV$^+$ neurons form a subcortical visual pathway that transmits threat-relevant visual information to the amygdala to trigger fear responses. These data, in alliance with earlier studies (*18*, *30*, *31*), suggest a "retina-SC-PBGN-amygdala-hypothalamus" pathway for vision-induced fear responses. Second, the SC PV$^+$ neurons in the SuG layer are predominantly glutamatergic

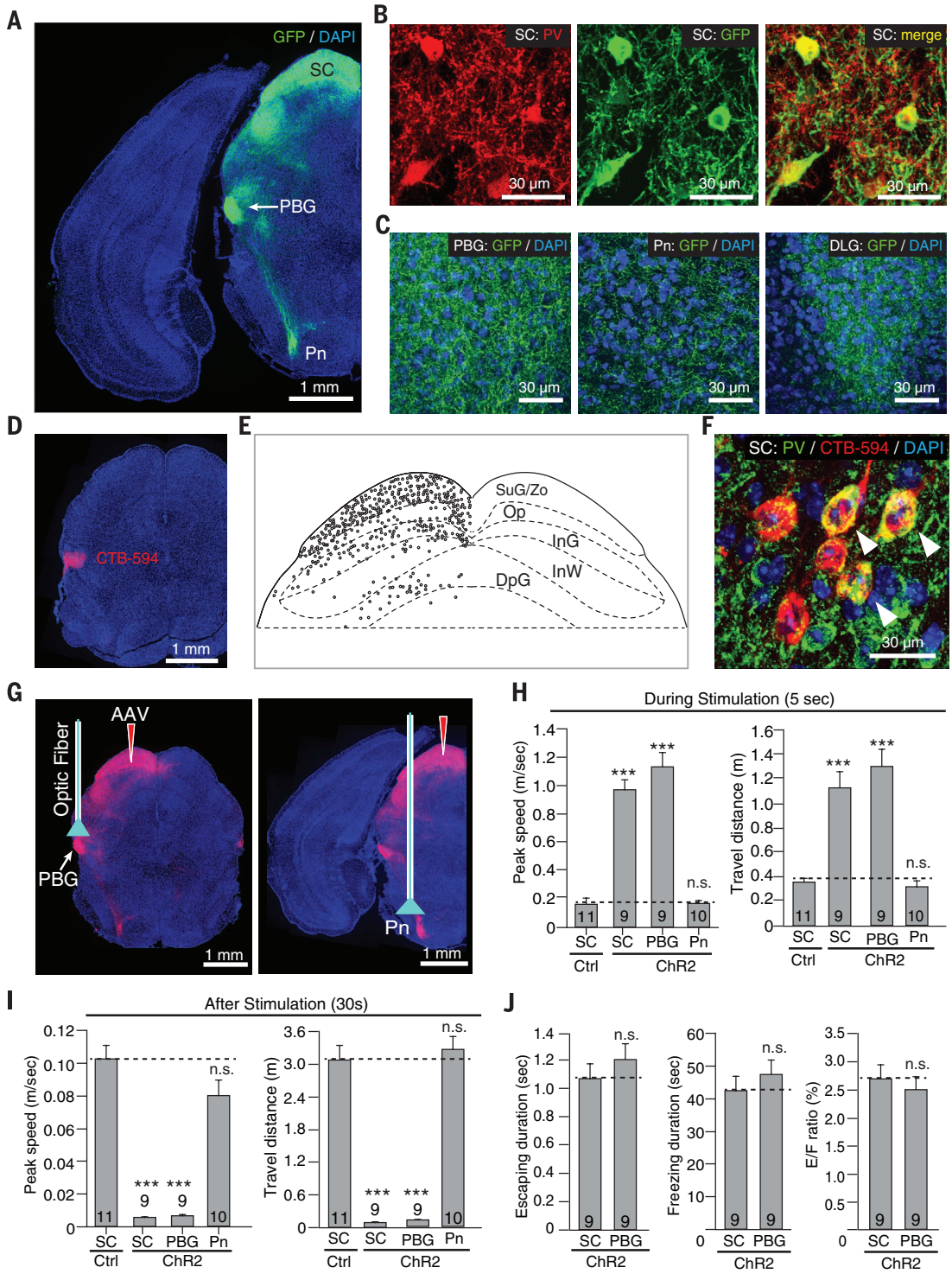

Fig. 4. PV$^+$ SC-PBGN pathway mediated fear responses. (**A** to **C**) Specific expression of mGFP in SC PV$^+$ neurons (B) of *PV-ires-Cre* mice resulted in labeling of their axon terminals in the PBGN, Pn, and DLGN [(A) and (C)]. (**D** to **F**) CTB-594 injected in the PBGN (D) retrogradely labeled cells in the SC (E), a large proportion of which were PV$^+$ (denoted by arrowheads) (F). DpG, deep gray layer; InW, intermediate white layer; Ing, intermediate gray layer; Op, optic nerve layer; Zo, zonal layer. (**G**) Diagrams showing the optic fibers implanted either above the PBGN or the Pn to stimulate ChR2-mCherry–positive axon terminals. (**H** and **I**) Locomotion analyses during and after the activation of PV$^+$ SC-PBGN and SC-Pn pathways. (**J**) Analyses of escaping, freezing, and E/F ratio in mice receiving activation of the PV$^+$ SC-PBGN pathway and SC PV$^+$ neurons. Data in (H) to (J) are means ± SEM (error bars); numbers of mice are in bars. Statistical analysis is *t* test (***P < 0.001; n.s. P > 0.1).

projection neurons with spiking patterns distinct from those of their counterparts in cortical regions. Thus, this finding broadens the concept of PV^+ neurons (*32*) and adds another perspective to understanding their functions. Third, the SC PV^+ neurons may belong to type-ρ looming detector, supporting the notion that mathematically defined computational units correspond to specific neuronal subtypes (*33*).

REFERENCES AND NOTES

1. E. A. Krusemark, W. Li, *J. Neurosci.* **33**, 587–594 (2013).
2. J. P. Johansen, C. K. Cain, L. E. Ostroff, J. E. LeDoux, *Cell* **147**, 509–524 (2011).
3. L. P. Morin, K. M. Studholme, *J. Comp. Neurol.* **522**, 3733–3753 (2014).
4. E. H. Feinberg, M. Meister, *Nature* **519**, 229–232 (2015).
5. R. J. Cork, S. Z. Baber, R. R. Mize, *J. Comp. Neurol.* **394**, 205–217 (1998).
6. R. R. Mize, *Prog. Brain Res.* **112**, 35–55 (1996).
7. B. D. Corneil, D. P. Munoz, *Neuron* **82**, 1230–1243 (2014).
8. N. Sahibzada, P. Dean, P. Redgrave, *J. Neurosci.* **6**, 723–733 (1986).
9. P. Dean, P. Redgrave, G. W. Westby, *Trends Neurosci.* **12**, 137–147 (1989).
10. J. D. Cohen, M. A. Castro-Alamancos, *J. Neurosci.* **30**, 8502–8511 (2010).
11. J. T. DesJardin *et al.*, *J. Neurosci.* **33**, 150–155 (2013).
12. F. Zhang *et al.*, *Nat. Protoc.* **5**, 439–456 (2010).
13. J. P. Johansen, S. B. Wolff, A. Lüthi, J. E. LeDoux, *Biol. Psychiatry* **71**, 1053–1060 (2012).
14. Experimental procedures are explained in the supplementary materials on *Science* Online.
15. L. Madisen *et al.*, *Nat. Neurosci.* **15**, 793–802 (2012).
16. S. Hippenmeyer *et al.*, *PLOS Biol.* **3**, e159 (2005).
17. H. Taniguchi *et al.*, *Neuron* **71**, 995–1013 (2011).
18. T. A. Münch *et al.*, *Nat. Neurosci.* **12**, 1308–1316 (2009).
19. L. Madisen *et al.*, *Nat. Neurosci.* **13**, 133–140 (2010).
20. V. F. Descalzo, L. G. Nowak, J. C. Brumberg, D. A. McCormick, M. V. Sanchez-Vives, *J. Neurophysiol.* **93**, 1111–1118 (2005).
21. Y. J. Liu, Q. Wang, B. Li, *Brain Behav. Evol.* **77**, 193–205 (2011).
22. M. Yilmaz, M. Meister, *Curr. Biol.* **23**, 2011–2015 (2013).
23. X. Zhao, M. Liu, J. Cang, *Neuron* **84**, 202–213 (2014).
24. P. Anikeeva *et al.*, *Nat. Neurosci.* **15**, 163–170 (2012).
25. J. Y. Cohen, S. Haesler, L. Vong, B. B. Lowell, N. Uchida, *Nature* **482**, 85–88 (2012).
26. E. Comoli *et al.*, *Front. Neuroanat.* **6**, 9 (2012).
27. W. Xu, T. C. Südhof, *Science* **339**, 1290–1295 (2013).
28. A. Pitkänen, V. Savander, J. E. LeDoux, *Trends Neurosci.* **20**, 517–523 (1997).
29. J. F. Medina, J. C. Repa, M. D. Mauk, J. E. LeDoux, *Nat. Rev. Neurosci.* **3**, 122–131 (2002).
30. A. S. Jansen, X. V. Nguyen, V. Karpitskiy, T. C. Mettenleiter, A. D. Loewy, *Science* **270**, 644–646 (1995).
31. T. Ono, P. G. Luiten, H. Nishijo, M. Fukuda, H. Nishino, *Neurosci. Res.* **2**, 221–238 (1985).
32. H. Hu, J. Gan, P. Jonas, *Science* **345**, 1255263 (2014).
33. H. Fotowat, F. Gabbiani, *Annu. Rev. Neurosci.* **34**, 1–19 (2011).

ACKNOWLEDGMENTS

We thank T. Südhof, K. Deisseroth, Y. Wang, B. Li, and M. Luo for providing plasmids, instruments, and technical support for this study. This work was supported by the Thousand Young Talents Program of China. We declare no conflicts of interest. All data are archived in the Institute of Biophysics, Chinese Academy of Sciences.

SUPPLEMENTARY MATERIALS

www.sciencemag.org/content/348/6242/1472/suppl/DC1
Materials and Methods
Supplementary Text
Figs. S1 to S12
Table S1 and S2
Reference (*34*)
Movies S1 to S5
Data S1

6 February 2015; accepted 28 May 2015
10.1126/science.aaa8694

STRUCTURAL BIOLOGY

A Cas9–guide RNA complex preorganized for target DNA recognition

Fuguo Jiang,[1] Kaihong Zhou,[2] Linlin Ma,[2] Saskia Gressel,[3] Jennifer A. Doudna[1,2,4,5,6,7]*

Bacterial adaptive immunity uses CRISPR (clustered regularly interspaced short palindromic repeats)–associated (Cas) proteins together with CRISPR transcripts for foreign DNA degradation. In type II CRISPR-Cas systems, activation of Cas9 endonuclease for DNA recognition upon guide RNA binding occurs by an unknown mechanism. Crystal structures of Cas9 bound to single-guide RNA reveal a conformation distinct from both the apo and DNA-bound states, in which the 10-nucleotide RNA "seed" sequence required for initial DNA interrogation is preordered in an A-form conformation. This segment of the guide RNA is essential for Cas9 to form a DNA recognition–competent structure that is poised to engage double-stranded DNA target sequences. We construe this as convergent evolution of a "seed" mechanism reminiscent of that used by Argonaute proteins during RNA interference in eukaryotes.

CRISPR-Cas proteins function in complex with mature CRISPR RNAs (crRNAs) to identify and cleave complementary target sequences in foreign nucleic acids (*1*). In type II CRISPR systems, the Cas9 enzyme cleaves DNA at sites defined by the 20-nucleotide (nt) guide segment within crRNAs, together with a trans-activating crRNA (tracrRNA) (*2*) that forms a crRNA:tracrRNA hybrid structure capable of Cas9 association (*3*). Once assembled on target DNA, the Cas9 HNH and RuvC nuclease domains cleave the double-stranded DNA (dsDNA) sequence within the strands that are complementary and noncomplementary to the guide RNA segment, respectively (*3*, *4*) (Fig. 1A). By engineering a synthetic single-guide RNA (sgRNA) that fuses the crRNA and tracrRNA into a single transcript of 80 to 100 nt (Fig. 1B), Cas9:sgRNA has been harnessed as a two-component programmable system for genome engineering in various organisms (*5*, *6*).

The utility of Cas9 for both bacterial immunity and genome engineering applications relies on accurate DNA target selection. Target choice relies on base pairing between the DNA and the 20-nt guide RNA sequence, as well as the presence of a 2– to 4–base pair (bp) protospacer adjacent motif (PAM) proximal to the target site (*3*, *4*). The target complementarity of a "seed" sequence within the guide segment of crRNAs is critical for DNA recognition and cleavage (*7*, *8*). In type II CRISPR systems, Cas9 binds to targets by recognizing a PAM and searching the adjacent DNA for complementarity to the 10- to 12-nt "seed" sequence at the 3′ end of the guide RNA segment (Fig. 1B) (*3*, *9*–*11*). Crystal structures of Cas9 bound to sgRNA and a target DNA strand, with or without a partial PAM-containing nontarget strand, show the entire 20-nt guide RNA segment engaged in an A-form helical interaction with the target DNA strand (*12*, *13*). How the "seed" region within the guide RNA specifies DNA binding has remained unknown.

To determine how Cas9 assembles with and positions the guide RNA prior to substrate recognition, we solved the crystal structure of catalytically active *Streptococcus pyogenes* Cas9 (SpyCas9) in complex with an 85-nt sgRNA at 2.9 Å resolution (Fig. 1 and table S1). The overall structure of the Cas9-sgRNA binary complex, representing the pre–target-bound state of the enzyme, resembles the bilobed architecture of the target DNA–bound state, as observed in electron microscopic studies (*14*), with the guide segment of the sgRNA positioned in the central channel between the nuclease and helical recognition lobes (Fig. 1, C to E). This structural architecture and guide RNA organization is maintained in the crystal structure of a widely used nuclease-inactive version of Cas9 (D10A/H840A, referred to as dCas9) in complex with sgRNA (fig. S1).

Comparison of SpyCas9 crystal structures representing the protein alone and the RNA-bound and RNA-DNA–bound states of the enzyme reveals the nature of Cas9's conformational flexibility during sgRNA binding and target DNA recognition (Fig. 2A and figs. S2 and S3). The helical recognition lobe undergoes substantial rearrangements upon sgRNA binding but before DNA association, especially in helical domain 3, which moves as a rigid body by ~65 Å into close proximity with the HNH domain (fig. S2D). Superposition of the Cas9-sgRNA pre–target-bound complex onto the target DNA–bound structures reveals further

[1]Department of Molecular and Cell Biology, University of California, Berkeley, CA 94720, USA. [2]Howard Hughes Medical Institute, University of California, Berkeley, CA 94720, USA. [3]Max Planck Institute for Biophysical Chemistry, 37077 Göttingen, Germany. [4]California Institute for Quantitative Biosciences, University of California, Berkeley, CA 94720, USA. [5]Department of Chemistry, University of California, Berkeley, CA 94720, USA. [6]Physical Biosciences Division, Lawrence Berkeley National Laboratory, Berkeley, CA 94720, USA. [7]Innovative Genomics Initiative, University of California, Berkeley, CA 94720, USA.
*Corresponding author. E-mail: doudna@berkeley.edu

Downloaded from www.sciencemag.org on June 26, 2015

conformational changes, including a modest shift in helical domains 2 and 3, as well as a concomitant displacement of the HNH domain toward the target strand (Fig. 2A and fig. S2, E and F). Together with limited proteolysis data (Fig. 2B and fig. S4), these results show that sgRNA binding drives the major conformational changes within Cas9 (*14*), although additional structural rearrangements occur upon substrate DNA binding. Interestingly, a guide-target mismatched DNA duplex yields a proteolytic pattern similar to that observed for sgRNA-bound Cas9 (fig. S4B), indicating that Cas9-sgRNA pretarget conformation is competent for PAM recognition because no further conformational change is required prior to target DNA binding.

The single-stranded guide RNA binding triggers ordering of the PAM recognition region of Cas9. In the absence of sgRNA, Cas9's PAM-interacting C-terminal domain (CTD) is largely disordered (fig. S2A) (*14*). However, in the Cas9-sgRNA pre–target-bound complex and target DNA–bound structures, the PAM-interaction CTD domain is structured to accommodate the PAM duplex (Fig. 2C). Two critical arginine resides (Arg^{1333} and Arg^{1335}) involved in 5′-NGG-3′ PAM recognition (*13*) are pre-positioned in the Cas9-sgRNA structure to recognize the GG dinucleotide on the nontarget DNA strand. This explains biochemical data indicating that the Cas9-sgRNA complex uses PAM recognition as an obligate step to identify potential DNA target sites (*9*).

In the Cas9-sgRNA structure, the RNA adopts an L-shaped configuration in which the 5′ guide segment lies in close spatial proximity to stem loop 1 of the sgRNA (Fig. 1C and fig. S5). Similar to the DNA-bound Cas9 complexes, Cas9 in the pre–target-bound state makes extensive hydrogen-bonding contacts and aromatic stacking interactions with the crRNA repeat:tracrRNA anti-repeat duplex and stem loop 1 (fig. S6) (*12*, *15*). In contrast to the sgRNA scaffold (nucleotides G21 to U82) for which clear electron density is observed, we observed unambiguous electron density for only 10 of the 20 nucleotides of the guide RNA segment (nucleotides 11 to 20; Fig. 1, B and C), all of which are located in the seed region. Nucleotides 1 to 10 of the guide RNA segment, although present in

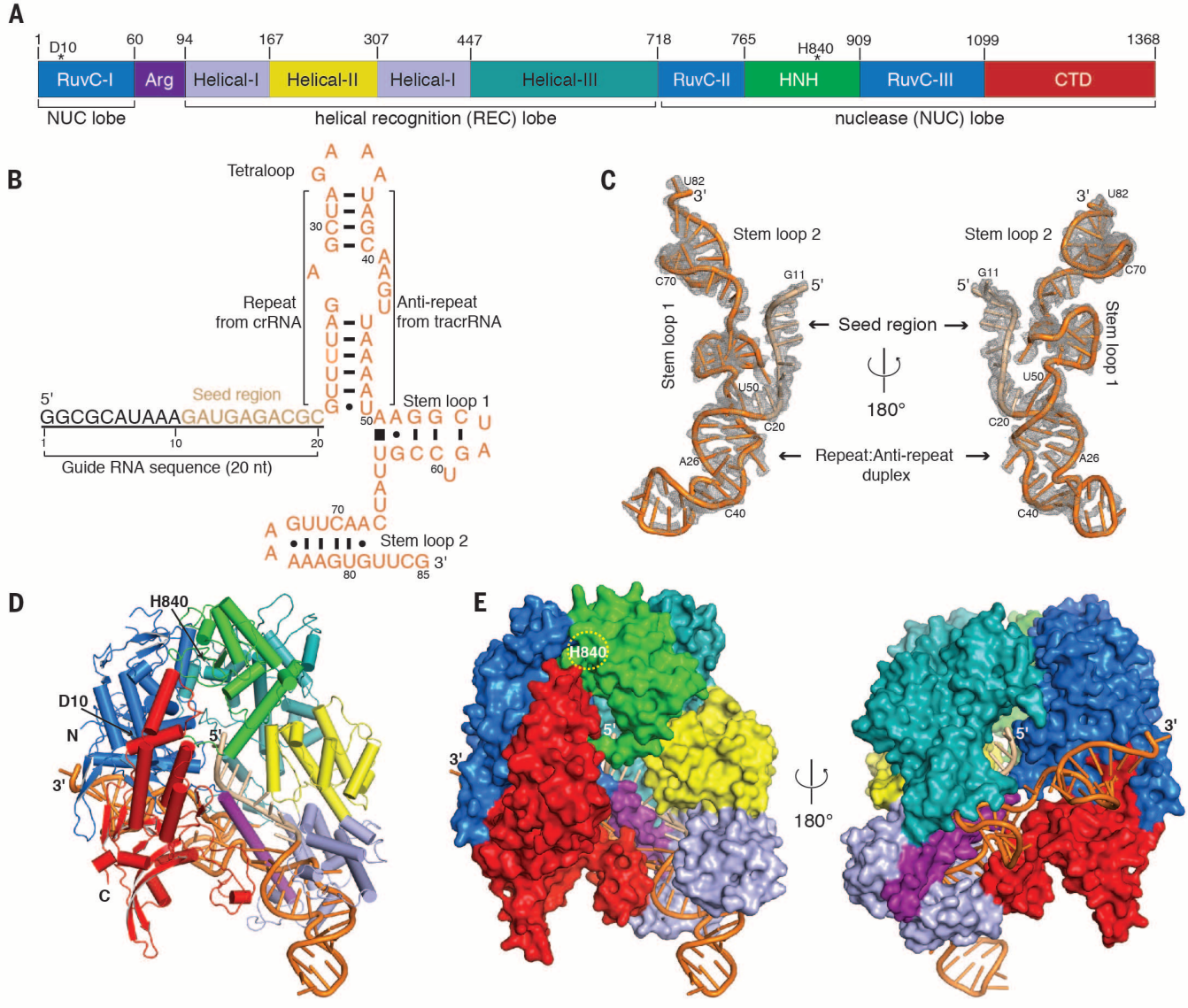

Fig. 1. Overall structure of SpyCas9-sgRNA binary complex. (**A**) Domain organization of the type II-A Cas9 protein from *S. pyogenes* (SpyCas9). (**B**) Secondary structure diagram of sgRNA bearing complementarity to a 20-bp region λ1 DNA. The seed sequence is highlighted in beige. Bars between nucleotide pairs represent canonical Watson-Crick base pairs; dots indicate noncanonical base-pairing interactions. The base stacking interaction is indicated by a filled square. (**C**) Tertiary structure of sgRNA in ribbon representation, with a sigma-A weighted composite-annealed omit $2F_{obs} - F_{calc}$ electron density map contoured at 1.5σ. (**D**) Ribbon diagram of SpyCas9-sgRNA complex, color-coded as defined in Fig. 1, A and B. (**E**) Surface representations of the crystal structure of SpyCas9 in complex with sgRNA (depicted in cartoon) showing the same view as in Fig. 1D and a 180°-rotated view.

the crystals (fig. S1), are disordered. The ordered seed nucleotides (G11 to C20, counting from the 5′ end of the sgRNA) are threaded through the narrow nucleic acid–binding channel formed between the two Cas9 lobes, with their bases facing outward (Fig. 2D and fig. S7). Nucleotides G19, C20, and G11 to U13 are exposed to bulk solvent, whereas nucleotides G14 to C18 are shielded from solvent by helical domain 2. The solvent-exposed PAM-proximal seed nucleotides G19 and C20 are therefore positioned to serve as the nucleation site for initiating target binding. This explains how a 2-bp mismatch immediately adjacent to the PAM in the DNA abolishes Cas9 binding and cleavage activity (*9*).

The single-stranded guide RNA within the seed region maintains a nearly A-form conformation along the ribose-phosphate backbone (Fig. 2E). To maintain this helical configuration, Cas9 makes extensive hydrogen-bonding interactions with phosphates and 2′-hydroxyl groups of the seed nucleotides (Fig. 2F). Such presentation of the seed sequence in a conformation thermodynamically favorable for helical guide:target duplex formation (*16*) is reminiscent of the guide RNA positioning observed in eukaryotic Argonaute complexes that recognize transcripts by base pairing with a 6-nt RNA seed sequence (fig. S8, A and B) (*17*–*19*). This situation is distinct from that observed in the type I CRISPR-Cascade targeting complex, in which the entire crRNA guide region is preordered, rather than just the seed segment (fig. S8C) (*20*–*22*).

Another similarity between the Cas9-bound sgRNA guide segment and the Argonaute-bound microRNA guide segment is the synchronized tilting of bases at each half-helical turn of the RNA strand. In the Cas9-sgRNA complex, a kink introduced by insertion of Tyr^{450} between seed nucleobases A15 and G16 results in coordinated tilting of nucleobases G11 to A15 relative to the same region of the guide RNA in the target-bound state (Fig. 2, E and F, and fig. S8A). Notably, the orientation of Tyr^{450} shifts by ~120° upon target binding (Fig. 2F). The bases G16 to C20 remain in an untilted orientation that is immediately ready for target DNA base pairing. This nonuniformity in base orientation may account for previous observations showing that the 5-nt sequence of the guide RNA that binds to DNA immediately adjacent to the PAM is the most critical segment for Cas9 binding (*23*).

Structural and biochemical data suggest that guide RNA binding triggers a large structural rearrangement in Cas9. To test whether the seed segment of the RNA itself contributes to formation of an activated Cas9 conformation, we monitored Cas9-sgRNA assembly with the use of a set of progressively truncated guide RNAs containing 0 to 20 nt of the guide segment (N_0 to N_{20}; table S2). Limited proteolysis showed that guide RNA binding confers protection from trypsin digestion only when the guide segment has a length of at least 10 nt of the target recognition sequence (N_{10}) (Fig. 3A and fig. S9). The absence of the guide segment results in moderately decreased Cas9

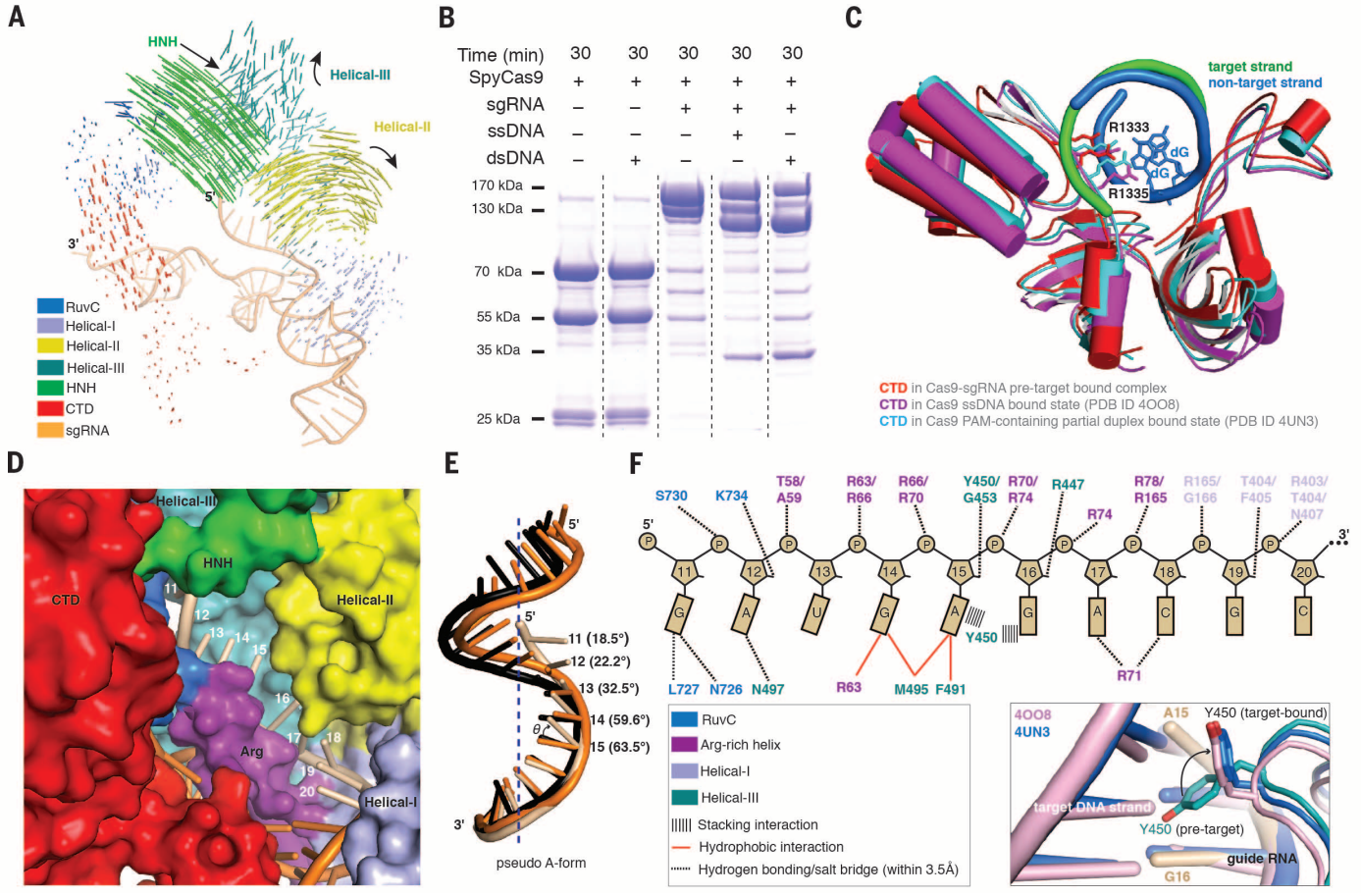

Fig. 2. Preordering of seed RNA sequence and PAM-recognition cleft for target DNA recognition. (**A**) Structural comparison between Cas9-sgRNA complex (pretarget) and target DNA–bound structure (PDB ID 4UN3) (see also movies S1 and S2). Vector length correlates with the domain motion scale. Black arrows indicate domain movements within Cas9-sgRNA upon target DNA binding. (**B**) Limited proteolysis to test for large-scale conformational changes of Cas9 upon sgRNA binding and target DNA recognition. (**C**) Overlay of the Cas9-sgRNA pre-target bound complex with the target DNA–bound structures. For clarity, only the PAM-containing CTD domain is shown. (**D**) Close-up view of the seed-binding channel in surface representation. (**E**) Superimposed sgRNAs in the pretarget (beige) and target DNA–bound states (black and orange) with only the guide segments shown for clarity. Helical axis is indicated by dotted line. Dihedral angles (θ) between guide segment nucleobases and those of the A-form RNA-DNA heteroduplex in target DNA–bound structures are shown in parentheses. (**F**) Schematic showing key interactions of SpyCas9 with the sgRNA seed sequence. The inset highlights the conformational change of Tyr^{450} upon target binding.

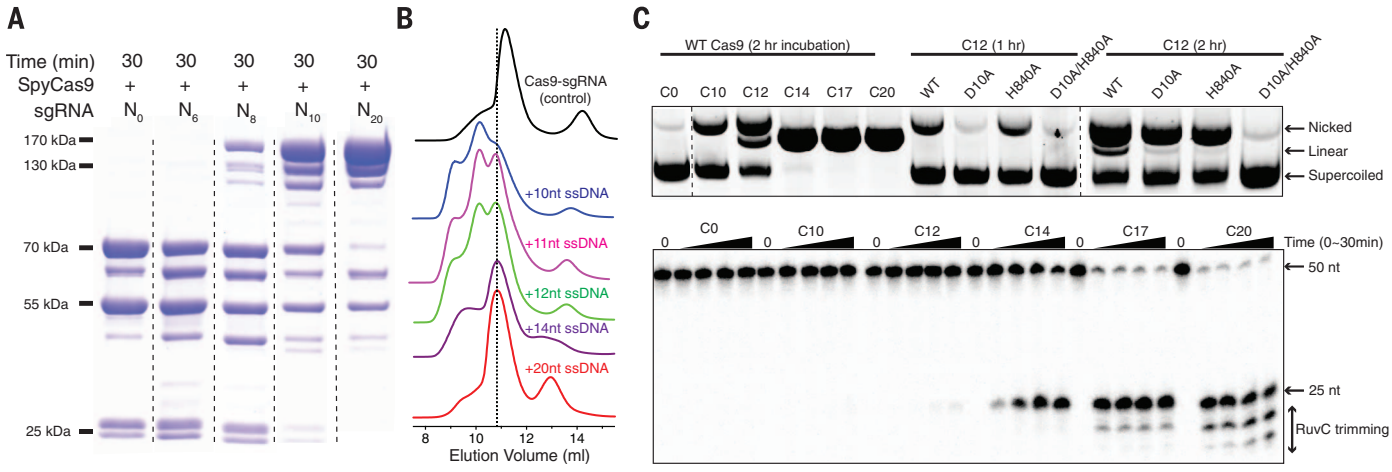

Fig. 3. The seed sequence triggers Cas9 to reach a target recognition-competent conformation. (**A**) SDS–polyacrylamide gel electrophoresis of limited trypsin digestion of SpyCas9 in the presence of truncated guide RNAs. (**B**) Analytical size-exclusion chromatograms of SpyCas9-sgRNA in the absence or presence of single-stranded target DNA with the indicated number of complementary nucleotides. The dashed line indicates the peak position of stably bound SpyCas9-sgRNA-ssDNA ternary complex eluting from the gel filtration column. (**C**) Cas9-mediated endonuclease activity time course assays using plasmid and oligonucleotide DNA (^{32}P-labeled on both strands) containing a 20-bp λ1 DNA target sequence and a 5′-TGG-3′ PAM motif. Cn (*n* = 0, 10, 12, 14, 17, or 20) represents the number of potential guide-target base pairs counted from the PAM end.

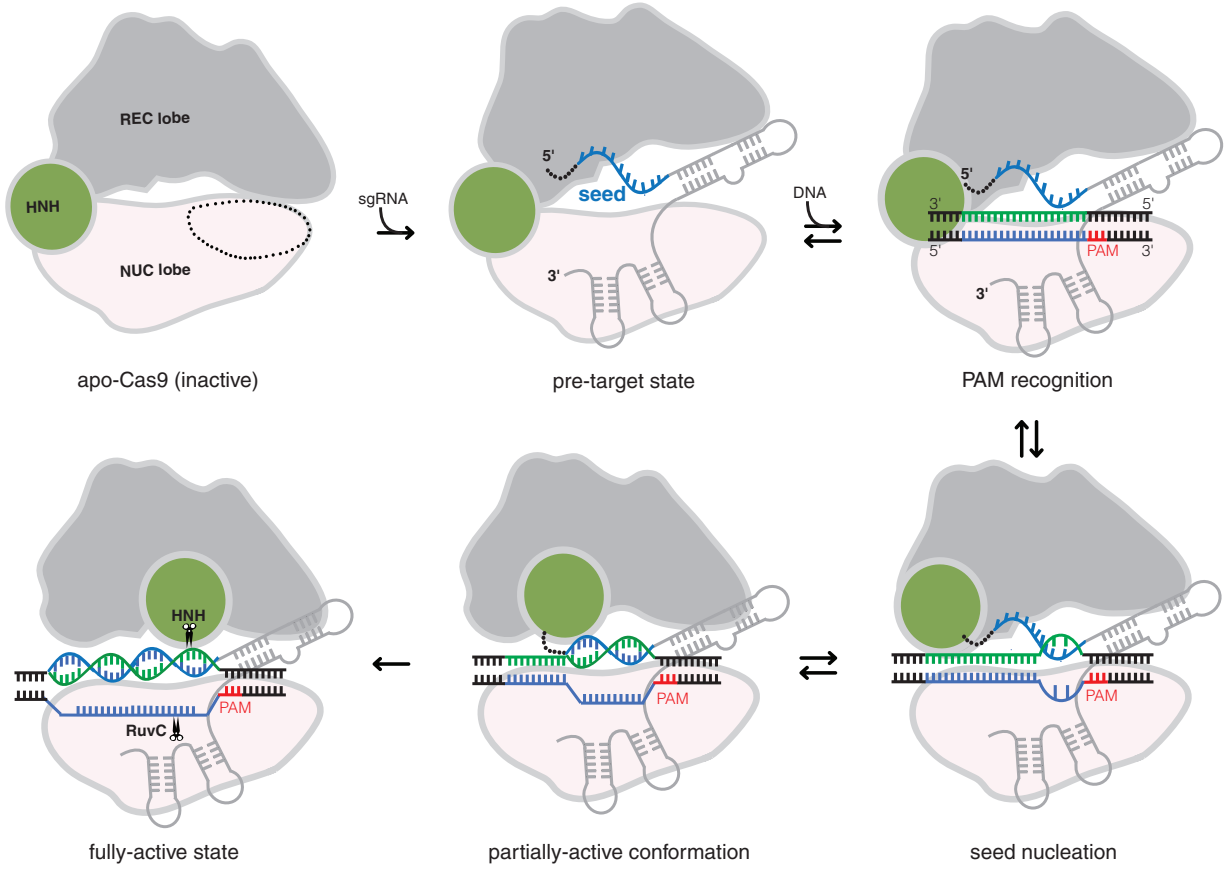

Fig. 4. Proposed mechanism for Cas9-mediated DNA targeting and cleavage. When Cas9 is in the apo state, its PAM-interacting cleft (dotted circle) is largely disordered. In the pretarget state, the PAM-interacting domain and seed sequence from guide RNA are preorganized for PAM recognition, followed by dsDNA melting next to PAM. The nonseed region is disordered and indicated as a dotted line. Base pairing between the seed sequence and the target DNA drives Cas9 into a near-active conformation; complete base pairing between the full guide segment and the target DNA strand enables Cas9 to reach a fully active state.

binding affinity for the RNA (fig. S10). Together, these results indicate that despite forming a stable complex with Cas9 (fig. S11), the crRNA:tracrRNA scaffold region of the sgRNA alone fails to induce the target recognition–competent conformation of Cas9.

To assess the molecular mechanism of Cas9-mediated RNA-DNA hybridization, we first used size exclusion chromatography to evaluate the effects of DNA length on the formation of Cas9-sgRNA-ssDNA (single-stranded DNA) ternary complexes. This analysis showed that target ssDNA length must be at least 10 nt to form a kinetically stable ternary complex with Cas9-sgRNA (Fig. 3B), in good agreement with the requirement for a 10- to 12-bp RNA-DNA heteroduplex to ensure strand propagation observed in Cas9 single-molecule experiments (*9*, *24*). To further explore the importance of the seed region for Cas9-mediated DNA cleavage, we conducted endonuclease activity assays using both plasmid and oligonucleotide DNA substrates and our truncated guide RNAs. The plasmid cleavage assay revealed that the 12-bp seed:DNA heteroduplex is necessary for Cas9-mediated supercoiled plasmid cleavage, which proceeds by nicking first by the RuvC nuclease domain, then by the HNH nuclease domain (Fig. 3C and table S2). These data are consistent with structural observations indicating that the flexible HNH domain can adopt multiple non–catalytically productive states during sgRNA binding and target DNA recognition. In line with previous studies (*25*), the oligonucleotide cleavage assay showed that the N_{17} guide RNA displays an almost comparable cleavage rate but much reduced RuvC 3′-5′ exonuclease-trimming activity (*3*) relative to the N_{20} guide RNA (Fig. 3C). This trimming activity is more pronounced with the H840A nickase version of Cas9 relative to the D10A nickase version (fig. S12). This observation may explain why the D10A nickase is more efficient than the H840A nickase version of Cas9 when using a double-nicking strategy to enhance genome editing specificity (*26*).

We propose that the preordered PAM recognition region of the Cas9-sgRNA complex initiates DNA interrogation, followed by base pairing between a short PAM-proximal segment of DNA (1 or 2 bp) and the 3′ end of the seed sequence in the sgRNA (Fig. 4). Conformational changes of Cas9 upon initial DNA binding then accommodate guide RNA strand invasion into and beyond the seed region, triggering additional structural changes necessary for Cas9 to reach a cleavage-competent state. Recent crystal structures of human Argonaute2 bound to a microRNA guide and short RNA target sequences underscore the importance of seed region base pairing for accuracy of target selection (*27*).

Our results suggest the apparent convergent evolution of a similar mechanism for CRISPR-Cas9. Collectively, our structural and biochemical data show that Cas9 is subject to multilayered regulation during its activation. The preordered RNA seed sequence and protein PAM-interacting cleft enable the Cas9-sgRNA complex to interact productively with potential DNA sequences for target sampling. The inactive conformation of apo Cas9, as well as the additional conformational changes required for the complex to reach its ultimate catalytically active state, could help to avoid spurious DNA cleavage within the host genome and hence minimize off-target effects in Cas9-based genome editing.

REFERENCES AND NOTES

1. B. Wiedenheft, S. H. Sternberg, J. A. Doudna, *Nature* **482**, 331–338 (2012).
2. E. Deltcheva *et al.*, *Nature* **471**, 602–607 (2011).
3. M. Jinek *et al.*, *Science* **337**, 816–821 (2012).
4. G. Gasiunas, R. Barrangou, P. Horvath, V. Siksnys, *Proc. Natl. Acad. Sci. U.S.A.* **109**, E2579–E2586 (2012).
5. P. D. Hsu, E. S. Lander, F. Zhang, *Cell* **157**, 1262–1278 (2014).
6. J. A. Doudna, E. Charpentier, *Science* **346**, 1258096 (2014).
7. E. Semenova *et al.*, *Proc. Natl. Acad. Sci. U.S.A.* **108**, 10098–10103 (2011).
8. B. Wiedenheft *et al.*, *Proc. Natl. Acad. Sci. U.S.A.* **108**, 10092–10097 (2011).
9. S. H. Sternberg, S. Redding, M. Jinek, E. C. Greene, J. A. Doudna, *Nature* **507**, 62–67 (2014).
10. L. Cong *et al.*, *Science* **339**, 819–823 (2013).
11. W. Jiang, D. Bikard, D. Cox, F. Zhang, L. A. Marraffini, *Nat. Biotechnol.* **31**, 233–239 (2013).
12. H. Nishimasu *et al.*, *Cell* **156**, 935–949 (2014).
13. C. Anders, O. Niewoehner, A. Duerst, M. Jinek, *Nature* **513**, 569–573 (2014).
14. M. Jinek *et al.*, *Science* **343**, 1247997 (2014).
15. A. E. Briner *et al.*, *Mol. Cell* **56**, 333–339 (2014).
16. T. Künne, D. C. Swarts, S. J. J. Brouns, *Trends Microbiol.* **22**, 74–83 (2014).
17. K. Nakanishi, D. E. Weinberg, D. P. Bartel, D. J. Patel, *Nature* **486**, 368–374 (2012).
18. N. T. Schirle, I. J. MacRae, *Science* **336**, 1037–1040 (2012).
19. E. Elkayam *et al.*, *Cell* **150**, 100–110 (2012).
20. R. N. Jackson *et al.*, *Science* **345**, 1473–1479 (2014).
21. H. Zhao *et al.*, *Nature* **515**, 147–150 (2014).
22. S. Mulepati, A. Héroux, S. Bailey, *Science* **345**, 1479–1484 (2014).
23. X. Wu *et al.*, *Nat. Biotechnol.* **32**, 670–676 (2014).
24. M. D. Szczelkun *et al.*, *Proc. Natl. Acad. Sci. U.S.A.* **111**, 9798–9803 (2014).
25. Y. Fu, J. D. Sander, D. Reyon, V. M. Cascio, J. K. Joung, *Nat. Biotechnol.* **32**, 279–284 (2014).
26. X. Ren *et al.*, *G3* **4**, 1955–1962 (2014).
27. N. T. Schirle, J. Sheu-Gruttadauria, I. J. MacRae, *Science* **346**, 608–613 (2014).

ACKNOWLEDGMENTS

Atomic coordinates of Cas9-sgRNA and dCas9-sgRNA structures have been deposited in the Protein Data Bank with accession codes 4ZT0 and 4ZT9. We thank G. Meigs, J. Holton (beamline 8.3.1 of the Advanced Light Source, Lawrence Berkeley National Laboratory), and M. Miller for helpful discussion about data collection and processing; D. King and A. Iavarone for mass spectrometric data analysis; and S. H. Sternberg, M. L. Hochstrasser, M. Jinek, and C. Anders for critical reading of the manuscript. Supported by NSF grant 1244557 (J.A.D.). F.J. is a Merck Fellow of the Damon Runyon Cancer Research Foundation (DRG-2201-14); J.A.D. is a Howard Hughes Medical Institute Investigator.

SUPPLEMENTARY MATERIALS

www.sciencemag.org/content/348/6242/1477/suppl/DC1
Materials and Methods
Supplementary Text
Figs. S1 to S12
Tables S1 and S2
Movies S1 and S2
References (*28*–*41*)

17 March 2015; accepted 22 May 2015
10.1126/science.aab1452

GENE SILENCING

Epigenetic silencing by the HUSH complex mediates position-effect variegation in human cells

Iva A. Tchasovnikarova,[1]* Richard T. Timms,[1]* Nicholas J. Matheson,[1] Kim Wals,[1] Robin Antrobus,[1] Berthold Göttgens,[2] Gordon Dougan,[3] Mark A. Dawson,[4] Paul J. Lehner[1]†

Forward genetic screens in *Drosophila melanogaster* for modifiers of position-effect variegation have revealed the basis of much of our understanding of heterochromatin. We took an analogous approach to identify genes required for epigenetic repression in human cells. A nonlethal forward genetic screen in near-haploid KBM7 cells identified the HUSH (human silencing hub) complex, comprising three poorly characterized proteins, TASOR, MPP8, and periphilin; this complex is absent from *Drosophila* but is conserved from fish to humans. Loss of HUSH components resulted in decreased H3K9me3 both at endogenous genomic loci and at retroviruses integrated into heterochromatin. Our results suggest that the HUSH complex is recruited to genomic loci rich in H3K9me3, where subsequent recruitment of the methyltransferase SETDB1 is required for further H3K9me3 deposition to maintain transcriptional silencing.

The positioning of a normally active gene into heterochromatin can result in epigenetic silencing, a phenomenon known as position-effect variegation (PEV) (*1*). Forward genetic screens in the fruit fly *Drosophila melanogaster* for mutations that act as suppressors or enhancers of PEV have identified a range of key regulators of heterochromatin (*2*). These include heterochromatin protein 1 (HP1) (*3*) and Su(var)3-9 (*4*),

which respectively bind and deposit the key repressive histone modification: trimethylated Lys[9] of histone H3 (H3K9me3) (*5*, *6*). Here, we set out to identify genes involved in PEV in human cells, using an analogous forward genetic screen in the haploid human KBM7 cell line.

We transduced KBM7 cells with a lentiviral construct encoding a green fluorescent protein (GFP) fusion protein driven by the spleen focus-forming virus promoter (SFFV) (Fig. 1A). Although the majority of transduced cells displayed high GFP expression, ~20% of the cells exhibited lower GFP expression (Fig. 1B), likely because of reporter integration into a repressive chromatin environment. To identify the genes required for this epigenetic suppression, we isolated the population of GFP^{dim} cells by fluorescence-activated cell sorting (FACS), mutagenized them with a gene-trap retrovirus, and enriched for rare mutant GFP^{bright} cells via two rounds of FACS (Fig. 1C). Mapping the gene-trap integration sites among the GFP^{bright} cells identified several genes that were significantly enriched for inactivating insertions relative to an unselected control population, including *SETDB1*, *FAM208A*, *MPHOSPH8*

[1]Department of Medicine, Cambridge Institute for Medical Research, Addenbrooke's Hospital, Cambridge CB2 0XY, UK. [2]Department of Haematology, Cambridge Institute for Medical Research, Addenbrooke's Hospital, Cambridge CB2 0XY, UK. [3]Wellcome Trust Sanger Institute, Wellcome Trust Genome Campus, Cambridge CB10 1SA, UK. [4]Peter MacCallum Cancer Centre, East Melbourne, Victoria 3002, Australia.
*These authors contributed equally to this work. †Corresponding author. E-mail: pjl30@cam.ac.uk

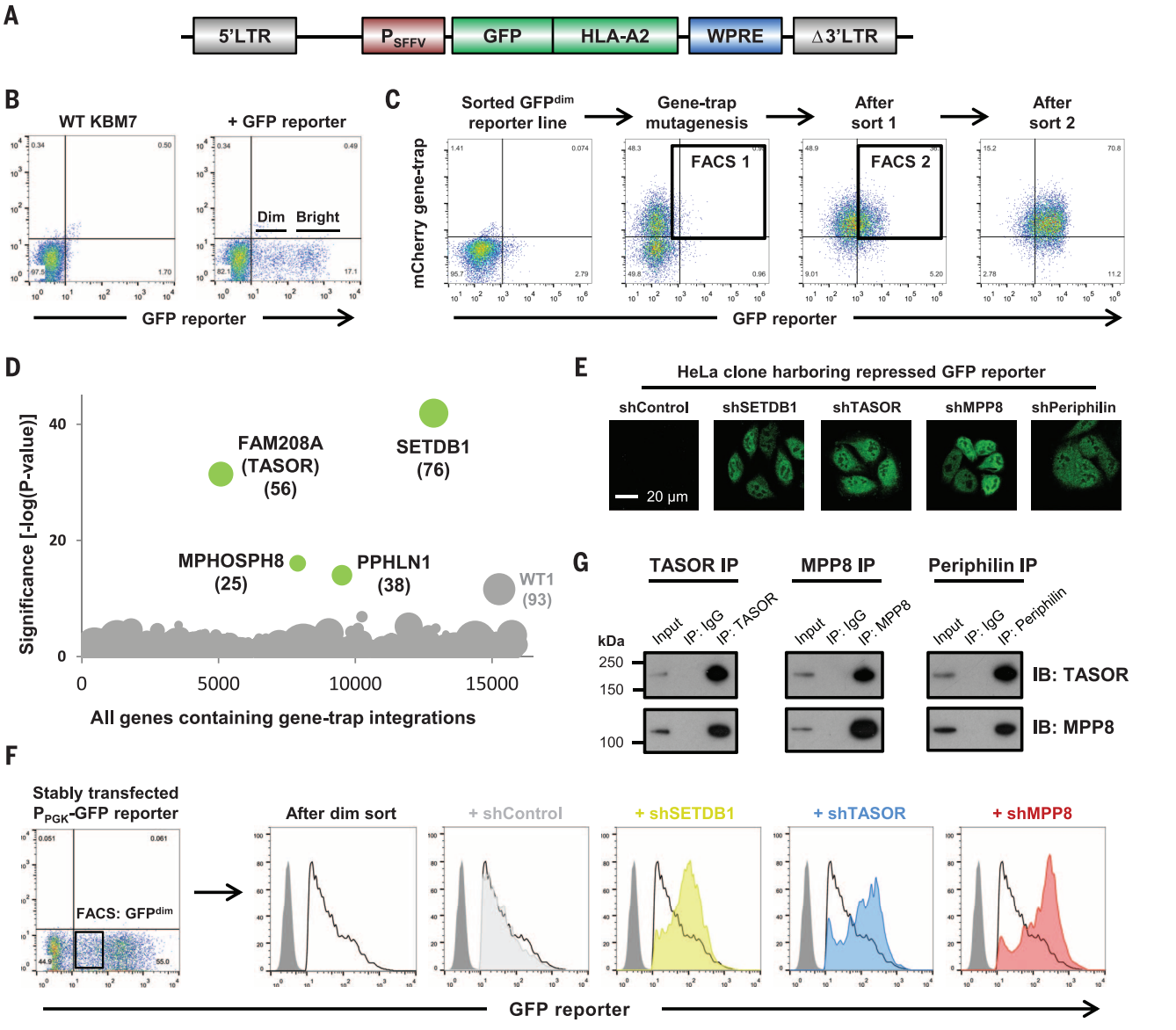

Fig. 1. A haploid genetic screen identifies a requirement for the HUSH complex for epigenetic repression in human cells. (**A**) Schematic view of the GFP reporter construct (*14*). LTR, long terminal repeat; SFFV, spleen focus-forming virus; HLA, human leukocyte antigen; WPRE, woodchuck hepatitis virus posttranscriptional regulatory element. (**B**) Transduction of KBM7 cells with the GFP reporter results in a majority GFP^{bright} population plus a repressed GFP^{dim} population. (**C**) A haploid genetic screen to identify genes required for repression of the GFP reporter. (**D**) Bubble plot illustrating the hits from the screen. Bubble size is proportional to the number of independent inactivating gene-trap integrations identified (shown in parentheses). (**E** and **F**) Validation of the screen hits in HeLa cells, using an independent lentiviral reporter (E) and a nonviral reporter containing the phosphoglycerate kinase 1 (PGK) promoter driving GFP delivered by transfection (F). Histograms were gated on GFP^{+} cells. (**G**) TASOR, MPP8, and periphilin form a complex. Endogenous TASOR, MPP8, and periphilin were immunoprecipitated (IP) from KBM7 cells, and the indicated coimmunoprecipitating proteins were identified by immunoblot (IB). We were unable to blot for periphilin because the antibody does not recognize its epitope after NP-40 lysis.

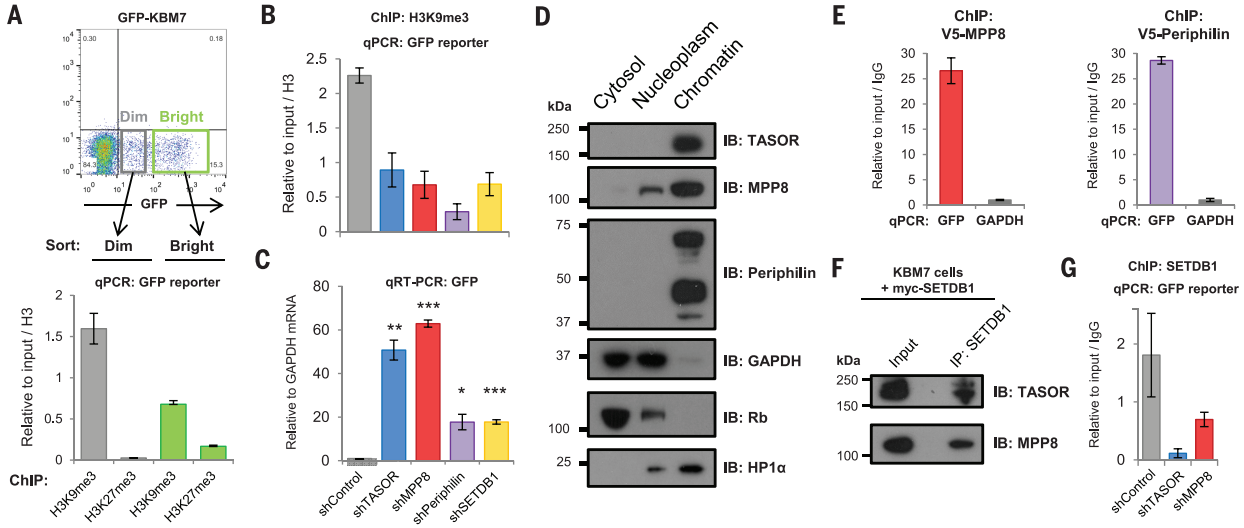

Fig. 2. The HUSH complex functions through H3K9me3 via the targeted recruitment of SETDB1. (**A**) GFP^{dim} integrations are marked by H3K9me3 but not H3K27me3. H3K9me3 and H3K27me3 levels across the reporter were assessed by ChIP combined with quantitative polymerase chain reaction (ChIP-qPCR) in sorted GFP^{dim} and GFP^{bright} populations. (**B** and **C**) Knockdown of HUSH components results in a loss of H3K9me3 across a GFP^{dim} reporter as assessed by ChIP-qPCR (B), concomitant with an increase in GFP transcript levels (C). *P < 0.05, **P < 0.01, ***P < 0.001. (**D**) Subcellular fractionation showing that HUSH subunits are found in the chromatin fraction. GAPDH, Rb, and HP1α were used to validate the fractionation. (**E**) V5-tagged HUSH subunits bind to a repressed GFP reporter as assessed by ChIP-qPCR. (**F**) Coimmunoprecipitation of TASOR and MPP8 with SETDB1. (**G**) Knockdown of HUSH components results in impaired recruitment of SETDB1 to a GFP^{dim} reporter, as assessed by ChIP-qPCR.

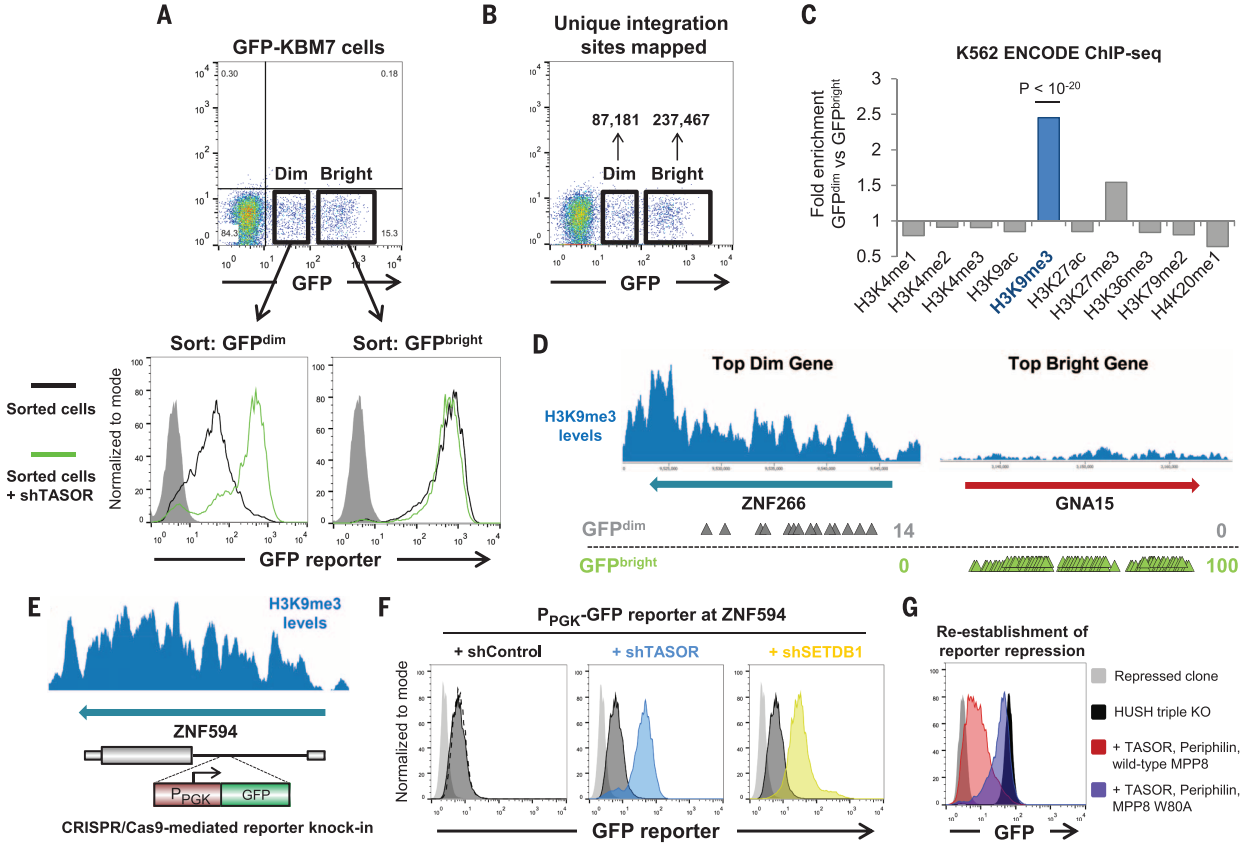

Fig. 3. The HUSH complex functions at genomic loci rich in H3K9me3. (**A**) HUSH represses the majority of GFP^{dim} reporter integrations. Populations of GFP^{dim} and GFP^{bright} cells were isolated by FACS and subjected to knockdown of TASOR. (**B** to **D**) The HUSH complex acts at genomic loci marked by high levels of H3K9me3. Reporter integration sites were mapped among the GFP^{dim} and GFP^{bright} populations (B). Correlating integration sites with ENCODE ChIP-seq peaks for K562 cells showed that GFP^{dim} integration sites were most enriched in proximity to H3K9me3 (C). Examples of the top "dim" and "bright" genes are shown in (D). (**E** and **F**) HUSH-mediated repression of a GFP reporter construct targeted to ZNF594. (**G**) Reestablishment of reporter repression upon reconstitution of a HUSH triple knockout clone.

[encoding M-phase phosphoprotein 8 (MPP8)], and *PPHLN1* (encoding periphilin) (Fig. 1D and fig. S1A). The uncharacterized gene *FAM208A* was renamed *TASOR* (transgene activation suppressor).

We validated the role of these four genes by short hairpin RNA (shRNA)–mediated knockdown in KBM7 cells (fig. S1, B and C) and with the use of an independent GFP reporter construct in HeLa cells (Fig. 1E and fig. S2). This effect was not limited to retroviral constructs, because stably integrated reporter constructs delivered by transfection were similarly repressed (Fig. 1F and fig. S3), and was apparent using both viral and cellular promoters (fig. S4). The variable proportion of GFP^{dim} cells observed with different reporter constructs, however, did suggest that the DNA sequence of the reporter may influence the degree of silencing. Thus, repression by these four genes appeared to be predominantly governed by the genomic landscape surrounding the transgene integration site, but could also be modulated by the sequence composition of the reporter.

To determine whether these genes act as part of a multiprotein complex, we analyzed TASOR immunoprecipitates from KBM7 nuclei by mass spectrometry. After discounting proteins also present in control immunoprecipitates, two putative interacting proteins remained: MPP8 and periphilin (table S1 and fig. S5A), the same proteins identified by our genetic screen (Fig. 1D). Thus, both genetic and proteomic approaches converged on a repressive complex comprising TASOR, MPP8, and periphilin, which we named the HUSH (human silencing hub) complex (fig. S5B). TASOR, MPP8, and periphilin all localized to the nucleus (fig. S5, C and D). Interactions between HUSH complex members were readily confirmed by coimmunoprecipitation experiments (Fig. 1G), and knockdown of each of the three proteins resulted in decreased levels of the other HUSH complex subunits (fig. S5, E and F). This was not the case upon knockdown of SETDB1 (fig. S5G), which did not appear to be a constitutive member of the HUSH complex.

Because the leading hit in the genetic screen was the H3K9 methyltransferase SETDB1 (*7*) and because the chromodomain of MPP8 binds H3K9me3 (*8*–*10*), our investigation into the mechanism of repression by the HUSH complex focused on the repressive H3K9me3 histone mark. High levels of H3K9me3 were found on repressed (GFP^{dim}) reporters but not on active

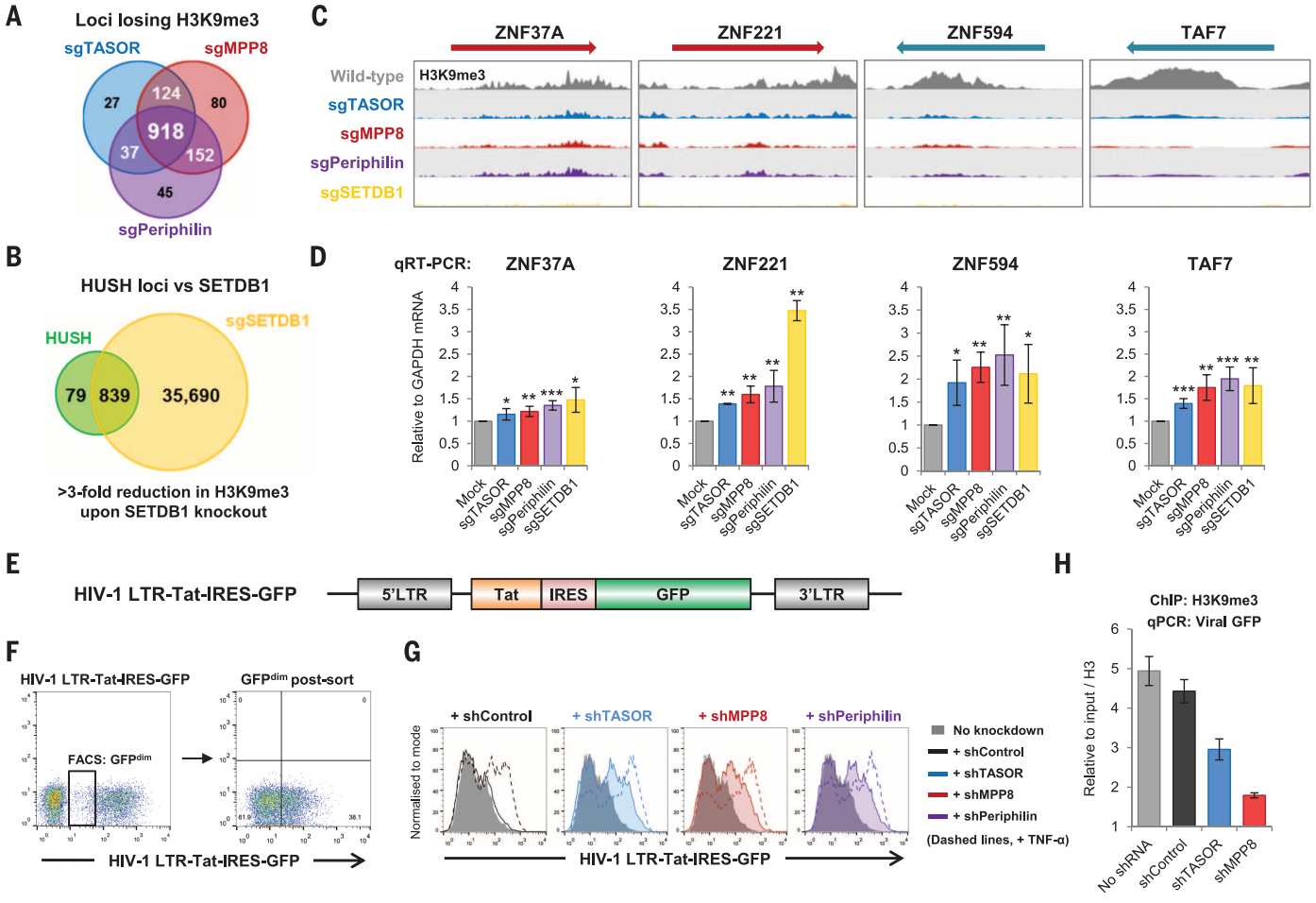

Fig. 4. The HUSH complex maintains H3K9me3 at endogenous loci and represses viruses integrated into heterochromatin. (**A** to **C**) Loss of HUSH results in decreased H3K9me3 at endogenous genomic loci. Global levels of H3K9me3 were measured by ChIP-seq in wild-type HeLa cells and cells lacking HUSH subunits and SETDB1. The CRISPR/Cas9-mediated disruption of TASOR, MPP8, and periphilin resulted in decreased H3K9me3 at shared loci (A). Knockout of SETDB1 resulted in decreased H3K9me3 at more than 99% of these loci, with the majority (91%) showing a factor of >3 reduction (B). Four example loci are shown in (C). (**D**) Loss of HUSH resulted in increased expression of the four example genes from (C), as measured by quantitative reverse transcription PCR (qRT-PCR). (**E** to **H**) Proviral repression by the HUSH complex. Schematic view of the HIV-1 LTR-Tat-IRES-GFP virus (E) (IRES, internal ribosome entry site). Infection of Jurkat cells resulted in a range of GFP expression levels (F); the proviruses in the GFP^{dim} cells were repressed by the HUSH complex (G) through H3K9me3 (H). Tumor necrosis factor–α (TNF-α) activates transcription from the HIV-1 LTR through the NF-κB pathway (*18*).

(GFP^{bright}) reporters (Fig. 2A and fig. S6). Consistent with a role for the HUSH complex in facilitating the deposition of H3K9me3, depletion of HUSH subunits resulted in a decrease in H3K9me3 across the reporter (Fig. 2B), concomitant with an increase in GFP mRNA expression (Fig. 2C). Furthermore, HUSH subunits were chromatin-associated (Fig. 2D), and we detected binding of epitope-tagged HUSH subunits to a repressed reporter (Fig. 2E). HUSH subunits coimmunoprecipitated with SETDB1 (Fig. 2F), and knockdown of HUSH complex members impaired the recruitment of SETDB1 to a repressed GFP reporter (Fig. 2G). Thus, the HUSH complex appeared to facilitate the deposition of the repressive H3K9me3 histone modification through the targeted recruitment of SETDB1.

HUSH repressed almost all GFP^{dim} reporter integrations (Fig. 3A and fig. S7). Thus, by comparing the integration sites of the GFP reporter in the GFP^{dim} versus GFP^{bright} populations, we could determine where HUSH acted in the genome (Fig. 3B). GFP^{dim} integrations were most enriched in proximity to H3K9me3 and were underrepresented in proximity to histone marks correlated with active chromatin (Fig. 3C and fig. S8A). We also compared genes that were highly enriched for GFP^{dim} insertions over GFP^{bright} insertions ("dim" genes) or vice versa ("bright" genes). H3K9me3 levels across dim genes were much higher than across bright genes (Fig. 3D and fig. S8B). The majority of the leading dim genes were KRAB-ZNF genes (fig. S8, C to E), which are covered with high levels of H3K9me3 (*11*) deposited by SETDB1 (*12*). To validate these observations directly, we used the CRISPR/Cas9 system to integrate a nonretroviral GFP reporter construct at an example KRAB-ZNF gene (Fig. 3E). This construct was indeed subject to HUSH-mediated repression (Fig. 3F and fig. S9). Thus, the HUSH complex preferentially silenced transgenes integrating into chromatin marked by high levels of H3K9me3.

Recruitment of the HUSH complex to loci rich in H3K9me3 could be mediated through the chromodomain of MPP8 (*8*–*10*). An H3 peptide trimethylated at Lys^9, but not an unmodified H3 peptide, pulled down MPP8 together with TASOR from a nuclear lysate (fig. S10A). TASOR recruitment to H3K9me3 was dependent on MPP8 and was lost following MPP8 depletion (fig. S10A). Additionally, the purified chromodomain of MPP8 has been shown to bind chromatin marked by high levels of H3K9me3 (fig. S10B) (*13*), and we detected binding of epitope-tagged HUSH subunits to genes rich in H3K9me3 (fig. S10C). To determine whether the chromodomain of MPP8 was essential for reestablishment of reporter repression, we used CRISPR/Cas9 technology to generate a HUSH triple knockout reporter clone lacking expression of TASOR, MPP8, and periphilin (fig. S11). Reexpression of wild-type HUSH subunits resulted in re-repression of the reporter, but this was severely abrogated upon reconstitution with an MPP8 chromodomain mutant (Trp^{80} → Ala, W80A) that cannot bind H3K9me3 (*8*) (Fig. 3G and fig. S12A). In contrast, in cells lacking MPP8 alone, a functional chromodomain was not absolutely critical for re-repression of the reporter, as the W80A MPP8 mutant could partially restore reporter repression (fig. S12, B and C). This result suggested that another member of the HUSH complex must also contribute to HUSH localization at target sites. Indeed, we found that in the absence of either TASOR or MPP8, periphilin was still able to localize to chromatin (fig. S12, D and E). Thus, the chromodomain of MPP8 was required for the initial targeting of the HUSH complex to H3K9me3-marked loci, but periphilin also contributed to the maintenance of the complex at chromatin.

Given that the HUSH complex regulates H3K9me3 levels across integrated reporter constructs, we asked whether it maintains H3K9me3 at endogenous genomic loci. Chromatin immunoprecipitation followed by deep sequencing (ChIP-seq) in CRISPR/Cas9-generated TASOR, MPP8, periphilin, and SETDB1 knockout HeLa cells (fig. S11) identified 918 shared genomic loci (*14*) with markedly reduced levels of H3K9me3 upon loss of HUSH subunits (Fig. 4A and table S2). Furthermore, knockout of SETDB1 resulted in a decrease in H3K9me3 at 916/918 (99.6%) of the shared loci affected by loss of HUSH, with the majority (91%) showing a factor of >3 reduction (Fig. 4B). This confirmed a functional association between this critical methyltransferase and the HUSH complex. At four example loci, the decrease in H3K9me3 levels as a result of loss of HUSH or SETDB1 (Fig. 4C) resulted in modest increases in gene expression (Fig. 4D).

Retroviral integration into heterochromatin is a natural mimic of PEV. As such, we reasoned that viruses—and not merely transgenes delivered in the context of self-inactivating vectors—might also be subject to HUSH-mediated repression. We infected the CD4$^+$ lymphoid cell line Jurkat with a standard HIV-1 reporter virus that contains the wild-type HIV-1 LTR promoter driving both the HIV-1 transactivator Tat and GFP (*15*) (Fig. 4E). Again we observed a range of GFP expression levels (Fig. 4F). The repressed proviruses in the GFP^{dim} cells were subject to HUSH-mediated repression, because knockdown of HUSH subunits resulted in transcriptional activation (Fig. 4G) accompanied by a decrease in H3K9me3 levels (Fig. 4H). Depletion of HUSH subunits also resulted in derepression of silent HIV-1 reporter proviruses in J-Lat clones (fig. S13), a widely used cellular model of HIV-1 silencing (*15*, *16*), and similarly in an analogous "K-Lat" model that we generated in KBM7 cells (fig. S14). This effect was not limited to the HIV-1 LTR; we also found that HUSH acted on repressed murine leukemia virus (MLV) integrations (fig. S15). Thus, the HUSH complex mediates epigenetic regulation of both endogenous and viral genes at heterochromatic loci marked by H3K9me3.

By replicating a classic *Drosophila* forward genetic screen for modifiers of PEV in cultured human cells, we identified the HUSH complex, which mediates epigenetic repression through the recruitment of SETDB1 and the deposition of H3K9me3. Surprisingly, we did not identify a role for canonical heterochromatin regulators required for PEV in *Drosophila*, such as HP1 (fig. S16) (*17*). HUSH complex subunits are absent from *Drosophila* but conserved from fish to humans, suggesting an additional, more recently acquired route to H3K9me3-mediated heterochromatin regulation in mammalian cells.

REFERENCES AND NOTES

1. G. Schotta, A. Ebert, R. Dorn, G. Reuter, *Semin. Cell Dev. Biol.* **14**, 67–75 (2003).
2. S. C. R. Elgin, G. Reuter, *Cold Spring Harb. Perspect. Biol.* **5**, a017780 (2013).
3. T. C. James, S. C. Elgin, *Mol. Cell. Biol.* **6**, 3862–3872 (1986).
4. G. Reuter, R. Dorn, G. Wustmann, B. Friede, G. Rauh, *Mol. Gen. Genet.* **202**, 481–487 (1986).
5. S. Rea *et al*., *Nature* **406**, 593–599 (2000).
6. A. J. Bannister *et al*., *Nature* **410**, 120–124 (2001).
7. D. C. Schultz, K. Ayyanathan, D. Negorev, G. G. Maul, F. J. Rauscher 3rd, *Genes Dev.* **16**, 919–932 (2002).
8. K. Kokura, L. Sun, M. T. Bedford, J. Fang, *EMBO J.* **29**, 3673–3687 (2010).
9. Y. Chang, J. R. Horton, M. T. Bedford, X. Zhang, X. Cheng, *J. Mol. Biol.* **408**, 807–814 (2011).
10. J. Li *et al*., *PLOS ONE* **6**, e25104 (2011).
11. H. O'Geen *et al*., *PLOS Genet.* **3**, e89 (2007).
12. S. Frietze, H. O'Geen, K. R. Blahnik, V. X. Jin, P. J. Farnham, *PLOS ONE* **5**, e15082 (2010).
13. G. Kungulovski *et al*., *Genome Res.* **24**, 1842–1853 (2014).
14. See supplementary materials on *Science* Online.
15. A. Jordan, P. Defechereux, E. Verdin, *EMBO J.* **20**, 1726–1738 (2001).
16. A. Jordan, D. Bisgrove, E. Verdin, *EMBO J.* **22**, 1868–1877 (2003).
17. J. C. Eissenberg *et al*., *Proc. Natl. Acad. Sci. U.S.A.* **87**, 9923–9927 (1990).
18. E. J. Duh, W. J. Maury, T. M. Folks, A. S. Fauci, A. B. Rabson, *Proc. Natl. Acad. Sci. U.S.A.* **86**, 5974–5978 (1989).

ACKNOWLEDGMENTS

We thank J. Sinclair, L. Dölken, A. Schuldt, N. Wilson, and F. Calero-Nieto for helpful discussion; R. Schulte and his team for FACS; M. Gratian, M. Bowen, and K. Jayawardena (Cambridge Institute for Medical Research); N. Smerdon (Wellcome Trust Sanger Institute); and S. Andrews (Babraham Institute) for SeqMonk customization. Supported by Wellcome Trust Principal Research Fellowship 101835/Z/13/Z (P.J.L.), a Wellcome Trust studentship (I.A.T.), an MRC Centenary Award (R.T.T.), and the Cambridge Biomedical Research Centre. The Cambridge Institute for Medical Research is in receipt of a Wellcome Trust Strategic Award. Raw sequence data are archived at Gene Expression Omnibus (GSE60056 and GSE63116) and Sequence Read Archive (PRJNA257239).

SUPPLEMENTARY MATERIALS

www.sciencemag.org/content/348/6242/1481/suppl/DC1
Materials and Methods
Figs. S1 to S16
Tables S1 to S4
References (*19*–*30*)

23 January 2015; accepted 15 May 2015
Published online 28 May 2015;
10.1126/science.aaa7227

RNA BIOCHEMISTRY

Factor-dependent processivity in human eIF4A DEAD-box helicase

Cuauhtémoc García-García,[1]* Kirsten L. Frieda,[2]* Kateryna Feoktistova,[3] Christopher S. Fraser,[3] Steven M. Block[1,4]†

During eukaryotic translation initiation, the small ribosomal subunit, assisted by initiation factors, locates the messenger RNA start codon by scanning from the 5′ cap. This process is powered by the eukaryotic initiation factor 4A (eIF4A), a DEAD-box helicase. eIF4A has been thought to unwind structures formed in the untranslated 5′ region via a nonprocessive mechanism. Using a single-molecule assay, we found that eIF4A functions instead as an adenosine triphosphate–dependent processive helicase when complexed with two accessory proteins, eIF4G and eIF4B. Translocation occurred in discrete steps of 11 ± 2 base pairs, irrespective of the accessory factor combination. Our findings support a memory-less stepwise mechanism for translation initiation and suggest that similar factor-dependent processivity may be shared by other members of the DEAD-box helicase family.

DEAD-box proteins are ubiquitous enzymes responsible for RNA remodeling. Found in eukaryotes as well as eubacteria and archaea, DEAD-box proteins participate in different stages of the mRNA life cycle, including translation initiation (*1*–*3*), ribosome biogenesis (*4*), pre-mRNA splicing (*5*), and RNA chaperoning (*6*). A key initiation factor that unwinds secondary structure during mRNA recruitment and scanning is eukaryotic initiation factor 4A (eIF4A) (*1*). This protein is a member of helicase superfamily 2 (SF2) and comprises the minimal helicase module within the DEAD-box family (*7*). As such, eIF4A possesses two RecA-like domains that contain the core conserved motifs necessary for adenosine triphosphate (ATP) binding and hydrolysis, as well as RNA binding and melting (*8*). Like most DEAD-box proteins, eIF4A is generally associated with a number of accessory proteins, including eIF4G, eIF4B, and eIF4H (*1*). These proteins help recruit eIF4A to the 5′ end of the mRNA, where it unwinds duplex regions to promote mRNA recruitment to the ribosome (*9*). eIF4G, eIF4B, and eIF4H synergistically activate the duplex unwinding activity of eIF4A, enhancing its RNA binding affinity and accelerating the cycling of its RecA-like domains between open and closed conformations (*10*–*14*). Nevertheless, it is still not understood whether duplex unwinding by eIF4A occurs via a distributive or processive mechanism. In fact, both mechanisms have been previously suggested (*2*, *13*, *15*–*17*).

To determine the mechanism used by eIF4A during translation initiation, we developed a high-resolution, single-molecule, optical trapping assay to study the helicase activity of eIF4A in conjunction with known accessory factors eIF4B, eIF4H, and eIF4G. The assay used purified human eIF4A, eIF4B, and eIF4H, as well as a previously characterized truncation mutant of eIF4G ($eIF4G_{682\text{-}1105}$) that retains the evolutionarily conserved eIF4A binding domain (*18*–*20*). The experimental geometry consisted of a "dumbbell" arrangement formed by two optically trapped beads, with a nascent RNA transcript stretched between them. This transcript was attached to one bead via hybridization to a DNA "handle" and to the other bead via RNA polymerase (RNAP) arrested at a roadblock (Fig. 1). The RNA transcript comprised a reporter hairpin [with a 72–base pair (bp) stem and a 4-nucleotide (nt) loop, and either 25 or 50% GC content] placed adjacent to a 20-nt, single-stranded RNA region at the 5′ end of the hairpin stem, which formed a target for the loading of a single eIF4A helicase (based on helicase footprint size) (Fig. 1 and fig. S1) (*21*, *22*). In this assay, loading of the helicase onto the RNA, followed by subsequent unwinding of the reporter hairpin during directional translocation (5′-to-3′, based on assay geometry), increases the bead-to-bead distance, which can be measured with nanometer-level accuracy (Fig. 1B). Any reannealing of a previously opened hairpin, arising from either enzyme dissociation or reverse translocation along the RNA, decreases this distance.

When eIF4A helicase was studied alone in the presence of ATP, only a very few stepwise unwinding events were observed, consistent with previous reports of nonprocessivity in bulk assays (*23*). Any RNA unwinding by eIF4A was typically characterized by a single step forward, followed either by a single step backward or by enzyme dissociation (Fig. 2A and fig. S3). The introduction of a single additional factor, whether eIF4B, eIF4H, or $eIF4G_{682\text{-}1105}$, slightly enhanced eIF4A's ability to unwind RNA in a forward or backward direction. The addition of factors $eIF4G_{682\text{-}1105}$ and eIF4B together increased the 5′-to-3′ processivity of eIF4A synergistically, permitting the ternary complex to efficiently melt the entire 72-bp reporter hairpin. This finding suggests that the minimal unit for ribosomal scanning may include a minimum of three initiation factors: eIF4A, eIF4B, and eIF4G. Although eIF4B and eIF4H are homologous proteins, and although each conferred an increase in processivity when complexed with eIF4A and $eIF4G_{682\text{-}1105}$, the eIF4A•B•$G_{682\text{-}1105}$ complex melted hairpins more efficiently than eIF4A•H•$G_{682\text{-}1105}$ (Fig. 2A and fig. S3). Previous experiments have shown that at least three translation initiation factors are required for efficient strand separation (*10*, *19*, *24*–*26*). The present observations argue that strand separation by eIF4A•B/H•$G_{682\text{-}1105}$ can be a direct consequence of processive translocation by a

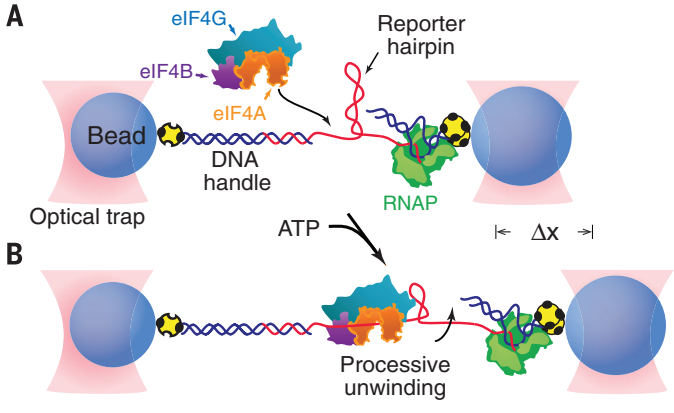

Fig. 1. Experimental geometry of the single-molecule eIF4A helicase assay (not to scale). (**A**) A single 72-bp RNA reporter hairpin (red) is tethered between two microscopic avidin-coated beads (blue) held in optical traps (pink) by a DNA handle and a biotinylated RNA polymerase (green) transcriptionally stalled at a biotin-avidin roadblock (yellow). The tether contains a short single-stranded RNA flanking sequence adjacent to the 5′ side of the hairpin for loading eIF4A helicase, shown here complexed with eIF4B and eIF4G. (**B**) As eIF4A, alone or bound to combinations of eIF4B, eIF4H, and eIF4G, translocates along the RNA, its helicase activity unwinds the hairpin, leading to an increase in distance (Δx) between the trapped beads. In all figures, "eIF4G" corresponds to the truncation mutant $eIF4G_{682\text{-}1105}$.

[1]Department of Biology, Stanford University, Stanford, CA 94305, USA. [2]Biophysics Program, Stanford University, Stanford, CA 94305, USA. [3]Department of Molecular and Cellular Biology, University of California at Davis, Davis, CA 95616, USA. [4]Department of Applied Physics, Stanford University, Stanford, CA 94305, USA.
*These authors contributed equally to this work. †Corresponding author. E-mail: sblock@stanford.edu

Downloaded from www.sciencemag.org on June 26, 2015

helicase complex based on eIF4A, not of a distributive mechanism requiring multiple binding events (supplementary text).

We next identified the specific changes in eIF4A behavior responsible for the factor-mediated increase in processivity. Because thermal noise in displacement often masks individual steps, the step size for eIF4A was determined by computing the pairwise distribution of distances moved in single records: Power spectra derived from such distributions display peaks at the corresponding spatial frequencies of any underlying steps (*27*). Whether eIF4A was scored alone or in complex with other factors, the power spectra from records of its activity all displayed peaks near 11 ± 2 bp (mean ± SEM), a spacing comparable to the helicase footprint and which corresponds closely to a single turn of the RNA duplex (Fig. 2B) (*8*). The measured step size did not differ among assays conducted under conditions that produced a comparatively high proportion of backsteps (eIF4A, eIF4A•B, eIF4A•H, and eIF4A•$G_{682\text{-}1105}$) and those that did not (eIF4A•B•$G_{682\text{-}1105}$ and eIF4A•H•$G_{682\text{-}1105}$).

When the noise levels in individual records are sufficiently low, it is possible to search for the presence of substeps within the ~11-bp steps. An analysis was therefore carried out by fitting selected segments of individual records using a step-finding algorithm whose robustness has been previously established (*28*). Substeps were identified, ranging in size from 2 to 4 bp (3 ± 1 bp, mean ± SEM; figs. S8 and S9). In this respect, the behavior of eIF4A is similar to that of the NS3 DEAD-box helicase from hepatitis C virus (supplementary text) (*29*).

To examine whether different cofactors might affect the directionality of eIF4A, we computed the probability ratio of forward to backward stepping, a measure of directional persistence (*23*). For eIF4A alone, this ratio was slightly higher than unity (~1.1), consistent with nonprocessive motion (Fig. 3A and fig. S11). For binary complexes eIF4A•B, eIF4A•H, and eIF4A•$G_{682\text{-}1105}$, the ratio increased only moderately (to ~1.7) and was, within error, the same for each complex. In contrast, ternary complexes eIF4A•B•$G_{682\text{-}1105}$ and eIF4A•H•$G_{682\text{-}1105}$ displayed a dramatic increase in persistence ratio, with values of ~7 and ~4, respectively. These results indicate that one role of cofactors eIF4B, eIF4H, and eIF4$G_{682\text{-}1105}$ is to enhance the directionality of eIF4A translocation. The topology of eIF4A•H•G has been studied (*10*), but unlike in the case of NS3, it is unclear which eIF4A residues mediate changes in processivity (supplementary text) (*30*).

In single-molecule records, mechanical steps were occasionally separated by pauses, corresponding to comparatively longer periods of invariant tether extension. Pause lifetimes were exponentially distributed for eIF4A, both alone and in combination with accessory factors, and were well fitted by single exponentials (Fig. 3B and fig. S12). We found that eIF4A displayed the longest measured pause lifetime, 9.0 ± 0.4 s (mean ± SEM). The complexes eIF4A•B, eIF4A•H, and eIF4A•$G_{682\text{-}1105}$ exhibited similar lifetimes within

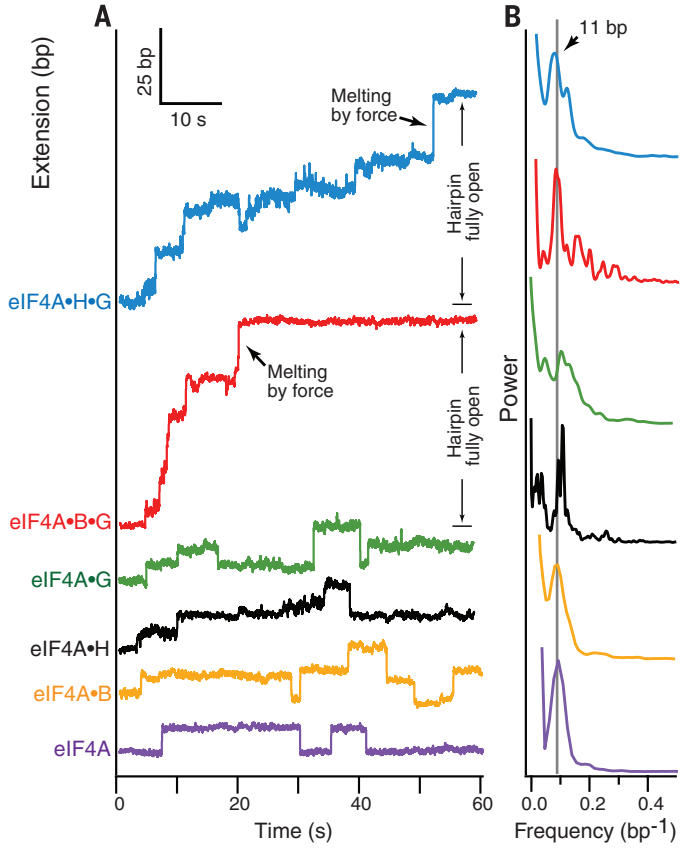

Fig. 2. Factor-dependent processivity of eIF4A. (**A**) Representative single-molecule records of helicase activity of eIF4A (purple), eIF4A•B (yellow), eIF4A•H (black), eIF4A•G (green), eIF4A•B•G (red), and eIF4A•H•G (blue) over a 60-s interval under constant load; traces are offset vertically for clarity. Note instances of forward motion corresponding to hairpin unwinding (extension increase) and rearward motion corresponding to hairpin reannealing (extension decrease). The final extension increase leading to full opening of the hairpin was facilitated by force, once the ever-shortening duplex region remaining became unstable under the constant load (black arrows; red and blue traces). (**B**) Normalized power spectra of the pairwise distances derived from multiple records of helicase and cofactor activities, color-coded as in (A), showing prominent peaks at a spatial frequency (0.09 bp^{-1}, gray line) corresponding to an ~11-bp step. Each power spectrum represents an average of at least 50 different single-molecule records.

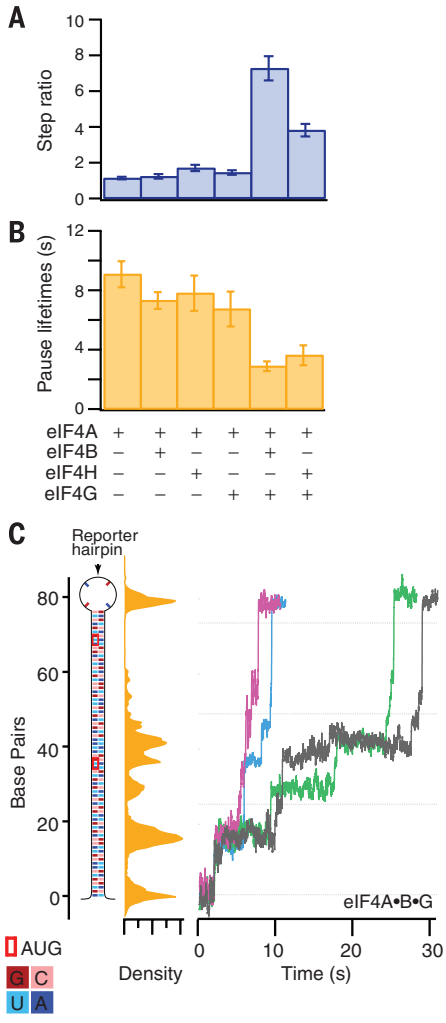

Fig. 3. Translocation properties of eIF4A helicase and accessory factor combinations. (**A**) Forward-to-backward stepping ratio for the indicated complexes (legend, bottom), with errors (SEM). (**B**) Mean pause lifetime with errors (SEM) for the indicated complexes (legend, bottom). (**C**) eIF4A•B•G melting of a reporter hairpin with the sequence shown (left), color-coded according to the legend (bottom). Five representative single-molecule records, expressed as base pairs unwound, are shown over a 30-s interval (right). The positions of these records were histogrammed in a single density plot (middle, yellow); strong peaks in this plot indicate locations where the complex pauses, which were not correlated with the location of the AUGs.

experimental error (~7 s), but these were not statistically different from that of eIF4A alone. However, ternary complexes eIF4A•B•$G_{682\text{-}1105}$ and eIF4A•H•$G_{682\text{-}1105}$ had pause lifetimes three times shorter than that of eIF4A, with durations of 2.9 ± 0.1 s and 3.6 ± 0.2 s (mean ± SEM), respectively. These findings suggest that, in addition to enhancing the directionality of eIF4A, the accessory factors eIF4B, eIF4H, and eIF4$G_{682\text{-}1105}$ also increase the mRNA unwinding efficiency by decreasing pausing. Pause locations were distributed along the reporter hairpin (Fig. 3C and fig. S3). The two reporter hairpins used in this study were based on randomized nucleotide sequences, and we could identify no obvious relationship between the locations and durations of pauses and the local base composition. However, many additional sequences would need to be scored to identify any possible sequence dependence of helicase activity.

Finally, analysis of unwinding activity indicates that eIF4A, alone or in complexes, has no memory associated with a given series of steps and that the translocation mechanism is governed by a single rate-limiting step (supplementary text).

Although DEAD-box helicases have sometimes been regarded as nonprocessive enzymes (*29*), we find here that eIF4A displays a factor-mediated processivity requiring at least two cofactors (eIF4B/H and eIF4$G_{682\text{-}1105}$). This acquired processivity is characterized by a preferential directionality (presumably 5′-to-3′), with burst openings of 11 ± 2 bp (mean ± SEM) and dramatically reduced pausing. In eukaryotic translation initiation, the eIF4A•B•$G_{682\text{-}1105}$ complex comprises a minimal processive unit that is thought to facilitate sequential, step-by-step ribosomal scanning. In light of our findings, we anticipate that the processivity and dynamics of other DEAD-box family members may be influenced by accessory cofactors, so that enzymatic activities scored in their absence may not fully reflect the in vivo function of the proteins.

REFERENCES AND NOTES

1. A. Parsyan *et al.*, *Nat. Rev. Mol. Cell Biol.* **12**, 235–245 (2011).
2. P. Linder, E. Jankowsky, *Nat. Rev. Mol. Cell Biol.* **12**, 505–516 (2011).
3. I. Jarmoskaite, R. Russell, *Annu. Rev. Biochem.* **83**, 697–725 (2014).
4. S. Rocak, P. Linder, *Nat. Rev. Mol. Cell Biol.* **5**, 232–241 (2004).
5. I. Jarmoskaite, R. Russell, *Wiley Interdiscip. Rev.: RNA* **2**, 135–152 (2011).
6. S. A. Woodson, *RNA Biol.* **7**, 677–686 (2010).
7. M. E. Fairman-Williams, U.-P. Guenther, E. Jankowsky, *Curr. Opin. Struct. Biol.* **20**, 313–324 (2010).
8. J. M. Caruthers, E. R. Johnson, D. B. McKay, *Proc. Natl. Acad. Sci. U.S.A.* **97**, 13080–13085 (2000).
9. C. E. Aitken, J. R. Lorsch, *Nat. Struct. Mol. Biol.* **19**, 568–576 (2012).
10. A. Marintchev *et al.*, *Cell* **136**, 447–460 (2009).
11. K. H. Nielsen *et al.*, *Nucleic Acids Res.* **39**, 2678–2689 (2011).
12. Y. Sun *et al.*, *Nucleic Acids Res.* **40**, 6199–6207 (2012).
13. R. D. Abramson, T. E. Dever, W. C. Merrick, *J. Biol. Chem.* **263**, 6016–6019 (1988).
14. Y. Sun *et al.*, *Structure* **22**, 941–948 (2014).
15. F. Liu, A. Putnam, E. Jankowsky, *Proc. Natl. Acad. Sci. U.S.A.* **105**, 20209–20214 (2008).
16. M. Kozak, *J. Cell Biol.* **108**, 229–241 (1989).
17. A. Z. Andreou, D. Klostermeier, *RNA Biol.* **10**, 19–32 (2013).
18. E. De Gregorio, T. Preiss, M. W. Hentze, *EMBO J.* **18**, 4865–4874 (1999).
19. K. Feoktistova, E. Tuvshintogs, A. Do, C. S. Fraser, *Proc. Natl. Acad. Sci. U.S.A.* **110**, 13339–13344 (2013).
20. N. L. Korneeva, E. A. First, C. A. Benoit, R. E. Rhoads, *J. Biol. Chem.* **280**, 1872–1881 (2005).
21. J. R. Lorsch, D. Herschlag, *Biochemistry* **37**, 2194–2206 (1998).
22. M. L. Peck, D. Herschlag, *RNA* **5**, 1210–1221 (1999).
23. F. Rozen *et al.*, *Mol. Cell. Biol.* **10**, 1134–1144 (1990).
24. G. W. Rogers Jr., N. J. Richter, W. F. Lima, W. C. Merrick, *J. Biol. Chem.* **276**, 30914–30922 (2001).
25. G. W. Rogers Jr., N. J. Richter, W. C. Merrick, *J. Biol. Chem.* **274**, 12236–12244 (1999).
26. A. Z. Andreou, D. Klostermeier, *J. Mol. Biol.* **426**, 51–61 (2014).
27. M. J. Schnitzer, S. M. Block, *Nature* **388**, 386–390 (1997).
28. J. W. J. Kerssemakers *et al.*, *Nature* **442**, 709–712 (2006).
29. A. M. Pyle, *Annu. Rev. Biophys.* **37**, 317–336 (2008).
30. S. Myong, M. M. Bruno, A. M. Pyle, T. Ha, *Science* **317**, 513–516 (2007).

ACKNOWLEDGMENTS

We thank R. Landick for providing RNAP and J. Hershey, E. Abrash, and members of the Fraser and Block labs for helpful comments. This work was supported by National Institute of General Medical Sciences grants R37GM057035 (S.M.B.) and R01GM092927 (C.S.F.), an Alejandro and Lisa Zaffaroni Graduate Fellowship (C.G.G.), a Stanford Graduate Fellowship (K.L.F.), and training grant T32 GM-007377 (K.F.).

SUPPLEMENTARY MATERIALS

www.sciencemag.org/content/348/6242/1486/suppl/DC1
Materials and Methods
Supplementary Text
Figs. S1 to S15
References (*31*–*51*)

2 January 2015; accepted 20 May 2015
10.1126/science.aaa5089

GENE REGULATION

Discrete functions of nuclear receptor Rev-erbα couple metabolism to the clock

Yuxiang Zhang,[1]* Bin Fang,[1]* Matthew J. Emmett,[1] Manashree Damle,[1] Zheng Sun,[1,2] Dan Feng,[1] Sean M. Armour,[1] Jarrett R. Remsberg,[1] Jennifer Jager,[1] Raymond E. Soccio,[1] David J. Steger,[1] Mitchell A. Lazar[1]†

Circadian and metabolic physiology are intricately intertwined, as illustrated by Rev-erbα, a transcription factor (TF) that functions both as a core repressive component of the cell-autonomous clock and as a regulator of metabolic genes. Here, we show that Rev-erbα modulates the clock and metabolism by different genomic mechanisms. Clock control requires Rev-erbα to bind directly to the genome at its cognate sites, where it competes with activating ROR TFs. By contrast, Rev-erbα regulates metabolic genes primarily by recruiting the HDAC3 co-repressor to sites to which it is tethered by cell type–specific transcription factors. Thus, direct competition between Rev-erbα and ROR TFs provides a universal mechanism for self-sustained control of the molecular clock across all tissues, whereas Rev-erbα uses lineage-determining factors to convey a tissue-specific epigenomic rhythm that regulates metabolism tailored to the specific need of that tissue.

Circadian rhythmicity is a common feature of nearly all physiological processes (*1*–*4*). Each cell of the body contains a molecular clock composed of transcription factors that act on one another in interlocking feedback loops that generate near–24-hour oscillations (*3*, *5*). A core component of the molecular clock, the nuclear receptor Rev-erbα, is expressed with a circadian rhythm (*6*) and represses BMAL1, a positive regulator of clock output genes (*7*). Rev-erbα represses many genes, often to regulate metabolism in a circadian and tissue-dependent manner (*8*–*11*). Thus, Rev-erbα is central to complex interactions between the core clock and metabolism.

Because Rev-erbα is a core clock component but also has tissue-specific functions, we were interested in comparing its cistromes in different mouse tissues, including liver, brain, and epididymal adipose tissue. The majority of Rev-erbα binding sites were tissue-specific (Fig. 1A), and gene ontology analyses were consistent with specialized functions of Rev-erbα (fig. S1). However, a common Rev-erbα cistrome included binding at clock genes in all tissues, consistent with its universal function in the core clock (fig. S1) (*6*, *7*, *12*).

[1]Division of Endocrinology, Diabetes, and Metabolism, Department of Medicine, Department of Genetics, and the Institute for Diabetes, Obesity, and Metabolism, Perelman School of Medicine, University of Pennsylvania, Philadelphia, PA 19104, USA. [2]Department of Molecular and Cellular Biology, Division of Diabetes, Endocrinology and Metabolism, Department of Medicine, Baylor College of Medicine, Houston, TX 77030, USA.
*These authors contributed equally to this work. **†Corresponding author. E-mail: lazar@mail.med.upenn.edu**

Downloaded from www.sciencemag.org on June 26, 2015

RevDR2 and retinoid-related orphan receptor (ROR)–response element (RORE) were the most enriched motifs at Rev-erbα binding sites shared among tissues (Fig. 1A). This is consistent with earlier reports that the function of Rev-erbα as a repressive component of the molecular clock involves binding to two RORE motifs that function in the transcriptional regulation of the *Bmal1* gene (*7*, *13*). Rev-erbα recruits the nuclear receptor co-repressor–histone deacetylase 3 (NCoR-HDAC3) complex to actively repress *Bmal1* transcription (*13*), and liver-specific deletion of HDAC3 induced *Bmal1* expression (fig. S2B) at Zeitgeber time (ZT) 10, consistent with previous reports (*9*, *13*). However, the loss of HDAC3 did not dampen circadian rhythmicity of *Bmal1* or other clock components as much as the loss of Rev-erbα itself, suggesting an additional mechanism (fig. S2, A and B).

Another, non–mutually exclusive mechanism posits competition with the activating nuclear receptor ROR for the DNA binding site, which contains RevDR2/RORE motifs bound by both receptors (*14*–*17*). The α and γ isoforms of ROR are most abundant in liver (*18*) and are expressed in a circadian manner with a peak at ZT18, antiphase to Rev-erbα (*19*), although the circadian variation of RORα is modest and of unclear biological importance (fig. S3, A and B) (*19*). Liver-specific deletion of RORα and γ markedly dampened the circadian oscillation of core clock genes in liver (fig. S3, C to E), consistent with previous reports (*19*). To determine target genes common to RORs and Rev-erbα, we compared gene expression in livers depleted of RORα and γ, at their peak time of expression, with gene expression from Rev-erbα knockout (KO) livers (*9*) (Fig. 1B). Intriguingly, genes regulated both by Rev-erbα and the RORs included clock genes such as *Bmal1*, *Npas2*, *Cry1*, and *E4bp4* (Fig. 1B and fig. S3F) and were expressed with large circadian amplitudes, consistent with the model that Rev-erbα and RORs are both critical regulators of the clock (Fig. 1C). By contrast, Rev-erbα–specific genes had modest circadian rhythms and were enriched for liver metabolic processes (Fig. 1C and fig. S3F).

Although RORα expression was similar at ZT10 and ZT22, there was a marked difference between RORα binding to REREs at the clock genes *Bmal1* and *Npas2* at these times (fig. S4A). Deletion of Rev-erbα enhanced RORα recruitment to these sites at ZT10, and this was potentiated by loss of Rev-erbβ (Fig. 1D), consistent with lower binding of RORα at ZT10 being due to competition with Rev-erbs. Conversely, hepatic overexpression of Rev-erbα reduced RORα recruitment to *Bmal1* and *Npas2* sites at ZT22 (Fig. 1E). Genome-wide, ~44% of RORα binding sites overlapped with Rev-erbα, and these were more likely to be circadian than were RORα-specific sites (Fig. 1F). In addition, sites of increased RORα binding at ZT22 were enriched for the RevDR2/RORE motifs bound by both Rev-erbα and RORα (fig. S4, B and C). Moreover, oscillating RORα binding sites were enriched near common target genes of RORs and Rev-erbα (Fig. 1G), further suggesting that RORα and Rev-erbα compete for binding at highly circadian genes, including core components of the molecular clock. In contrast, consistent with its expression, RORγ had a circadian binding pattern at overlapped and non-overlapped sites (fig. S4D).

To understand why Rev-erbα and ROR tended to compete near clock genes but not Rev-erbα–specific genes, we performed chromatin immunoprecipitation (ChIP)–exonuclease followed by high-throughput sequencing (ChIP-exo) (*20*) in mouse liver at ZT10 to better resolve Rev-erbα binding (fig. S5A). At clock genes regulated by Rev-erbα and RORs, exemplified by *Bmal1* and *Cry1*, the RevDR2/RORE motif was detected at ChIP-exo peaks (Fig. 2A, left). However, Rev-erbα

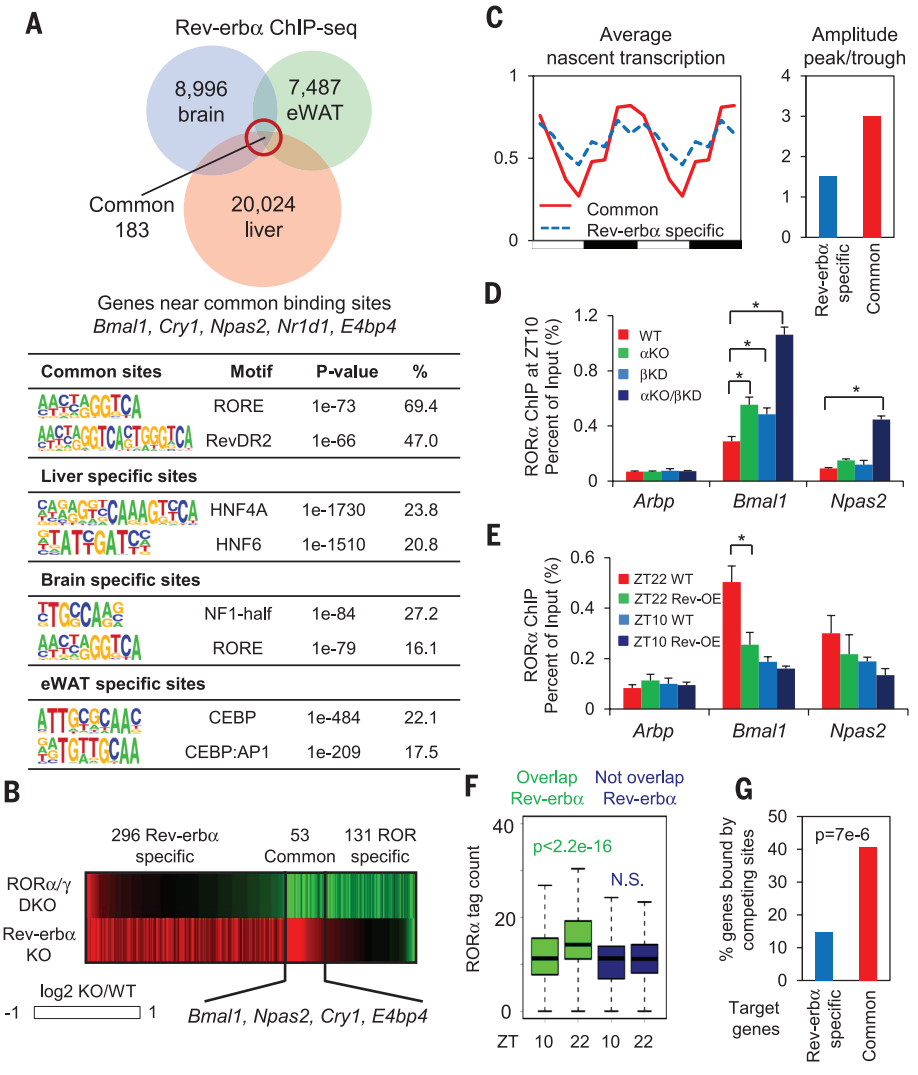

Fig. 1. Rev-erbα represses clock genes by competing with RORα at its cognate sites. (**A**) Overlap of Rev-erbα cistromes in liver (*9*), brain, and epididymal adipose tissue (eWAT). Most significantly enriched known motifs (abundance >10%) in common and tissue-specific cistromes are shown. (**B**) Heat map showing expression fold changes of genes deactivated by RORα/γ double KO (DKO/WT < –1.3, $P < 0.01$) and derepressed by Rev-erbα KO (αKO/WT > 1.3, $P < 0.01$). (**C**) Mean relative global run-on sequencing (GRO-seq) transcription (left) throughout 24-hour light–dark cycle, as well as oscillation amplitudes (right) of RORs/Rev-erbα common targets (red) and Rev-erbα–specific targets (blue). Time points were duplicated for clearer visualization. (**D**) RORα binding at clock and control genes promoters at ZT10, in WT, Rev-erbα KO (αKO), Rev-erbβ knockdown (βKD), and αKO/βKD mice liver, analyzed by ChIP-PCR. Data are expressed as mean ± SEM (* Student's *t* test, $P < 0.05$, $n = 4$ mice). (**E**) RORα binding at clock and control gene promoters at ZT10 or ZT22 in Rev-erbα overexpression (OE) mouse liver, analyzed by ChIP-PCR. Data are expressed as mean ± SEM (* Student's *t* test, $P < 0.05$, $n = 6$ or 7 mice). (**F**) Circadian binding of RORα at sites overlapped or not overlapped with Rev-erbα cistrome (N.S., not significant; Student's *t* test, $P > 0.05$). (**G**) Percentage of common or Rev-erbα–specific target genes containing high-confidence oscillating RORα binding sites [ZT22 > 2 reads per million (rpm), ZT22/ZT10 > 1.5] within 50 kb of transcription start sites (*P* value from hypergeometric test).

ChIP-exo peaks were most commonly enriched for the motif bound by liver-lineage determining TF hepatocyte nuclear factor 6 (HNF6) (Fig. 2B). As exemplified by *Cyp2b13* and *Slc45a3*, these Rev-erbα binding sites colocalized with HNF6 in mouse liver (Fig. 2A, right). Overall, the HNF6 motif was found at 1108 Rev-erbα ChIP-exo sites (Fig. 2C), the vast majority of which were also detected by HNF6 ChIP-exo in liver (*21*) yet did not have an RORE motif nearby (fig. S5B). The genes located nearest to these Rev-erbα/HNF6 binding sites ("Rev-erbα/HNF6-exo sites") were enriched for lipid metabolic processes (fig. S5C), similar to Rev-erbα–specific gene regulation. Indeed, enhancer RNAs (eRNAs) at these sites bound by Rev-erbα and HNF6 had a robust circadian expression pattern (Fig. 2D) and were markedly up-regulated in livers depleted of Rev-erbα, indicating active repression of enhancer function at these sites (Fig. 2E) (*22*).

To test whether the binding of Rev-erbα to the genome can be indirect, we used a mouse model with a conditional deletion of the Rev-erbα DNA binding domain (DBD). These mice have been previously studied as a model of Rev-erbα deletion (*12*, *23*), but the targeting strategy is predicted to lead to in-frame deletion of the DBD (fig. S6A), and Rev-erbα immunoblot of mouse liver after Cre-recombination revealed an abundant species at the approximate molecular weight of the protein lacking the DBD (fig. S6B). The identity of this protein as full-length Rev-erbα lacking its DBD was confirmed by mass spectrometric analysis of Rev-erbα immunoprecipitates from recombined liver extracts (fig. S6C). Thus, this model is actually a knock-in of a DBD mutation, rather than a complete knockout of the Rev-erbα protein. We studied the function of this Rev-erbα DBD mutant in mice whose livers were also depleted of Rev-erbβ to eliminate its compensatory effects (*6*, *12*).

ChIP-seq analysis of Rev-erbα in livers expressing only the Rev-erbα DBD mutant ("DBD^{m}") revealed a comparable level of binding at a subset of wild-type (WT) sites ("DBD-independent sites"), whereas binding was markedly reduced at many other sites ("DBD-dependent sites") (Fig. 2E and fig. S7, A and B). HNF6 ChIP-seq signals (*24*) were more enriched at Rev-erbα DBD-independent sites than at the DBD-dependent sites (fig. S7C), suggesting that HNF6 might tether Rev-erbα to the DNA even in the absence of Rev-erbα DBD domain.

DBD-dependent sites were enriched in RORE as well as dimeric RevDR2 motifs, in agreement with direct DNA binding (fig. S7D). These motifs are also recognized by ROR, and indeed the binding of RORα at these sites decreased markedly at ZT10, when Rev-erbα competition is strongest (fig. S7E). RevDR2 motifs were depleted in DBD-independent sites, whereas ROREs still exist in a minority of sites (fig. S7D), suggesting that the RORE may facilitate, but is not required for, DBD-independent binding. The HNF6 motif was markedly enriched at DBD-independent sites (fig. S7D), and Rev-erbα binding at Rev-erbα/HNF6-exo sites was comparable between WT and DBD^{m} mice, following the same pattern as that seen at DBD-independent sites (fig. S7F). The simultaneous binding of Rev-erbα and HNF6 at these sites was confirmed by ChIP-re-ChIP experiments in WT liver, whereas HNF6 and Rev-erbα were not colocalized at DBD-dependent sites (Fig. 2G and fig. S7G). Enhancer RNA transcription showed circadian oscillation in phase ZT22, at DBD-dependent and -independent sites (fig. S7H), suggesting active repression of Rev-erbα in both cases. In agreement with Rev-erbα functioning by recruiting the co-repressor complex, HDAC3 binding at Rev-erbα sites was reduced in Rev-erb–depleted livers (fig. S7I). In addition, the HDAC3 ChIP-seq signal in the DBD^{m} was reduced at DBD-dependent sites but not at sites that are DBD-independent (Fig. 2H), suggesting active repression by Rev-erbα via recruitment of HDAC3.

To determine whether HNF6 is required for Rev-erbα DBD-independent binding, we performed ChIP-seq for Rev-erbα in the liver of 129S1/SvlmJ mice and compared this result with that obtained in the C57BL/6J mice. The two

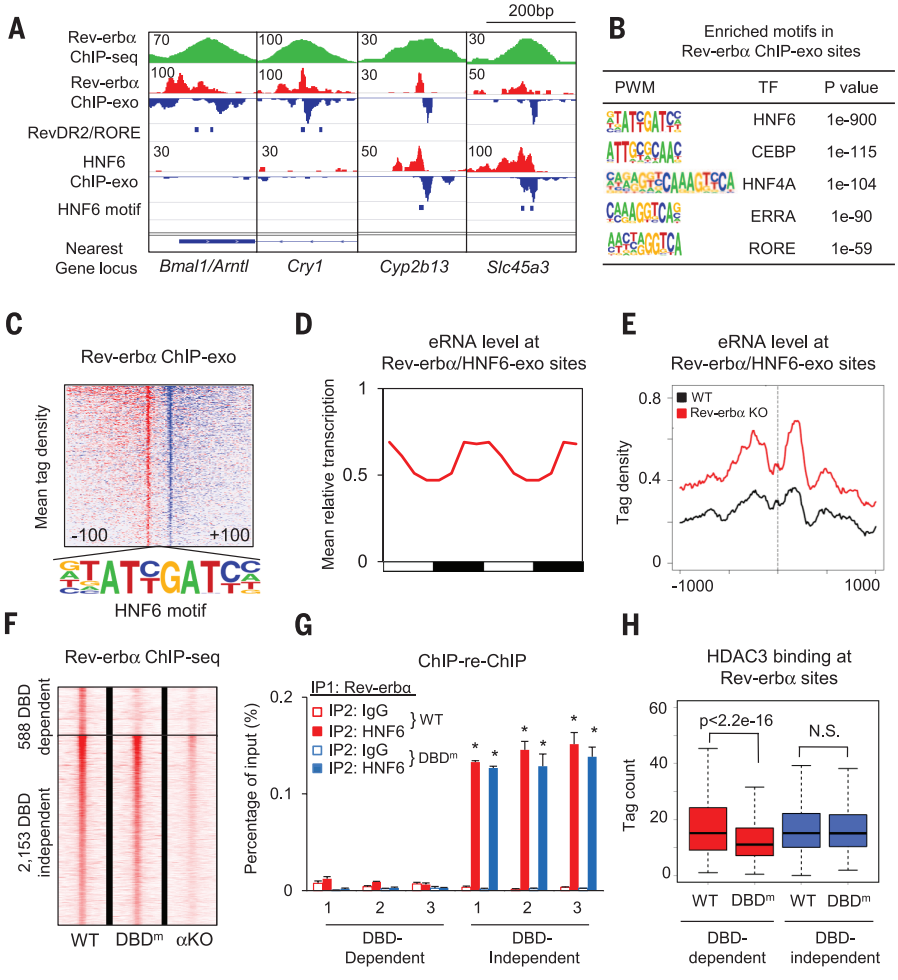

Fig. 2. Rev-erbα binds to the genome using both DBD-dependent and DBD-independent mechanisms. (**A**) Genome browser view of Rev-erbα and HNF6 ChIP-exo signals under Rev-erbα ChIP-seq peaks near clock and metabolic genes. Blue bars indicate locations of RevDR2/RORE and HNF6 motif. (**B**) Highly enriched known motifs found in Rev-erbα ChIP-exo peak pairs 22 to 26 base pairs apart. (**C**) Heat map showing 5′-end tag densities of Rev-erbα ChIP-exo centered at HNF6 motifs within 1108 peak pairs. Red and blue indicate tag density on the plus and minus strand, respectively. (**D**) Mean relative eRNA transcription (*22*) at Rev-erbα/HNF6-exo sites throughout 24-hour light–dark cycles. Data were double plotted for clearer visualization. (**E**) eRNA tag density (*22*) centered at Rev-erbα/HNF6-exo sites near Rev-erbα target genes, in Rev-erbα KO and WT liver. (**F**) Heat map showing Rev-erbα ChIP-seq tag densities (at ZT10) in WT, DBD mutant (DBD^{m}), and Rev-erbα KO (αKO) mice, at DBD-dependent and -independent sites identified among 5792 high-confidence Rev-erbα peaks (peak height > 1 rpm, WT/Rev-erbα KO > 3). (**G**) Sequential ChIP of Rev-erbα followed by either HNF6 or immunoglobulin G ChIP in WT and DBD^{m} mouse liver at ZT10. Data are expressed as mean ± SEM (* Student's *t* test, $P < 0.05$, $n = 3$ or 4 mice per group). (**H**) Binding of HDAC3 at DBD-dependent and -independent sites in WT and DBD^{m} liver (N.S., Student's *t* test, $P > 0.05$).

strains differ by ~5.4 million single-nucleotide polymorphisms (SNPs), and SNPs were predicted to cripple the HNF6 motif at 107 Rev-erb binding sites in C57BL/6J mice and 71 Rev-erb binding sites in 129S1/SvlmJ mice. Notably, Rev-erbα binding was markedly diminished at the sites in which the SNPs disrupt either the RevDR2/RORE or the HNF6 motif in C57BL/6J or 129S1/SvlmJ mice, whereas Rev-erbα binding at random SNPs tended to be unaffected (Fig. 3, A and B, and fig. S8A). Specific examples of strain-dependent binding of Rev-erbα at HNF6 sites are shown in Fig. 3, A and B, and differential binding in the two mouse strains was confirmed by ChIP–polymerase chain reaction (PCR) for HNF6 and Rev-erbα (fig. S8, B and C). Interestingly, although the HNF6 motif was most significantly associated with strain specific Rev-erbα binding by the same analysis, we also found significant association with motifs for several other TFs that play important roles in liver function, suggesting involvement of other partners in Rev-erbα binding in the absence of RORE and RevDR2 (Fig. 3C).

The preserved binding of HDAC3, mediated by Rev-erbα DBD mutant, at metabolic genes suggested that hepatic expression of these genes might also be intact relative to livers of mice in which the Rev-erbα protein is deleted. To test this hypothesis, we compared the gene expression changes in mice lacking Rev-erbα in liver with published results using the DBD^m mouse model used here, in which Rev-erbα is converted to the DBD mutant and Rev-erbβ is also deleted (*12*). Circadian clock genes were derepressed in both situations, demonstrating that the regulation of these genes required direct binding at RevDR2/RORE sites by Rev-erbα. Overall, only ~25% of Rev-erbα target genes that were derepressed in Rev-erbα KO mice were also derepressed in the DBD^m mice ("DBD-dependent Rev-erbα targets") (Fig. 4A). Genes derepressed specifically in Rev-erbα KO mice ("DBD-independent Rev-erbα targets") showed circadian expression peaking at ZT22 (fig. S9A) and were enriched for lipid metabolic functions (fig. S9B), suggesting that Rev-erbα regulates circadian

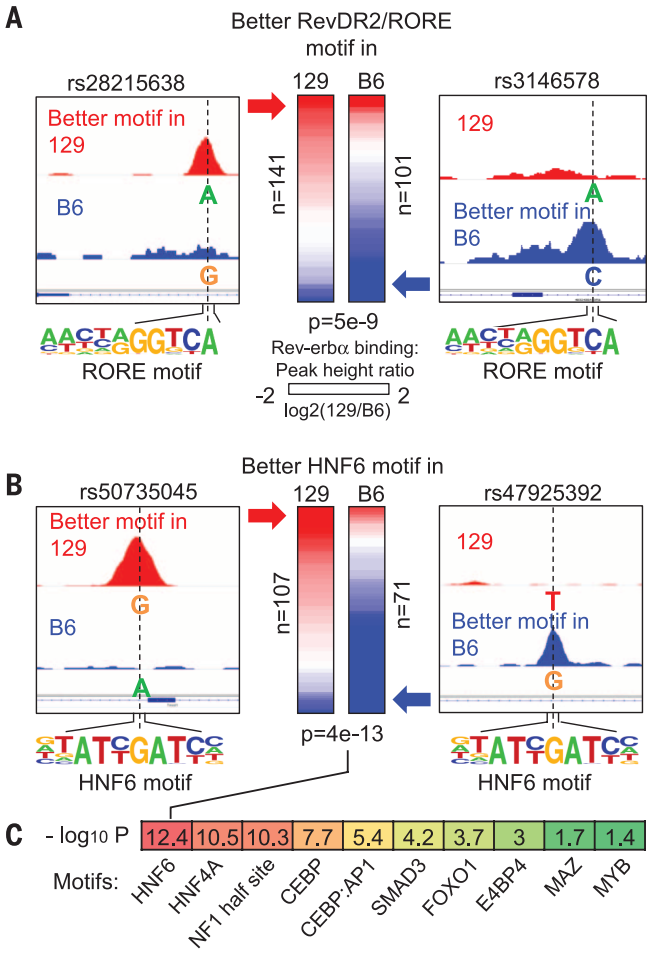

Fig. 3. SNP-associated strain-specific occupancy suggests HNF6-mediated binding of Rev-erbα. (**A**) Heat map showing $\log_2$ fold changes of Rev-erbα binding in 129 and B6 mice. The left column in the heat map contains 141 Rev-erbα peaks where RevDR2/RORE motif scores are higher in 129 mice and lower in B6 mice, owing to the SNPs (illustrated in the left panel). Similarly, the right column contains 101 SNP-bearing Rev-erbα peaks with better RevDR2/RORE in the B6 genome. *P* value was calculated with Student's *t* test. (**B**) Same analysis as in (A), focusing on SNPs disrupting HNF6 motif under Rev-erbα peaks. (**C**) Heat map showing –log10 *P* values for other motifs that are enriched in DBD-independent Rev-erbα peaks.

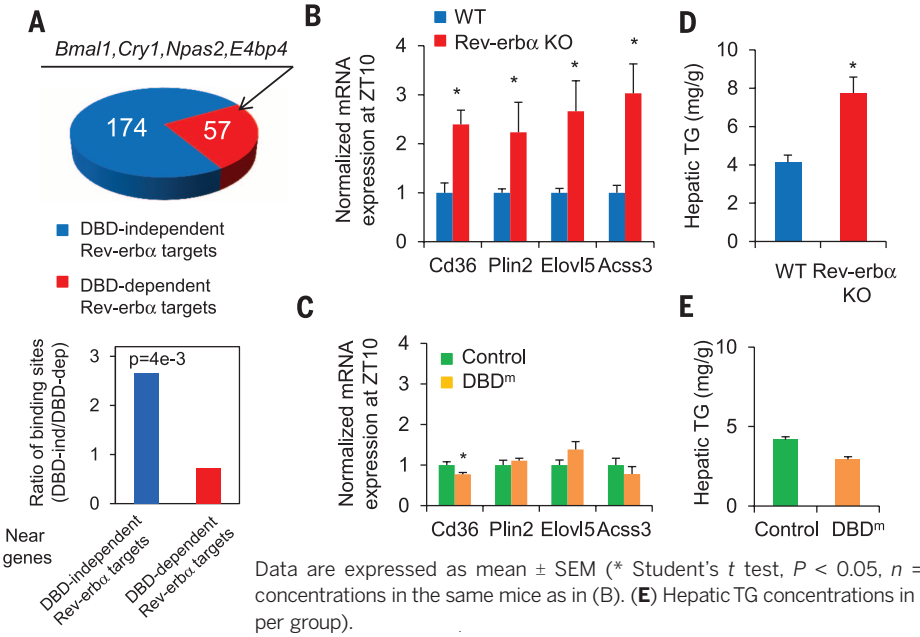

Fig. 4. DBD-independent Rev-erbα sites regulate metabolic genes in liver. (**A**) Top panel shows the number of DBD-dependent and -independent Rev-erbα target genes identified with microarrays in Rev-erbα KO (*9*) and DBD^m mice (*12*). Bar graph shows ratios of DBD-independent and -dependent Rev-erbα/HDAC3 binding sites (*29*) located near two groups of Rev-erbα target genes (*P* value from hypergeometric test). (**B**) mRNA expression of lipid metabolic genes normalized to *Arpp*, measured by reverse transcription–quantitative polymerase chain reaction (RT-QPCR), in livers of Rev-erbα KO mice and WT mice at ZT10. (**C**) mRNA expression of lipid metabolic genes normalized to *Arpp*, measured by RT-QPCR, in livers of Rev-erbα DBD^m (Rev-erbα/β double floxed mice injected with adeno-associated virus expressing cre-recombinase under a hepatocyte-specific thyroxine-binding globulin promoter (AAV-Tbg-Cre)) or control mice (floxed mice injected with AAV-Tbg–green fluorescent protein (GFP)) at ZT10. Data are expressed as mean ± SEM (* Student's *t* test, $P < 0.05$, $n = 4$ mice per group). (**D**) Hepatic triglyceride (TG) concentrations in the same mice as in (B). (**E**) Hepatic TG concentrations in mice as in (C) (* Student's *t* test, $P < 0.05$, $n = 4$ mice per group).

lipid metabolic genes independent of its DBD. In support of this, DBD-independent Rev-erbα/HDAC3 sites were enriched near DBD-independent Rev-erbα targets, whereas DBD-dependent Rev-erbα/HDAC3 sites, where Rev-erbα and HDAC3 binding was markedly reduced in DBD^m mice, were more enriched near DBD-dependent Rev-erbα targets (Fig. 4A). Examples of the deletion-specific regulation of metabolic genes are shown in Fig. 4, B and C. Consistent with preserved metabolic gene expression in the DBD^m mice livers, these mice did not display hepatosteatosis as is characteristic of the mice with complete deletion of Rev-erbα (Fig. 4, D and E, and fig. S9C) (*6*, *9*).

These findings demonstrate that Rev-erbα has a DBD-independent function that contributes to its regulation of liver metabolism. Other nuclear receptors, including estrogen receptor and glucocorticoid receptor, have DBD-independent activities through protein-protein interactions with other TFs, either directly or indirectly (*25*, *26*). In liver, Rev-erbα is tethered to chromatin by hepatic lineage–determining TFs (fig. S10), and this mechanism of binding explains much of the non-overlapping cistromes of Rev-erbα in different tissues, as well as the large proportion of binding sites without the RevDR2/RORE motif. In liver, the tethered cistrome is more enriched for genes with specialized function in hepatic metabolism, whereas the DBD-dependent cistrome is enriched for circadian clock genes and common to multiple tissues.

Circadian clocks and metabolism are tightly connected (*1*, *3*, *4*), and Rev-erbα has emerged as a transcriptional link from circadian rhythms to metabolism in multiple tissues (*8*). Our findings delineate a molecular hierarchy that governs how the clock is wired with metabolism. Direct competition between Rev-erb and ROR provides a universal mechanism for self-sustained control of the molecular clock across all tissues. On top of this basic landscape, circadianly expressed Rev-erb uses lineage-determination factors to convey a tissue-specific epigenomic rhythm that, through co-repressor and HDAC3, regulates metabolism tailored to the specific need of that tissue. These two modes of action may bestow on Rev-erbα the ability to stabilize the circadian oscillations of clock gene, while coupling liver metabolism to environmental and metabolic changes, perhaps through its endogenous ligand heme (*27*, *28*). This raises the possibility that synthetic ligands that specifically affect Rev-erbα interaction with NCoR/HDAC3 without disrupting DNA binding could modulate liver metabolism with lesser effects on the integrity of the circadian clock.

REFERENCES AND NOTES

1. D. Feng, M. A. Lazar, *Mol. Cell* **47**, 158 (2012).
2. G. Asher, P. Sassone-Corsi, *Cell* **161**, 84 (2015).
3. J. S. Takahashi, H. K. Hong, C. H. Ko, E. L. McDearmon, *Nat. Rev. Genet.* **9**, 764 (2008).
4. J. Bass, J. S. Takahashi, *Science* **330**, 1349 (2010).
5. P. E. Hardin, S. Panda, *Curr. Opin. Neurobiol.* **23**, 724 (2013).
6. A. Bugge *et al.*, *Genes Dev.* **26**, 657 (2012).
7. N. Preitner *et al.*, *Cell* **110**, 251 (2002).
8. L. J. Everett, M. A. Lazar, *Trends Endocrinol. Metab.* **25**, 586 (2014).
9. D. Feng *et al.*, *Science* **331**, 1315 (2011).
10. Z. Gerhart-Hines *et al.*, *Nature* **503**, 410 (2013).
11. E. Woldt *et al.*, *Nat. Med.* **19**, 1039 (2013).
12. H. Cho *et al.*, *Nature* **485**, 123 (2012).
13. L. Yin, M. A. Lazar, *Mol. Endocrinol.* **19**, 1452 (2005).
14. V. Giguère *et al.*, *Genes Dev.* **8**, 538 (1994).
15. B. M. Forman *et al.*, *Mol. Endocrinol.* **8**, 1253 (1994).
16. H. P. Harding, M. A. Lazar, *Mol. Cell. Biol.* **15**, 4791 (1995).
17. E. Stashi *et al.*, *Cell Rep.* **6**, 633 (2014).
18. L. A. Solt, T. P. Burris, *Trends Endocrinol. Metab.* **23**, 619 (2012).
19. Y. Takeda, R. Jothi, V. Birault, A. M. Jetten, *Nucleic Acids Res.* **40**, 8519 (2012).
20. H. S. Rhee, B. F. Pugh, *Cell* **147**, 1408 (2011).
21. L. Wang *et al.*, *Nucleic Acids Res.* **42**, e156 (2014).
22. B. Fang *et al.*, *Cell* **159**, 1140 (2014).
23. M. T. Lam *et al.*, *Nature* **498**, 511 (2013).
24. A. J. Faure *et al.*, *Genome Res.* **22**, 2163 (2012).
25. N. Heldring *et al.*, *Mol. Endocrinol.* **25**, 564 (2011).
26. C. K. Glass, K. Saijo, *Nat. Rev. Immunol.* **10**, 365 (2010).
27. L. Yin *et al.*, *Science* **318**, 1786 (2007).
28. S. Raghuram *et al.*, *Nat. Struct. Mol. Biol.* **14**, 1207 (2007).
29. Materials and methods are available as supplementary materials on *Science* Online.

ACKNOWLEDGMENTS

ChIP-seq and microarray data have been deposited in the Gene Expression Omnibus (GSE67973). We thank S. Sidoli and B. A. Garcia for assistance with mass spectrometry. We acknowledge the Functional Genomics Core and the Viral Vector Core of the Penn Diabetes Research Center (P30 DK19525) for next-generation sequencing and virus preparation, respectively. We thank the Penn Digestives Disease Center Morphology Core (P30 DK050306) for histology studies and the Molecular Profiling Core for microarray analysis. This work was supported by NIH R01 DK45586 (M.A.L.), K08 DK094968 (R.E.S.), R00 DK099443 (Z.S.), R01 DK098542 (D.J.S.), F32 DK102284 (S.M.A.), F30 DK104513 (M.J.E.), T32 GM0008275 (J.R.R.), and the Cox Medical Research Institute.

SUPPLEMENTARY MATERIALS

www.sciencemag.org/content/348/6242/1488/suppl/DC1
Materials and Methods
Figs. S1 to S10
Table S1
References (*30*–*39*)

14 April 2015; accepted 22 May 2015
Published online 4 June 2015;
10.1126/science.aab3021

Science Careers Advertising

For full advertising details, go to ScienceCareers.org and click For Employers, or call one of our representatives.

Tracy Holmes
Worldwide Associate Director
Science Careers
Phone: +44 (0) 1223 326525

THE AMERICAS

E-mail: advertise@sciencecareers.org

Fax: +1 (202) 289 6742

Tina Burks
Phone: +1 (202) 326 6577

Nancy Toema
Phone: +1 (202) 326 6578

Online Job Posting Questions
Phone: +1 (202) 312 6375

EUROPE / INDIA / AUSTRALIA / NEW ZEALAND / REST OF WORLD

E-mail: ads@science-int.co.uk

Fax: +44 (0) 1223 326532

Sarah Lelarge
Phone: +44 (0) 1223 326527

Kelly Grace
Phone: +44 (0) 1223 326528

Online Job Posting Questions
Phone: +44 (0) 1223 326528

JAPAN

Katsuyoshi Fukamizu (Tokyo)
E-mail: kfukamizu@aaas.org
Phone: +81 3 3219 5777

Hiroyuki Mashiki (Kyoto)
E-mail: hmashiki@aaas.org
Phone: +81 75 823 1109

CHINA / KOREA / SINGAPORE / TAIWAN / THAILAND

Ruolei Wu
Phone: +86 186 0082 9345
E-mail: rwu@aaas.org

All ads submitted for publication must comply with applicable U.S. and non-U.S. laws. *Science* reserves the right to refuse any advertisement at its sole discretion for any reason, including without limitation for offensive language or inappropriate content, and all advertising is subject to publisher approval. *Science* encourages our readers to alert us to any ads that they feel may be discriminatory or offensive.

ScienceCareers
FROM THE JOURNAL SCIENCE AAAS

ScienceCareers.org

ScienceCareers

Cernet

“《科学》职业” 已经与Cernet/赛尔互联开展合作。中国大陆的高校可以直接联系Cernet/赛尔互联进行国际人才招聘。

请访问
Sciencecareers.org/CER
点得联系信息。

中国大陆高校以外的 招聘广告，或者高校的其它业务，请与国际合作、出版副总监吴若蕾联系：
+86-186 0082 9345 rwu@aaas.org

招募学术精英，《科学》是您的不二之选 Science

Main building of the University of Hong Kong

The globalization of universities and science in Southern China

Universities in south China are taking the lead in an array of reforms aimed at making academic centers and scientific collaboration more international and more dynamic. Leaders of universities across southern Guangdong Province are expanding award schemes designed to recruit researchers and scientists who have obtained advanced degrees or taught in the United States or Europe. These measures are increasing openings for scholars trained abroad, and are helping globalize university faculties and joint scientific research. In the process, China is strengthening its position as a world power in science. **By Kevin Holden**

As the new millennium unfolds, reform-minded leaders of Chinese universities and academies, and of independent scientific institutes, are all pushing for research discoveries and applications that will bolster China's rise in diverse spheres of science.

These leaders—many of whom have received advanced degrees in the United States or Europe—likewise support making colleges and scientific collaboration more international and dynamic.

This trend is gaining momentum in south China's Guangdong Province and is creating new openings for scientists trained abroad.

For centuries, coastal Guangdong has been China's main portal for contact with the West—everyone from Italian astronomers to British tea traders ended their seafaring passage from Europe at one of the province's harbors—and the region is moving to expand these intercontinental connections.

Capped on one side by the South China Sea and by mountains to the north, Guangdong features the palm-tree–lined megacities of Guangzhou and Shenzhen along the Pearl River Delta, one of the planet's most densely populated regions.

Zhuhai, a smaller seaside outpost opposite the former Portuguese colony of Macau, hosts China's biggest space technology exhibition every 2 years. Daya Bay, a boating resort in eastern Guangdong, holds a massive nuclear power complex.

On the island of Hainan, just off Guangdong's coast, China is constructing its most technologically advanced spacecraft launch center—the first spaceflight complex to be open to international visitors.

Although Guangzhou, the provincial capital, has been the academic center of south China for hundreds of years, Shenzhen—a sleepy checkerboard of coastal villages when the People's Republic was founded nearly 6 decades ago—is now experiencing a construction boom in terms of new colleges.

Guangdong's simultaneous moves to expand universities and to attract scholars worldwide to conduct research or teach at these academic centers are rapidly boosting progress across a spectrum of scientific areas.

Guangzhou's universities are magnets for scholars trained abroad

In Guangzhou, which has been an export powerhouse in terms of manufactured goods since the launch of China's market-oriented reforms more than three decades ago, academic leaders are ramping up campaigns to "import" scholars who can help shape the transition to a knowledge-based economy.

At Guangzhou's Sun Yat-sen University, President Luo Jun is using an assortment of talent schemes, along with perks like access to one of the world's fastest supercomputers, to attract scientists worldwide to the university's School of Advanced Computing, School of Engineering, and School of Life Sciences.

The university was founded by Sun Yat-sen, the Hawaiian-educated leader of the 1911 revolution that toppled 2,000 years of imperial rule and gave birth to the Republic of China. Sun, a medical scholar who became the first president of the new republic, envisioned a rejuvenated China guided by "science and democracy," and he promoted ever-closer ties with the West.

These days, the university he created is transforming itself into an international center for the life sciences and engineering, partly by forging partnerships with American schools: Sun Yat-sen University has teamed up with Johns Hopkins University to create the Medical Research Center for Clinical and Translational Research, and with Carnegie Mellon University to launch the Joint Institute of Engineering.

The university recently received international attention after a group of 16 scientists based at the Key Laboratory of Gene Engineering published the results of a controversial experiment in which they genetically modified single-cell human embryos to repair the human β-globin (HBB) gene in a procedure aimed at preventing a serious blood disorder (www.sciencemag.org/content/348/6234/486.full).

Some scholars argue that the Chinese scientists have crossed an ethical line by editing the human genome, but others welcome China's comparatively liberal regulation of this area of experimentation, which allows genetics researchers to push the scientific envelope.

Meanwhile, Sun Yat-sen University and other academic centers across Guangdong are competing continued>

PHOTO: © NORMAN CHAN/SHUTTERSTOCK.COM

Upcoming Features

Postdoc Careers—August 28 ■ *Faculty Careers—September 18* ■ *Regional Focus: China—October 2*

South University of Science and Technology

> **"Over 95% of the current faculty members are Chinese scholars returning from abroad."**
>
> **— Chen Shiyi**

to attract Chinese scientists who have relocated to Europe or North America after studying there.

For example, Jinan University, which has five campuses spread across the cities of Guangzhou, Zhuhai, and Shenzhen, is stepping up recruitment of researchers who have obtained a degree or taught abroad, says university president **Hu Jun**.

Jinan University's academic focus ranges from aquatic ecology and biotechnology to medical bioengineering and traditional Chinese medicine.

The university's globe-spanning headhunting campaign covers the fields of biology, medicine, information science, and engineering; this effort has been so successful that more than half of the scholars currently joining the faculty have been trained abroad, Hu says.

"Talent from overseas have more expansive academic views and international ways of thinking," Hu explains. These scholars likewise tend to develop innovative approaches to research and thinking about science.

Shenzhen's new universities and their global alliances

In the seaside city of Shenzhen, which borders the former British enclave of Hong Kong, the speed of change across the sciences and the university system has been dramatic.

At Shenzhen's South University of Science and Technology of China, which was launched just 5 years ago, "over 95% of the current faculty members are Chinese scholars returning from abroad," says university President **Chen Shiyi**.

Chen, a former Oppenheimer Fellow at the Los Alamos National Laboratory in New Mexico, says: "This high ratio of professors with [training from] foreign universities makes South University a leader in Chinese academic and scientific communities in terms of the level of globalization."

The university, which holds departments in physics, chemistry, life sciences, electronic engineering, and environmental engineering, "was built with a mission to serve as an experimental ground to reform the Chinese higher education system," he explains.

Many courses are taught in English, with textbooks from North America or Europe, Chen says. He adds that South University is currently searching for experts in the fields of neural and cognitive sciences, biology and gene engineering, physics, nanotechnology, environmental sciences, large-scale computational research, robotics, and artificial intelligence. The university is also searching for candidates to serve as dean of the School of Engineering or the School of Life and Health Sciences.

"South University of Science and Technology of China is also making a huge effort to increase the level of globalization by recruiting more high-quality non-Chinese professors and international students to its campus," Chen says.

Many new academic centers launched across China, he adds, are becoming testing grounds for reforms aimed at connecting universities and students through a global network of partnerships.

At South University, which has woven a web of collaboration with 18 world-leading universities, Chen says, "The goal is to provide the opportunity for every student to take part in an international exchange."

A new Chinese-Danish college in Guangdong

South University is also co-founding a new college in a unique union with the University of Copenhagen in Denmark and with Shenzhen-based BGI, one of the world's leading genome research institutes.

The new BGI Genomic College will recruit scientists and students globally, says **Wang Jun**, executive director of BGI.

Wang says the experimental structure of the new college, in contrast with China's traditional universities, will foster innovation across the life sciences, and will feature cutting-edge research in medicine, biology, genomics, and bioinformatics.

BGI—which is part research institute and part genomics applications developer—has already launched satellite research groups in Europe and the United States and aims to move its talent from city to city, continent to continent, to promote scholarly collaboration.

This worldwide rotation of talent will allow scientists to understand different cultures and approaches to research.

BGI was set up as an independent research institute in 1999 in order to represent Chinese scientists in the Human Genome Project (www.genome.gov/10001772), and recently signed an agreement with the Bill and Melinda Gates Foundation to collaborate on genetics studies tied to global health and agricultural breakthroughs envisioned as part of the United Nations Millennium Development Goals (www.un.org/millenniumgoals).

The leaders of BGI, which was founded in the Chinese capital, say they opted to move the institute's headquarters to Shenzhen due to the city's openness to international trends and thinking.

Shenzhen was a sparsely populated region of rice paddies with a tightly guarded, barbed-wire border with British-ruled Hong Kong during the isolationist rule of Chairman Mao Zedong. It was transformed into China's first "special economic zone," aimed at integrating the country into the global market, after Mao's successors began jettisoning the chairman's most radical policies.

Shenzhen, now one of the globe's fastest-growing cities, is also seeking ever-closer economic, academic, and cultural ties with post-colonial Hong Kong.

And as Shenzhen adopts components of Hong Kong's capitalist-model economy and open, international education system, it has begun competing with the former British outpost to build China's biggest stock market, attract biotech startups, and recruit leading scientists.

South China's global collaboration in visual computing

The Shenzhen Institutes of Advanced Technology, part of the Chinese Academy of Sciences, have tapped continued>

PHOTOS: SOUTHERN UNIVERSITY OF SCIENCE AND TECHNOLOGY

COLD SPRING HARBOR ASIA | 冷泉港亚洲

Suzhou, China

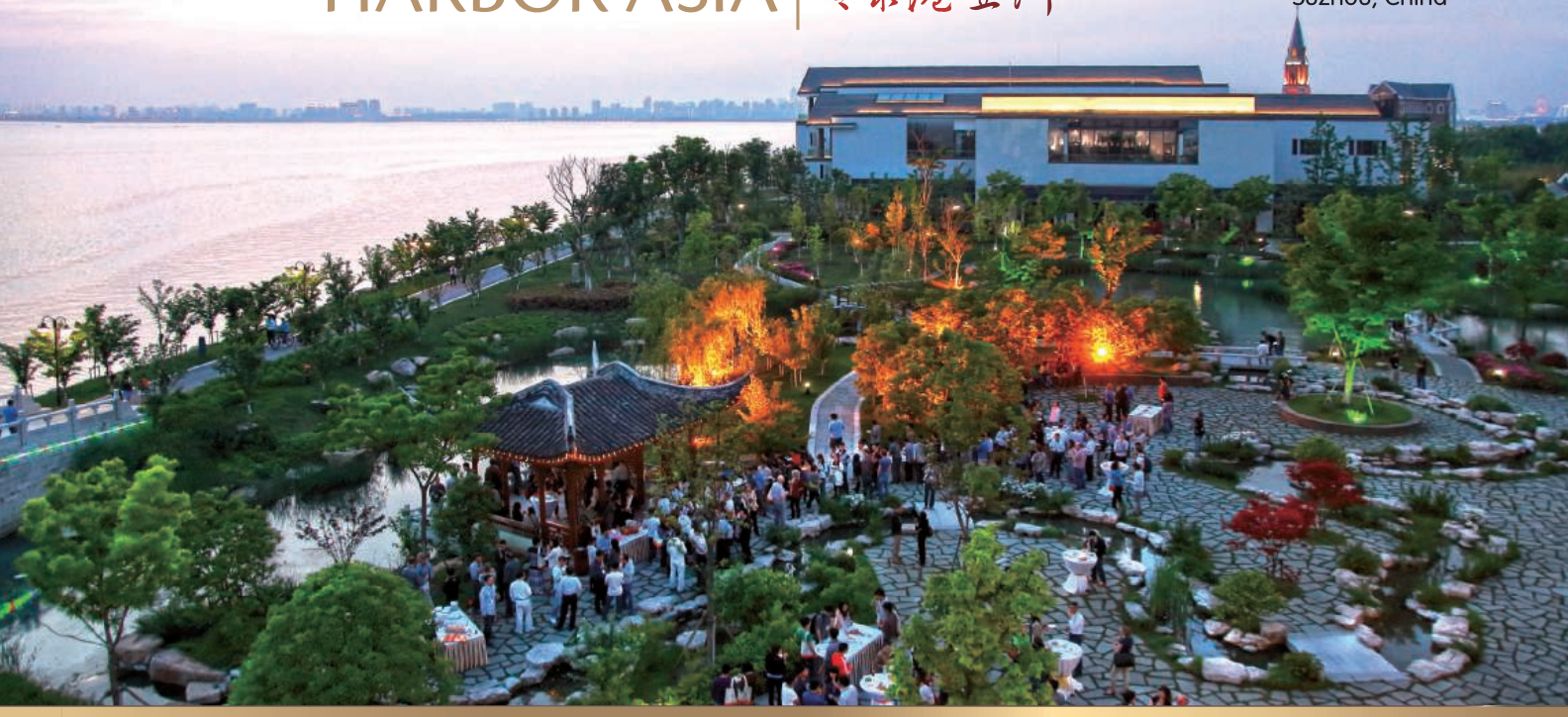

2015 FALL MEETINGS

Molecular Basis of Aging and Disease / September 14-18
Adam Antebi, Jing-Dong Jackie Han, Brian Kennedy, Jan Vijg
Abstract Deadline: June 26

Tumor Immunology and Immunotherapy / September 21-25
Xuetao Cao, Olivera J. Finn, Shimon Sakaguchi, Laurence Zitvogel
Abstract Deadline: July 3

Mitochondria / October 12-16
Xiaodong Wang, Andrew Dillin, Paolo Bernardi
Abstract Deadline: July 24

CSHA/ISSCR Joint Meeting – Stem Cells: from Basic Biology to Disease Therapy / October 19-22
Hongkui Deng, Andrew Elefanty, Gordon Keller, Duanqing, Pei, Kathrin Plath
Abstract Deadline: July 31

Biological Rhythms / October 26-30
Carla Green, Michael Hastings, Joseph Takahashi, Hiroki Ueda, Han Wang
Abstract Deadline: August 7

Bacterial Infection and Host Defense / November 2-6
Kenya Honda, Sam Miller, Craig Roy, Feng Shao, Jörg Vogel
Abstract Deadline: August 14

Targeting Cell Death Mechanisms for the Treatment of Human Diseases / November 9-13
Junying Yuan, Jiahuai Han, Douglas Green, Domagoj Vucic
Abstract Deadline: August 21

Development and Pathophysiology of Respiratory Systems / November 16-20
Paul Noble, Min Wu, Nanshan Zhong
Abstract Deadline: August 28

CSHA/AACR Joint Meeting - Big Data, Computation and Systems Biology in Cancer /December 1-5
Andrea Califano, William C. Hahn, Satoru Miyano, Xuegong Zhang
Abstract deadline September 11

New Advances in Optical Imaging of Live Cells and Organisms / December 7-11
Guoqiang Bi, Wenbiao Gan, Arthur Konnerth, Akihiro Kusumi
Abstract Deadline: September 18

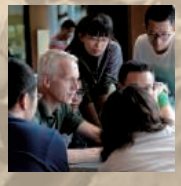
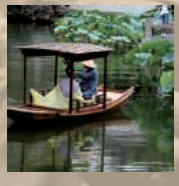

For the most updated information, plesae visit our website at
www.csh-asia.org

Tel: +86-512-62729029 | Email: meetings@csh-asia.org | Address: No. 299, Qiyue Road, Suzhou, China

暨南大學
JINAN UNIVERSITY

百年暨大，誠聘英才
携手暨大，共創未來

Faculty Position Available at Jinan University

Jinan University is the first overseas Chinese university founded by the government in China, and the key comprehensive "211 Project" university under the Overseas Chinese Affairs Office of the State Council. It has 15 post-doctorial research stations, 4 national key disciplines, 8 key disciplines of the Overseas Chinese Affairs Office of the State Council, 20 Guangdong Province Level-I key disciplines, and 4 Guangdong Province Level-II key disciplines. There are four campuses of Jinan University located in three cities, Guangzhou, Shenzhen and Zhuhai, covering a total area of 1,461,300m².

The Institute of Photonics Technology of Jinan University is founded in 2009. It specializes in research into fundamental research and development in the fields of advanced photonic devices, fiber sensor techniques, high speed optical communications, microwave photonics and micro-nanophotonics. The institute has an excellent research team consisting of the winner of "National Science Fund for Distinguished Young Scholars", the Recruitment Program of Global Youth Experts, the New Century Excellent Talents and so on. Open research positions for lecturers and postdoctoral researchers are available now.

I. Requirement

1. Lecturers: having the Ph.D in the domestic or oversea high-level university, or research institutes, with excellent academic records. We encourage applications from candidates with backgrounds in microwave photonics, optical communication and fiber sensor technology. Candidates with oversea study and work experience are highly desirable.
2. Postdoctoral researchers: having the Ph.D in the domestic or oversea university, or research institutes.A strong expertise in optical communication, fiber sensing, microwave photonics, Bio-photonics, polymer photonics, micro-nano photonics, and being under the age of 35, are required.

II. Salary and benefits

Refer to the relevant documents of the university on the talent introduction, and the specific is negotiable. For the postdoctoral researchers, an annual salary for each successful applicant is valued at RMB130,000 (before tax). During the postdoctoral period, an extra RMB 50,000, RMB 30,000 and RMB 30,000 bonus will be rewarded for each success winner of the National Science fund, the provincial and ministerial fund, or each SCI indexed 1-level publication, respectively.

III. Application procedures

Applications including a full CV and photocopies of published academic papers should be sent to Prof. Guan (head of our institute) by E-mail: tguanbo@jnu.edu.cn.

Contact information

Web Site:http://ipt.jnu.edu.cn
Tel: +86-20-85222046

蘇州大學 SOOCHOW UNIVERSITY

FACULTY POSITIONS

Soochow University
Institutes for Translational Medicine

The Soochow University Institutes for Translational Medicine (SU-ITM) is a new research establishment with a mission to accelerate the advancement in strategies for patient care and healthy improvement through bridging strong university-wide foundation in basic research with clinicians, patients and pharmaceutical industry. SU-ITM strives for its excellence in translating discoveries from basic research in immunology, stem cells and cancer into prophylactically and therapeutically novel strategies and new products by soliciting expertise in various research enterprises across all campuses of Soochow University and affiliated hospitals. Through developing close ties with Suzhou Industrial Park, Suzhou municipal government, Jiangsu provincial government and the Yangtze River Delta region, SU-ITM is anticipated to contribute to the social need and prosperity rising locally and nationally. SU-ITM will focus on unmet medical needs of autoimmune, metabolic and degenerative disorders, and cancers. Excellent research platforms have been established for the SU-ITM mission in precision medicine, strategies of stem cell and regenerative medicine, immunological therapies, and novel diagnostic techniques.

SU-ITM seeks outstanding scholars to fill academic positions at different levels to strengthen the research programs in cancer, immunology, stem cell biology, and drug discovery with strong emphasis on translational research. Qualified applicants should have a doctoral degree (Ph.D., M.D./Ph.D., or an equivalent) and received minimally 3 years of post-doctoral training. A good publication record is required.

SU-ITM offers generous start-up funding, newly renovated laboratory space and state-of-the art research equipment and facilities. SU-ITM has an outstanding research environment including adjacent Suzhou Cold Spring Harbor meeting facility, excellent opportunities to collaborate with colleagues at Soochow University and affiliated hospitals as well as other institutes in nearby Shanghai metropolitan (25 min by train). Excellent recruitment package including relocation fees, competitive stipend and social benefits will be offered. Soochow University is highly experienced in assisting application for national scholar programs such as Thousand Talents Program and Young Thousand Talents Program.

Interested applicants should forward their curriculum vitae, a statement of research proposal, 3-5 exemplary publications, and 2-3 recommendation letters to Dr. Yufang Shi, the Dean of Soochow University Institutes for Translational Medicine (shiyufang2@gmail.com) or Dr. Bingxue Shang (bingxueshang@suda.edu.cn), Soochow University Institutes for Translational Medicine, Soochow University, 199 Ren Ai Road, Suzhou Industrial Park, Suzhou 215123, China.

安徽工程大学 Anhui Polytechnic University

Talents Recruitment Program of Anhui Polytechnic University

1. Disciplines Required
Those to be recruited should major in one of the following disciplines: Mechanical Engineering, Material Science & Engineering, Electrical Engineering, Controlling Science & Engineering, Information & Communication Engineering, Textile Science & Engineering, Costume Design & Engineering, Business Administration, Management Science & Engineering, Design Art, Computer Science & Technology, Finance Engineering, English Language & Literature, PE Sociology, Civil Engineering and Architecture.

2. Recruiting Posts

2.1 Innovation Teams (full-time or flexible-time)
AHPU is of great interest to recruit those excellent innovation teams which have already gained some significant achievements in fields related to AHPU's disciplines or have manifested remarkable potential of innovation with significant breakthrough in related core technologies.

2.2 Leading Academics (full-time or flexible-time)
Leading academics include: members of Chinese Academy of Science, members of Chinese Academy of Engineering; academicians or research teams of internationally renowned academic institutes; heads of 863 Projects; winners of Top 1000 National Talents Program, the National Science Fund for Distinguished Young Scholars, or the National Famous Teachers Award; the Yangtse Scholars; Professors or the like in renowned universities or institutes overseas; nominees of National Hundred, Thousand & Ten Thousand Talents Project.

2.3 Specially-appointed professors (full-time or flexible-time)
The said professors are those with a doctorial degree conferred by renowned universities overseas, doctors of renowned universities overseas, professors in 985 or 211 Project universities, or researchers in the Institutes under Chinese Academy of Science.

2.4 Specially-appointed associate professors (full-time or flexible-time)
The said associate professors are those with a doctorial degree conferred by renowned universities overseas, doctors of renowned universities overseas, or associate professors in 985 or 211 Project universities with a doctorial degree.

3. Salary and Allowance
Those who are enrolled by AHPU will be provided with 500,000 to 2,000,000 RMB for house purchase, 150,000 to 500,000 RMB for accommodation, and 2,000,000 to 10,000,000 RMB as research funding. All these privileges are offered depending on the enrollees' previous academic achievements, and spouses will be assigned to appropriate posts according to their educational backgrounds. The salary and allowance for innovation teams can be negotiated.

4.Recruiting Procedures and Contact Information

4.1 Recruiting procedures
Applicants should email their application forms to the email box of the Personnel Office and those of corresponding colleges (please see the column of "Personnel Recruitment"). The email subject should be in the format of "Global Talent + Applicant's Name –University –Discipline–Title (Doctor, Professor or Team in a specific field).

4.2 Contact Information
This recruitment information is perennial effective.

Look forward to your joining AHPU!

Contact Person:
WANG Zhong-jiang, YANG Ji-long
Contact Department:
Personnel Office, Personnel Department, Anhui Polytechnic University
Contact Telephone:
+86 0553 2871214
Contact Email: 2006rsc@sina.com
Website:www.ahpu.edu.cn

Young 1000 Talents Global Recruitment Program
South University of Science and Technology
Shenzhen, China
http：//www.sustc.edu.cn

The South University of Science and Technology in Shenzhen, China (SUSTC) is seeking outstanding candidates for the "Young 1000 Talents Global Recruitment Program" sponsored by the Central Government of China. Applications are invited for all major scientific and engineering disciplines. Successful applicants wilal be appointed to the faculty of SUSTC at a level commensurate with each applicant's background and experience, from assistant, or associate to full professor. SUSTC offers a generous salary and startup package for "Young 1000 Talents Program" recipients, including: a) starting salaries from 350,000 to 600,000 RMB for appointments at different ranks; b) a living subsidy of up to 1.75 million RMB over 3-5 years; c) a start-up fund of up to 9.5 million RMB; d) two fully paid research assistants; and e) housing accommodation in an on-campus apartment of 100-150 m^2.

Applicants should have a Ph.D. degree in a relevant science and engineering field and three years or more of post-doctoral research or work experience. Applicants must have a proven track record of high-quality scientific publications. They must also have excellent communications skills and are capable of teaching classes in English. Those interested are invited to apply through the job website at http://talent.sustc.edu.cn/en/enindex.aspx. For additional information, please contact: Ms. Jing Long, phone: +86-755-88010968; email: 1000plan@sustc.edu.cn, talents@sustc.edu.cn.

SUSTC was founded in 2011 in the southern city of Shenzhen, the epicenter of China's economic miracle and ingenuity over the past 35 years. Situated on a tranquil and picturesque campus of rolling hills and wandering creeks, SUSTC is widely known as a pioneer for higher education reform and innovation in China. With an outstanding faculty trained globally, SUSTC is making great strides toward its goal of building a world-class institution of higher education and cutting-edge research with broad societal impacts. The successful candidates will have great opportunities to contribute to the advancement of science and technology in an increasingly global economy.

ScienceCareers online @sciencecareers.org
OPPORTUNITIES IN CHINA

The Chinese Academy of Sciences has similarly attracted Western scientists who are co-powering progress in such fields as "electric vehicles, integrated circuits, pharmaceutical development, and computer science."

— Hui Huang

Featured Participants

BGI
www.genomics.cn/en/index

Chinese Academy of Sciences
english.cas.cn

Daya Bay Reactor Neutrino Experiment
dayabay.ihep.ac.cn/twiki/bin/view/public

Jinan University
oiss.jnu.edu.cn/category_81/index.aspx

Lawrence Berkeley National Laboratory
www.lbl.gov

Shenzhen Institutes of Advanced Technology, CAS
english.siat.cas.cn

Sun Yat-sen University
www.sysu.edu.cn/2012/en/index.htm

South University of Science and Technology of China
www.sustc.edu.cn/en

University of California, Berkeley
www.berkeley.edu

University of Copenhagen
www.ku.dk/english

University of Hong Kong
www.hku.hk

the national Thousand Talents program to attract a circle of scholars including German computer scientist **Oliver Deussen** into the new Visual Computing Research Center. Deussen, one of the world's leading experts on modeling three-dimensional urban scenes, architecture, natural objects, and biological processes, has developed a sophisticated series of software packages to render these subjects in videos, computer graphics, or animations.

Based at Germany's University of Konstanz and recently nominated for an American Academy Award for scientific achievement, Deussen is now working with his Chinese colleagues at the visual computing outpost on everything from transforming human models into animation characters to creating abstract renderings of architectural works or even entire city sectors.

"In my area of visual computing, which includes computer graphics, image analysis, and data visualization, the Chinese Academy of Sciences [has been] able to gather top international scientists," Deussen says. A new research group that combines these international scientists with their Chinese colleagues is already making significant contributions to the field of visual computing, he adds.

One of the primary challenges facing researchers in southern China, he says, is government pressure to make internationally recognized advances in their field at hyper-speed. "Change is happening so fast," Deussen notes, "that individuals and systems can hardly follow."

Hui Huang, the Canadian-educated director of the Visual Computing Center, says the Chinese Academy of Sciences has similarly attracted Western scientists who are co-powering progress in such fields as "electric vehicles, integrated circuits, pharmaceutical development, and computer science."

These scholars, she adds, are helping transform southern China into a globally linked hub for new frontiers of research in science and technology.

Nuclear reactors and neutrino experiments at Daya Bay

Due east along Guangdong's coastline, one of the region's most sophisticated technological projects, the Daya Bay Nuclear Power Complex, is also the stage for a cutting-edge experiment in high-energy physics: measuring the proportion of electron antineutrinos from the nuclear reactors that morph into other types, or generations, of these leptons as they speed through space.

Ghost-like particles that were first created in the instant following the Big Bang, antineutrinos and their partner neutrinos travel at close to the speed of light and are notoriously difficult to observe as they move through space, passing through planets, star systems, and galaxies with scant interactions with other forms of matter.

But Daya Bay's nuclear reactors produce billions of trillions of electron antineutrinos every second, emitted by neutrons during a process called "beta decay," and scientists have finally been able to measure their metamorphosis as they pass through a series of detectors positioned outside the reactors.

Physicists from south China's Shenzhen University, Dongguan University of Technology, the Chinese University of Hong Kong, and the University of Hong Kong, along with counterparts from the Lawrence Berkeley National Laboratory in California, are all part of the Daya Bay collaboration measuring this antineutrino transformation with increasing precision.

Many of the Chinese researchers leading the Daya Bay experiment have been trained in the United States or Europe, and the Chinese Academy of Sciences is now searching for international experts in particle physics to work on similar experiments in the future.

Kam-Biu Luk, a professor of physics at the University of California, Berkeley and a visiting professor at the University of Hong Kong, heads the United States' participation in the China-based neutrino experiment. The Daya Bay project, which is being co-led by China and the United States, "is one of the most productive experiments in particle physics [being] carried out by an international collaboration," he says.

The success of Daya Bay "has captured the attention of the international community of particle physics," adds Luk.

Chinese breakthroughs in understanding these fundamental particles, like its progress in human spaceflight, Luk says, "demonstrate the capability and potential of China in science and technology, which are on the rise."

"With the steady decline in supporting basic science in the Western world," Luk predicts, "China could well be the future Mecca for particle physics."

Kevin Holden, a writer based on the east coast of China and the west coast of the United States, covers advances in science and technology across the Pacific Rim.

DOI: 10.1126/science.opms.r1500155

Director of Clinical Cancer Genetics

Roswell Park Cancer Institute, an NCI-Comprehensive Cancer Center in Buffalo, NY, invites applications for the position of Director of Clinical Cancer Genetics. Candidates are sought with M.D., M.D./Ph.D. or Ph.D. degrees at the Associate or Full Professor level. The successful applicant will work in a leadership position with our Center for Personalized Medicine in the use of genetic sequencing and epigenetic data to guide clinical treatment, to identify at-risk populations and to define genetic biomarkers in clinical trials that will be part of the new Clinical and Translational Science Center. Ideal candidates will have a proven track-record in funded research programs involving clinical genomic- and epigenomic-based approaches such as next-gen sequencing to identify and characterize cancer-related driver mutations, genes, expression signatures and/or genetic components relating to cancer initiation, progression and/or treatment response. Applicants will be highly collaborative, eager to develop "team science" and involved in translational projects with applications to clinical samples, thereby strengthening the mission of the Comprehensive Cancer Center Genetics Program, the Center for Personalized Medicine and the Institute.

America's first cancer center founded in 1898 by Dr. Roswell Park, the mission of the Roswell Park Cancer Institute is to provide total care to cancer patients, conduct research into the cause, treatment, and prevention of cancer, and to educate the public and the next generation of researchers who study and treat cancer. Over its long history, Roswell Park Cancer Institute has made fundamental contributions to reducing the cancer burden and has successfully maintained an exemplary leadership role in setting the national standards for cancer care, research and education. The campus spans 25 acres in downtown Buffalo and consists of 15 buildings with about 1.6 million square feet of space. A new hospital building, completed in 1998, houses a comprehensive diagnostic and treatment center. In addition, the Institute built a new medical research complex and renovated existing education and research space to support its future growth and expansion.

Applicants for this position must have a distinguished record of scientific achievement, demonstrated leadership skills, a productive research program recognized at the national and international level, and a commitment to education and mentorship of students and faculty. Please submit a CV, a letter of interest addressing research, educational, administrative and leadership goals and vision, and contact information on three referees to Irwin H. Gelman, Ph.D., John and Santa Palisano Chair of Cancer Genetics, Roswell Park Cancer Institute, Elm & Carlton Streets, Buffalo, NY 14263, care of Amy Troutman at **amy.troutman@roswellpark.org**.

RPCI is an M/F/D/V Affirmative Action Employer.

ROSWELL PARK CANCER INSTITUTE

CONFERENCE

"These ideas could dramatically transform life worldwide."
Scientific American

FALLING WALLS BERLIN 8/9 NOV 2015

WHICH ARE THE NEXT WALLS TO FALL?

FALLING WALLS is a unique international platform for leaders from the worlds of science, business, politics, the arts and society.

THE FALLING WALLS CONFERENCE (9 November, 9 am - 7 pm) is at the heart of the Falling Walls days in Berlin. 20 world-class scientists from top institutions around the globe present in only 15 minutes each the break-throughs they are working on.

FALLING WALLS VENTURE (8 November, 11 am - 6 pm) is an international forum for outstanding science based start-up companies, venture capital companies and strategic investors. It is supported by the European Private Equity and Venture Capital Association (EVCA).

Falling Walls attracts an audience from more than 80 nations and is covered by media globally.

More information and registration: **www.falling-walls.com**

REGISTER NOW!

REGISTER BEFORE 31 AUGUST 2015
to take advantage of the Early Bird Ticket
www.falling-walls.com/registration

ScienceCareers online @sciencecareers.org

For recruitment in science, there's only one Science

What makes *Science* the best choice?

- Read and respected by 570,400 readers around the globe
- 78% of readers read *Science* more often than any other journal
- Your ad sits on specially labeled pages to draw attention to the ad
- Your ad dollars support AAAS and its programs, which strengthens the global scientific community.

Why choose this immunology section for your advertisement?

- Relevant ads lead off the career section with special Immunology banner
- Bonus distribution to:

  8th International AIDS Society (IAS) Conference
  July 19–22, Vancouver, British Columbia, Canada

  Malaria
  July 25–26, Girona, Spain.

Expand your exposure. Post your print ad online to benefit from:

- Link on the job board homepage directly to immunology jobs
- Dedicated landing page for jobs in immunology
- Additional marketing driving relevant job seekers to the job board.

* Ads accepted until July 6 on a first-come, first-served basis.

SCIENCECAREERS.ORG

ScienceCareers
FROM THE JOURNAL SCIENCE AAAS

To book your ad: **advertise@sciencecareers.org**

The Americas
202-326-6582

Europe/RoW
+44(0)1223-326500

Japan
+81-3-3219-5777

China/Korea/Singapore/Taiwan
+86-186-0082-9345

PRINCETON UNIVERSITY

Vice President for Princeton Plasma Physics Laboratory

Princeton University seeks nominations and applications for the position of Vice President (VP) for the Princeton Plasma Physics Laboratory (PPPL). Princeton University manages and operates PPPL under contract with the U.S. Department of Energy (DOE), and funding for the Laboratory comes primarily from the Office of Fusion Energy Sciences within the DOE Office of Science. As one of the 10 National Laboratories owned by the DOE Office of Science, PPPL employs a staff of approximately 450 to conduct a leading program in fusion energy research and plasma science, funded at approximately $90M per year.

Reporting to the Provost, the Vice President (VP) is responsible for representing the university's interests with respect to the contract, including all aspects of oversight, financial and contractual issues, relations with the DOE, and other matters associated with the management and operation of the laboratory. The VP oversees the performance of PPPL in science, operations and strategic planning, and serves on the PPPL Management Group Board of Directors, the entity of Princeton University having corporate responsibility for the laboratory. The VP, the PPPL Director (who reports to the VP) and the DOE Site manager work together to ensure a transparent and effective Contractor Assurance System. An important additional responsibility is to identify and support opportunities for collaborative research and other activities between PPPL and the main campus. The VP also represents Princeton University on relevant associations, such as the Brookhaven Science Associates Board of Directors, and the Council of Presidents of Universities Research Association.

Princeton is seeking a candidate with a proven record of scientific or technical accomplishment and success in leading and managing complex scientific programs or organizations. Prior experience with and understanding of the operations and expectations of the DOE are highly desirable. Ability to communicate effectively with staff, researchers, and government officials is essential. The responsibilities of the Vice President for PPPL constitute approximately 50% of a full-time position.

Applications should be submitted online to **http://jobs.princeton.edu**

Nominations may be sent to:
Pablo G. Debenedetti, Dean for Research
91 Prospect Avenue
Princeton University
Princeton, NJ, 08540
dfr@princeton.edu

To receive full consideration, nominations and applications should be received by **July 31, 2015**.

Princeton University is an Equal Opportunity Employer and all qualified applicants will receive consideration for employment without regard to race, color, religion, sex, sexual orientation, gender identity, national origin, disability status, protected veteran status, or any other characteristic protected by law.

EGL Charitable Foundation

The EGL Charitable Foundation invites you to apply to the

Gruss Lipper Post-Doctoral Fellowship Program

Eligibility

- Israeli citizenship
- Candidates must have completed PhD and/or MD/PhD degrees in the Biomedical Sciences at an accredited Israeli University/Medical School or be in their final year of study
- Candidates must have been awarded a postdoctoral position in the U.S. host research institution.

Details regarding the fellowship are available at www.eglcf.org

NW210508R

TAM BIOLOGY TEXAS A&M UNIVERSITY

Two Faculty Positions in Evolutionary Genomics

The Department of Biology at Texas A&M University invites applications for two tenure-track Assistant Professor positions in evolutionary genomics, starting in the fall of 2016.

We will consider candidates pursuing innovative research in any area of evolutionary genomics, including empirical, theoretical or computational approaches applied to any taxonomic group. The criteria for selection will be uniqueness, creativity and excellence in research and scholarship. We require all candidates to have a Ph.D. and strongly encourage applications from candidates who will increase the exposure of our students to a diverse culture.

Successful candidates will be expected to develop externally funded research programs and to teach undergraduate and graduate courses. The Department of Biology (www.biology.tamu.edu) is part of an interactive and collegial research environment, offering a modern infrastructure and competitive startup packages. The broader Texas A&M research community includes a number of exciting interdepartmental programs, such as the new Ecology and Evolutionary Biology Doctoral Program (eeb.tamu.edu), the Texas A&M Institute for Genome Sciences and Society (genomics.tamu.edu), and the Genetics Interdisciplinary Graduate Program (genetics.tamu.edu).

Applicants should email a letter of intent, *curriculum vitae*, statements of research and teaching interests, and should arrange to have three letters of recommendation sent to **evosearch@bio.tamu.edu**. Review of applications will begin **September 1, 2015**. Questions regarding this search should be directed to **Dr. Adam G. Jones**, chair of the search committee, at **evosearch@bio.tamu.edu**.

Texas A & M University is an Equal Opportunity/Affirmative Action Employer that is dedicated to the goal of building a culturally diverse and pluralistic faculty and staff who are committed to teaching and working in a multicultural environment. We strongly encourage applications from women, minorities, veterans, individuals with disabilities, and the LGBTQ community. In addition, the University is responsive to the needs of dual career couples.

ScienceCareers online @sciencecareers.org

myIDP: A career plan customized for you, by you.

For your career in science, there's only one Science

my IDP ScienceCareers

Recommended by leading professional societies and the NIH

Features in myIDP include:

- Exercises to help you examine your skills, interests, and values.
- A list of 20 scientific career paths with a prediction of which ones best fit your skills and interests.
- A tool for setting strategic goals for the coming year, with optional reminders to keep you on track.
- Articles and resources to guide you through the process.
- Options to save materials online and print them for further review and discussion.
- Ability to select which portion of your IDP you wish to share with advisors, mentors, or others.
- A certificate of completion for users that finish myIDP.

Visit the website and start planning today!
myIDP.sciencecareers.org

ScienceCareers In partnership with:

advancing the life sciences 1912-2012 FASEB Federation of American Societies for Experimental Biology

UCSF University of California San Francisco

Medical College of Wisconsin

Burroughs Wellcome Fund

Faculty Positions at the Indian Institute of Science Education and Research Bhopal

The Indian Institute of Science Education and Research (IISER) Bhopal (**www.iiserb.ac.in**) offers various degree programmes in Biological Sciences, Chemistry, Earth and Environmental Sciences, Engineering Sciences, Mathematics, and Physics.

IISER Bhopal (**www.iiserb.ac.in**) seeks candidates for faculty positions at all levels in the Departments of Engineering Sciences & Earth and Environmental Sciences. The Institute is also looking for Post-Doctoral Fellows in the above departments.

Areas

- **Engineering Sciences** (**www.iiserb.ac.in/engr**): Various areas of Engineering Sciences including but not limited to Computer Science, Electronics and Communication, Material Science, and Electrical, Chemical, and Mechanical Engineering.
- **Earth and Environmental Sciences (EES)** (**www.iiserb.ac.in/ees**): Various areas of EES including but not limited to Geochemistry (Stable and Radioactive), Atmospheric Sciences (Dynamics and Chemistry), Structural Geology, Sedimentology, Geophysics, Paleontology, Soil and Water Sciences, Oceanography, Remote Sensing and GIS.

Eligibility criteria, recruitment procedure, pay/perks, and a format of the application form are accessible online via **http://www.iiserb.ac.in/ofa**

Applicants residing in India should send hard copies of the applications in the prescribed format to:

Dr. Ramya Sunder Raman
Head, Department of Earth and Environmental Sciences &
Head, Engineering Sciences
IISER Bhopal, Bhopal Bypass Road, Bhauri,
Bhopal 462 066, Madhya Pradesh, INDIA
Email: hod_ees@iiserb.ac.in; hod_engr@iiserb.ac.in
Phone: +91 755 6692 369

Applicants residing abroad may submit their application via e-mail to **hod_engr@iiserb.ac.in** or **hod_ees@iiserb.ac.in**, as the case may be, with a copy to **dofa@iiserb.ac.in**

Download the
Science Careers jobs app from Science

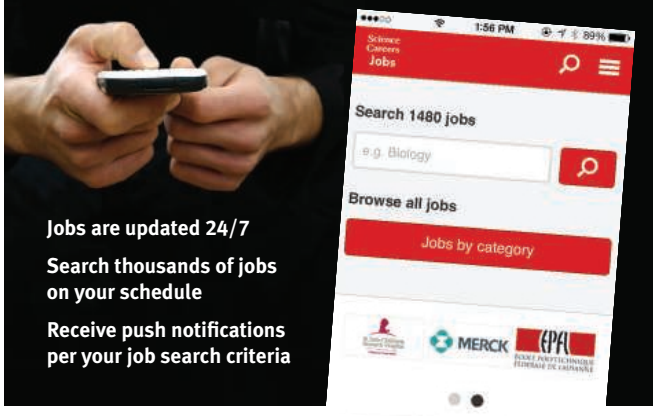

Jobs are updated 24/7

Search thousands of jobs on your schedule

Receive push notifications per your job search criteria

Get a job on the go.

Search worldwide for thousands of scientific jobs in academia, industry, and government. The application process is seamless, linking you directly to job postings from your customized push notifications.

Scan this code to download app or visit **apps.sciencemag.org** for information.

ScienceCareers | AAAS
FROM THE JOURNAL SCIENCE

ScienceCareers.org

NANYANG TECHNOLOGICAL UNIVERSITY

Asian School of the Environment,
Nanyang Technological University, Singapore

Young and research-intensive, Nanyang Technological University (NTU Singapore) is the fastest-rising university in the world's Top 50 and ranked 39th globally. NTU is also placed 1st amongst the world's best young universities.

FOUR FACULTY POSITIONS

The Asian School of the Environment (ASE) at NTU Singapore seeks to hire faculty for four professor-level positions (rank commensurate with experience) as part of a terrestrial and marine initiative in Southeast Asia. ASE, a new interdisciplinary School, focuses on Asian environmental challenges integrating Earth systems, environmental life sciences, ecology, and the social sciences to address key issues of the environment and sustainability. Strong interdisciplinary links between ASE and the Singapore Centre on Environmental Life Sciences Engineering (SCELSE), the Earth Observatory of Singapore (EOS) and the Complexity Institute provide an excellent community for tackling large, cutting-edge research questions. Successful candidates will also contribute to development and execution of new undergraduate programmes.

1. Aquatic Chemistry (open professor rank)

We seek a creative and cutting edge aquatic chemist who focuses on environmental sustainability of natural systems and who has an interest in addressing research questions in Southeast Asia. Research interests may include but are not limited to, natural and anthropogenic contaminants of fresh water systems, nutrient cycling and the carbon cycle, redox chemistry using tools such as stable isotopes and water sediment interactions amongst other areas.

2. Environmental Organic Chemistry (open professor rank)

We seek a creative and cutting-edge marine chemist focusing on environmental sustainability of natural systems and who has an interest in addressing research questions in Southeast Asia. Research interests may include but are not limited to, organic contaminant fate and transport, synthesis and processing of organic molecules in the environment, stable isotope techniques to evaluate the sources, sinks and cycling of organic matter in aquatic or marine environments.

3. Environmental Microbiology (open professor rank)

We seek a creative and cutting-edge microbiologist exploring microbial diversity and activity in natural systems and their implications on ecosystem functions and services. The successful applicant should have a clearly defined interest in addressing research questions in Southeast Asia. Research interests may include but are not limited, to microbial physiology, environmental virology, bacterial genetics and diversity, microbe-host interactions using tools such as genomics and metagenomics amongst other areas.

4. Biogeochemistry (open professor rank)

We seek a creative and cutting-edge biogeochemist investigating biological, chemical and geological processes on societally relevant time-scales in wetlands, rivers, soils or oceans. The successful applicant should have a clearly defined interest in addressing research questions in Southeast Asia. Research interests may include but are not limited to, global carbon and nutrient cycling, ocean-atmosphere interactions, and microbial or organic biogeochemistry amongst other areas.

The candidates are expected to:

- Establish a world-class research programme
- Play a leading role in the formation of the new Asian School of the Environment
- Enhance the new School's visibility as an international leader in education and research in Environmental Earth System Science
- Teach undergraduate and graduate classes in Environmental Earth System Sciences
- Actively collaborate with NTU faculty and researchers with existing strengths in Earth Systems Science and Environmental Life Sciences

Applications, including the applicant's experience/ philosophy of research, teaching, a CV, and contact information for two professional references should be sent to Chairman of Search Committee, NTU, at ASE-EnvSc@ntu.edu.sg.

Review of applications will begin in August 2015 and will continue until the positions are filled. NTU offers highly competitive salaries and on-campus housing. A start-up package will be available. NTU is an equal opportunity employer.

More information can be found at:
www.ase.ntu.edu.sg
www.earthobservatory.sg
www.scelse.sg
www.complexity.ntu.edu

www.ntu.edu.sg

Two Fantastic Recruiting Opportunities!

POSTDOC CAREERS | August 28, 2015

Be sure to promote your openings to the thousands of scientists who read *Science* to find out about the latest postdoc opportunities.

Reserve space by August 11, 2015.

FACULTY CAREERS | September 18, 2015

Gear up to recruit for the faculty positions at your university with this much anticipated issue that reaches thousands of Ph.D. scientists looking for positions in academia.

Reserve space by September 1, 2015.

Produced by the *Science*/AAAS Custom Publishing Office.

SCIENCECAREERS.ORG

ScienceCareers
FROM THE JOURNAL SCIENCE AAAS

To book your ad: **advertise@sciencecareers.org**

The Americas
202-326-6582

Europe/RoW
+44(0)1223-326500

Japan
+81-3-3219-5777

China/Korea/Singapore/Taiwan
+86-186-0082-9345

"What I do with my Octet HTX time? Climb."

Shave weeks off your lead selection programs.

Broader antibody cross-competition ups your odds of finding the best candidates, but larger epitope binning studies take time. The Octet HTX system lets you use any binning assay format, any size matrix, start a run and get analyzed results the same day or the next day for larger studies. You can also combine multiple experiments into one dataset to easily visualize and cluster antibodies in similar bins or binding groups.

Lucy gets out of the lab more often now to climb. What will you do with your extra time?

fortéBIO®
A Division of ***Pall Life Sciences***

fortebio.com | 888-OCTET-75

PALL Life Sciences

Fast. Accurate. EASY.

Host Cell Protein Detection and Quantification

The Gyrolab CHO-HCP Kit 1 detects and quantifies host cell proteins (HCP) from Chinese hamster ovary (CHO) cells used in bioprocessing of biotherapeutics. HCP are measured throughout the production process, as they may affect the safety and efficacy of the biotherapeutic. Gyrolab CHO-HCP Kit 1 has been validated for use on Gyrolab xP workstation and the new Gyrolab xPlore and is ready to use, eliminating the need for time-consuming assay development. The automation capabilities of Gyrolab systems enable 96 data points to be generated in approximately one hour without manual intervention, saving time, and reducing errors and repeats. The kit broadens the analytical range from typically two orders of magnitude to four, and therefore requires fewer dilutions and fewer reruns than alternative methods. Gyrolab CHO-HCP Kit 1 contains all the reagents needed to produce 96 data points, including a specific Bioaffy CD that has been optimized for this HCP assay.

Gyros
For info: +46-(0)-18-56-63-00
www.gyros.com

IHC Reference Standards

A unique range of genetically defined, highly characterized HDx Reference Standards are now available for immunohistochemistry (IHC) assays. The introduction of IHC HDx Reference Standards provides histopathology laboratories with a consistent and reproducible source of reference material for the development and quality control of IHC assays. The independent external controls contain precisely defined protein expression levels presented on one slide, providing scientists the ability to easily determine the sensitivity of their assay. These standards are unique in having undergone a high level of characterization at a molecular and protein level, including Quantitative Digital Pathology, to quantify the intensity of staining. Variability in the quality of clinical samples and immunohistochemistry staining is a major concern within pathology laboratories as these techniques are used to confirm diagnoses. The use of independent external controls enables consistency, reproducibility, and accuracy to be maintained and monitored across the laboratory workflow, including operators, assays, manufacturers, and platforms.

Horizon Diagnostics
For info: 800-860-1567
www.horizondx.com/ihc

Automated Western Blot Processing

Based on proprietary sequential lateral flow (SLF), the new iBind Flex Western System is designed to enable a more versatile walk-away solution for the immunodetection step in a Western blotting workflow. Researchers now have the ability to adapt the iBind Flex Western Device to a variety of blot formats and sample throughput. Compatible with downstream chemiluminescent, colorimetric, or fluorescent detection protocols and optimized for higher sensitivity and reproducibility, there is potential for a significant reduction in primary antibody required when compared with manual blot processing. Experimental results can be achieved without the need for power, pumps, or vacuums through the use of SLF technology, which is designed to automate the blocking, primary and secondary antibody binding, and washing steps for immunodetection of proteins transferred to a nitrocellulose or PVDF membrane. The sequential and uniform flow of solutions across a glass fiber matrix ensures a consistent antigen-antibody interaction to deliver robust protein detection.

Thermo Fisher Scientific
For info: 800-955-6288
www.lifetechnologies.com/ibindflex

Protein Interactions Assay

NanoBRET Protein Interaction Assays use a new Bioluminescence Resonance Energy Transfer (BRET) technology that enables scientists to quantitatively measure protein:protein interactions in live cells. With NanoBRET Protein Interaction Assays, researchers can study both induction and inhibition of protein interactions in real time using full-length proteins expressed at physiologically relevant levels. Conventional BRET measures the interaction of proteins using a bioluminescent donor fused to a protein of interest and a fluorescent acceptor fused to its binding partner; the donor does not excite the fluorophore using light, but transfers resonance energy through dipole-dipole coupling. The optimized NanoBRET Protein Interaction Assays use NanoLuc Luciferase as the energy donor and HaloTag protein as the energy acceptor. NanoBRET Technology has improved spectral overlap, increased signal, and provided lowered background. In addition, the brighter light output from NanoLuc enables use of NanoBRET even at low expression levels, while still providing efficient energy transfer.

Promega
For info: 608-274-4330
www.promega.com

Gel Imager

The easy-to-use PXi Access systems offer major advances on film detection and can rapidly generate high-quality images of virtually all types of large blots and gels. The new compact PXi 6 or 9 Access systems are complete with high-performance cameras capable of imaging a wide range of blot and gel types and sizes. The camera in each PXi Access features superb optics, which means scientists can set up quickly and detect even the faintest amounts of DNA or protein with a much greater sensitivity than film. PXi Access is so flexible that the systems can image stain-free gels and blots or those stained with any commercial chemiluminescence, fluorescence, visible, and IR dyes. For imaging chemi blots, the PXi Access uses a wide dynamic range to optimize exposure for each protein, accurately quantifying abundant and poorly expressed proteins, making this a much simpler method than using film for producing Western blot results.

Syngene
For info: +44-(0)-1223-727123
www.syngene.co.uk/pxi-pxi-touch

Electronically submit your new product description or product literature information! Go to www.sciencemag.org/products/newproducts.dtl for more information.

Newly offered instrumentation, apparatus, and laboratory materials of interest to researchers in all disciplines in academic, industrial, and governmental organizations are featured in this space. Emphasis is given to purpose, chief characteristics, and availability of products and materials. Endorsement by *Science* or AAAS of any products or materials mentioned is not implied. Additional information may be obtained from the manufacturer or supplier.

Will you be meeting a Nobel Prize winner this December?

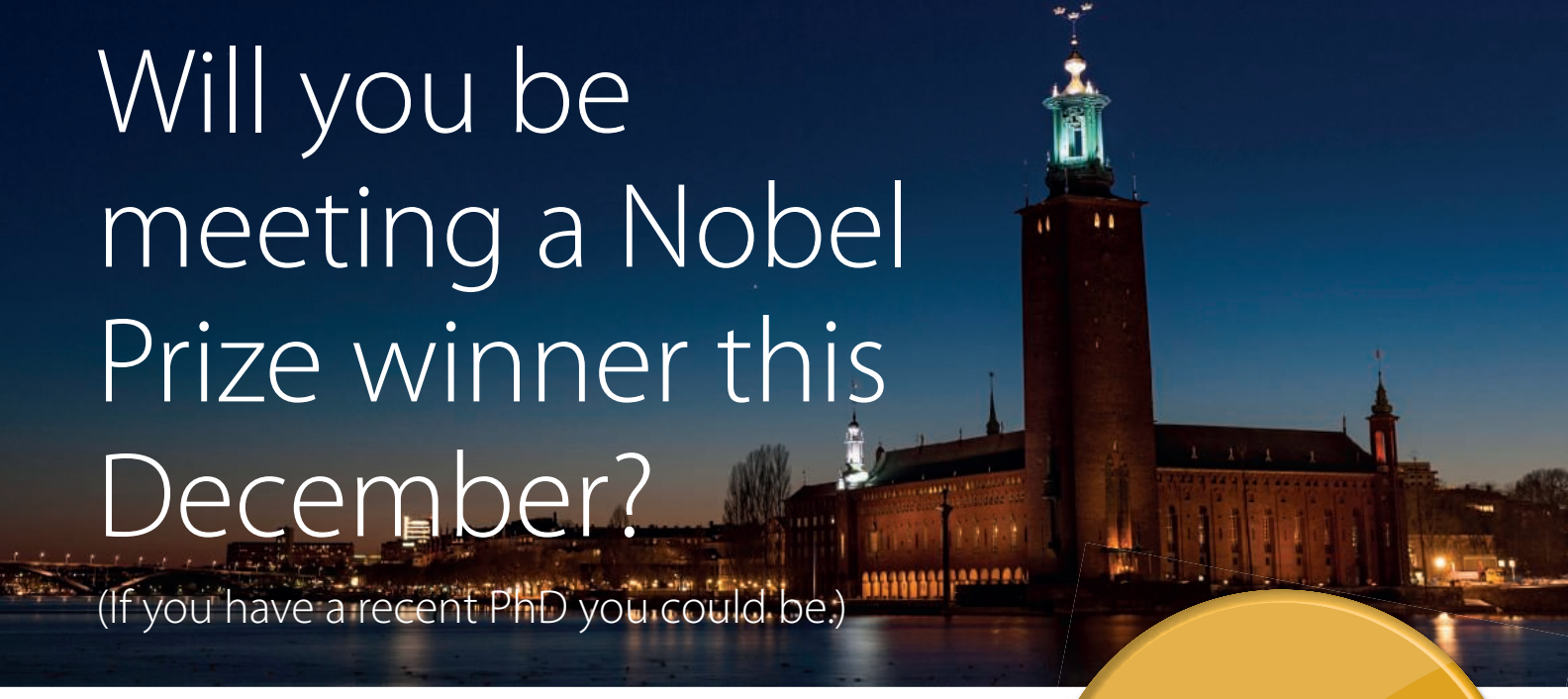

(If you have a recent PhD you could be.)

Stockholm in the second week of December is a special place. The city is alive with excitement as it welcomes and celebrates the new Nobel Laureates at the annual Nobel Prize ceremony.

If you are a PhD student, you could be here too – meeting a Nobel Laureate and receiving a rather special prize yourself.

The journal *Science* & SciLifeLab have established The *Science* & SciLifeLab Prize for Young Scientists, to recognize and reward excellence in PhD research and support young scientists at the start of their careers. It's about bright minds, bright ideas and bright futures.

Four winners will be selected for this international award. They will have their essays published in the journal *Science* and share a new total of 60,000 USD in prize money. The winners will be awarded in Stockholm, in December, and take part in a unique week of events including meeting leading scientists in their fields.

"The last couple of days have been exhilarating. It has been an experience of a lifetime. Stockholm is a wonderful city and the Award winning ceremony exceeds my wildest dreams."
–Dr. Dan Dominissini, 2014 Prize Winner

Who knows, The *Science* & SciLifeLab Prize for Young Scientists could be a major stepping stone in your career and hopefully one day, during Nobel week, you could be visiting Stockholm in December once again.

Science & SciLifeLab PRIZE FOR YOUNG SCIENTISTS

This prize is made possible with the kind support of the Knut and Alice Wallenberg Foundation. This Foundation grants funding in two main areas; research projects of high scientific potential and individual support of excellent scientists.

The 2015 Prize is now open. The deadline for submissions is August 1, 2015.
Enter today: www.sciencemag.org/scilifelabprize

The 2015 Prize categories are:

- Cell and Molecular Biology
- Ecology and Environment
- Genomics and Proteomics
- Translational Medicine

Knut och Alice Wallenbergs Stiftelse

Science AAAS

SciLifeLab

Finding cures starts with research tools that actually work...

- Proteomic products and services
- Focused product portfolio
- Products tested for specificity and sensitivity
- Antibodies rigorously tested across a wide range of research applications
- Custom formulations
- cGMP compliant ASRs*
- Bulk orders and lot reservations

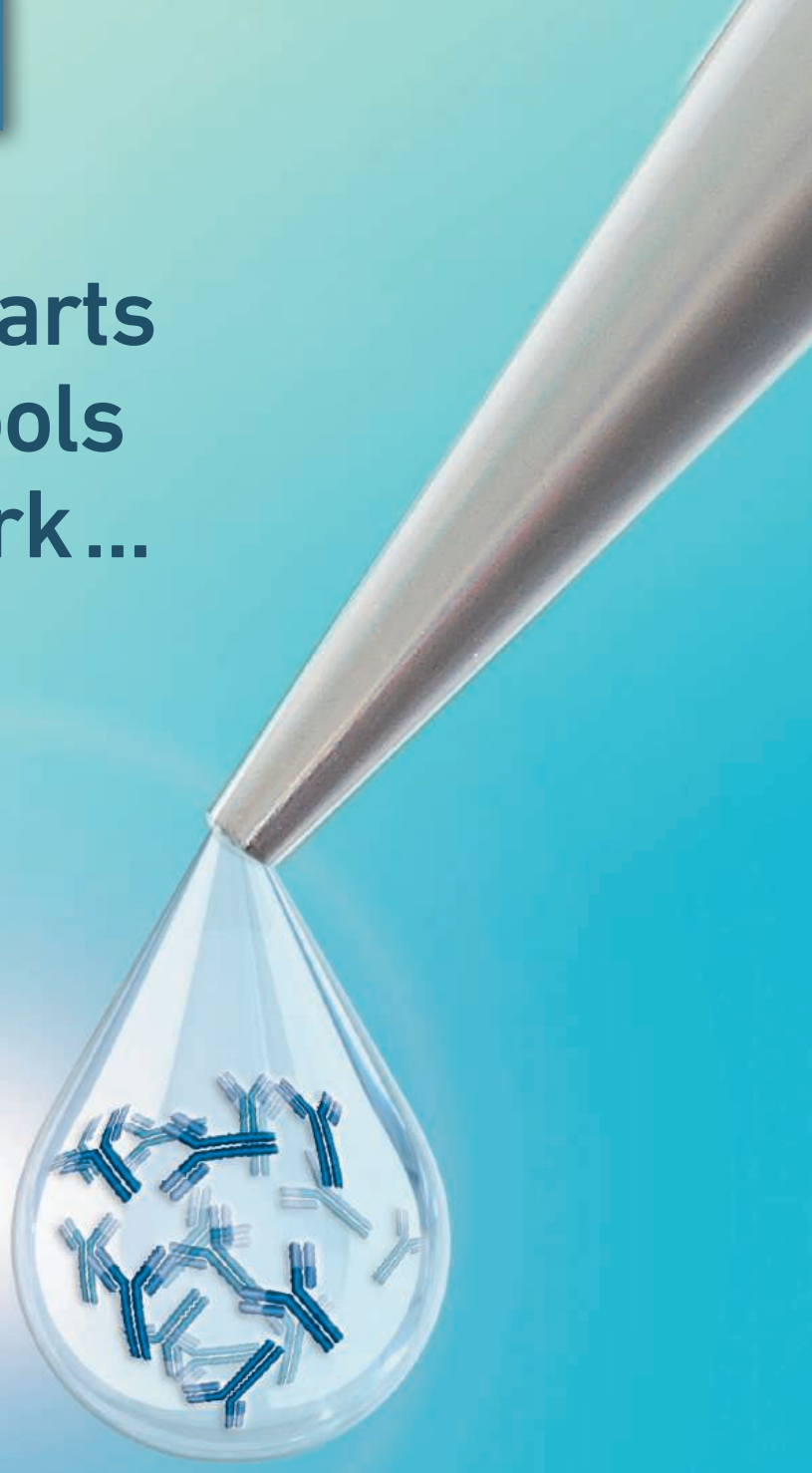

* Custom formulations of certain monoclonal antibodies can be produced by CST in compliance with FDA regulations governing ASRs. Such products would be classified as Analyte Specific Reagents. Analytical and performance characteristics are not established. All other products are for Research Use Only. Not For Use In Diagnostic Procedures.

Learn more at: www.cellsignal.com/drugdiscovery

cGMP CURRENT GOOD MANUFACTURING PRACTICE

bsi. ISO 9001 Quality Management

Cell Signaling TECHNOLOGY®

© 2015 Cell Signaling Technology, Inc. Cell Signaling Technology, and CST are trademarks of Cell Signaling Technology, Inc.

15PADINDUPHAR0001ENG_00

By **Rachel Bernstein**

The health of those who study health

Behavioral scientist Warren Holleman spent much of his career serving the homeless at a community health center, but about 5 years ago he began serving a different population: university faculty. As the director of the Faculty Health & Well-Being Program at the University of Texas MD Anderson Cancer Center in Houston, "I went from encouraging homeless people to take better care of their health to encouraging doctors and scientists to take better care of their health." Sometimes, he adds, "the homeless people are easier to access because the doctors and the scientists are so busy."

Academic life can be hard: Extreme pressure to publish and an exceptionally competitive funding environment can cripple morale, Holleman says. But there's not much information about how faculty members are faring physically and mentally. "It seems so ironic to me that biomedical scientists, the people who study the health of everybody else, ... have barely had their own health studied," Holleman says.

The Faculty Health & Well-Being Program was created in 2001 after a faculty member died by suicide. Shortly after Holleman took the helm, he interviewed 19 department chairs to learn how the faculty was doing. The answer: Stress was high and morale was low. He tried to expand his work by collaborating with scientific societies, but the three he approached turned him down. "It seems to me that there might be a sense in which they really don't want to know what the situation might be," he says.

Burning the candle at both ends is "just not sustainable."

The primary underlying issues—scarce funding, publish-or-perish culture, bureaucratic challenges—are systemic and beyond the scope of what a single person, study, or institution can solve, but Holleman believes his program helps by promoting better health and well-being practices among faculty members. Some of the events—lectures, panel discussions, and workshops addressing work-life balance and resilience—are typical fare for an academic campus. Others, though, may raise eyebrows: weekly meditation, yoga, and tai chi classes; "stress-buster" concerts; faculty art shows.

"Some programs will help some people; others will help others," Holleman says. For Pratip Bhattacharya, a professor of cancer systems imaging, attending yoga and meditation classes about once a month is "an effortless stress relief" that provides "an overall sense of being centered and focused." The program, he says, "allows me to be more creative at work, more effective at time management, and to develop better interpersonal skills and emotional intelligence."

Beyond the specifics of each event, the social contact can have a positive impact, Holleman says. "Social connections help people cope with stress and be satisfied with their job." Scientists, though, may miss out on these benefits because they "tend to be introverts, and their work tends to isolate them to some extent in their labs. ... We keep trying to come up with ways to encourage social connection."

"I think there are a lot of people who would benefit from our programs who don't come," Holleman continues. But he believes the benefits of his efforts will be felt beyond the immediate participants. "I feel that [our events] have an overall benefit of encouraging everybody to find what works for them. ... A big part of what we do is being kind of a beacon for culture change in the area of work-life balance and good physical and mental health."

"I think many faculty [members] would like to participate in theory, but they haven't managed the time to figure out how," Bhattacharya says. "I guess it's not very high on the priority list of most faculty [members], who are very preoccupied with day-to-day work." For those who are having a hard time tearing themselves away from the lab, Holleman emphasizes that burning the candle at both ends is "just not sustainable. You'll be less productive in the long run, as well as less happy and less healthy." ■

Rachel Bernstein is a staff writer for Science *Careers. For more on life and careers, visit ScienceCareers.org. Send your story to SciCareerEditor@aaas.org.*

ILLUSTRATION: ROBERT NEUBECKER

Downloaded from www.sciencemag.org on June 26, 2015

Published by AAAS